WIND AND SEISMIC EFFECTS

Proceedings
of the
Eighteenth
Joint
Meeting

**U.S. DEPARTMENT
OF COMMERCE**
National Bureau
of Standards

*T*he National Bureau of Standards[1] was established by an act of Congress on March 3, 1901. The Bureau's overall goal is to strengthen and advance the nation's science and technology and facilitate their effective application for public benefit. To this end, the Bureau conducts research and provides: (1) a basis for the nation's physical measurement system, (2) scientific and technological services for industry and government, (3) a technical basis for equity in trade, and (4) technical services to promote public safety. The Bureau's technical work is performed by the National Measurement Laboratory, the National Engineering Laboratory, the Institute for Computer Sciences and Technology, and the Institute for Materials Science and Engineering.

The National Measurement Laboratory

Provides the national system of physical and chemical measurement; coordinates the system with measurement systems of other nations and furnishes essential services leading to accurate and uniform physical and chemical measurement throughout the Nation's scientific community, industry, and commerce; provides advisory and research services to other Government agencies; conducts physical and chemical research; develops, produces, and distributes Standard Reference Materials; and provides calibration services. The Laboratory consists of the following centers:

- Basic Standards[2]
- Radiation Research
- Chemical Physics
- Analytical Chemistry

The National Engineering Laboratory

Provides technology and technical services to the public and private sectors to address national needs and to solve national problems; conducts research in engineering and applied science in support of these efforts; builds and maintains competence in the necessary disciplines required to carry out this research and technical service; develops engineering data and measurement capabilities; provides engineering measurement traceability services; develops test methods and proposes engineering standards and code changes; develops and proposes new engineering practices; and develops and improves mechanisms to transfer results of its research to the ultimate user. The Laboratory consists of the following centers:

- Applied Mathematics
- Electronics and Electrical Engineering[2]
- Manufacturing Engineering
- Building Technology
- Fire Research
- Chemical Engineering[2]

The Institute for Computer Sciences and Technology

Conducts research and provides scientific and technical services to aid Federal agencies in the selection, acquisition, application, and use of computer technology to improve effectiveness and economy in Government operations in accordance with Public Law 89-306 (40 U.S.C. 759), relevant Executive Orders, and other directives; carries out this mission by managing the Federal Information Processing Standards Program, developing Federal ADP standards guidelines, and managing Federal participation in ADP voluntary standardization activities; provides scientific and technological advisory services and assistance to Federal agencies; and provides the technical foundation for computer-related policies of the Federal Government. The Institute consists of the following centers:

- Programming Science and Technology
- Computer Systems Engineering

The Institute for Materials Science and Engineering

Conducts research and provides measurements, data, standards, reference materials, quantitative understanding and other technical information fundamental to the processing, structure, properties and performance of materials; addresses the scientific basis for new advanced materials technologies; plans research around cross-country scientific themes such as nondestructive evaluation and phase diagram development; oversees Bureau-wide technical programs in nuclear reactor radiation research and nondestructive evaluation; and broadly disseminates generic technical information resulting from its programs. The Institute consists of the following Divisions:

- Ceramics
- Fracture and Deformation [3]
- Polymers
- Metallurgy
- Reactor Radiation

[1]Headquarters and Laboratories at Gaithersburg, MD, unless otherwise noted; mailing address Gaithersburg, MD 20899.
[2]Some divisions within the center are located at Boulder, CO 80303.
[3]Located at Boulder, CO, with some elements at Gaithersburg, MD.

NF-R
DU100
156
87-3540
1987

WIND AND SEISMIC EFFECTS

PROCEEDINGS OF
THE 18th JOINT
MEETING OF
THE U.S. - JAPAN
COOPERATIVE PROGRAM
IN NATURAL RESOURCES
PANEL ON WIND AND
SEISMIC EFFECTS

Issued April 1987

Noel J. Raufaste,
EDITOR

Center for Building Technology
National Engineering Laboratory
National Bureau of Standards
Gaithersburg, MD 20899

PREFACE

The U.S.-Japan Cooperative Program in Natural Resources (UJNR) was established in 1964 for the exchange of technical information and experience mutually beneficial to the economics and welfare of both countries. The Panel on Wind and Seismic Effects held its first joint meeting in 1969 in Tokyo, Japan. The joint meeting has been held annually ever since, alternately in Japan and the United States.

The Eighteenth Joint Meeting was held at the National Bureau of Standards, Gaithersburg, Maryland, May 12-15, 1986. Under five themes, thirty-two technical papers were presented and discussed; thirty-eight manuscripts were authored. Ten task committees on the Panel also held their meetings during this period.

These proceedings include the program of the Eighteenth Joint Meeting, the formal panel resolutions, all technical papers, and the task committee reports. The text of the papers had been edited for clarity.

Preparation of the proceedings was partially supported by funds from the National Science Foundation, Department of State, Bureau of Reclamation, Department of Navy, Department of Army, Federal Emergency Management Administration, Nuclear Regulatory Commission, and the National Bureau of Standards.

Noel J. Raufaste, Secretary
U.S. Panel on Wind and Seismic Effects

iii

ABSTRACT

The Eighteenth Joint Meeting of the U.S.-Japan Panel on Wind and Seismic
Effects was held at the National Bureau of Standards, Gaithersburg,
Maryland, from May 12 - 15, 1986. This publication, the proceedings of
the Joint Meeting, includes the program, list of members, formal resolutions,
task committee reports, and technical papers.

There were five themes under which papers were presented to the Panel.
These were:

    Theme I   - WIND ENGINEERING
    Theme II   - EARTHQUAKE ENGINEERING
    Theme III - STORM SURGE AND TSUNAMIS
    Theme IV   - U.S.- JAPAN COOPERATIVE RESEARCH PROGRAM
    Theme V   - MEXICO CITY AND CHILIAN EARTHQUAKES

Subjects covered in the papers presented include:

    (1) characteristics of stongwinds;
    (2) wind loads on structures and design criteria;
    (3) earthquake ground motions;
    (4) soil liquefaction studies and methods to improve liquefaction
        resistance;
    (5) seismic loads on structures and design criteria;
    (6) stress analyses of pipelines during earthquakes;
    (7) full-scale seismic experiments;
    (8) earthquake hazard reduction program;
    (9) use of the microcomputer for earthquake studies;
    (10) quantitative evaluation of damages caused by winds and earthquakes;
        and,
    (11) tsunami research projects.

KEYWORDS: Accelerograph; codes; design criteria; disaster; earthquakes;
           earthquake hazards; geotechnical engineering; ground failures;
           liquefaction; pipeline; seismicity; solids; standards; struc-
           tural engineering; structural response; tsunami; wind loads;
           and winds.

CONTENTS

CONTENTS

CONTENTS

CONTENTS

SATURDAY 10 MAY

     1800, DCA NW-4 JAPANESE TEAM ARRIVES WASHINGTON DC

     2000, INFORMAL GATHERING HOSTED BY US SIDE IN GAITHERSBURG

        HOTEL, HOLIDAY INN GAITHERSBURG

SUNDAY 11 MAY

     1830, RECEPTION HOSTED BY DR. AND MRS WRIGHT AT THEIR
     HOME

MONDAY 12 MAY

          OPENING CEREMONIES (1000 - 1145)

    1000   CALL TO ORDER BY NOEL RAUFASTE, SECRETARY
           US SIDE UJNR PANEL
          OPENING REMARKS BY DR. ERNEST AMBLER,
           DIRECTOR NATIONAL BUREAU OF STANDARDS
          REMARKS BY MR. KANAME IKEDA, COUNSELLOR FOR
           SCIENCE AND TECHNOLOGY, EMBASSY OF JAPAN
          REMARKS BY DR. RICHARD WRIGHT, CHAIRMAN
           US SIDE UJNR PANEL
          REMARKS BY DR. MASATERU TOMINAGA,
           CHAIRMAN JAPANESE SIDE
          INTRODUCTION OF US MEMBERS BY US CHAIRMAN
          INTRODUCTION OF JAPANESE MEMBERS BY
           JAPANESE CHAIRMAN
           ELECTION OF TECHNICAL SESSION CHAIRMEN
          APPROVAL OF AGENDA
          GROUP PHOTOGRAPH

    1145   LUNCH (HOSTED BY DR. ERNEST AMBLER)

          TECHNICAL SESSIONS

          SESSION 1 - WIND ENGINEERING
             CHAIRMAN R.N. WRIGHT

    1300 - 1320 THE EFFECTS OF LARGE-SCALE UPSTREAM
    GUSTING ON THE AEROELASTIC BEHAVIOR OF SECTION MODELS,
    BY D. HUSTON, H. BOSCH, H. TANAKA (Presented by D.
    HUSTON)
    1320 - 1340 ON THE EVALUATION OF WIND-INDUCED
    VIBRATIONS OF LONG-SPAN BRIDGES USING TAUT-STRIP
    MODELS, BY N. NARITA, H. TADA, K. YOKOYAMA, H. SATO,
    K. KANZAKI, M. FUKUDA (Presented by H. TADA)
    1340 - 1400 THE RESPONSE OF TAUT STRIP MODELS,
    COMPARISONS OF THEORETICAL AND EXPERIMENTAL RESULTS,
    BY R. SCANLAN, R. MARSHALL (Presented by R. MARSHALL)
    1400 - 1420 DISCUSSIONS

    1420 - 1440 A FULL-SCALE MEASUREMENT OF WIND LOAD ON
    A SOLAR WATER HEATER, BY H. OKADA, T. MUROTA
    (Presented by H. OKADA)
    1440 - 1500 DESIGN CRITERIA FOR GLASS SUBJECTED TO
    WIND LOADS, BY E. SIMIU, E. HENDRICKSON (Presented
    by E. SIMIU)
    1500 - 1520 DISCUSSION

    1520 - 1540 BREAK

SESSION 2 - EARTHQUAKE ENGINEERING
CHAIRMAN R.N. WRIGHT

1540 - 1600 MICROZONING AND PROBABILISTIC HAZARD
            ASSESSMENT, BY T. ALGERMISSEN
1600 - 1620 SPECTRAL CHARACTERISTICS OF GROUND MOTION
            IN THE TOKYO METROPOLITAN AREA, BY K. OHTANI,
            S. KINOSHITA (Presented by K. OHTANI)
1620 - 1640 STRONG-MOTION RECORDINGS FROM THE
            HOLLISTER, CALIFORNIA, AREA M5.5 EARTHQUAKE,
            JANUARY 26, 1986, BY A.G. BRADY, R.P. MALEY,
            G.N. BYCROFT (Presented by A.G. BRADY)
1640 - 1700 DENSE INSTRUMENT ARRAY SYSTEM BY PWRI FOR
            OBSERVING STRONG EARTHQUAKE MOTION, BY T. IWASAKI,
            Y. SASAKI, K. TAMURA, K. AIZAWA, K. TAKAHASHI
            (Presented by Y. SASAKI)
1700 - 1720 DISCUSSION

1720 ADJOURN

1930 DINNER - BULL FEATHERS RESTAURANT OF CAPITOL HILL
      (HOSTED BY US MEMBERS)

TUESDAY 13 MAY
                SESSION 3 - EARTHQUAKE ENGINEERING
                    CHAIRMAN M. TOMINAGA

840 - 900 VIBRATION TESTS OF AN ASPHALTIC FACING COFFERDAM
           BY BLASTINGS, BY N. MATSUMOTO, N. YASUDA,
           M. SHIGA (Presented by H. TADA)
900 - 920 SUMMARY OF THE RICHARD B. RUSSELL CONCRETE
           DAM VIBRATION STUDY, BY V.P. CHIARITO, R.J. SMITH
           (Presented by R.J. SMITH)
920 - 940 SHAKING TABLE TEST ON SEISMIC STABILITY OF
           REINFORCED EMBANKMENTS, BY Y. KOGA, E. TANIGUCHI,
           Y. ITO (Presented by Y. SASAKI)
940 - 1000 DISCUSSION

1000 - 1020 STATUS REPORT ON NEW STUDY OF LOWER VAN
            NORMAN DAM, BY A.G. FRANKLIN
1020 - 1040 SEISMIC DESIGN PROCEDURE AND DYNAMIC
            STRENGTH OF "CAB", BY T. IWASAKI, K. KAWASHIMA,
            N. OBINATA, S. UNJOH   (Presented by H. TADA)
1040 - 1100 LARGE-SCALE BRIDGE COLUMN TESTS - A
            PROGRESS REPORT, BY E.V. LEYENDECKER, W. STONE, G.
            CHEOCK (Presented by E.V. LEYENDECKER)
1100 - 1120 DISCUSSION
1120 - 1140 BREAK

1140 - 1200 OUTLINE OF MANUAL FOR REPAIR METHODS FOR
            CIVIL ENGINEERING STRUCTURES DAMAGED BY EARTHQUAKES,
            BY T. IWASAKI, S. KOBAYASHI, T. UDA, Y. ASAI,
            Y. KOGA, Y. SASAKI, K. KAWASHIMA (Presented by
            Y. SASAKI)
1200 - 1220 EFFECTS OF VERTICAL CONTRACTION JOINTS ON
            THE DYNAMIC RESPONSE OF ARCH DAMS, BY H. BOGGS,
            J. MAYS (Presented by H. BOGGS)
1220 - 1240 DISCUSSION

1240 LUNCH (HOSTED BY DR. EDWARD BRADY, ASSOCIATE
             DIRECTOR FOR INTERNATIONAL AFFAIRS)

SESSION 4   EARTHQUAKE ENGINEERING
CHAIRMAN R.N. WRIGHT

1340 - 1400   DECISION ANALYSIS FOR EMBANKMENT DAMS
        UNDER SEISMIC LOADS, BY T. LUEBKE (Presented by
        F. McLEAN)
1400 - 1420   A NEW CRITERION FOR ASSESSING LIQUEFACTION
        POTENTIAL, BY S. IAI, H. TSUCHIDA, S. NODA (Presented
        by H. TSUCHIDA)
1420 - 1440   EARTHQUAKE SAFETY INVESTIGATION OF
        EXISTING FACILITIES   BY J.TYRRELL
1440 - 1500   THEMATIC MAPPING WORKS FOR SEISMIC
        DISASTER PREVENTION IN GEOGRAPHICAL SURVEY INSTITUTE,
        JAPAN, BY M. NAGAOKA, H. MATSUDA, (Presented by
        M. NAGAOKA)
1500 - 1520   DISCUSSION
1520 - 1540   BREAK

TASK COMMITTEE MEETINGS (1540 - 1800)

        TASK COMMITTEE A, STRONG MOTION INSTRUMENTATION
            ARRAYS AND DATA
        TASK COMMITTEE B, LARGE SCALE TESTING PROGRAM
        TASK COMMITTEE D, EVALUATION OF PERFORMANCE OF
            STRUCTURES
        TASK COMMITTEE H, SOIL BEHAVIOR AND STABILITY
            DURING EARTHQUAKES
        TASK COMMITTEE J, WIND AND EARTHQUAKE ENGINEERING
            FOR TRANSPORTATION SYSTEMS

1900   DINNER - JAPANESE MEMBERS HOSTED BY US MEMBERS

WEDNESDAY 14 MAY

SESSION 5   STORM SURGE AND TSUNAMI
CHAIRMAN   M. TOMINAGA

900 - 920   SATELLITE APPLICATION IN MARINE AREAS, BY
        C. BARRIENTOS
920 - 940   DISCRIMINATION OF FLOODED AREAS CAUSED BY
        TSUNAMI OR STORM SURGE USING SATELLITE DATA, BY
        A. TAKEDA, Y. TSUJI, H. TAKAHASHI (Presented by
        K. OHTANI)
940 - 1000 FAULT DISPLACEMENT SEICHE WAVES ON INLAND
        RESERVOIR AND LAKES, BY R. DEWEY, K. DISE
        (Presented by R. DEWEY)
1000 - 1020   DISCUSSION
1020 - 1040   BREAK

SESSION 6   US JAPAN COOPERATIVE RESEARCH
PROGRAM   CHAIRMAN   M. TOMINAGA

1040 - 1100   US-JAPAN COORDINATED EARTHQUAKE RESEARCH
PROGRAM ON REINFORCED MASONRY BUILDINGS, BY
S. OKAMOTO, Y. YAMAZAKI, T. KAMINOSONO,
M. TESHIGAWARA, H. HIRAISHI (Presented by
H. YAMANOUCHI)
1100 - 1120   US JAPAN COORDINATED PROGRAM ON MASONRY
RESEARCH, BY S. OKAMOTO, J. NOLAND (Presented by
M. PORTER)
1120 - 1140   SEISMIC BEHAVIOR OF A FULL-SCALE K-BRACED
STEEL BUILDING STRUCTURE, BY H. YAMANOUCHI,
M. MIDORIKAWA, I. NISHIYAMA, T. MUROTA (Presented
by H. YAMANOUCHI)
1140 - 1200   FULL-SCALE STUDIES OF STEEL STRUCTURES,
BY R. HANSON
1200 - 1220   DISCUSSION

1220 - LUNCH (HOSTED BY DR. JOHN LYONS, DIRECTOR,
NATIONAL ENGINEERING LABORATORY)

TASK COMMITTEE MEETINGS (1400 - 1700)

TASK COMMITTEE C, REPAIR AND RETROFIT OF EXISTING
    STRUCTURES
TASK COMMITTEE E, LAND USE PROGRAM FOR CONTROLLING
    NATURAL HAZARD EFFECTS
TASK COMMITTEE F, DISASTER PREVENTION METHODS FOR
    LIFELINE SYSTEMS
TASK COMMITTEE G, WIND CHARACTERISTICS AND
    STRUCTURAL RESPONSE
TASK COMMITTEE I, STORM SURGE AND TSUNAMIS

1800   DINNER   JAPANESE MEMBERS HOSTED BY US MEMBERS

THURSDAY 15 MAY

SESSION 7   MEXICO CITY AND CHILIAN EARTHQUAKES,
CHAIRMAN   M. TOMINAGA

900 - 920   EARTHQUAKE DAMAGE IN MEXICO CAUSED BY THE
SEPTEMBER 1985 EARTHQUAKES, BY E.V. LEYENDECKER,
W. STONE, F. YOKEL (Presented by E.V. LEYENDECKER)
920 - 940   JAPAN-MEXICO TECHNICAL COOPERATION ON
DAMAGE EVALUATION, REPAIR AND STRENGTHENING FOR
BUILDINGS DAMAGED BY 1985 MEXICO EARTHQUAKE, BY
M. HIROSAWA, T. MUROTA (Presented by H. OKADA)
940 - 1000   ASPECTS OF STRONG MOTION FROM THE MICHOACAN,
MEXICO EARTHQUAKE OF SEPTEMBER 19, 1985, BY J.
ANDERSON, J. BRUNE, J. PRINCE, E. MENA, P. BODIN,
M. ONATE, R. QUAAS, S.K. SINGH (Presented by J.
ANDERSON)
1000 - 1020   DISCUSSION
1020 - 1040   BREAK

1040 - 1100   SEISMIC DAMAGE TO PORT FACILITIES BY THE
1985 CHILE EARTHQUAKE AND IMPROVEMENT OF SEISMIC
SAFETY OF THE DAMAGED PORTS, BY H. TSUCHIDA,
S. NODA (Presented by H. TSUCHIDA)
1100 - 1120   OBSERVATIONS OF THE STRUCTURAL DAMAGE
CAUSED BY THE 3 MARCH 1985 CHILE EARTHQUAKE, BY
M. SOZEN
1120 - 1140   DISCUSSION
1140 - 1200   BREAK

1200 - 1300   LUNCH (HOSTED BY DR. RICHARD WRIGHT)

FRIDAY 16 MAY

    STUDY TOUR HOSTED BY US SIDE TO THE BALTIMORE HARBOR TUNNEL
    AND BALTIMORE HARBOR RECONSTRUCTION/RENOVATION

    1830 DINNER HOSTED BY US MEMBERS

SATURDAY 17 MAY

    VISIT BRIDGE SITES AND THE WORLD TRADE CENTER (Hosted
    by ASCE)

    900 EA-1420 LV DCA
    1000 AR NYC
        HOTEL; DORAL HOTEL

SUNDAY 18 MAY

    TEAM TRAVELS TO VICKSBURG, MS
    1101 EA-543 LV LGA
    1427 EA-595 AR JACKSON, MS
    1600 ARRIVE VICKSBURG
        HOTEL; RAMADA INN, Vicksburg

MONDAY 19 MAY

    900   TEAM VISIT TO WATERWAYS EXPERIMENT STATION
    1400 DEPART BY AUTO TO JACKSON
    1635 DP JACKSON DL-557
    2010 AR SAN FRANCISCO DL-143
        HOTEL; BEVERLY PLAZA HOTEL

TUESDAY 20 MAY

    1000 TEAM VISIT TO USGS MENLO PARK

WEDNESDAY 21 MAY

    TEAM TRAVELS TO HONOLULU
    930   NW-101 LV SAN FRANCISCO
    1135 ARRIVES HONOLULU
    VISIT PACIFIC TSUNAMI WARNING CENTER AT EWA BEACH
    91-270 Ft. Weaver Road, Ewa Beach
    1915 LV HONOLULU AQ-48
    1955 AR HILO
        HOTEL; HILO HAWAIIAN

THURSDAY 22 MAY

    900   TEAM VISITS HAWAIIAN VOLCANO OBSERVATORY
    1535 LV HILO
    1615 AR HONOLULU
        HOTEL; KAIMANA BEACH HOTEL,

FRIDAY 23 MAY

    TEAM DEPARTS FOR JAPAN
    1105 NW-009

LIST OF MEMBERS

U.S. PANEL ON WIND AND SEISMIC EFFECTS
MEMBERSHIP LIST
1986

Dr. Richard N. Wright, Chairman
Director, Center for Building Technology
National Bureau of Standards
Gaithersburg, MD 20899
(301) 921-3377

Mr. Noel J. Raufaste, Secretary US Side
Structures Division
Center for Building Technology
National Bureau of Standards
Gaithersburg, MD 20899
(301) 921-3106

Dr. S. T. Algermissen
Office of Earthquake Studies
Branch of Earthquake Tactonics, USGS
Denver Federal Center
Stop 978, Box 25046
Denver, CO 80225
(303) 236-1611

Dr. Celso S. Barrientos
Supervisory Physicist Scientist
NOAA/NESDIS
3300 Whitehaven Street, NW
Washington, DC 20235
(202) 634-7379

Dr. Eddie N. Bernard
Director, Pacific Marine
  Environmental Laboratory
7600 San Point Way, NE
Seattle, WA 98115
(206) 526-6239 FTS 292-6800

Dr. Roger D. Borcherdt
Chief, Branch of Engineering
Seismology and Geology
Office of Earthquake Studies, USGS
345 Middlefield Road
Menlo Park, CA 94025
(415) 323-8111 x2755

Dr. A. Gerald Brady
Physical Scientist
Office of Earthquake Studies
U.S. Geological Survey
345 Middlefield Road
Menlo Park, CA 94025
(415) 323-8111

Dr. John J. Burns, Jr.
Head, Structures Section
Office of Research
U.S. Nuclear Regulatory Commission
Washington, DC 20555
(301) 443-7860

Mr. H. Lee Butler
Chief, Research Division
Coastal Engineering Research Center
Waterways Experiment Station
U.S. Army Corps of Engineers
Vicksburg, MS 39108
(601) 634-3462

Dr. James Choromokos, Jr.
Director, Research and Development
Department of the Army
DAEN-RDZ-A
Washington, DC 20314
(202) 272-0254

Dr. A. G. Franklin
Chief, Earthquake Engineering
  and Geophysics Division
Geotechnical Laboratory
U.S. Army Engineer Waterways
  Experiment Station
Vicksburg, MS 39180
(601) 634-2658

Mr. G. Robert Fuller
Chief, Standards Branch
Manufactured Housing Construction
  Standards Division, Room 9156
Housing and Urban Development
Washington, DC 20410-8000
(202) 755-6920

Mr. James Gates
Office of Structures Design
Department of Transportation
1120 N Street
Sacramento, CA 95807
(916) 445-1439

Dr. Michael P. Gaus
Section Head of Critical Engineering
Division of Emerging and Critical
  Engineering Systems
National Science Foundation
1800 G Street, NW
Washington, DC 20550
(202) 357-9500

Mr. Peter E. Gurvin
A/FBO, SA-6
Department of State
Washington, DC 20620
(202) 235-3689

Dr. Walter W. Hays
Deputy for Research Application
U.S. Geological Survey
Office of Earthquake Survey
905 National Center
Reston, VA 22043
FTS 928-6472 or (703) 860-6471

Dr. William B. Joyner
Geophysicist
Office of Earthquake Studies
Branch of Ground Motion and
  Faulting, USGS
342 Middlefield Road
Menlo Park, CA 94025
(415) 323-8111

Mr. Richard W. Kramer
Civil Engineer
Technical Review Staff, D-3210
Bureau of Reclamation
P.O. Box 25007
Denver, CO 80225
FTS 776-8539 or (303) 236-8539

Mr. Richard Krimm
Office of Natural and
  Technological Hazards
Federal Emergency Management Agency
Washington, DC 20472
(202) 646-2871

Mr. Paul K. Krumpe
Office of Foreign Disaster Assistance
Agency for International Development
Department of State
Washington, DC 20523
(202) 647-9758

Mr. James F. Lander
Deputy Director
National Geophysical Data Center
NOAA/NESDIS
325 Broadway
Boulder, CO 80303
FTS 320-6215 or (303) 497-6215

Dr. H. S. Lew
Leader, Construction Safety Group
Structures Division
Center for Building Technology
National Bureau of Standards
Gaithersburg, MD 20899
(301) 921-2647

Dr. E. V. Leyendecker
Leader, Earthquake Hazards Reduction
  Group, Structures Division
Center for Building Technology
National Bureau of Standards
Gaithersburg, MD 20899
(301) 921-3471

Dr. Shih-Chi Liu
Director, Earthquake Hazards
  Mitigation
National Science Foundation
1800 G Street, N.W. Room 1128
Washington, DC 20550
(202) 357-9780

Mr. Robert MacDonald
Geological Services Branch, Code D
1630 Bureau of Reclamation
Denver Federal Center, Building 67
Denver, CO 80225
FTS 776-4195 or (303) 236-4915

Dr. Richard Marshall
Structural Research Engineer
Structures Division
Center for Building Technology
National Bureau of Standards
Gaithersburg, MD 20899
(301) 921-2170

Dr. Richard D. McConnell
Office of Construction
Veterans Administration
811 Vermont Avenue, NW
Washington, DC 20420
(202) 389-3103

Dr. Francis G. McLean
Chief, Division of Research and
  Laboratory Services, D-1500
Bureau of Reclamation
P.O. Box 25007
Denver, CO 80225
FTS 776-5981 or (303) 234-3303

Mr. John F. Meehan
Research Director
Structural Safety Section
Office of the Architect
Department of General Services
State of California
Sacramento, CA 95805
(916) 445-8730

Dr. John B. Scalzi
Program Director, Systems
  Engineering for Large Structures
National Science Foundation
1800 G Street, NW, Room 1130
Washington, DC 20550
(202) 357-7710

Mr. Joseph T. Schaefer
Chief, Scientific Services Division
National Weather Service, NOAA
Federal Building, Room 1836
601 East 12th Street
Kansas City, MO 64106
(816) 374-5672

Dr. Charles Scheffey
Science Advisor, Offices of Research,
  Development and Technology
Federal Highway Administration
6300 Georgetown Pike
McLean, VA 22101
(703) 285-2054

Mr. Robert J. Smith
Office of the Chief of Engineers
Department of the Army
DAEN-ECE-D
Washington, DC 20314-1000
(202) 272-0220

Dr. Lawrence A. Soltis
Supervisory Research Engineer
Engineering Design Criteria
Forest Products Laboratory
Forest Service
U.S. Department of Agriculture
Madison, WI 53705
(608) 364-5910

Mr. Joseph Tyrrell
Director, Civil/Structural Div. (O4BA)
Naval Facilities Engineering Command
200 Stovall Street
Alexandria, VA 22332
(703) 325-0047

ALTERNATES

Dr. Clifford Astill
National Science Foundation
1800 G Street, NW
Washington, DC 20550
(202) 357-9500

Mr. Michael Changery
National Climatic Center
Federal Building
Asheville, NC 28787
(704) 259-0765

Mr. Vincent Chiarito
U.S. Army
Waterways Experiment Station
P.O. Box 631
Vicksburg, MS 39180
FTS 542-2000

Dr. A. J. Eggenberger
National Science Foundation
1800 G Street, NW
Washington, DC 20550
(202) 357-9500

Mr. Lucian G. Guthrie
Structural Engineer
Office Chief of Engineering
Engineering Division
Directorate of Engineering
  and Construction
HQUSACE (DAEN-ECE-D)
Washington, DC 20314-1000
(202) 272-8673

Mr. James Houston
Division Chief
Waterways Experiment Station
P.O. Box 631
Vicksburg, MS 39180-0631
FTS 542-2000

Mr. Roger Kenneally
Structures Division
Office of Research
U.S. Nuclear Regulatory Commission
Washington, DC 20555
(301) 443-7860

Mr. Robert R. Ledzian
Senior Staff Assistant for Research
Bureau of Reclamation, WO-220
Department of the Interior
18th and C Streets, NW
Washington, DC 20240
(202) 343-6703

Mr. T. K. Lew
Commanding Officer
Naval Civil Engineering Laboratory
Port Hueneme, CA 93043
(805) 982-5785

Dr. Herbert Meyers
Chief, Solid Earth Geophysics Division
National Geophysical Data Center
NOAA
325 Broadway
Boulder, CO 80303
(303) 497-6215

Ms. Janina Z. Mirski
Chief, Southern/Western Structural
  Division 0853
Office of Construction
Veterans Administration
Washington, DC 20420
(202) 389-2394

Mr. Ronald J. Morony
Program Manager
Building Technology Research Staff
Department of Housing and
  Urban Development
7th and D Street, SW
Washington, DC 20410
(202) 755-0640

TEMPORARY

Mr. Harold H. Boggs
Bureau Reclamation
P.O. Box 25007
Denver, CO 80225
(303) 234-3303

Mr. Harold R. Bosch
Research Structural Engineer
Structures Division HNR-10
Federal Highway Administration
6300 Georgetown Pike
McLean, VA 22101
(703) 285-2446

Mr. Robert L. Dewey
Civil Engineer
Bureau of Reclamation
P.O. Box 25007
Denver, CO 80225
(303) 234-3303

Mr. Karl M. Dise
Civil Engineer
Bureau of Reclamation
P.O. Box 25007
Denver, CO 80225
(303) 234-3303

Professor Robert D. Hanson
Department of Civil Engineering
University of Michigan
2340 GG Brown Building
Ann Arbor, MI 48109-2125
(313) 764-5617

Mr. T. A. Luebke
Bureau of Reclamation
P.O. Box 25007
Denver, CO 80225
(303) 234-3303

Mr. J. R. Mays
University of Colorado
Denver, CO 80202

Mr. James Noland
Principal, Atkinson-Noland Associates
Consulting Engineers
2619 Spruce Street
Boulder, CO 80302
(303) 444-3620

Professor Max Porter
Department of Civil Engineering
Iowa State University
416 A Town Engineering Building
Ames, Iowa 50011
(515) 294-7456

Professor Robert Scanlan
Department of Civil Engineering
Johns Hopkins University
202 Lathrobe Hall
Baltimore, MD 21218
(301) 338-7138

Mr. Emil Simiu
Structural Research Engineer
Structures Division
Center for Building Technology
National Bureau of Standards
Gaithersburg, MD 20899
(301) 921-3169

Dr. Masateru Tominaga, Chairman
Director-General
Public Works Research Institute
Ministry of Construction
Asahi 1-banchi, Toyosato-machi, Tsukuba-gun
Ibaraki-ken 305
Tel. 0298-64-2211

Mr. Toshiaki Fujii, Secretary-General
Director
Planning and Research Administration Department
Public Works Research Institute
Ministry of Construction
Asahi 1-banchi, Toyosato-machi,
Tsukuba-gun, Ibaraki-ken 305
Tel. 0298-64-2211

Dr. Yoshimi Goda
Deputy Director-General
Port and Harbour Research Institute
Ministry of Transport
3-1-1, Nagase, Yokosuka-shi, Kanagawa-ken 239
Tel. 0468-41-5410

Dr. Tatsuo Hanafusa
Chief, Second Research Laboratory
Physical Meteorology Research Division
Meteorological Research Institute (MRI)
Japan Meteorological Agency (JMA)
1-1, Nagamine, Yatabe-machi, Tsukuba-gun
Ibaraki-ken 305
Tel. 0298-51-7111

Dr. Sadaiku Hattori
Director
International Institute of Seismology and
   Earthquake Engineering (I.I.S.E.E.)
Building Research Institute
Ministry of Construction
Tatehara 1-banchi, Oh-ho-machi, Tsukuba-gun
Ibaraki-ken 305
Tel. 0298-64-2151

Dr. Masaya Hirosawa
Director
Research Planning and Information Department
Building Research Institute
Tatehara 1-banchi, Oh-ho-machi, Tsukuba-gun
Ibaraki-ken 305
Tel. 0298-64-2151

Dr. Masaji Ichikawa
Head, Seismology and Volcanology Division
Meteorological Research Institute (MRI)
Japan Meteorological Agency (JMA)
1-1, Nagamine, Yatabe-machi, Tsukuba-gun
Ibaraki-ken 305
Tel. 0298-51-7111

Dr. Yuji Ishiyama
Head of Planning and Investigation Division
Research Planning and Information Department
Building Research Institute
Ministry of Construction
Tatehara 1-banchi, Oh-ho-machi, Tsukuba-gun
Ibaraki-ken 305
Tel. 0298-64-2151

Dr. Toshio Iwasaki
Director, Earthquake Disaster Prevention Department
Public Works Research Institute
Ministry of Construction
Asahi 1-banchi, Toyosato-machi, Tsukuba-gun
Ibaraki-ken 305
Tel. 0298-64-2211

Dr. Kazuhiko Kawashima
Head, Earthquake Engineering Division
Earthquake Disaster Prevention Department
Public Works Research Institute
Ministry of Construction
Asahi 1-banchi, Toyosato-machi, Tsukuba-gun
Ibaraki-ken 305
Tel. 0298-64-2211

Mr. Yasuyuki Koga
Head, Soil Dynamics Division
Construction Method and Equipment Department
Public Works Research Institute
Ministry of Construction
Asahi 1-banchi, Toyosato-machi, Tsukuba-gun
Ibaraki-ken 305
Tel. 0298-64-2211

Dr. Keizo Masamura
Head, Typhoon Research Division
Meteorological Research Institute (MRI)
Japan Meteorological Agency (JMA)
1-1, Nagamine, Yatabe-machi, Tsukuba-gun
Ibaraki-ken 305
Tel. 0298-51-7111

Dr. Norihisa Matsumoto
Head, Fill Type Dam Division
Dam Department
Public Works Research Institute
Ministry of Construction
Asahi 1-banchi, Toyosato-machi, Tsukuba-gun
Ibaraki-ken 305
Tel. 0298-64-2211

Mr. Tatsuo Murota
Director
Structural Engineering Department
Building Research Institute
Ministry of Construction
Tatehara 1-banchi, Oh-ho-machi, Tsukuba-gun
Ibaraki-ken 305
Tel. 0298-64-2151

Mr. Masatoshi Nagaoka
Head of Second Geographic Division
Geographical Survey Institute
Ministry of Construction
Kitazato 1-banchi, Yatabe-machi, Tsukuba-gun
Ibaraki-ken   305
Tel. 0298-64-1111

Dr. Nobuyuki Narita
Deputy Director-General
Public Works Research Institute
Ministry of Construction
Asahi 1-banchi, Toyosato-machi,
Tsukuba-gun, Ibaraki-ken   305
Tel. 0298-64-2211

Dr. Setsuo Noda
Chief, Earthquake Resistant Structures Laboratory
Structure Division
Port and Harbour Research Institute
Ministry of Transport
3-1-1, Nagase, Yokosuka-shi, Kanagawa-ken   239
Tel. 0468-41-5410

Mr. Keiichi Ohtani
Head, Earthquake Engineering Laboratory
Second Research Division
National Research Center for Disaster Prevention
Science and Technology Agency
3-1, Tennodai, Sakura-mura, Niihari-gun
Ibaraki-ken   305
Tel. 0298-51-1611

Mr. Michio Okahara
Head, Foundation Engineering Division
Structure and Bridge Department
Public Works Research Institute
Ministry of Construction
Asahi 1-banchi, Toyosato-machi, Tsukuba-gun
Ibaraki-ken   305
Tel. 0298-64-2211

Mr. Shin Okamoto
Director, Production Department
Building Research Institute
Ministry of Construction
Tatehara 1-banchi, Oh-ho-machi, Tsukuba-gun
Ibraki-ken   305
Tel. 0298-64-2151

Dr. Yasushi Sasaki
Head, Ground Vibration Division
Earthquake Disaster Prevention Department
Public works Research Institute
Ministry of Construction
Asahi 1-banchi, Toyosato-machi, Tsukuba-gun
Ibaraki-ken   305
Tel. 0298-64-2211

Mr. Hiroshi Shinohara
Head, Bridge Division
Structure and Bridge Department
Public Works Research Institute
Ministry of Construction
Asahi 1-banchi, Toyosato-machi, Tsukuba-gun
Ibaraki-ken 305
Tel. 0298-64-2211

Dr. Yoshihiro Sugimura
Head, Foundation Engineering Division
Structure Engineering Department
Building Research Institute
Ministry of Construction
Tatehara 1-banchi, Oh-ho-machi, Tsukuba-gun
Ibaraki-ken 305
Tel. 0298-64-2151

Dr. Hirohiko Tada
Director, Structure and Bridge Department
Public Works Research Institute
Ministry of Construction
Asahi 1-banchi, Toyosato-machi, Tsukuba-gun
Ibaraki-ken 305
Tel. 0298-64-2211

Dr. Hiroshi Takahashi
Director-General
National Research Center for Disaster Prevention
Science and Technology Agency
3-1, Tennodai, Sakura-mura, Niihari-gun
Ibaraki-ken 305
Tel. 0298-51-1611

Dr. Hajime Tsuchida
Director, Structures Division
Port and Harbour Research Institute
Ministry of Transport
3-1-1, Nagase, Yokosuka-shi, Kanagawa-ken 239
Tel. 0468-41-5410

Dr. Takaaki Uda
Head, Coastal Engineering Division
River Department
Public Works Research Institute
Ministry of Construction
Asahi 1-banchi, Toyosato-machi, Tsukuba-gun
Ibaraki-ken 305
Tel. 0298-64-2211

Dr. Hiroyuki Yamanouchi
Head, Structure Division
Structural Engineering Department
Building Research Institute
Ministry of Construction
Tatehara 1-banchi, Oh-ho-machi, Tsukuba-gun
Ibaraki-ken 305
Tel. 0298-64-2151

Mr. Koichi Yokoyama
Head, Structure Division
Structure and Bridge Department
Public Works Research Institute
Ministry of Construction
Asahi 1-banchi, Toyosato-machi, Tsukuba-gun
Ibaraki-ken 305
Tel. 0298-64-2211

LIST OF TASK COMMITTEE MEMBERS

Task Committee	U.S. Side	Japanese Side
A. Strong-Motion Instrumen- tation Arrays & Data	*A.G. Brady W.B. Joyner J.F. Lander F.G. McLean	*Hajime Tsuchida Sadaiku Hattori Masaji Ichikawa Yuji Ishiyama Keiichi Ohtani Yasushi Sasaki
B. Large-Scale Testing Programs	*E.V. Leyendecker H.S. Lew J.B. Scalzi C.F. Scheffey	*Keiichi Ohtani Yuji Ishiyama Yasuyuki Koga Setsuo Noda Shin Okamoto Koichi Yokoyama
C. Repair and Retrofit of Existing Structures	*J.B. Scalzi P.E. Gurvin H.S. Lew R.D. McConnell C.F. Scheffey	*Masaya Hirosawa Yuji Ishiyama Toshio Iwasaki Shin Okamoto Hirohiko Tada
D. Evaluation of Performance	*G.R. Fuller R.D. McConnell J.F. Meehan J.B. Scalzi	*Shin Okamoto Yuji Ishiyama Kayuya Ohshima Hirohiko Tada
E. Natural Hazard Effects Land Use Program for Controlling	*S.T. Algermissen A.G. Brady G.R. Fuller R.D. Marshall	*Kazuhiko Kawashima Sadaiku Hattori Toshio Iwasaki Masatoshi Nagaoka Yoshihiro Sugimura
F. Disaster Prevention Methods for Lifeline Systems	*S.C. Liu J.B. Scalzi E.V. Leyendecker	*Toshio Iwasaki Kazuhiko Kawashima Tatsuo Murota Setsuo Noda Keiichi Ohtani Yasushi Sasaki
G. Wind Characteristics and Structural Response	*R.D. Marshall C.S. Barrientos M.P. Gaus C.F. Scheffey	*Keikichi Naito Keizo Masamura Tatsuo Murota Nobuyuki Narita Koichi Yokoyama
H. Soil Behavior and Stability During Earthquakes	*A.G. Franklin F.G. McLean R.J. Smith	*Yasushi Sasaki Yasuyuki Koga Norihisa Matsumoto Kayuya Ohshima Yoshihiro Sugimura Hajime Tsuchida

xiv

I. Storm Surge and Tsunamis   *C.S. Barrientos   *Yoshimi Guda
                                   E.N. Bernard   Masaji Ichikawa
                                   M.P. Gaus   Keizo Masamura
                                   J.F. Lander   Hiroshi Takahashi
                                                         Takaaki Uda

J. Wind and Earthquake   *C.F. Scheffey   *Hirohiko Tada
    Engineering for   A.G. Franklin   Toshio Iwasaki
    Transportation Systems   H.S. Lew   Kazuhiko Kawashima
                                  E.V. Leyendecker   Nobuyuki Narita
                                                        Kayuya Ohshima
                                                        Yasushi Sasaki
                                                        Hiroshi Shinohara
                                                        Koichi Yokoyama

---

*Chairman

LIST OF JAPANESE PARTICIPANTS

<u>Member</u>

Dr. Masateru Tominaga
Director General
Public Works Research Institute
Ministry of Construction

Mr. Masatoshi Nagaoka
Head, Second Geographic Division
Geographical Survey Institute
Ministry of Construction

Mr. Keiichi Ohtani
Chief, Earthquake Engineering Laboratory
Second Research Division
National Research Center for Disaster Prevention
Science and Technology Agency

Dr. Yasushi Sasaki
Head, Ground Vibration Division
Earthquake Disaster Prevention Department
Public Works Research Institute
Ministry of Construction

Dr. Hirohiko Tada
Director, Structure and Bridge Department
Public Works Research Institute
Ministry of Construction

Dr. Hajime Tsuchida
Director, Structure Division
Port and Harbour Research Institute
Ministry of Transport

Dr. Hiroyuki Yamanouchi
Head, Building Structure Division
Structural Engineering Department
Building Research Institute
Ministry of Construction

<u>Temporary Member</u>

Dr. Hisashi Okada
Senior Researcher, Building Aerodynamics Division
Structural Engineering Department
Building Research Institute
Ministry of Construction

Mr. Akira Endoh
Researcher, New Transportation Systems Division
Road Department
Public Works Research Institute
Ministry of Construction

FORMAL RESOLUTIONS

RESOLUTIONS OF THE EIGHTEENTH JOINT MEETING
U.S.-JAPAN PANEL ON WIND AND SEISMIC EFFECTS (UJNR)

National Bureau of Standards
Gaithersburg, Maryland

May 12-15, 1986

The following resolutions are hereby adopted:

1. The Eighteenth Joint Panel Meeting provided valuable exchange of technical information which was beneficial to both countries. In view of the importance of cooperative programs on the subject of wind and seismic effects, the continuation of Joint Panel Meetings is considered essential.

2. The following activities have been carried out since the Seventeenth Joint Meeting:

   a. In December 1985 this Panel's activities were reported at the 11th UJNR Plenary Conference.

   b. Technical documents, strong motion records, research reports, earthquake damage records, and workshop proceedings were exchanged.

   c. Workshops were held that continued joint research and development activities on methodologies for wind and seismic disaster mitigation.

   d. The Coordinated Research Program on Large-Scale Testing of Masonry Structures which is currently underway. Research is coordinated by the Joint Technical Coordinating Committee on Masonry Research (JTCCMAR).

3. A Charter was drafted for this Panel on Wind and Seismic Effects as suggested at the 11th UJNR Plenary Conference, December 1985, Tokyo (attached). The draft will be studied and considered for adoption at the nineteenth joint meeting.

4. The Panel endorses the following workshops and conferences proposed by the Task Committees:

   a. Planning conference on Disaster Prevention Methods for Lifeline Systems and Task Committee (F) participation in the Third U.S. National Conference on Earthquake Engineering, August 1986, Charleston, South Carolina.

   b. Workshop on Repair and Retrofit, Task Committee (C), to be held, if possible, in conjunction with the 19th UJNR Joint Meeting.

   c. Fourth Workshop on Evaluation of Seismic Resistance of Existing Buildings, Task Committee (D), to be held in Japan prior to the 19th Joint UJNR Meeting.

   d. Second Workshop on Tsunami and Storm Surge Workshop, Task Committee (I), to be scheduled in conjunction with the 19th UJNR Joint Meeting.

   e. Third Bridge Workshop held by Wind and Earthquake Engineering for Transport Systems, Task Committee (J), to be held in conjunction with the 19th Joint UJNR Panel Meeting or in conjunction with the completion of Honshu Shikoku Bridges in October 1987.

   f. Workshop on Strong-Motion Earthquake Observation, Task Committee (A), to be held in the San Francisco area, August 1987.

Scheduling for workshops and conferences shall be performed by the chairmen of each Task Committee with concurrence of the Joint Panel chairmen. Results of each workshop shall be presented at subsequent Joint Panel Meeting.

5. The Panel endorses the recommended change in Task Committee (E) title "Land Use Programs for Controlling Natural Hazard Effects" to reflect the Task Committee's full scope, "Natural Hazard Assessment and Mitigation through Land Use Programs".

6. The Panel recognizes the importance of continued exchange of personnel, technical information, research data and recorded data on significant earthquakes and strong winds, and use of available facilities in both countries. Thus, these activities should be strengthened and expanded. To facilitate the exchange of personnel, the Panel will continue to encourage such exchanges and provide official Panel sponsorship.

7. The Panel recommends that for future Joint Panel Meetings, priority attention be given to the following items:

   a. Task Committee Chairmen should give attention to identifying joint research needs, priorities, development plans, and recommendations for future research programs. Each Task Committee Chairman is encouraged to examine his Committee's objectives and to modify the objectives, as appropriate, to meet the need for improved technology.

   b. Task Committee Chairmen are encouraged to increase communication with each other for improved understanding of Panel activities. Task Committee Chairmen should furnish copies of appropriate Task Committee correspondence to the Secretariat of both sides for proper dissemination.

8. Recognizing that wind and seismic disaster mitigation plans benefit disaster-prone countries worldwide, that many developing countries suffer from natural disasters such as extreme winds, storm surges, earthquakes and tsunamis, and that both the U.S. and Japan have been involved in international technical cooperative programs, the Panel will continue efforts to develop and coordinate projects which provide aid and training to developing countries and maintain the exchange of technical information.

9. The Nineteenth Joint Meeting of the UJNR Panel on Wind and Seismic Effects will be held at the Tsukuba Science City, Japan, May 1987. Specific dates, program, and itinerary will be proposed by the Japan Panel with concurrence by the U.S. Panel.

THEME I

Wind Engineering

THE EFFECTS OF LARGE-SCALE UPSTREAM GUSTING
ON THE AEROELASTIC BEHAVIOR OF SECTION MODELS

BY

D. R. Huston[1], H. R. Bosch,[2] and H. Tanaka[3]

ABSTRACT

This paper will describe the results of a recent wind tunnel study which examined the effect of large-scale upstream gusting upon the aeroelastic behavior of bridge deck section models. The large-scale upstream gusts were created with a flapping-airfoil gust generator. The results of the section model studies demonstrate that the method of active gust generation can produce large-scale upstream gusts which are capable of inducing measurable changes in the flutter stability and buffeting response of bridge deck section models. The changes which were induced in the aeroelastic behavior of the section models by upstream gusting will be presented along with an interpretation of these preliminary results.

KEYWORDS: Aeroelasticity; Large-scale; Section model; Turbulence

1. INTRODUCTION

The interaction of a flexible structure and a moving fluid, such as a large suspended-span bridge subjected to wind loading, is an inherently complex problem. The complexities arise because the fluid and structural motions are coupled by the continuity of displacements and tractions at the fluid-structure interface. The presence of turbulence in the flow introduces an additional complication to the interaction problem. An understanding of fluid-structure interaction problems usually requires the introduction of mildly restrictive theoretical assumptions which are then used to formulate parsimonious semi-empirical models with easily measured parameters.

The flexibility and exposure to the wind of the deck structure on a long suspended-span bridge enables an analysis of the wind loading to be conducted by considering only the action of the wind loading upon the flexible bridge deck. If, in addition, "strip-theory" aerodynamics is valid for the bridge deck structure, then it is possible to examine the effects of wind loading on the full bridge structure by studying the dynamics of a conceptual two-dimensional slice of the bridge deck, i.e. a section model. Section models are extremely useful in the theoretical modeling of the aeroelastic behavior of elongated structures. The simplicity of section models also facilitates their use in wind tunnel simulations.

The equations of motion for a two-degree-of-freedom section model take the form:

$$M[\ddot{h} + 2\zeta_h \omega_h \dot{h} + \omega_h^2 h] = -L(t) \qquad [1]$$

$$I[\ddot{\alpha} + 2\zeta_\alpha \omega_\alpha \dot{\alpha} + \omega_\alpha^2 \alpha] = M(t) \qquad [2]$$

where

$h(t)$ = the vertical displacement of the section model

$\alpha(t)$ = the torsional displacement of the section model

$L(t)$ = the lift

$M(t)$ = the aerodynamic moment

The generalized aerodynamic forces are theoretically calculated by integrating the instantaneous local surface pressures which act on the deck section as the section undergoes a virtual vertical or torsional displacement. The fluctuating aerodynamic pressures and the associated generalized forces depend upon the upstream flow conditions, the deck section geometry, the motion history of the deck section and local topographical considerations. Since the theoretical calculation of the local aerodynamic pressures requires an integration

[1] Dept. of Civil Engin., The Johns Hopkins University, Baltimore, MD 21218

[2] Federal Highway Administration, HNR-10, 6300 Georgetown Pk., McLean, VA 20212

[3] Hitachi-Zosen Corp., 3-40, Sakurajima 1-chome, Konohana-ku, Osaka 554, Japan

of the partial differential equations of the unsteady fluid motion around the bluff body, it is usually necessary to invoke additional simplifying assumptions so that the fluid forces can be faithfully modeled. A primary simplifying assumption is to model the fluctuating aerodynamic forces by conceptually separating the aerodynamic forces into two components, one which depends on the motion of the deck section the other being a buffeting force . which depends on the upstream gusting, i.e.:

$$L(t) = L_m(t) + L_b(t) \qquad [3]$$

$$M(t) = M_m(t) + M_b(t) \qquad [4]$$

where the subscripts m and b correspond to the motion-dependent and the buffeting aerodynamic forces, respectively.

Stability of dynamical systems, such as bridge decks subjected to wind loading, about positions of equilibrium can be assessed from the linearized motion-dependent forces acting on the system in the neighborhood of the equilibrium position, ref. (1). The motion-dependent aerodynamic forces are usually expressed in terms of the flutter derivative coefficients as follows, refs. (2) and (3):

$$L_m(s) = \rho U^2 B \left[K H_1^* (K) \frac{h'}{B} + K H_2^*(K) \alpha' + K^2 H_3^* (K)\alpha + K^2 H_4^* (K) \frac{h}{B} \right] \qquad [5]$$

$$M_m(S) = \rho U^2 B^2 \left[K A_1^* (K) \frac{h'}{B} + K A_2^* (K)\alpha' + K^2 A_3^* (K) \alpha + K^2 A_4^* (K) \frac{h}{B} \right] \qquad [6]$$

where s and K are the reduced time and frequency, respectively.

The aeroelastic stability of a bridge deck depends upon whether the combined action of motion-dependent aerodynamic and structural forces will cause a net increase or decrease in the total energy of the system. If the system acts to input energy from the airstream, then the deck motion will become excessively large and eventually result in damage to the structure. Otherwise, the aeroelastic deck-

section system will dissipate the energy contained in incipient motions, thereby forming a stable system. The calculations which assess the aeroelastic stability of the deck sections and the corresponding prototype bridge structures are usually iterative procedures that search for the lowest mean velocity corresponding to a neutrally stable system.

Experiments conducted with bluff bodies indicate that aeroelastic instabilities are usually of the single-degree-of-freedom type which are associated with a negative effective aerodynamic damping. The effective torsional and vertical aerodynamic damping are represented in terms of the $A_2^* (K)$ and the $H_1^*(K)$ flutter derivative coefficients, respectively. Positive trends in either of these flutter coefficients are indicative of destabilizing tendencies. Therefore, a measurement of the $A_2^* (K)$ and the $H_1^* (K)$ flutter derivatives will usually give a very good indication of the tendencies towards bluff-body flutter.

If it is assumed that the motion-dependent aerodynamic forces are indeed independent of the upstream wind gusts, then the stability of the aeroelastic system about a position of equilibrium will be independent of the presence of upstream turbulence and the flutter derivatives will not change under smooth and turbulent flow conditions. However, if the aeroelastic stability is affected by upstream gusting, then the flutter derivatives will be noticeably different under different flow conditions.

Flutter derivatives are usually measured with initial conditions experiments that extract the effective aeroelastic damping from the response that ensues from giving the section model either an initial torsional or vertical displacement.

The buffeting effect of upstream turbulence is to produce generalized aerodynamic forces that are presumably independent of the deck section motion. The turbulent wake downstream of the bluff body, i.e. the signature turbulence, will also produce a buffeting effect, regardless of the presence of upstream turbulence. The combination of upstream turbulence with signature turbulence will presumably produce larger buffeting forces than those which form in smooth flow which are solely attributed to the signature turbulence.

Wind tunnel simulations of the prototype turbulent flow conditions are usually hampered by problems of scale. The wind gusts encountered at the bridge site are, in general, several times larger than the width of a typical bridge deck, ref. (4). The gusts which can be simulated in a wind tunnel by passive methods such as grids, strakes, wooden blocks,

etc. are usually somewhat smaller than the typical bridge deck section model, ref. (5). Two alternative solutions are available for the gust scale simulation problem. One alternative is to use significantly smaller section models, ref. (6). The use of small section models will alleviate the gust scaling problem but will exacerbate Reynolds number scaling problems and problems associated with faithfully reproducing the geometry of the prototype deck sections. The other alternative solution to the gust scaling problem is to use active gust generation techniques such as flapping airfoils or air-jet injectors.

This paper will present some of the results of a wind tunnel investigation of turbulent-wind bridge aeroelasticity. The section models were tested under under smooth and gusting flow conditions. The gusting flow conditions were passively created, in one set of tests, by a grid and actively induced, in another set of tests, by a flapping-airfoil gust generator. The flapping-airfoil gust generator is capable of producing gusts that are several times larger than the width of a deck section.

The following sections will discuss, in succession, the experimental procedures and apparatus, the results of some of the experiments and a preliminary interpretation of the experimental results.

2. EXPERIMENTAL APPARATUS AND PROCEDURES

The innovative apparatus in this project were the flapping airfoil gust generators. The gust generators are positioned upstream of the deck section and create two-dimensionally coherent gusts by flapping an array of airfoils in unison. Two gust generators were used in this manner. One generator, referred to as the in-phase gust generator, flapped all of the airfoils in one direction, thereby controlling vertical gusts. The other generator, referred to as the out-of-phase gust generator flapped two airfoil arrays in opposite directions, thereby tending to choke off the flow and controlling the horizontal gust action.

The use of flapping-airfoil type gust generators for wind engineering purposes was originally proposed by Scanlan, ref. (7). The development of the gust generator technology was conducted at the Colorado State University Fluid Dynamics and Diffusion Laboratories, ref. (8). The result of these studies was the fabrication and installation of flapping-airfoil gust generators in the Federal Highway Administration's G. S. Vincent Wind Tunnel, McLean, VA. Details of some of the flow patterns that can be produced with the active gust generators can be found in ref. (9). A schematic diagram of the flapping-airfoil gust generator mechanism is shown in fig. 1.

The experiments that are reported in this paper represent the first use of the flapping-airfoil gust generators, described above, to the testing of bridge deck section models. Therefore, the experiments were designed so that the influence of the gust generators could be easily detected and evaluated. This design entailed performing standard state-of-the-art testing procedures on section models in both smooth and gusting flow patterns.

Two types of smooth flow patterns were employed in this study. One type was formed when the gust generators were removed from the wind tunnel. The resulting undisturbed airstream was quite smooth with a turbulence intensity of less than 1%. This approximately laminar flow will be referred to as the "Laminar" flow. The other type of smooth flow was produced, while the gust generators were installed in the wind tunnel. This flow was created by passing the air through the generators with the airfoils held in a neutral stationary position. The resulting flow was reasonably smooth flow with an intensity of approximately 3%. The flow produced by holding the gust generator airfoils in a neutral position, will be referred to as the "Neutral" flow.

Large-scale gusting flow patterns were induced by flapping the airfoils on the in-phase gust generator with a large-amplitude, 2.0 Hz. cutoff, low-pass filtered white noise random driving signal. This driving signal was selected so that the gust generators would produce produce one of the more violently turbulent flow patterns that the gust generators were capable of synthesizing. The gusting flow, which formed downstream of the generators and upstream of the section models, with this driving signal, was not intended to simulate any specific prototype field condition, but rather it was simply a large-scale high intensity flow pattern. Since the flow was produced by driving the in-phase gust generator with a 2.0 Hz. low-pass filtered white noise random signal, hereinafter it will be referred to as the "Low-Pass" flow. The intensity of the turbulence contained in the "Low-Pass" flow was measured at 20%. The length of the resulting gusts was quite large and could be extended, in theory, to infinity.

An additional type of turbulent flow was created by placing a 4x4 wood lath grid across the mouth of the wind tunnel. The wooden grid induced turbulence intensities that ranged from 10% to 20%. The flow pattern produced by the wooden grid will be referred to as the "Grid Turbulent" flow. The scale of the "Grid" turbulence and the spanwise coherence was somewhat smaller than that of the "Low-Pass" flow.

Three different section models were tested under these four flow regimes. The deck section models were geometrically faithful slices of the Deer Isle-Sedgewick, Maine, bridge, a proposed fairing-modified version of the Deer Isle bridge and the Golden Gate Bridge, San Francisco, Calif., figs. 2.a-c. The unmodified Deer Isle bridge is of the plate girder or H-type. The proposed fairing-modified version of the Deer Isle bridge forms a rather streamlined deck section. The Golden Gate deck section is of the open-truss type.

The standard section model tests consisted of: 1.) measuring the motion-dependent aerodynamic forces, i.e. the flutter derivatives, by initial condition experiments, 2.) recording the stationary response of the section model to stationary wind conditions. Both sets of experiments were performed with the deck section models mounted on flexible springs. This elastic support structure was constructed to permit motion in the vertical direction and in a torsional direction about as spanwise-running axis. The support structure was designed to restrain or enable the vertical and the torsional degrees of freedom separately, if desired. Therefore, the section model could be configured as either a single-degree-of-freedom system or as a two-degree-of-freedom system.

All of the flutter derivatives were measured with the section model configured to act as a single degree of freedom system. The flutter derivatives that could be measured with an S.D.O.F. setup were measured the $A_2^*(K)$, $A_3^*(K)$, $H_3^*(K)$ and the $H_4^*(K)$ flutter derivatives, i.e. the auto-excited flutter derivatives. The stationary time histories were recorded with the deck sections mounted in three different configurations, one which permitted single degree of freedom vertical motion, one which permitted single degree of freedom torsional motion and one which permitted two degree of freedom combined vertical and torsional motion.

3. EXPERIMENTAL RESULTS

3.1 Flow Measurements

The ability of the gust generators to produce controllable gusts is demonstrated by figs. 3-5. Figs. 3.a and 3.b are strip chart recordings of the flow that resulted from holding the airfoils in a stationary neutral position, i.e. the "Neutral" flow, at a mean velocity of 7 ft./sec, with an intensity of about 3%. An observation of these traces indicates that the "average" gust size is of the order of 1 ft. or less. Figs. 4.a, 4.b and 4.c are traces of the actuator motion and the gust velocities that result from flapping the in-phase airfoils with a 2.0 Hz. low-pass filtered, large-amplitude, white noise signal. The intensity of the resulting turbulence was 20%. An observation of figs. 4.b and 4.c

indicates that the "average" gust size which results from using these flow patterns is at least 7 ft, which is several times larger than the 1ft.-2ft. range of typical section model widths. Spectra of the actuator motion, vertical gust velocity, and the horizontal gust velocities which correspond to the "Low-Pass" flow are shown in fig. 5.

3.2 Flutter Derivative Measurements

The $A_2^*(K)$, $A_3^*(K)$, $H_3^*(K)$, and $H_4^*(K)$ flutter derivatives were extracted from the three section models under smooth and gusting flow patterns. fairing-modified Deer Isle deck section and the Golden Gate deck section were all measured under smooth and gusting flow conditions. Both versions of the Deer Isle deck section were tested under the "Laminar," "Neutral," "Grid Turbulent," and "Low-Pass" flows. The Golden Gate deck section was tested only under the "Neutral" and the "Low-Pass" flows.

The flutter derivatives which were measured by initial condition experiments are shown in figs. 6-8. Figs. 6.a-6.d contain the flutter derivatives that were extracted from the unmodified Deer Isle deck section. Figs. 7.a-7.d are the flutter derivatives which were extracted from the fairing-modified version of the Deer Isle deck section. Figs. 8.a-8.d are the flutter derivatives which were extracted from the Golden Gate deck section.

All of the flutter derivatives that are shown in figs. 6-8 were calculated from estimates of the effective aeroelastic damping and natural frequency. These estimates were performed with a digital version of the logarithmic decrement procedure that used all of the local maxima and minima in the free vibration response of the deck section to calculate the desired system parameters, ref. (10).

Since the logarithmic decrement procedure is strictly applicable to the case where a linear system is oscillating as the result of nonzero initial conditions without any applied external forces, such as buffeting forces, it was decided to verify some of the measured flutter derivatives with an independent procedure. One alternative method of estimating damping ratios and natural frequencies of elastically supported section models, is to measure the width of the peak that occurs in the spectrum of the displacement that results from buffeting the section with a broadbanded stationary random excitation. A modified version of this procedure which used a least-squares spectral curve fitting procedure, ref. (10), coupled with the use of a Maximum Entropy spectral estimator, ref. (11), was used to remeasure the $A_2^*(K)$ flutter derivative under smooth and gusting flow conditions. The results of this independent flutter derivative extraction

procedure to the stationary response of the Golden Gate deck section are shown in fig. 9.

Since it is impractical to measure the reference zero-velocity viscous damping ratio by the spectral width procedure, the vertical positioning of the horizontal axis in fig. 9 is uncertain. If the mean of viscous damping ratios where were measured with transient initial condition experiments was employed, then the horizontal-axis takes the position of the solid line in fig. 9. However, since the $A_2^*(K)$ flutter derivative should approach zero as the reduced velocity approaches zero the horizontal axis in fig. 9 should be shifted to reflect this physical constraint. The dashed horizontal axis which appears in fig. 9 reflects this ad hoc axis shift, which is based on physical reasoning.

3.3 Stationary Buffeting Response

The motions which resulted from allowing the elastically-supported section models to oscillate freely in the presence of buffeting forces due to upstream and signature turbulence were digitized and recorded on magnetic tape. Figs. 10-12 contain plots of the dimensionless root mean square displacement versus the reduced velocity for four different motion conditions. The torsional displacement is expressed in terms of radians, the vertical motion is rendered nondimensional by dividing the motion by the deck width. The wind velocity is reduced by the free vibration natural frequency of the particular degree of freedom under consideration and by the deck width.

The use of three different end support conditions required the observation of four different types of motion. The four displacement-types were: 1.) vertical single-degree-of-freedom motion, 2.) torsional single-degree-of-freedom motion, 3.) the vertical component of a two-degree-of-freedom motion, and 4.) the torsional component of two-degree-of-freedom motion. Figs. 10.a.-c. contain the RMS vs reduced velocity plots for the unmodified Deer Isle deck section under four flow conditions. Fig. 11.a.-d. contain the rms displacement vs. reduced velocity plots for the fairing-modified Deer Isle deck section. Figs. 12.a.-12.d. contain the RMS displacement vs. reduced velocity plots for the Golden Gate deck section.

4. INTERPRETATIONS AND CONCLUSIONS

The measurements of the flow conditions downstream of the gust generators indicated that the flapping airfoils are indeed capable of producing controllable large-scale gusts. If the airfoils are held in a neutral stationary position the resulting turbulence flow field is probably smooth enough to be used

as a nongusting reference flow condition. The ability of the gust generators to simulate prototype field conditions has not been entirely verified, although these studies indicate that it should at least be possible for those prototype conditions where the turbulence intensity exceeds 10%.

The flutter derivative measurements indicated that the presence of upstream turbulence will produce noticeable changes in the flutter derivatives. The $A_2^*(K)$ flutter derivative for the unmodified Deer Isle deck section displayed a moderate change under smooth and gusting flow conditions. The $A_2^*(K)$ derivative for the "Laminar" flow was unmeasurable in the reduced velocity range of 2-4 because of strong vortex-shedding action. The results indicate that the presence of the upstream turbulence in the "Low-Pass" flow have indicated causes a slight positive trend in the $A_2^*(K)$ derivative, which indicates a destabilizing tendency due to the upstream gusting. The fairing-modification to the Deer Isle deck section produced radically different flutter derivatives from those of the unmodified Deer Isle deck section. Nevertheless, the presence of upstream gusting in both the "Grid Turbulent" and the "Low-Pass" flow causes an increased positive (destabilizing) trend in the $A_2^*(K)$ derivative. Likewise the $A_2^*(K)$ derivative for the Golden Gate Deck section also showed this same destabilizing trend in the $A_2^*(K)$ derivative for the smooth and gusting flows.

Since the tendency of upstream gusting to produce an increased aeroelastic torsional instability is somewhat contrary to the conventional wisdom that turbulence is a stabilizing factor in bluff-body aerodynamics, the $A_2^*(K)$ flutter derivative for the Golden-Gate deck section was also measured by the alternative least-squares spectral width procedure. The remeasured $A_2^*(K)$ derivative shows the same destabilizing tendencies due to upstream gusting as that of the transient response measurements. Therefore, in addition to verifying the result that upstream gusting can indeed exert a destabilizing influence upon the torsional dynamic motion of bridge deck section models, the two methods of system identification were verified.

The RMS displacement vs. reduced velocity curves exhibited a behavior that was consistent with the results of the flutter derivative experiments. The unmodified Deer Isle deck section showed an increased RMS response due to the upstream gusting except for certain isolated peaks which may be attributed to the vortex-shedding action in the smoother "Laminar" and "Neutral" flows. The changes in the flutter stability of the flutter stability of the unmodified Deer Isle deck section were not extremely dramatic. The fairing-modified Deer Isle deck section showed a considerable

7

increase in the vertical motion due to the presence of upstream turbulence. Since the addition of fairings produced a deck section that was quite stable, no changes were observable in the aeroelastic stability of the fairing-modified Deer Isle deck section. The Golden Gate section also exhibited an increased vertical response to upstream gusting. The presence of turbulence in the "Low-Pass" flow caused to section to become unstable at a lower velocity than that which was encountered in the smoother "Neutral" flow. This destabilizing trend was verified by the flutter derivative measurements. The instability which appeared in the Golden Gate motion was a torsional flutter-type instability, in spite of rather larger vertical buffeting motions.

Some of the overall conclusions that can be drawn from this study are that the use of flapping-airfoil type gust generators is a viable method of producing controllable large-scale gusting flow patterns. The future research capabilities of this apparatus are virtually unlimited. The measured changes in the aeroelastic behavior of the section models, at present forms a rather small data base. However, the preliminary conclusions that can be drawn from these results are that large-scale upstream gusting may, in some circumstances, be destabilizing and the gusting will possibly suppress vortex-shedding action.

ACKNOWLEDGMENTS

REFERENCES

(1) Meirovitch, L., Methods of Analytical Dynamics, McGraw-Hill, 1970.

(2) Scanlan, R. H. and Tomko, J. T., " Airfoil and Bridge Deck Flutter Derivatives" ASCE, Jnl. Eng. Mech. Div., pp. 1717-1737, Dec. 1971.

(3) Beliveau, J. G. Suspension Bridge Aeroelasticity Nonlinear Least Squares Techniques for System Identification, doctoral dissertation, Dept. of Civil Engineering, Princeton University, Sept. 1973.

(4) Counihan, J. "Adiabatic Atmospheric Boundary Layers: A Review and Analysis of Data from the Period 1880-1972" Atmos. Environ., 9(1975), 871-905.

(5) Jancauskas, E. D. and Melbourne, W. H., "The Aerodynamic Admittance of Two-Dimensional Rectangular Section Cylinders in Turbulent Flow," Proc. Fifth U.S. National Conference on Wind Engineering, Lubbock, Texas, 1985.

(6) Lin, W. H., Forced and Self-Excited Responses of a Bluff Structure in a Turbulent Wind, Ph.D. dissertation, Princeton University, 1977.

(7) Bienkiewicz, B., Cermak, J. E., Peterka, J., and Scanlan, R. H., "Active Modeling of Large-Scale turbulence," J. Wind Eng. Ind. Aerodyn,. 13(1983), 465-476.

(8) Cermak, J. C., Bienkiewicz, B. and Peterka, J., Active Modeling of Turbulence for Wind Tunnel Studies of Bridge Models, Final Report FHWA/RD-82/148.

(9) Huston, D. R., and Bosch, H., "Active Modeling of Turbulence for Section Model Studies," Presented at the 16th U.S.-Japan Joint Panel on Wind and Seismic Effects, National Bureau of Standards, Gaithersburg, MD, May 1984.

(10) Huston, D. R., The Effects of Upstream Gusting Upon the Aeroelastic Behavior of Long Suspended-Span Bridges, doctoral dissertation, Princeton University, Department of Civil Engineering, May 1986.

(11) Robinson, E. A., Multichannel Time Series Analysis With Digital Computer Programs, Holden-Day, San Francisco, 2nd Ed., 1978.

A = Horizontal Gust Control

B = Vertical Gust Control

C = Linkage

D = Hydraulic Actuators

E = Bridge Model
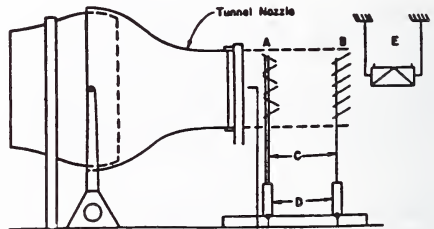
Fig. 1. Line drawing of the flapping-airfoil gust generators positioned downstream of the wind tunnel exhaust nozzle and upstream of the section model.

8
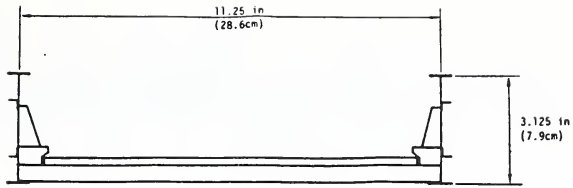
Fig. 2.a. Unmodified Deer Isle-Sedgewick, Maine, bridge deck section.
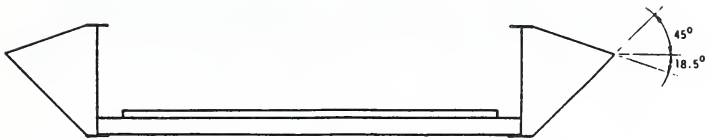
Fig. 2.b. Fairing-modified version of the Deer Isle deck section.
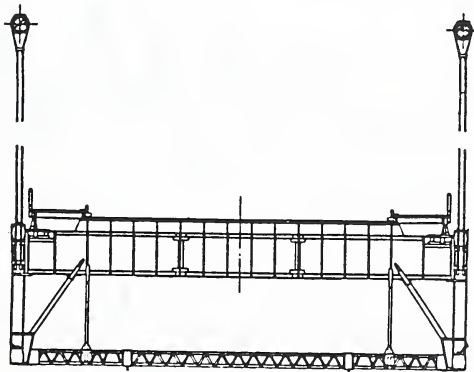
Fig. 2.c. Golden Gate deck section.

a. Horizontal gusting.
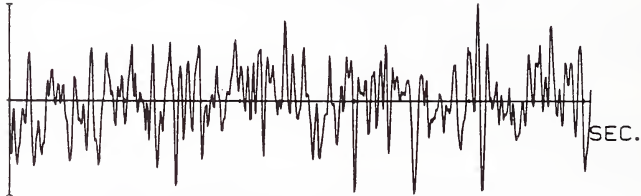
b. Vertical gusting.

Fig. 3. Typical simultaneous gust velocity time histories for the "Neutral" flow at a nominal mean velocity of 7 ft./sec.
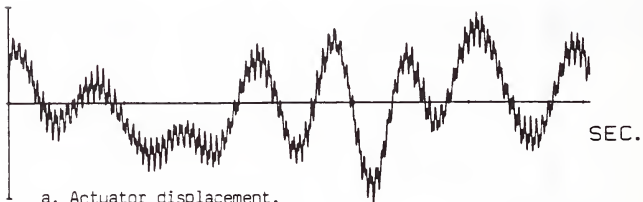
a. Actuator displacement.
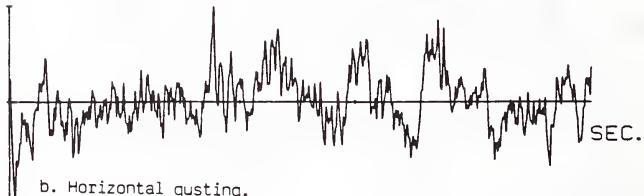
b. Horizontal gusting.

Fig. 4. Typical simultaneous gust velocity time histories for the "Low-Pass" flow at a nominal mean velocity of 7 ft./sec.

SEC.

c. Vertical gusting.
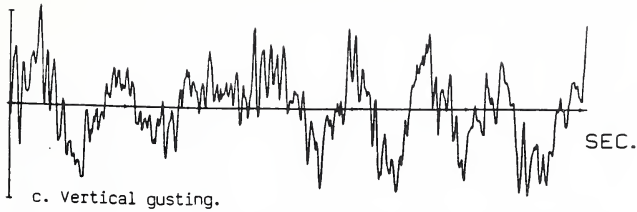
Fig. 4. (cont.) Typical simultaneous gust velocity time
histories for the "Low-Pass" flow at a nominal
mean velocity of 7 ft./sec.

Horizontal Velocity Spectrum   Hz.

Vertical Velocity Spectrum   Hz.

Actuator Displacement Spectrum
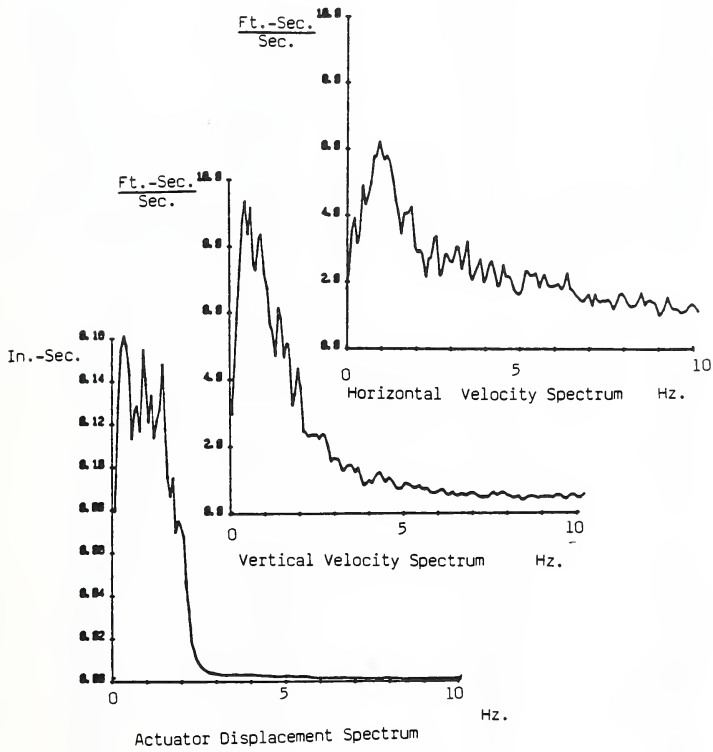
Fig. 5. Actuator and gust velocity spectra
corresponding to the "Low-Pass" flow.
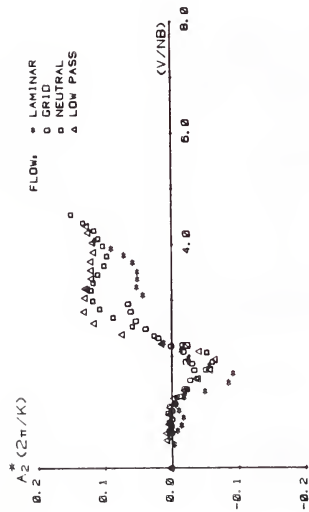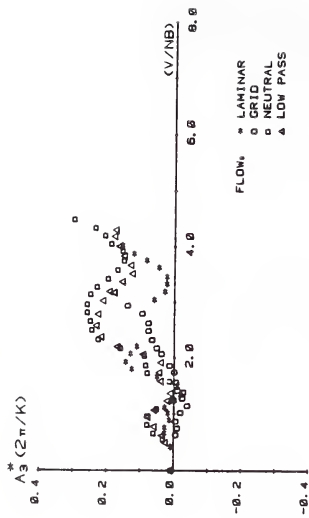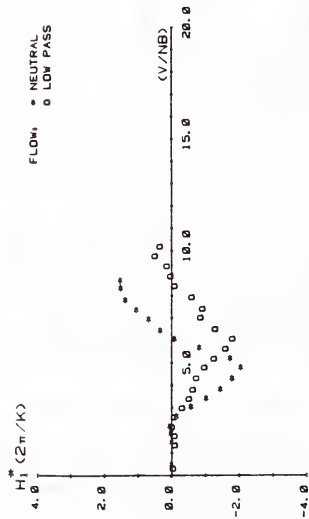
11

Fig. 6. Unmodified Deer Isle bridge: flutter derivatives, extracted from initial condition experiments.
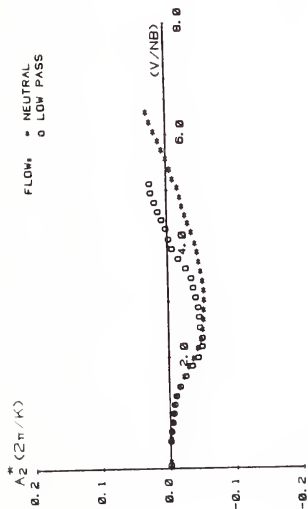
a. A_2^* vs. reduced velocity.

b. A_3^* vs. reduced velocity.

c. H_1^* vs. reduced velocity.

d. H_4^* vs. reduced velocity.

Fig. 7. Fairing-modified version of the Deer Isle bridge: flutter derivatives, extracted from initial condition experiments.

a. A_2^* vs. reduced velocity.

b. A_3^* vs. reduced velocity.

c. H_1^* vs. reduced velocity.

d. H_4^* vs. reduced velocity.

13

a. A_2^* vs. reduced velocity.
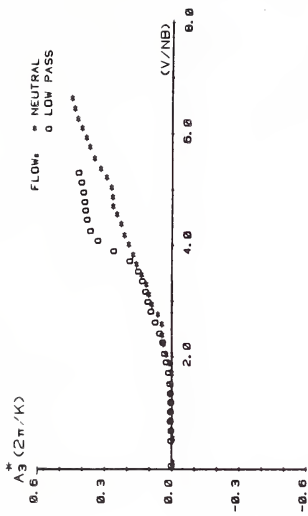
b. A_3^* vs. reduced velocity.
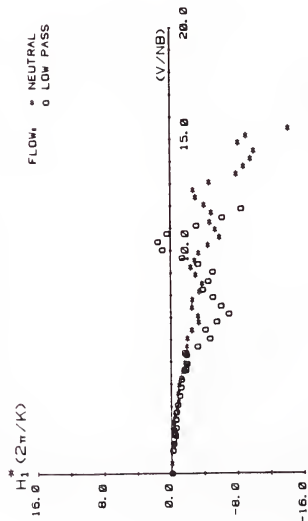
c. H_1^* vs. reduced velocity.
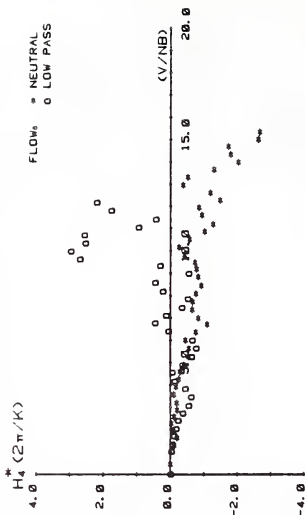
d. H_4^* vs. reduced velocity.

Fig. 8. Golden Gate deck section: flutter derivatives extracted from initial condition experiments.

14
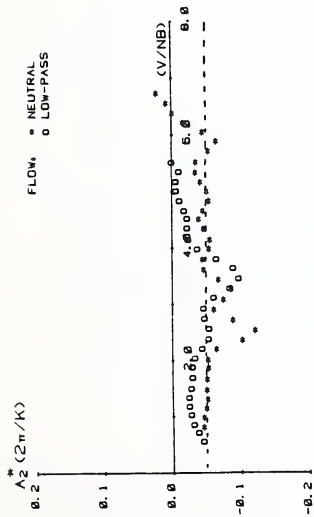
Fig. 9   Golden Gate Bridge deck section flutter derivative, extracted by the stationary time history method, (-----) indicates ad hoc shift in the vertical axis.
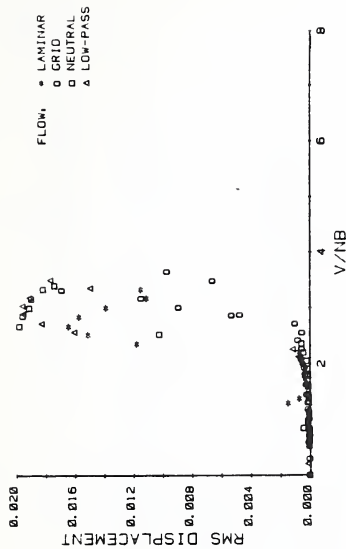
Fig. 10.a.   Unmodified Deer Isle deck section, RMS torsional disp. vs. reduced velocity, torsion and vertical D.O.F. enabled.
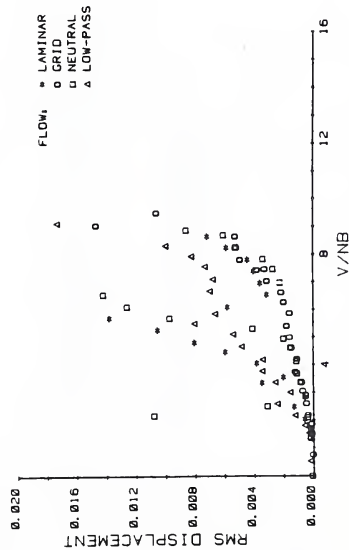
Fig. 10.b.   Unmodified Deer Isle deck section, RMS vertical disp. vs. reduced velocity, torsion and vertical D.O.F. enabled.
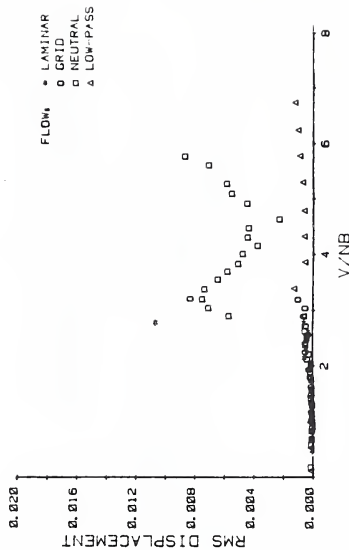
Fig. 10.c.   Unmodified Deer Isle deck section, RMS torsional disp. vs. reduced velocity, torsion D.O.F. enabled.

15
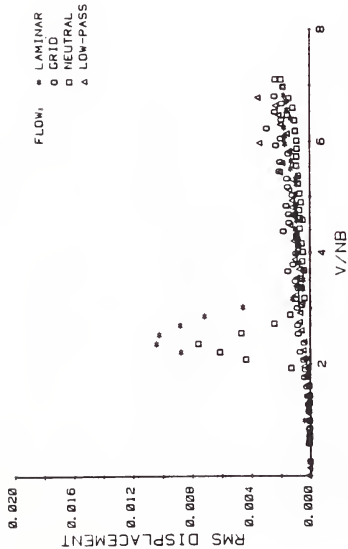
Fig. 11.a. Fairing modified Deer Isle deck section, RMS torsional disp. vs. reduced velocity, torsion and vertical D.O.F. enabled.
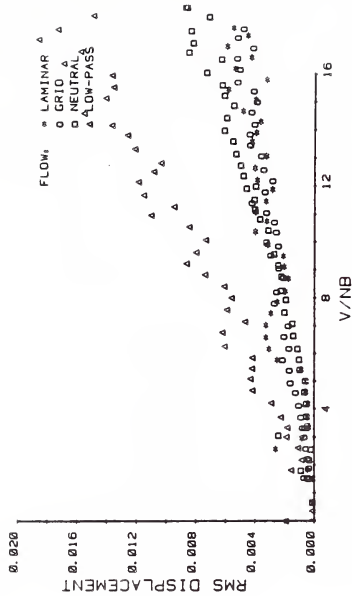
Fig. 11.b. Fairing modified Deer Isle deck section, RMS vertical disp. vs. reduced velocity, torsion and vertical D.O.F. enabled.
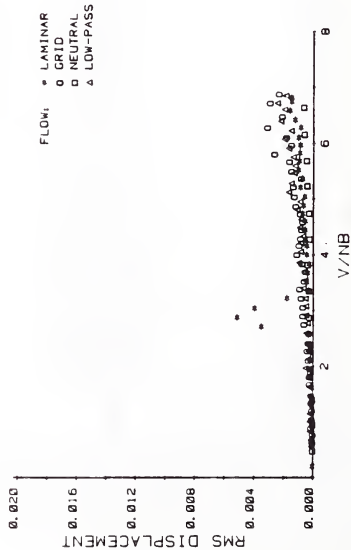
Fig. 11.c. Fairing modified Deer Isle deck section, RMS torsional disp. vs. reduced velocity, torsion D.O.F. enabled.
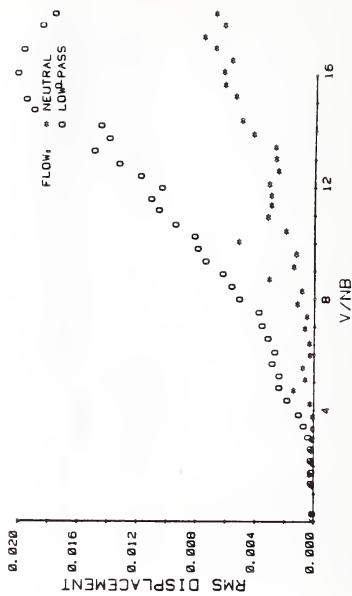
Fig. 11.d. Fairing modified Deer Isle deck section, RMS vertical disp. vs. reduced velocity, vertical D.O.F. enabled.

16
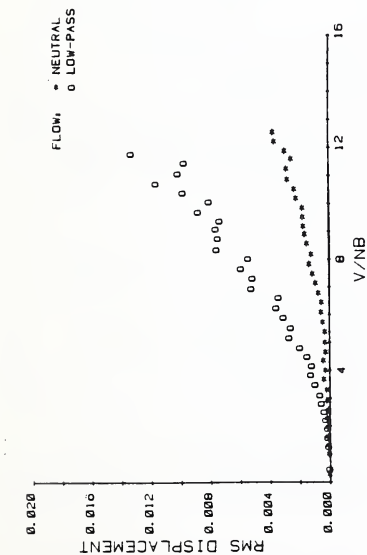
Fig. 12.a. Golden Gate deck section, RMS vertical disp. vs. reduced velocity, torsion and vertical D.O.F. enabled.
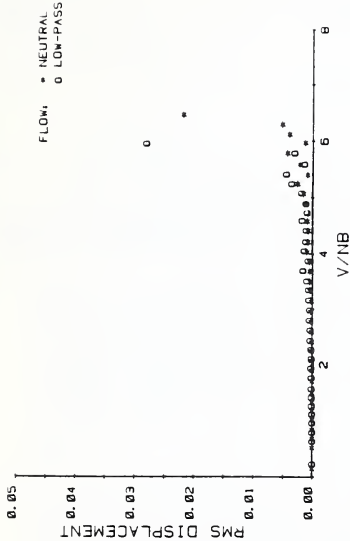
Fig. 12.b. Golden Gate deck section, RMS torsional disp. vs. reduced velocity, torsion and vertical D.O.F. enabled.
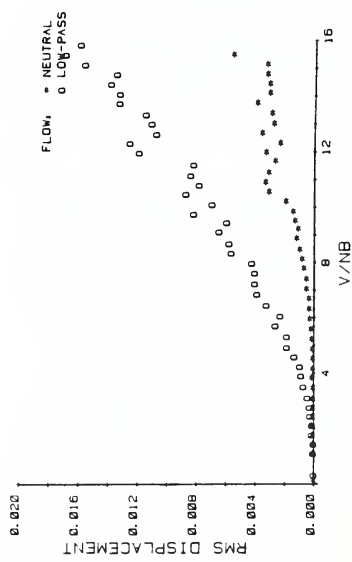
Fig. 12.c. Golden Gate deck section, RMS vertical disp. vs. reduced velocity, vertical D.O.F. enabled.
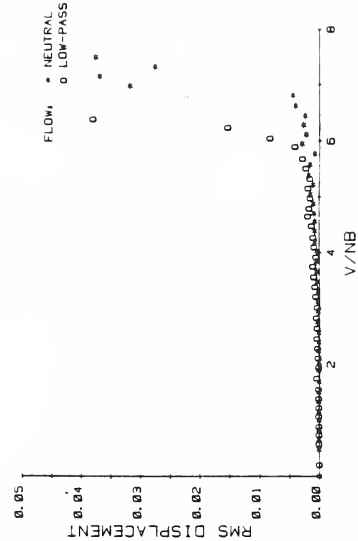
Fig. 12.d. Golden Gate deck section, RMS torsional disp. vs. reduced velocity, torsion D.O.F. enabled.

17

ON THE EVALUATION OF WIND-INDUCTED VIBRATIONS OF LONG-SPAN
BRIDGES USING TAUT-STRIP MODELS

Nobuyuki Narita*, Hirohiko Tada*, Koichi Yokoyama*,
Hiroshi Sato*, Kazuo Kanzaki*, and Makoto Fukuda*

ABSTRACT

The taut-strip model test is a new wind tunnel
technique. A bridge deck model is attached to
two parallel taut piano wires, and its respon-
ses to wind are measured. The advantages of
the taut-strip model test over the section
model test are that the model can be tested in
turbulent boundary layer flow, and that the
model is three dimensional. Therefore, the
properties of wind and bridge vibrations for
taut-strip model tests are more similar to
prototype than those for section model tests.
Also, the construction cost of the taut-strip
model is less expensive than that of full
bridge model.

This paper describes the design method of the
taut-strip model, the simulation method of
turbulent boundary layer flow, and the test
results on the wind-induced vibrations of the
taut-strip models. The flutter speed of the
flat plate model was compared with the one
calculated from Selberg's formula, and the
vibrations of the box girder model were
compared with those observed at the real cable
stayed bridge. It was confirmed that the taut-
strip model test is one of the effective
techniques for evaluation of the wind-induced
vibrations of long-span bridges with box girder
deck.

1. INTRODUCTION

The wind-resistance of long-span bridges in
Japan have been investigated and proved through
the section model tests in smooth flow.
Natural wind, however, is turbulent flow, whose
wind speed varies with time and space, and the
vibrational displacement of bridge deck varies
along the bridge axis. Therefore, the wind-
induced vibrations of long-span bridges can not
be predicted directly from the section model
tests in smooth flow. On the other hand, the
wind-induced vibrations can be obtained
directly through the full bridge model tests in
turbulent boundary layer flow if the structural
properties and flow properties are kept similar
to those of prototype. The construction of
full bridge model, however, is more expensive
and difficult than that of section model.

*Public Works Research Institute, Ministry of
Construction, Tsukuba, Japan.

Recently, a new technique called taut-strip
model test has been developed (1,2). In taut-
strip model tests, the bridge deck model is
attached to two parallel taut piano wires, and
its responses to wind are measured. The
advantages of the taut-strip model test over
the section model test are that the model can
be tested in turbulent boundary layer flow, and
that the model is three dimensional. There-
fore, the properties of wind and bridge vibra-
tions for taut-strip model tests can be kept
more similar to prototype than those for sec-
tion model tests. Another advantage is the
construction cost of the taut-strip model is
less expensive than that of full bridge model.

This paper describes the design method of the
taut-strip model, the simulation method of
turbulent boundary layer flow, and the test
results on the wind-induced vibrations of the
taut-strip models. The flutter speed of the
flat plate model was compared with the one
calculated from Selberg's formula, and the
vibrations of the box girder model were
compared with those observed at the real cable
stayed bridge.

2. DESIGN METHOD OF TAUT-STRIP MODEL

2.1 Similarity Requirements

In the wind tunnel test of long-span bridges,
the following nondimensional parameters should
be kept the same between prototype and model.

$$\sigma = m/(\rho B^2), \quad \gamma = I/(\rho B^4),$$

$$U/(f_h B), \quad U/(f_\theta B), \quad \delta_h, \quad \delta_\theta, \quad f_\theta/f_h$$

where, m: mass per unit length of the bridge,
    ρ: air density
    B: bridge deck width
    I: mass moment of inertia per unit
       length of the bridge
    U: mean wind speed
    f_h: natural frequency of vertical bending
       mode
    f_θ: natural frequency of torsional mode
    δ_h: logarithmic decrement of vertical
       bending vibration
    δ_θ: logarithmic decrement of torsional
       vibration

To simulate the natural wind, the following
parameters should be kept the same.

$$U_{Z2}/U_{Z1}, \quad I_u, \quad I_w, \quad L_u/B, \quad L_w/B$$

where, U_{Z1}: mean wind speed at the height of Z1
U_{Z2}: mean wind speed at the height of Z2
I_u: turbulence intensity of u(longitudinal component of fluctuating wind speed)
I_w: turbulence intensity of w(vertical component of fluctuating wind speed)
L_u: integral scale of turbulence of u
L_w: integral scale of turbulence of w

The structural dimensions of the taut-strip model can be determined by the following process.

a. The scale ratio should be decided considering the width of the test section of the wind tunnel, span length of the bridge, the integral scale of turbulence of the natural wind at the construction site, and that of the boundary layer generated in the wind tunnel.

b. The required values of m and I should be calculated using the scale ratio.

c. The natural frequencies f_h and f_θ should be decided so that the wind-induced vibrations for the required wind speed range may be investigated in the wind tunnel. Attension should be paid to the sag when small values of f_h and f_θ are applied.

2.2 Natural Frequency

Since the required values for m and I are given from similarity requirements, the natural frequencies should be adjusted by changing the stiffness of the taut-strip model. The stiffness of the model is given by the taut piano wires and the bridge deck model. When the bridge deck model is separated into several segments and attached to the taut piano wires, the bending stiffness of the bridge deck model does not contribute to that of the whole taut-strip model. Only the stiffness due to the piano wires should be considered. For the torsional stiffness, the contribution of the bridge deck model depends on the length where the road deck model is attached to the piano wires. If each deck segment is attached by point, the torsional stiffness of the deck model can be neglected. In the case that the length of the attached part is not negligibly small, the effect of the torsional stiffness of the bridge deck should be considered.

The natural frequencies f_h and f_θ of the taut-strip model can be calculated by the following formulae when the bridge deck model segments are fully attached to the taut piano wires.

$$f_h = (2l)^{-1}(2P/m)^{\frac{1}{2}}$$

$$f_\theta = (b/(4l)) \; (2P/I)^{\frac{1}{2}}(1+(2GJ)/(Pb^2))^{\frac{1}{2}}$$

$$f_\theta/f_h = (b/2) \; (m/I)^{\frac{1}{2}}(1+(2GJ)/(Pb^2))^{\frac{1}{2}}$$

where, P: tension per one piano wire
l: length of the taut-strip model
b: separation of the two piano wires
GJ: torsional stiffness of the bridge deck model

f_h can be adjusted by P, and f_θ/f_h can be adjusted by GJ and b.

When the each bridge deck segment is attached by point, the formulae can be rewritten as follows.

$$f_h = (2l)^{-1}(2P/m)^{\frac{1}{2}}$$

$$f_\theta = (b/(4l)) \; (2P/I)^{\frac{1}{2}}$$

$$f_\theta/f_h = (b/2) \; (m/I)^{\frac{1}{2}} = (b/(2B)) \; (\sigma/\gamma)^{\frac{1}{2}}$$

To keep the piano wires inside the deck model, b should be less than B. Therefore f_θ/f_h is less than $0.5(\sigma/\gamma)^{\frac{1}{2}}$. If the required f_θ/f_h is larger than this value, the taut-strip model should be constructed so the torsional stiffness of the bridge deck model may contribute to the whole taut-strip model.

3. SIMULATION OF TURBULENT BOUNDARY LAYER FLOW

3.1 Simulation Method

For the simulation of turbulent flow, the turbulence properties of natural wind at the bridge construction site should be investigated. In the case that field observations can not be made, the properties may be estimated from the references (3,4,5).

Among many non-dimensional parameters for similarity requirement, the power law exponent α was chosen as a fundamental parameter, because it reflects the effect of the terrain roughness in a simple manner. Typical values of α for several terrain conditions are as follows (3,4).

Rough Sea	$\alpha=0.12$
Open Grassland	$\alpha=0.16$
Suburban Areas	$\alpha=0.28$
City Centres	$\alpha=0.40$

In the wind tunnel, turbulent boundary layer flow can be generated by floor roughness and spires. The relation between the shape of spires and α is shown in the reference (6). Appropriate floor roughness should be chosen to make α a required value.

3.2 Experiment

The low speed wind tunnel of the Public Works Research Institute, with test section of 2.5m wide, 4m high and 10m long, was used for the experiment. The four corners of the test section have been cut by 0.4m, and the width of the tunnel floor is 1.7m. To use the full width of the test section, the surface floor was installed 0.4m above the wind tunnel floor as is shown Fig. 1. At the upstream end of the surface floor, the fairing plate was attached to prevent the separation of the flow. In the case of the generation of smooth flow, a shorter surface floor was used as is shown in the table of Fig. 1.

The aim of the experiment was the generation of turbulent boundary layer flows whose power law exponents correspond to the natural wind over rough sea (turbulent flow I), open grassland (turbulent flow II) and suburban area (turbulent flow III). The arrangement of the spires and the floor roughness for each turbulent flow is shown in Fig. 1. The measurement was made by hot-wire anemometer.

3.3 Results

3.3.1 Wind Profile

The vertical profiles of the mean wind speed of the turbulent boundary layer flow are shown in Fig. 2. The power law distributions are also plotted in the figure. Although the exponent of the turbulent flow III is slightly higher than the typical value for suburban areas, the wind profiles of the turbulent flow generated in the wind tunnel are fairly similar to those of the natural wind.

3.3.2 Properties of the Turbulence

The power spectral density functions (PSD) S of the fluctuating wind speed were calculated and reduced by frequency f and mean wind speed at the height of Z, U_Z. The reduced PSD, fS/U_Z^2 are plotted against reduced frequency fB/U_Z (where B is bridge deck width) in Fig. 3. The values of Z and B for the experiment are 0.14m and 0.0925m, respectively, which correspond to the height and the deck width of the 1/200 bridge deck model, whose wind-induced vibrations are described in Chapter 4. The PSD's of natural wind for typical surface conditions are also plotted in Fig. 3, using the Engineering Science Data Unit (5). The surface roughness parameters z_0 were assumed as follows (5).

Large Expanses of Water	$z_0=0.001m$
Fairly Level Grass Plains	$z_0=0.01m$
Outskirts of Towns	$z_0=0.4m$
Centres of Large Towns	$z_0=1m$

In this case, the values of the prototype cable stayed bridge were used for B and Z.

Since

$$fS/U_Z^2 = I^2 \ (fS/\sigma^2)$$

$$f_B/U_Z = B/L \ (Lf/U_Z)$$

where σ is standard deviation of fluctuating · wind speed, the extent of similarity about turbulence intensity I and scale of turbulence L can be judged by comparing the plotted PSD of the experiment with that of the prototype. From the figure, it is shown that the turbulence scales are almost similar between model and prototype when the scale ratio of the model is about 1/200. As for the turbulence intensities, the turbulent flow generated in the wind tunnel may be regarded as the model of natural wind over the following surface conditions.

Turbulent Flow I	Large Expanses of Water
Turbulent Flow II	Fairly Level Grass Plains
Turbulent Flow III	Outskirts of Towns or Centres of Large Towns

4. WIND-INDUCED VIBRATIONS OF TAUT-STRIP MODEL

4.1 Cases and Conditions of Experiment

To confirm the applicability of the taut-strip model test to the resistant design of long-span bridges, flat plate models and box girder models were constructed. The flutter speed of the flat plate model can be compared with the theoretical value. The 1/200 model of the cable stayed bridge, where wind and responses of the bridge deck have been observed (7), was constructed so the responses of the model could be compared with the ones observed at the bridge site.

The taut-strip models are shown in Fig. 4. For the flat plate, two models with different frequency ratio f_θ/f_h were constructed. For the box girder, the model with the flap plates was constructed as was the model with usual handrails. The flap plate is one of the aerodynamic devices for reduction of the vortex-induced vibrations, and it was applied to this cable stayed bridge.

The structural properties of the taut-strip models and those of the prototype cable stayed bridge are shown in Table 1. Except for the logarithmic decreasement of the torsional vibration, the structural properties of the box girder model is fairly similar to those of the prototype.

The experimental cases are shown in Table 1. Wind-induced vibrations were measured in the smooth flow and in the turbulent flow II. The turbulent flow II was chosen because its turbulence properties are similar to those of the wind at the cable stayed bridge site.

In the experiment, the displacement at the center of the model was measured by the optical displacement meter. The wind direction was perpendicular to the model axis, and the angle of inclination was 0.

4.2 Results

4.2.1 Flat Plate Model

The relations between the vibrational displacement and the mean wind speed are shown in Fig. 5. The maximum and the root mean square of the displacement were calculated using 1 minute data, and reduced by the deck width B. The main findings are as follows:

a. Coupled flutter was observed for the model of small frequency ratio tested in the smooth flow (Case 1).

b. The reduced flutter speed ($U_Z/(f_\theta B)$) was about 8, which agreed fairly well with the one ($U_Z/(f_\theta B)$)=7.8) calculated from Selberg's formula (8).

c. Buffeting of vertical bending mode and torsional mode was observed for the model of small frequency ratio tested in the turbulent flow (Case 2).

d. For the model of large frequency ratio, coupled flutter or remarkable buffeting of torsional mode was not observed (Case 3,4), because of the reduced wind speed range tested was low.

4.2.2 Box Girder Model

The experimental results of the box girder models are shown in Fig. 6 in the same manner as those of the flat plate models. The main findings are as follows.

a. Vortex-induced vibrations of vertical bending mode were observed in the reduced wind speed ($U_Z/(f_h B)$) from 2.0 to 2.5 for the usual handrail model tested in the smooth flow (Case 5).

b. The amplitudes of the vibrations were reduced remarkably by attaching the flap plate (Case 7).

c. In the turbulent flow, no vortex-induced vibration was observed, but the buffeting of vertical being mode was observed for the usual handrail model and for the flap model (Case 6,8).

Since the experimental condition of Case 8 was regarded as the most similar to the prototype cable stayed bridge, its responses were compared with those observed at the bridge. The results are shown in Fig. 7. At the bridge, wind and response data have been collected up to the mean wind speed of 30 m/s, and responses are regarded as the buffeting of vertical bending mode. As far as this wind speed range is concerned, the responses estimated from the taut-strip model test agree fairly well with those observed at the prototype cable stayed bridge.

5. CONCLUSIONS

The taut-strip models for flat plate and box girder deck of cable stayed bridge were constructed, turbulent flow was simulated, and their responses to the smooth flow and the turbulent flow were measured. The major findings are as follows:

a. The structural properties of the taut-strip model can be kept almost similar to those of the prototype bridge deck, except for the logarithmic diminishing of torsional mode of the large frequency ratio model.

b. The turbulent flow generated in the wind tunnel were found to be applicable to the taut-strip model whose scale ratio is about 1/200.

c. The flutter speed for the flat plate model in the smooth flow agreed fairly well with the one calculated from Selberg's formula.

d. The wind-induced vibration of vertical bending mode of the box girder model agreed fairly well with that observed at the prototype cable stayed bridge.

e. From the findings above, the taut-strip model test is on effective technique for estimating wind-induced vibrations of long-span bridges with box girder deck.

6. REFERENCES

(1) Davenport, A. G., N. Isymov, and T. Miyata, The Experimental Determination of the Responses of Suspension Bridges to Turbulent Flow, Proc. 3rd Int. Conf. on Wind Effects on Bldgs. and Strcts., Tokyo, 1971.

(2) Davenport, A. G., The Use of Taut Strip Models in the Prediction of the Responses of Long Span Bridges to Turbulent Wind, Proc. Symp. on Flow Induced Strct. Vibrations, Karlsruhe, 1972.

(3) Davenport, A. G., Wind Structure and Wind Climate, Safety of Structures under Dynamic Loading, Trondheim, TAPIR, 1978.

(4) Davenport, A. G., The Interaction of Wind and Structures, Engineering Meteorology, Amsterdam, Elsevier, 1982.

(5) ESDU, Engineering Science Data, Wind
     Engineering, Volume 1, Wind and Turbulence
     Data, Engineering Science Data Unit Ltd.,
     1982.

(6) Irwin, I. P. A. H., The Design of Spires
     for Wind Simulation, J. of Wind Engineer-
     ing and Industrial Aerodynamics, 7, 1981.

(7) Okubo, T., N. Narita, K. Yokoyama and H.
     Sato; Field Observations of Aerodynamic
     Behavior of Long-Span Bridges, Proc. Fifth
     Int. Conf. on Wind Engineering, Colorado,
     1979.

(8) Selberg, A., Oscillation and Aerodynamic
     Stability of Suspension Bridges, ACTA
     Polytechnica Scandinavica, CII3, 1961.

Table 1. Conditions and Cases of Experiment

Case No.	Model	$m/(\rho B^2)$	$I/(\rho B^4)$	f_h/f_θ	δ_h	δ_θ	Flow	Note
1	Flat Plate I	26	1.8	1.7	0.013	0.023	smooth flow	compared with Selberg's formula
2	Flat Plate I	26	1.8	1.7	0.013	0.020	turbulent flow II	
3	Flat Plate II	27	1.8	4.0	0.022	0.060	smooth flow	
4	Flat Plate II	27	1.8	3.9	0.027	0.066	turbulent flow II	
5	Box Girder (hand rails)	25	1.1	3.6	0.017	0.097	smooth flow	
6	Box Girder (hand rails)	25	1.1	3.5	0.021	0.118	turbulent flow II	
7	Box Girder (flap plates)	25	1.1	3.6	0.018	0.099	smooth flow	
8	Box Girder (flap plates)	25	1.1	3.6	0.021	0.117	turbulent flow II	compared with the field observation result
Prototype Box Girder		23	0.94	3.1	0.026~0.039	0.014~0.018		
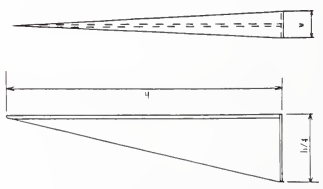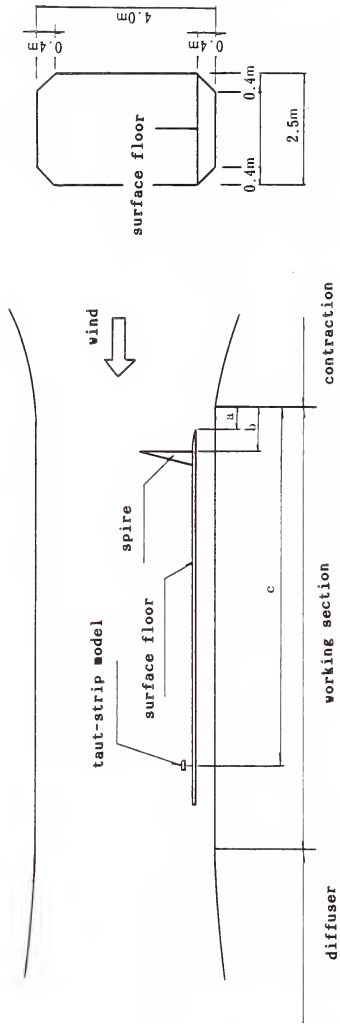
| | a | b | c | spires | | | floor roughness |
				number	w	h	
smooth flow	5.7m	----	8.0m	-------	----	----	-------------
turbulent flow I	0.5m	0.1m	8.0m	4	0.14m	1.6m	-------------
turbulent flow II	0.5m	1.0m	8.0m	4	0.13m	1.2m	artificial grass, 7mm thick
turbulent flow III	0.5m	1.0m	8.0m	4	0.17m	1.2m	14 rows of 0.1m cube blocks

Fig. 1. Wind Tunnel Arrangement
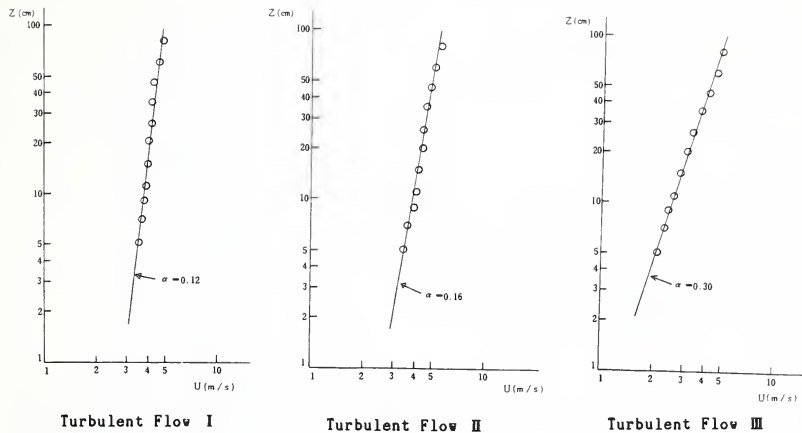
Turbulent Flow I   Turbulent Flow II   Turbulent Flow III

Fig. 2. Vertical Profiles

Longitudinal Component
of Fluctuating Wind Speed

Vertical Component
of Fluctuating Wind Speed

Fig. 3. Power Spectral Density Functions

25

Flat Plate Model I

Flat Plate Model II

Box Girder Model

Fig. 4. Taut-Strip Models

26
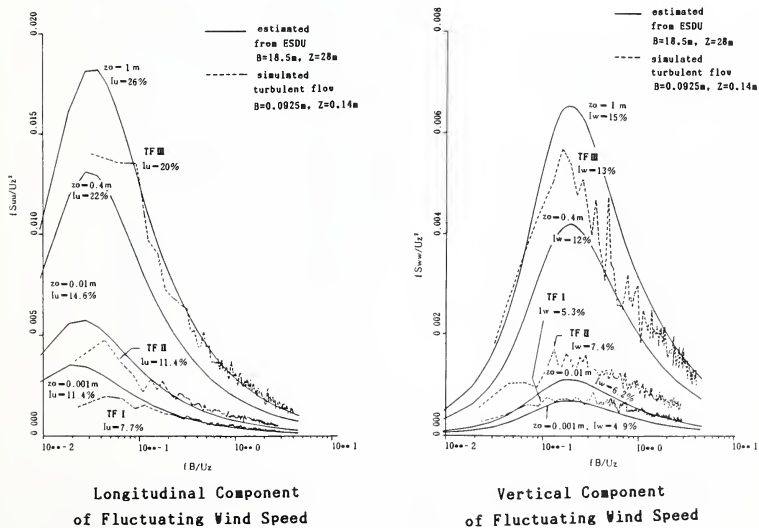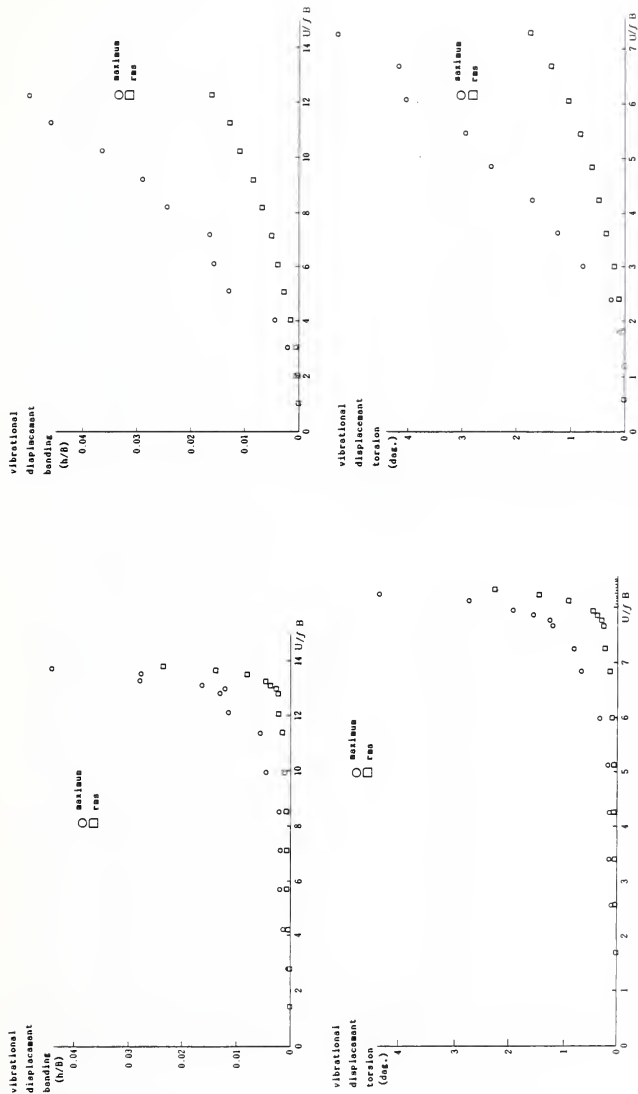
Fig. 5.1. Wind-Induced Vibrations (CASE 1)

Fig. 5.2. Wind-Induced Vibrations (CASE 2)
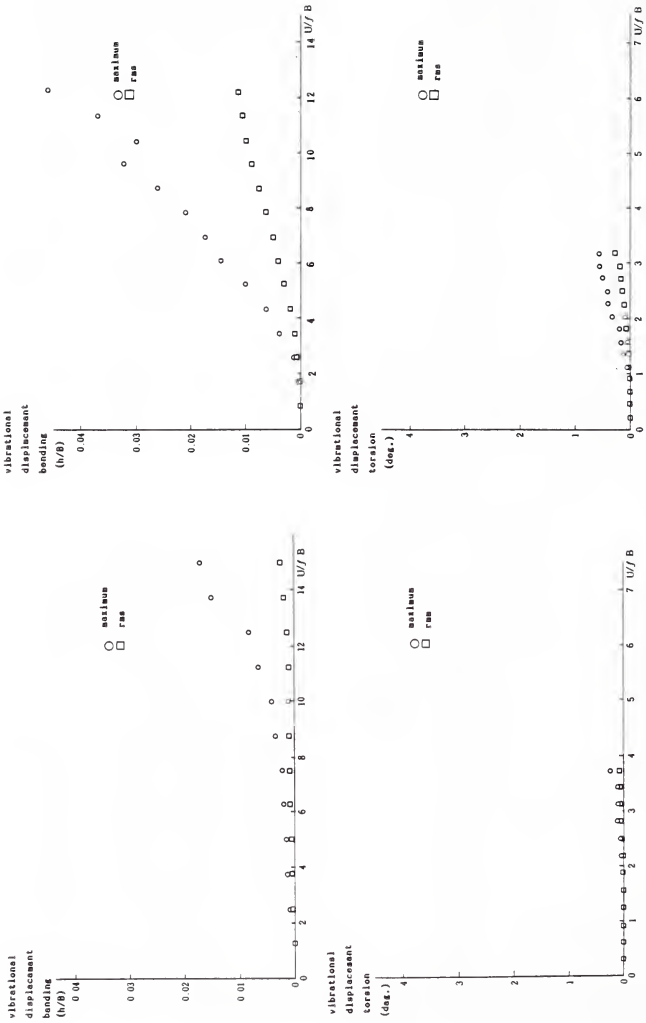
Fig. 5.3. Wind-Induced Vibrations (CASE 3)

Fig. 5.4. Wind-Induced Vibrations (CASE 4)
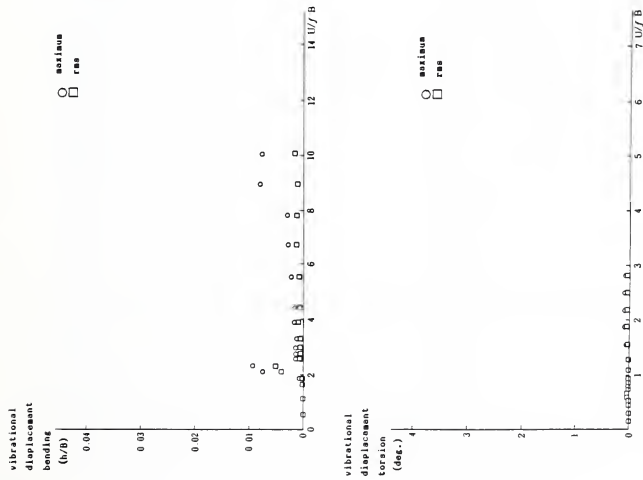
Fig. 6.1. Wind-Induced Vibrations (CASE 5)
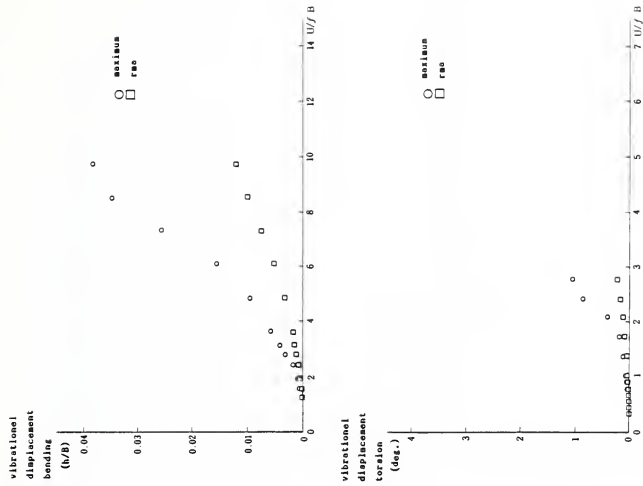
Fig. 6.2. Wind-Induced Vibrations (CASE 6)
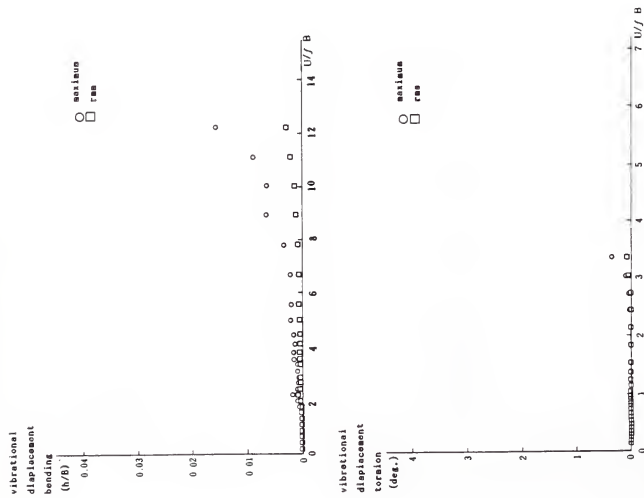
Fig. 6.3. Wind-Induced Vibrations (CASE 7)
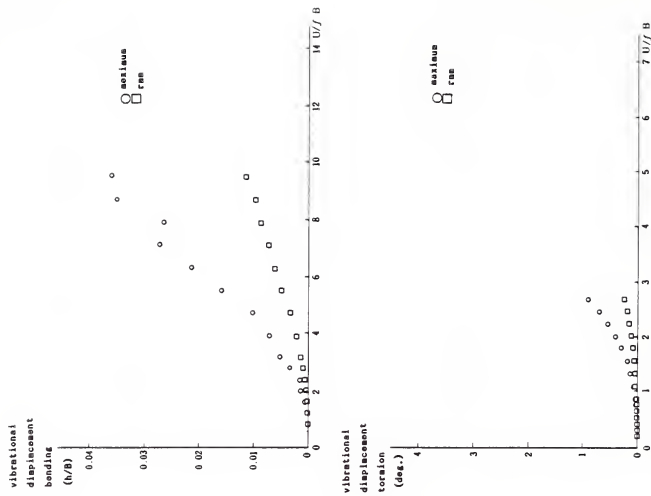
Fig. 6.4. Wind-Induced Vibrations (CASE 8)
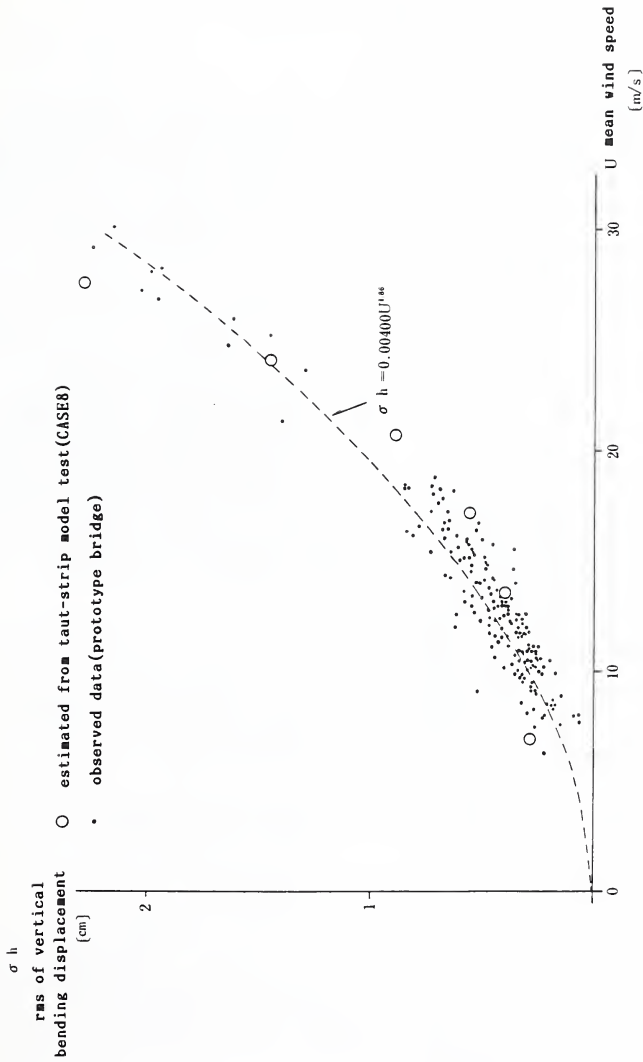
Fig. 7. Taut-Strip Model Responses
Compared with the Field Observation Results

○ estimated from taut-strip model test(CASE8)

● observed data(prototype bridge)

σ h
rms of vertical
bending displacement
(cm)

$\sigma h = 0.00400U^{1.46}$

U mean wind speed
(m/s)

THE RESPONSE OF TAUT STRIP MODELS:
COMPARISONS OF THEORETICAL AND EXPERIMENTAL RESULTS

BY

R.H. SCANLAN[1] AND R.D. MARSHALL[2]

ABSTRACT

This paper tests, by representative calcula-
tions, the applicability of certain existing
theories of flutter, vortex-shedding, and
galloping to the corroboration of results found
experimentally for the response of four
taut strip models in the wind tunnel. The
report shows that the theories yield plausi-
ble predictions but are very sensitive to
values of input parameters. Therefore it is
imperative to acquire accurate values of such
parameters for any given system to which the
theories are to be applied.

KEYWORDS: AERODYNAMICS; FLUTTER; VORTEX
EXCITATION; GALLOPING; TAUT STRIP MODEL

1. INTRODUCTION

Experimental findings on the response of a
series of 4 taut strip models of rectangular
section that were excited by wind in a wind
tunnel are summarized in reference 1. The
extent to which existing aerodynamic response
theory for bluff bodies can be used to
predict the observed responses has been
reported in reference 2. This paper presents
certain highlights of the work of reference 2
and the main experimental findings. The
ratios of width B to depth D of the taut
strip models were respectively 1,2,5 and 10.
Essentially what was done in the experimental
work was to excite the 4 different taut strip
models each through a range of velocities
until instability of its response became
apparent, the environment consisting of
either smooth flow or successively 3 dif-
ferent levels of turbulent flows, realized at
different heights in the boundary layer.
Figures 1 through 4 portray the main experi-
mental observations, which consisted of
either rms vertical or torsional displace-
ments at midspan of the models.

As is generally accepted, theories of
aeroelastic response rely, except in extreme-
ly simple cases -- such as that of the thin
airfoil and a few other streamlined bodies --
upon measured, rather than purely theoretical
flutter derivatives [3]. Fortunately, some
limited experimental torsional damping deri-
vatives exist for three of the four
rectangular section models examined in refer-

ence 1. Since the reported study is explora-
tory and not intended to be based upon
further experimentation, recourse is made to
existing flutter derivatives and to other
information that appears in the literature
[3,4,5,6,8,9]. Using these derivatives and
related data, a plausible case is made for
the ability of theory to corroborate the taut
strip results observed experimentally.

2. ANALYTIC BACKGROUND FOR FLUTTER INSTABIL-ITY

According to reference 4, most bluff-body
flutter is associated with
single-degree-of-freedom instability in tor-
sion. This means that, even in those cases
where vertical and twist motions couple (as
they do in so-called "classical" flutter),
with bluff bodies it is usually the unstable
torsion mode that "drives" the flutter
motion. Under these conditions a close
approximation to the situation can be real-
ized via a mathematical model permitting the
torsion degree of freedom only. This is
written as follows (4):

$$I[\ddot{\alpha} + 2\zeta_\alpha \omega_\alpha \dot{\alpha} + \omega_\alpha{}^2 \alpha] = 1/2\ \rho U^2 [2B^2][KA_2{}^* \frac{B\dot{\alpha}}{U} + K^2 A_3{}^* \alpha] \quad (1)$$

where

    I = mass moment of inertia per unit span
         of bluff body (taut strip model)
    α = twist degree of freedom of model
    ζ_α = torsional mechanical damping ratio of
         model

    ω_α = natural circular frequency of model
    U = mean cross-wind velocity
    B = model width (along-wind direction)
    K = $\frac{B\omega}{U}$ = "reduced frequency"

    ρ = air density
    ω = $2\pi n$ ($\cong \omega_\alpha$) = flutter circular
frequency
    $A_2{}^*$ = $A_2{}^*(K)$ = flutter damping
coefficient, function of reduced frequency
    $A_3{}^*$ = $A_3{}^*(K)$ = flutter stiffness
coefficient, function of reduced frequency
In particular, flutter occurs when the net
system damping becomes zero, i.e., when
$\dot{\alpha}$ terms on the left and right are equal:

$$2I\zeta_\alpha \omega_\alpha = 1/2\ \rho U^2 [2B^2][KA_2{}^* \frac{B}{U}] \quad (2)$$

---
[1] The Johns Hopkins University
Baltimore, Maryland 21218
[2] National Bureau of Standards
Gaithersburg, Maryland 20899

Since experimentally it is found that the flutter frequency departs very little from the natural torsional frequency ($\omega \cong \omega_\alpha$), then

$$K \cong \frac{B\omega_\alpha}{U} \qquad (3)$$

Using (3) in (2) results in the net condition that holds at flutter:

$$(A_2^*)_{cr} = \frac{2I\zeta_\alpha}{\rho B^4} \qquad (4)$$

Thus, for a particular set of mechanical parameters, the critical flutter coefficient $(A_2^*)_{cr}$ is determined. Since it in turn is an experimental function of K, (usually given as curves of A_2^* vs. the parameter U/nB, where $n = \omega/2\pi$) the value of K for flutter can be found. This then reveals the critical value of velocity, $U_{critical}$ for the flutter condition.

2.1 Application of Theory to Corroborate Critical Velocities of Experimental Cases Involving Torsional Flutter Instability

Reference 5 provides results on the torsional flutter instability of several rectangular-section prisms, including those with B/D = 1,2, and 5. As is shown in reference 2, the data given in reference 5 for the torsional damping coefficient $C_{M\theta I}$ may be translated into the notation used here by the formulas below:

$$A_2^* = \frac{C_{M\theta I}}{2(\frac{B}{D})^2 K^2} \qquad (5)$$

$$\frac{U}{nB} = \bar{V}/(B/D) \qquad (6)$$

$$K = \frac{2\pi}{\bar{V}} (\frac{B}{D}) \qquad (7)$$

Note that $\bar{U}_r$ as employed in reference 1 bears the following relation to $\bar{V}$ of reference 5:

$$\bar{U}_r = \frac{n_\alpha}{n_h} \bar{V}$$

Plots of $C_{M\theta I}$ vs. $\bar{V}$, as given by reference 5, are presented in Figs. 5 to 7. Mechanical data for the four strip models are listed in Tables 1 and 2. In these tables the following symbols are used:

- B = model width (streamwise dimension)
- D = model depth (vertical)
- L = total model span
- M_t = total model mass
- I_t = total model mass moment of inertia about its rotation axis
- ρ = air density
- ζ_h = mechanical damping ratio in vertical motion
- ζ_α = mechanical damping ratio in rotation

- n_h = vertical frequency (Hz.)
- n_α = torsional frequency (Hz.)

It should be noted that the mechanical damping ratios ζ_h and ζ_α given in Table 2 are derived from logarithmic decrements. The average values of damping ratio (ζ_z and ζ_θ) listed in reference 1 were not used since, used as mechanical damping ratios, they did not, in general, lead to as good a match between theory and experiment as those given in Table 2. Characteristics of the turbulent boundary layer established in the wind tunnel are listed in Table 3.

CASE B/D = 1

The curves of $C_{M\theta I}$ vs. $\bar{V}$ for smooth and turbulent flow are given in Fig. 5. Clearly, only those regions where $C_{M\theta I}$ is greater than zero are of interest in predicting instability. Hence attention will be focused here on such regions.

First, the criterion for oscillatory instability is recalled. This is given by eq. (4). Applying this here with data from Tables 1 and 2 yields

$$(A_2^*)_{cr} = 0.3635$$

Inspection of the curve (Fig. 5) of $C_{M\theta I}$ vs. $\bar{V}$ for smooth flow reveals an interruption (probably due to erratic model behavior associated with instability) between $\bar{V} \cong 7.4$ and $\bar{V} \cong 9.8$. If, in the region of $\bar{V}=8$, the value of $C_{M\theta I}$ had attained the very plausible value of 0.45, the corresponding A_2^* value would have been, according to eq. (5): $A_2^* = 0.3648$ which is very near the predicted instability criterion. The corresponding value of $\bar{U}_r$ would have been 8.64, whereas Fig. 1(b) shows a strong measured instability somewhat earlier at $\bar{U}_r \cong 6.6$ However, as it stands, Fig. 5 (Ref. 5) does not actually provide the critical data needed. Note that calculation of A_2^* in the region of $\bar{V} \cong 3$, yielding $A_2^* = 0.0684$, does not reveal any torsional instability, which is consistent with Fig. 1(b) in this region.

For turbulent flow, the curve (Fig. 5) of $C_{M\theta I}$ vs. $\bar{V}$ reveals potential instability regions $3.4 \leq \bar{V} \leq 5.3$ and $7.4 \leq \bar{V} \leq 20$. Calculation of A_2^* by eq. (5) in the first of these regions reveals that the instability criterion for A_2^* is not met, consistent with the results of Fig. 1(b). However, for the values $\bar{V}=7.7$, $C_{M\theta I} = 0.5$, the corresponding calculation for A_2^* reveals $A_2^* = 0.3755$, very close to the critical criterion. The corresponding $\bar{U}_r$ value is $\bar{U}_r = 1.08\bar{V} = 8.32$, again somewhat later than actual instability onset ($\bar{U}_r \cong 6.5$) of the taut strip model, as seen in Fig. 1(b).

Essentially the process used here amounts to comparing two experimental performances: one, the rigid block section model of reference 5, considered as a source of flutter derivative data, the other being the 3D taut strip model. The intermediary employed is the theory given in eq. (1). A number of discrepancies can obviously occur between predicted and measured taut strip results for experimental and other reasons. The process does, however, continually yield reasonable values qualitatively consistent with observation.

Case B/D = 2

Inspection of the source curves (Fig. 6) reveals potential instability regions under smooth flow as follows

$$2 \leq \overline{V} \leq 3$$

$$4.7 \leq \overline{V} \leq 8$$

$$9.8 \leq \overline{V} \leq 15(?)$$

and under turbulent flow as follows

$$5.5 \leq \overline{V} \leq 6.3$$

$$9.4 \leq \overline{V} < ?$$

The criterion for flutter, eq. (4), is first calculated as follows, using data from Tables 1 and 2:

$$\left(A_2{}^*\right)_{cr} = 0.0628$$

Employing, in the present case, B/D = 2, the process reviewed above for B/D = 1, the values for smooth flow yield $A_2{}^* = 0.0693$, close to the criticality criterion, and $\overline{U}_r = 6.6$. Reference to Fig. 2(b) reveals a strong critical region (probably associated with vortex shedding) in the region of $\overline{U}_r \cong 5$, both for smooth and turbulent flow. Subsequently, regions of taut-strip instability are approached in $\overline{U}_r \gtrsim 14$. In both smooth and turbulent flow, instability is indicated in reference 5 for $\overline{V} \gtrsim 10$, which corresponds to $\overline{U}_r \gtrsim 14$; this is in fact borne out in Fig. 2(b).

Case B/D = 5

Background for this case is provided in the curves of Fig. 7. The flutter criterion of eq. (4) in this case, with data from Tables 1 and 2, is

$$\left(A_2{}^*\right)_{cr} = 0.0975$$

Inspection of Fig. 7 for smooth flow reveals that at $\overline{V} = 24.3$, $C_{M\theta I} = 8.5$, the value of $A_2{}^*$ reaches the above critical value. The corresponding $\overline{U}_r$ value is

$$\overline{U}_r = 1.43\overline{V} = 34.75$$

Fig. 3(b) shows in fact that in the region of $\overline{U}_r = 35$ there is a strong instability under smooth flow.

Under turbulent flow the instability is postponed to $\overline{U} = 40$. However, the $C_{M\theta I}$ and corresponding $A_2{}^*$ values for turbulent flow given by reference 5 (Fig. 7) do not reveal any instability tendency in the range of $0 \leq \overline{V} \leq 50$. Beyond $\overline{V} \cong 30$, however, they approach zero. It is a fact (confirmed, for example, by the curves of the case B/D = 1) that turbulence can increase instability tendencies. It may be, then, that the particular intensity and scale of turbulence used with the taut strip model differed enough from those of reference 5 that for B/D = 5, destabilizing conditions, (i.e., necessary turbulence levels), missing in the tests of reference 5, were provided under the conditions of taut strip testing.

In the present case then, smooth-flow instability of the taut strip is predicted with the results of reference 5 but the turbulent flow instability is not, most likely due to differences in turbulence level.

Treatment of the Case B/D = 10

Up to this point, no background data have been introduced that are directly applicable to this case, to which, unfortunately, the information of reference 5 does not extend. An approach is suggested here, however, that permits some corroboration.

During the research done for reference 3, a number of curves of $A_2{}^*$ plotted vs. U/nB were acquired for various shapes of bridge deck. In particular, for a certain set of decks, the data of Fig. 8 were assembled. For decks 2 and 3 of this group, the associated curves 2 or 3 for $A_2{}^*$ were found to have some relation to the bluff-body case B/D = 10.

First, the flutter criterion for the taut strip (cf. Tables 1 and 2) is calculated to be

$$\left(A_2{}^*\right)_{cr} = 0.0582$$

while the critical reduced velocity parameter for instability (from Fig. 4b) is $\overline{U} \cong 106$, which corresponds to $\overline{V} = 106/1.45 = 73.1$ and to $K = 2\pi(B/D)/\overline{V} = 0.8595$ or U/nB = 7.31. Correspondingly, curves 2 or 3 of Fig. 8 yield U/nB $\cong 7$, for $A_2{}^* = 0.06$. The corresponding value of $\overline{U}_r$ is $\overline{U}_r^2 = 102$.

It should be commented that the curves 1 to 4 of Fig. 8 were obtained in the early 1970's by methods not necessarily as detailed as those used in reference 5 or presently employed in other studies to get $A_2{}^*$ results. In particular, the lower (negative) values of

$A_2{}^*$ have subsequently, in other cases, been found to be more irregular than shown in Fig. 8, corresponding to a variety of flow nuances, including low speed vortex excitation. In spite of this possible discrepancy, the use of curves 2 or 3 from Fig. 8 seems to bear out typical trends of $A_2{}^*$ curves in the higher U/nB region of instability.

2.2 Summary on Prediction of Critical Reduced Velocities for Torsional Instability

Theory, dependent on measured flutter derivatives, was used above to predict the critical value of $\overline{U}_F$ as observed in the experimental studies of reference 1. Table 4 summarizes the obtainable results.

Discrepancies that occur can be ascribed to a number of sources, including all measured physical parameters. Further, the theory used is considered reliable for small amplitudes only and for spanwise uniform flow, either of which conditions could have been violated in references 1 and 5. Lastly, it is to be emphasized that the theory applied to this point is intended to predict critical wind velocities only, and not response amplitudes. Typically, when theoretically critical velocities are reached, the systems in question do not exhibit "instant" onset of "infinite" amplitudes. This is due in part to the fact that the systems are not strictly linear, with parameters that remain unchanged by amplitude, frequency, etc. Also, the cross-sections dealt with are bluff, giving rise to at least "signature" turbulence effects, even under laminar onset flow.

3. GALLOPING THEORY

Across-wind galloping of a structure can be described [9] by the equation

$$m[\ddot{h} + 2\zeta_h\omega_h\dot{h} + \omega_h{}^2 h] = -1/2\rho U^2 B \left[\frac{dC_L}{d\alpha} + C_D\right]\frac{\dot{h}}{U} \quad (8)$$

where

$\quad$ m = structure mass per unit span

$\quad$ h = vertical (across-wind) amplitude

$\quad \zeta_h$ = vertical damping ratio

$\quad \omega_h = 2\pi n_h$ = natural frequency of across-wind oscillation

$\quad$ U = wind velocity

$\quad$ B = along-wind dimension of object

$\quad C_L$ = dimensionless lift coefficient (referred to dimension B)

$\quad \alpha$ = wind angle of attack

$\quad C_D$ = dimensionless drag coefficient (referred to dimension B)

(Note: If C_D is not referred to B, but to the across-wind dimension D, then it is replaced above by $\frac{D}{B}C_D$.)

3.1 Galloping Effects

The Den Hartog Criterion

$$\frac{dC_L}{d\alpha} + C_D < 0 \quad (9)$$

governs incipient across-wind galloping tendencies in the vertical mode. (It is understood that C_L and C_D are both based on the same reference length.) Inspection of laminar flow lift and drag information presented in reference 8 reveals that the model with side ratio B/D = 1 is susceptible to this type of galloping instability through the limited range $-12 \leq \alpha \leq 12$ degrees for which

$$\frac{dC_L}{d\alpha} = -4.06 \qquad 1.7 \leq C_D \leq 2.3$$

Hence, at least in this range of α, the Den Hartog criterion for incipient galloping is satisfied, in fact for all wind speeds.

Galloping may exhibit the nonlinear characteristic requiring motion to be initiated, however, before it can proceed. Furthermore, the Den Hartog condition is necessary, not a sufficient condition, the sufficient condition being [9]:

$$2m\zeta_h\omega_h + 1/2\rho UB\left(\frac{dC_L}{d\alpha} + C_D\right) < 0 \quad (10)$$

where m is model mass per unit span and ω_h is circular frequency in cross-wind oscillation.

Case B/D=1

Taking $C_L{}' = -4.06$, $C_D \cong 1.9$, yields, for the taut strip model with B/D = 1, (see data of Tables 1,2):

$$U = 0.6113 \text{ m/s}$$

This corresponds to a reduced velocity

$$\overline{U}_r = 1.99$$

Fig. 1a shows in fact that a slight instability tendency in vertical motion under smooth flow occurs for $1.4 \leq \overline{U}_r \leq 1.8$.

On the other hand, it is observed that the presence of turbulence suppresses this galloping tendency. Therefore, instabilities encountered elsewhere in the $\overline{U}_r$ range are not associated with classic Den Hartog across-flow galloping for B/D=1.

It is important to emphasize that the above galloping calculation is quite sensitive to assumed values of $C_L{}'$ and C_D. What actual effective values held during the experiment is not presently known.

Case B/D = 2

Reference 8 provides graphs of drag, lift and moment coefficients for rectangular sections. From these graphs, for B/D =2 (d/b = 0.5), values of C_D , C_L , and C_M for smooth flow are obtainable for $0 \leq \alpha \leq 90°$. Near $\alpha = 0°$, the slope C_L' of the lift curve is negative, suggesting the possibility of instability in this region. In fact

$$C_L' = \frac{dC_L}{d\alpha} = -4.78 \text{ per radian}$$

while

$$C_D \cong 0.8$$

These yield

$$C_L' + C_D = -3.98$$

Using these values in the galloping criterion with data from Tables 1 and 2 yields U = 0.342 m/s, corresponding to $\overline{U}_r$ = 0.93. Clearly this low value of $\overline{U}_r$ is not witnessed experimentally.

There are some possibilities, however, that the circumstances of the test (cf. results Fig. 2) did not correspond to the parameters used above. One strong possibility is a mean twist of the model by a few degrees, about which oscillation occurred. Another possibility is that the value of mechanical damping ratio ζ_h given in Table 2 did not hold during the test wherein high amplitude response was evidenced.

It may be observed from reference 8 that the slope C_L' of the lift curve for B/D = 2 makes a rapid reversal, over a very few degrees of angle of attack, from negative to positive values; this takes place in the vicinity of $\alpha = 8°$. If the equilibrium angle of the taut strip model were to approach this value, C_L' could be radically different from its $\alpha = 0$ value. Furthermore, effective mechanical damping might increase to a considerably greater value than that shown in Table 2.

Leaving mechanical damping at its measured value, however, it is of interest to see what value of C_L' would correspond, for example, to the observed peak response region $\overline{U}_r$ =5. This implies a velocity U = 5(12.31)(0.03) = 1.846 m/s. Using this, with $C_D \cong 0.7$, in the galloping criterion yields the value C_L' = -1.438.

Again, for a doubled value of mechanical damping (ζ_h =0.0026), the value C_L' =-2.17 is obtained.

These exploratory results tend to illustrate that quite reasonable values of damping and lift slope could correspond to the observed experimental response seen at $\overline{U}_r$ =5

Fig. 2. It would experimentally be difficult to measure either of these values under wind-on, oscillatory conditions.

It may be concluded that the so-called galloping theory, while encountering the difficulty of correct parameter assessment, nonetheless approximates certain of the phenomena viewed experimentally. These phenomena, for B/D =1,2 may therefore, with some assurance, be classified as "galloping."

Cases B/D = 5 and 10

From the results of Figs. 3 and 4, it would appear reasonable to rule out galloping in these cases and explore only flutter and buffeting excitations for them.

It may be remarked in general that, in the absence of detailed flow visualization and other more deeply investigative methods in regard to a flow-induced oscillation, it is difficult to categorize any given phenomenon uniquely as "vortex-induced," "galloping," or "flutter," due in part to the inherently fuzzy boundaries (and, in fact, inherent shortcomings) of these classes of description.

4. VORTEX SHEDDING EFFECTS

Referring to response amplitude, those cases investigated in reference 1 that suggest the vortex shedding phenomenon in strongest fashion are shown in Figs. 1 and 2, for sections with B/D = 1 and 2, respectively. When vortex-induced motion occurs it can evidence itself both across-wind and in twist.

Case B/D = 1

Figure 1 shows strong displacement in both bending and torsion at the value

$$\overline{U}_r = \frac{U}{n_z D} \cong 6.6$$

where n_z is the vertical (across-wind) frequency. This correspond to a Strouhal number of

$$S = 0.15$$

Most researchers, however, of which reference 6 is representative, place the Strouhal number of a square section at zero angle of attack at S=0.12 to 0.125. Fig. 9, which is a reproduction of Fig. 3 of reference 6, suggests (cf. label "BT") that both bending and torsion excitations are associated with this Strouhal number.

It is of interest to note that, for B/D = 1, the U_r value corresponding to S = 0.12 is $\overline{U}$ = 8.33, much closer to the first theoretically "expected" value of $\overline{U}_r$ (i.e., $U \cong 8.6$) discussed earlier in this report (under torsional instability). This value was for a nominal angle of attack $\alpha = 0°$. However, in case the taut strip model twisted ("blew back") to a non-zero mean angle, this could account for a different Strouhal number holding in the experiments of reference 1. In fact, Fig. 9 suggests that a Strouhal number $S \cong 0.15$ could obtain for a mean wind angle of about $\alpha \cong 12°$. Another possibility is that oscillation amplitudes influenced the net effective Strouhal number. Either of these effects could explain the anomaly observed for B/D = 1.

Case B/D = 2

Figure 2 suggests the possibility of a vortex-shedding instability close to $\overline{U}$ = 5, or S = 0.2. Again, according to Fig. 9 of the present report, this is far from a zero-angle-of-attack Strouhal number for B/D = 2. In fact, an appropriate Strouhal number at $\alpha = 0°$ for B/D = 2 is about S = 0.08 (cf. Fig. 9 [6]). It is probably more nearly correct, therefore, to assign the early peaks (in both vertical motion and twist) of Fig. 2 to galloping than to vortex shedding.

For B/D = 5 or 10, no strong vortex-induced instability appears to be present, according to the results given in Figs. 3 and 4.

5. BUFFETING BY TURBULENCE

The theory and measurements discussed above are concerned only with locating the critical velocities associated with instability. These theories do not attempt to predict amplitudes of response. Attempts to predict buffeting response amplitudes have been made in references 4 and 7. The methods of reference 4 have been employed to predict response amplitudes for the taut strip models described herein [2]. Highlights of this work will be the subject of a future paper.

6. COMMENTS AND CONCLUSIONS

A set of experimental results presented in reference 1 has been examined. They represent the wind-induced response of a series of four taut-strip models with bluff, rectangular sections. Theories of flutter, vortex response and buffeting have been recalled from the literature and used in this report to predict the velocities of critical instabilities of the models and the model response amplitudes at selected points.

The general process has demonstrated that the theories used are capable of yielding results consistent with observation. However, the process of attempting to closely match experimental results reveals both the high sensitivity of the theories to certain parameter inputs and the need to acquire highly accurate parameter estimates in order to obtain dependable results from the predictions.

The data provided by reference 1, while extensive, were not fully adequate to support the theories used. Neither were the literature sources relied upon in the present study.

Clearly, extensive further work could be done in this area to fill the gap in knowledge required to tighten up the effectiveness of the theoretical predictions. In particular, whole sets of accurate flutter derivatives were lacking for the present study, forcing recourse to somewhat inadequate literature data and to the pressing into use of static derivative data as a substitute for true flutter derivative information. In spite of these difficulties, the theories called up appeared to yield plausible results based on reasonably argued parameter choices.

Generally, experiments with taut strip models should be accompanied by rigid, sprung section model experiments for the same cross-sections. Such models are accurate sources of indispensable data to be used in forecasting taut strip behavior. The theories used were found most sensitive to the input parameters concerned with aerodynamic derivatives, both static and dynamic, and to damping values.

REFERENCES

1. Marshall, R.D., Yamamoto, K., Nakagami, Y., and Kanjaki, K., "Response of Taut Strip Models to Smooth and Turbulent Flows," Proceedings of the Fifteenth Joint UJNR Panel Conference on Wind and Seismic Effects, Tsukuba, Japan, May 1983.

2. Scanlan, R.H., "Comparison of Theoretical and Experimental Results In Response of Taut Strip Models to Smooth and Turbulent Flows", Report prepared for National Bureau of Standards, August 1985.

3. Scanlan, R.H. and Tomko, J.J., "Airfoil and Bridge Deck Flutter Derivatives," Jnl. Engrg. Mech. Div., ASCE, Vol. 97, No. EM6, Dec. 1971, pp. 1717-1737.

4. Scanlan, R.H., "State-of-the-Art Methods
    for Calculating Flutter, Vortex-Induced,
    and Buffeting Response of Bridge
    Structures," Report FHWA/RD-80/050,
    Federal Highway Administration,
    Washington, D.C., April 1981.

5. Nakamura, Y. and Yoshimura, T., "Flutter
    and Vortex Excitation of Rectangular
    Prisms in Pure Torsion in Smooth and
    Turbulent Flows," Jnl. of Sound and
    Vibration (1982), Vol. 84, No. 3, pp.
    305-317.

6. Otsuki, Y., Washizu, H., Tomizawa, H.,
    Ohya, A. and Fujii, K., "Experiments on
    the Aeroeslastic Instability of
    Prismatic Bars with Rectangular
    Sections," Proceedings, Conf. on Wind
    Effects on Bldgs. & Structures, Tokyo,
    1971, Paper IV 24, pp. 891-898

7. Scanlan, R.H. and Gade, R.H., "Motion of
    Suspended Bridge Spans under Gusty
    Wind," Jnl. Struct. Div. ASCE, Vol. 103,
    No. ST9, Sept. 1977, pp. 1867-1883.

8. Okauchi, I., Ito, M. and Miyata, T., Wind
    Resistant Structures (in Japanese),
    Tokyo, 1977.

9. Simiu, E. and Scanlan, R.H., Wind
    Effects on Structures, Second Edition,
    John Wiley & Sons, New York, 1986.

Table 1

PHYSICAL PROPERTIES OF TAUT STRIP MODELS

B/D Dimension	M_T (Kgf s^2 m^{-1})	$10^4 I_T$ (Kgf m s^2)	ρ (Kgf m^{-4} s^2)	B (m)	D (m)	L (m)
1	0.0437	0.2625	0.12	0.06	0.06	1.3
2	0.0317	0.1244	0.12	0.06	0.03	1.3
5	0.0240	0.0821	0.12	0.06	0.012	1.3
10	0.0153	0.0535	0.12	0.06	0.006	1.3

Table 2

MECHANICAL DAMPING RATIOS AND NATURAL

FREQUENCIES OF TAUT STRIP MODELS

B/D Dimension	ζ_h	ζ_α	n_h (Hz.)	n_α (Hz.)	n_α/n_h	$\dfrac{n_\alpha B}{n_h D}$
1	0.0011	0.014	10.23	11.05	1.08	1.08
2	0.0013	0.0051	12.31	16.74	1.36	2.72
5	0.0010	0.012	13.98	19.99	1.43	7.15
10	0.0018	0.011	15.86	23.00	1.45	14.50

Table 3

CHARACTERISTICS OF TURBULENT BOUNDARY LAYER

Z (cm)	$\overline{U}_z/U_o$	I_u (Percent)	I_w (Percent)	L_u (m)	L_w (m)
35	0.62	20.8	14.7	0.21	0.08
60	0.85	11.4	8.8	0.22	0.07
70	0.91	7.1	6.2	0.20	0.07

Table 4

COMPARISON OF CRITICAL VALUES OF $\overline{U}_r$ IN TORSION

B/D	Smooth Flow		Turbulent Flow	
	Theory	Taut Strip Experiment	Theory	Taut Strip Experiment
1	8.6(?)	6.6	8.3	~6.6
2	6.8;14	~5.0;~14.5	~4.8;14	~5.0;≥14
5	34.8	~36		~40
10	102	106		~85
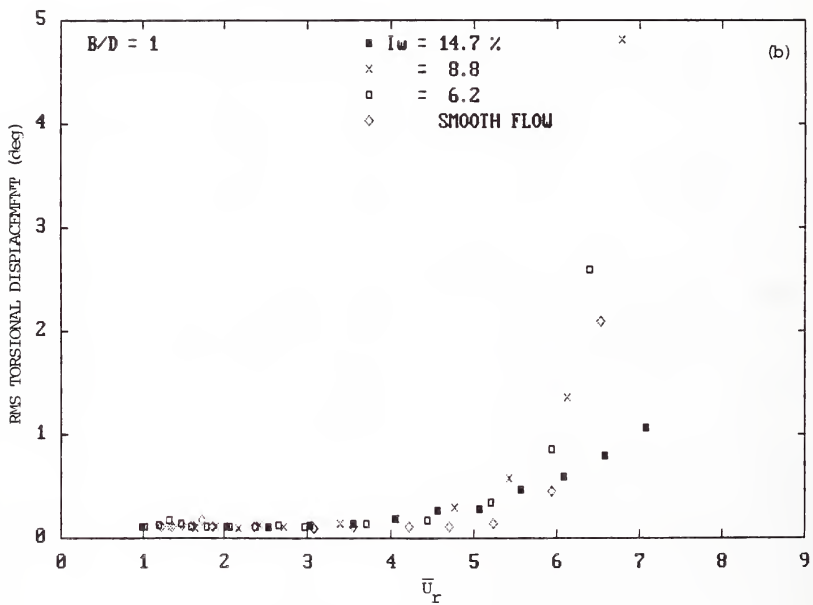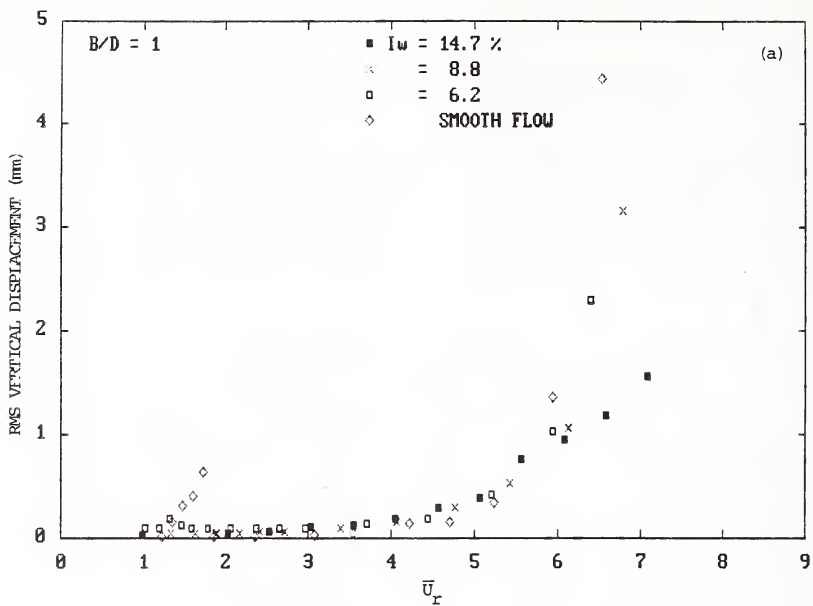
Fig. 1. RMS Displacement at Midspan. B/D = 1.
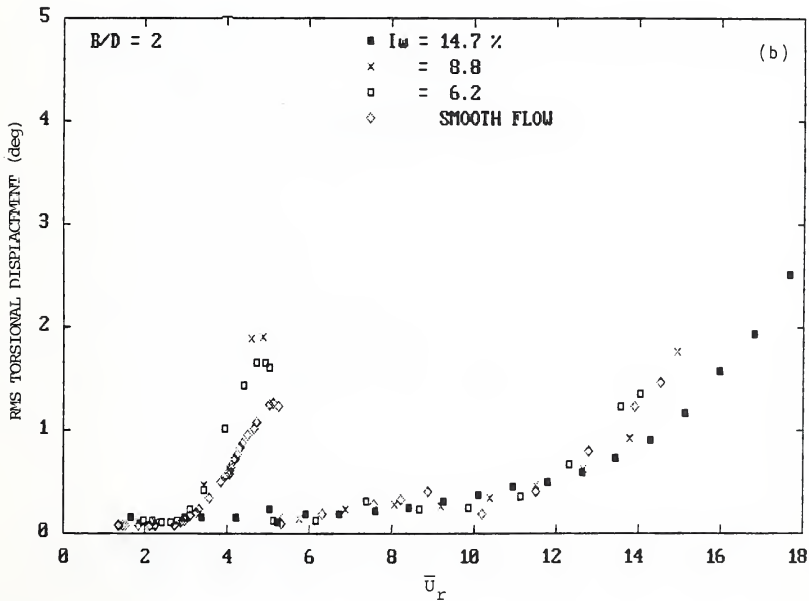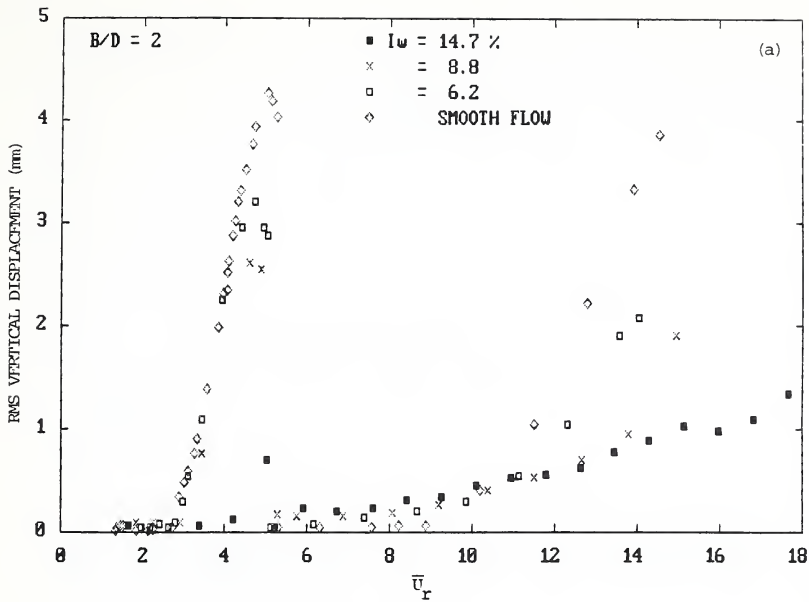
Fig. 2. RMS Displacement at Midspan. B/D = 2.
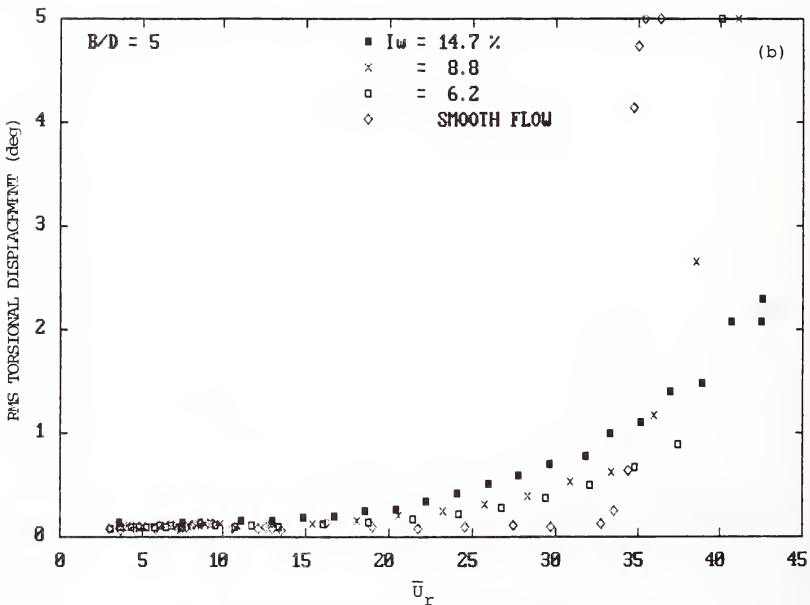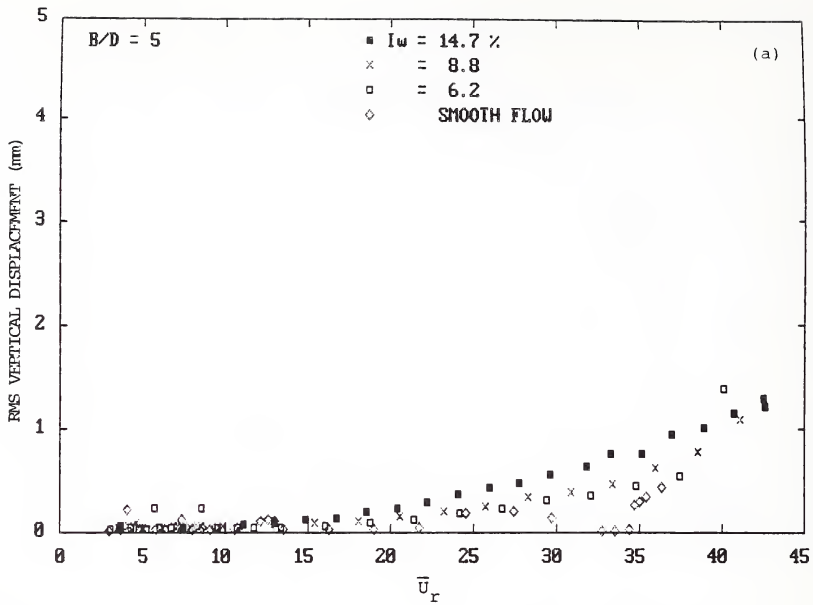
Fig. 3.   RMS Displacement at Midspan.   B/D = 5.
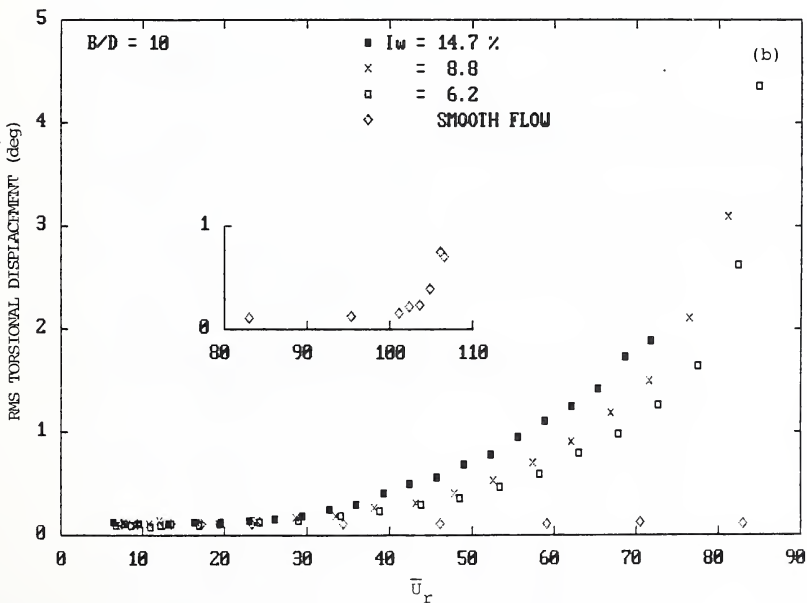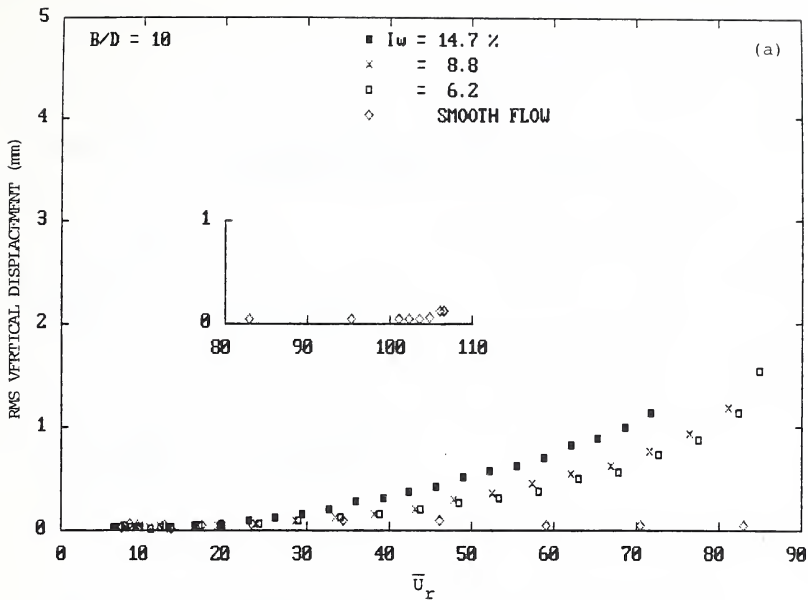
Fig. 4.   RMS Displacement at Midspan.   B/D = 10.
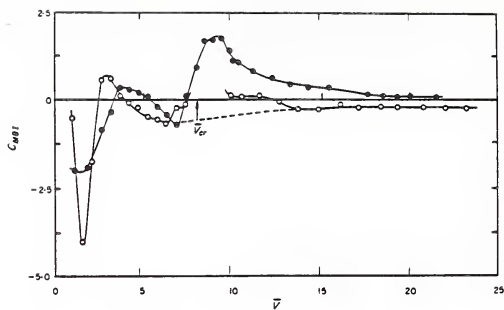
Fig. 5.   Torsional Damping Coefficient.   B/D = 1.   (Ref. 5)

             ° Smooth Flow
             • Turbulent Flow
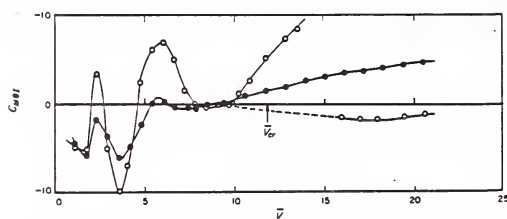
Fig. 6.   Torsional Damping Coefficient.   B/D = 2.   (Ref. 5)
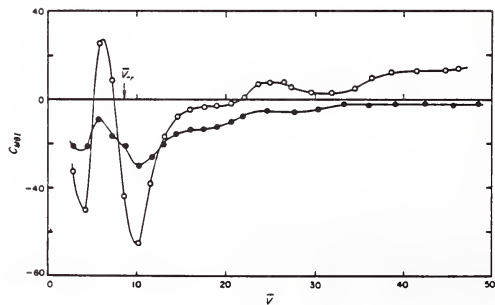
Fig. 7.   Torsional Damping Coefficient.   B/D = 5.   (Ref. 5)
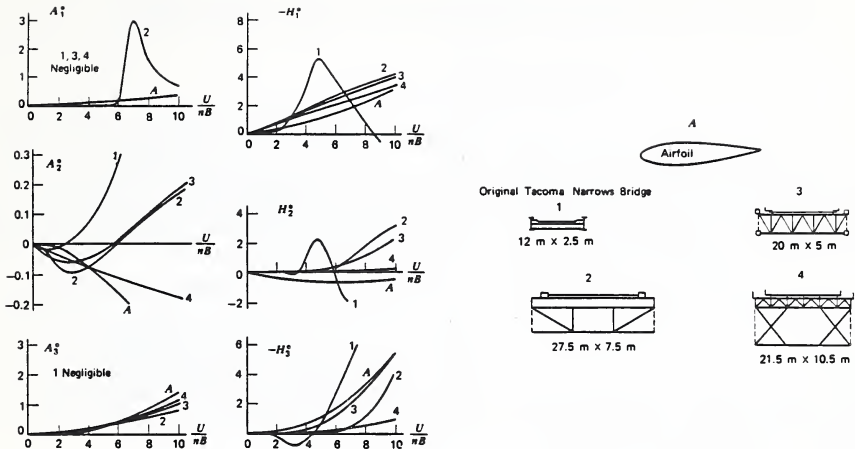
Fig. 8.   Aerodynamic Coefficients.   (Ref. 4)
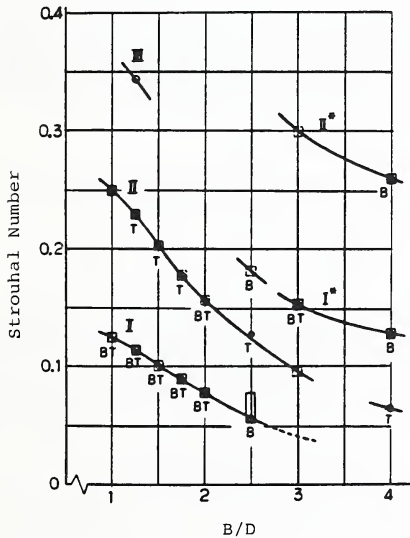
"B" denotes Strouhal numbers closely related to critical speeds for across-wind oscillation.

"T" denotes Strouhal numbers closely related to critical speeds for torsional oscillation.

Fig. 9.   Strouhal Number in the Wake of Rectangular Sections. (Ref. 6)

45

A FULL-SCALE MEASUREMENT OF WIND LOAD ON A SOLAR WATER HEATER

BY

Hisashi Okada and Tatsuo Murota[1]

ABSTRACT

Results of a full-scale field observation of wind loads on a solar water heater, mounted on a house roof, are described and compared with wind tunnel tests obtained by the authors. Wind force coefficients estimated from wind tunnel tests were 10 to 20% larger than those observed in the field. This suggests that the design pressure coefficients obtained by wind tunnel tests are good estimates for designing solar heater mountings.

1. INTRODUCTION

Solar water heaters for energy conservation are coming into wide use in Japan. Most are mounted on roofs of residential houses where they are exposed to strong winds. It is the structural engineer's concern to prevent heater damage from high winds. It is difficult to assess the possibility of damage because technical information is scarce. Under those circumstances, the authors conducted wind tunnel tests(1) in 1982 to produce information about wind forces on solar water heaters. Full-scale field observations were performed at the same time. This report presents the outline of the field observation and compares wind forces obtained by wind tunnel tests and field observations.

2. DESCRIPTION OF FULL-SCALE OBSERVATION

2.1 Observation Field

A full-scale test specimen was located in a flat open ground at the south east corner of the site of the Building Research Institute, Ministry of Construction (Fig. 1 and Photo 1). A transmission tower is located about 30m south-east of the specimen. Except for the tower, nothing else is within the area 40m to the west, 70m to the east, and more than 100m to the north and south of the specimen.

2.2 Test Specimen

Test specimen is a full-scale solar water heater mounted on the center of a roof as shown in Fig 2. The house is 9m x 5.46m in plan and has a gable roof of 3/10 pitch. The height of the eaves is 2.54m. The heater has a laid-L-like section, and its size is 2m x 2.23m in plan. It was mounted on a steel frame fixed to the house roof of 30° inclination to the horizontal plane. Three sets of load cell were installed between the heater and the steel frame to measure wind forces on the heater.

Upper surfaces (collector) of solar water heaters generally face south. In this observation, however, it faced east taking predominant direction of winds into consideration. Therefore, in applying the observation results, wind directions should be changed by 90 degrees: east and west for observation must be considered to be south and north, respectively.

2.3 Wind Direction and Wind Speed Measurements

To observe wind direction and wind speed in the field, a 10m high mast was erected 6m south-east of the specimen as shown in Fig. 1. A vane-type anemometer and three 3-cup-anemometers were mounted at the top, 6, 4 and 2m levels of the mast, respectively.

2.4 Data Acquisition

Wind and load data observed were processed by the following two methods: 1) data are sampled at 20 second intervals during 10 minutes at every 1 hour and the 10 minutes are recorded, 2) data are sampled and recorded at 1 second intervals during 10 minutes. The first method was adopted for strong wind conditions. Turbulence intensities and power spectra presented later are calculated using the data acquired by the second method.

3. WIND TUNNEL TEST

Before presenting the results of field observation, the wind tunnel test in 1982 will be described.

3.1 Model

Fig. 3 shows a model for the wind tunnel test. The size reduction ratio is 1/20. The house with the heater mounted on its roof is assumed to be 2 stories and with plan dimension of 6.4m x 8.2m. It has a gable roof of 3/10 pitch. A heater is assumed to be a flat plate type having the size of 2m x 2m in plan. It is mounted on a ridge in 30° inclination to the horizontal plane.

3.2 Wind Profile in Wind Tunnel Test

Profiles of mean wind velocity and turbulence intensity are shown in Fig. 4 and Fig. 5, respectively. Mean wind velocity profile

---
[1]Building Research Institute, Ministry of Construction, Tsukuba

46

approximated to the following log-law equation:

$$U(Z) \propto \ln(Z/Z_0) \qquad (1)$$

in which, $U(Z)$ = mean wind velocity (m/s) at height over wind tunnel floor Z(m)

Z_0 = roughness parameter

= 0.70cm(14cm in conversion to full-scale)

Turbulence intensity at ridge height is about 15% and a power spectrum of turbulence at the same height is shown in Fig. 6. It approximated the Davenport's empirical equation(2):

$$\frac{S(n)}{\sigma^2} = \frac{2}{3n} X^2 (1+X^2)^{-4/3} \qquad (2)$$

in which, $S(n)$ = power spectral density at n(Hz)
η^2 = variance of turbulence
X = $nL/U(10)$
L = $\sqrt{3}$ x wave length giving power spectral peaks
$U(10)$ = mean wind velocity(m/s) at height of 10m in conversion to full-scale

Sprectrum in Fig. 6 was expressed by eq. (2) with L=14.6m ($U(10)$=8.1m). The value of L was converted to 298m in full-scale.

3.3 Summary of Results

Values of wind force coefficients for the heaters changed with wind directions as shown in Fig. 7. Those coefficients are normalized by the dynamic pressure at height of eaves as follows:

$$C = F/A/q_0 \qquad (3)$$

in which, C = wind force coefficient
F = mean wind force
A = projected area of heaters to a plane parallel to lower surfaces
q_0 = mean dynamic pressure at eaves height

Positive and negative signs of coefficients are defined as: when wind forces push heaters toward the roof, corresponding coefficients are positive and when wind forces pull heaters off roofs, corresponding coefficients are negative. Fig. 7 shows wind force coefficients are positive in directions $0°$ to $90°$, and are negative in directions $90°$ to $180°$. The values of coefficients for $0°$ and $180°$ are about 0.80 and -0.97, respectively. The coefficients reach a positive peak value at about $45°$ and a negative peak value at about $135°$.

4. RESULTS OF FIELD OBSERVATION

4.1 Characteristics of Wind
Wind directions observed are mostly west and east. Figs. 8 and 9 show 10 minute mean wind

velocity profiles of east and west wind at rather strong velocities, respectively. Here, directions west or east correspond to the true west or east $\pm$ 12.5°. Fitting these profiles for eq. (1), we get roughness length Zo of about 5cm. This is considerably small compared with wind tunnel in open fields. Fig. 10 shows a turbulence intensity profile in west winds. Turbulence intensities are 30 to 40% and are greater than those for wind tunnel flows. Fig. 11 shows power spectrum of turbulence at 10m high in west winds. It approximates Davenport's spectrum for X=200n as shown in the figure. The wave length giving a peak value of power spectrum agrees with one proposed by Davenport for natural winds, but it is much larger than that for wind tunnel flows.

4.2 Wind Forces

Relationships between 10 minute mean wind forces and 10 minute mean wind velocities at 10m high are shown in Figs. 12 and 13 for west and east wind, respectively. Positive and negative signs of wind forces are used following the same definition as stated in Fig. 7. These figures show that wind forces on heaters increase in proportion to the square of wind velocity. Curves of quadratic equation in these figures show regression equations obtained by assuming the relationship between wind forces(F) and wind velocities($U(10)$) at 10m high to be $F = a \, U(10)^2$, where a is a constant. Wind force coefficients can be derived from the constants as follows:

$$C = 2a \frac{1}{\rho A} \left(\frac{U(10)}{U_{ref}} \right)^2 \qquad (4)$$

in which, ρ = air density
U_{ref} = 10 min. mean wind velocity at height of eaves

C is calculated as -0.87 or 0.57 in case of west or east wind, respectively.

5. DISCUSSION OF RESULTS

Values of wind force coefficients and corresponding major parameters for full-scale field observations listed in Table 1 are compared with those for wind tunnel tests. Values of wind force coefficients observed outdoors are 10 to 20% less than those obtained in the wind tunnel. The differences are caused by the effects of:

(1) Scale of turbulence
(2) Intensity of turbulence
(3) Reynolds Number
(4) Sectional figure of heater
(5) Number of house stories

It was demonstrated by wind tunnel tests that the effects of parameters (4) and (5) of wind forces on heaters are small. Parameter (3) has little effects of wind forces on bluff bodies. Therefore, differences in values of parameters (1) and/or (2) in wind tunnel tests and full-scale field observations are considered major

47

reasons that caused the difference in wind force
coefficients.

6. CONCLUDING REMARKS

Wind force coefficents obtained by wind tunnel
tests are 10 to 20% larger than those from full-
scale observations. Therefore, by adopting wind
tunnel test results to design of heater mount-
ings, wind loads will be estimated with a factor
of safety. To determine a more accurate estima-
tion of wind forces on solar water heaters,
effects of scale and/or intensity of turbulence
should be investigated.

7. REFERENCE

(1) Hisashi Okada and Tatsuo Murota, "Wind Loads
    on Solar Water Heaters," 14th Joint Meeting,
    U.S.-Japan Panel on Wind and Seismic
    Effects, 1982.

(2) A.G. Davenport, "The Dependence of Wind
    Loads on Meteorological Parameters," Wind
    Effects on Buildings and Structures, 1967.

Table 1 Comparison between wind tunnel test and full-scale observation

	wind tunnel test	full-scale observation
wind force coefficient		
(west wind)	-0.97	-0.87
(east wind)	0.80	0.57
wave length giving a power spectral peak	170m	660m
turbulence intensity at height of eaves	15%	35%
roughness parameter	14cm	5cm
plan and dimensions of heater	rectangle 2m × 2m	rectangle 2m × 2.36m
cross-sectional figure of heater	flat plate	laid-L-like
plan and dimensions of house	rectangle 6.4m × 8.2m	rectangle 5.46m × 9m
number of story of house	2	1
roof	gable roof	gable roof
pitch of roof	3/10	3/10
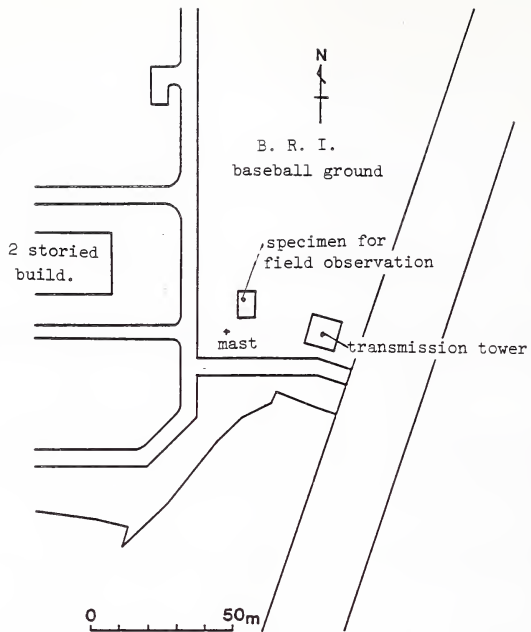
Fig.1 Layout of observation field

Photo 1 Observation field viewed from W-N-W
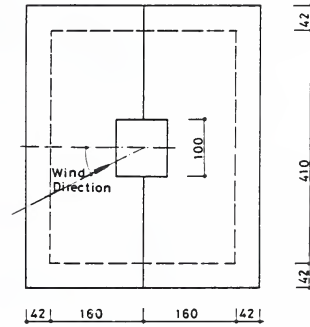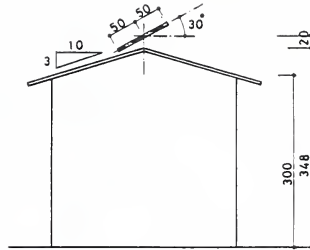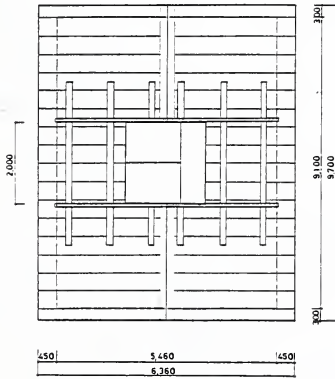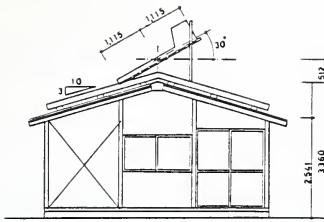
Fig.2 Specimen for field observation

Fig.3 Model for wind tunnel test
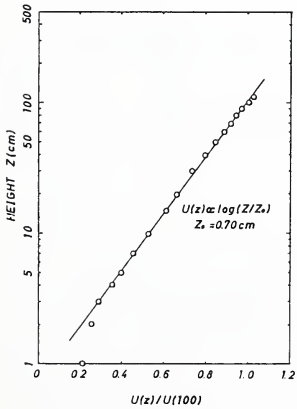
Fig.4 Mean wind velocity profile
of wind tunnel flow
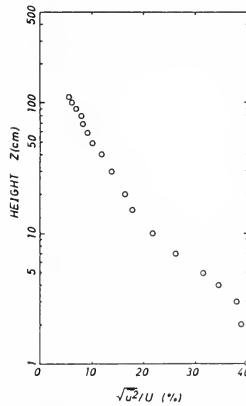
Fig.5 Turbulence intensity profile
of wind tunnel flow
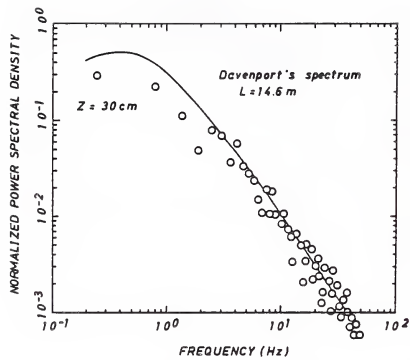
Fig.6 Power spectrum of turbulence
of wind tunnel flow
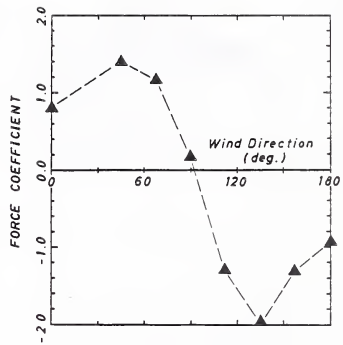
Fig.7 Wind force coefficients
(wind tunnel tests)
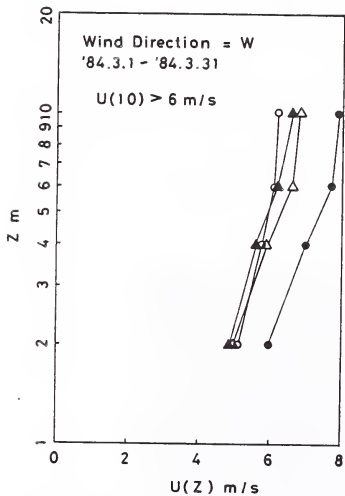
Fig.8 Mean wind velocity profile
(west wind)
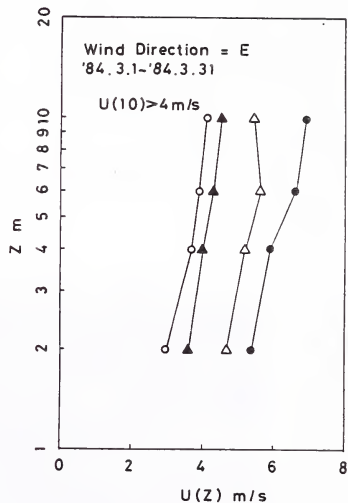
Fig.9 Mean wind velocity profile
(east wind)
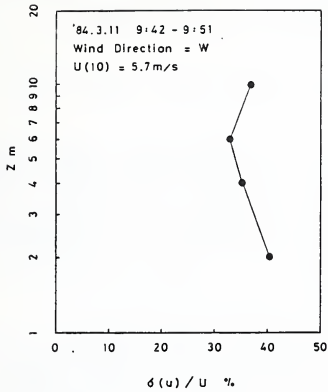
Fig.10 Turbulence intensity profile (west wind)
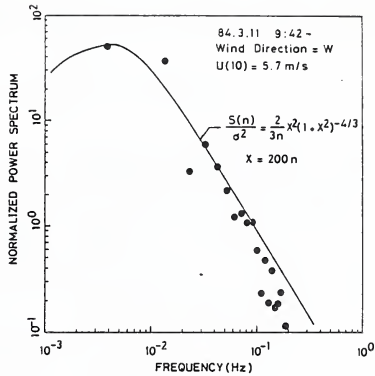
Fig.11 Power spectrum of turbulence (west wind)
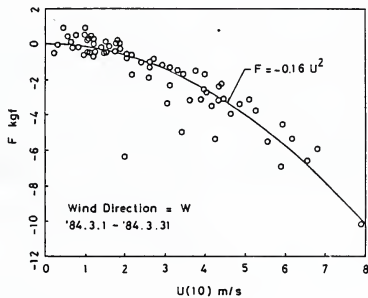
Fig.12 Relationship of mean wind force to wind velocity (west wind)
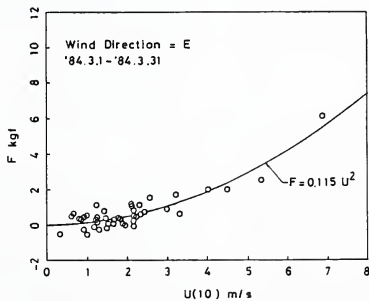
Fig.13 Relationship of mean wind force to wind velocity (east wind)

DESIGN CRITERIA FOR GLASS CLADDING SUBJECTED TO WIND LOADS

by

Emil Simiu[1] and Erik M. Hendrickson[1]

ABSTRACT

The safety and cost of glass cladding facades subjected to wind loads depend upon the criteria used for their design. These criteria specify the design wind loads and the allowable panel loads. The present paper reviews: the evolution in recent years of methods for the estimation and specification of design wind loads for building facades; recent developments concerning the estimation and specification of allowable loads for glass cladding panels, and controversies surrounding these developments; and recent developments in structural reliability as applied to glass cladding, which allow rational decisions to be made concerning the adoption of satisfactory design criteria specifying both design wind loads and allowable panel loads. It is shown that, in view of recent changes in methods for estimating design wind loads and allowable panel loads, it would be imprudent or wasteful to adopt a standard specifying allowable panel loads without giving due consideration to the overall reliability aspects of the cladding glass design problem. Comments are offered concerning the development of such a standard. The paper is addressed to members of the ASTM E06.51.13 Task Group on the Structural Performance of Glass and to other individuals and bodies concerned with the behavior and design of glass cladding under wind loads.

KEYWORDS

Design; Glass cladding; Probability; Wind Loads.

1. INTRODUCTION

A glass panel subjected to wind loads is designed so that the underlined design wind load, q_w, does not exceed the design value of the load capacity, q_a, referred to as the allowable load. A design criterion consists of the specification of the values q_w and q_a.

To each set of values q_w and q_a there correspond probabilities P_w and P_a, representing, respectively, the probability that the wind load on the panel will exceed the value q_w in any one year and the probability that the panel will break if subjected to a load q_a. A design criterion may thus be redefined as consisting of the specification of the probabilities P_w and P_a. For example, it might be specified that panels be designed so that $P_w = 0.02/year$ (corresponding to a 50-year mean recurrence interval of the wind load), and $P_a = 0.008$ (corresponding to a load that, if applied to the panel, would cause eight out of 1,000 panels to fail). It is required that the specification of q_w and q_a (or of P_w and P_a) be such that the safety level for the cladding glass facade as a whole is acceptable. It is noted

that the safety level depends on both q_w and q_a (or P_w and P_a). Thus, assuming that a design criterion has been proven by experience to result in acceptable designs, such a criterion should not be tampered with by changing the specification of the wind load without modifying accordingly the specification of the allowable load, and conversely.

The purpose of this paper is to examine various proposed design criteria in light of this observation. Such an examination is rendered necessary by various changes in the specification of design wind loads q_w, or of allowable loads q_a, proposed in the last decade without sufficient regard for the inextricable interconnection of these two quantities from a reliability viewpoint.

To provide the requisite background for this effort, we first review briefly the evolution in recent years of methods for the estimation and specification of design wind loads for building facades. We then review recent developments concerning the estimation and specification of allowable loads on glass cladding panels, and controversies surrounding these developments. Finally, we review the structural reliability framework that enables rational decisions to be made concerning the adoption of a design criterion specifying both design wind loads and allowable panel loads.

In attempting to assess various proposed design criteria, we will define 'acceptable safety level' as one that, in light of past experience with the behavior of glass facades under wind loads, is satisfactory from a public safety point of view and does not entail wasteful overdesigns.

2. DESIGN WIND LOADS

It will be useful for our purposes to illustrate two methods that have been widely used to specify design wind loads. To this end we reproduce two examples of wind load calculations from the Technical Service Memorandum issued by the Glass Division, PPG Industries, titled 'Design Wind Loads, ANSI A58.1-1972,' dated June 21, 1974. The examples show the calculation of wind loads in accordance with the City of Atlanta Building Code and the American National Standard ANSI A58.1-1972. They pertain to a 12-story building with dimensions 50 ft by 50 ft (15.24 m x 15.24 m) in plan and 150 ft (45.72 m) tall, assumed to be located in downtown Atlanta, Georgia.

----

[1]Center for Building Technology, National Bureau of Standards, Gaithersburg, Md.

2.1 City of Atlanta Building Code Requirements

The City of Atlanta Building Code wind load requirements, as quoted in the PPG Memorandum, are listed below.

Height of Structure (feet)	Wind Pressure (psf)
Under 30	25
30 - 49	30
50 - 99	40
100 - 499	45
500 - 1199	55
1200 and Over	60

(1 ft = 0.3048m; 1psf = 47.9 kPa)

The design pressure distribution required by the City of Atlanta Building Code is represented in Fig. 1, extracted from the PPG Memorandum. Note that the pressures at any one elevation of the building are uniform, i.e., pressures on corner and center panels are assumed to have the same value.

2.2 ANSI A58.1-1972 Requirements

Figure 2, also excerpted from the PPG Memorandum, shows pressures and suctions on the glass panels of the building, calculated in accordance with the provisions of the American National Standard ANSI A58.1-1972 [1] under the following assumptions:

(1) the building is not exceptional in terms of its degree of sensitivity to wind or of its degree of hazard to life and property, and

(2) the terrain upwind of the building is built up for at least one-half mile in all directions, with at least 50 percent of the buildings in excess of six stories; in addition, the terrain for at least one more mile is of the suburban type.

In Fig. 2, positive and negative numbers indicate pressures and suctions, respectively. It is seen that pressures on corner strips (having, according to the ANSI Standard, width = 0.1 x 50 ft = 5 ft (1.52 m) on all faces) are higher than pressures elsewhere on the building faces. (The pressures in Fig. 2 are consistent with the provisions of ANSI A58.1-1972 except for a few minor numerical differences.)

Three points concerning the ANSI Standard requirements deserve comment. First, these requirements make allowance for the effect of terrain exposure on the wind loads. In contrast, the City of Atlanta Building Code, and similar codes, specify the same wind loads regardless of whether the building being designed benefits from a favorable exposure or not. It is seen from Figs. 1 and 2 that the maximum (corner) loads specified by the ANSI Standard are in this case lower than the loads specified by the City of Atlanta Building Code. However, it can be verified that they would have been higher had the conditions listed under assumption (2) above not been satisfied.

Second, the requirements of the City of Atlanta Code (and of similar codes) imply the use of a single pressure coefficient for the entire building. In contrast, the ANSI Standard specifies a different pressure coefficient for each distinct aerodynamic zone of the facade. For example, the negative external pressure coefficient at a building corner is $C_p = -2.0$. Thus, as seen in Fig. 2 and pointed out earlier, loads are not uniform over the width of the building, and if architectural and construction considerations permit, it is possible to limit the use of stronger glass to the zones of high pressure, rather than using the same glass thickness throughout the entire facade.

Third, in the ANSI Standard — as in the City of Atlanta Building Code Loads -- the directional features of the extreme wind climate and of the aerodynamic flow around the building, are not accounted for. Indeed, the external pressures calculated in accordance with the ANSI Standard are proportional to the product of the appropriate pressure coefficient and the square of the wind speed from any direction, v_N, corresponding to a N-year mean recurrence interval (usually, N = 50, or, in the case of buildings with an unusually high degree of sensitivity to wind, or an unusually high degree of hazard to life and property, N = 100).

Since our object is to review only the broad features of methods for specifying design wind loads, we do not discuss here revisions included in the 1982 version of ANSI A58.1. Although pressure distributions in ANSI A58.1-1982 are somewhat different from those indicated in Fig. 2, in general they would not affect the three points just commented upon.

2.3 Design Loads Based on Wind Tunnel Tests

Methods for estimating design wind loads have evolved in recent years following the increasingly widespread use of the wind tunnel as a design tool.

In the first years during which wind tunnel testing of individual buildings became relatively common, external pressures were calculated by using essentially the same method as the ANSI Standard, except that pressure coefficients were determined from wind tunnel measurements, rather than being taken from ANSI Standard tables. In wind tunnel tests external pressure coefficients are measured at a large number of points on the building facade for as many as 32 or more directions. The pressure coefficient at a point was assumed to be the largest of the coefficients measured for the various wind directions at that point. The design pressure was then assumed to be proportional to that pressure coefficient and to the square of the wind speed, v_N. Thus, the dependence of pressures upon the directionality of the extreme wind climate was ignored, just as in the 1972 or 1982 ANSI Standard. It is convenient to summarize the procedure for calculating design wind loads just described by the formula

$$q = 1/2 \ \rho \ \max[C_p(\alpha)]v_N^2 \qquad (1)$$

where C_p is the pressure coefficient for the point being considered, α is the wind direction, ρ is the air density, and v_N is the design wind speed.

The main motivation for conducting wind tunnel studies was to identify areas on the building facades where pressures could be higher than indicated in tables, such as those included in the ANSI Standard. Areas with high pressures could be expected to exist on buildings with unusual geometric shapes, re-entrant corners, and so forth, or buildings subjected to channeling or other aerodynamic effects due to the proximity of other structures. It was found that areas with pressure coefficients higher than those specified in the ANSI Standard or than those implicit in various codes are quite common indeed. At the same time it was found that, most commonly, high pressures were not only confined to relatively small areas, but also corresponded to pressure coefficients that decreased rapidly as a function of direction, as suggested, for example, in Fig. 3. It could, then, be argued that the chances of the wind speed having the value v_N and having precisely the most unfavorable possible direction are small, and that a reduction of design pressures would be in order. For reasons not explained satisfactorily, a blanket reduction factor of about 0.8, meant to account for the favorable effect of directionality, has been proposed (see, e.g., [2]).

It is in fact possible to estimate wind loads with any given mean recurrence interval by taking into account both the directional dependence of the pressure coefficients and the directional dependence of the extreme wind climate. For details, see Ref. 3, Chapt. 8. To illustrate the effect of directionality, consider the following simple example. Assume that the pressure coefficient and the largest wind speed in a given year are $C_p(\alpha_1) = 1.0$ and $v(\alpha_1) = 30$ m/s for direction α_1, and that $C_p(\alpha_2) = 2.0$ and $v(\alpha_2) = 20$ m/s for direction α_2. The air density is assumed to be $\rho = 1.2$ kg/m^3. If the pressure is obtained by an expression similar to Eq. 1, the calculated largest pressure for that year would be

$$q = 0.5 \times 1.2 \times 2.0 \times 30^2 = 1080 \text{ Pa}$$

Actually, at the point of interest, during the year in question, the largest pressure from direction α_1 is

$$q(\alpha_1) = 0.5 \times 1.2 \times 1.0 \times 30^2 = 540 \text{ Pa}$$

and the largest pressure from direction α_2 is

$$q(\alpha_2) = 0.5 \times 1.2 \times 2.0 \times 20^2 = 480 \text{ Pa}$$

i.e., the largest wind pressure during the year is 540 Pa, rather than 1080 Pa, as would be indicated by the calculation based on the largest wind speed from any direction. In reality, we would of course have to perform calculations for, say, 8 or 16 directions. However, from this deliberately simple example it can be inferred that, in most cases, a wind load with a 50-year (or 100-year) mean recurrence interval calculated by taking wind directionality into account is smaller than the

wind load calculated by Eq. 1 in which the wind speed v_N is the wind from any direction, obtained, for example, from the ANSI Standard.

Within the last decade, rather than using Eq. 1, commercial wind tunnel laboratories usually have provided information on design wind pressures based on calculations that account for the directional dependence of both the pressure coefficients and the extreme wind climate. Interestingly, the mean recurrence interval is quite often not specified by the building official, perhaps because not enough building officials are sufficiently familiar with the relatively new developments and issues involved in such specification. It is common for the wind tunnel laboratory to provide design wind pressures corresponding to 50- and 100-year mean recurrence intervals, and the choice of which to use in design is left to the developer or building owner, in spite of the public safety issues such a choice obviously entails.

It is clear from what has been said above that design pressures with a 50- or 100-year mean recurrence interval calculated by taking into account the directional dependence of the pressure coefficients and of the extreme wind climate may be lower than the values obtained from the ANSI Standard or from codes of the type exemplified by the City of Atlanta Building Code. The question then arises whether the safety levels of glass cladding facades designed on the basis of such pressures are acceptable. To attempt an answer to this question it is first necessary to examine the matter of estimating and specifying allowable loads, q_a.

3. ALLOWABLE LOADS ON GLASS PANELS

3.1 Design Charts

Although other sources of information on this topic exist, the major documents available for use by designers in the United States are those issued by LOF Glass [4], PPG Industries [5,6], and the American Society for Testing and Materials (ASTM E 330 Standard) [7]. These documents specify 60-second loads causing glass panel failure. Differences among the charts of [4], [5], and [7] are relatively minor. While [4] and [7] are essentially unmodified versions of documents that have been in existence for almost two decades, the PPG Industries charts first issued in 1979 [6] represent a major departure from the PPG Industries charts issued in 1974 [5], and therefore also differ substantially from [4] and [7].

It is useful at this point to present the following excerpts from the LOF Technical Information document ATS-108 [8] concerning the ASTM charts [7] and the departures from them in the charts of [6]:

> "Starting in 1964 a consensus on glass strength began to develop within the building industry. Within five years, strength of glass information in building codes and the standards of trade associations and technical societies became uniform for practical

purposes. Of these documents the one exposed to the most critical study is ASTM Standard E 330, Structural Performance of Exterior Windows, Curtain Walls, and Doors by Uniform Pressure Difference. A glass strength chart included in the appendix to this Standard ... generally considered to be an 'industry standard' for glass exposed to uniform loads....

"On April 23, 1979, the Glass Division of PPG Industries issued a technical bulletin on glass strength.... The information therein differs significantly from the ASTM chart and all other current publications....

"The PPG charts are more conservative than existing information. In some cases the discrepancies in the PPG information are large.... The specification writer faces a dilemma. His indicated choice of glass may depend upon the manufacturer. PPG information suggests one thickness and the data used by the remainder of the industry will lead him to another thickness, most often thinner....

"In a letter of February 13, 1979 to ASTM, PPG characterizes the ASTM chart referenced earlier as presenting 'possibly dangerous information.' Persuasive reasons for these opinions are not included...."

The drastic changes embodied in the 1979 PPG charts [6] might well have appeared all the more surprising to the industry as the previous PPG document [5] (whose charts did not, by and large, differ substantially from the LOF [4] or the ASTM [7] charts), contained a section entitled 'Current Practice on Firm Foundation,' which stated:

"For more than 20 years, empirical tables developed by PPG were accepted internationally as references for determining glass thickness and size. A chart including failure probability considerations, published in 1962, established a more reliable procedure, which is now in general use. The new product recommendations presented here are based on recent research, analysis, and experience."

Prompted by discrepancies between [6] and other charts, the task group ASTM E06.51.13 (Structural Performance of Glass) of the ASTM E06.51 Committee on Component Performance of Windows, Curtain Walls, and Doors is currently examining a draft proposal submitted by the task group chairman, which includes proposed charts for allowable loads q_a on annealed glass panels simply supported on four sides, corresponding to a probability of failure $P_a = 0.008$. In a number of instances, especially for thinner glass, the loads in these proposed charts are relatively close to those of [6]. However, in other instances the loads in the proposed charts are substantially lower than the loads in [6] (and, therefore, even more substantially lower than the loads in [4], [5], and [7]). To illustrate differences among various available charts, listed below are values of the

load corresponding to a probability of breakage $P_a = 0.008$ as given in the LOF charts [4], the 1974 PPG Industries charts [5], the ASTM E 330 Standard [7], the 1979 PPG charts [6], and the E06.51.13 draft, for two annealed glass panels supported on four sides: panel 1 is assumed to have a 15 ft^2 (1.39 m^2) area, 3/16 in. (5 mm) thickness, and aspect ratio (ratio of long side to short side) equal to 2.0; panel 2 is assumed to have a 20 ft^2 (1.86 m^2) area, 5/16 in. (8 mm) thickness, and aspect ratio 1.0. It is noted that the dependence of the allowable loads on aspect ratio is reflected only in the 1979 PPG charts [6] and in the charts from the E06.51.13 draft document. The loads q_a are listed below.

Reference	Panel 1	Panel 2
LOF [4]	52 psf	82 psf
PPG (1974) [5]	50 psf	78 psf
ASTM [7]	50 psf	81 psf
PPG (1979) [6]	28 psf	70 psf
E06.51.13 Draft	29 psf	50 psf

1 psf = 47.9 kPa

Additional comparisons among values q_a taken from various sources are presented later.

Reference 4 contains information, based on test results, on allowable loads corresponding to failure probabilities P_a ranging from 0.2 to 0.0005. Similar information is given in [6] for probabilities P_a ranging from 0.5 to 0.001, based on the assumption that the strength of glass has a normal distribution with a coefficient of variation of 25% for annealed glass and 20% for heat strengthened glass.

3.2 Sources of Differences Among Load Charts

Differences among loads corresponding to a failure probability $P_a = 0.008$ specified in the various charts can be attributed to: (1) differences in the definition of the basic strength of glass as affected by in-service degradation, (2) differences among the respective methods for estimating the load capacity, and (3) effects of statistical errors.

3.2.1 Effect of In-Service Degradation

The 1974 PPG document [5] states: "The curves plotted for each nominal thickness represent the expected performance of glass of PPG minimum thickness after _normal_ surface depreciation has occurred. These curves are not applicable to glass that has obvious surface damage, such as abrasion, scratches, or welding splatter tracks.... In the interest of public safety, prompt replacement of damaged glass is imperative."

According to [4], the LOF charts "are based on testing glass to destruction. In effect they are a summary of test results." It is further stated in [4] that "float glass, plate glass, and sheet glass had the same strengths for practical purposes. Any differences are not significant

enough to warrant distinguishing between the three methods of production." No explicit statements are made in [4] on whether any allowance was made for surface degradation, but from the similarity between the values of [4] and [5] one might infer that surface degradation was accounted for in essentially the same manner in the respective sets of charts.

As noted earlier, the loads in the new PPG charts [6] are in most cases substantially lower than those given in the 1974 PPG document [5]. The principal reason for these reductions lies in the decision by PPG to reduce the strength of annealed glass by 33 percent to account for in-service surface degradation, presumably beyond what was referred to in the earlier PPG document [5] as normal surface depreciation. This decision is justified as follows [9]: "While the average breaking stress of as-produced glass is approximately 9000 psi; limited strength data using in-service float glass, in conjunction with engineering judgement and experience, indicate that a 60-second average breaking stress of 6000 psi with a coefficient of variation of 0.22 probably represents the strength of in-service float glass reasonably well for architectural design purposes with respect to wind loads." Note that the 'average breaking stress' of 6000 psi and the coefficient of variation of 0.22 are also listed in [6] for annealed glass.

As far as the E06.51.13 Draft is concerned, it is the writers' understanding that it is based on tests conducted on glass panels removed after about 20 to 25 years of service from three buildings subjected to renovation or wrecking and salvage operations [10]. Of these buildings, the Great Plains Life Building was severely damaged during the May 11, 1970 Lubbock tornado, which caused the loss of a substantial part of the glass panels (e.g., on the south and west elevations of the building, about 50 percent of the panels were lost [11]). The reduction in strength for in service glass with respect to new glass given in [10] is on the order of 66 percent, rather than 33 percent as in the case of [6].

3.2.2 Effect of Methods for Estimating Load Capacity

As mentioned above, the LOF charts were obtained by fitting curves to test results. The charts in [6] were developed using the following criterion: panel breakage occurs if the maximum stress in the plate is equal to the breaking stress. It was further assumed that for annealed glass the breaking stress has a normal distribution with a mean of 6000 psi and a coefficient of variation of 0.22, as indicated earlier [9]. For example, to calculate the breaking load corresponding to a 0.008 probability of panel failure, it is necessary to obtain the breaking stress corresponding to the value 0.008 of the cumulative distribution function of the breaking stress. From normal distribution tables it follows that this breaking stress is equal to the mean breaking stress minus 2.41 times the standard deviation of the breaking stress, i.e., $6000 - (2.41 \times 0.22 \times 6000) = 2819$ psi. (The

value listed in [6] is 2800 psi.) The load that corresponds to a 0.008 failure probability for the panel being considered is then assumed to be equal to the load that causes a maximum stress in that panel equal to 2800 psi.

The charts in the E06.51.13 draft are based on the glass failure model developed in [10]. In this model a glass panel is viewed as a weakest link system that will fail when the strength at any of its points and in any direction is lower than corresponding applied normal stress. The strength is assumed to be modeled by a two parameter Weibull distribution. The probability of failure of the panel is then calculated in accordance with Weibull's classic theory. Conversely, it is possible to estimate from failure tests conducted on a sufficient number of panels the best fitting parameters of the Weibull distribution of the strength.

Comments on the possible effects of load capacity estimation methods and on differences between values given in various documents are presented subsequently.

3.2.3 Effect of Statistical Errors

Statistical errors are likely to have affected the values of the load capacities specified, e.g., by the LOF charts. Note, in particular, that the methods of analysis used in [6] and in the E06.51.13 draft, and the respective charts, reflect the influence of the aspect ratio of the plate on the stresses and therefore on the failure loads, while the LOF charts [4], the old PPG charts [5], and the ASTM charts [7] do not. It is stated in [4] that: "The ratio of the width and length of a pane of glass ... may have an effect on its ability to withstand uniform loads. Test data show that adjustments for this ratio are small and follow no readily predictable pattern.... When the ratio of the long edge to the short edge does not exceed 5:1 any adjustment would not influence the choice of glass type or thickness." In the writers' opinion, the failure of [4] (as well as [5] and [7]) to reflect the influence of the aspect ratio is due to statistical errors. Such errors can be significant, since the coefficient of variation of the failure loads can be as high as 0.20 or so, and the number of specimens in any one set of tests is, as a rule, relatively small (from 10 to 30, say). Statistical errors could thus easily obscure the aspect ratio effect. This point will be taken up again subsequently against the background of comparisons between graphs of various specified allowable loads.

Statistical errors due to insufficient testing are also likely to affect values of the prestress used in methods for estimating the load capacity of heat strengthened and tempered glass panels.

3.3 NBS Method for Estimating Load Capacity

A more recent method for estimating the load capacity of glass panels has been developed at the National Bureau of Standards (NBS). The method

entails two phases: obtaining basic strength information, and estimating the load capacity of glass panels once this information is available. The basic strength information consists of the parameters of the Weibull distribution of the glass strength. It is possible to obtain this information from results of ring-on-ring tests performed on new glass, using a method based on fundamental fracture mechanics considerations, described in [12]. The method for estimating the probability distribution of the load capacity of the panel is also based on fundamental fracture mechanics considerations. Its essential features are described in [13], and a listing of the computer program used to implement the method is included in [12]. The computer program used in the investigation presented in this work was an updated version of the program listed in [12] and is available from the authors.

An interesting result obtained in [12] is that the Weibull distribution of the glass strength, and the Weibull distributions of the load capacity of the panels, have location parameters with positive values, rather than with zero value, as assumed in [10]. This is an indication that the load capacities of panels have positive, rather than zero, lower bounds. A similar result was obtained by independent tests conducted at Nippon Sheet Glass Company in Ichihara City, Japan, and communicated to the writers by S. Kawabata. It was also shown in [12] that the procedure for estimating the load capacity of glass panels developed at NBS is insensitive to the shape of flaws causing panel failure. Further research conducted on the validity of the fracture mechanics models used in this procedure is reported in [14], in which these models were validated against results of failure tests on about 100 annealed glass panels with dimensions 1.52 m x 2.43 m x 6mm, conducted recently by the Ontario Research Foundation [15].

Load capacities corresponding to the failure probability $P_a = 0.008$ estimated for new glass by the NBS method are shown in Figs. 4 to 8. For the heat strengthened glass the estimates were obtained by using strengths, based on ring-on-ring tests conducted on annealed glass specimens, augmented by a value assumed to be equal to the prestress due to the heat strengthening process. The prestress can be inferred from information on breaking strengths tabulated for annealed and heat strengthened glass in [6]. The value of the prestress in the heat strengthened glass used in the calculations was 4,200 psi. A similar procedure can be applied to tempered glass.

3.4 Comparisons Between Estimated Load Capacities

Figures 4 to 8 also include values of the load capacity corresponding to the failure probability $P_a = 0.008$ taken from the LOF charts [4] and from the PPG charts [6]. Recall that the PPG values from [6] pertain to glass assumed to have lost 33 percent of its mean strength owing to surface degradation in service. Approximate values for the mean strength of new glass (based on the values

given for old glass in [6]) can be estimated as follows. In the case of annealed glass, the values of [6] are multiplied by 1.5, i.e., by the ratio (9000/6000) between the average breaking stress for new glass and for old glass assumed in the PPG calculations. This simple procedure assumes, first, that stresses at the failure points are proportional to the applied load. Since it is indicated in [9] that the vast majority of annealed glass panels were found to break in high stress regions, and since in such regions stresses are approximately proportional to the loads, this assumption is acceptable to a first approximation. A second assumption is that the coefficients of variation of the breaking stresses are the same for new and old glass. For heat strengthened glass the multiplying factor, rather than being 1.5, is assumed to be equal to the ratio between the sum of the prestress and the breaking stress for new glass, and the sum of the prestress and the breaking stress for old glass. In both cases the values of the breaking stress corresponding to a failure probability $P_a = 0.008$ are used. In Figs. 4 to 8 the PPG values from [6] are labeled 'PPG [6] (old glass)', and their counterparts for new glass are labeled 'PPG [6] (new glass)'. It is emphasized that these new glass strength values are only approximate estimates.

It can be seen that the NBS estimates for new glass are very close to the new glass values derived from the PPG charts [6]. It is also noted that the influence of surface degradation on the estimated allowable loads becomes smaller in the presence of prestressing due to heat treatment. Finally, note that the general shapes of the curves expressing the dependence of the load capacity upon aspect ratio support the conjecture that, in the absence of guidance by structural theory, this dependence was clouded by sampling errors and was missed in LOF and other charts for this reason.

It is seen in Fig. 8 that there are instances where the PPG values from [6] are _higher_ than the LOF values, i.e., there does not appear to be a uniform pattern as far as the relative magnitudes of the values in the two sets of charts is concerned. An examination of the LOF [4] and PPG [6] charts reveals that PPG values tend to be lower than LOF values (in some cases by as much as 50 percent) for the thinner annealed glass panels with relatively small areas, and tend to be higher than LOF values (in some instances by as much as 100 percent) for the thicker annealed glass panels with larger areas (i.e., about 80 ft^2 or more), heat strengthened glass panels, and the thicker tempered glass panels.

Comparisons between various estimates of the load capacities, such as those presented herein can reveal apparent anomalies that might be attributable to deficiencies in the methods of analysis. For example, in spite of apparently similar stress analyses and of the apparent use in developing the E06.51.13 draft of basic strengths lower than those implicit in [6], a 3/16 in. annealed glass panel with 10 ft^2 area and aspect ratio 1.0 has a marginally higher load in the

E06.51.13 draft than in [6] (29 psf versus 28 psf), while for a 3/4 in. annealed glass panel with 100 ft^2 area and aspect ratio 1.0 the E06.51.13 load is considerably lower (42 psf versus 80 psf). Such an inconsistency suggests that, in this case, at least one of the methods of analysis on which the two documents are based performs inadequately. One possible explanation is that the simplified model on which [6] is based, which was briefly described earlier, may, for certain ranges of glass thickness, panel area, and aspect ratio, result in load capacity estimates with unacceptable deviations from the actual load capacities. Another possibility is that, for certain ranges of these variables, unacceptable deviations may be the result of forcing the location parameter of the Weibull distribution of glass strength to vanish, as was done in [10] and in the E06.51.13 draft. This might bring the value of the variate corresponding to the 0.008 percentage point closer to zero than is actually the case. Further studies of panel test results are necessary to verify the validity of such possible explanations.

4. RELIABILITY CONSIDERATIONS

4.1 Assessment of Past Practice

As stated earlier, the safety level inherent in a design criterion for glass cladding is regarded as acceptable if, in light of past experience with the behavior of glass facades, (1) it is satisfactory from a public safety point of view, and (2) it does not entail wasteful overdesigns. A first and indispensable step in any attempt to develop new design criteria is to assess past design practice from these two points of view.

Glass cladding started to develop as a major architectural component primarily in the 1950's. It would appear that for a period of at least 20 years a large number of designs have been carried out on the basis of the criterion $q_{wc} < q_{ac}$, in which q_{wc} denotes a conventional design wind load, i.e., a design wind load taken from codes with wind loading requirements of the same type as those of the Uniform Building Code (or codes such as the City of Atlanta Building Code) and q_{ac} denotes a conventional allowable load, i.e., an allowable load taken from charts such as those issued by LOF [4], PPG [5], or ASTM [7]. Such designs will be referred to here as conventional designs.

Data on glass cladding failures due to high winds are not readily available in a form suitable for analysis; however, it appears that, with the possible exception of a few local code jurisdictions, failures have generally not occurred owing to the inadequacy of provisions in building codes and standards and glass design charts but, rather, owing to such causes as:

 − design errors

 − inadequate quality of panels being used (due, e.g., to substandard manufacturing, as in the case of glass with nickel sulfide inclusions

causing spontaneous failure, or to mishandling of the panels before or during construction)

 − poor construction details

 − the occurrence of exceptional storms such as tornadoes the effects of which are deliberately not accounted for in building codes

 − wind-borne missiles, e.g., gravel blown by wind from the roofs of adjacent buildings (this was apparently a major cause of damage to glass facades in downtown Houston during hurricane Alicia).

This suggests that, in general, conventional designs have been satisfactory from a public safety standpoint. Should there be any reasons to doubt the acceptability of this assumption in any particular instance, a clear and well documented case should be made for the opposite view.

As to the question whether conventional designs are acceptable from an economic standpoint, it can be argued that had they been viewed as wasteful, the probability of failure $P_a = 0.008$ associated with the conventional allowable loads would have been increased. To the writers' knowledge there have been no proposals to this effect.

4.2 Design Calibration: Case $q_w = q_{wc}$

If it is assumed that conventional designs have been satisfactory from a safety standpoint, it follows that designs based on the inequality $q_w < q_a$, in which $q_w = q_{wc}$ but q_a is lower than q_{ac}, would have safety levels higher than those inherent in conventional designs. This appears to be unnecessary, and would impose an undesirable economic penalty on the glass cladding component of building construction.

It has been argued that design values $q_a < q_{ac}$ should be specified for the following reason. If the failure probability corresponding to the conventional value q_{ac} is $P_a = 0.008$ after normal surface degradation (as understood in [5], see section 3.2 above), the failure probability will be higher after the degradation that may occur following 20 years of service. Thus, the use of the conventional allowable load in design would not ensure that the failure probability of the panel under the action of the design wind load will be at most 0.008 during the entire anticipated life of the panel. Thus, it has been argued that the allowable load used in design should be the value corresponding to a failure probability $P_a = 0.008$ of the panel degraded as apparently assumed in the E06.51.13 draft (i.e., with a loss of about 66 percent of the original strength).

In reality, 0.008 is not a 'magic number,' and it represents nothing more than a nominal value arrived at by experienced and competent professionals within the context of conventional design practice. This value appears to have worked well within that context, i.e., it has resulted in an acceptably small number of panel failures under wind loads. It is true that, implicit in

conventional practice are actual values of the failure probability under the load q_{wc} that are equal to or lower than 0.008 toward the beginning of the panel's service life, and possibly higher than 0.008 at a later time. However, this does not matter as long as the corresponding number of panel failures during the lifetime of the building is sufficiently low. Therefore, for design wind loads $q_w = q_{wc}$, the use of allowable load charts based on drastically reduced strengths (e.g., the charts of the E06.51.13 draft) would not be justified.

3.3 Design Calibration: Case $q_w \neq q_{wc}$

It has been shown earlier that design wind loads calculated in accordance with the 1972 (or 1982) ANSI Standard A58.1 can be lower than conventional designs loads, e.g., for buildings in terrain classified as urban, and/or for portions of the facades away from building edges. Design wind loads incorporating aerodynamic and climatological wind directionality effects also tend to be lower than conventional wind loads, with the possible exception of a few 'hot spots.'

First, we consider facades in which, by design, all the panels have the same allowable load. For such facades, the design criterion $q_w < q_a$ becomes

$$\max\{q_w\} < q_{ac} \qquad (2)$$

where $\max\{q_w\}$ is the largest design wind pressure on the facade (e.g., in Fig. 1, $\max\{q_w\} = 45$ psf). If $\max\{q_w\} > q_{wc}$, the design criterion given by Eq. 2 will result in a safe design. However, if $\max\{q_w\} < q_{wc}$, the resulting design may be unsafe, i.e., the number of panel failures during the lifetime of the building would be higher than that inherent in a conventional design.

Second, we consider the case in which architectural and construction considerations permit the division of the facade into, say, two distinct zones with panels having conventional allowable loads q_{a1c} and q_{a2c}. The largest design wind loads on the two zones are denoted by $\max\{q_{w1}\}$ and $\max\{q_{w2}\}$. Two design inequalities are then used:

$$\max\{q_{w1}\} < q_{a1c} \qquad (3a)$$

$$\max\{q_{w2}\} < q_{a2c} \qquad (3b)$$

Usually $\max\{q_{w2}\} < q_{wc}$. Therefore, even if $\max\{q_{w1}\} > q_{wc}$, it still is possible that the total number of panel failures during the structure's lifetime will be higher than that inherent in a conventional design. This is of course even more strongly true if $\max\{q_{w1}\} < q_{wc}$.

Thus, unless the design wind load $q_w > q_{wc}$ for all panels, the safety level inherent in a facade for which $q_a = q_{ac}$ is lower than for a conventional design. The safety level further decreases if $q_a < q_{ac}$.

For the sake of definiteness, we consider again Figs. 1 and 2. We assume that the panels are designed on the basis of the loads on the upper part of the structure, that their dimensions are 4 ft x 6 ft, and that annealed glass is used. The glass thicknesses corresponding in various charts to the 45 psf load specified by the City of Atlanta Building Code and to the 32 psf and 15.5 psf loads specified by ANSI A58.1-1972 are listed below.

	$q_w = q_{wc} = 45$ psf	$q_w = 32$ psf	$q_w = 15.5$ psf
LOF [4]	1/4 in.	3/16 in.	1/8 in.
1974 PPG [5]	1/4 in.	3/16 in.	1/8 in.
1979 PPG [6]	5/16 in.	1/4 in.	1/8 in.
E06.51.13 Draft	3/8 in.	5/16 in.	5/32 in.

It can be seen that a conventional design would consist of annealed glass panels with 1/4 in. thickness. However, if the panels were designed in accordance with the ANSI A58.1-1972 Standard and the allowable loads were taken from [4] or [5], the panel thicknesses would be reduced to 1/8 in. over most of the facade and to 3/16 in. near the corners. Obviously, the expected number of panel failures during the lifetime of the building would be considerably higher for this design than for the conventional design.

It therefore becomes understandable that following the development of the ANSI Standard A58.1-1972 some professionals may have felt uncomfortable with situations such as the one just illustrated, and may have felt the need to counterbalance trends toward less safe designs inherent, at least in some cases, in design provisions such as those of the ANSI A58.1 Standard. Even though the PPG Technical Service Memo dated June 21, 1974 states that "PPG does not recommend ... safety factors," it is permissible to interpret PPG's changes in allowable loads as changes in the factors of safety inherent in glass cladding designs. The same could be said of the E06.51.13 draft.

Assuming that the technical information included in the revised PPG charts [6] or in the E06.51.13 draft was correct, the question arises whether the safety margins implicit in their respective choices of glass strength (e.g., 67 percent of the value for new glass in the case of [6]) lead to acceptable safety levels for cladding glass designs. For example, if the revised PPG charts [6] are used in conjunction with the City of Atlanta Building Code, it can be seen from the glass thicknesses listed above the resulting design would be uneconomical compared to a conventional design. However, if those charts are used in conjunction with the ANSI A58.1-1972 Standard, the resulting design would be less safe than that inherent in a conventional design. This is true because the thickness of the majority of the panels (i.e., of all the panels not located in corner zones) would be 1/8 in., instead of 1/4 in. as in a conventional design, and the chances of failure of some of those panels would therefore be greater than for a conventional design.

It is seen that the disadvantage of, in effect, increasing safety factors by reducing the glass strength on which design charts are based is that such increases affect indiscriminately designs

based on different loading criteria, so that while the increases may be warranted for some loading criteria, they may well be unwarranted for others. In the absence of guidance to the designer, and depending upon the loading criterion being used, there would result in some instances facades that are unnecessarily expensive; in some instances the facades would have acceptable safety levels; and in some instances the resulting facades would be unsafe in relation to conventional designs.

4.4 Reliability-Based Glass Cladding Design

The existence of different criteria with respect to design wind loads and to allowable panel loads inevitably creates confusion and dilemmas that have yet to be resolved. This can be done by an explicit use of modern structural reliability procedures. Within the context of glass cladding design, such a procedure has already been developed and successfully applied (see, e.g., [3, Chapter 9] for a detailed description). For any given glass cladding design of any given building, the procedure makes it possible to estimate the expected number of panel failures during the lifetime of the building. Conversely, given a specified safety level (i.e., a specified expected number of panel failures during the lifetime of the building), the procedure makes it possible to design the glass cladding so that it meets this safety requirement. The procedure is computerized, and can account for the strength degradation of the glass panels as a function of time. Its inputs consist of relevant wind climate and aerodynamic information, and of the mean value and the coefficient of variation of the load capacity of the glass panels.

By applying the reliability-based procedure just mentioned to a sufficient number of typical designs, it is possible to obtain information on the expected number of panel failures per lifetime inherent in those designs. Such information can then be used to establish safety level criteria (i.e., acceptable expected numbers of panel failures per lifetime). The latter would serve as a basis for risk-consistent design criteria for glass cladding subjected to wind loads, which would supersede the present unsatisfactory state of affairs. Specifications involving the use of 'design factors' of the type included in the LOF [4] or PPG [5] charts could be contemplated. A research effort on practical methods for achieving risk-consistent designs, involving the National Bureau of Standards, Colorado State University, and Gordon B. Smith Corporation, has recently been planned.

4.5 Comments on a Future ASTM Standard

The evolution of consistent criteria outlined above can take time, and should be gradual. The effort currently being undertaken by the ASTM E06.51.13 task group, whose scope is limited to preparing a standard concerning the load capacity of glass panels, could contribute usefully to such an evolution. For this to be the case, such a standard should meet the following requirements:

- Its charts should be derived from a basic strength of glass (as expressed, e.g., by the parameters of the probability distribution of the strength of glass) (a) defined explicitly in terms of the basic strength of glass implicit in the ASTM E 330 Standard [7] or of the basic strength of new glass, and (b) meeting with the explicit approval of the ASTM E06.51.13 task group.

- It should be based on an acceptable method of calculation. In the writers' opinion, the method developed in [10] and used in the E06.51.13 draft would be acceptable if it were modified to be compatible with experimental evidence that the lower bound of the glass strength is not zero, as assumed in [10] (i.e., that the assumed Weibull distribution of the glass strength has three, rather than two parameters). As mentioned earlier, the assumption that the glass strength is described probabilistically by a two-parameter Weibull distribution could have significant effects on the extrapolation of test results to low probabilities of failure (e.g., $P_a = 0.008$).

- Allowable loads included in the standard, calculated by the method of [10] or by any other acceptable method of calculation, should be verified for an acceptable number of types of panels against reliable test results.

- The information on load capacity included in the standard could, if desired, consist of the 0.008 percentage point. However, in addition to the 0.008 percentage point, the standard should include the mean values and the coefficients of variation of the load capacities as well. Failure to include such information would seriously impair the usefulness of the standard in achieving rational and risk-consistent designs, and would represent a step backward with respect to the LOF and PPG charts, which include useful probabilistic information in addition to the 0.008 percentage point.

5. SUMMARY AND CONCLUSIONS

The safety and cost of glass cladding facades subjected to wind loads depends upon the criteria used for their design. These criteria specify the design wind loads and the allowable panel loads. In this paper a review has been presented of: the evolution in recent years of methods for the estimation and specification of design wind loads for building facades; recent developments concerning the estimation and specification of allowable loads on glass cladding panels, and controversies surrounding those developments; and recent developments in structural reliability as applied to glass cladding, which allow rational decisions to be made concerning the adoption of satisfactory design criteria specifying both design loads and allowable panel loads. In view of recent changes in methods for estimating design wind loads and allowable panel loads, it would be imprudent or wasteful to adopt a standard specifying allowable panel loads without giving due consideration to the overall reliability aspects of the cladding glass design problem.

6. ACKNOWLEDGMENT

7. REFERENCES

(1) _American National Standard A58.1, Building Code Requirements for Minimum Design Loads in Buildings and Other Structures_, National Standards Institute, New York, N.Y., 1972.

(2) Ravindra, M.K., Cornell, C.A., and Galambos, T.V., 'Wind and Snow Load Factors for Use in LRFD,' _Journal of the Structural Division_, ASCE, Vol. 104, 1978, 1443-1457.

(3) Simiu, E., and Scanlan, R.H., _Wind Effects on Structures_, Wiley-Interscience, New York, N.Y., 1986.

(4) _LOF Technical Information — Strength of Glass Under Wind Loads_, 805-109, Toledo, Ohio, January, 1980.

(5) _PPG Industries Glass Product Recommendations: Wind Load Performance_, Technical Service Report No. 101A, PPG Industries, Pittsburgh, 1974.

(6) _PPG Glass Thickness Recommendations to Meet Architects Specified 1-Minute Load_, Technical Services/Flat Glass Division, PPG Industries, Pittsburgh, April 23, 1979.

(7) _ANSI/ASTM E330 - 70, Standard Test Method for Structural Performance of Exterior Windows, Curtain Walls, and Doors Under the Influence of Wind Loads_, 1978 Annual Book of ASTM Standards, American Society for Testing and Materials, Philadelphia, 1978.

(8) _Glass and Uniform Loads_, LOF Technical Information, ATS-108, File #1 - Strength of Glass, Toledo, Ohio, April 30, 1979.

(9) Krall, W.R., et.al., 'The Behavior of Float Glass Under Uniform Wind Loading,' _Proceedings_, Fourth U.S. National Conference on Wind Engineering Research, Department of Civil Engineering, University of Washington, Seattle, 1981.

(10) Beason, W.L., and Morgan, J.R., 'Glass Failure Prediction Model,' _Journal of Structural Engineering_, ASCE, Vol. 110, 1984, 197-212.

(11) Somes, N.F., Dikkers, R.D., and Boone, T.H., _Lubbock Tornado: A Survey of Damage in an Urban Area_, Technical Note 558, National Bureau of Standards, Washington, D.C., March 1971.

(12) Simiu, E., et al., _Ring-on-Ring Tests and Load Capacity of Cladding Glass_, NBS Building Science Series 162, National Bureau of Standards, Gaithersburg, Md., August 1984.

(13) Reed, D.A., and Simiu, E., 'Wind Loading and Strength of Cladding Glass,' _Journal of Structural Engineering_, ASCE, Vol. 110, 1984, 715-729.

(14) Simiu, E., Nolan, W.A., and Lechner, J., 'Glass Fracture Phenomenology and Loading Rate,' submitted for publication to the _Journal of Structural Engineering_, April, 1986.

(15) Johar, S., _Dynamic Fracture of Glass, Part III_, Ontario Research Foundation, Mississauga, Ontario, Canada, July, 1982.
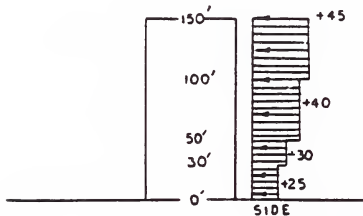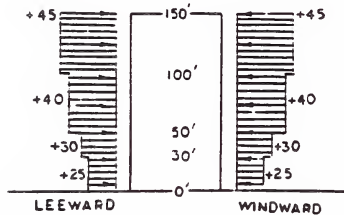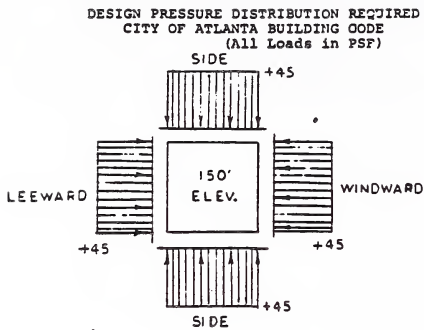
Figure 1. City of Atlanta Building Code wind loads (from PPG Technical Service Memorandum, June 21, 1974).
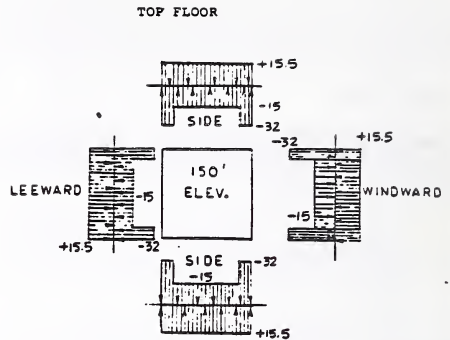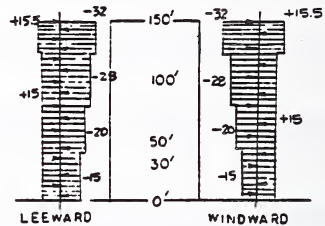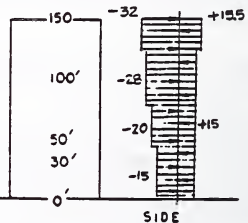
Figure 2. ANSI A58.1-1972 wind loads (from PPG Technical Service Memorandum June 21, 1974).
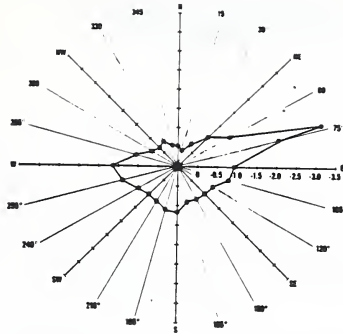
Figure 3.   Dependence on direction of the
pressure coefficient near a building corner.
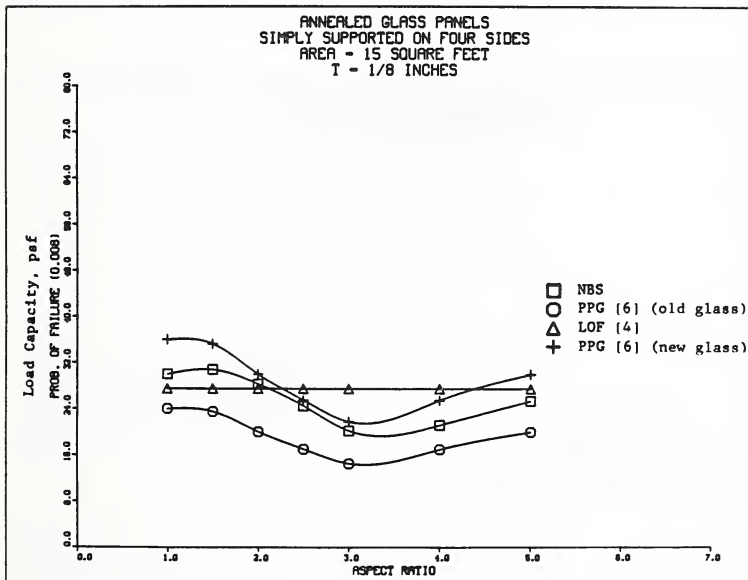
Figure 4
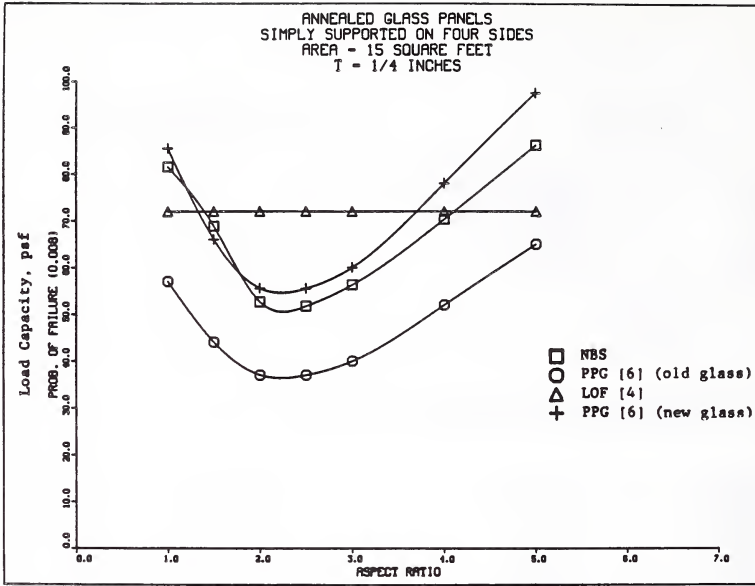
Figure 5
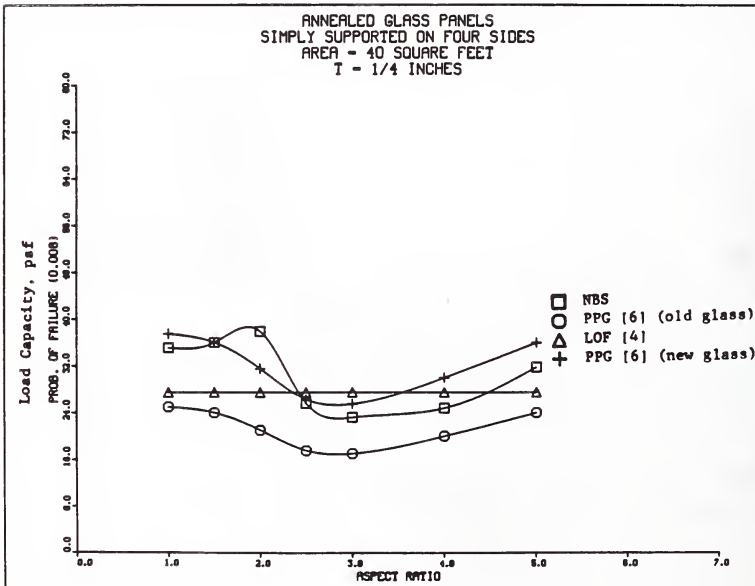
Figure 6
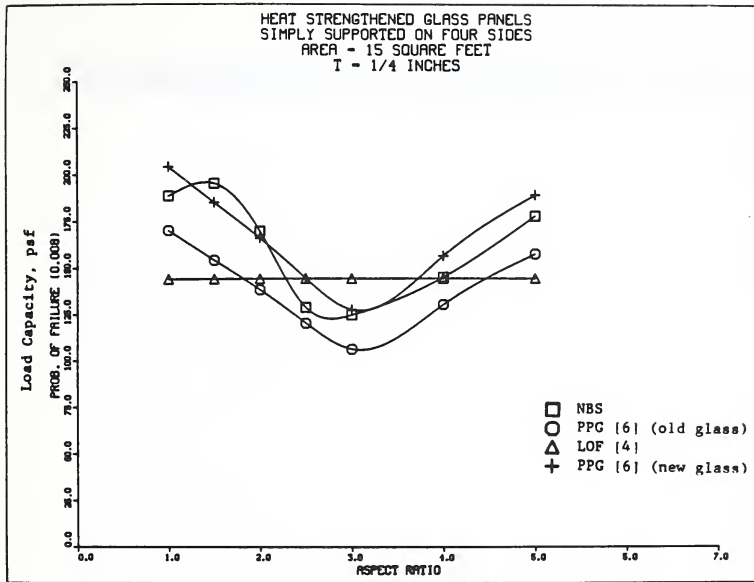
Figure 7
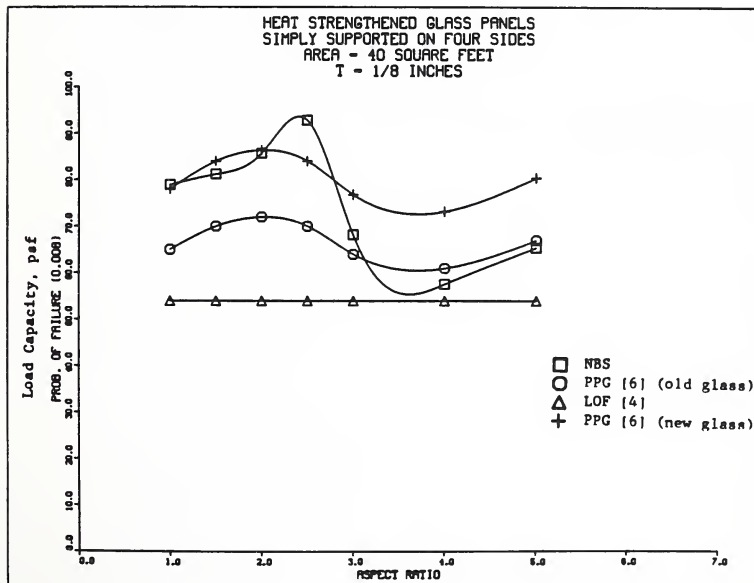
Figure 8

Earthquake Engineering

SPECTRAL CHARACTERISTICS OF GROUND MOTION
IN THE TOKYO METROPOLITAN AREA

BY

Keiichi Ohtani, and Shigeo Kinoshita

National Research Center for Disaster Prevention
Science and Technology Agency

ABSTRACT

The authors propose a tentative estimation procedure to estimate the average amplification characteristics of a sedimentary layer with a thickness of several kilometers for the short period S-waves (0.2-2 s) in a specific region of the Tokyo metropolitan area. The average amplification characteristics are given by the average of ratios of the zero-damped velocity response spectra of surface strong-motion to those of bedrock motion. The zero-damped velocity response spectra of bedrock motion are given by the models which were constructed by using the data of accelerometers installed at the bottoms of deep boreholes in the pre-Tertiary basement. The results obtained by using our method are compared with the calculated wave-transfer function of the thick sedimentary layer for the SH-waves.

INTRODUCTION

To investigate the earthquake response of the alluvium, observation of the earthquake motions by using seismometers installed on ground and under the alluvium by a borehole, was performed. The thickness of the alluvium is a hundred meters; in the Tokyo metropolitan area, borehole observation was practical and economical. During the last ten years, the earthquake response of the alluvium was investigated using borehole observation at many sites in this area.

Recently, in Japan, we learned that the pre-Tertiary basement is seismic bedrock. As a result, it is necessary to investigate the earthquake response of thick sedimentary layers of several kilometers of bedrock. The method used to investigate the earthquake response of the alluvium became impractical because observations of earthquake motions in the pre-Tertiary basement by means of boreholes are expensive and difficult to perform.

Instead of using bedrock motion data, which are directly observable by deep boreholes, it is economical and acceptable to use a statistical model to estimate the spectral characteristics of bedrock motions. In this report, as a tentative method to estimate the earthquake response of thick sedimentary layer, we examined a method that used the data of the surface strong-motions and models for estimating the spectral characteristics of bedrock motions. The models are constructed using acceleration records obtained at the bottom of three deep boreholes in the Tokyo metropolitan area.

2. METHOD

The amplification characteristics of the sedimentary layer are defined as

$$G(T) = SV_o(T) / SV_i(T),$$

where $SV_i(T)$ and $SV_o(T)$ are the zero-damped velocity response spectra at the period T of the bedrock motion and the surface ground motion, respectively. $SV_i(T)$ is obtained from the practical model and $SV_o(T)$ is obtained from the data observed on the surface ground. The average amplification characteristics of $G(T)$ is estimated by the following relation;

$$\bar{G}(T) = \frac{1}{k} \sum_{n=1}^{k} SV_o(T; M_n, R_n) / SV_i(T; M_n, R_n),$$

where M_n and R_n are the JMA magnitude and the hypocentral distance (in km) of the n-th earthquake, respectively. $\bar{G}(T)$ means the average of earthquake response of the thick sedimentary layer at the specific site. The zero-damped velocity response spectrum $SV_i(T; M, R)$ of the bedrock motions is estimated by the following relations;

$$SV_i(T; M, R) = 10^{a(T)M - b(T)\log_{10}R + c(T)}.$$

The coefficients $a(T)$, $b(T)$ and $c(T)$ at each period T, are given in Fig. 1. Model I is obtained by using the earthquakes whose epicenters were located out of the volcanic front in Japan and Model II is obtained by the earthquakes whose epicenters were located in and around the volcanic front. The results in Fig. 1 were constructed by using the acceleration data obtained at the bottom of deep boreholes in the three sites shown in Fig. 2; Iwatsuki (IWT, GL-3510 m), Shimohsa (SHM, GL-2300 m) and Fuchu (FCH, GL-2750 m).

3. RESULTS

The average amplification characteristics of sedimentary layer at the sites were investigated; Iwatsuki (IWT; 35° 55′ 33″N, 139° 44′ 17″E), Urayasu (URAYA SU; 35° 39′ 00″N, 139°

54' 19"E) and Tama (NT2; 35° 37' 65"N, 139° 26'
09"E). The earthquake data are shown in Table
1. These earthquakes belong to the earthquakes
used to construct the Model I of bedrock
motions. Table 2 shows the estimated velocity
structure at three sites. Estimated average
amplification characteristics of sedimentary
layer are shown in Fig. 3 (IWT), Fig. 4
(URAYASU) and Fig. 5 (NT2). $\bar{G}$ is the estimated
average amplification characteristics. G_1 is
the gain of transfer function of sedimentary
layer calculated by using the velocity struc-
ture in Table 2. SG_o is the gain of transfer
function of surface alluvium.

The results show that the average amplification
characteristics are mainly influenced by the
response of sedimentary layer for the SH-waves
and have maximum amplification factors of
several ten times. Also, the average amplifi-
cation characteristics have an envelope similar
to the amplification characteristics of soft
alluvium for the SH-waves.

4. CONCLUDING REMARKS

Based on the models used to estimate the
spectral characteristics of the bedrock
motions, we proposed a tentative method to
estimate the average amplification characteris-
tics of sedimentary layer for the short period
S-waves. The results obtained indicate that
our tentative method may be used to estimate
the average response characteristics of
sedimentary layer in the Tokyo metropolitan
area.

Table 1-1 Data of earthquakes for IWT site

No.	Date	Latitude	Longitude	Depth (km)	Magnitude
1	Oct. 5, 1977	36°08'	139°52'	60	5.5
2	Dec. 17, 1977	36°35'	141°05'	50	5.6
3	Feb. 20, 1978	38°45'	142°12'	50	6.7
4	Mar. 20, 1978	36°05'	139°53'	60	5.5
5	Jul. 11, 1979	36°36'	141°19'	40	5.9
6	Sep. 24, 1980	35°58'	139°48'	80	5.4
7	Sep. 25, 1980	35°31'	140°13'	80	6.1
8	Jul. 23, 1982	36°11'	141°57'	30	7.0
9	Feb. 27, 1983	35°54'	140°09'	70	6.0

Table 1-2 Data of earthquakes for URAYASU site

No.	Date	Latitude	Longitude	Depth (km)	Magnitude
1	Sep. 24, 1980	35°58'	139°48'	80	5.4
2	Sep. 25, 1980	35°31'	140°13'	80	6.1
3	Jul. 23, 1982	36°11'	141°57'	30	7.0
4	Feb. 27, 1983	35°54'	140°09'	70	6.0
5	Jan. 17, 1984	36°27'	141°15'	40	5.6
6	Jan. 18, 1984	36°27'	141°16'	40	5.9
7	Sep. 19, 1984	34°03'	141°33'	10	6.6

Table 1-3 Data of earthquakes for NT2 site

No.	Date	Latitude	Longitude	Depth (km)	Magnitude
1	Mar. 20, 1978	36°05'	139°53'	60	5.5
2	Jun. 12, 1978	38°09'	142°10'	40	7.4
3	Sep. 24, 1980	35°58'	139°48'	80	5.4
4	Sep. 25, 1980	35°31'	140°13'	80	6.1
5	Feb. 27, 1983	35°54'	140°09'	70	6.0
6	Jul. 2, 1983	36°54'	141°12'	50	5.8
7	Sep. 19, 1984	34°03'	141°33'	10	6.6

Table 2-1 Estimated velocity structure at IWT site

Layer No.	S-wave velocity (km/s)	Density (g/cm^3)	Thickness (m)
1	o.189	1.7	5.0
2	0.155	1.7	6.0
3	0.3	1.8	6.0
4	0.18	1.7	2.0
5	0.54	1.9	181.0
6	0.78	2.0	750.0
7	1.17	2.2	800.0
8	2.5	2.5	

Table 2-2 Estimated velocity structure at URAYASU site

Layer No.	S-wave velocity (km/s)	Density (g/cm^3)	Thickness (m)
1	0.14	1.7	3.0
2	0.2	1.8	5.0
3	0.12	1.7	15.0
4	0.15	1.7	9.0
5	0.2	1.8	4.0
6	0.45	1.9	264.0
7	0.67	2.0	1000.0
8	1.5	2.2	1000.0
9	2.5	2.5	

Table 2-3 Estimated velocity structure at NT2 site

Layer No.	S-wave velocity (km/s)	Density (g/cm^3)	Thickness (m)
1	0.16	1.7	12.5
2	0.13	1.8	2.5
3	0.33	1.9	27.0
4	0.37	1.8	9.0
5	0.33	1.8	14.0
6	0.41	2.0	17.0
7	0.36	1.9	20.0
8	0.44	2.0	218.0
9	0.76	2.1	670.0
10	1.3	2.5	980.0
11	1.6	2.6	830.0
12	2.5	2.7	
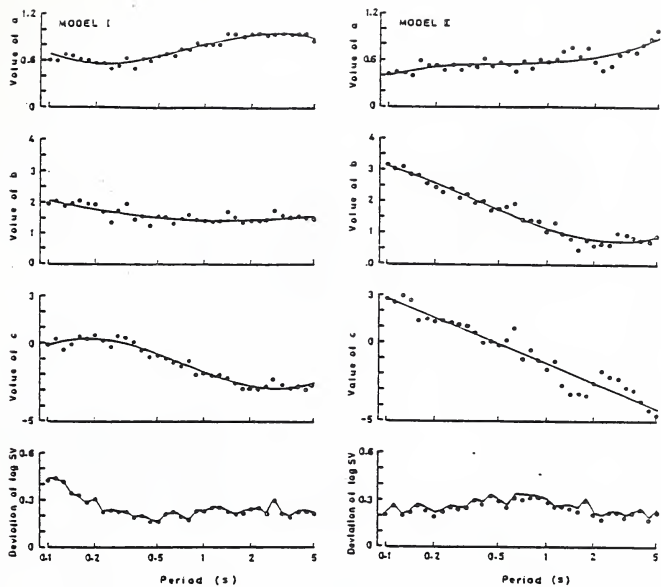
Fig. 1 The coefficients a, b and c
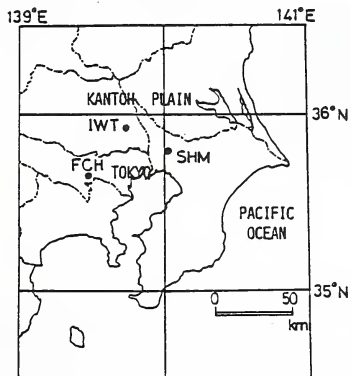
Fig. 2 Location of deep borehole observatories
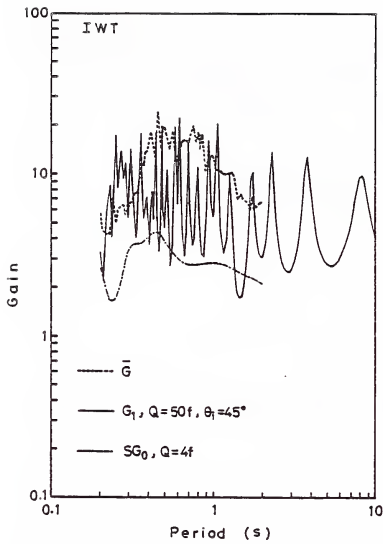
Fig. 3 Estimated average amplifi-
cation characteristics of
sedimentary layer (IWT)
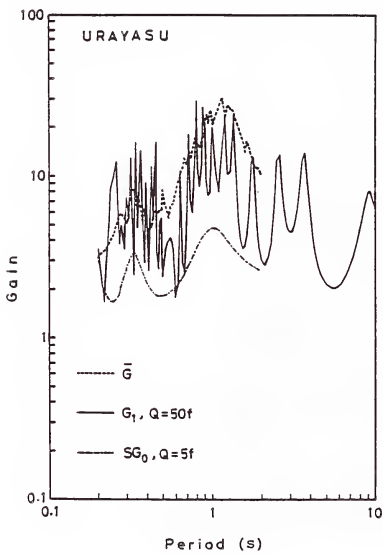
Fig. 4 Estimated average amplifi-
cation characteristics of
sedimentary layer (URAYASU)
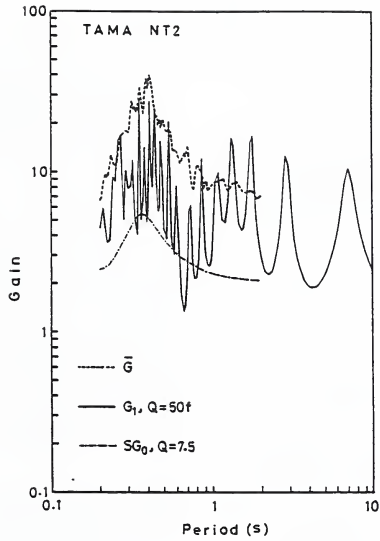
Fig. 5 Estimated average amplification characteristics of
sedimentary layer (NT2)

STRONG-MOTION RECORDINGS FROM THE
HOLLISTER, CALIFORNIA, AREA M5.5 EARTHQUAKE,
26 JANUARY 1986

BY

A. Gerald Brady, Richard P. Maley,
and G. Noel Bycroft[1]

ABSTRACT

On January 26, 1986, a moderate earthquake
(magnitude M_L5.5, Berkeley; M_L5.5 Caltech)
occurred approximately 12 km SE of Hollister,
California. The coordinates of the
earthquake's epicenter were 36° 48.32' North
and 121° 16.94' West, which is located along
the southern end of the little-known Quien
Sabe fault, 7 km east of the Calaveras Fault.
The right-lateral strike slip event occurred
at a depth of 8.2 km.

Among the stations operated by the United
States Geological Survey (USGS) that recorded
this event are:

1. Five stations in the Hollister vicinity,
   with film recorders.
2. The Hollister Digital Differential
   Array, located at the airport 4 km north
   of Hollister.
3. Six stations of the Bear Valley array,
   spreading over an area reaching 46 km
   south of Hollister, with film recorders.

The main purpose of this report is to bring to
the attention of the earthquake engineering
and scientific communities the existence of a
set of film and digital recordings of the
earthquake from strong motion accelerographs
operated and maintained by the USGS. A
preliminary analysis is made of the digital
recordings and their relationships.

KEYWORDS: accelerograms; earthquake;
processing.

1. INTRODUCTION

On January 26, 1986, 1920:50.9 GMT, a moderate
earthquake (magnitude M_L5.5, Berkeley;
M_L5.5 Caltech; Mb5.2, NEIS) occurred approx-
imately 12 km SE of Hollister, California.
The coordinates of the earthquake's epicenter
were 36° 48.32' North and 121° 16.94' West,
which is located along the southern end of the
Quien Sabe fault of D. Herd (unpubl.), 7 km
east of the Calaveras Fault. The event
occurred at a depth of 8.2 km and its movement
was right-lateral strike slip. (Rob
Cockerham, USGS, oral communication, 1986).

Among the stations operated by the United
States Geological Survey (USGS) (Ref. 1) that

recorded this event are (see Table 1):

1. Stations near Hollister (see Fig. 1).
2. the Hollister Digital Differential
   Array, located at the airport 4 km north
   of Hollister (Ref. 2 and Fig. 2).
3. the Bear Valley array, spreading over an
   area reaching 46 km south of Hollister
   (Ref. 3).

The main purpose of this report is to bring to
the attention of the earthquake engineering
and scientific communities the existence of a
set of film and digital recordings of the
earthquake from strong motion accelerographs
operated and maintained by the USGS. Although
the report is not complete, the earthquake
occurred sufficiently close to the Western
Region Headquarters of the USGS in Menlo Park
that most of the triggered records were
recovered within a few days, and some
preliminary analysis was possible on the
digital recordings.

Updated information on the earthquake,
records, and processing will be provided in
subsequent data reports. Further study of the
set of records from the Bear Valley array will
be required before a decision is made on their
digitization. As for all earthquakes (for
example, San Fernando, 1971) the more remote
triggered stations are of much less interest,
and their digitization and processing is less
cost-efficient than those with accelerations
of 10% g or higher.

This report contains copies of the film
records obtained from 11 of these stations and
processed records from the Hollister array.
The stations at Anderson Dam and Pinnacles did
not trigger. The San Justo Dam instruments
are maintained by the USGS under a cooperative
agreement with the Bureau of Reclamation.

The Hollister array (located 11 km from the
San Andreas Fault) is a 24-channel, two-dimen-
sional system with two legs at 33° separation
with accelerometers placed at 0, 61, 457, and
610 m on one leg, and 244 and 305 m on the
second. The sensors are Kinemetrics triaxial
force balance accelerometers mounted at the
center of a 2.1 m diameter concrete pad, well
coupled to the soil. The system has a 2.5
second pre-event memory (allowing the record-

---

[1]U.S. Geological Survey, Menlo Park,
California.

ing of pre-triggering onset motions) and is triggered by vertical motions exceeding 0.01 g in the range of 1 to 10 Hz. The data are digitized at a rate of 200 samples per second with a total recording time capability of 20 minutes. Two additional triaxial accelerographs, including the Differential Array film recorder, are mounted on an isolated pier in the recorder house.

2. DESCRIPTION OF RECORDS

Epicentral and hypocentral distances for the stations, rounded to the nearest kilometer, are given in Table 1. Table 2 lists the scaled peak accelerations for each component.

Film records from the Hollister area have epicentral distances ranging from 11 to 16 km, with peak horizontal acceleration of 0.17 g (Damler Residence) and vertical acceleration of 0.29 g (Hollister City Hall Annex). Copies of the first 20-25 seconds of these film records are shown in Figure 3. Half-second time marks appear at the lower edge.

Digital records from the Hollister Differential Digital Array, 15 km from the epicenter, have peak horizontal accelerations ranging from 0.09 to 0.12 g, and vertical, 0.08 to 0.17 g. Station 2 failed to operate correctly (A/D converter problem) and one horizontal channel of Station 4 failed.

Film records from the Bear Valley Array, with epicentral distances ranging from 17 to 37 km, exhibit peak horizontal accelerations ranging from 0.12 g down to the approximate triggering level at 0.01 g.

The Pinnacles and Anderson Dam stations did not trigger. Further distant stations have not been visited for this report.

3. DIGITIZATION AND PROCESSING

The digital records from the Differential Array are processed by the following steps. Further details may be found in Ref. 4.

1. The uncorrected data are prepared by subtracting the mean. The instrument sensitivities, determined by peak-to-peak voltages, are used to scale the ordinates to acceleration.

2. The data are passed through a correction algorithm that applies a 50 Hz (high-frequency) low-pass filter, instrument correction, base-line correction in the form of a 0.2 Hz low-frequency (5 second, long-period) filter, and decimation to 200 sps. This initial preliminary selection of 5 seconds for the long-period filter is based on the convention of retaining a period content somewhat longer than the strong-motion duration of the records (Ref. 5), here estimated at 2-3 seconds.

Fig. 4 shows the preliminary calculated displacements from the Differential Array stations, arranged by component, and aligned for simultaneous timing. Further analysis and processing is required to differentiate between the differences that are due to noise and the differences that the array is designed to study.

4. SUMMARY

Although in this preliminary report the quoted values for the earthquake epicenter may eventually be altered, it appears that a significant set of records has been obtained from the magnitude 5.5 event. Current epicentral distances indicate five records to the west within 15 km. A set of five digital records obtained at the Hollister array are 15 km from the epicenter. A further set of film records to the southeast has been recovered at epicentral distances in the range 17-37 km.

Digitization and further processing of the film records will await a decision on the overall significance of the event. Further corrections applied to the digital recordings, and investigations on the total ground motion at the Hollister array will be described in subsequent reports.

5. ACKNOWLEDGEMENTS

We appreciate the kindness of the property owners, where the Bear Valley Array instruments are located, for permission originally to install the array and subsequently annually to maintain it. The cooperative agreement with the Bureau of Reclamation has resulted in the San Justo Dam records, from instruments installed prior to the dam being built.

6. ATTRIBUTIONS

A. G. Brady leads the Data Management project with P. N. Mork and B. L. Silverstein; R. P. Maley heads the Network Operations project with E. C. Etheredge and technicians D. A. Johnson, A. V. Acosta, R. D. Forshee and M. J. Salsman. Text, figures, tables, and records were prepared through the efforts of all.

7. APPENDIX

The appendix contains three tables listing processed records since 1978.

8. REFERENCES

(1) Switzer, L., Johnson, D., Maley, R., and Matthiesen, R., 1981; Western Hemisphere Strong-Motion Station List - 1980; U.S. Geological Open-File Report No. 81-664, 162 p.

(2) Maley, R. P., and Etheredge, E. C., 1984; The Development of Ground and Structural Response Strong-Motion Instrumentation Arrays in the United States: Eighth World conference on Earthquake Engineering, San Francisco, California, 8 p.

(3) Dielman, R. J., Hanks, T. C., and

Trifunac, M. D., 1975; An array of strong-motion accelerographs in Bear Valley, California; BSSA, v. 65 no. 1.

(4) Converse, A. M., 1984; AGRAM: A Series of Computer Programs for Processing Digitized Strong-Motion Accelerograms, Version 2.0: U.S. Geological Survey Open-File Report 81-525, 118 p.

(5) Basili, M., and Brady, A. G., 1978; Low Frequency Filtering and the Selection of Limits for Accelerogram Corrections: Sixth European Conference on Earthquake Engineering, Dubrovnik, Yugoslavia.

Table 1.- Epicentral and Hypocentral Distances

Earthquake coordinates: 36.805°N, 121.282°W
depth: 8.2 kilometers

Station Name	Latitude (North)	Longitude (West)	Epicentral Distance(km)	Hypocentral Distance(km)	Azimuth from Epicenter
Bear Valley 5 Callens Ranch	36.673	121.195	17	19	152.10
Bear Valley 1 CDF Fire Station	36.573	121.184	27	28	161.22
Bear Valley 6 James Ranch	36.504	121.101	37	38	154.18
Bear Valley 7 Pinnacles (a)	36.483	121.184	37	38	165.68
Bear Valley 2 Stone Canyon West	36.636	121.234	19	21	167.10
Bear Valley 14 (b) Upper Butts Ranch	36.569	121.043	34	35	140.85
Bear Valley 10 Webb Residence	36.532	121.143	33	34	157.72
Bear Valley 12 Williams Ranch	36.658	121.249	17	19	169.71
Anderson Dam (a)	37.166	121.626	50	51	322.83
Hollister City Hall Annex	36.851	121.402	12	14	295.53
Hollister SAGO Vault	36.765	121.446	16	18	251.40
Hollister Damler Residence	36.807	121.408	11	14	272.65
Hollister Differential Array	36.888	121.413	15	17	308.37
San Justo Damsite Abutment	36.815	121.447	15	17	274.37
San Justo Damsite Dike	36.827	121.445	15	17	279.45

Notes: (a) No trigger
(b) Not yet visited

Table 2.- Peak Accelerations, scaled from original film or preliminary digital processing

Station Name	Station Number	Components			Scaled peaks (g)		
		L	V	T	L	V	T
Bear Valley Array:							
Callens Ranch	1474	310	Up	220	0.05	0.06	0.04
CDF Fire Station	1210	310	Up	220	0.04	0.02	0.04
James Ranch	1475	310	Up	220	0.02	0.01	0.01
Pinnacles (a)	1476	310	Up	220			
Stone Canyon West	1343	130	Up	040	0.03	0.02	0.04
Upper Butts Ranch (b)	1483	310	Up	220			
Webb Residence	1479	310	Up	220	0.04	0.01	0.04
Williams Ranch	1481	310	Up	220	0.12	0.06	0.12
Hollister							
City Hall Annex	1575	180	Up	090	0.10	0.29	0.12
SAGO Vault	1032	360	Up	270	0.04	0.04	0.04
Damler Residence	1657	360	Up	270	0.17	0.09	0.14
Hollister Differential Array	1656						
Station 1		255	Up	345	0.09	0.17	0.11
Station 2		255	Up	345	---	---	--- (c)
Station 3		255	Up	345	0.10	0.12	0.10
Station 4		255	Up	345	0.10	0.08	--- (d)
Station 5		255	Up	345	0.11	0.17	0.12
Station 6		255	Up	345	0.10	0.15	0.11
Recorder building		255	Up	165	0.10	0.15	0.10
San Justo Damsite	1655						
Abutment		360	Up	270	0.16	0.07	0.14
Dike		360	Up	270	0.09	0.04	0.08

Notes: (a) No trigger
(b) Not yet visited
(c) No operation
(d) No op, one channel
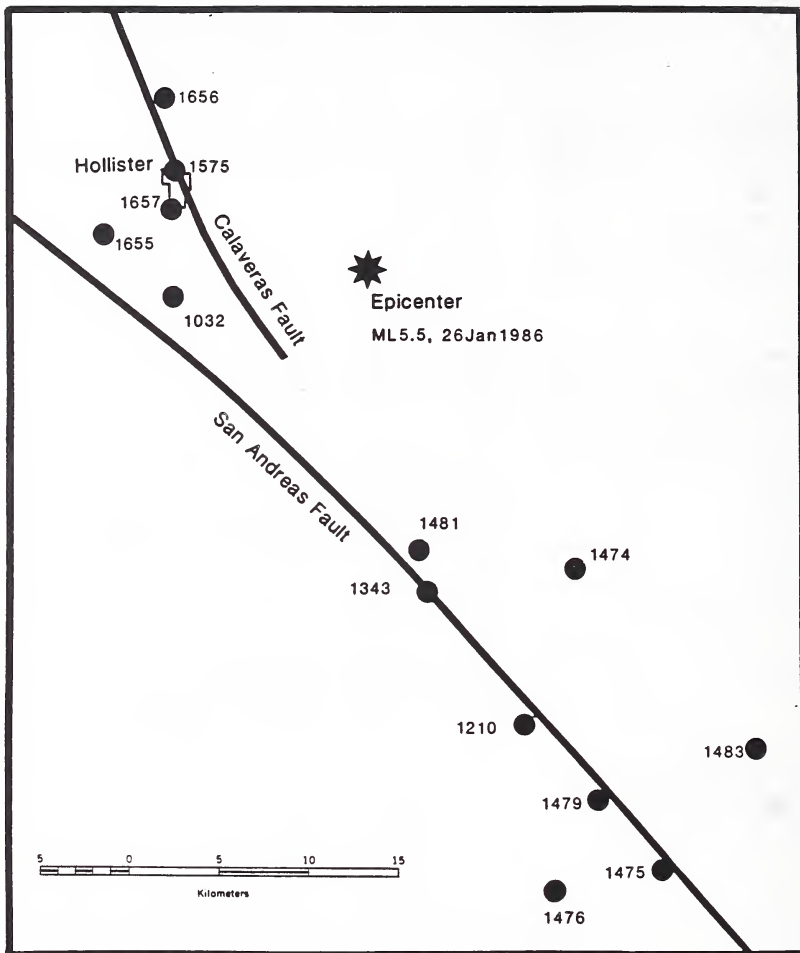
Figure 1.
Instrument locations coded with Station Numbers from Table 1, epicenter, and adjacent faults.
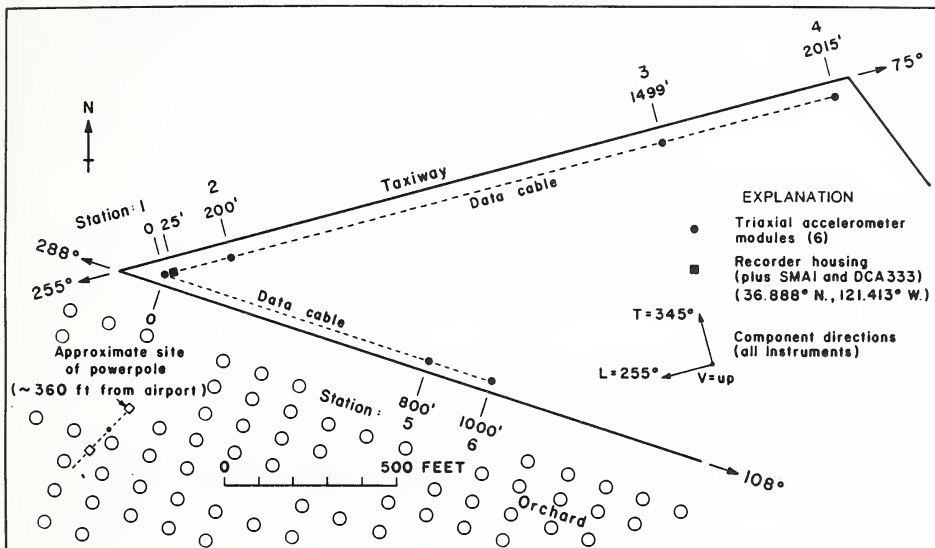
Figure 2.

Instrument locations at Hollister Digital Differential Array.

HOLLISTER: CITY HALL ANNEX

180

UP

90

HOLLISTER DIFFERENTIAL ARRAY

255

UP

165

HOLLISTER: DAMLER RESIDENCE

360

UP

270

BUREAU OF RECLAMATION

SAN JUSTO DAMSITE: DIKE

360

UP

270

SAN JUSTO DAMSITE: ABUTMENT

360

UP

270
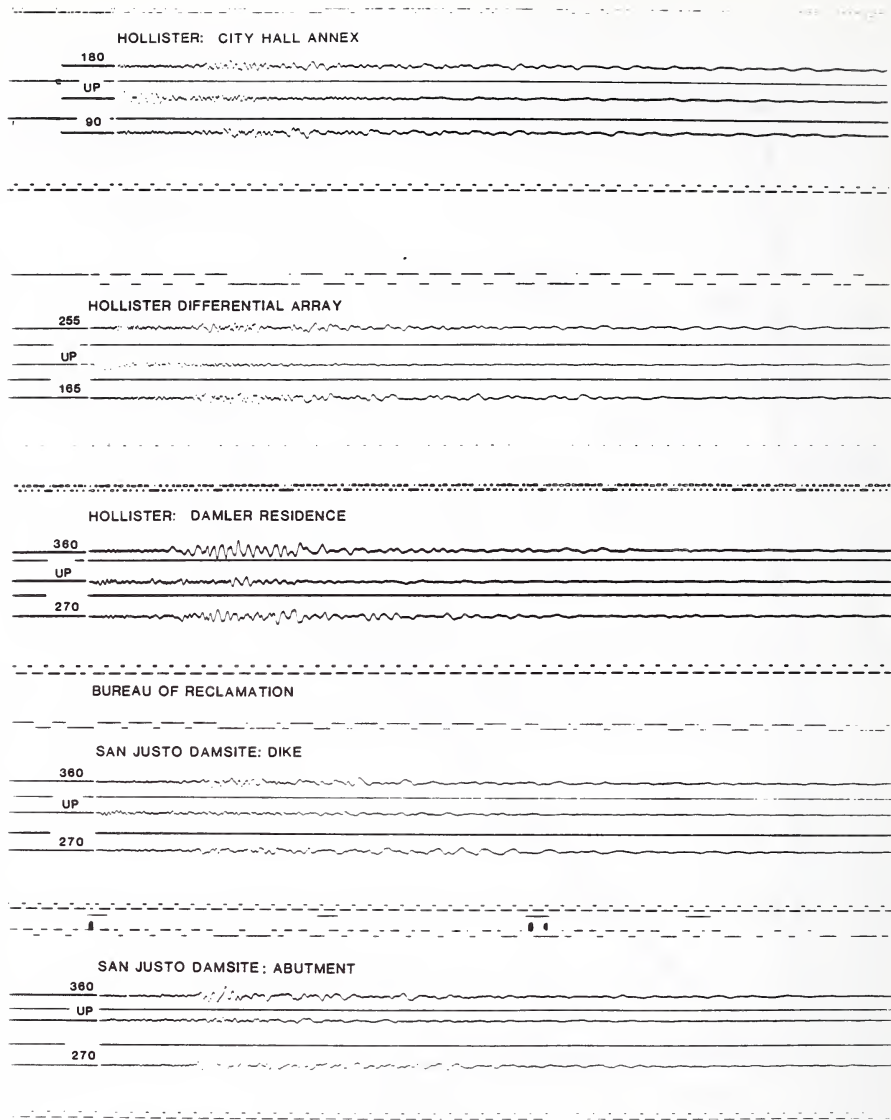
Figure 3.

Copies of the first 20-25 seconds of the film records. Most ran for at
least 60 seconds for the WWVB time record. Refer to Table 1 for peak
values.
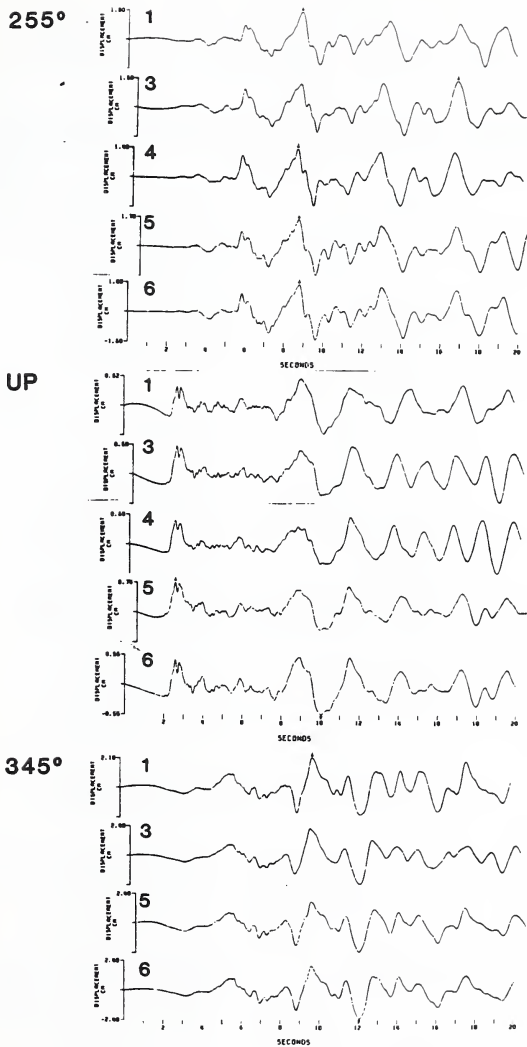
Figure 4. Hollister array aligned displacements from preliminary accelerogram correction, using band-pass filter from 50 Hz to 5 sec.

CURRENT LIST OF PROCESSED RECORDS   January, 1987

USGS processing of records from the USGS permanent network of strong-motion
accelerographs and associated networks. Strong motion data from earthquakes 1978
and later including an isolated earlier event.

TABLE A1. Chronological list of events and associated reports describing the
          existence/processing/analysis/availability of digital data on tape, or
          at the National Strong Motion Data Center in Menlo Park.

Date & Time	Earthquake	Reference (see attached list)
January 1, 1975; 0355 GMT	Southern Alaska	OFR 86-191 (Ref. 16)
March 25, 1978	Coyote Dam, California	OFR 83-166 (Ref. 6)
August 27, 1978 and two later shocks	Monticello Dam, Jenkinsville, South Carolina	OFR 81-0448 (Ref. 2)
August 6, 1979	Coyote Lake, California	OFR 81-42 (Ref. 4)
October 15, 1979	Imperial Valley, California	OFR 80-703 (Ref. 5)
October 15, 1979	Imperial Valley, California	OFR 82-183 (Ref. 11)
October 15, 1979; 2317:41, 2318:20, 2318:40 GMT	Imperial Valley California aftershock	OFR 86-441 (Ref. 3)
October 16, 1979, 0706 GMT	Monticello Dam, Jenkinsville, South Carolina	OFR 81-1241 (Ref. 10)
December 13, 1981 and March 18, 1983	Solomon Islands	OFR 86-264 (Ref. 15)
February 13, 14, and 23, 1983	Monasavu Dam, Fiji	OFR 85-375 (Ref. 12)
May 2 and May 9, 1983	Coalinga, California	OFR 84-626 (Ref. 9)
July 9, 1983; 0740 GMT	Coalinga, California	OFR 85-584 (Ref. 13)
July 22, 1983; 0239 GMT	Coalinga, California	OFR 85-250 (Ref. 14)
April 24, 1984	Morgan Hill, California	OFR 84-498, Vol I and II (Refs. 7 and 8) (Compiled by Seena Hoose)
December 23, 1985; 0516 GMT and Nov. 9, Dec. 23, Dec 25	Northwest Territories, Canada	OFR 86-____, (Ref. 17)
January 26, 1986; 1920 GMT	Hollister, California	OFR 86-156, (Ref. 1)

TABLE A2. Processed records in each report

January 1, 1975; 0355 GMT; southern Alaska; OFR 86-191.
    Records (4):   Anchorage, 500 W. Third St., Basement
                   Anchorage, Alaskan Methodist University
                   Anchorage, Government Hospital
                   Talkeetna, FAA-VOR Building

March 25, 1978; Coyote Dam, California; OFR 83-166.
    Records (3):   Coyote Dam, Ukiah, California: abutment, toe, crest

August 27, 1978, 1023 GMT and 2 later shocks; Monticello Dam, South Carolina,
    OFR 81-0448.
    Records (3):   Jenkinsville, Monticello Dam
                   Shared abutment (center crest)

August 6, 1979, Coyote Lake, California; OFR 81-42.
    Records (6):   Coyote Creek, San Martin, California
                   Gilroy Array: Station 6, San Ysidro
                   Gilroy Array: Station 4, San Ysidro School
                   Gilroy Array: Station 3, Sewage Treatment Plant
                   Gilroy Array: Station 2, Mission Trails Motel
                   Gilroy Array: Station 1, Gavilan College

October 15, 1979, 2317 GMT; The Imperial Valley Earthquake; OFR 80-703.
    Records (22): El Centro Array 7, Imperial Valley College
                   El Centro Array 6, Huston Road
                   El Centro, Bonds Corner, Hiways 98 & 115
                   El Centro Array 8, Cruickshank Road
                   El Centro Array 5, James Road
                   El Centro Differential Array
                   El Centro Array 4, Anderson Road
                   Brawley, Brawley Municipal Airport
                   Holtville, California, Holtville Post Office
                   El Centro Array 10, Keystone Road
                   Calexico, California, Calexico Fire Station
                   El Centro Array 11, McCabe School
                   El Centro Array 3, Pine Union School
                   Parachute Test Facility
                   El Centro Array 2, Keystone Road
                   El Centro Array 12, Brockman Road
                   Calipatria, California, Calipatria Fire Station
                   El Centro Array 13, Strobel Residence
                   El Centro Array 1, Borchard Ranch
                   Superstition Mountain, California
                   Plaster City, California, Storehouse
                   Coachella Canal Number 4, California

October 15, 1979, 2317:41 GMT; Imperial Valley Aftershocks; OFR 86-441
    Records (6)   El Centro Array 5, James Road
                   El Centro Array 6, Huston Road
                   El Centro Array 7, Imperial Valley College
                   El Centro Array 8, Cruickshank Road
                   El Centro Array 9, Commercial Ave.
                   El Centro Differential Array
October 15, 1979, 2318:20 GMT; Imperial Valley Aftershocks; OFR 86-441
    Records (6)   El Centro Array 5, James Road
                   El Centro Array 6, Huston Road
                   El Centro Array 7, Imperial Valley College
                   El Centro Array 8, Cruickshank Road
                   El Centro Array 9, Commercial Ave.
                   El Centro Differential Array

87

TABLE A2. Processed records in each report (continued)

October 15, 1979, 2318:40 GMT; Imperial Valley Aftershock; OFR 86-441
    Records (7)   El Centro Array 6, Huston Road
                    El Centro Array 7, Imperial Valley College
                    El Centro Array 8, Cruickshank Road
                    El Centro Array 9, Commercial Ave.
                    El Centro Differential Array
                    Bonds Corner, Highways 115 & 98
                    Holtville Post Office

October 15, 1979; The Imperial Valley, California; OFR 82-183;
    Records (22): This report contains the time-dependent response spectrum
                plots for the same records in OFR 80-703, above.

October 16, 1979, 0706 GMT, Monticello Dam, South Carolina, OFR 81-1214.
    Records (1): Jenkinsville, South Carolina, Monticello Dam
               shared abutment (center crest)

December 13, 1981 and March 18, 1983; Solomon Islands, OFR 86-264
    Records (5): Dec. 13, 1981, 0129 GMT: 460 Beach, Panguna Mine,
                                        Bougainville Island.
              Dec. 13, 1981, 1324 GMT: "
              March 18, 1983:   Arawa Town
                               Bato Bridge
                               BVE80, Panguna Mine.

February 13, 14, and 23, 1983; Monasavu Dam, Fiji; OFR 85-375
    Records (3): Feb 13, 14, 23, 1983: Monasavu Dam.

May 2 and May 9, 1983; Coalinga, California; OFR 84-625.
    Records (13): May 2, 1983, 2342 GMT:
              Pleasant Valley Pump Plant: switchyard, basement

              May 9, 1983, 0249 GMT
              Anticline Ridge: freefield and pad
              Burnett Construction
              Oil City
              Oil Fields Fire Station
              Palmer Avenue
              Skunk Hollow
              Pleasant Valley Pump Plant: switchyard, basement,
                                               1st floor, roof

July 9, 1983; 0740 GMT; Coalinga, California; OFR 85-584
    Records (9): Anticline Ridge: freefield and pad
              Burnett Construction
              Oil City
              Oil Fields Fire Station: freefield and pad
              Palmer Avenue
              Skunk Hollow
              Transmitter Hill

July 22, 1983; 0239 GMT; Coalinga, California; OFR 85-250
    Records (13): Anticline Ridge: pad site
              Burnett Construction
              Oil City
              Oil Fields Fire Station: freefield and pad
              Palmer Avenue
              Pleasant Valley Pump Plant: 1st floor, basement, roof,
                                         switchyard, freefield
              Skunk Hollow
              Transmitter Hill

TABLE A2. Processed records in each report. (continued)

April 24, 1984; Morgan Hill, California; OFR 84-498B, Vol. II.
    Records (11): Anderson Dam: downstream, crest
                  Hollister City Hall Annex
                  Hollister Differential Array
                  San Justo Damsite: right abutment, left abutment
                  San Jose 101/280/680 bridge
                  Hollister Differential Array No. 1, 3, 4, 5

December 23, 1985; with foreshock and aftershocks; Northwest Territories,
    Canada; OFR 86-___.
    Records (6):   Nov. 9, 1985; 0446 GMT: Nahanni Site 2
                   Dec. 23, 1985; 0516 GMT: Nahanni Sites 1, 2, 3
                   Dec. 23, 1985; 0548 GMT: Nahanni Site 1
                   Dec. 25, 1985; 1543 GMT: Nahanni Site 3

January 26, 1986; Hollister, California; OFR 86-156
    Records (5):   Hollister Digital Differential Array, Stations 1, 3, 4, 5, 6

References

(1) Brady, A. G., Etheredge, E. C., Maley, R. P., Mork, P. N., Silverstein, B. L., Johnson, D. A., Acosta, A. V., Forshee, R. D., and Salsman, M. J., 1986, Preliminary report on records from the USGS-maintained strong-motion network in the Hollister area, January 26, 1986: USGS Open-File Report 86-156, 43 p.

(2) Brady, A. G., Mork, P. N., and Fletcher, J. P., 1981, Processed accelerograms from Monticello Dam, South Carolina, 27 August 1978, and two later shocks: USGS Open-File Report 81-0448, 35 p.

(3) Brady, A. G., Mork, P. N., and Silverstein, B. L., 1986, Processed strong-motion records from the 2317:41, 2318:20 and 2318:40 aftershocks of the October 15, 1979, 2313:53 GMT earthquake; Imperial Valley. USGS Open File-Report 86-441.

(4) Brady, A. G., Mork, P. N., Perez, Virgilio, and Porter, L. D., 1980, Processed data from the Gilroy Array and Coyote Creek records, Coyote Lake, California earthquake, 6 August 1979. USGS Open-File Report 81-42, 171 p.

(5) Brady, A. G., Perez, Virgilio, and Mork, P. N., 1980. The Imperial Valley earthquake, October 15, 1979. Digitization and processing of accelerograph records: USGS Open-File Report 80-703, 309 p.

(6) Brady, A. G., and Perez, Virgilio, 1983, Processed accelerograms from Coyote Dam, California, March 25, 1978: USGS Open-File Report 83-166, 82 p.

(7) Brady, A. G., Porcella, R. L., Bycroft, G. N., Etheredge, E. C., Mork, P. N., Silverstein, B., and Shakal, A. F., 1984, Strong-motion results from the main shock of April 24, 1984, S. Hoose, compiler, in The

Morgan Hill, California earthquake of April 24, 1984, USGS Open-File Report 84-498A, v. I, p. 18-26, and v. II, 103 p.

(8) _____, 1984. Strong-motion results from the main shock of April 24, 1984, in The Morgan Hill, California Earthquake of April 24, 1984, (S. Hoose, compiler) USGS Open File Report 84-498B, V. II, 103 p.

(9) Maley, R. P., Etheredge, E. C., Johnson, D. A., Switzer, J. C., Mork, P. N., and Brady, A. G., 1984, Strong-motion data recorded near Coalinga, California (May 2, 1983) and processed data from May 2 and May 9, 1983: USGS Open-File Report 84-626, 258 p.

(10) Mork, P. N., and Brady, A. G., 1981, Processed accelerogram from Monticello Dam, Jenkinsville, South Carolina, 16 October 1979, 0706 Gmt: USGS Open-File Report 81-1214, 20 p.

(11) Perez, Virgilio, 1982, The Imperial Valley, California earthquake, October 15, 1979; time dependent response spectrum plots: USGS Open-File Report 82-183, 96 p.

(12) Silverstein, Barry, 1985a, Processed strong-motion records from Monasavu Dam, Fiji; Earthquakes of February 13, 14, and 23, 1983: USGS Open-File Report 85-375, 58 p.

(13) _____, 1985b, Processed strong-motion records from the Coalinga, California aftershock of July 9, 1983; 0740 GMT: USGS Open-File Report 85-584, 169 p.

(14) Silverstein, B., and Brady, A. G., 1985, Processed strong-motion records from the Coalinga, California, aftershock of July 22, 1983, 0239 Gmt: USGS Open-File Report 85-250, 229 p.

(15) Silverstein, B. L., Brady, A. G., and

Mork, P. N., 1986a, Processed strong-motion records from Bougainville Island, Papua New Guinea; earthquakes of December 13, 1981 and March 18, 1983: USGS Open-File Report 86-264, 148 p.

(16) _____, 1986b, Processed strong-motion records from the southern Alaska earthquake of January 1, 1975; 0355 Gmt: USGS Open-File Report 86-191, 99 p.

(17) Weichert, D. H., P. N. Mork, and others, 1986. The November and December, 1985, earthquakes in the Nahanni region of the Northwest Territories, Canada. USGS Open-File Report, in press.

DENSE INSTRUMENT ARRAY SYSTEM BY PWRI FOR
OBSERVING STRONG EARTHQUAKE MOTION

by

Toshio Iwasaki, Yasushi Sasaki, Keiichi Tamura,
Koh Aizawa and Kazuyuki Takahashi

ABSTRACT

This paper presents the Dense instrument
Array Program for observing strong
earthquake motions by the public Works
Research Institute (PWRI), Ministry of
Construction.

PWRI has installed dense array
accelerographs at its Tsukuba campus in
1979. PWRI created a program to observe
strong motions at four sites; Sagara,
Yaizu, Numazu and Matsuzaki around
Suruga Bay, Sizuoka Prefecture. This
research was completed by March, 1985.
At each site, 14-18 3-component
accelerographs were deployed at 10-14
points at ground surface and in
down-holes. By July 1985, records of 56
earthquakes were obtained at Tsukuba
campus; 11 earthquakes were observed at
sites around Suruga Bay.

This report introduces the summary of
the PWRI's Dense Instrument Array system
with the preliminary analysis on
amplification of ground motion and the
velocity of horizontal propagation of
the ground motion by using the data
obtained at the Tsukuba campus.

----

1) Dr. Eng., Director, Earthquake
   Disaster Prevention Department,
   PWRI, MOC

2) Dr. Eng., Head, Ground Vibration
   Division, Earthquake Disaster

Prevention Dept., PWRI, MOC

3) Research Engineer, Ground Vibration
   Division, Earthquake Disaster
   Prevention Dept., PWRI, MOC

4) Ground Vibration Division,
   Earthquake Disaster Prevention
   Dept., PWRI, MOC

5) Kanto Regional Construction Bureau,
   MOC

1. INTRODUCTION

Based on knowledge accumulated through
past strong-motion observations, it is
widely recognized that characteristics
of ground motion differ, site by site,
and that characteristics of short period
ground motions are strongly dependent on
seismic source mechanism, seismic wave
path conditions from source area to
observation station, and local
geological and topographical conditions
near the station. To precisely
investigate these effects, observation
through dense instrumentation array,
deployed in concentration and
systematically in specific zones, is
indispensable, to currently adopted
conventional observation of strong
motion.

Considering this situation PWRI
formulated a dense instrument array
program to deploy a number of
accelerographs at its own campus in

91

Tsukuba Science City and at four local observatory sites in the Suruga Bay – Izu region. The latter was designated as one of six high priority sites at the International Workshop on Strong-Motion Earthquake Instrument Arrays (Ref. 1). Fig. 1 shows the locations of the five sites, i.e., Tsukuba, Sagara, Yaizu, Numazu and Matsuzaki. The observation at Tsukuba campus was initiated in 1979, and deployment of arrays at Sagara, Yaizu, Numazu and Matsuzaki was completed in March 1985.

The International Workshop on Strong-Motion Earthquake Instrument Arrays classifies local effects arrays into two categories, ground motion arrays and special arrays. Ground motion arrays consisted of three subcategories; local laboratory arrays, simple extended arrays, and elementary arrays and Special arrays consist of two categories; soil-structure interaction arrays and liquefaction arrays.

PWRI's array at its Tsukuba campus is a local laboratory array; its arrays in the Suruga Bay – Izu region are simple extended arrays. The purpose of simple extended arrays is to study the influence of local geology and topography on the earthquake motions at different locations. To establish the criteria on response spectra for practical design applications it is recommended to use three component instruments, measuring two horizontal and one vertical components of acceleration.

2. SIMPLE EXTENDED ARRAYS AROUND SURUGA BAY – IZU REGION [Ref. 2-4]

In Fig. 1, the location of four local observatory sites around Suruga Bay – Izu region are shown. At these four sites, the digital type records of every accelerograph with absolute time are independently acquired in each cartridge recorder which has a pre-event memory of 5 seconds. Main specifications of the accelerographs are listed in Table 1. Maximum range of acceleration is 1.0 g and signals are digitized with time interval of 1/200 second and are stored on digital cartridge tapes. Time code generators having an automatic time corrector by NHK time signal are equipped for each recording system so that exact triggering time can be recorded at each station.

The deployments of array with subsoil conditions for each of the four sites

are described below.

2.1 Array at Sagara Site

Sagara site is located near Omaezaki in Shizuoka Prefecture facing Suruga Bay, approximately 170 km south-west of Tokyo as shown in Fig. 1. Fig. 4 shows the array. Most of the surface of Sagara site is covered by soft alluvial clay deposits. Baserock is of the Sagara Group, tertiary layers consists of alternating sandy and clayey rocks which are common at the site; it has shear wave velocity of approximately 70 m/s. The thickness of the Sagara Group is approximately 1000 meters.

Ten 3-component strong-motion accelerographs are installed on the surface along an approximate L-shaped configuration. Four 3-component down-hole accelerometers are installed at four points as deep as 36-meters to obtain baserock motions. The signals of each down-hole accelerometer (same specifications as those installed on the surface) are transmitted via cable to the recorders. Fourteen accelerographs were installed at 10 points at the Sagara site. The observation operation started in February, 1982.

2.2 Array at Yaizu Site

The Yaizu site is located near Yaizu Port approximately 20 kilometers north of the Sagara site. The array consists of 12 ground-surface accelerographs and 3 down-hole accelerometers as shown in Fig. 3. The left bank of the Seto river is covered by soft silty materials as deep as 110 meters. This bank has shear wave velocity of about 100 m/s. The right bank of the Seto river is covered by stiff gravel formations. It is expected that response characteristics of subsurface ground between the banks of the Seto river are very different. The baserock at the site is of the Takakusa Group; basalt in Neocene period, which exists at the ground surface at observing point No. 1 and the depth gradually increases in a direction along observing point Nos. 4, 7, 8, 9, 10 and 12. The depth of baserock at the observing point No. 9 is about 110 meters from the surface, and the deepest down-hole accelerometer is installed at this level. The strong-motion accelerographs, the down-hole accelerometers and time code generators used at this site are the same as those used at the Sagara site.

2.3 Array at Numazu Site

The Numazu site is located in a western part of Numazu city, Shizuoka Prefecture. At the site, an array deploys approximately north to south from the foot of Ashitaka mountain to the coastal dune, crossing the low land of Ukishimagahara. Ground surface at the district is covered by organic soils of 10 - 15 meters deep, underlayed by gravel, sand and silt formation. Baserock in this area is tuff breccia and inclines from north to south, shallow in north and deep in south. At the southern end of the array line, bedrock lies at the depth of 160 meters. Shear wave velocity of surface soil ranges from 70 to 200 m/s and that of baserock is approximately 650 m/s.

In 1980, PWRI initiated the deployment of dense strong-motion observation at this site using the array of five accelerographs [Ref. 5]. This time the site was called Ashitake site. Later, the array at this site was reinforced and the five accelerographs were combined with new ones; the present array was named Numazu site.

The array configuration at this site is shown in Fig. 4. As shown in this figure, the array deploys 9 points along the line from the foot of Ashitaka mountain to coast dune and 3 points along the line perpendicular to this deployment. Furthermore 2 more points are settled at No. 11 and No. 12 points. Total number of the points at this site is 14, and total number of accelerographs is 18 including 5 down-hole accelerometers.

2.4 Array at Matsuzaki Site

Matsuzaki site is located at Matsuzaki town on the south west coast of the Izu peninsula. The array deploys along the slope of Ushibara mountain with stations at the flat area, as shown in Fig. 5. The central part of Matsuzaki extends on the alluvial fan made by the river Nakagawa and surrounded by mountains 200 meters high. The main line of stations deploys from the low flat area of the alluvial deposit to the slope of the Ushibara mountain in a north south direction. Five points are located on the slope, an additional five points are located on the lowland along the main line and one reference station is deployed on lowland apart from the main line.

Fifteen accelerographs are installed at 11 points including four down-hole accelerometers installed at stations No.

5, 6, 8 and 9. The observation phase at this site started in March 1985.

3. PRELIMINARY ANALYSIS PROGRAM FOR DENSE INSTRUMENT ARRAY RECORDS

Prior to analysis of records obtained at dense instrument array sites, it is necessary to check the characteristic features of each data set which constitutes many components obtained by 14 - 18 accelerometers for one site during an earthquake event. To save time for this preliminary analysis, PWRI developed a computer processing system consisting of:

1) Graphic display of the epicentral location with the location of four observation sites.

2) Figure of the time history of recorded motion.

3) Figure of the calculated response acceleration spectra and Fourier spectra.

4) Display of the maximum acceleration at each station.

5) Display of the duration time of observed ground motion at each station.

6) Display of the rate of maximum acceleration at each station to one at an arbitrary station.

7) Display of the rate of response acceleration spectrum at each station to one at an arbitrary station.

8) Display of the arriving absolute time of ground motion at each station.

In Figs. 6 - 8, the examples of the output obtained by this system are shown for the case of the records of the Naganoken-Seibu Earthquake of September 14, 1984, (M=6.8).

4. LOCAL LABORATORY ARRAY AT PUBLIC WORKS WORKS RESEARCH INSTITUTE CAMPUS [Ref. 5]

PWRI moved to Tsukuba Science City, Ibaraki Prefecture in March 1979, and installed a local laboratory array for observing propagation of seismic ground strain in vertical and horizontal directions.

PWRI is located about 60 kilometers north-east of Tokyo and occupies 126 hectares (320 acres) of land. As shown in Fig. 9, two field stations (A and B Fields) were selected for dense array observation.

Subsurface soil condition of the campus is comparatively uniform in the horizontal direction. The ground consists of alternating clay, silt and sand with 100-meter depth; gravel and sand exist below the 100-meter depth. Upper layers are alluvial deposits with thicknesses of 50 meters and lower layers are diluvial. Shear wave velocities of the alluvial and diluvial deposits are approximately 250 m/s and 400 m/s, respectively.

Fig. 10 schematically shows the deployment of array instruments at Fields A and B. At Field A, thirteen 3-component accelerographs are installed along a cross-shaped configuration with 100-meter limb length and with instrumental arrangement consisting of three on the ground, five at 2-meter depth, and five at 50-meter depth. At Field B, six 3-component accelerographs are installed along a L - Shape configuration. The configuration has a 100-meter and a 50-meter leg; arrangements are one at 2-meter depth, four at 50-meter depth, and one at 96-meter depth. The direction of each limb at Fields A and B is north to south or east to west, same as the direction of each accelerograph component. Characteristics of accelerographs are listed in Table 2. Signals from each accelerograph are transmitted by cables embedded in a duct to a central processing room.

The observation by this local laboratory array was initiated in July 1979. By July 1985, records were obtained during 56 earthquakes.

5. ANALYSIS ON AMPLIFICATION OF MOTION IN THE GROUND [Ref. 6]

5.1 Amplification of Maximum Acceleration

Amplification of maximum acceleration in the ground is analyzed for the sets of records obtained at the 2 m and 50 m below ground surface (for example at points A2C0 and A46C0) at Field A of the Tsukuba campus.

Records with relatively large accelerations (larger than 10 gals horizontally and 5 gals vertically)

obtained during 56 earthquakes with magnitudes of 4 or higher were analyzed. The record sets analyzed are summarized in Table 3.

Fig. 11 shows an example of maximum accelerations which were obtained at A2C0 and A46C0 during the event of EQ-28. The ratio of maximum acceleration of the point at 50 m below surface, a_{max}^{GL-50m} to the maximum acceleration at 2 m below the surface, a_{max}^{GL-2m}, is defined as follows.

$$\alpha = \frac{a_{max}^{GL-50m}}{a_{max}^{GL-2m}} \qquad (1)$$

The value of α for the case shown in Fig. 11 is calculated as shown in Fig. 12. Average trend of α for all analyzed record is shown by the mean value of α, $\bar{\alpha}$, and the standard deviation, σ_{α} as shown in Fig. 13. It is known from Fig. 13 that the value of $\bar{\alpha}$ for the records obtained at Tsukuba campus is 0.35-0.5 for horizontal component and is 0.4-0.5 for vertical component. Therefore, the amplification ratio in the ground of the maximum acceleration is 2-3 times for horizontal motion and is 2-2.5 times for vertical motion.

5.2 Amplification of Acceleration Response Spectrum

An example of acceleration response spectrum is shown in Fig. 14, which is drawn for the records at A2C0 and A46C0 during the EQ-28 earthquake. The ratio of the acceleration response spectrum (5% damping to critical) of the record at 50 m below the surface for each period, S_A^{GL-50m}, (T, 0.05) to the one at 2 m below the ground surface for each period, S_A^{GL-2m} (T, 0.05) is defined as follows:

$$\gamma(T) = \frac{S_A^{GL-50m}(T, 0.05)}{S_A^{GL-2m}(T, 0.05)} \qquad (2)$$

The value of $\gamma(T)$ for the case of Fig. 14 is obtained as shown in Fig. 15. The mean value of $\gamma(T)$, $\bar{\gamma}(T)$ and the standard deviation $\sigma_{\gamma}(T)$ for points A2C0 and A46C0 are shown in Fig. 16. Data from Fig. 16 suggests that;

94

1) The mean value of acceleration response spectrum varies with the period, but generally, (T) in region of period less than 1 sec. is equal to 0.3-0.6 (Amplification; 1.5-3) for horizontal components and 0.4-0.7 (Amplification; 1.3-2.5) for vertical components. This means that the amplification in the horizontal direction is slightly larger than that in the vertical direction in accordance with the amplification tendency of maximum acceleration. For the region with period more than 1 second, the ratio scatters fairly wide; the mean value in this region seems to be bigger than that in the region with periods less than 1 second. This implies that the amplification for the component in the region with periods longer than 1 second is comparatively small.

2) The ratio of the acceleration spectrum has the minimum value of about 0.7 second in period. Amplification is maximum at this period. This is in accordance with the estimated predominant period of the ground equal to 0.79 second. Calculated from the shear wave velocities and the thickness of the layers.

6. ANALYSIS ON PHASE VELOCITY OF GROUND MOTION [Ref. 7]

6.1 Comparison between the Epicentral Direction and the Predominant Direction of Ground Motion propagation.

If it is assumed that the ground motion in horizontal plane propagates in a predominant direction, the cross correlation between the two components of a recorded ground motion in this predominant direction and in the direction perpendicular to this direction is thought to be minimum.

Prior to the calculation of the cross correlation, the two components of ground motion along two direction of an arbitrary direction and its perpendicular direction are calculated from the recorded data measured along north-south direction and east-west direction. Assuming the east-west component of the recorded ground motion

is expressed by $a_x(t)$, and the north-south component is expressed by $a_y(t)$, as shown in Fig. 17, the components of the ground motion along the X axis and Y axis are rotated by θ in anticlockwise, $a_X(\theta, t)$ and $a_Y(\theta, t)$ respectively, are expressed as follows:

$$a_X(\theta, t) = a_x(t)\cos\theta + a_y(t)\sin\theta \quad (3)$$

$$a_Y(\theta, t) = -a_x(t)\sin\theta + a_y(t)\cos\theta \quad (4)$$

The cross correlation coefficient of $a_X(\theta, t)$ and $a_Y(\theta, t)$, $R(\theta)$ is obtained by the following equation:

$$R(\theta) = \frac{\int_0^T a_X(\theta, t)\, a_Y(\theta, t)\, dt}{\sqrt{\int_0^T a_X^2(\theta, t)\, dt \cdot \int_0^T a_Y^2(\theta, t)\, dt}} \quad (5)$$

where, T denotes the duration time of the recorded data. As equations (3) and (4) apparently leads that $a_X(\theta+\pi, t) = -a_X(\theta, t)$ and $a_Y(\theta+\pi, t) = -a_Y(\theta, t)$, then the relation $R(\theta+\pi) = R(\theta)$ is reduced. Fig. 18 shows an example of the results of $R(\theta)$ reduced from the equation (5) by varying every 10° from 0° to 180°, using the recorded ground motions observed at the points of 2 m below the ground surface (A2CO, A2N2, A2S2, A2E2, A2W2) and at the points of 50 m below the ground surface (A46CO, A47N2, A45S2, A47E2, A46W2) during the earthquakes of EQ-28 and EQ-34. In Fig. 18, epicentral direction angle, θ_{EP}, which is measured anticlockwise from the east direction, is also illustrated.

If the principal motion propagates in its predominant direction, the maximum value of the horizontal acceleration of the reduced component in this direction is thought to be smaller than that in the direction perpendicular to the propagating direction. Then, among the directions in which the cross correlation coefficient becomes zero, such direction in that the maximum acceleration is smaller than the maximum acceleration in the other direction, is taken as the predominant direction of the ground motion propagation.

The predominant propagation directions for each observing point and the epicentral directions are shown in Fig. 9. Although there are some earthquakes where the predominant direction does not coincide with the epicentral direction, in cases of three earthquakes, EQ-21, EQ-34 and EQ-45, both directions coincide well at points 2 m below ground surface. For earthquakeS EQ-21, EQ-22,

EQ-34 and EQ-39, one sees that both
directions coincide well at points 50 m
below the ground surface.

6.2 Calculation of the Phase Velocity
of Ground Motion

Based on the results described above,
the horizontal phase velocity of the
ground motion can be calculated for the
five earthquakes, which the predominant
propagation directions coincide well
with the epicentral directions. The
five earthquakes are EQ-21, EQ-22 (only
for the data obtained at points 50 m
below the ground surface), EQ-34, EQ-39
(only for data obtained at points 50 m
below the ground surface) and EQ-45
(only for data obtained at points 2 m
below the ground surface). The
horizontal phase velocities of the
ground motion in epicentral direction
and perpendicular to the epicentral
direction between two points on a
horizontal plane are respectively
calculated by dividing the horizontal
distance of these points by the phase
lags which make the cross correlation
coefficients of the ground motions at
two points maximum in each direction.
The phase velocity in a vertical
direction of the ground motion
calculated from the phase differences of
the records between two points coincides
fairly well with the shear wave
velocity.

As for the records obtained at two
points i and j in Fig. 20, by denoting
the components at points i and j along X
axis which is rotated by θ_0
(epicentral direction components) by
$a_{i,x}(t)$ and $a_{j,x}(t)$ respectively, the
cross correlation coefficient of these
values, $R_{ij}(\tau)$, is expressed by the
following equation.

$$R_{ij}(\tau) = \frac{\int_0^T a_{i,x}(t)\, a_{j,x}(t+\tau)\, dt}{\sqrt{\int_0^T a_{i,x}^2(t)\, dt \cdot \int_0^T a_{j,x}^2(t)\, dt}} \qquad (6)$$

where,   means the phase lag. Let the
phase lag at which $R_{ij}(\tau)$ becomes
maximum value, R_{max},   be denoted by
τ_{max}, and the projected distance between
two points to the epicentral direction
be expressed by ℓ (refer to Fig. 20),
then the phase velocity, v, is
expressed as follows.

$$v = \frac{\ell}{\tau_{max}} \qquad (7)$$

The expression for the phase velocity of
the component along Y-axis (component
perpendicular to the epicentral
direction) can be reduced similarly.
Table 5 summarizes the calculated
results by these procedures taking four
sets of data at (A2N2, A2S2),(A2E2,
A2W2), (A47N2, A45S2) and (A47E), A46W2)
as the combination of points (i, j). In
this table, the negative values mean
that the propagating direction is
opposite to the apparent direction.
Although the shear wave velocity around
these points is 250 m/sec for the layer
from ground surface to the depth of 50
m, and 400 m/sec for deeper layer, the
phase velocity estimated by equation (7)
is extremely large. Also there are many
cases where the propagating directions
are opposite to the apparent ones.

Next, the phase velocity of the treated
records obtained by filtering the
original records by band pass filter in
frequency domain is calculated for each
period by the same procedure mentioned
above.

Fig. 21 shows an example of the results
of this calculation for the case of
EQ-34. It is reduced from the analysis
for the phase velocity of various period
as follows:

   1)   The apparent velocity iN
horizontal direction of the
            ground motion in any period is
            generally larger than the
            shear wave velocity.

   2)   There are no apparent relations
            between the period and the
            phase velocity as far as the
            range up to 5 second of period
            which is examined by this
            analysis. However, it seems
            that the phase velocity
            generally becomes smaller in
            longer periods.

   3)   It is difficult to recognize
            the general relation among the
            magnitudes of calculated phase
            velocities from records
            obtained at the points 2 m
            below the ground surface and
            the points 50 m below the
            ground surface.

It is concluded from the above results,
that the apparent horizontal velocity of
ground motion is extremely large for the
data analyzed here because the ground
motion propagates vertically around the
ground surface.

7. SUMMARY AND CONCLUSIONS

1) A dense instrument array system was constructed and maintained by PWRI for observing strong ground motion during earthquakes.

2) The amplification factor of the motion in the ground of 50 m thickness analyzed from the data observed at PWRI campus was 2-3 for horizontal motion and was 2-2.5 for vertical motion.

3) The phase velocity in a horizontal plane calculated from the data observed at PWRI campus was extremely large compared with the shear wave velocity. The reason is considered that the ground motion propagates vertically during the observed earthquakes.

8. ACKNOWLEDGMENTS

9. REFERENCES

1) International Association for Earthquake Engineering: Strong-Motion Earthquake Instrument Arrays, Proc. of the International Workshop on Strong-Motion Earthquake Instrument Arrays, Edited by Iwan, W. D., Honolulu, Hawaii, U.S.A., May, 1978

2) Tadayoshi Okubo: On the Dense Array Observation of Strong Earthquake Motion (in Japanese), Civil Engineering Journal, Vol. 22, No. 4, April, 1980

3) Toshio Iwasaki, Yasushi Sasaki, Keiichi Tamura, Koh Aizawa: Dense Instrument Array Program by Public Works Research Institute for Observing Strong Earthquake-Motion, ASCA Seminar, Tsukuba, Japan, February, 1985

4) Yasushi Sasaki, Keiichi Tamura, Koh Aizawa, Kazuyuki Takahashi: Dense Instrument Array Observation by Public Works Research Institute (in Japanese), Civil Engineering Journal Vol. 28, No. 1, January 1986

5) Tadayoshi Okubo, Toshio Iwasaki, Kazuhiko Kawashima: Dense Instrument Array Program of the Public Works Research Institute and Preliminary Analysis of Some Records, U.S.-Japan Panel on Wind and Seismic Effects, U.J.N.R., 13th Joint Meeting, May 1981

6) Yasushi Sasaki, Keiichi Tamura, Koh Aizawa, Kazuyuki Takahashi: Analysis on Strong Ground Motions during Earthquakes observed by Dense Array at P.W.R.I. -- Study on Characteristic of amplification and Spatial Variation of Ground Motion -- (in Japanese), Technical Memorandum of Public Works Research Institute, No. 2270, December, 1985

7) Yasushi Sasaki, Keiichi Tamura, Koh Aizawa, Kazuyuki Takahashi: Analysis on Strong Ground Motions during Earthquakes observed by Dense Array of P.W.R.I. -- Study on Apparent Velocity of Wave Propagation -- (in Japanese), Technical Memorandum of Public Works Research Institute, No. 2271, December 1985

Table 1 Main Specifications of Accelerograph used for Simple
Extended Arrays around Suruga Bay

	Type	Triaxial, Velocity Feed-Back with Calibration Coil
Accelerometer	Full Scale Range	± 1G
	Natural Frequency	5 Hz
	Damping Ratio	>30
Trigger System	Sensitive Direction	Vertical
	Acceleration Set Point	0.005G (Changeable)
	Operation Cycle	Self-actuating for duration of earthquake, with automatic reset 5 seconds after averaged acceleration in horizontal direction becomes less than 5 gals
Recording System	Type	Digital
	Number of Truck	4
	Magnetic Tape	Digital Cartridge; 60 inch/sec.
	Number of Bits	16 bits
	Dynamic Range	± 92 dB
	Sampling Rate	200 Samples/sec/channel
	Max. Recording Time	Approximately 40 minutes
	pre-event Memory	5 seconds for each channel
Time Code Generator	Accuracy of Crystal	± 10^{-7}
	Auto Adjustment of Time of Crystal	Each 1 hour by NHK Time Signal
Power Requirement	Voltage	12 VDC
	Battery Charger	Float Charger Supplied; Approved for less than 25 hours after suspention of commercial electricity
Case		Water tight case for proof of twice of atmospheric pressure

Table 2 Main Specifications of Accelerometer used
by Local Laboratory Array at PWRI

Number of Component	3
Type	Velocity Feed Back
Natural Frequency	5 Hz
Frequency Range	0.1 - 50 Hz ; within 1 dB
Maximum Acceleration	± 650 gals
Diameter, Length	φ 13 cm, 125 cm
Weight	50 kg

Table 3 Number of Records used for Analysis on Amplification
of the Motion in the Ground

Component / Combination	N – S	E – W	U – D
A46C0 / A2C0	30	25	29
A47N2 / A2N2	30	25	30
A45S2 / A2S2	31	30	30
A47E2 / A2E2	30	27	29
A46W2 / A2W2	23	19	25

Table 4 Earthquake Records used for Analysis on Wave Propagation

Earthquake No.	Date	Hypocenter				Epicentral Distance (km)	JMA Magnitude
		Region	Longitude	Latitude	Depth (km)		
EQ – 13	1980. 9. 25	Central Chiba Pref.	140°13'	35°31'	80	69	6.1
EQ – 16	1981. 9. 2	Off Ibaraki Pref.	141°08'	35°48'	40	102	5.8
EQ – 21	1982. 3. 7	Kashima-nada	140°39'	36°28'	60	64	5.5
EQ – 22	1982. 7. 23	Off Ibaraki Pref.	141°57'	36°11'	30	169	7.0
EQ – 28	1983. 2. 27	S.Ibaraki Pref.	140°09'	35°56'	72	22	6.0
EQ – 31	1983. 7. 2	Off Fukushima Pref.	141°07'	36°54'	50	127	5.8
EQ – 34	1983. 10. 28	SE Ibaraki Pref.	139°59'	36°13'	60	13	5.2
EQ – 39	1984. 1. 1	S off Kinki	136°59'	33°16'	400	425	7.4
EQ – 44	1984. 2. 21	SE Ibaraki Pref	140°06'	36°06'	70	3	5.2
EQ – 45	1984. 3. 6	Near Torishima	139°08'	29°28'	460	745	7.9

Table 5 Apparent Velocity of Wave Propagation

Earthquake No.	Epicentral Direction θ_{EP}	Predominant Direction θ_g	Observing Points	Propagation Distance ℓ [m]	Component[1]	Max. Cross Correlation R_{max}	Phase Lag τ_{max} [sec]	Propagation[2] Velocity ν [m/sec]
EQ-21	42.6	40	A2N2 → A2S2	64.3	LG	0.577	0.01	6430
					TR	0.613	0.00	∞
			A47N2 → A45S2	64.3	LG	0.374	−0.05	−1286
					TR	0.497	−0.05	−1286
			A47E2 → A46W2	76.6	LG	0.536	0.01	7660
					TR	0.753	0.00	∞
EQ-22	2.8	0	A47E2 → A46W2	100.0	LG	0.796	0.00	∞
					TR	0.834	0.00	∞
EQ-34	122.3	120	A2N2 → A2S2	86.6	LG	0.398	0.00	∞
					TR	0.657	−0.02	−4330
			A2W2 → A2E2	50.0	LG	0.209	0.05	1000
					TR	0.528	0.035	1429
			A47N2 → A45S2	86.6	LG	0.261	0.52	167
					TR	0.506	0.01	8660
			A46W2 → A47E2	50.0	LG	0.497	−0.02	−2500
					TR	0.623	−0.02	−2500
EQ-39	228.3	230	A45S2 → A47N2	76.6	LG	0.477	−0.01	−7660
					TR	0.609	−0.02	−3830
			A46W2 → A47E2	64.3	LG	0.670	−0.01	−6428
					TR	0.724	−0.01	−6428
EQ-45	264.3	270	A2S2 → A2N2	100.0	LG	0.850	0.00	∞
					TR	0.877	0.00	∞

1) LG: Epicentral direction   TR: Perpendicular to LG

2) Negative velocity means that the propagating direction is opposite to the apparent direction.
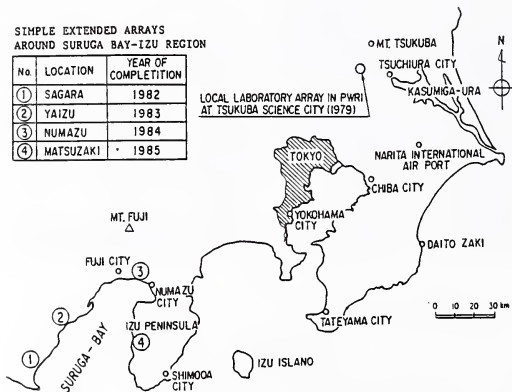

Figure 1 Location of Dense Instrument Arrays by PWRI

Figure 2 Array at Sagara Site


Figure 3 Array at Yaizu Site

Figure 4 Array at Numazu Site
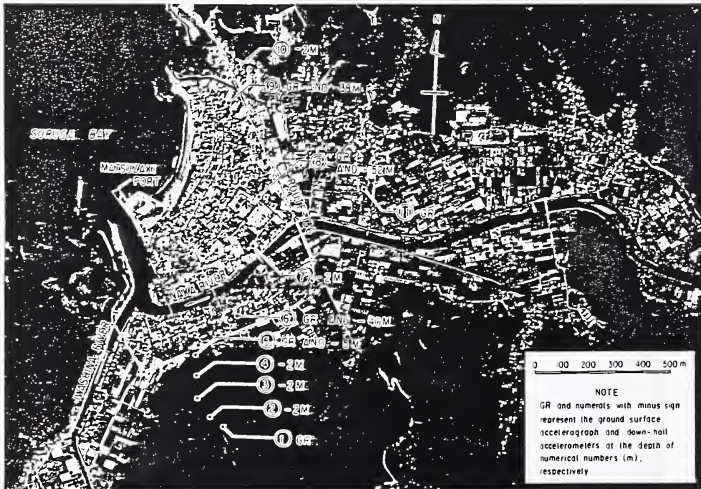
Figure 5 Array at Matsuzaki Site

Figure 6 Location of Epicenter (Nagano-Ken-Seibu
Earthquake, 1984)

NAGANO-KEN-SEIBU EARTHQUAKE.1984   1984-09-14
TAIZU AREA MAXIMUM ACCELERATION (UNIT:GAL)

TOMEI EXPRESSWAY

NO.4	GA	
N-S	E-W	U-D
26	19	10

NO.1	-TOM	
N-S	E-W	U-D
2	3	2

NO.5	GA	
N-S	E-W	U-D
23	18	9

NO.6	GA	
N-S	E-W	U-D
25	25	7

HIGASHI-MASHIZU
ELEMENTARY SCHOOL

HIGASHI-MASHIZU
JUNIOR HIGH SCHOOL

NO.8	GA	
N-S	E-W	U-D
33	26	9

ASAHINA
RIVER

NO.3	GA	
N-S	E-W	U-D
-	-	-

NO.2	GA	
N-S	E-W	U-D
19	18	7

NO.7	GA	
N-S	E-W	U-D
-	-	-

NO.9	GA	
N-S	E-W	U-D
30	29	7

SETO RIVER

NO.11	GA	
N-S	E-W	U-D
14	14	3

SURUGA BAY

NO.10	GA	
N-S	E-W	U-D
22	24	8

TOKAIDO SHINKANSEN

TAIZU

TAIZU
PORT

0 100 200 300 400 500 m

TOKAIDO LINE

LOCATION OF STRONG MOTION ACCELEROGRAPH

TAIZU-NISHI ELEMENTARY SCHOOL

| NO.12	GA	
N-S	E-W	U-D
12	16	3

NOTE : NUMERALS WITH PARENTHESES ARE NOT GOOD

Figure 7 Maximum Acceleration of Yaizu Site

103

Figure 8 Maximum Acceleration of 4 Sites around Suruga Bay

Figure 9 Local Laboratory Array at PWRI
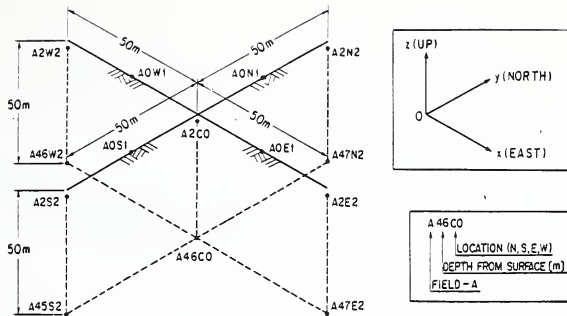
Field A

Note   AOE1: Observation has been stopped since September
          16, 1982.
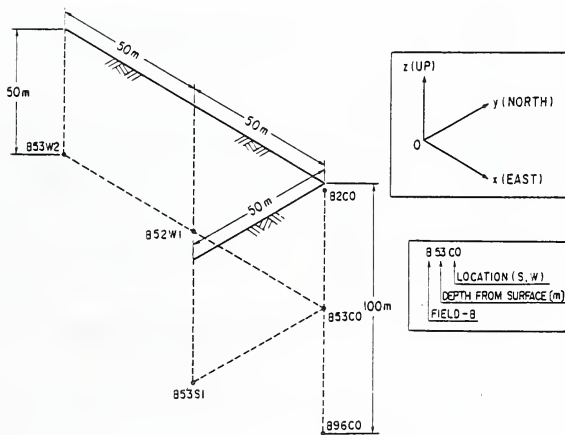
Field B

Figure 10   Array Configuration at PWRI Campus
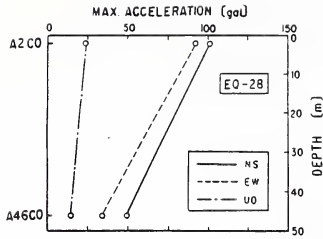
Figure 11   Example of Maximum
Acceleration (EQ-28)
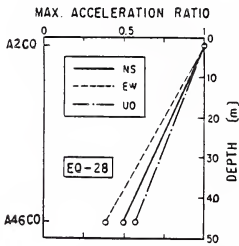
Figure 12   Example of Maximum
Acceleration Ratio (EQ-28)
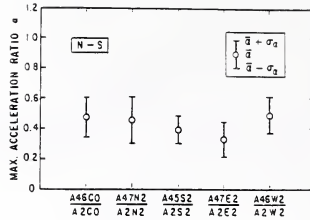
(a) N-S Component
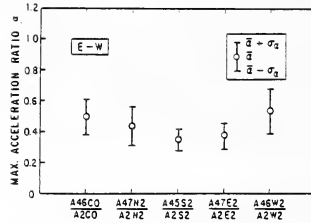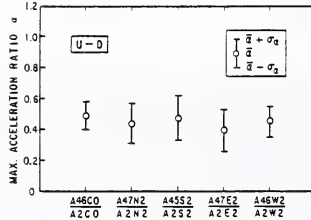
(b) E-W Component

(c) U-D Component

Figure   13   Average and Standard Deviation of
Maximum Acceleration Ratio
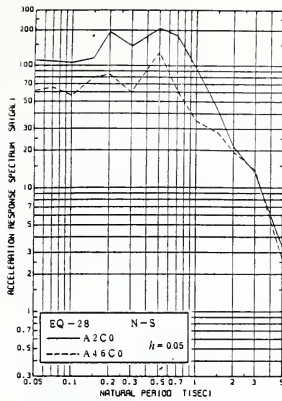
Figure 14   Example of Acceleration
Response Spectrum (EQ-28)
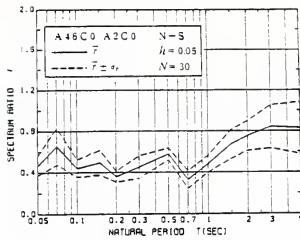
(a) N-S Component
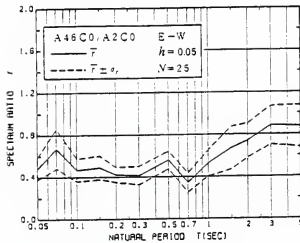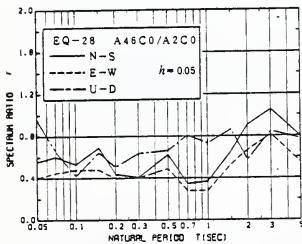
(b) E-W Component

Figure 15   Example of Acceleration
Response Spectrum Ratio (EQ-28)
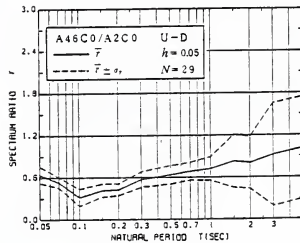
(c) U-D Component

Figure 16   Average   and   Standard
Deviation   of   Acceleration
Response Spectrum Ratio
(A46C0/A2C0)
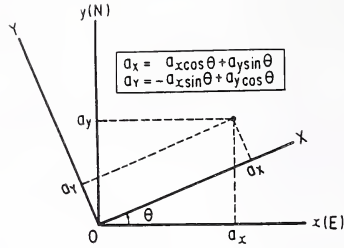
Figure 17 Rotation of Coordinate
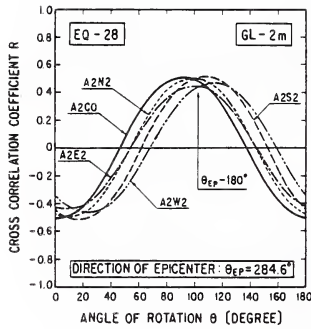
(a) EQ-28, GL-2m
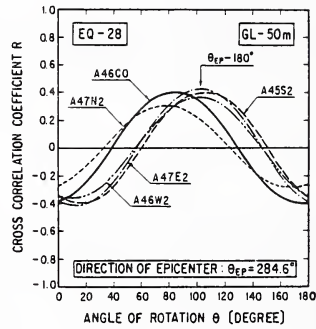
(b) EQ-28, GL-50m
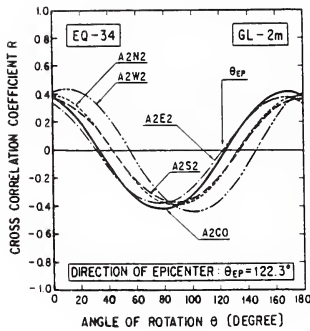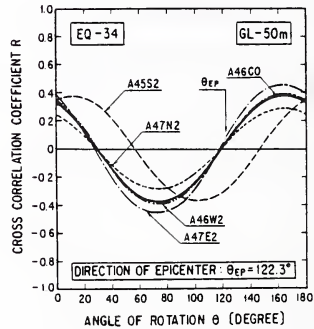
(c) EQ-34, GL-2m

(d) EQ-34, GL-50m

Figure 18 Relation between Rotation Angle and Cross
Correlation Coefficient

(a) EQ-28, GL-2m (b) EQ-28, GL-50m

(c) EQ-34, GL-2m (d) EQ-34, GL-50m
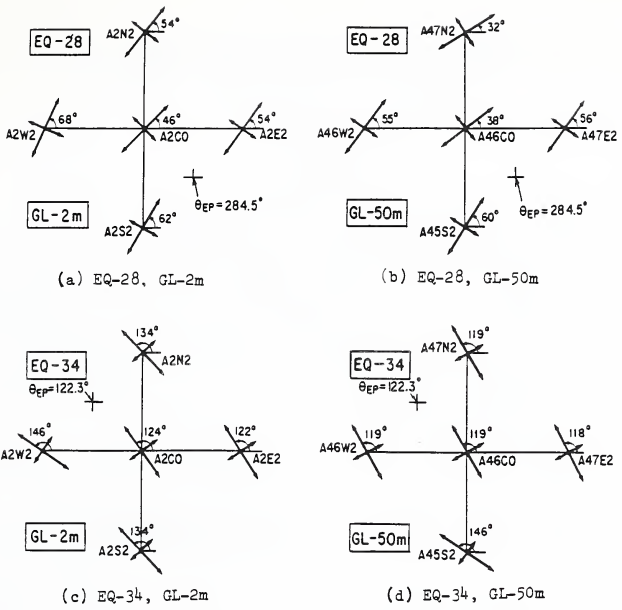
Figure 19 Predominant Propagation Direction

$\ell = L \sin \theta_0$
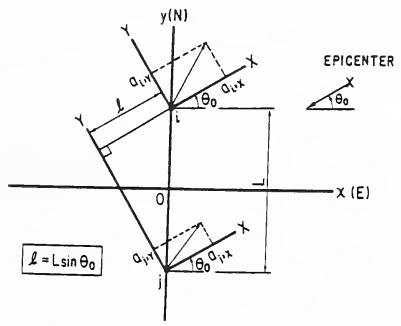
Figure 20 Definition of Propagation Distance
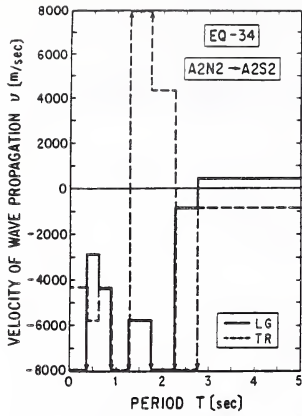
(a) EQ-34, A2N2→A2S2
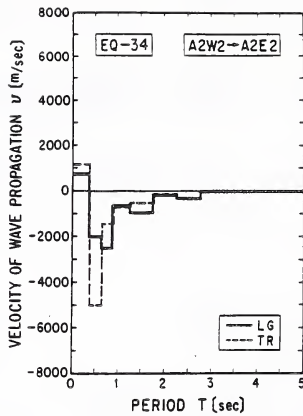
(b) EQ-34, A2W2→A2E2
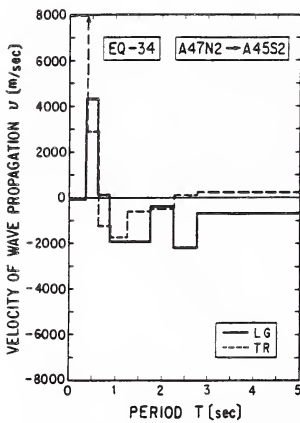
(c) EQ-34, A47N2→A45S2
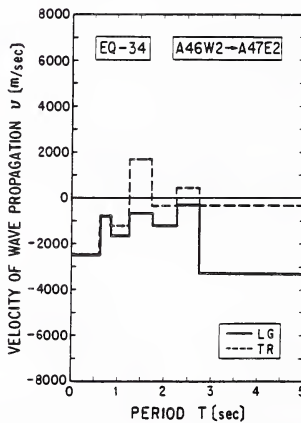
(d) EQ-34, A46W2→A47E2

Note   LG: Epicentral direction   TR: Perpendicular to LG

Figure 21   Propagation Velocity of Various Period

VIBRATING TESTS OF AN ASPHALTIC FACING
COFFERDAM BY BLASTINGS

BY

N. Matsumoto[1]
N. Yasuda
M. Shiga

ABSTRACT

Rockfill dams with upstream impervious facings have advantages in rapid construction and economical construction cost. However, impervious facings are vulnerable to damage caused by the settlement of the dam and earthquake motion. Therefore, dams of this type have pervious rock zones capable of draining leakage, if any, and adequate means of lowering water level for repairing the impervious facing.

On the other hand, compaction of the rockfill by vibratory roller and use of well graded materials enabled minimization of the post construction settlement. Vulnerability of the facings of the rolled fill dam decreased compared to the dumped fill. Dams with facing often have been designed in areas where seismic activity is low. The seismic resistance design of this type of the dam is important to Japan with its frequency of strong earthquakes. So the vibration test test of a 16.5-m-high asphaltic facing dam by using blastings at the quarry site was performed. Seismographs, accelerations and dynamic strain gauges were placed in the asphaltic facing dam and its dynamic behavior was investigated. The quarry site was exploded when the reservoir level of the dam was at its lowest, intermediate, and the highest. Accelerations recorded at the dam foundation ranged from 4 gals to 30 gals.

In this paper, the effects of the reservoir level to natural frequency and response amplitude at the dam crest are reported. Also, the behavior of an asphaltic facing during vibrating and the comparison with calculated results by a computer program are discussed.

1. GENERAL DESCRIPTION OF A COFFER DAM AND BLASTINGS

The 110-m high rockfill dam (central core zone type) is now under construction by Hokuriku Regional Construction Bureau of the Ministry of Construction. A 16.5-m-high asphaltic facing dam was constructed as the upstream No. 1 cofferdam, the downstream slope was covered with concrete.

In this cofferdam seismographs, accelerometes, and strain gauges were installed to monitor dynamic behaviors during explosions. Seven seismographs were located in the dam. Four were inside the dambody and the others were at the surface of the dam. Seismographs (made by Katsujima Co., Ltd.) were servo-type strong motion accelerometers which were composed of three components (up-down stream, dam axis, and vertical directions); 21 components of earthquake motion were observed. Figure-1 shows the positions of the seismographs.

Accelerometers (made by Kyowa Electric Co., Ltd) were strain gauge type. Each meter was composed of up-down stream and vertical direction, and 12 components of earthquake motion were obtained. Figure-2 shows the locations of accelerations and strain gauges. The vibrating tests by blastings were performed at the upstream No.-1 cofferdam (Asphaltic facing dam) and the response to the shaking of a cofferdam was investigated.

The blastings were conducted three times corresponding to three different water levels, i.e. at the water level before filling the reservoir, at the top water level and at the intermediate water level (twice). Table-1 shows the list of blasting tests. The locations of explosions were at the downstream side of a quarry site (400 m in the horizontal distance) during the time of an intermediate water level and the downstream side of a quarry site (400 m in the horizontal distance) for the others. Powder quantity used were 1,004 kgf--1,715 kgf for each case.

2. BEHAVIORS OF A COFFERDAM DURING BLASTINGS

Observed waves were digitized at every 0.002 seconds. The maximum accelerations, the maximum displacements and power spectra were obtained for each explosion wave. Each spectrum was smoothed by 0.4Hz of Parzen's spectral window. Figures 3 & 4 show time histories of accelerations and spectra at the crest and foundation. The maximum accelerations, the maximum displacements and predominant frequencies observed by each seismographs are indicated in Tables 2 & 3.

The maximum acceleration of the foundation in the up-down stream direction ranges from 4.7 gals to 20.1 gals; for the dam crest it ranges from 16.4 gals to 67.7 gals. The response amplitude at crest to foundation is about 3.5.

The dynamic behaviors of asphaltic facing are shown by Figure 5. Time histories are presented of displacement gained by integration of accelerations which were observed at V-2 (the surface

of an asphaltic facing) and V-7 (the inside of a facing).

The relative displacement between an asphaltic facing and the dam body is very small, as are the phase difference between them. The behaviors of a facing appear to be almost the same with that of the dam body. This is distinct from the power spectra of V-2 and V-7 both in the up-down stream direction because their spectra have similar shapes when the reservoir is empty and full. Table-4 shows the maximum accelerations observed by accelerometers and the maximum strains by strain gauges, both types are located at the asphaltic facing. In the case the maximum acceleration at the foundation is more than 10 gals, the maximum in up-down stream direction tend to be larger than those of vertical direction. The maximum strains range from 1×10^{-6} to 1×10^{-5} and likely to decrease in lower level.

The wave velocities at the facing and the dam body were 122-167m/sec and 341-441 m/sec respectively during the empty reservoir, and 122-192 m/sec and 341-375 m/sec respectively during the full reservoir. In disregard of the path of wave propagations in the dam body, the wave velocities were calculated from distances between seismographs and start of waves. The propagation speed at an asphaltic facing was the half of the dam body. Both velocities decreased after the reservoir was filled.

The natural frequency of the dam body can be estimated from the power spectrum of acceleration observed at the dam crest, but the frequency characteristics of foundation has to be eliminated from this spectrum. The time history of acceleration of the foundation and the dam crest were assumed to be $f(t)$ and $g(t)$ respectively. Fourier spectra $F(w)$ and $G(w)$ are obtained as follows:

$$F(w) = \int_{-\infty}^{\infty} f(t) e^{-iwt} dt \qquad (1)$$

$$G(w) = \int_{-\infty}^{\infty} g(t) e^{-iwt} dt \qquad (2)$$

The frequency response function of the dam crest to the foundation Zw is given by the equation:

$$Z(w) = G(w) / F(w) \qquad (3)$$

Upstream-No. 1 is a three-dimensional structure, the vertical motion of the foundation, for example, contributes to the vertical and to the horizontal motions of the dam. However, ignoring this coupling motion, the frequency response functions of up-down stream component, shown in Figure-7, were obtained from equation (3).

From this response function, the first natural frequency of the dam is 8.1 Hz when the reservoir is empty. Figure-7 also shows the

frequency response of the reservoir function during filling. During filling, the first natural frequency becomes smaller and the response amplitude decreases from 16 to 10. The authors reported test results of a two-dimensional dam model by a shaking table during the sixteenth (1984) joint meeting of UJNR. This result coincided with the above-mentioned one i.e., the response amplitude and the natural frequency decreases as it is being filled (see Figure-8).

3. DYNAMIC ANALYSIS OF AN ASPHALTIC FACING DAM

Using the time histories of acceleration of the foundation during blastings, the observed response accelerations of the dam body are compared with computed ones. The computer program used was DINAS; modal damping method was used. The part of kinetic energy accumulated in each mode dissipated as damping energy. At first, kinetic energy of each element is calculated from the mass matrix of each element for every natural frequency of free vibration. Damping ratio of each natural mode is given as follows:

$$h_i = \frac{\sum_{j=1}^{n} C_j x_i^t m_j x_i}{\sum_{j=1}^{n} x_i^t m_j x_i} = \frac{\sum_{j=1}^{n} C_j x_i^t m_j x_i}{X_i^t M X_i} \qquad (4)$$

m_j : Mass matrix of each element j
c_j : Damping ratio of element j
M : Mass matrix of structure
xi : $i - th$ mode shape

The Westergaard's added mass concept is adopted for the hydro-dynamic effect of the upstream face. The filldam body may be considered elastic when very small strain is expected to occur. The maximum strain observed at the dam body was 1×10^{-5} during blastings, so two-dimensional elastic analysis was performed as in the concrete dam. Figure-9 shows the finite element idealization.

It is known that shear modulus of rock materials depends on the confining pressure. However, the modulus of the dam body was assumed to be independent of the pressure and 2,997 kgf/cm^2 of modulus was adopted in this computation. Poisson's ratio and damping ratio is 0.36 and 10%, respectively. The input properties used for computation were obtained after the equations of Sawada et al. The characteristics of the asphaltic facing were determined from laboratory tests as shown in Table-6. The calculated and observed results are indicated in Table-7. Table-8 shows the maximum computed strain of an asphaltic facing. Figures-10 to 12 show the time histories of acceleration and displacements and frequency response functions during the empty reservoir (case-1) and full (case-2). There were coincidences between the computed result and the observed data, especially about the natural frequency and the accelerations

of the dam body.

4. CONCLUSION

The following are results from investigations of dynamic behaviors of the asphaltic facing dam.

1. The response amplitude of the dam crest to the foundation is about 3.5.

2. Relative displacements between the asphaltic facing and the dam body was very small, and the phase difference was difficult to recognize; their dynamic behaviors during blasting were near similar to each other.

3. The natural frequencies and the response amplitude of the dam body decreased as the reservoir was filled. The same results were obtained from a two-dimensional dam model using a shaking table.

4. The computed vertical accelerations of the dam crest were nearly equal to the observed ones in every case. The response displacements and frequencies were the same in vertical and horizontal directions.

ACKNOWLEDGEMENTS

REFERENCES

(1) N. Matsumoto, M. Toyoda, M. Shiga, "Dynamic Tests of Rockfill Dam Models," 16th UJNR, 1982.

(2) "Dynamic Interaction Problem Analysis System," C.R.C. Co., LTD.

(3) Y. Sawada, T. Takahashi, A. Sakurai and H. Yajima, "Material Property Distribution and Dynamic Characteristics of Rockfill Dams--A Consideration Based on Elastic Wave--," Central Research Institute of Electric Power, Report No. 377008, 1977 (in Japanese).

(4) N. Matsumoto, N. Yasuda, M. Shiga, " Measured Behaviors of Asphaltic Concrete Facing Dam," 1986 (unpublished).

Table 1 General Description of blastings

| | Water level (m) | Temperature of Asphalt | | Location of Blastings (m) | Horizontal Distance (m) |
		Surface	10 cm below		
EMPTY	empty	38.0	41.0	Upstream side of Quarry EL = 420	200
FULL	EL = 368.22	36.5	33.0	Upstream side of Quarry EL = 400 ~ 420	200
INTERMEDIATE-1	EL = 364.01	34.0	32.0	Downstream side of Quarry EL = 550	400
INTERMEDIATE-2	EL = 362.33	36.0	38.0	Downstream side of Quarry EL = 550	400
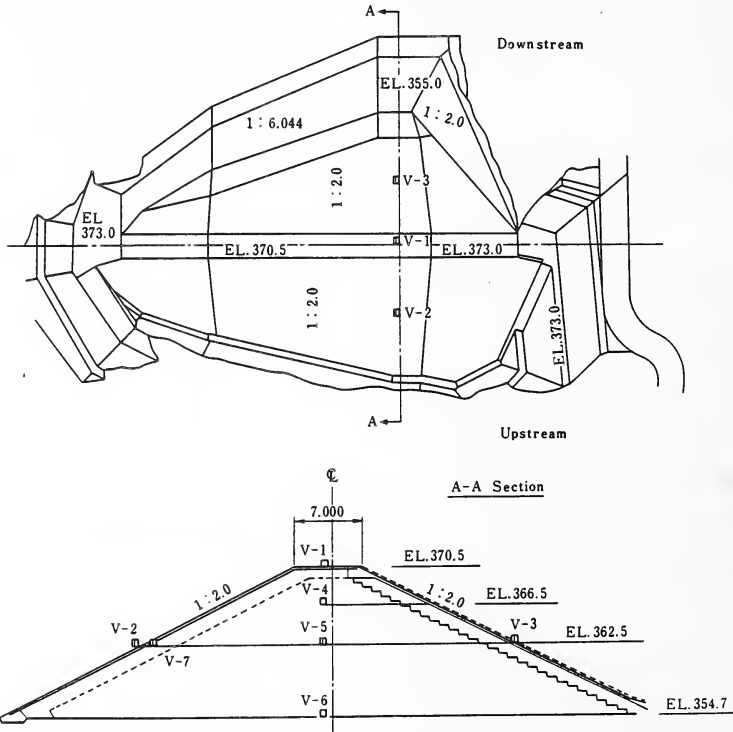
Figure-1   Positions of seismographs

114

Table 2 The maximum acceleration and displacement in each explosion

Seismograph	Direction	Empty Acceleration gal	Empty Displacement cm	Full Acceleration gal	Full Displacement cm	Intermediate-1 Acceleration gal	Intermediate-1 Displacement cm	Intermediate-2 Acceleration gal	Intermediate-2 Displacement cm
V-1	Up-down stream	46.4	0.016	67.7	0.016	16.4	0.008	27.3	0.016
	Dam axis	67.3	0.022	65.9	0.016	16.0	0.008	25.3	0.013
	Vertical	48.6	0.009	68.5	0.015	8.0	0.002	14.2	0.003
V-2	Up-down stream	36.2	0.006	32.5	0.006	10.3	0.004	14.8	0.008
	Dam axis	40.3	0.009	33.1	0.006	6.4	0.003	10.7	0.005
	Vertical	55.0	0.006	48.4	0.001	8.9	0.001	20.6	0.003
V-3	Up-down stream	32.0	0.009	63.9	0.011	9.3	0.004	20.0	0.009
	Dam axis	67.8	0.012	66.7	0.011	9.3	0.004	8.8	0.005
	Vertical	54.3	0.008	106.2	0.009	8.1	0.001	20.3	0.003
V-4	Up-down stream	39.2	0.015	41.6	0.016	14.9	0.008	26.4	0.015
	Dam axis	69.8	0.021	62.7	0.016	15.1	0.007	25.4	0.013
	Vertical	39.1	0.010	56.8	0.015	6.4	0.002	14.1	0.003
V-5	Up-down stream	21.8	0.010	26.1	0.011	11.4	0.006	18.6	0.011
	Dam axis	43.0	0.014	44.7	0.013	9.3	0.005	21.1	0.010
	Vertical	35.0	0.009	58.9	0.013	5.9	0.002	8.8	0.003
V-6	Up-down stream	15.5	0.004	20.1	0.004	4.7	0.003	8.4	0.005
	Dam axis	20.7	0.005	24.0	0.006	4.0	0.002	8.5	0.004
	Vertical	24.8	0.005	50.4	0.009	4.3	0.001	9.7	0.003
V-7	Up-down stream	32.0	0.007	32.9	0.008	9.6	0.004	15.1	0.008
	Dam axis	35.3	0.009	31.6	0.006	6.6	0.003	12.0	0.005
	Vertical	42.9	0.007	64.5	0.012	8.8	0.001	21.6	0.003

Table 3 The predominant frequencies of observed accelerations in each explosion

Predominant frequencies Hz

Seismograph	Direction	Empty	Full	Intermediate-1	Intermediate-2
V-1	X	6.3 8.0 **10.8** 14.4 18.0 19.6	**6.4** 10.8 12.4 14.4 17.5	6.6 11.1	**6.3**
	Y	**6.9** 8.0 11.1 12.5 14.8	6.9 8.1 10.8 14.7	6.6 8.2 9.2	6.5 8.0
	Z	**9.1** 12.8 15.9 17.3 18.7	9.1 12.9 15.3	8.8 11.9	5.5 **8.9** 14.0 17.7 18.5 21.1
V-2	X	8.3 9.3 14.0 15.9 19.3 20.9 24.0	**6.3** 8.4 9.3 14.0	6.0 6.6 8.5 9.5 10.9 13.4 17.7	**6.0** 13.2 17.5
	Y	6.8 **11.1** 12.0 15.2 18.5 22.0 30.0	6.8 9.3 **12.0** 14.8 17.7 22.4 30.0	**6.0** 6.6 8.2 10.0 10.9	6.0 6.6 8.0 11.2 15.4 17.7 20.0
	Z	8.8 12.7 14.8 19.1 20.3 21.5 29.8	8.7 12.8 **15.5** 20.8 22.3	8.5 11.4 18.2	8.5 11.4 15.9 **18.0** 20.0
V-3	X	6.4 **12.0** 18.5 21.6 25.3 27.1 28.5	6.4 **10.4** 12.0 13.9 15.3 17.3 27.6	6.8 8.0 8.9 11.2 14.6 17.8 18.3 20.0	**6.0** 8.2 10.6 14.5 17.5
	Y	6.5 **10.4** 12.8 16.3 17.5 18.8	6.5 8.8 **12.3** 17.6	5.8 7.5 9.5 14.2	5.9 6.6 7.5 9.2 13.1 41.2 14.9
	Z	8.9 15.1 **19.8** 21.3 26.8	8.7 14.0 16.9 **20.0** 25.3 30.5 42.0	8.6 11.7 17.5 21.8 22.6	8.3 12.0 14.3 17.9 19.5
V-4	X	6.3 **10.3** 14.0 15.5 18.0	6.4 10.4 14.0	6.8 10.9	6.3
	Y	6.8 10.8	**8.8** 8.0 10.8 12.5 14.7	6.5 8.0 9.2	6.8 8.0
	Z	9.1 13.1 17.6 20.3	9.1 13.1 6.4	8.9	8.9 13.5
V-5	X	8.4 8.7 10.0 12.5 18.0	6.4 10.0 17.5	8.8	6.0
	Y	6.8 10.8 12.5 16.5 18.0	**8.9** 8.0 10.8 12.7 15.5 17.8	6.0 6.5 8.2 9.2	6.5 8.0
	Z	9.1 13.1 18.0 20.0	9.1 13.3	8.8	8.8 13.5
V-6	X	6.1 10.1 14.0 17.3 20.8	**8.3** 8.3 10.9 13.7 16.8 19.3 33.1 35.1	6.0 8.3 10.8	6.0
	Y	8.5 13.6 18.7 26.0	6.8 10.8 **14.0** 18.0	6.0	5.9 6.6
	Z	8.8 18.0 19.3	8.8	~~8.6~~	8.8 20.0
V-7	X	6.1 10.0 14.0	6.3 9.9 14.0 19.1	8.6 6.8 8.3 9.5 13.2 17.8	6.0 17.5
	Y	6.8 **11.1** 12.3 15.1 23.6	6.9 9.3 12.0 14.8 17.3 22.3	6.0 6.6 8.2 10.0 10.9	6.6 11.1 15.2
	Z	8.8 12.5 **14.9** 23.2	8.8 12.7 15.6	8.5 11.2 16.3 17.8 18.5 18.9	9.6 11.5 **16.0** 18.2

Note) Thick numbers mean the maximum power spectra

115
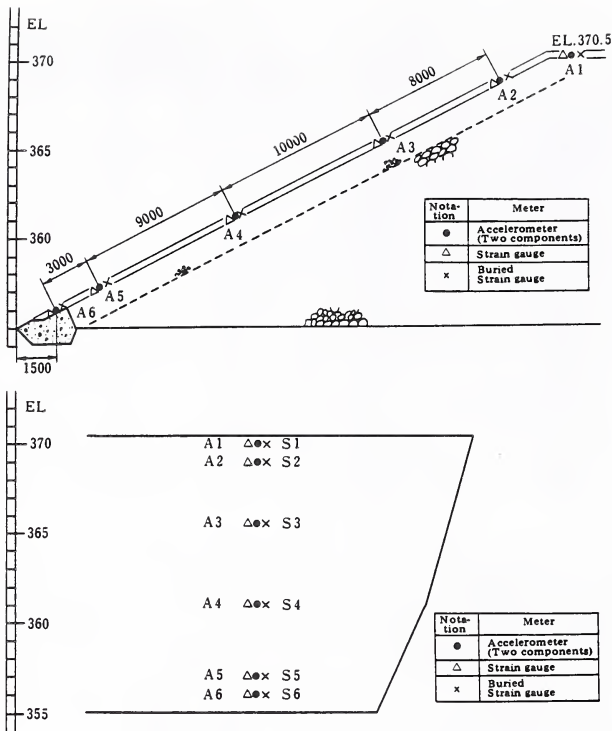
Figure-2   Positions of accelerometers and strain gauges

Table-4   The maximum acceleration (by accelerometers) and the maximum strain (by strain gauges) in each explosion

Accelero-meter	Direction	Empty		Full		Intermediate-1		Intermediate-2	
		Accelera-tion gal	Strain x10^{-6}	Accelera-tion gal	Strain x 10^{-6}	Accelera-tion gal	Strain x 10^{-6}	Accelera-tion gal	Strain x 10^{-6}
A-1	Up-down stream	39.3	1.448 [1]	56.5	1.272	16.6	0.680	25.4	0.712
(S-1)	Vertical	47.7	2.425 [2]	68.3	1.817	11.6	0.668	15.4	0.775
A-2	Up-down stream	31.5	2.207 [1]	34.4	2.094	12.9	0.655	20.8	1.048
(S-2)	Vertical	56.7	1.228 [2]	83.5	0.802	14.3	0.805	19.8	0.807
A-3	Up-down stream	37.0	2.708 [1]	50.8	2.078	11.4	0.850	17.6	1.368
(S-3)	Vertical	38.1	1.857 [2]	54.3	1.110	8.4	1.011	19.1	0.883
A-4	Up-down stream	39.9	0.841 [1]	36.0	0.863	8.1	0.760	17.1	0.732
(S-4)	Vertical	28.7	1.068 [2]	31.7	1.929	8.4	0.672	12.7	0.827
A-5	Up-down stream	30.6	0.963 [1]	24.9	0.791	4.3	0.668	7.6	0.770
(S-5)	Vertical	39.3	0.977 [2]	27.1	0.831	4.3	0.699	10.4	0.745
A-6	Up-down stream	16.2	0.907 [1]	24.9	0.848	4.0	0.707	6.7	0.757
(S-6)	Vertical	25.5	0.870 [2]	26.0	0.726	3.2	0.740	9.4	0.886

1) Strain on the surface   2) Strain of the inside

116

Up-down stream (V-6)

Dam axis (V-6)

Vertical (V-6)

Up-down stream (V-1)

Dam axis (V-1)

Vertical (V-1)
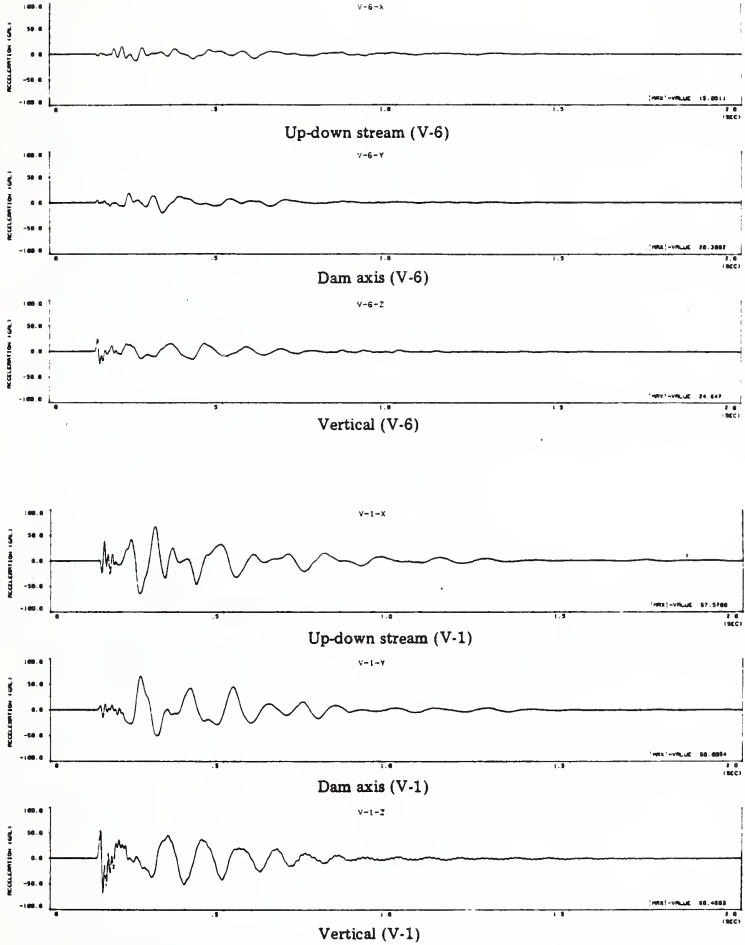
Figure-3(a) Time histories of accelerations at the foundation
(V-6) and dam crest (V-1) during the empty
reservoir

— 8 —
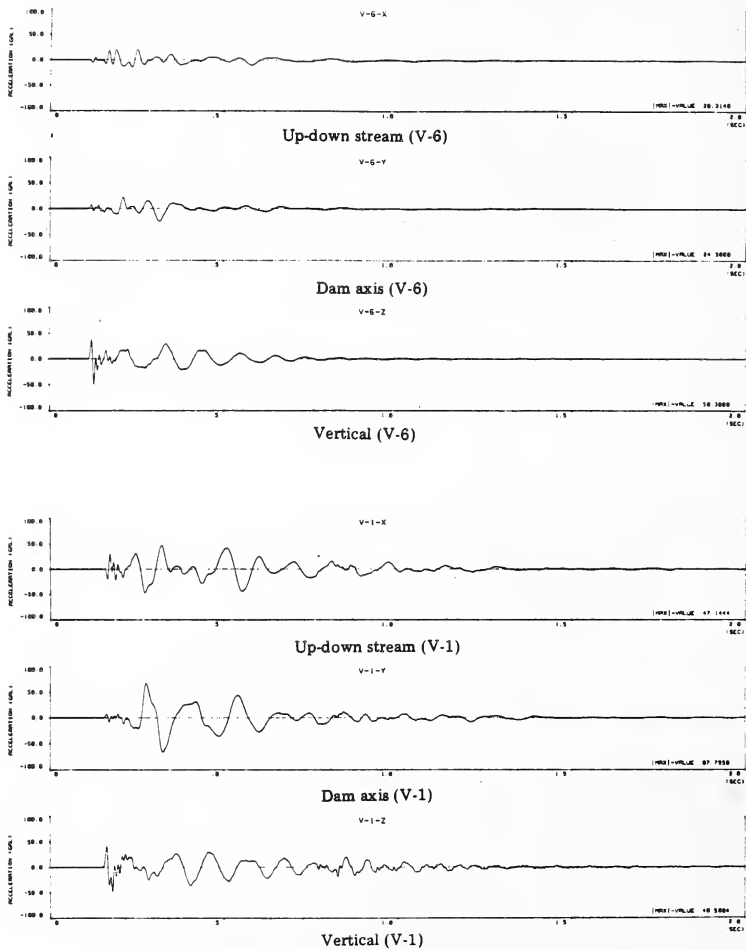
Figure-3(b) Time histories of accelerations at the foundation
(V-6) and dam crest (V-1) during the full reservoir
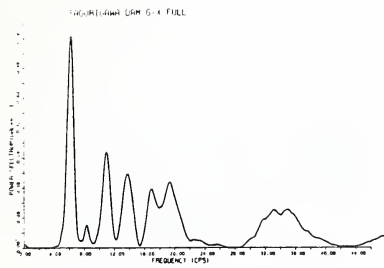
Up-down stream (V-6)
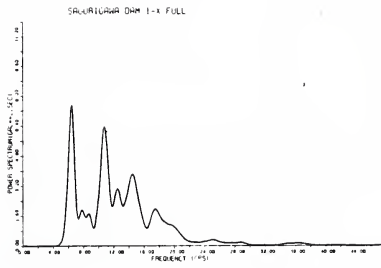
Up-down stream (V-1)
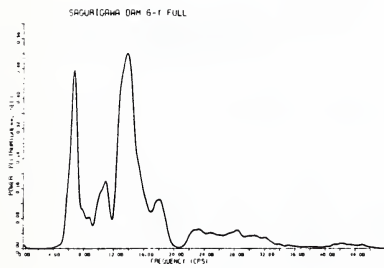
Dam axis (V-6)
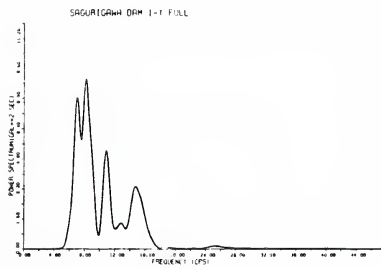
Dam axis (V-1)
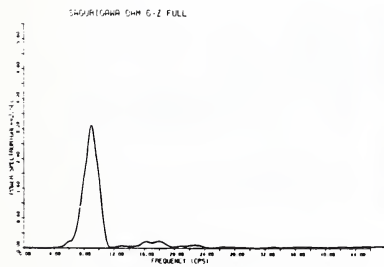
Vertical (V-6)
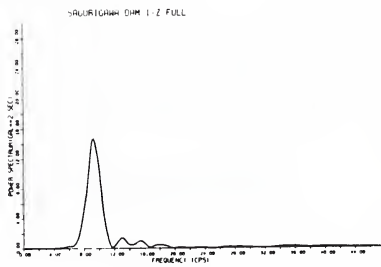
Vertical (V-1)

Figure-4   Power spectra of accelerations at the foundation
(V-6) and dam crest (V-1) during the full reservoir
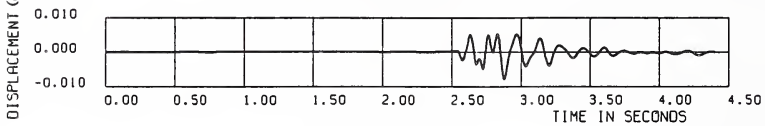
Figure-5(a) Time histories of displacements at V-2 and V-7
during the empty reservoir

Figure-5(b) Time histories of displacements at V-2 and V-7
during the full reservoir

SHGAKIGAWA DAM 2-X EMPTY

Empty reservoir (V-2)

SHGAKIGAWA DAM 2-X FULL

Full reservoir (V-2)

SHGAKIGAWA DAM 7-X EMPTY

Empty reservoir (V-7)

SHGAKIGAWA DAM 7-X FULL
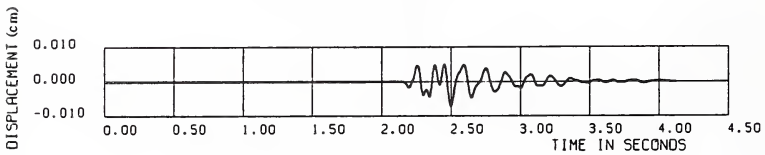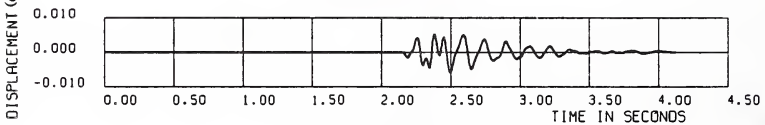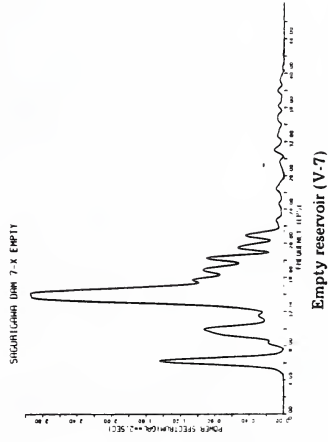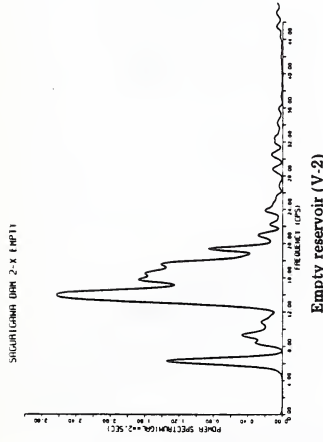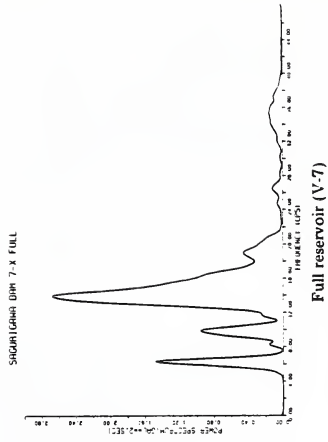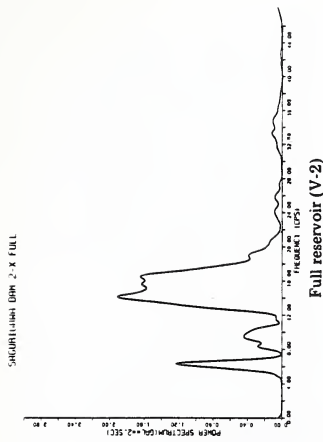
Full reservoir (V-7)

Figure-6   Power-spectra of vertical accelerations at V-2
and V-7 during the empty and full reservoir

121
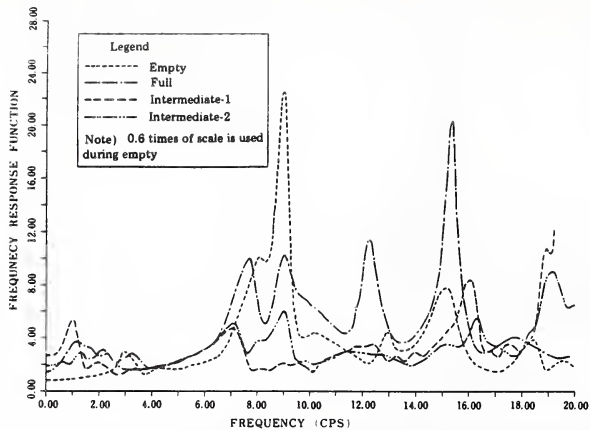
Figure-7 Frequency response function of up-down stream direction at the dam crest in each explosion
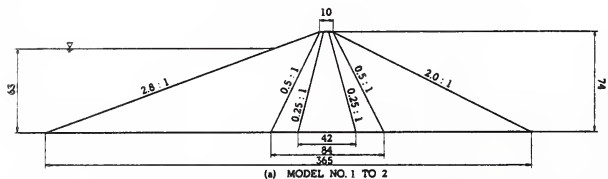
Figure-8(a) Section of two-dimensional filldam model
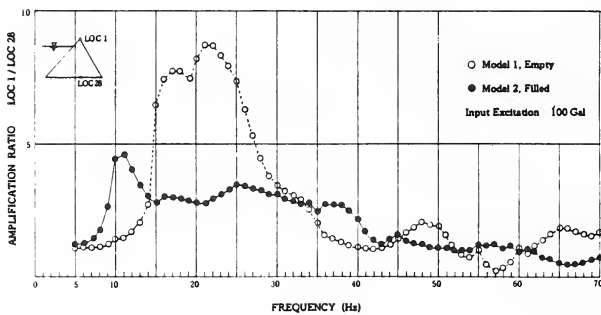
Figure-8(b) Comparison of the frequency response functions of two-dimensional dam model during the full and empty reservoir

122

Table-5 Computed cases

CASE	Water Level	Input Wave	Evaluation of Hydro-dynamic Force
1	Empty	Vertical and Horizontal	
2	Full	Vertical and Horizontal	Westergaard
3	Intermediate-1	Vertical and Horizontal	Westergaard
4	Intermediate-2	Vertical and Horizontal	Westergaard

Table-6 Inputed properties of materials

	Asphalt	Rock
Unit Weight (t/m^3)	2.36	2.1
Elastic Modulus (t/m^2)	5500	70730
Poisson's Ratio	0.40	0.36
Damping Ratio (%)	10	10
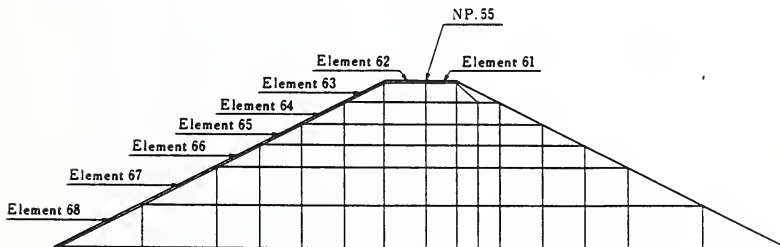
Figure-9 F.E.M. discritization for computation
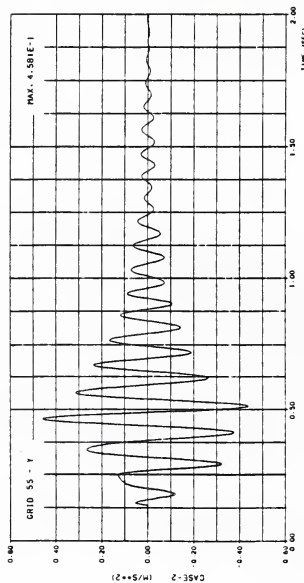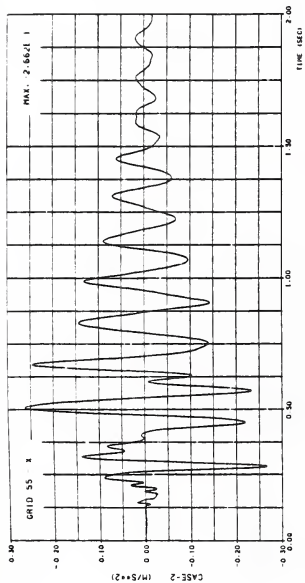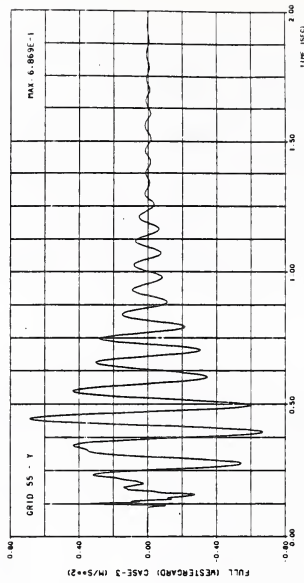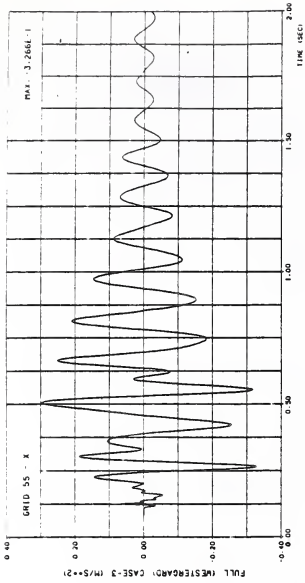
Acceleration at N.P.55 during empty (Case 1)

Acceleration at N.P.55 during full (Case 2)

Figure-10 Computed accelerations of the dam crest

124
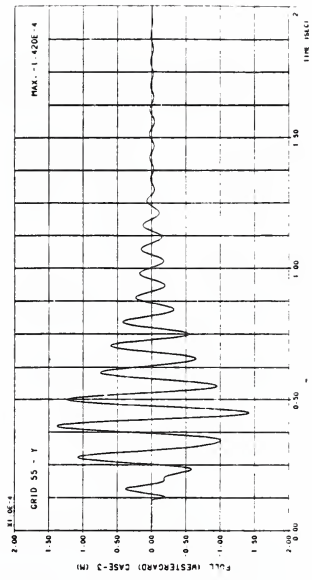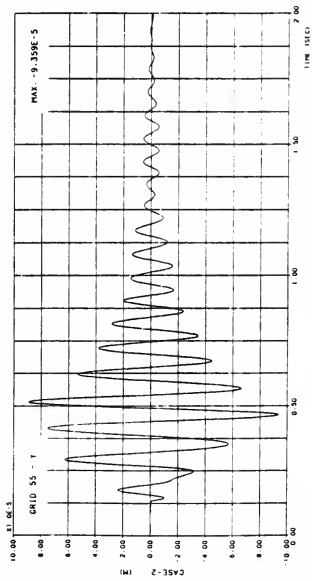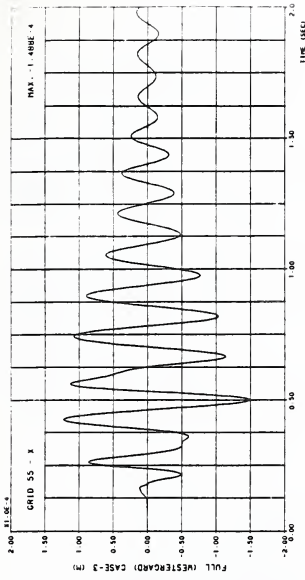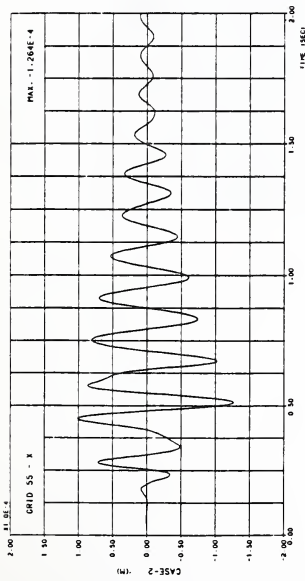
Displacement at N.P.55 during empty (Case 1)

Displacement at N.P. 55 during full (Case 2)

Figure-11 Computed displacements of the dam crest

125

Frequency response function at N.P.55 during empty (Case 1)

Frequency response function at N.P.55 during full (Case 2)
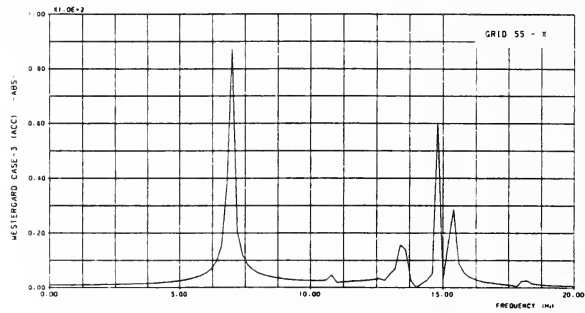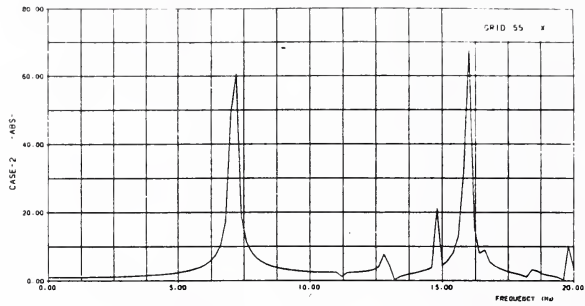
Figure-12 Frequency response function of the dam crest

Table-7 Observed and computed results

| Case	Natural Frequency (Hz)			Maximum Acceleration (cm/s^2)		Maximum Displacement (cm)	
	1st	2nd	3rd	Horizontal	Vertical	Horizontal	Vertical
Empty (CASE-1)	7.11 (8.0)	11.19 (9.0)	12.91 (13.0)	−26.6 (46.4)	45.8 (48.6)	−0.013 (0.016)	−0.009 (0.009)
Full (CASE-2)	6.94 (7.7)	10.84 (9.1)	12.81 (12.2)	−32.7 (67.7)	68.7 (68.5)	−0.015 (0.016)	−0.014 (0.015)
Intermediate-1 (CASE-3)	7.08 (7.1)	11.10 (9.0)	12.89 (12.4)	18.5 (16.4)	10.1 (8.0)	0.009 (0.008)	−0.002 (0.002)
Intermediate-2 (CASE-4)	7.10 (7.1)	11.16 (9.0)	12.90 (16.4)	32.5 (27.3)	−14.1 (14.2)	0.017 (0.016)	0.003 (0.003)

Note) (   ) is the observed value

Table-8 The computed maximum strains in an asphaltic facing

Case \ Element	Empty (CASE-1)	Full (CASE-2)	Intermediate-1 (CASE-3)	Intermediate-2 (CASE-4)
61	1.82^{E-6}	4.12^{E-6}	0.394^{E-6}	1.15^{E-6}
62	1.66	3.59	0.357	1.00
63	0.822	1.41	−0.312	−0.608
64	3.03	−6.70	−1.18	−1.96
65	−3.39	−13.3	−1.66	−3.11
66	−3.01	−26.8	−1.43	2.65
67	−2.73	−28.3	−3.94	−3.32
68	0.581	−31.8	−3.20	−3.62

SUMMARY OF THE RICHARD B. RUSSELL CONCRETE DAM VIBRATION STUDY

BY

Mr. Vincent P. Chiarito[1]
Mr. Robert J. Smith[2]

ABSTRACT

The forced-vibration tests of the 200-foot high
Richard B. Russel gravity dam were conducted
before and after reservoir impoundment. The
experimentally measured dynamic properties of
the dam without and with hydrodynamic
interaction were compared to results from three-
dimensional (3-D) finite element (FE) modal
analyses. Flexible and rigid foundation models
were used in the FE analyses, and the reservoir
was modelled as added mass to the dam. Mode
shapes from the prototype test and FE results
were compared using a modal assurance
criterion. The results reveal the dynamic
characteristics of the complex structure with
and without hydrodynamic interaction. The
natural frequencies and mode shapes are
consistent with the results of 2-D and 3-D FE
analyses. Modal damping ratios were greater
than independently measured concrete specimen
values but were scattered between 1.4 and 5.2
percent. Relative joint motion was observed
above a low response threshold. Ambient
vibrations recorded after impoundment of the
reservoir provided another measure of the dam's
dynamic characteristics.

KEYWORDS: Ambient Vibrations; Damping Ratios;
Finite Element Analysis; Forced-Vibration Test;
Frequencies; Mode Shapes

1. INTRODUCTION

Results of prototype vibration tests (2,3) of
the Richard B. Russell Dam, with and without
reservoir, were compared to linear elastic
three-dimensional (3-D) dynamic finite-element
(FE) analyses of the dam. This comparison
provides one basis for assessing the accuracy of
linear elastic FE models for predicting dynamic
properties of concrete gravity dams.

The Richard B. Russell Dam, recently built by
the Corps of Engineers, is approximately 170
miles (272 kilometers) from the mouth of the
Savannah River between Georgia and South
Carolina. A view of the completed dam is shown
in Figure 1. As shown in Figure 2, the crest of
the concrete gravity part of the dam is 1,884 ft
long (574 meters). It is composed of 13
nonoverflow, 8 intake, and 11 spillway
monoliths, the tallest of which is approximately
200 ft high (61 meters). The average reservoir
height was 174 ft (52 meters) during the second
test.

The grid for the 3-D FE analyses of the dam is
shown in Figure 3. A subspace iteration method

was used to solve for the undamped natural
frequencies and mode shapes in the FE analyses
(4). Four FE analyses were conducted: (a) fixed
base or foundation, without reservoir, (b) fixed
base, with reservoir, (c) flexible base, without
reservoir, and (d) flexible base, with
reservoir. The flexible base was modelled with
vertical and horizontal springs using an
appropriate spring constant. Concentrated
masses were added to model the mass due to the
reservoir and the tainter gates. A Modal
assurance criterion (1) was used to compare the
results of experimental and analytical
structural dynamics. Any attempts to completely
determine the dam-foundation-reservoir
interaction under dynamic conditions are beyond
the scope of this paper.

2. EXPERIMENTAL PROCEDURE

Richard B. Russel Dam was excited by a 17,000-lb
(7,711-kg) inertial mass driven by an
electrohydraulic servo-controlled actuator. The
shaker was welded to a 4-ft by 5-ft by 2-in.-
thick (1.22 by 1.52 by 0.0508 m) steel plate
which was epoxied to the mass concrete of the
dam. The force input to the dam was computed as
the product of the measured acceleration and the
17,000-lb mass. A typical force spectrum of the
shaker for the tests is shown in Figure 4. The
maximum stroke of the actuator is limited to 1
in. (0.0254 m). From 25 to 6 Hz (1z = 1 Hertz =
1 cycle/second), the force spectrum is flat (for
a peak force output of 20 kips (89 kN)). The
rolloff from 6 to 1 Hz is due to the stroke
limitation.

Servo-accelerometers with sensitivities ranging
from 0.25 to 5.0 volts/g were used to measure
the horizontal accelerations of the concrete
dam. The accelerometers have a frequency
response range from 0 to 500 Hz. Analog signals
were recorded on 32-track magnetic tapes. The
tape recorder has a frequency response range
from 0 to 2,500 Hz. A structural dynamics
analyzer was used to later digitize and process
the analog signals. All the recording
instrumentation was housed in a closed van
positioned on the crest of the monolith adjacent
to the drive point.

---

[1] U.S. Army Engineer Waterways Experiment
Station, Vicksburg, Mississippi 39180

[2] Office, Chief of Engineers, Washington, D.C.

3. PROTOTYPE TESTS

Two forced vibration tests were made on the Richard B. Russell Dam, before and after impoundment of the reservoir, to determine the natural frequencies, mode shapes, modal damping ratios, and relative joint movements. The first low-level forced vibration test was conducted during January and February 1982 and the second was conducted during June and July 1984. This provided an experimental measure of the prototype hydrodynamic interaction and a comparison of the changes of the dynamic properties.

The dam was excited at monoliths 7, 16, and 22 by a crest-mounted inertial mass (2,3). The force input was in an upstream-downstream direction. Three arrays of servo accelerometers measured the horizontal crest accelerations of 31 monoliths in the first test and all 32 monoliths in the second test. Measurements from drive point 16 overlapped measurements from drive points 7 and 22. In each test, accelerometers were placed at different elevations in the three drive point monoliths to measure the horizontal motions in the vertical planes.

The abutments on the sides of the dam restrained the end monoliths with some degree of fixity. However, the abutment on the Georgia side was not complete during the first test and was approximately 60 ft (18.3m) below the completed crest elevation. Therefore, a portion of monolith 1 was unrestrained above El. 430.00 on the Georgia side during the first test.

4. FINITE ELEMENT MODEL

4.1 Parameter Studies

The grid for the FE model was developed by conducting parameter studies of isolated nonoverflow, spillway, and intake monoliths (5). Modal analyses were used to obtain appropriate FE grid sizes for each of the monoliths. A compatible grid was found for all of the monoliths, thus making possible the generation of the nodal and element data with the computer. Favorable results were obtained when modal analyses of each monolith using uniform grids were compared to analyses using the grid for the entire 3-D FE model. Figures 5 through 7 show typical sections of the monoliths and the resulting 3-D grids of each monolith. In Figure 3, the resulting 3-D FE grid of the dam is shown.

Figure 6b shows the penstock tube opening in the intake monolith modelled as solid, or "smeared-hole," elements with 29 percent less stiffness and density than the mass concrete. Modal analyses showed good agreement between a finer FE grid that included the penstock opening and the grid shown in Figure 6b using solid elements.

4.2 Material Properties

The concrete properties used in the FE analyses were taken from previous measurements on 6- by 12- in. (152- by 305-mm) concrete cylinders. Dynamic modulus of elasticity values used were 5.1×10^6 psi (35.2×10^6 kPa) for exterior mass concrete and 4.26×10^6 psi (29.4×10^6 kPa) for interior mass concrete. From previous foundation tests, the dynamic elastic modulus of the foundation used to compute the spring constant was 6.05×10^6 psi (41.7×10^6 kPa). Using elastic theory, the average horizontal and vertical spring constant was 4×10^{10} lb/ft (5.8×10^{11} N/m) in the flexible base model (6).

4.3 Element Types

Four element types were used to model the dam (4). Variable-number-nodes (8 to 21 nodes) 3-D thick shell elements were used to model the mass concrete of the nonoverflow, intake, and spillway monoliths. Plate elements were used to model the concrete spillway piers, the concrete training walls at spillway monoliths 16 and 26, and the concrete deck of the spillway bridge. Beam elements were used to model the steel girders of the spillway bridge. Boundary (spring) elements were used along the base of the model in the flexible base analysis.

4.4 Boundary Conditions

By definition, the X, Y, and Z translations were defined on the 3-D thick shell elements. All degrees of freedom were deleted along the base of the model for the fixed base analysis. For the flexible base analysis, the longitudinal (Y) translations and all rotations were fixed along the base of the model. Except at the dam abutment interface, horizontal and vertical springs were placed at all nodes on the base in the X and Z directions.

In order to model the restraint due to the abutments, nodes along the two end sections (monoliths 1 and 32) had all degrees of freedom deleted. However, a few of the nodes had defined translational degrees of freedom on the Georgia side for the model of the dam without reservoir. As was discussed previously, this abutment was not completed at the time of the first vibration test.

For the model without reservoir, a total of 5,127 and 5,609 degrees of freedom were used for the fixed base and flexible base FE models, respectively. For the model with reservoir, a total of 5,100 and 5,582 degrees of freedom were used for the fixed base and flexible base FE models, respectively.

4.5 Modelling Of Added Mass

Concentrated masses were added at appropriate

nodes to model the mass due to the reservoir and the tainter gates. A constant 49.6 ft (15.1m) width mass of reservoir was applied to the model with reservoir. Parameter studies indicated that this constant width added the same amount of mass as more refined methods. The mass of the reservoir acting on the tainter gates and the mass of the gate was applied at the trunnion locations on the spillway piers.

5. RESULTS

5.1 Dam Without Reservoir

The 3-D shapes shown in Figure 8 are the first 6 normal mode shapes computed from the FE model with fixed base. At 7.7 Hz the major response is associated with the sideway of the roadway and concrete spillway pier system. The other mode shapes show that the major responses of the dam are associated with bending of the dam perpendicular to the longitudinal axis of the dam. Mode No. 5 at 10.4 Hz is the shape computed by the FE analysis but not measured experimentally. This was suspected to be due to the possibility of the exciter locations existing at nodes of that mode shape during the vibration test (2).

Comparisons of the dam crest mode shapes are shown in Figures 9-12. Note that the mode numbers correspond to bending modes of the dam crest. The solid symbols represent the normalized mode shape vectors of the experimental results. The solid and dotted lines, respectively, represent the normalized mode shapes for the flexible and fixed foundation models. Table 1 summarizes the results of the comparisons in Figures 9-12. Based upon the results of the modal assurance criterion values, the correlation between analytical and experimental mode shapes was favorable. The model with a fixed base had slightly better mode shape correlation than the model with a flexible base. For a qualitative comparison the mode shapes all appear to have the largest amplitude in the same general location on the crest of the dam. The modal assurance criterion does indicate quantitatively how good the comparison is among modes.

The frequencies estimated by the FE models were higher than frequencies measured experimentally. This is reasonable since the FE models are an approximation of the dam using a discrete number of degrees of freedom. The FE model in this case is stiffer than the actual dam. The flexible base model estimated frequencies closer to the experimentally measured frequencies than did the fixed base model.

Comparisons of the analytical and experimental mode shapes in cross section were also conducted. Results were favorable, with several modal assurance criterion MAC values greater

than 0.70. The governing mode shape in cross section resembles the fundamental mode shape of a cantilever beam (8).

5.2 Dam With Reservoir

The 3-D shapes shown in Figure 13 are the first five major bending modes of the dam crest and one mode shape associated with sideway of the roadway and concrete spillway pier system with a fixed base. Note that the mode numbers correspond to the eigenvector number obtained from analysis. The mode shapes not shown below 8.2 Hz are also associated with sideway of the spillway pier system.

Comparisons of the dam crest mode shapes are shown in Figures 14-18. Note that the mode numbers correspond to bending modes of the dam crest. Table 2 summarizes the results of these comparisons. Mode shape correlation between experiment and analysis was not as favorable as with the dam without reservoir. Both the fixed and flexible base models had approximately the same modal assurance criterion (MAC) values.

Various factors may have caused this lower correlation. Anomalies existed in the experimental mode shapes at the lower frequencies (modes 1 and 2) because the force input was not large enough to completely excite the entire structure at these frequencies. At the higher frequencies, the experimental data is more reliable because the force input was large enough to excite normal modes. Another source of error in these experimental mode shapes could have been the scale factors applied to the measurements from drive points 7 and 22 with respect to the measurements from drive point 16 (3). A least squares method should have been used to obtain scale factors (1).

Inadequacies in the FE model assumptions could have produced a lower correlation between experimental and analytical mode shapes. The FE model did not include the effects of the added mass of the soil at the abutments. The abutment on the Georgia side of the dam was not complete at the time the first vibration test was made. The additional soil during the second test might have caused a slight increase in the stiffness of the structure at the Georgia-side abutment. Assumptions used for the added mass distribution of the reservoir may have been slightly inaccurate, and nonlinearities due to joint slippage were not modelled.

Similar to the case of the dam without reservoir, the frequencies estimated by the FE models were higher than measured experimentally. The flexible base model frequencies better compared to the experiment then did the fixed base model frequencies.

Comparisons of the analytical and experimental mode shapes in cross section were conducted at

two sections. Results were favorable, with several MAC values greater than 0.90. The governing mode shape in cross section resembles the fundamental mode shape of a cantilever beam. It should be noted that some dam crest experimental mode shapes had better correlation with FE results of a different mode of vibration. The fourth experimental mode shape at 7.3 Hz resembled a fourth normal mode of vibration of a fixed at both ends (7). However, this shape had a better correlation with mode No. 14 (MAC = 0.63) than with mode No.16 (MAC = 0.14) from Figure 13. Engineering judgement was used in interpreting the experimental mode at 7.3 Hz as a fourth mode of vibration. But it is possible that the experimental modes exhibited measured local behavior not determined by the model. Also, it is possible there were significant bias errors in the estimates of the mode shape vectors of the spillway and South Carolina nonoverflow monoliths. In this way, the MAC can aid in illustrating complex responses not computed by the model, but measured in the prototype test.

6. CONCLUSIONS

Three-dimensional linear FE analyses have been compared with previous experimental estimates of the modal parameters of a concrete gravity dam. Using available dynamic material properties of the dam concrete and the foundation, a 3-D FE model was successfully developed to estimate the linear elastic modal properties of the dam. A mode shape that was not measured experimentally was computed by the 3-D FE analyses for the dam without reservoir.

The modal assurance criterion was useful for evaluating the correlation between the experimental and the FE mode shapes. Favorable correlations were computed for the dam without reservoir, indicating that a reasonable 3-D FE model was developed for computing the first three natural modes of vibrations. MAC values ranged from 0.53 to 0.68 for the first three modes.

Less favorable correlations were computed for the dam with reservoir, due to possible errors in the experimental mode shapes or the FE model boundary conditons. MAC values ranged from 0.15 to 0.44 for the first three modes. Low force input at lower frequencies caused discontinuities in experimental mode shapes, and the scale factors applied to the modes may have been inaccurate. The effects of the soil at the Georgia-side abutment and the reservoir effects may not have been modelled adequately.

The 3-D FE analyses estimated frequencies higher than those measured experimentally. This is reasonable since the FE models are an approximation of the dam using a discrete number of degrees of freedom. The FE model with flexible foundation predicted natural frequencies closer to the experimentally measured values than did the FE model with rigid foundation.

7. ACKNOWLEDGEMENTS

8. REFERENCES

1. Allemang, R. J., and Brown, D. L., "A Correlation Coefficient for Modal Vector Analysis," Proceedings of the 1st International Modal Analysis Conference, 1982, pp 110-116.

2. Chiarito, Vincent P., and Mlakar, Paul F. "Vibration Test of Richard B. Russell Concrete Dam Before Reservoir Impoundment," TR-SL-83-2, May, 1983.

3. Chiarito, Vincent P., Recent results of the second vibration test of Richard B. Russell Concrete Dam after reservoir impoundment (Final report in preparation).

4. Bathe, K. J., Wilson E. L., and Peterson, F. E., "SAPIV: A Structural Analysis Program for Static and Dynamic Response of Linear Systems," University of California, Earthquake Engineering Research Center, Richmond, California, 1973.

5. Chiarito, Vincent P. "Linear Finite Element Comparison with Experimental Modal Analysis for a Concrete Gravity Dam," Proceedings of the Third International Modal Analysis Conference, Vol. 1, 1985, pp 59-65.

6. Timoshenko, S. P., and Goodier, J. N., Theory of Elasticity, 3rd ed., McGraw-Hill, New York, 1970.

7. Shock and Vibration Handbook, C. N. Harris, and C. E. Crede, eds, McGraw-Hill, New York, 1961.

8. R. Stephen Wright and Vincent P. Chiarito, "Comparison of Experimental and Analytical Structural Dynamics Using a Modal Assurance Criterion," from SAE SP-635-Structural Dynamic Testing and Analysis, SAE Technical Paper Series 851928, Presented at Aerospace Technology Conference and Exposition, Long Beach, California, Oct 14-17, 1985.

Table 1. Crest Mode Shape Comparisons – Dam without Reservoir

| Crest Mode Number | Prototype Vibration Test Frequency (Hz) | 3-D FE Analyses | | | |
		Fixed Base Frequency (Hz)	MAC*	Flexible Base Frequency (Hz)	MAC*
1	5.9	7.1	0.67	6.6	0.68
2	6.8	7.9	0.55	7.4	0.53
3	7.6	9.3	0.58	8.7	0.55
5	8.2	10.7	0.43	10.0	0.13

* Modal Assurance Criterion (1)

Table 2. Crest Mode Shape Comparisons –Dam with Reservoir

| Crest Mode Number | Prototype Vibration Test Frequency (Hz) | 3-D FE Analyses | | | |
		Fixed Base Frequency (Hz)	MAC*	Flexible Base Frequency (Hz)	MAC*
1	5.3	6.2	0.20	5.7	0.19
2	6.2	6.8	0.44	6.4	0.38
3	6.6	7.8	0.17	7.3	0.15
4	7.3	8.2	0.14	7.6	0.23
5	8.1	8.7	0.09	8.0	0.33

* Modal Assurance Criterion (1)
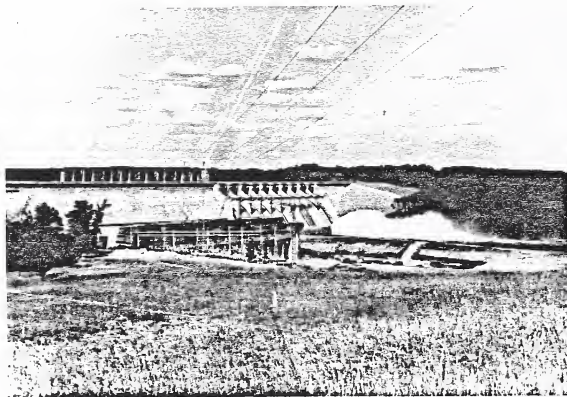
Figure 1. View of the Dam from the Downstream Georgia Side
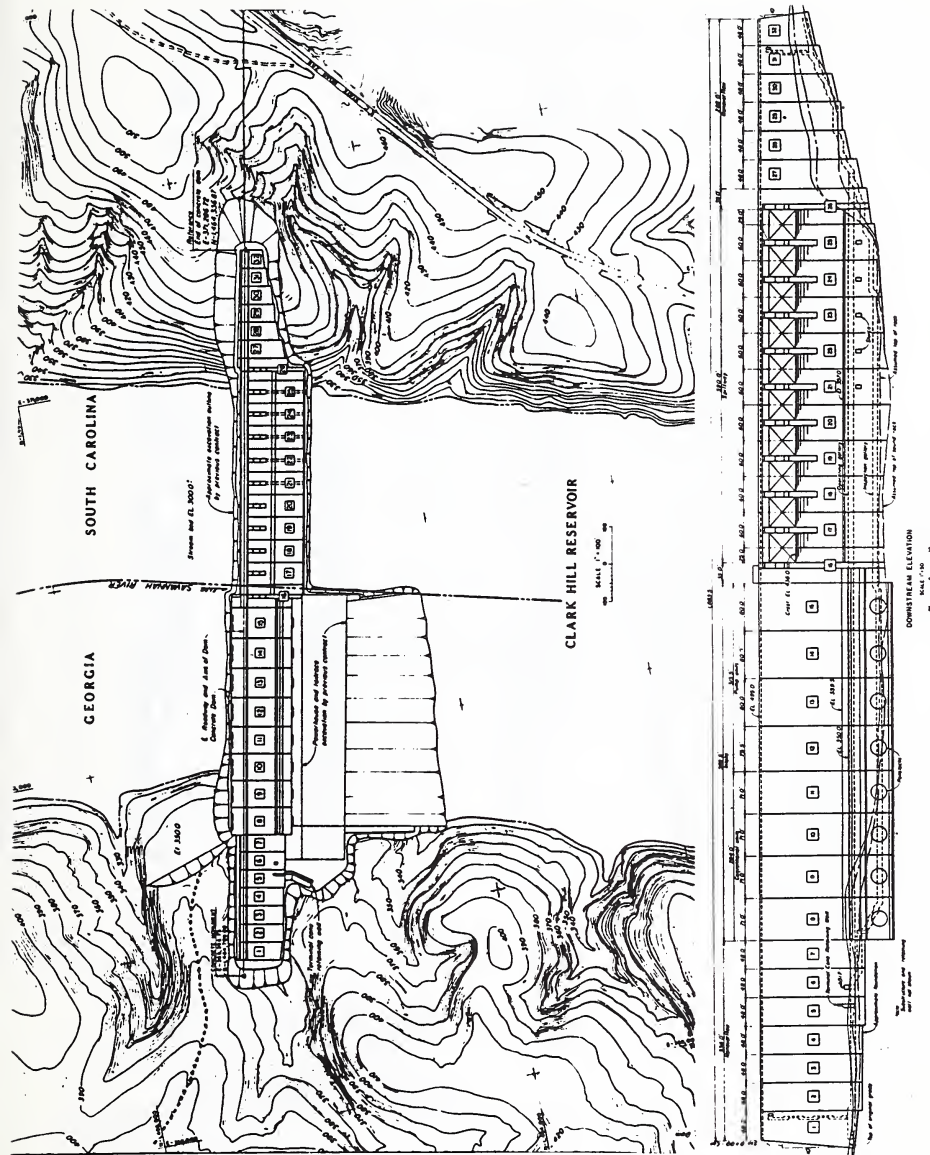
Figure 2. Plan and Elevation Views of Richard B. Russell Dam

MONOLITHS

NONOVERFLOW — INTAKE — SPILLWAY — NONOVERFLOW

← GA.

S.C. →

UNDEFORMED SHAPE FROM
DOWNSTREAM — SOUTH CAROLINA SIDE

← S.C.

GA. →

UNDEFORMED SHAPE FROM
UPSTREAM — SOUTH CAROLINA SIDE

Figure 3. Finite Element Grid of Entire Dam
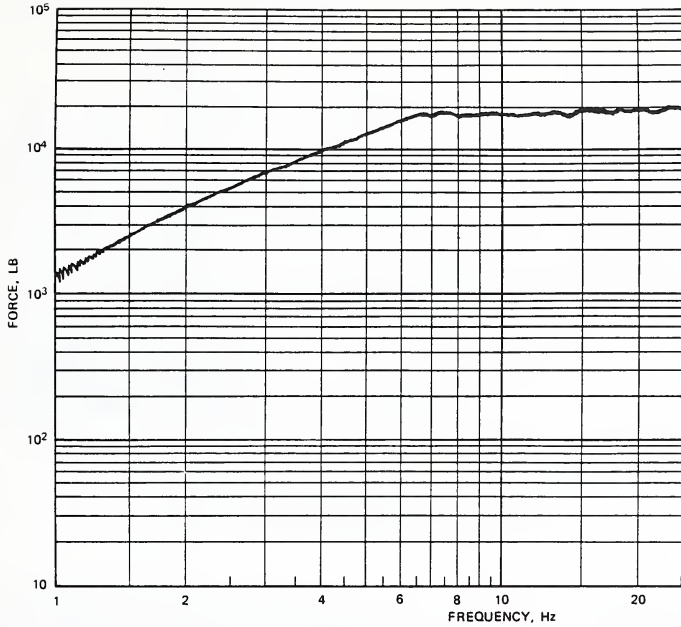
Figure 4. Typical force spectrum - force output of electrohydraulic vibrator versus frequency
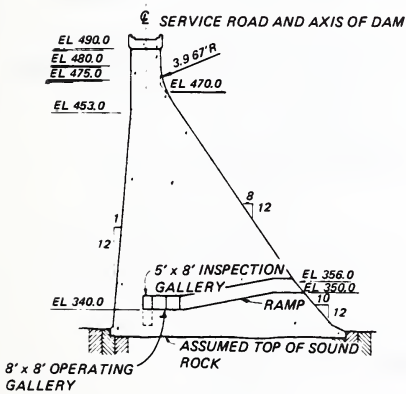
TYPICAL NONOVERFLOW

a. Cross-section
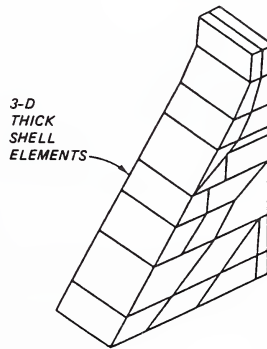
b. Finite-element model

Figure 5. Typical Nonoverflow Monolith

135

SERVICE ROAD AND AXIS OF DAM

EL 490.0
EL 480.0
EL 475.0
ROADWAY EL 495.0
39.67'R
EL 470.0

EL 437.24
EL 419.81
EL 410.70

8
12

EL 370.0
EL 359.0
EL 350.0
EL 340.0
EL 330.0

EL 350.0 ±

8 x 8 OPERATING GALLERY

EL 322.0 ±
EL 300.0
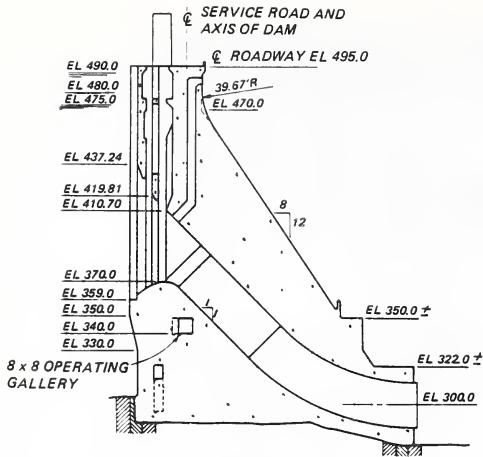
TYPICAL INTAKE

a. Cross-section

3-D THICK SHELL ELEMENTS

"SMEARED-HOLE" ELEMENTS

MODELLING EFFECTS OF PENSTOCK TUBE OPENING (SHADED AREA)
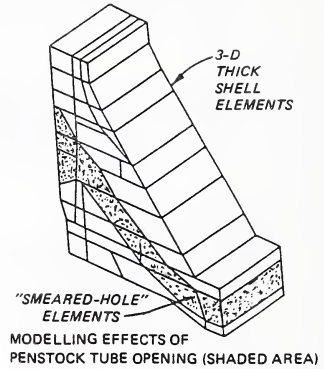
b. Finite–element model

Figure 6. Typical Intake Monolith

SERVICE ROAD AND AXIS OF DAM

EL 490.0
EL 480.0
EL 475.0
EL 495.0

TRUNNION LOCATION

10
12

EL 447.58

EL 436.0

EL 357.0

EL 340.0
EL 320.0

EL 327.0
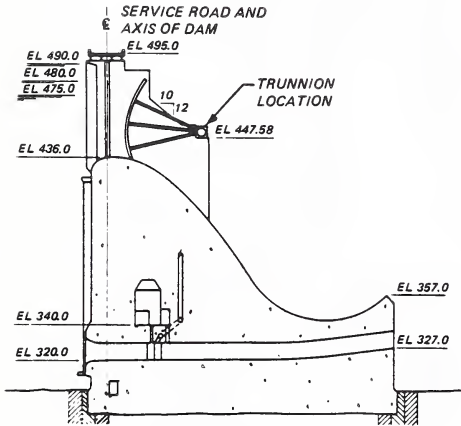
TYPICAL SPILLWAY

a. Cross-section

BEAM ELEMENTS

PLATE ELEMENTS

3-D THICK SHELL ELEMENTS
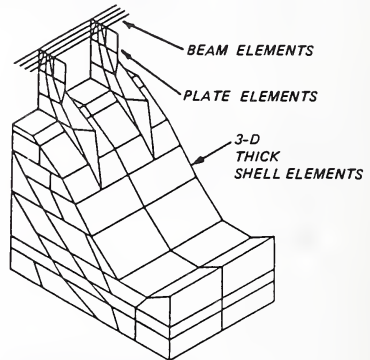
b. Finite–element model

Figure 7. Typical Spillway Monolith

136
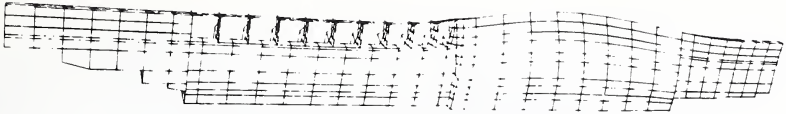
MODE NUMBER 1, 7.1 Hz

MODE NUMBER 2, 7.7 Hz

MODE NUMBER 3, 7.9 Hz

MODE NUMBER 4, 9.3 Hz
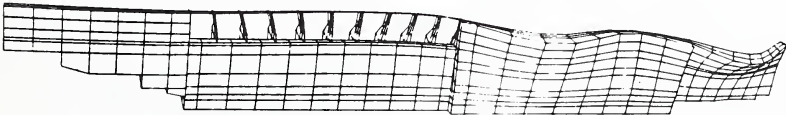
MODE NUMBER 5, 10.4 Hz
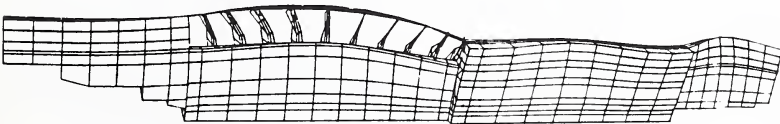
MODE NUMBER 6, 10.7 Hz

Figure 8. FE Model Mode Shapes - Dam Without Reservoir

137
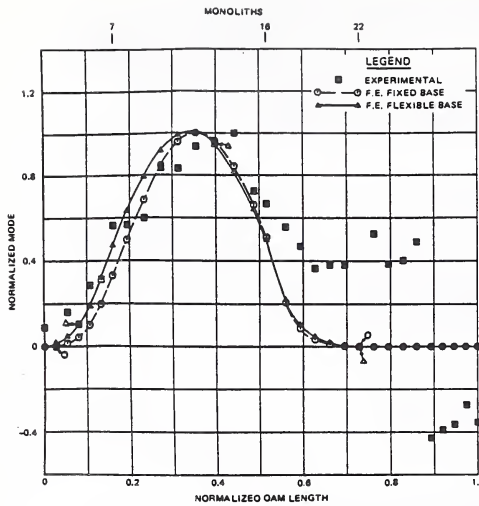
Figure 9. Mode 1 - Dam without Reservoir
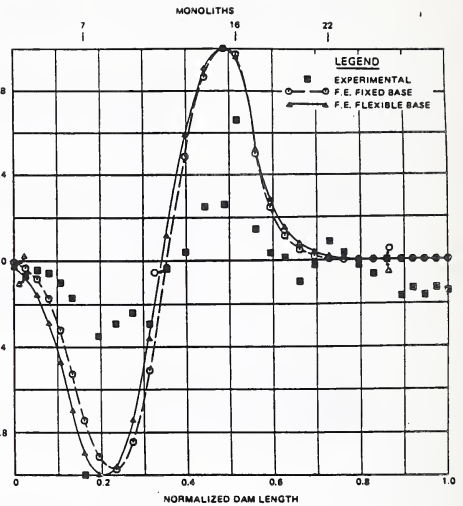
Figure 10. Mode 2 - Dam without Reservoir
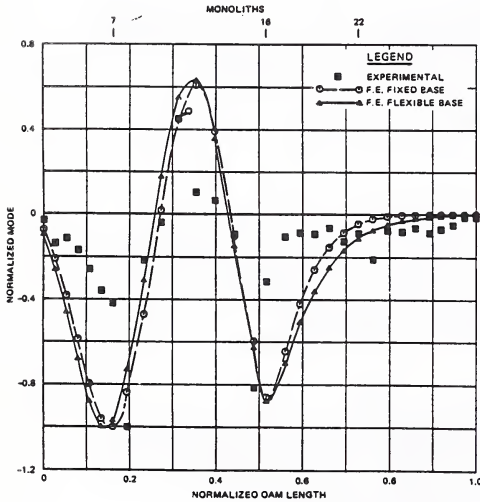
Figure 11. Mode 3 - Dam without Reservoir
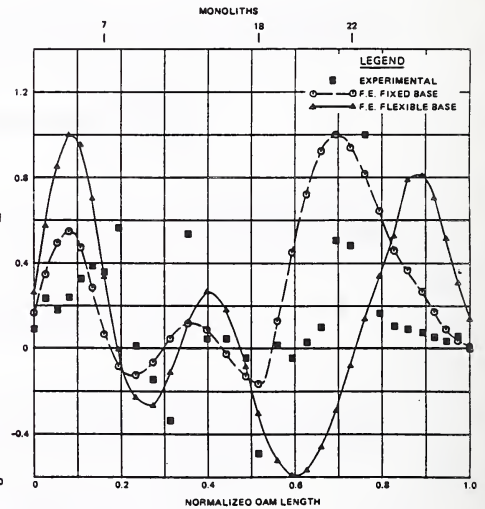
Figure 12. Mode 5 - Dam without Reservoir

138
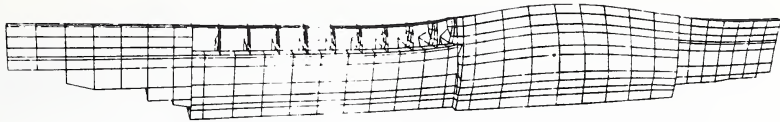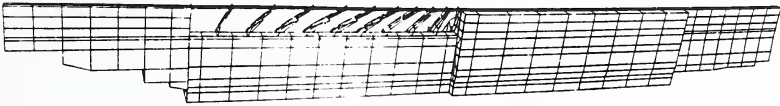
MODE NUMBER 1, 6.2 Hz

MODE NUMBER 2, 6.3 Hz
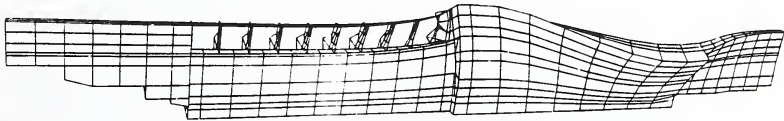
MODE NUMBER 11, 6.8 Hz

MODE NUMBER 14, 7.8 Hz

MODE NUMBER 16, 8.2 Hz

MODE NUMBER 17, 8.7 Hz

Figure 13. FE Model Mode Shapes - Dam with Reservoir

139
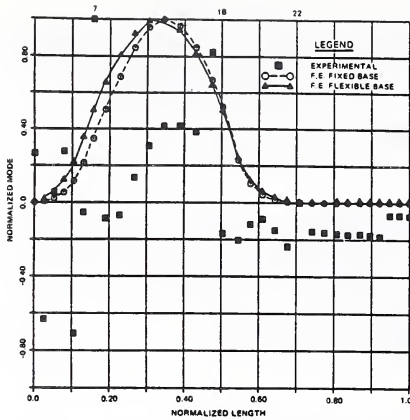
Figure 14. Mode 1 - Dam with Reservoir   Figure 15. Mode 2 - Dam with Reservoir
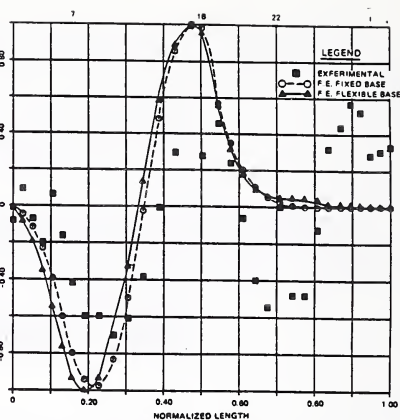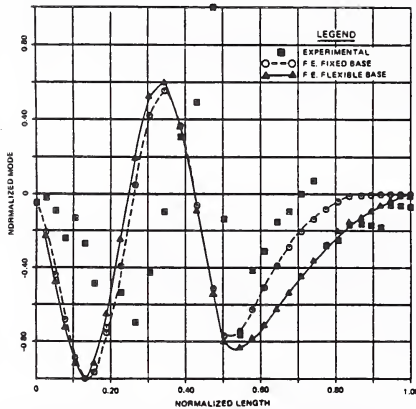
Figure 16. Mode 3 - Dam with Reservoir   Figure 17. Mode 4 - Dam with Reservoir
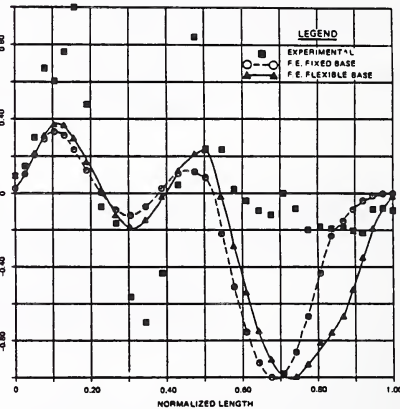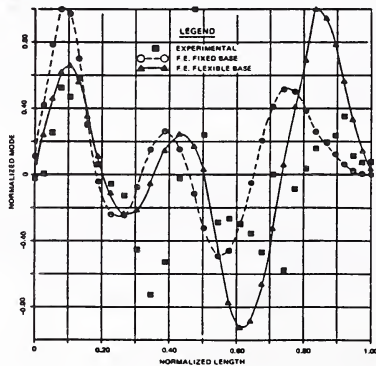
Figure 18. Mode 5 - Dam with Reservoir

SHAKING TABLE TESTS ON SEISMIC STABILITY OF REINFORCED EMBANKMENTS

BY

Yasuyuki Koga[1], Eiichi Taniguchi[2]
and Yoshihiro Ito[3]

ABSTRACT

Recently geotextile has been used for reinforcing embankments, but there remain some unknown points on the aseismicity of geotextile reinforced embankments. Shaking table tests were performed to clarify seismic effects on embankments reinforced by non-woven fabric. The tests consisted of two cases; reinforced embankments on liquefiable sand deposits and those on inclined ground. Test results showed that the settlement of a reinforced embankment due to cyclic loadings was smaller than that of a non-reinforced one. Moreover the reinforced embankment settled as a unified soil block during excitation and therefore it kept its original shape after it settled and very few cracks were observed on the surface of the embankment.

KEYWORDS: Earthquakes; Embankments; Geotextiles

1. INTRODUCTION

Recently geotextile has been used for reinforcing embankments, but there remain some unknown points on the aseismicity of geotextile embankments reinforced . Shaking table tests were performed to clarify seismic effects on embankments reinforced by non-woven fabric. The tests consisted of two cases; reinforced embankments on liquefiable sand deposits and those on inclined ground. Measurements carried out during the tests included acceleration, pore water pressure, displacement of the ground and embankment, and tension of the non-woven fabric. Test data were compared in reinforced and non reinforced cases.

2. PURPOSE

The purposes of shaking table tests described in this paper are:

(1) to determine if the reinforcement by non-woven fabric to embankments is effective against earthquakes,

(2) to understand the vibratory behavior and final failure pattern of embankments reinforced by a non-woven fabric during cyclic loadings.

3. PROCEDURE

3.1 Outline of Models

Fig. 1 shows the cross sections of four models used in the shaking table tests. Among these four models Models L-1 and L-2 have embankments on a liquefiable saturated sand deposit, and Models S-1 and S-2 have embankments on an inclined stiff ground.

The embankments and ground in Models L-1 and L-2 are constructed by using Sengenyama sand. Table 1 shows the physical properties of Sengenyama sand. Models L-1 and L-2 were prepared as follows: air dried Sengenyama sand was spread in a steel box at the thickness of 20 – 30 cm for ground and 10 cm for embankment, and compacted by men's feet, and then water was infiltrated from the bottom of the ground to saturate it. The ground of Model L-1 is in a loose condition with relative density of 53 – 62 percent, and the ground just beneath the embankment of Model L-2 is compacted to a dense condition with relative density of about 80 percent. The left side embankment is reinforced by placing non-woven fabric at 10 cm intervals; the right side is not reinforced. Table 2 shows the physical properties of the non-woven fabric.

The ground of Models S-1 and S-2 was prepared by fully compacting sandy silt (Table 1) by a wooden block to eliminate destruction by excitation. The embankment was made by 10 cm of Sengenyama sand that was compacted by men's feet. Its relative density is 43 – 65 percent. Both Models S-1 and S-2 have a reinforced embankment on the left side and a non-reinforced one on the right side. Although the boundary surface between the embankment and the ground is smooth in Model S-1, the boundary of Model S-2 is of bench shape. The non-woven fabric is fixed by 15 cm long nails at 5 cm intervals.

3.2 Scaling Law

The following scaling law was adopted in this series of tests; the reinforcement ratio R (non dimensional)(1) is defined by the following equation. It is the same for the prototype and the model.

$$R = \frac{(-\bar{\epsilon}_{3R}) \ E \cdot t}{\sigma_{30}\Delta H}$$

---

[1] Head

[2] Senior Research Engineer

[3] Research Engineer, Soil Dynamics Division, Public Works Research Institute, Ministry of Construction, Tsukuba Science City, Ibaraki 305 Japan

where $\bar{\epsilon}_{3R}$: average tensile strain of reinforced soil in horizontal direction ($\bar{\epsilon}_{3R} < 0$)

E : Young's modulus of reinforcing material

t : thickness of reinforcing material

σ_{30}: horizontal confining pressure acting on reinforced soil

ΔH: placement interval of reinforcing material

We assume that the reduced scale of the model is $\frac{1}{7}$ and $\bar{\epsilon}_{3R}$ of the model agrees with that of the prototype. Thus, the following equations can be drawn.

$$(\sigma_{30})_m = \frac{1}{7}(\sigma_{30})_p , \quad (\Delta H)_m = \frac{1}{7}(\Delta H)_p$$

$$\frac{(R)_m}{(R)_p} = \frac{\left(\dfrac{E \cdot t}{\sigma_{30} \cdot \Delta H}\right)_m}{\left(\dfrac{E \cdot t}{\sigma_{30} \cdot \Delta H}\right)_p} = 49 \frac{(E \cdot t)_m}{(E \cdot t)_p} = 1$$

$$\frac{(E \cdot t)_m}{(E \cdot t)_p} = \frac{1}{49} \tag{2}$$

The Young's modulus and the thickness of the non-woven fabric used in the prototype produced values as in Table 3; therefore Eq. (2) holds for non-woven fabric used in the tests.

3.3 Shaking Condition

Table 4 shows the shaking condition. The direction of shaking is only horizontal and longitudinal to the model. Tests No. L-1-1 - No. L-1-3 were performed by using one model. Test No. L-1-1 was performed and after pore water pressure in the model was dissipated, test No. L-1-2 was conducted, and then test No. L-1-3 was performed. Other tests were carried out in a similar way.

3.4 Measurement

In models L-1 and L-2, acceleration, pore water pressure, settlement of the ground surface, and tension of the non-woven fabric were measured at 16, 35, 3 and 3 points, respectively. In models S-1 and S-2, acceleration, settlement of the ground surface, tension of the non-woven fabric, and displacement of the non-woven fabric were measured at 16, 3, 3, and 3 points respectively. Small targets were placed on the surfaces of all models and the vertical and horizontal displacements were measured before and after each shaking test. The deformation of the model was observed through an acryl side panel; photographs were taken during excitation.

4. RESULTS AND DISCUSSIONS

4.1 Reinforced Embankment on Liquefiable Sand Deposits

Test results of Models L-1 and L-2 are described in this section. Fig. 2 shows the relationship between the acceleration on a shaking table and the cumulative settlement of the embankment. The settlement of an embankment reinforced by non-woven fabric is smaller than that of the non-reinforced one as illustrated by Models L-1 and L-2. In the test case for a shaking table acceleration of 173 gal, the settlement of reinforced embankment of Model L-1 is about half of that of non reinforced one. The settlement of reinforced embankment on the improved ground of Model L-2 is about one fifth of that of non-reinforced embankment on non-improved ground shown in Model L-1. These test results indicate that reinforcement by non-woven fabric is effective in reducing the settlement of embankments caused by liquefaction of the subsoil.

Fig. 3 shows the deformation of the side mesh of models in cases of Tests No. L-1-3 and No. L-2-4. The figure denotes that the deformation of the ground in Test No. L-1-3 occurs in the area above the line 30 cm high from the bottom. Ground deformation from Test No. L-2-4 occurs in the area above the line 70 cm high from the bottom resulting from ground improvement under the embankment.

Table 5 shows average horizontal strain ϵ_h at positions of A - J shown in Fig. 3. It was calculated from the displacements of intersections of the mesh before and after excitation. Table 5 indicates that the average horizontal strain in the reinforced embankment and the shallower part of its subsoil in Test No. L-1-3 is reduced to 26 - 42 percent of that in the non-reinforced one. In Test No. L-2-4 the average horizontal strain is decreased to 14 - 61 percent. It is shown that non-woven fabric, horizontally spread in the embankment, is able to reduce the horizontal tensile strain caused by cyclic loadings in the embankment and subsoil; this results in the reduction of the settlement of the embankment.

Photographs 1 and 2 show the view of the top of reinforced and non-reinforced embankment, respectively, after shaking in Test No. L-2-4. The non-reinforced embankment is considerably cracked and completely destroyed. On the other hand the embankment reinforced by non-woven fabric has few cracks and keeps its original shape; the effect of fabric reinforcement is clearly observed. It is shown from the test that an embankment reinforced by non-woven fabric settles if the subsoil is liquefied, but keeps its original shape because the embankment is unified by the non-woven fabric.

Figs. 4 and 5 show the change of acceleration, pore water pressure, settlement of embankment and tension of non-woven fabric with time in Tests No. L-1-3 and No. L-2-3. Fig. 6 shows the position of sensors and the ratio of pore water pressure to effective overburden pressure 10 seconds after the beginning of excitation. In Fig. 4 the accelerations at A13 and A14 have almost the same value before the ground begins to liquefy, 2 seconds after the beginning of excitation, and therefore there are almost no effects of reinforcement on the acceleration in the embankment. As the pore water pressure at P7 and P13 starts to increase 2 seconds after the beginning of excitation, the settlement of embankment D1 and D3 appears. The value of pore water pressure at P7 is about half of that at P13. A reason for it is that shear strain is not likely to increase in the ground just under the embankment because of confining effects by non-woven fabric. In Fig. 4 the tension T1 at the boundary between embankment and ground is four times larger than the tension T2 and T3 at the upper part of embankment. This result implies that if an embankment on liquefiable ground is reinforced by geotextile, it is necessary to decrease the placement interval of geotextile or place stronger geotextile in the lower part of the embankment. The value of tension T1 increases with time, but the value of tension T2 starts to decrease when the embankment begins to settle 2 seconds after the start of excitation; it then begins to increase again.

Fig. 5 shows that the pore water pressure P7 in the ground just under the reinforced embankment starts to increase 9 seconds after the beginning of excitation and reaches the peak value at 15 seconds, but that the pore water pressure P13 just under the non-reinforced embankment starts to increase 4 seconds after the beginning of excitation and reaches the peak value at 9 seconds. As the pore water pressures P7 and P13 increase, the reduction of acceleration A13 and A14 and the settlement of embankment D1 and D3 appears. The settlement D3 at the end of excitation, 8.8 cm, is twice as large as that of D1, 4.2 cm. Thus, the generation of pore water pressure just under the reinforced embankment is restrained and the required time to reach initial liquefaction becomes longer. This phenomenon is presumably due to the deformation of shallower ground being restrained by the fabric reinforcement. However such a phenomenon is not clearly observed in Model L-1, and so further investigation is needed. The tensions T2 and T3 increase with time until 15 seconds after the beginning of excitation when the embankment settlement suddenly increases and then the value T2 increases and T3 decreases.

Fig. 6 shows that the ratio of pore water pressure to effective overburden pressure u/σ_v' in the ground under the reinforced embankment is smaller than that under the non-reinforced one in Tests No. L-1-3 and No. L-2-3. In Test

No. L-2-3 the value of u/σ_v' in the improved area is smaller than in the non-improved area.

Figs. 7 and 8 show the change of the amplification ratio of acceleration with time. It can be noted from Figs. 7 and 8 that the amplification ratio of the reinforced embankment takes almost the same value as the non-reinforced one until the ground is liquefied. In Fig. 7 the acceleration amplification ratio of the reinforced embankment is larger than that of the non-reinforced one at 10 seconds after the beginning of excitation. This may caused by the effect of the inclination of the accelerometer in the liquefied ground. In Fig. 8, the delay of time when the initial liquefaction occurs in the ground under the embankment relates to the delay of time when the acceleration begins to decrease.

4.2 Reinforced Embankment on Inclined Ground

This section describes the test results of Models S-1 and S-2. Fig. 9 shows the deformation of the embankment after excitation with acceleration of about 850 gal. The result of Test No. S-1-6 indicates that almost the same value of settlement is induced by cyclic loadings to both reinforced and non-reinforced embankments. Actually the top of the slope of non-reinforced embankment is heavily destroyed, but the reinforced embankment is unified by the non-woven fabric as it settles as a single block of soil. Same failure pattern is seen in Test No. S-2-7. A considerably smaller number of cracks were observed on top of the reinforced embankment than on the top of non-reinforced one. It is observed from the comparison of the failure pattern of non-reinforced embankment in Test No. S-1-6 and No. S-2-7 that a large failure occurred in both cases at the top of the slope. However in Test No. S-1-6 a slip surface exists between the embankment and the inclined ground. A large slip occurs there, but in Test No. S-2-7 such a large slip is not observed because benching occurred between the embankment and the inclined ground. This difference appears more clearly for embankment reinforced by non-woven fabric; although in Test No. S-1-6 a clear slip surface is seen between the embankment and inclined ground. No clear slip surface is observed in Test No. S-2-7. The embankment holds its original shape because non-woven fabric is nailed on benches. A small slip is observed between the soil and the non-woven fabric. A smaller slip is observed in Model S-2 over S-1 where non-woven fabric is fixed on benches. Moreover if non-woven fabric is rolled into the embankment in the front of the slope, the slip will be reduced.

Fig. 10 shows the relationship between the acceleration on shaking table and the settlement of the embankment. The settlement was calculated by averaging the settlement of targets on the top of the embankment. Any type of embankment in Fig. 10 greatly settles when the acceleration reaches about 850 gal. A comparison

of the settlement of embankment in the case of acceleration of about 850 gal indicates that both the reinforced and non reinforced embankment have almost the same average settlement in Model S-1, but that the average settlement of the reinforced embankment in Model S-2 is considerably smaller than that of the non-reinforced one.

Fig. 11 shows the displacement of non-woven fabric during cyclic loadings in Test No. S-1-5. This figure shows that the non-woven fabric in the upper part of embankment first starts to move and every non-woven fabric does not start to move at the same time.

Fig. 12 shows the relationship between the acceleration on the shaking table and the maximum tension of non-woven fabric. It indicates that the tension increases with the increase of acceleration. The lower the position of non-woven fabric in the embankment, the larger tension occurs in Model S-1 in the case with acceleration of about 850 gal in which large deformation appears. In Model S-2 the maximum tension occurs at the position of No. 1 of the non-woven fabric which is located in the lowest part of embankment, and the second largest tension occurs at the position No. 5 of the non-woven fabric which is located in the highest part of the embankment. This is due to the effect of fixing the end of non-woven fabric on benches.

5. CONCLUSIONS

A. Reinforced embankments on liquefiable sand deposit:

(1) Embankments reinforced by non-woven fabric settle to some extent when the subsoil is liquefied. However the settlement of the reinforced embankment was about half that of a non-reinforced one. The settlement of reinforced embankment on the improved ground was about one fifth of a non-reinforced embankment on non-improved ground. It is found that the embankment reinforced by non-woven fabric is unified and deforms as a single soil block and the embankment is hardly cracked by cyclic loadings.

(2) Non-woven fabric is able to restrain the horizontal tensile strain in embankment and ground.

(3) The pore water pressure in the ground under the reinforced embankment is smaller than that in the ground under the non-reinforced one.

(4) The tension acting on the non-woven fabric in the lower part of embankment is about four times as large as that in the upper part of the embankment.

B. Reinforced embankment on inclined ground:

(1) An embankment on inclined ground is unified by reinforcing by non-woven fabric and the reinforcement can prevent the failure at the top of slope.

(2) The settlement of the embankment due to cyclic loadings can be considerably reduced by benching the inclined ground and fixing non-woven fabric on the benches.

(3) The maximum tension occurs at non-woven fabric in the lower part of the embankment.

6. ACKNOWLEDGEMENT

7. REFERENCES

(1) Tatsuoka, F. et al.: Reinforcement of clayey embankment by non-woven fabric, Tsuchi-To-Kiso, Vol. 33, No. 5, 1985 (in Japanese).

Table 1　Physical properties of material

soil name	Sengenyama sand	sandy silt
Japanese unified soil classification	SPu	ML
specific gravity　Gs	2.71	2.70
average grain size　D_{50} (mm)	0.28	0.057
uniformity coefficient　Uc	2.91	39.6
fine content rate　($< 74\,\mu$m)　(%)	2.4	53.0

Table 2　Properties of non-woven fabric

material	nylon　　70 %　polyester　30 %
thickness　(mm)	0.217
tensile strength at peak　σ_f (kgf/cm^2)	13.2 – 13.6
strain at peak　ϵ_f (%)	38 – 29
Young's modulus at　$\epsilon = 15$ %　E_{15} (kgf/cm^2)	47.3 – 57.3

Table 3　Data for non-woven fabric of model and prototype

model		prototype		$\dfrac{(E \cdot t)_m}{(E \cdot t)_p}$
Young's modulus E (kgf/cm^2)	thickness t (mm)	Young's modulus E (kgf/cm^2)	thickness t (mm)	
56.3	0.217	200	3.08	$\dfrac{1}{50.4}$
		150	4.49	$\dfrac{1}{55.1}$

Table 4　Shaking condition

test No.	model No.	acceleration on the shaking table (gal)	frequency (Hz)	duration time (sec)
L−1−1	L−1	25		
L−1−2		113		
L−1−3		173		
L−2−1	L−2	25	2	20
L−2−2		117		
L−2−3		173		
L−2−4		240		
S−1−1	S−1	26		
S−1−2		123		
S−1−3		248		
S−1−4		395		
S−1−5		580		
S−1−6		850		
S−2−1	S−2	25	4	10
S−2−2		122		
S−2−3		245		
S−2−4		400		
S−2−5		590		
S−2−6		700		
S−2−7		840		

Table 5　Average horizontal strain ϵ_h

test No.	average horizontal strain ϵ_h (%)			
	reinforced		non reinforced	
L−1−3	A	−2.4	F	−4.0
	B	1.6	G	3.8
	C	3.2	H	12.3
	D	11.4	I	8.2
	E	0.9	J	0
L−2−4	A	4.0	F	28.0
	B	18.9	G	33.0
	C	13.2	H	21.8
	D	0	I	0
	E	0	J	0

note :　ϵ_h

positive : tension
negative : compression

146
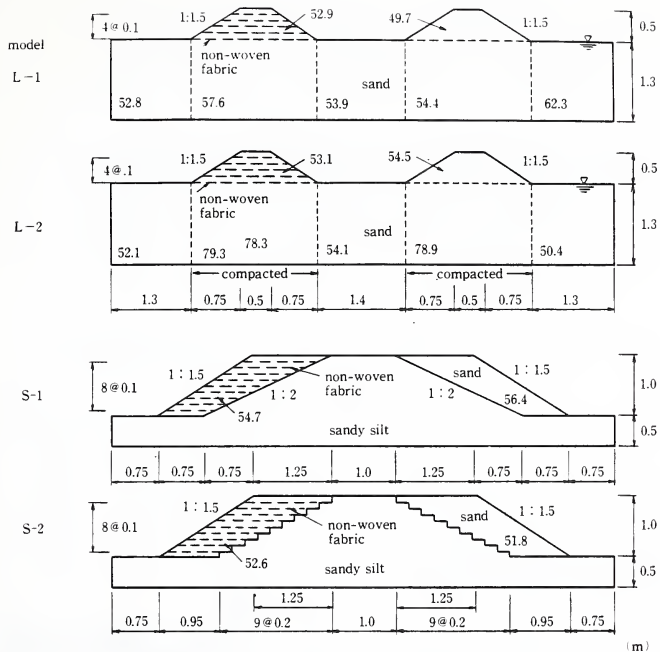
Figures in the models show relative density in per cent.

Fig. 1　Models used in tests
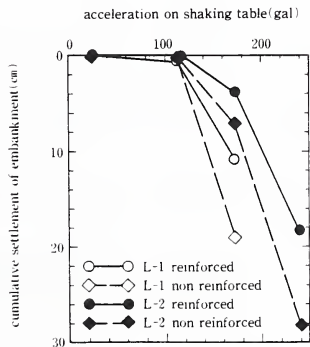
Fig. 2　Cumulative settlement of embankment and acceleration on shaking table

147

(A ~ J show the place where average horizontal strain ϵ_h was calculated.)
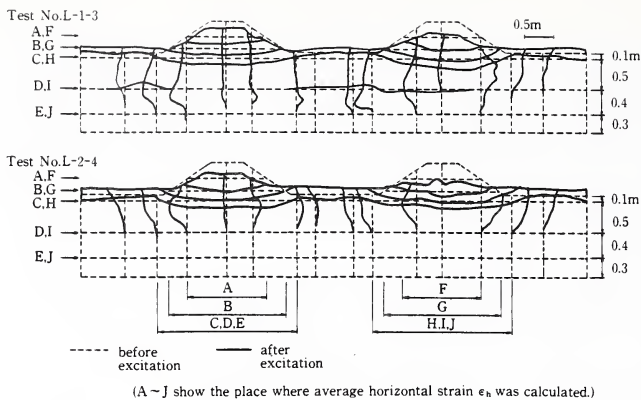
Fig. 3 Failure pattern of models
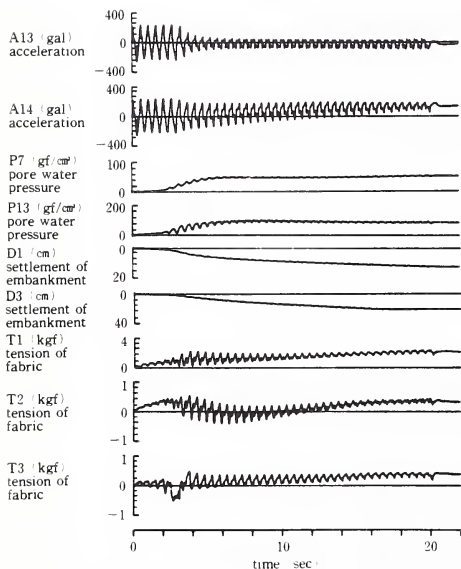
Fig. 4 Records of measurements (Test No. L-1-3)
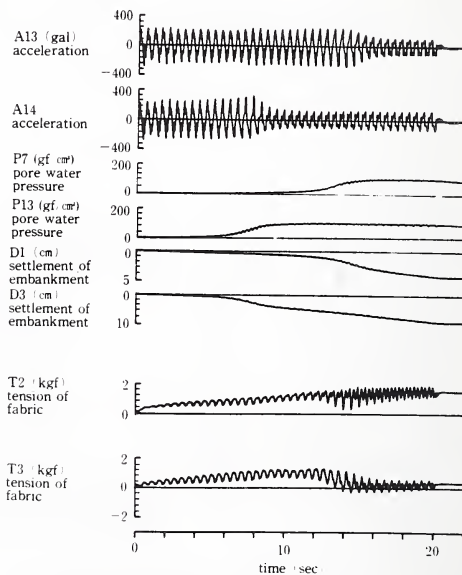
Fig. 5 Records of measurements (Test No. L-2-3)
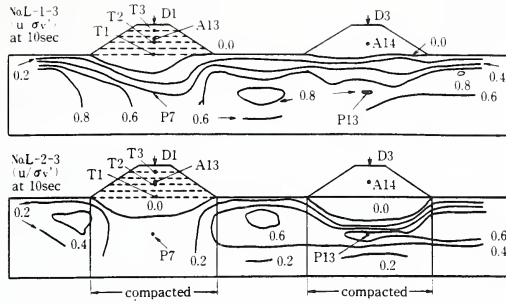
Fig. 6   Distribution of rate of pore water pressure to effective overburden pressure
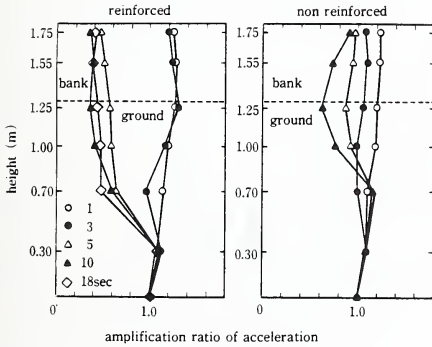
Fig. 7   Amplification ratio of acceleration
(Test No. L-1-3)
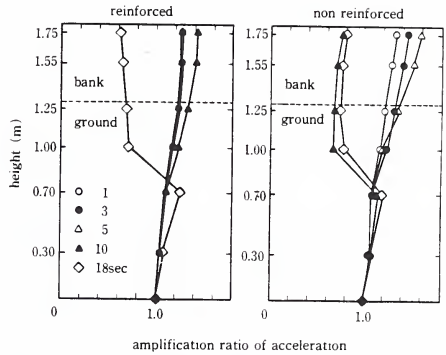
Fig. 8   Amplification ratio of acceleration
(Test No. L-2-3)

a) Test No S−1−6

b) Test No S−2−7

———— after excitation   —·—·— before excitation   —··—··— slip surface
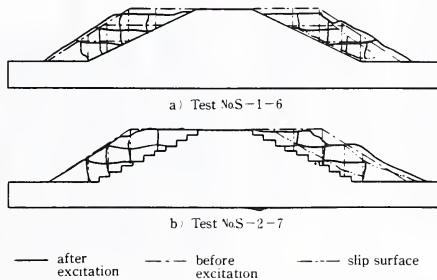
Fig. 9   Deformation of embankment after excitation

149
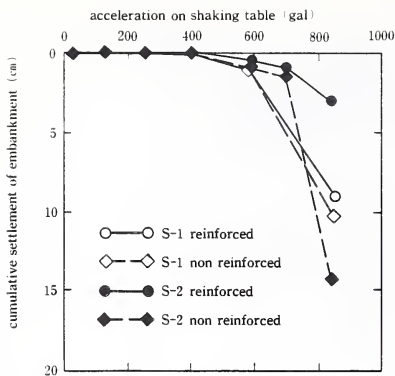
Fig. 10   Cumulative settlement of embankment
and acceleration on shaking table
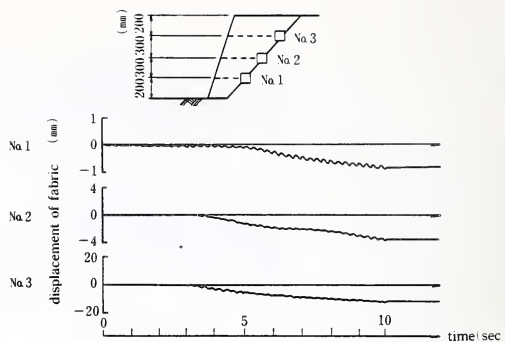
Fig. 11   Displacement of non-woven fabric during excitation
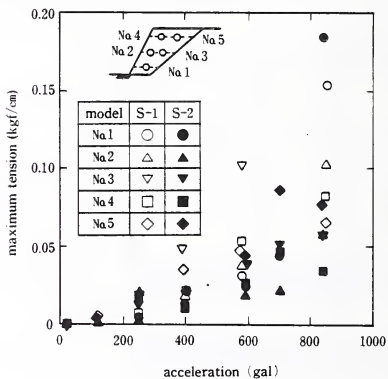
Fig. 12   Maximum tension in non-woven fabric and acceleration on shaking table
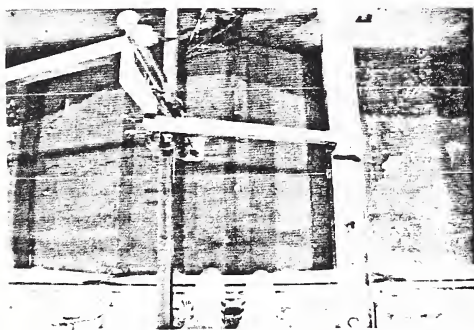
Photo. 1   View of top of reinforced embankment
after excitation   (Test No. L-2-4)
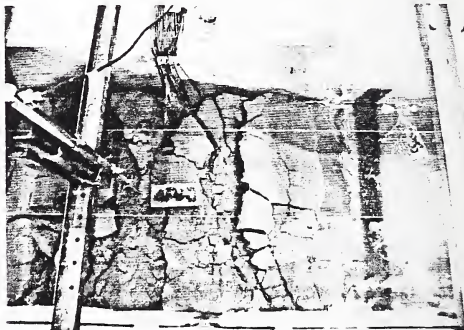
Photo. 2   View of top of non reinforced embankment
after excitation   (Test No. L-2-4)

STATUS REPORT ON NEW STUDY OF LOWER VAN NORMAN DAM

BY

A. G. Franklin[1]

ABSTRACT

This study consists of a re-analysis of the slide that occurred in the Lower Van Norman Dam during the 1971 San Fernando earthquake. In addition to information obtained in earlier investigations, new data are being obtained from field and laboratory investigations of the hydraulic fill sand in the remnant of the original dam. The objective is to validate a method of evaluating the post-earthquake stability of dams with liquefaction-susceptible soils, using either steady-state strength or some other form of residual strength. The approach is to compare strength values from field and laboratory tests of materials in the remnant of the original dam with those that can be inferred from its observed behavior during and immediately after the 1971 earthquake.

KEYWORDS: Earthquakes; Dams; Soils; Liquefaction

1. INTRODUCTION

The Lower Van Norman Dam, also known as the Lower San Fernando Dam, was severely shaken by the San Fernando Earthquake of 9 February 1971, and suffered a major slide of the upstream shell and crest. These events and the characteristics of the dam were studied exhaustively and reported by Seed, et al. (1975a,b). The investigations showed that the slide occurred as a consequence of earthquake-induced liquefaction of a zone of hydraulic fill sand in the upstream shell.

The dam was of hydraulic fill construction in its lower portions, with about 45 ft (14 m) of rolled fill at the top (Fig. 1). The slide which followed the 1971 earthquake resulted in the loss of a major part of the crest and the upstream shell (Fig. 2), and loss of the reservoir was averted only because the water level was fortuitously at a relatively low level. The dam was subsequently rebuilt, incorporating the remnant downstream of the slide. A replacement dam was built upstream, so that the original dam now serves only as an emergency detention structure.

The Corps of Engineers, with Professor H. Bolton Seed and Geotechnical Engineers, Inc. (GEI), is presently conducting a new study of the dam and the 1971 slide, using the information provided by the original investigations and new data being obtained from field and laboratory investigations of the hydraulic fill sand in the still extant remnant of the original dam.

2. PURPOSE AND OBJECTIVES

Conventional methods of evaluating liquefaction potential in embankment dams deal primarily with the development of excess pore water pressures in embankment and foundation soils, to predict whether or not excess pore pressure buildup and loss of shear strength will occur in the event that the structure is shaken by an earthquake of a size judged to be possible at the site. If the outcome of the analysis is the conclusion that such pore pressure buildup will occur, it is frequently assumed that the structure is therefore unsafe. However, very large strains can occur only if the shear strengths are reduced to values below the shear stresses produced by the static loading conditions. A complete evaluation of seismic stability thus requires the determination of the minimum values of shear strength that could be developed under conditions of liquefaction and large strain.

The earlier investigations of the 1971 slide provided, from field observations, particularly well-defined and well-documented description of the failure mechanism, including the zone of soil liquefaction and the locations of the slip surfaces. These observations provide a basis for obtaining from a stability analysis an upper bound value for the undrained residual shear strength of the soil in the liquefied zone, and an estimate of the shear strength at the time the slide was initiated. In the present investigation, the properties of the hydraulic sand fill are being re-examined to determine whether field and/or laboratory tests can be used to predict the post-liquefaction or residual strength, and so to determine the ultimate stability of the structure.

One of the participants in the current study is Geotechnical Engineers, Inc., whose Principals Gonzalo Castro and Steve Poulos have developed a theory and analytical procedure based on the concept of the steady state of deformation (Poulos, 1981). It is considered that "liquefaction" is the onset of continuing, large deformations under shear stresses that exceed the available shear strength (Castro, 1975). The

---

[1] Chief, Earthquake Engineering and Geophysics Division, Geotechnical Laboratory, U.S. Army Engineer Waterways Experiment Station, Vicksburg, Mississippi

undrained steady-state strength is defined as the shear stress in a saturated soil as it undergoes continuing deformation at constant void ratio and strain rate; and it is achieved only after liquefaction has occurred. The steady-state strength is similar to a residual undrained strength. It is believed to be dependent only on the void ratio of the soil, and is defined by the steady-state line on a plot of void ratio vs. initial effective minor principal stress, or approximately, the undrained steady-state strength (Fig. 3); obtained from strain-controlled, undrained, monotonically loaded shear tests. Because the steady-state strength is very sensitive to void ratio, accurate determination of the in-situ void ratio or density is essential in applying this theory. Detailed discussions of the application of the theory to liquefaction evaluation and to the lower Van Norman Dam are given by Poulos (1985) and Castro (1985).

Seed (1985, unpublished) has used back-calculation of shear strengths from several past occurrences of liquefaction to obtain a tentative correlation of residual strength with SPT "N" values (Fig. 4). This offers the possibility of using in-situ tests for evaluation of post-liquefaction strength. The Cone Penetrometer Test (CPT) may also prove useful for the purpose, either through correlation with the SPT or by direct comparison of CPT test values with back-calculated residual strengths.

The objective of the present study is to validate a procedure for evaluation of post-earthquake stability of embankment structures using post-liquefaction shear strengths obtained from field or laboratory tests. The approach being used is to compare the strength values obtained in the remnant of the original Lower Van Norman Dam with those that can be inferred from its observed behavior during and immediately after the earthquake of 9 February 1971.

3. PLAN AND PROGRESS OF STUDY

3.1 Review of Historical Data

Prior to initiation of field work, a review of historical records, including settlement and hydrological data, was done by GEI at the offices of the owner, the Los Angeles Department of Water and Power, and at State Government offices in Sacramento, California.

3.2 Field Investigations

The field phase of the study was completed in December 1985. Twelve CPT soundings were performed in September 1985, to depths ranging from 83 ft (25 m) to 123 ft (37 m) through the core and the downstream shell, but with most located to test shell materials. Six borings for split-spoon samples and SPT's were done by a Waterways Experiment Station (WES) drilling

rig, and the SPT system was later calibrated using dynamic energy measurements. Six additional borings were made to obtain high-quality undisturbed samples, using a Hvorslev fixed-piston sampler. Two more borings were drilled as observation wells.

A test shaft of 6-ft diameter (2 m) diameter was excavated through the downstream shell. (The location is shown in cross-section in Fig. 2.) This shaft provided access for visual and photographic examination of the shell materials, to take high-quality undisturbed samples by hand carving into tubes, to do in-place density tests, and to take remolded bag samples.

X-radiographs were made of all of the undisturbed samples, to evaluate any possible excessive disturbance and as an aid in selecting sample intervals for testing.

3.3 Laboratory Testing

Laboratory testing is being done at the laboratories of GEI, in Winchester, Massachusetts; at Stanford University; and at WES. Laboratory tests will include the following:

    Atterburg limits;
    Grain-size distribution;
    Compaction;
    Maximum and minimum density;
    Cyclic loading triaxial tests;
    Monotonic loading triaxial tests.

The cyclic loading and monotonic loading triaxial tests will be done on both undisturbed and remolded specimens. Laboratory testing is scheduled to be completed by the end of September 1986.

3.4 Analysis and Report

The final phase of the study is to be the analysis of the data and of the failure mechanism during the slide, from October 1986 to January 1987, and preparation of the final report, scheduled for completion in July 1987.

4. REFERENCES

(1) Castro, Gonzalo; Poulos, Steve J.; and Leathers, Francis D. 1985. "Re-Examination of the Slide of Lower San Fernando Dam," Journal of Geotechnical Engineering, Vol. 111, No. 9, pp. 1093-1107.

(2) Castro, Gonzalo 1975. "Liquefaction and Cyclic Mobility of Saturated Sands," Journal, ASCE, Vol. 101, No. GT6, pp. 551-569.

(3) Poulos, Steve J. 1981. "The Steady State of Deformation," Journal, ASCE, Vol. 107, No. GT5, pp. 553-562.

(4) Poulos, Steve J. 1985. "Liquefaction
     Evaluation Procedure," Journal of Geo-
     technical Engineering, ASCE, Vol. 111,
     No. 6, pp. 772-792.

(5) Seed, H. B.; Lee, K. L.; Idriss, I. M.;
     and Makdisi, F. I. 1975a. "The Slides of
     the San Fernando Dam During the Earthquake
     of 9 February 1971," Journal, ASCE,
     Vol. 101, No. GT7, pp. 651-689.

(6) _____ 1975b. "Dynamic Analyses of
     the Slide in the San Fernando Dam During
     the Earthquake of 9 February 1971," Jour-
     nal, ASCE, Vol. 101, No. GT9, pp. 889-911.
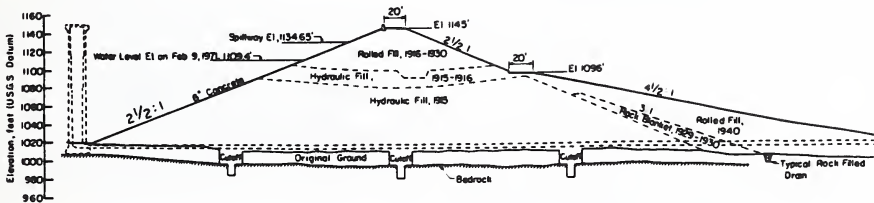
Figure 1. Cross-section through Lower Van Norman Dam
(Los Angeles Department of Water and Power)
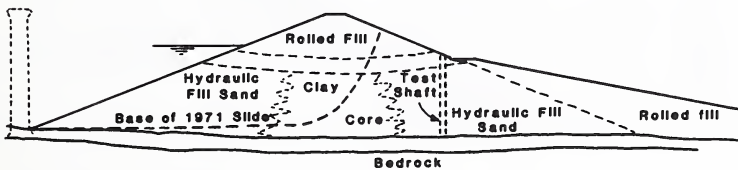
Figure 2. Cross-section through Lower Van Norman Dam,
showing location of base of 1971 slide and location of
test shaft.

153
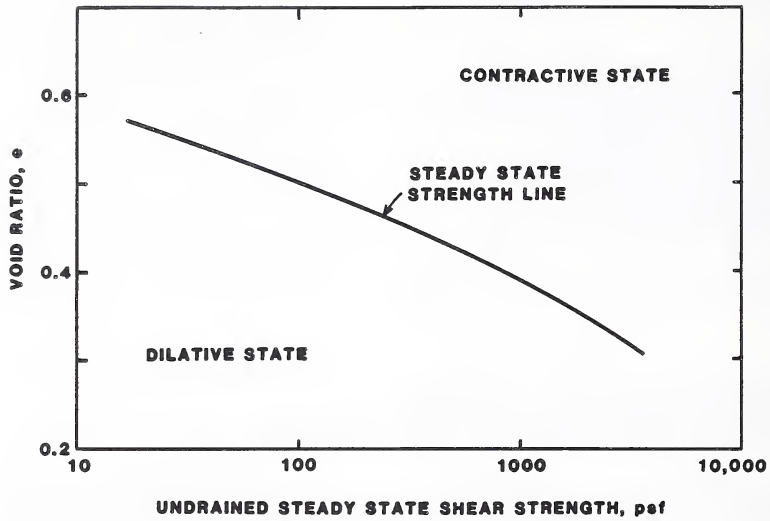
Figure 3. The Steady-State Line
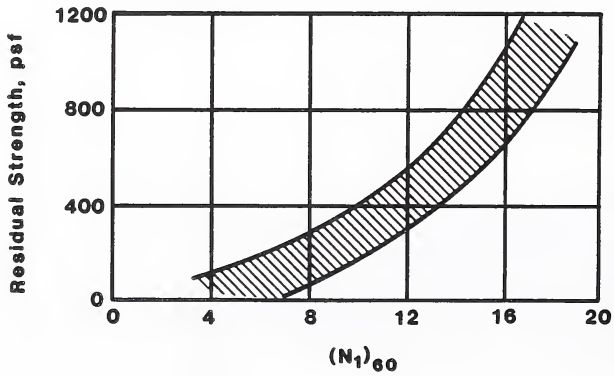
Figure 4. Tentative Relationship between Residual Strength and SPT N values. (After Seed, 1985, unpublished)

SEISMIC DESIGN PROCEDURE AND DYNAMIC STRENGTH OF CAB

BY

Toshio Iwasaki, Kazuhiko Kawashima, Naomi Obinata, and Shigeki Unjoh

ABSTRACT

The installation of CAB (Cable Box) is initiated to enhance underground distributing network services of electricity and telephone at populated cities in Japan. Draft Manuals for Design of CAB Systems were produced by the Ministry of Construction. This paper briefly describes the seismic design procedures and the dynamic load test results performed to verify the seismic performance of a standard CAB element.

1. INTRODUCTION

Special reinforced concrete ducts called CAB (abbreviation of cable box) housing transmitting lines (network service of electricity and telephone) are being constructed under city roads in Japan. The CAB network systems is generally more expensive than the current transmission systems which hangs the wires from electric poles. However, CAB has advantages such as disaster prevention and an increases available road space for service (refer to Fig. 1).

CAB has a standard cross section (see Fig. 2). One element of CAB is composed of an U-shaped duct with length of approximately 1.5 m; it has a concrete cover. Photographs 1 and 2 show an installation of the U-shaped duct and the cover, respectively. The Ministry of Construction developed the design procedures including the "Manuals for Design of CAB Systems (Draft)." In conjunction with examining seismic design procedures, a series of dynamic loading tests were performed to verify the seismic performance of CAB systems at the Public Works Research Institute. These tests were at the request of the Road Bureau and the Kantoh Regional Construction Bureau of the Ministry of Construction.

This paper presents a summary of the proposed draft seismic design procedures in the Manuals for Design of CAB Systems and the dynamic loading test results.

2. OUTLINE OF SEISMIC RESISTANT DESIGN PROCEDURE

The Manuals for Design of CAB Systems (Draft), hereafter referred as the manuals, stipulate that the design of CAB must resist seismic effects. CAB may be installed at soft ground

---

Earthquake Disaster Prevention Department.

sites and/or sites vulnerable to liquefaction. Seismic design testing is required for:

1) deformation of surrounding ground developed during earthquake and excessive pore water pressure,

2) longitudinal direction of CAB axis,

3) uplift when the surrounding subsoils are vulnerable to liquefaction.

2.1 Seismic Ground Strains Considered in Seismic Design

Designing for deformation of subsurface ground during earthquakes is accounted for in terms of seismic ground strains ϵ_G, and is represented as

$$\epsilon_G = \nu_1 \times \nu_2 \times \nu_3 \times \epsilon_0 \qquad (1)$$

in which ν_1, ν_2 and ν_3 represent the seismic zone factor, soil condition factor and liquefaction effect factor, respectively, and ϵ_0 represents a standard seismic ground strain (=1/100). Factors ν_1 and ν_2 are specified in Tables 1 and 2, respectively, in accordance with Part V of the Specifications of Highway Bridges. Factor ν_3 represents an amount of increase of subsoil deformations due to liquefaction, it is shown in Table 3. Even when the sublayer which CAB is to be buried is stable against liquefaction, the factor ν_3 shall be considered when sublayers underlying that sublayer are likely to cause liquefaction.

For seismic design of straight chain structures embedded in shallow ground like CAB, the ground strains developed along CAB axis has the controlling effect. The ground strains during earthquakes are contributed by several variables such as non-uniformity of subsurface ground and effect of wave propagation; the standard ground strain ν_0 was assumed as 1/100. Although the ground strains obtained by field observations are generally much smaller than 1/100, the value of 1/100 was adopted for ϵ_0 taking into account that significant cracks and subsidence associated with large deformations of subsoils were frequently observed in past large earthquakes.

2.2 Seismic Design

Seismic force P developed in CAB's axial direction and the magnitude of joint length Δ (avoid uncoupling of joint) are

$$P = D \times \ell \times \tau_0 \qquad (2)$$
$$\Delta = \epsilon_G \times \ell \qquad (3)$$

where D: width of CAB in touch with
          surrounding soils per unit length
          (m)
    ℓ : length of CAB element (m)
    τ_0 : frictional force between CAB and
        soils per unit contact area (tf/m^2)
    ϵ_G: seismic ground strain represented by
        Eq. (1)

The seismic force P defined by Eq. (2) represents the force transmitted from soils to CAB associated with deformations of surrounding subsoils. The joint length Δ by Eq. (3) represents the relative displacement between an interval CAB element associated with the seismic ground strains. Note, such relative displacement has to be absorbed by joints without causing uncoupling of joint.

2.3 Judgment of Liquefaction of Sandy Soil Layers and Countermeasures for Liquefaction

Vulnerability for liquefaction at certain depth may be represented in terms of liquefaction resistance factor F_L. However, F_L gives liquefaction vulnerability only at a specific depth considered and is not necessarily a suitable index representing stability of the site associated with liquefaction. Therefore, the liquefaction potential index P_L, which is designated as the integral of F_L from ground surface to 20 m below the surface, was adopted to evaluate the stability of the site.

It is stipulated in the manuals that the safety against uplift of CAB be checked when P_L becomes larger than 15 and when CAB is installed in the sandy layer with F_L less than 1.0. The excessive pore water pressure vs. F_L relation, which is used for evaluation of safety factor against uplift, is specified in the manuals.

Countermeasures for liquefaction should be conducted when the surrounding subsoils have high potentials for liquefaction ($P_L > 15$), and possible movement of surface layer associated with liquefaction is expected.

2.4 Structural Details in Seismic Design

For improving seismic performance of CAB, the following structural details are stipulated:

1) installation of joint at the points where sudden change of ground condition occurs,

2) adoption of joint to absorb required joint displacement given by Eq. (3),

3) installation of pull-out prevention device at the joint at sites where large ground deformations are likely to occur.

3. DYNAMIC LOADING TEST OF CAB-ELEMENT

3.1 Objectives

Underground structures similar to CAB such as drainage U-ducts, water supply and sewage pipes have sustained damages in past earthquakes. The damage features of these underground structures are characterized as:

1) Damage of Pipe Itself (refer to photograph 3)

Longitudinal and transverse cracks were developed, at times the pipe was crushed from large deformation and movement of subsurface soils during earthquakes.

2) Failure, Shift and Uncoupling of Pipe Joint (refer to photographs 4, 5, and 6)

The pipe joint is generally more vulnerable than the pipe itself and failure, shift, and uncoupling at pipe joints were frequently observed.

According to lessons learned through past earthquake damages, it is considered important to prevent future seismic damage of CAB by improving the strength of its main body including joints by providing pull-out prevention devices (stopper) at joints. Consequently, the purpose of these experiments verified the strength of CAB element and the effectiveness of the stopper.

3.2 Test Cases and Loading Condition

3.2.1 Test Cases

A series of four loading tests was conducted; the purpose of and specimen used for each test are described.

1) Test 1

In test, 1 the strength of CAB in its axial direction was studied. One side of the CAB specimen was pushed and/or pulled by a dynamic actuator, the other side was fixed to a reaction wall as shown in Fig. 3. Fig. 4 shows dimensions and reinforcement of the specimen used for test 1.

2) Test 2

In test 2, the strength of CAB's bending moment around a vertical axis was studied. A dynamic lateral force was applied by the actuator to the CAB specimen. The specimen was supported by two hinges placed at both ends using a two leg jig as shown in Fig. 5. It produced

156

constant bending moment in the specimen. Fig. 6 represents the dimensions and reinforcement of the specimen for test 2.

3) <u>Test 3</u>

In test 3, the effectiveness of the joint stopper was studied. Three elements of CAB were placed as shown in Fig. 7. Four stoppers were set for connecting two adjacent elements. One side of the end element was pushed and pulled by the dynamic actuator; the other end was fixed to the reaction frame. Fig. 8 represents the dimensions of the specimen for test 3. The reinforcement of this specimen is the same as denoted in Fig. 4.

4) <u>Test 4</u>

In test 4, the strength of joint in transverse direction was studied. Three elements of CAB were connected as shown in Fig. 9; the end of two side elements are supported by hinges. Dynamic lateral force was applied to the center element so shearing force could be applied at the joints. Fig. 10 represents dimensions of the specimen for test 4. The reinforcement of this specimen is essentially the same with that represented in Fig. 4.

The specimens used in the loading test are full-scale models of actual CAB's constructed as a pilot execution at one of the city roads in Tokyo metropolitan area by the Ministry of Construction in 1983 and 1984. In the loading tests, strains developed in the reinforcements and at the concrete and relative displacement between two adjacent elements at the joint were measured including the lateral dynamic force applied to the specimen. The strains were measured at 7 points as shown in Fig. 11.

3.2.2 Loading Conditions

The seismic force required for the seismic design was obtained in accordance with the manuals. The lateral dynamic force applied to the specimens (refer to Table 4) had an amplitude approximately three times as large as the required seismic force. The loading of sinusoidal wave with frequently of 0.5 Hz and with number of cycles of 10 was reproduced by a dynamic actuator installed at the dynamic structural laboratory, P.W.R.I.

3.3 <u>Test Results</u>

1) <u>Test 1</u>

The strain of reinforcement vs. loading force relations were obtained as shown in Fig. 12. Fig. 12 shows that differences of measured strains depending on the measuring points are very small. This implied that the specimen developed uniform extension and compression. Fig. 12 illustrates that the strains predicted,

assuming that full section of concrete resists for the force, agree well with the measured strains.

The strains for reinforcement and concrete corresponding to the seismic force of 11.1t, expected during earthquakes, are only 20 μ, i.e., stresses developed in the reinforcements and at the concrete are only 40 kg/cm^2, and 5 kg/cm^2, respectively.

The seismic performance of the specimen are shown in Fig. 13, i.e.,

i)   no damage was developed up to the lateral force of 15t.

ii) at lateral force of 15t, hair cracks were generated at the knockout, and they grew slightly in accordance with increase of the lateral force.

iii) at lateral force of 35t, only hair cracks developed around the knock-out. The CAB specimen resisted without serious damage for a force 3 times as large as the seismic force, which is expected to develop during earthquake.

2) <u>Test 2</u>

Fig. 14 shows the strain of reinforcement vs. loading force relation for test 2. As the case for test 1, predicted strains assuming that full section of concrete resists for bending moment agreed well with the measured strains.

The strains developed in the reinforcement and concrete at force level of 21t (three times the force supposedly developed during an earthquake) are only 70 μ, i.e., stresses of reinforcement and concrete are 150 kg/cm^2 and 20 kg/cm^2, respectively. Only hair cracks appeared at the knockout as shown in Fig. 15.

3) <u>Test 3</u>

Fig. 16 represents the hysteresis curve of relative displacement between two adjacent elements vs. force developed in the stopper at the joint. Because collision occurs at the instance when the relative displacement becomes zero, increase of force level is observed in the hysteresis curve.

Although some spalling of concrete occurred at the joint due to collision, it was confirmed that the stoppers work effectively to prevent pulling-out of one CAB element from the adjacent CAB element. Note, because the axial force developed in the specimen was small, no cracks appeared in the specimen.

4) Test 4

The redundancy between two adjacent specimen connected by tenon and mortise in the trans-verse direction is small (refer to Fig. 8(b)), few relative displacements occurred during excitation. The strains developed in the reinforcement and the stoppers were small; no cracks or damage occurred.

4. CONCLUSIONS OBTAINED FROM DYNAMIC LOADING TESTS

From the results of the dynamic loading tests of CAB-specimens, the following conclusions were derived:

1) the seismic performance of the CAB specimen for the four tests are summarized in Table 5. For seismic force, expected during an earthquake, no damages were observed except for minor hair cracks at the knock-out. For the seismic force three times as large as the expected developed seismic force, only hair cracks appeared at the specimen in the vicinity of the knout-out. From these results, it was confirmed that the CAB has sufficient strength to survive seismic forces,

2) the effect of the stopper, for prevention of pulling out at the joint, was significant, and

3) the strain developed in the reinforcement and concrete can be sufficiently predicted by assuming that the full-section concrete resists tension and bending moment.

5. ACKNOWLEDGMENT

This report presented the seismic design procedures of CAB adopted in the Manuals for Design of CAB System (Draft). It was issued by the Ministry of Construction in 1985; the dynamic loading test was conducted to verify the seismic safety of CAB.

Cooperation to perform the dynamic loading tests was received from the Road Bureau and the Kantoh Regional Construction Bureau of the Ministry of Construction, the Research Center for Land Development Technology, and the Highway Industry Development Institute. The authors appreciate all concerned for their cooperation during this study. Special appreciation also goes to members of the CAB Committee chaired by Prof. Masakatsu Koshi, University of Tokyo, for their valuable discussions in formulating the seismic design procedures and for conducting the dynamic loading tests.

6. REFERENCES

1) Highway Industry Development Institute, Technical Manual of CAB Systems, January 1986 (In Japanese).

2) Kawashima, K., N. Obinata, K. Gotoh, and T. Kanoh, Investigation on Seismic Perfor-mance of CAB, Part 1, Preliminary Study for Seismic Performance of Sandard Type CAB, Technical Memorandum No. 2138, Public Works Research Institute, 1984 (In Japanese).

3) Kawashima, K., et al., Investigation on Seismic Performance of CAB, Part 2, Dynamic Loading Tests of CAB, Technical Memorandum No. 2259, Public Works Research Institute, 1985 (In Japanese).

4) Kawashima, K., N. Obinata, K. Gotoh, and T. Kanoh, Damage of Sewage Facilities Caused by the Nihon-kai-chubu Earthquake of 1983, Part 1, Damage Features of Sewage Facilities, Technical Memorandum No. 2244, and Part 2, Photographs Showing Damage, Technical Memorandum No. 2237, Public Works Research Institute, 1985 (In Japanese).

5) Kawashima, K., N. Obinata, K. Gotoh, and T. Kanoh, Seismic Damage of Sewage Pipes Caused by the 1983 Nihon-kah-chubu Earthquake, Pressure Vessels and Piping Technology, ASME, New Orleans, Louisiana, U.S.A., 1985.

6) Japan Road Association, Specifications of Highway Bridges, Part V, Earthquake Resistant Design, 1980.

7) Iwasaki, T., Soil Liquefaction Studies in Japan, Soil Dynamic and Earthquake Engineering, Vol. 5, No. 1, 1986.

8) Katayama, T. and N. Sato, Ground Strain Measurements by a Very Densely Located Seismometer Array, Proc. of 6th Japan Earthquake Engineering Symposium, 1982.

9) Iwasaki, T., Earthquake Resistant Design of Underground Pipelines in Japan, Proc. of US-Japan Workshop on Seismic Behavior of Buried Pipelines and Telecommunications System, Tsukuba Science City, Japan, 1984.

10) Kawashima, K., K. Tamura, and K. Aizawa, Finite Ground Strains Induced During Earthquake for Application to Seismic Design of Underground Pipelines, Proc. of U.S.-Japan Workshop on Seismic Behavior of Buried Pipelines and Telecommunications System, Tsukuba Science City, Japan, 1984.

11) Iwamoto, T., N. Wakai, and T. Yamaji,
Observation of Dynamic Behavior of Buried
Pipelines During Earthquakes, Proc. 8th
World Conference on Earthquake
Engineering, San Francisco, U.S.A., 1984.

12) Kubo, K., M. Hamada, and R. Isoyama,
Measurement of Permanent Movement of
Subsurface Ground Due to Nihon-kai-chubu
Earthquake, Proc. of Earthquake
Engineering, JSCE, 1985 (In Japanese).

Table 1   Seismic Zone Factor ν_1

Zone	A	B	C
Value of ν_1	1.0	0.85	0.7

Table 2   Ground Condition Factor ν_2

Group	1	2	3	4
Value of ν_2	0.9	1.0	1.1	1.2

Table 3   Liquefaction Effect Factor ν_3

Group	Coefficient ν_3	Condition	Remarks
1	1.0	$P_L < 15$	
2	1.5	$P_L \geqq 15$ and CAB is installed within soil layers with $F_L \geqq 1$	$F_L \geqq 1$ $F_L < 1$
3	2.0	$P_L \geqq 15$ and CAB is installed within soil layers with $F_L < 1$	$F_L < 1$ $F_L < 1$
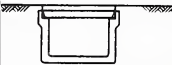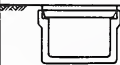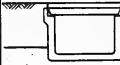
Table 4   Load and/or Displacement Subjected to CAB-Specimens

Case	Estimated Seismic Effect (Load and/or Displacement) Subjected to CAB during Earthquakes Ⓐ	Load and/or Displacement Applied to CAB Specimens by This Experiment		Ⓑ / Ⓐ	Procedure for Loading Control
		Static Loading Test	Dynamic Loading Test B		
Test-1	11.1 t	20 t	35 t	3.2	Load Control
Test-2	6.8 t	10 t	21 t	3.1	Load Control
Test-3	11.1 t and Relative Displacement at Joint between Two Adjacent CAB elements ± 10 mm	Compression 35 t Tension 4 t	Relative Displacement at Joint ± 10 mm	—	Load Control (Static) and Displacement Control (Dynamic)
Test-4	0.09 t	2 t	2 t	22.2	Load Control

Table 5   Summary of Loading Test Results

Case	CAB-Specimens Subjected to The Load and/or Displacement Expected to Develop during Earthquakes	CAB-Specimens Subjected to 3 Times as Large as The Load and/or Displacement Expected to Develop during Earthquakes
Test-1	No Damage	Hair Cracks at Knock-out
Test-2	Hair Cracks at Knock-out	Hair Cracks at Knock-out
Test-3	No Damage, but Slight Spalling-off of Concrete at Joint due to Collision	
Test-4	No Damage	No Damage
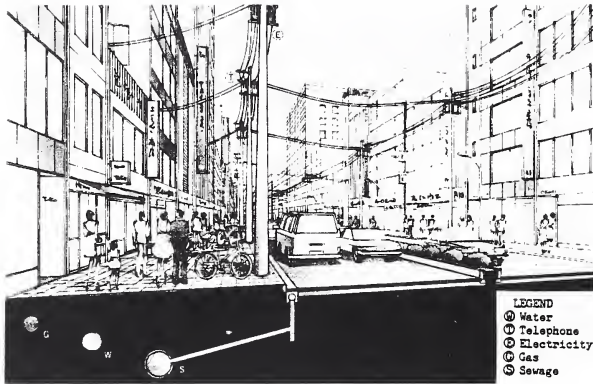
(a) Transmission Line Via Electric Poles
    and Telephone
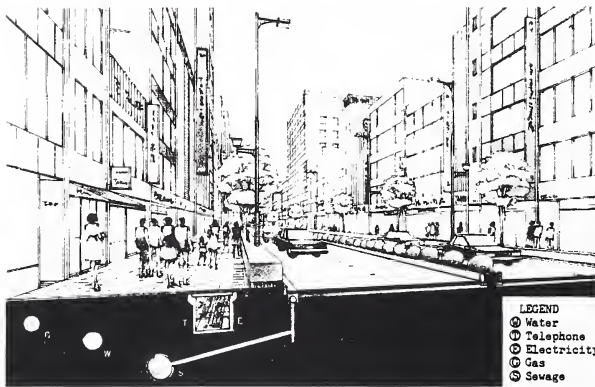
(b) Transmission Line Stored in CAB

Fig.1 Effect of CAB-System for Distributing Electricity
       and Telephone
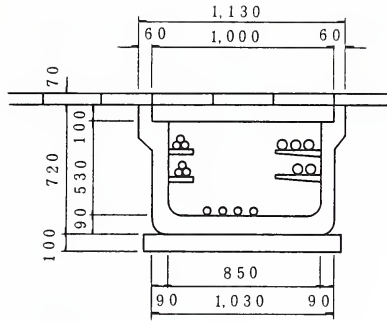
Fig.2 Standard Cross Section of CAB

(a) Plan View
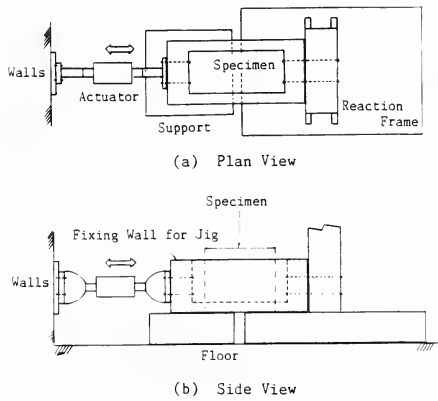
(b) Side View

Fig.3 Loading Procedure for Test 1

Fig. 4 CAB-Specimen for Test-1

164

Specimen

Support

2 Leg Loading Jig

Load Transmission Jig

Wall

Objective Part of Specimen

Actuator

Hinge

(a) Plan View

Wall

Floor

(b) Side View

Fig.5 Loading Procedure for Test 2

Fig.6 CAB-Specimen for Test-2

165
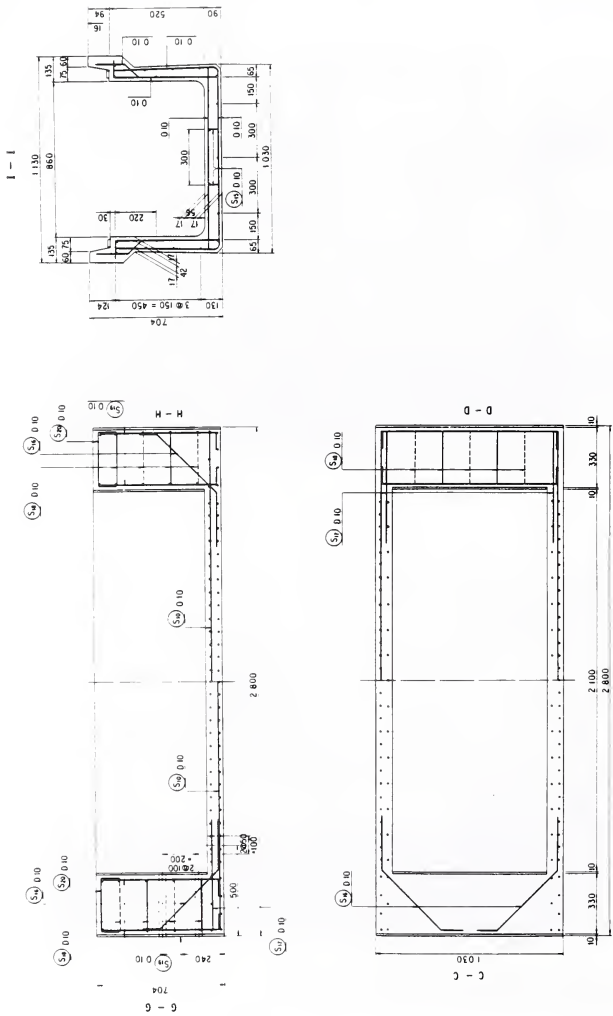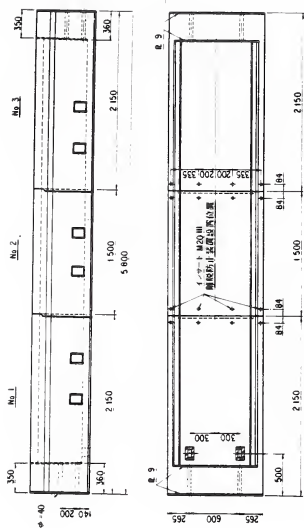
(a) CAB

(b) Detail of Joint and Stopper (Pulling-out Prevention Device)

Fig.8 CAB-Specimen for Test-3

Specimen

Reaction Frame

Support   Pulling-out Prevention Device

(a) Plan View

Actuator

Wall

Fixing Wall for Jig

Floor

Wall
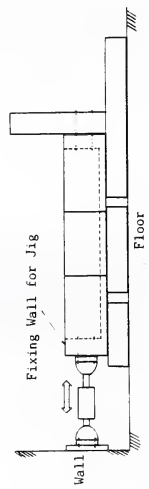
(b) Side View

Fig.7 Loading Procedure for Test 3
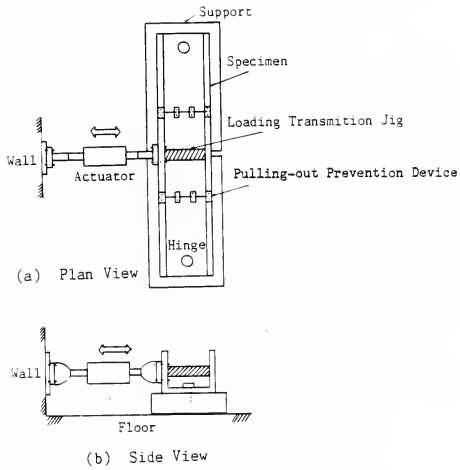
Fig.9 Loading Procedure for Test 4
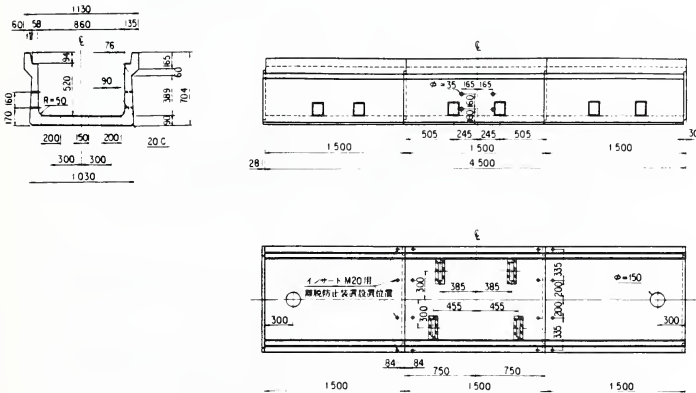
Fig.10 CAB-Specimen for Test-4

167
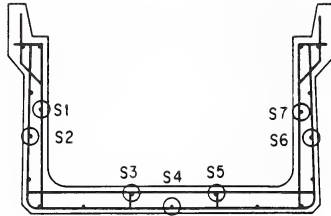
Fig.11   Measuring Points of Strains
         Developed in Reinforcing Bar
         (S1 - S7)
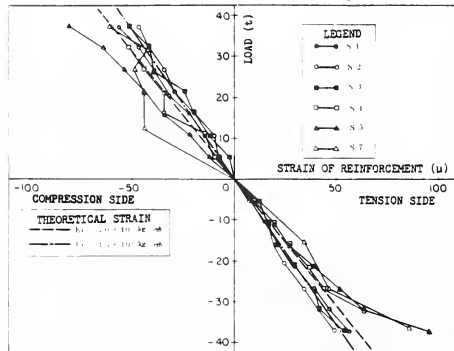
Fig.12 Load vs. Strain of Reinforcing Bar
        for Dynamic Loading Test with Frequency
        of 0.5Hz (Test 1, refer to Fig.11
        for measuring points of strain)
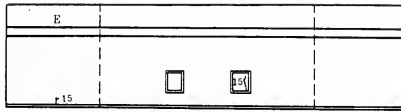
(a) Micro Cracks Observed After Dynamic Loading with
    Amplitude of $\pm$ 15t (f=0.5Hz)
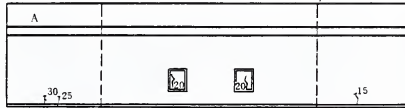
(b) Micro Cracks Observed After Dynamic Loading with
    Amplitude of $\pm$ 30t (f=0.5Hz)

Fig.13 Dynamic Loading Test Results for Test-1
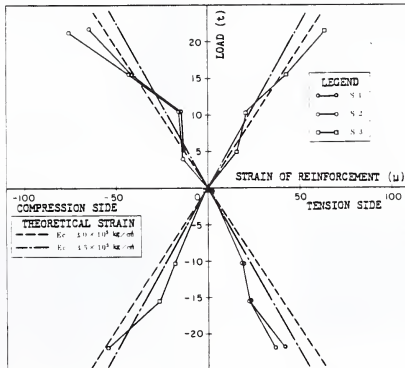
Fig.14 Load vs. Strain of Reinforcing Bar for Dynamic Loading
        Test with Frequency of 0.5Hz (Test 2, refer to Fig.11
        for measuring points of strain)
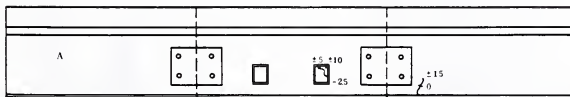
Fig.15 Micro Cracks Observed After Dynamic Loading with
        Amplitude $\pm$ 15t for Test-2
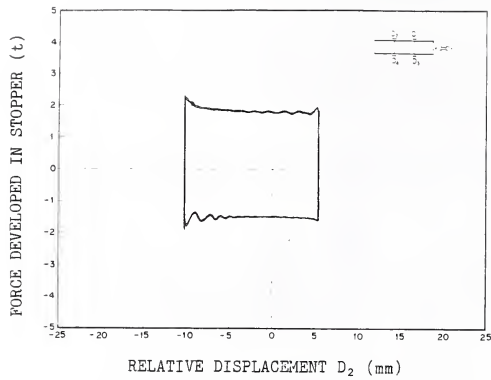
(a) Dynamic Loading with Frequency of 0.3Hz
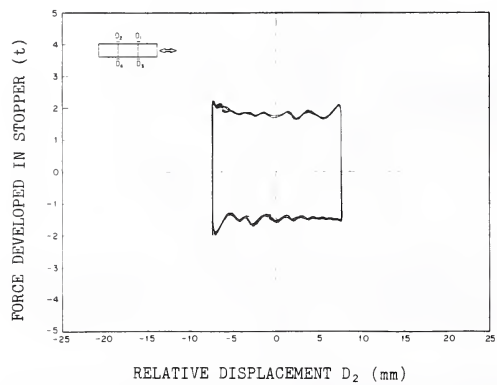
(b) Dynamic Loading with Frequency of 0.5Hz

Fig.16 Hysteresis of Force Developed in Stopper vs.
Relative Displacement at Joint (No.2 Joint)
for Test-3
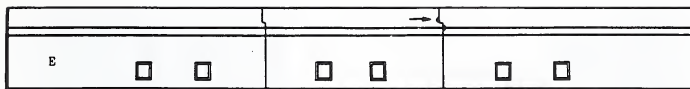
Fig.17 Spalling-off of Concrete Developed at Joint
due to Collision (Test-3)

Photo 1   Installation of CAB (U-Shaped Duct)
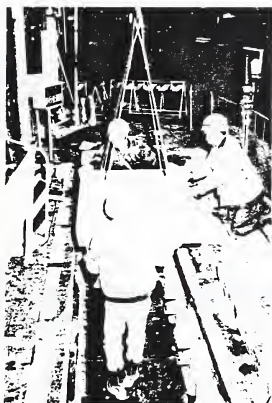
Photo 2   Installation of CAB
(Concrete Cover)

Photo 3 Damage of Drainage Flume
(Nihonkai-chubu Earthquake)
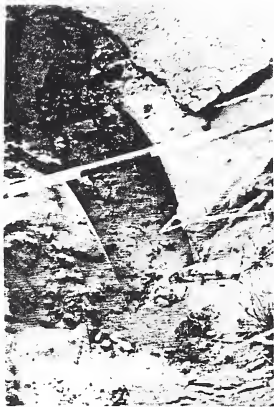
Photo 4   Pulled-Out of Sewage pipe
          at Joint
          (Nihonkai-chubu Earthquake)
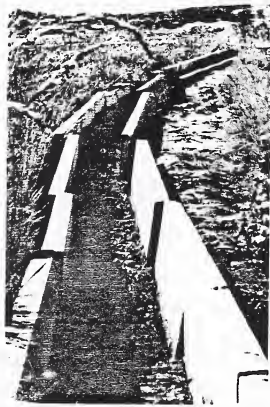
Photo 5   Offset of Flume at Joint
          (Nihonkai-chubu Earthquake)

Photo 6   Offset of Drainage Flume
          at Joint
          (Nihonkai-chubu Earthquake)
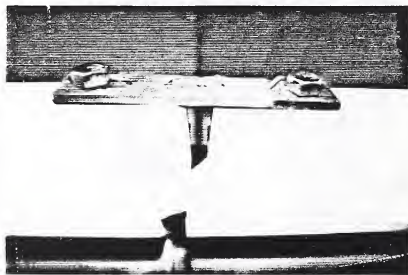
Photo 7   Effectiveness of Pulling
          Out Prevention Device

172

LARGE-SCALE BRIDGE COLUMN TESTS
A PROGRESS REPORT

BY

Edgar V. Leyendecker
William C. Stone
Geraldine S. Cheok[1]

ABSTRACT

An experimental program to assess the performance of full-scale bridge columns subjected to cyclic inelastic loading has been undertaken at the National Bureau of Standards. The objectives of this program are to determine the adequacy of existing California Department of Transportation (CALTRANS) reinforcement provisions for highway bridges constructed in zones of high seismicity, and to determine the feasibility of reproducting prototype behavior with 1/6-scale model replicates. A description of the on-going test program, as well as results from the first series of three 1/6-scale model tests, is presented.

1. INTRODUCTION

A large portion of modern bridge structures constructed in zones of high seismic activity are supported by bents consisting of one or more columns. Nearly all present design codes for bridge columns seismic details have had their basis in the extensive research done on building columns at relatively small scale. Inelastic response of these bridge structures under seismic loading normally involves plastic hinging of the columns. Behavior is consequently different in concept from that required of building frames, where a design approach is adopted to insure that beams hinge before columns.

In an effort to summarize the current state-of-knowledge and to establish research needs for seismic aspects of highway bridge design, the National Science Foundation sponsored a workshop on Earthquake Resistance of Highway Bridges. The Proceedings, published in January 1979, contained recommendations for future research, as well as state-of-the-art and state-of-practice papers. Research recommendations were called for in a number of areas.

A key recommendation was to perform experimental and analytical studies to determine the reserve capacities of bridge components. Much of the considerable research work on column behavior has been done on relatively small specimens and has been extrapolated for bridges from tests of columns typically used in buildings. Bridge columns are larger and lower stressed than building columns; extrapolation from the present wealth of building column data may no be appropriate. Therefore, work is needed to determine whether the behavior of small sections can be extrapolated to larger cross sections.

2. RESEARCH PROGRAM

A test program was developed using the variables shown in figure 1. Specimens include a flexural specimen and two shorter specimens with variable axial load. Tests are planned at full and reduced scale.

Two types of cantilevered bridge columns have been designed based on full-scale 60" (1.5 m) diameter bridge columns. The basic specimen properties are as shown in figure 1:

Type I) 30 foot (9 m) column(high moment-to-shear ratio) with continuous longitudinal reinforcement through the footing for evaluation of transverse reinforcement performance in the plastic hinge region (maximum ductility factor) under varying axial load.

Type II) 15 foot (4.6 m) column (low moment-to-shear ratio) to investigate shear performance of transverse reinforcement.

[1] Structures Division, National Bureau of Standards, Gaithersburg, Maryland 20899

3. FULL-SCALE TESTS

The facilities at the National Bureau of Standards (NBS) provide the experimental means to perform large scale structural testing. The basic loading scheme is simple and includes a combination of vertical and lateral load. This is shown schematically in figure 2. Vertical load is applied using an existing testing machine and lateral load is applied using a reaction wall to move the test specimen base. Although simple in concept, the test facility, shown in figure 3, is complex in practice. The structural laboratory includes a 12 million pound universal testing machine. Specimen sizes of up to 58 feet in height and 8 feet in width can be accommodated in the machine. Lateral loads can be imposed on the specimen by means of the newly completed 45 foot (14 m) high reaction wall.

The first of three planned full-scale test specimens 5-foot (1.5 m) diameter and 30-feet (9 m) high) has been fabricated, see figure 4. Testing is planned for early July, 1986.

4. MODEL TESTS

Model tests are being conducted at 1/6-scale using both microconcrete and conventional aggregate concrete. These are being tested using the NBS Tri-Directional Testing Facility shown in figure 5. A model of the column is shown in figure 5.

Various stages of the model program are shown in figure 6 (model of the 30 foot (9 m) specimen). Note the fractured vertical reinforcement.

Four 1/6-scale models tested during May of 1986. A set of three specimens modelling the parameters in figure 1 using microconcrete have been completed. These are being repeated using small aggregate concrete, but not scaled as microconcrete.

Preliminary results from the microconcrete tests are shown in figure 7. Only the tip deflection data are shown in the figure. Much more data have been collected but are still in the process of being analyzed.

The following points are noted for the three specimens:

30-foot (9 m) model, 1000 kips (450 tons) vertical load
o   spiral did not fracture
o   vertical steel fractured at 8 times the yield displacement, first cycle
15-foot (4.6 m) model, 2000 kips (900 tons) vertical load
o   spiral fractured at 10 times yield displacement, first cycle
o   vertical steel fractured at 10 times yield displacement, third cycle

5. SUMMARY

The current status of the NBS research on the large-scale bridge column has been briefly presented. Preliminary model data have been reviewed. The full-scale experimental program is scheduled to continue through the spring of 1987 with the test of the first large-scale specimen scheduled for July, 1986. Reports on the model tests are due in October. Final reports on the comparison of full-scale and model specimens are planned for September 1987.

NBS LARGE SCALE BRIDGE COLUMN TESTS
(Series A)

CONCRETE: f'_c = 4000 psi (27.6 MPa)

STEEL: 2% MAIN COLUMN

SPIRAL #5 at 3-1/2" – I

#6 at 2-1/8" – II,III

TYPE I

2000 kips (9 MN) AXIAL LOAD

30' (9m)

SEISMIC LOAD

9' (2.8m)

5' (1.5m)

26' (8m)

TYPE II

2000 kips (9 MN) AXIAL LOAD

15' (4.5m)

SEISMIC LOAD

5' (1.5m)

26' (8m)

TYPE II

1000 kips (4.5 MN) AXIAL LOAD

15' (4.5m)

SEISMIC LOAD

5' (1.5m)

26' (8m)
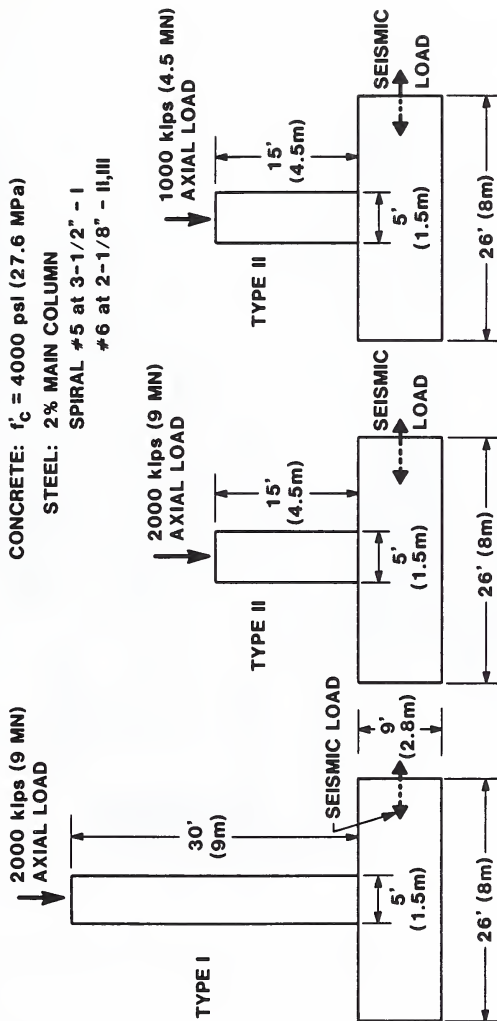
Figure 1. Summary of Test Specimens
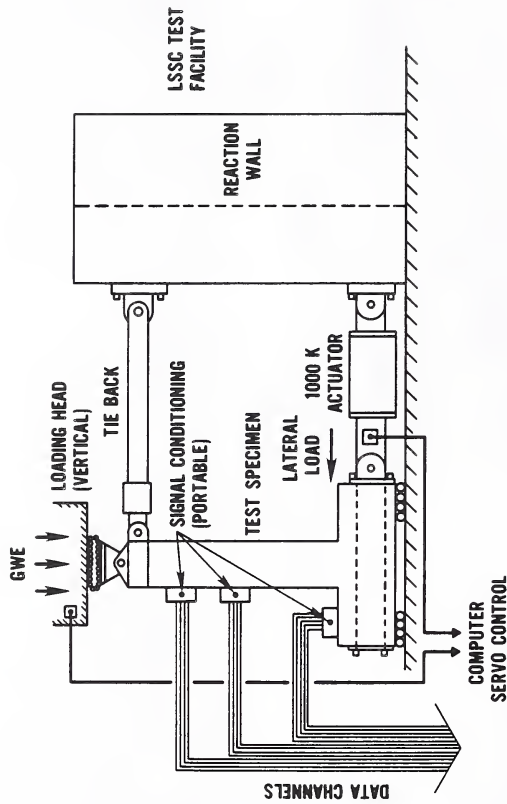
Figure 2. Application of Forces on Large-Scale Specimens
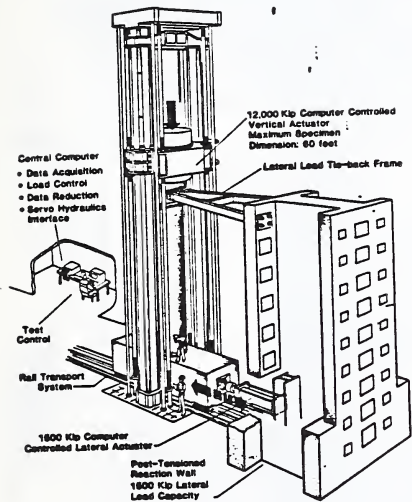
Schematic of Column under Test
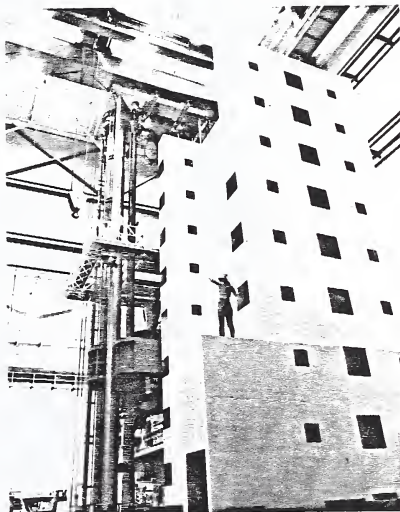
Reaction Wall and Testing Machine

Figure 3. Testing Facility for the Large-scale Bridge Project
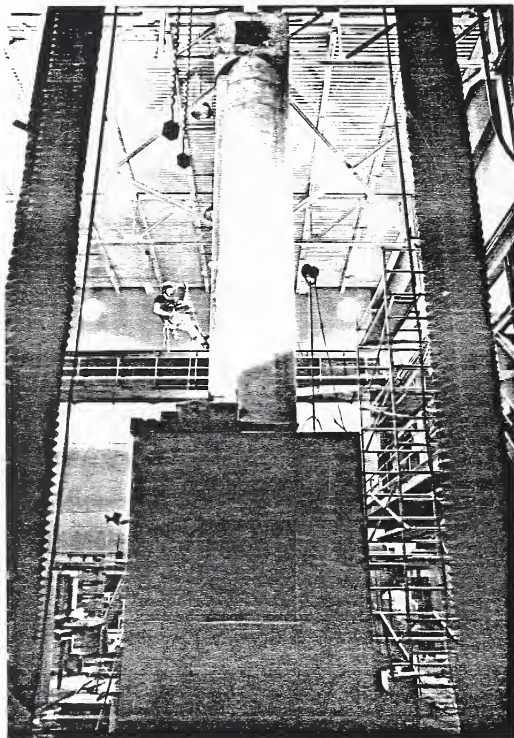
Figure 4. Large-Scale Specimen
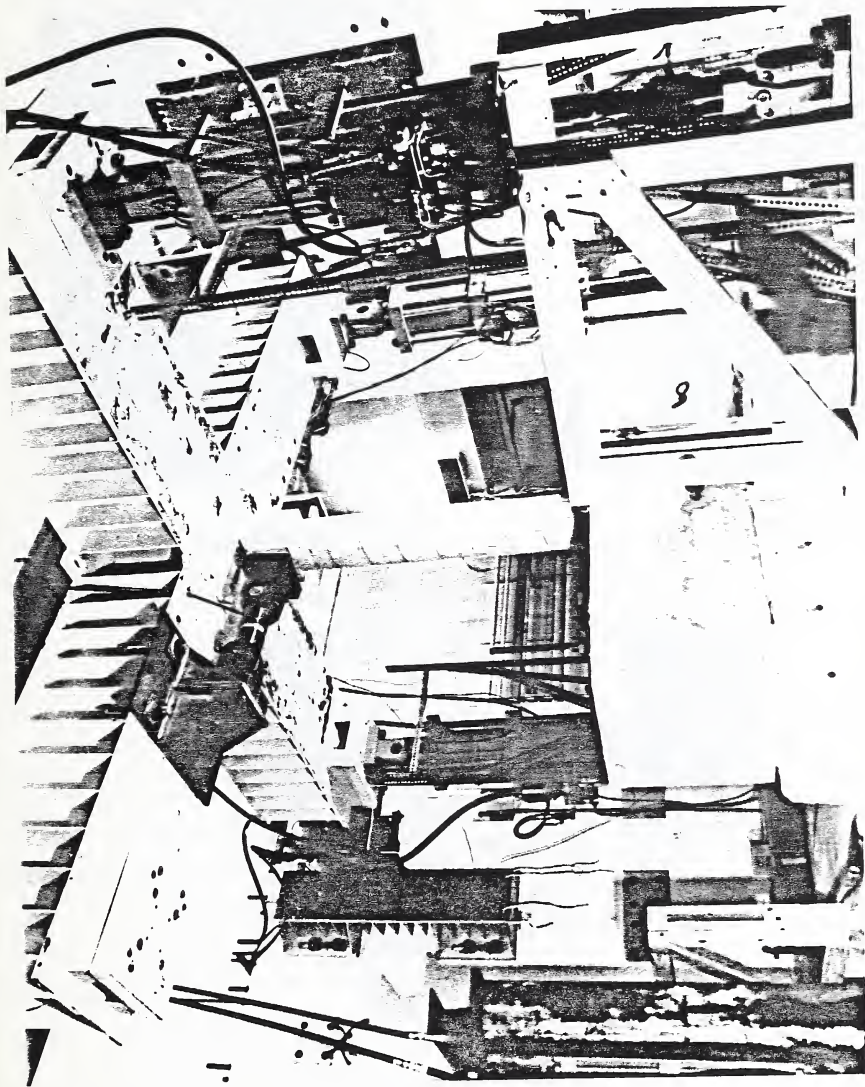
Figure 5. Tri-Directional Testing Facility with 1/6-scale Model
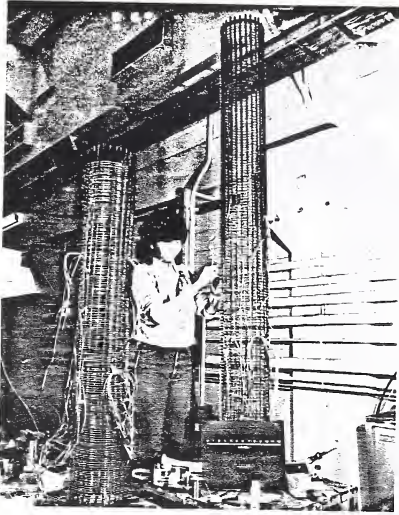
Column Cage Fabrication
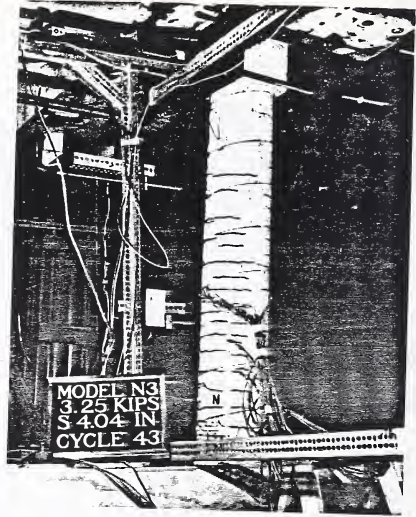
Column under Test

Crushed Concrete and Fractured Vertical Reinforcement

Figure 6. One-sixth Scale Model

180

Figure 7. Load-Displace Cycles for 1/6-scale Models
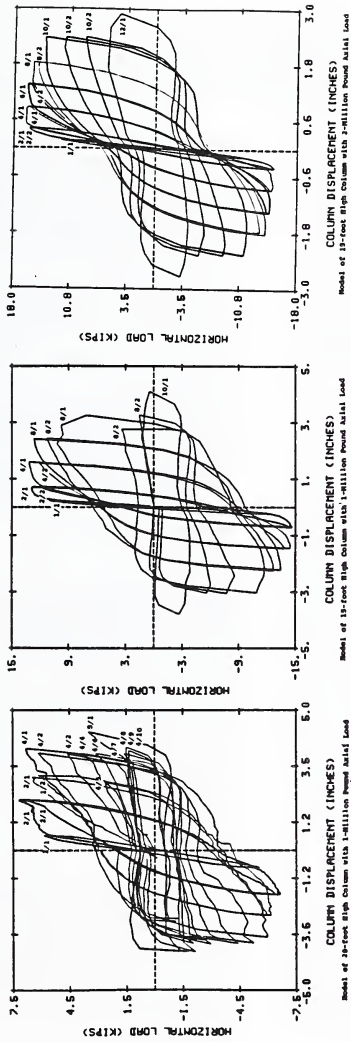
NOTATION:

MULTIPLE OF YIELD DISPLACEMENT/CYCLE NUMBER

181

OUTLINE OF MANUAL FOR REPAIR METHODS
FOR CIVIL ENGINEERING STRUCTURES
DAMAGED BY EARTHQUAKES

by

Toshio Iwasaki, Shigetoshi Kobayashi,
Takashi Uda, Yohtaroh Asai, Yasuyuki Koga,
Yasushi Sasaki, and Kazuhiko Kawashima[1]

ABSTRACT

The Ministry of Construction completed a 5-year research project entitled "Development of Repair Methods for Structures Damaged by Earthquakes," in March, 1986. The purposes of this project is to develop a guideline for inspection and measurement, assessment repair, and overall evaluation methods of repairing, for structures and natural slopes affected/damaged by earthquakes. This paper describes an outline of "Manual for Repair Methods for Civil Engineering Structures Damaged by Earthquakes," which is an important part of the results of the 5-year project conducted at the Public Works Research Institute and the Geographical Survey Institute, the Ministry of Construction.

1. INTRODUCTION

Located along the Pacific Seismic Region, Japan is one of the seismically disastrous countries in the world and has often suffered from large earthquakes. The recent advancement in structural and earthquake engineering, however, has enabled us to safely design and construct huge structures such as long-span bridges, underwater tunnels, high-rise buildings, etc. The research entitled "Development of New Seismic Design Methods for Buildings and Structures," was performed by the Ministry of Construction in 1972 through 1977 using lessons gained from the Tokachi-oki Earthquake of 1968 and the San Fernando Earthquake of 1971. This research has led to the advancement of Japanese seismic design codes.

As a result, catastrophic disasters due to entire collapses of buildings and structures have decreased and the numbers of human fatalities have become comparatively lower during recent large earthquakes. It is considered, however, that minor damages and partial failures may still break out in

future earthquakes, as observed in the Miyagiken-oki Earthquake of 1978 and the Nihon-kai-chubu Earthquake of 1983. In view of this fact, post-earthquake measures including the development of repair methods for partially damaged structures have become significant concerns.

The Ministry of Construction initiated a comprehensive research project, "Development of Repair Methods for Structures Damaged by Earthquakes," in April, 1981, and completed it in March, 1968. This project developed post-earthquake measures by providing procedures of inspection and measurement, assessment of damage extent, repair methods, and overall evaluation for repairing seismically damaged structures. This paper introduces an outline of "Manual for Repair Methods for Civil Engineering Structures Damaged by Earthquakes," an important part of the results.

In executing this project (between 1981 and 1985), the Technology Research Center for National Land Development established a Committee for Development of Repair Methods for Civil Engineering Structures Damaged by Earthquakes (Chairman: Prof. Shunzo Okamoto) to discuss and examine the Manual, with the commission from the Public Works Research Institute, the Ministry of Construction. At the same time, four Sub-Committees, namely Sub-Committee on Earth Works (Chairman: Prof. Kenji Ishihara), Sub-Committee on Bridge Structures (Chairman: Prof. Motohiko Hakuno), Sub-Committee on Underground Structures (Chairman: Prof. Tsuneo Katayama), and Sub-Committee on Evaluation Methods of Repair (Chairman: Prof. Keizaburo Kubo), were organized under the above Committee to prepare a draft Manual. Comprehensive experiments and investigations were conducted at the Public Works Research Institute and the Geographical Survey Institute, the Ministry of Construction. Research for each of the four Sub-Committees

[1]Public Works Research Institute, Ministry of Construction, Tsukuba, Japan

are listed in Table 1 in chronological order.

2. FLOW OF REPAIR AND RESTORATION

2.1 Flow of Repair and Restoration

Repair and restoration of seismically damaged civil engineering structures shall be correctly and immediately conducted because it significantly affects restoration activities of the public and stabilization of national life. Repair and restoration shall be done in accordance with the disaster plans by correctly understanding the whole damage, and by consulting and exchanging information with related organizations and authorities. Flow of repair and restoration after an earthquake may be classified into three stages as shown in Fig. 2-1. The fundamental aims of the three stages are the following;

1) First Stage of Repair and Restoration

Inspect damage with emphasis on the important and/or critical facilities as early as possible, and also decide the strategy for repair and restoration. When it is judged that a large secondary disaster is likely to develop, conduct appropriate treatment.

2) Second Stage of Repair and Restoration

Inspect damage of all facilities, and judge the necessity of temporal repair and

restoration based on the consideration for large possible secondary disaster, emergency for restoration, types and importance of the facilities, and the time required for initiation of permanent restoration. When it is judged that the temporal repair and restoration is required, conduct it by the most appropriate method considering priority and restoration level.

3) Third Stage of Repair and Restoration

Determine the level required for permanent repair and restoration based on importance, location of damage, damage degree, difficulties of repair and restoration, and future plan. Conduct permanent repair and restoration by considering the future development and restoration plans of the site.

2.2 Items to be Considered for Conducting Repair and Restoration

1) First Stage of Repair and Restoration

Conducting urgent damage inspection and urgent treatment in the first stage of repair and restoration; the following items should be considered.

a) Characteristics of main shock, aftershock, tsunami and weather

b) Characteristics of damage area

c) Potential for secondary disaster

d) Damage of other facilities

2) Second Stage of Repair and Restoration

Determine fundamental strategy for repair and restoration in the second stage; the following items should be considered.

a) Characteristics and degree of damage

b) Influence of secondary effect including secondary disaster

c) Possibility of occurrence of secondary effect including secondary disaster

d) Restrictions for conducting repair and restoration

Table 2-1 represents major items which should be taken into account for the second stage.

3) Third Stage of Repair and Restoration

Conduct permanent repair and restoration; the following items should be considered.

a) Future plan of the damaged area and facility

b) Possibility for sustaining damage in future

c) Adjustment with related other facilities

The repair and restoration level shall be determined based on the possible increase of function of damaged facility, possibility and appropriateness to restore the facility,

feasibility of repair and restoration, and required increase of seismic performance. Fig. 2-2 shows a flow chart to select permanent repair and restoration.

3. REPAIR AND RESTORATION TECHNIQUES FOR RIVER, COASTAL AND SABO FACILITIES

This manual describes the restoration and repair techniques for seismically damaged river, coastal and sabo facilities. River facilities include river dykes, water embankments, sluice gates, etc. Coastal facilities are coastal dykes, water embankments, detached breakwater, wave dissipation breakwaters, etc. Sabo facilities are concerned with erosion control works, landslide prevention works, steep slope collapse prevention works, and slope failures including enormous slope failures related to these facilities.

3.1 Fundamental Plan

1) Fundamental Plan for Restoration and Repairing of River, Coastal and Sabo Facilities

The fundamentals in the restoration of seismically damaged facilities is in temporarily protecting secondary disaster to be caused by rainfall, flood, high water, aftershock, etc. and executing permanent repair and restoration.

2) Flow of Repair and Restoration

Fig. 3.1 shows the flow chart from occurrence of an earthquake to investigation and end of the restoration. This flow can be roughly divided into three stages considering time, object and content. The first stage in the restoration is from the occurrence of an earthquake that caused damage to understanding the outline of damages, and executing some immediate treatment to prevent a secondary disaster. The duration is roughly one day, through it depends on the area and the amount of damage. Next, in the second stage the damage is investigated in detail and temporary repair and restoration is executed where required. Finally in the third stage permanent repair and restoration is executed to regain the original function of damaged facilities.

3) The First Stage of Repair and Restoration

In the first stage, the sites which need urgent treatment against possible secondary disaster, are selected and the strategy for the inspection and restoration thereafter is considered. The urgent treatment in this stage is generally limited in a slight action without essential construction.

4) The Second Stage of Repair and Restoration

In the second stage, the damage situation in the whole administration area is investigated in detail mainly by site reconnaissance taking a few days to a week. Based on investigation results, it is judged whether restoration should be conducted, and whether temporary repair and restoration is needed, that is, whether restoration is conducted under two stages of temporary and permanent repair and restoration, or under only one stage of permanent repair and restoration.

Moreover technical methods for temporary and permanent restoration works are selected and the approximate amount of temporary and permanent restoration works is estimated. Based on such judgement temporary restoration works are executed. For the judgement of the need for restoration works and temporary restoration works, the damage pattern and rank, the period until the permanent restoration is executed, and the expected magnitude of external load during the restoration period must be taken into account. When temporary repair and restoration works should be executed, damage scale, allowable construction period, appropriate restoration level, technical methods, extent of the works and priority order of construction sites are to determined.

5) The Third Stage of Repair and Restoration

In the third stage, to select and to design technical methods for permanent restoration works, and to clarify damage mechanism, several types of investigation, mainly ground investigation, are performed. Based on investigation results, permanent repair and restoration works are executed. For the judgement of the restoration level, the

selection of suitable technical methods and appropriate extent for restoration works, the original function of damaged facilities, the damage scale and mechanism, and the possibility of future damage must be taken into account.

3.2 Restoration of River Facilities

1) Damage Inspection and Judgement of River Facilities

The length of dykes and levees are particularly large among the river facilities, it is necessary to investigate their damages by car along a dyke administration road to grasp the outline and location of heavy damage. When restoration is needed a longitudinal and cross sectional survey is performed in addition to site reconnaissance.

In the site reconnaissance, the damage to the facilities is classified into several patterns and ranks through measuring the extent, width, depth and length of the crack, settlement, tilting, gap, etc. The classification is used for the judgement of restoration need and selection of technical restoration methods. The pattern and rank classification as in Table 3.1 (a) (b) is proposed concerning earthen river dykes.

2) Repair and Restoration Methods of River Facilities

Several technical restoration methods used in the second and the third stage are classified based on restoration purposes considering damage pattern. More over the fundamental idea for each method and the points to be considered in the designing and construction are arranged for the use of engineers. Repair and restoration methods for river dykes are classified and shown in Tables 3.2 and 3.3.

3.3 Repair and Restoration of Coastal Facilities

Coastal facilities may be damaged by tsunami, earthquake motion, combination of these and high water after the earthquake which induces secondary damage. As regard to damages due to tsunami, damage patters are classified by examining various damages of the previous tsunamis, and tsunami forces related to them are also classified. In the

inspection of the damage due to tsunami, not only the damage situation of respective facilities but also the survey of innundated area of tsunami is important.

In the restoration, most appropriate technical methods must be selected considering the degree of the damage, and the restoration to the original level.

3.4 Repair and Restoration of Sabo Facilities

When a failure of a natural slope occurs, a large amount of soil is piled on a river bed and after forms a damaged lake. When an inspection by a visual observation from ground or observation, videotape, and oblique photograph indicates that such dangers as a slope failure from cracks at nearby slopes, a secondary debris flow by a rainflow from the accumulated collapsed soil at a river bed and a break of dammed lake, warning and evacuation must be considered. Several viewpoints for the judgement in the investigation are arranged separating the cases into a mountain slope, a river bed, a landslide, and a steep slope.

The viewpoints of the measure level of temporary and permanent restoration works are described. The technical methods concerning those facilities are arranged and classified considering the feature of the phenomena, and the applicability of these methods is also summarized.

4. REPAIR AND RESTORATION TECHNIQUES FOR ROAD FACILITIES

4.1 Fundamental Strategy for Repair and Restoration of Road Facilities

Post-earthquake functions required for roads may consist of connectivity, reliability, mass transportation and safety as shown in Table 4.1. Although functions required for roads depend on the magnitude of earthquake damage and characteristics of the area damaged; they change principally in the sequence as connectivity - reliability - mass transportation - safety in accordance with time after the end of an earthquake. Therefore, it should be considered when determining the target of repair and restoration that post-earthquake demand required for roads change with time.

4.2 Urgent Damage Inspection and urgent
Treatment

Main targets for urgent damage inspection
are the following;

1) Is the road passable?

2) Investigate damage, especially critical
damage.

3) Investigate for possible large secondary
disaster.

Table 4-2 represents major check points.
The urgent damage inspection shall be
conducted in accordance with Fig. 4-1.

4.3 Repair and Restoration of Highway
Bridge

1) Temporal repair and restoration

Table 4-3 summarizes major damage patterns
of bridges observed in past earthquakes.

Among these damage patterns are pier
failures, failure of seat concrete, and
failure of main members of superstructure.
They are considered the most susceptible
which are most likely to to result in bridge
failure. Consequently, damage inspection
for temporal repair and restoration shall be
done for these three main items, and
subsequently conduct inspection in detail.

The damage degree for temporal repair and
restoration shall be judged based on the
result of damage inspection.

i) Damage Judgement in View of Bearing
Capacity

A : No Damage - No special damages are
detected

B : Slight Damage - Damaged, but not
influential for short term service

C : Medium Damage - Influential damage, but
structure may be used for short-term service
unless progress of damage due to aftershock
and live load is not developed

D : Critical Damage - Possible
superstructure failure is expected due to
damage

E : Falling-off - Falling-off
superstructure is developed

ii) Damage Judgement in View of Passable
Condition

a : No Damage - No special damages are
detected

b : Passable With Care - Damaged, but
passable with care

c : Unpassable - Badly damaged, and
unpassable

Fig. 4-2 is an example how damage judgement
in view of bearing capacity is made based on
simple informations detected from out-view
of the facility, i.e., this example
represents a check point for judging the
degree of damage to reinforced concrete pier
which sustained bending failure at its
base.

Fig. 4-3 represents a flow chart for
required traffic restriction as well as
temporal repair and restoration based on
damage judgement in view of both bearing
capacity and passable condition. Table 4-4
summarizes major temporal repair and
restoration methods.

2) Permanent Repair and Restoration

The damage degree for permanent repair and

restoration shall be judged based on damage
investigation as

A : No Damage - No damage or minor damage
which does not influence function of bridge
from the view of long-term service

B : Slight Damage - Damage which does not
affect bearing capacity

C : Medium Damage - Damage which affects
bearing capacity

D : Critical Damage - Damage which
significantly affects bearing capacity

For selecting the permanent repair and
restoration method, time required, cost,
workability, availability of construction
materials and out-view aspect after
repairing shall be considered. Table 4-5

represents permanent repair and restoration method of reinforced concrete pier which sustained bending failure at its base.

4.4 Road Embankments

This article discusses road embankments which include the road surface, the embankment, the slope of the embankment and the drainage facilities for surface water. The paper describes the purpose, content and method of the inspection and judgement in the second and third stage of restoration. The fundamental idea is the same as described in Chapter 3, River, coastal and Sabo facilities, Art. 3.1 Fundamental plan. To judge appropriate restoration levels, technical methods, aerial surveys and priority order for temporary restoration, is necessary to classify the damage pattern and rank which governs the serviceability and stability of the road embankment considering the location, depth, and magnitude of cracks and settlements of the road surface, embankment slope and slope protection works. The classification of the damage pattern and rank is proposed in Table 4.6 and Table 4.7. For temporary restoration it is necessary to consider the damage degree, the period length until the full restoration is completed and the expected function of the road during the restoration works.

The design level of permanent restoration works must be determined considering the previous functions of the facilities, the importance of the road, the influence of the damage, the past damage history, the future damage possibility, etc.

The purpose of technical methods for temporary restoration works can be classified into the protection of an embankment failure and the security of transportation. The purposes of these restoration works is classified into security of transportation function and the measure of stabilize embankments. The idea of the applicability of the methods and the attentions in design and instruction are summarized. Table 4.8 and 4.9 show the classification of restoration methods of road embankments.

4.5 Natural and Out Slope

This article addresses cut slopes, natural slopes, and slope protection structures concerning these slopes. The purpose, content and method of the investigation and judgement in the second and third stage in restoration is described as in road embankments in 4.4 In the investigation the collapsed soil and rock piled on the road surface from the slope and damage behavior and stability degree of the slope must be given attention. To judge the appropriate restoration level technical method, aerial extent, and priority order, it is necessary to classify the damage pattern and rank, which governs the serviceability of the road and the stability of the slope, through the damage behavior such as swelling, crack movements, etc. and geomorphological and geological condition of the slope. The need and procedure of the restoration must be judged considering the presence of a detour, importance of the road, damage degree and construction period. The classification of damage pattern and rank is proposed considering thickness, relative depth to a supporting ground, assess if falling rocks are predominant and the scale of the failure. The design level and appropriate technical method in the permanent restoration works must be determined considering the overall stability of the slope before damage, damage scale, damage mechanism, and the possibility of future damage.

The purpose of temporary restoration works can be classified into urgent security of transportation and protection of the secondary disaster. The purpose of permanent restoration works is classified by the types of restraint and protection phenomena. The idea of the applicability of methods and attentions in design and construction are summarized for use.

5. REPAIR AND RESTORATION TECHNIQUES FOR SEWAGE PIPELINES

5.1 Scope of Description

Part 4 of the Manual describes the repair and restoration techniques for sewage pipelines. Sewage facilities are composed

of pipelines, machinery, electrical, and building facilities. In these facilities, independently located facilities such as treatment station or pump station are comparatively easy to investigate or to repair their damage because most exist above ground surface. On the contrary, since pipeline facilities are buried beneath ground surfaces having long total length spreading in wide area, they tend to be damaged by the direct effect of ground deformation and furthermore, once they are damaged by earthquakes, it is not easy to determine the damaged portions, rate of damage and restoration of their function.

In this part of the manual, information describes the techniques for repairing the seismically damaged sewage works pipeline facilities.

Since the installation of modern sewage facilities has had a short history, no large-scale sewage facilities in each large cities has suffered from earthquake damage. However, since the Niigata earthquake in 1964, those sewage facilities in several cities with population between the tens to few hundred thousand had suffered damage due to several earthquakes.

Among these earthquakes, the experience obtained during repairing works after the Miyagiken-oki Earthquake (1978, M = 7.4) and the Nihonkai-chubu Earthquake (1983, M = 7.7) were used in developing the technical manual for repairing works described in this part of the manual.

Part 4 of this Manual is composed of two parts, one is the lessons learned from damaged sewage pipelines from past earthquakes and the other describes the repair and restore techniques for sewage pipelines damaged by earthquakes. The table of contents of Part 4 is included in the Appendix of this report, and the basic idea of the contents follows.

5.2 Damage of Sewage Pipelines Due to Past Earthquakes

Outline of damage of sewage facilities due to the past earthquakes since Niigata Earthquake is summarized in Table 5.1.

Intensity of seismic ground motion which starts to cause damage to sewage facilities is 4 in JMA scale. And there are lower bound in the earthquake magnitude varing with the epicentral distances which caused damage to sewage facilities as shown in Fig 5.1.

Weak ground, adjacency to the rigid structure such as manhole and shallow embedment tends to cause pipeline damage during earthquakes. In case of the occurrence of liquefaction of the ground where pipelines are buried, pipelines may suffer severe damage such as snaking deformation, uplift, uncoupling and/or shift at pipe joints and in some cases the pipelines may be filled up by the sand flowed in from surrounding liquefied layer.

Fig. 5.2 shows an example of damage caused by liquefaction.

From these damage experiences during past earthquakes, it is learned that there are sites where post-earthquake inspection should be carried out in detail and that there are several typical damage types of pipelines due to earthquakes.

These lessons are part of the Manual.

5.3 Inspection and Investigation Methods for Seismically Damaged Sewage Pipelines

After an earthquake, restoration work is implemented step by step in three stages which are urgent, temporal, and permanent repairing stages. At the first stage of repair and restoration, it is necessary to grasp whether the damage of sewage pipelines may or may not causes secondary disaster such as depression of road pavement or inundation from the result of urgent inspection to perform necessary treatment at the severely damaged portions. At this stage, it is important to perform the inspection at whole sites of facilities as soon as possible. The inspection is mainly implemented by observation from the ground surface without using equipment nor devices because of the shortage of time, equipments, and devices. The key during this inspection is to determine if there are deformations in ground surface at damage-prone sites as described in the previous section.

At the second and third stage of repair and restoration, it is possible to investigate the pipelines from inside of manholes or pipelines as the consumable time for investigation becomes longer. At these stages, it is necessary to clarify the locations of damaged portion, original structure and buried condition with their damage degree by the investigation so that temporal or permanent repair works can be carried out according to the damage condition.

The investigation method for this purpose is classified into two methods; one is the direct investigation method and the other is the indirect investigation method. The direct method is to investigate pipeline damage by observation or measurement directly using devices usually from inside of pipelines. When the inner diameter of pipeline is too small for the investigator to enter, it is effective to use a TV camera mounted on a skid or self-driving crawler to obtain information about pipeline damage.

The indirect method is used for investigation of pipeline damage when it is difficult to enter the pipelines. The generally used indirect method is to determine damage of pipeline judging from discontinuity of fluid flow. For this purpose of investigation, measurements are employed such as the observation of the leakage of poured water from manhole or leakage of smoke injected from manhole or measurement of water flow at two points in the pipe.

Applicability of these investigating methods are summarized in Table 5.2.

Considering the complex actions involved in earthquake investigations which are generally performed by many persons, it is effective to have given the unified standards for judgement of damage and for reporting format of the investigation results. Therefore in this manual, guideline for evaluating pipeline damage and reporting the damage are proposed.

5.4 Repairing Method of Sewage Pipeline Damage

When damage of pipeline facilities is found by the investigation, damage is classified

into one of three categories of repair works--to implement urgent-treatment, to repair temporally and to repair permanently according to the degree of functional damage and the possibility of causing secondary disaster to neighboring facilities.

The purpose of urgent treatment is to prevent secondary disaster by controlling the traffic at the depressed point of road or by pumping out the overflowed water.

The temporal repair is implemented to recover the pipeline function temporarily until the completion of permanent repair. This category of repair includes removing sand which flowed into the pipeline or manhole. High pressure cleaning mobile and vacuum cleaning mobile are used to remove sand.

The method for the permanent repair is selected from the investigation on the damage form and the damage degree.

When performing permanent repairs, one should consider the existing life of the pipeline system and if the pipeline system is expected to be expanded. Considering these conditions, basic policy of repair works to recover the facility function should be decided whether to repair pipelines as they were, original-level repairing, or to repair pipelines that result is a significant improvement to this performance. Following the basic policy, the repairing method should be selected by assessing the period of repair works and implementation circumstances besides the above mentioned damage form and damage degree.

Pipeline facilities are composed of various type of construction such as manhole, well, small diameter service pipe, large diameter pipe of trunk line, etc. The repairing methods for these structures are divided into two groups, 1) manhole and 2) pipe. They are shown in Table 5.3.

These repairing methods are classified into two groups by considering the purpose of works. One is to prevent leakage and the other is to recover the strength. The characteristics and applicability of each methods are introduced in the Manual.

Actual example of repair methods for various damage form and degree are shown in Table 5.4, which were employed to repair actual damage of pipelines caused by recent earthquakes.

6. SUMMARY

This paper introduces an outline of "Manual for Repair Methods for Civil Engineering Structures Damaged by Earthquakes." It is a result of the Ministry of Construction's project "Development of Repair Methods for Structures Damaged by Earthquakes" performed 1981 through 1986. Although this Manual is still a draft and is not a mandatory regulation, it can be used as a reference guideline when practical engineers conduct repair works for seismically damaged structures such as river engineering structures, coastal structures, highway structures, and sewer pipelines, etc.

7. ACKNOWLEDGMENTS

Table 1   Research Items of Four Sub-Committees

Fiscal Year	A. Sub-Committee on Earth Works	B. Sub-Committee on Bridge Structures	C. Sub-Committee on Underground Structures	D. Sub-Committee on Evaluation Methods of Repair
1981	a. Existing measurement technology b. Post-earthquake damages	a. Highway bridge damages due to the Niigata Earthquake and the Miyagi-ken-oki Earthquake	a. Damages to underground structures (water supply systems, sewer systems, gas facilities, electric supply systems, tele-communication systems)	
1982	a. Measurement technology necessitated for assessment of damage b. Damage assessment with use of photographs (PWRI, GSI) c. Damage assessment of earth structures d. Assessment of damage degree e. Brief survey on repair methods f. Planning of experiments and execution	a. Highway bridge damages due to the Urakawa-oki Earthquake and repair methods b. Flow chart of damage assessment c. Repair experiment of RC bridge piers with use of resin injection (preliminary tests) d. Examination of effectiveness of repair methods done for highway bridges damaged by the Miyagi-ken-oki Earthquake	a. Damage assessment, repair methods, and post-earthquake measures for sewer facilities in post earthquakes (Miyagi-ken-oki and San Fernando) b. Damage and repair methods for water gates and conduits c. Damage assessment (with use of micro TV cameras) and repair methods for sewer pipelines	
1983	a. Accuracy of measurement with use of oblique photographs b. Damage measurement with use of vibro-cone penetrometers c. Earthworks damages due to the Nihon-kai-chubu Earth-quake d. Frame work of damage degree assessment e. Experiments on repair methods (archoring method, sheet pile method)	a. Highway bridge damages and repair works due to the Nihon-kai-chubu Earthquake b. Damage assessment of RC single bridge pier clolumns (in case of fractural failue) c. Repair experiment of RC bridge piers with use of resin injection	a. Damage and repair for sewer facilities, water gates and con-duits due to the Nihon-kai-chubu Earthquake b. Damage and repair for tunnels due to the Izu-Ohshima Kinkai Earthquake c. Questionnaires on inspection, assessment, and repair for pipe-line damages d. Regulations for maintenance of common utility ducts	a. Intensity and frequency of aftershocks b. Post-earthquake measures in post earthquakes c. Laws and regulations regarding repair technology for seismic damages d. Periods of post-earthquake time to be considered for respective facilities e. Frame work of manual of repair methods for seismically dam-aged structures

Table 1 Continued

1984	a. Analysis of oblique photographs and its manual (GSI) b. Survey on tsunami damages c. Examination of damage degree assessment for earth structures (vibro-cone penetrometers) d. Experiments on repair methods (pile method, sheet pile method) e. Draft of manual of repair methods (mainly earth works)	a. Damage assessment of superstructures, bearing supports, and foundations of highway bridges b. Damage assessment of RC single bridge pier columns (in case of shear failure) c. Repair experiment of RC bridge piers with use of reinforced concrete d. Damage assessment of steel piers e. Repair experiments of steel piers f. Draft of manual of repair methods (mainly bridge structures)	a. Rationality of immediate assessment of damage to sewer facilities in post earthquakes (Nihon-kai-chubu) b. Relation between damage characteristics and repair methods for sewer facilities in Nihonkai-chubu Eq, and construction management for repair works c. Technology used in maintenance and management, and new technology d. Measures against damage to common utility ducts e. Draft of manual of repair methods (mainly sewer pipelines)	a. Post-earthquake measures in the Nagano-ken-seibu Earthquake (Priority of repair and evaluation items) b. Damage and repair methods in the Nagasaki Flood Disaster (Priority of repair and evaluation items) c. Draft of manual of repair methods (mainly common matters and repair evaluation methods)
1985	a. Damage assessment methods (earth works) b. Repair methods (retaining pile method, sheet pile method) c. Final version of manual of repair methods (mainly earth structures)	a. Examination of damage asessment methods (highway bridge structures) b. Repair experiment of RC piers by adding steel plates c. Final version of manual of repair methods (mainly bridge structures)	a. Application of damage assessment methods b. Application of repair methods c. Final version of manual of repair methods (mainly sewer pipelines)	a. Repair evaluation methods b. Final version of manual of repair methods (mainly common matters and repair evaluation methods)

Table 2.1 Items To Be Considered in Executing Temporal Repair and Restoration

Items	Examples
Damage Degree	○ Damage of facilities not only administrated but non-administrated ○ Functional damage of the area ○ Degree of degradation of structural performance of facilities ○ Stability of damaged structure ○ Influence of functional damage
Probability of Occurrence of Large Secondary Disaster	○ Factor depending on human activities ○ Factors depending on aftershock, tsunami, rain-fall etc.
Influence of Secondary Disaster	○ Area affected by secondary disaster ○ Damage potential such as number of residence inside the affected area
Restriction for Initiation of Temporal Repair and Restoration	○ Restriction from social aspect ○ Restriction from approach to the site ○ Restriction from materials, instrument and operaters ○ Adjustment with other restoration
Restriction for Completion of Temporal Repair and Restoration	○ Restriction from natural condition such that temporal repair and restoration be completed before rainy reason ○ Restriction from social condition
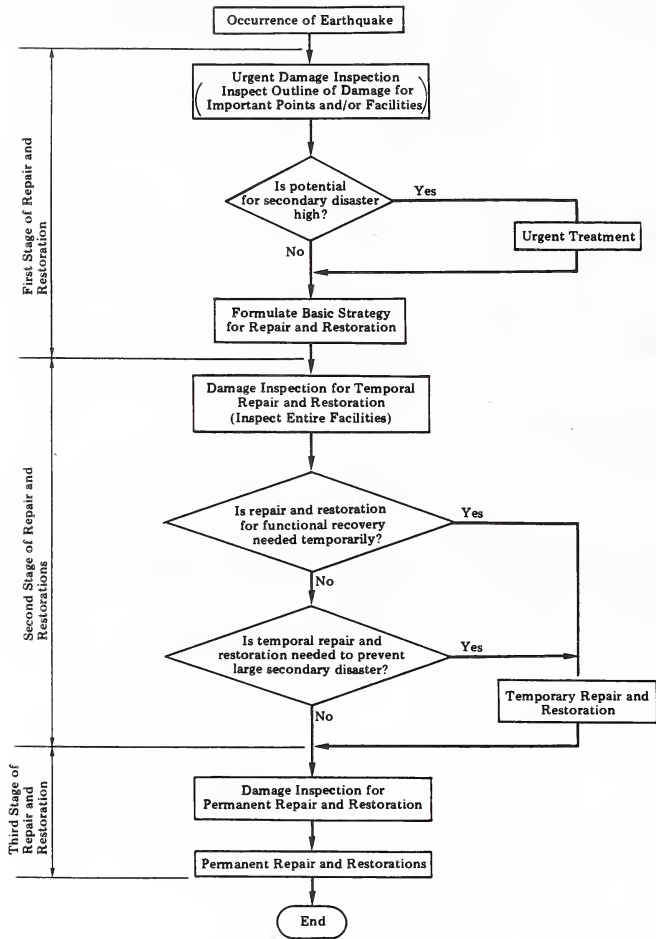
Fig. 2-1   Flow of Repair and Restoration of Seismically
Damaged Facilities
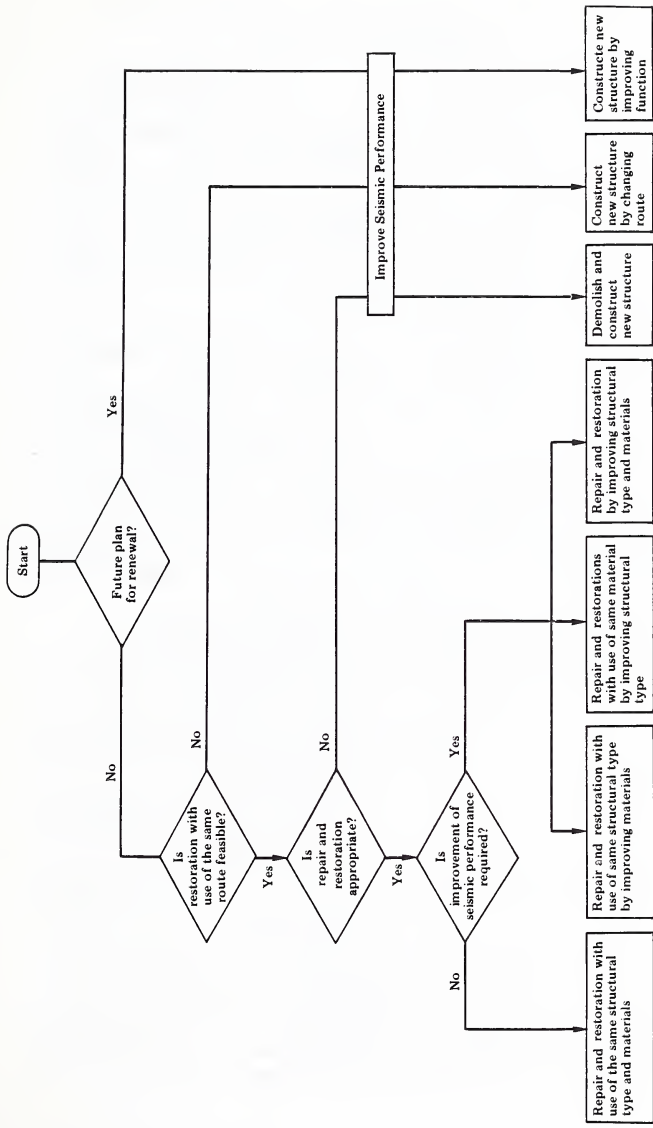
Fig. 2-2   Classification of Permanent Repair and Restoration

195

Table 3.1　Classification of Damage Pattern and Damage Rank of River Dyke

(a) Classification of Damage Pattern

Damage Pattern	Schematic Figure	Form of Damage
Type I		Slope failure, collapse, cracks, and faulting are limited at the dyke shoulder.
Type II		Sliding failure or longitudinal cracks and faulting reach the central part of dyke crown.
Type II'		Transversal cracks and faulting occur in the dyke.
Type III		Failure reaches to the subsoils, and the dyke does not show the original shape.
Type IV		Uniform settlement deforms the dyke with keeping the shape to a certain extent.
Type V		Settlement and cracks occur in dykes behind structures.
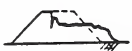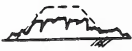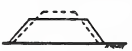
(b) Classification of Damage Rank

Damage Pattern	Damage Rank	Description of Damage Rank
I	β	$w \geq 15$ cm, or $\delta \geq 20$ cm
I	γ	$w < 15$ cm, and $\delta < 20$ cm
II	α	$w > 30$ cm, and $\delta > 50$ cm
II	β	$w \leq 30$ cm, or $\delta \leq 50$ cm, and not equals γ
II	γ	$w < 15$ cm, and $\delta < 20$ cm
II'	α	$w > 30$ cm and $\delta > 50$ cm
II'	β	$w \leq 30$ cm or $\delta \leq 50$ cm, and not equals γ
II'	γ	$w < 15$ cm and $\delta < 20$ cm
III	α	—
IV	α	$S \geq 100$ cm
IV	β	50 cm $\leq S < 100$ cm
IV	γ	$S < 50$ cm
V	α	$S \geq 50$ cm
V	β	20 cm $\leq S < 50$ cm
V	γ	$S < 20$ cm

w : Crack width, δ : faulting, S: settlement

196

Table 3.2 Temporary Restoration Technical Methods

Main Purpose	Methods
Prevention of Rainfall Seepage	San filling, Excavation and filling
Securing of Embankment Hight	Sand filling, Excavation and filling, Sand-bag piling, Temporary coffering
Prevention of Leak through Dyke	Sand filling, Sand-bag piling, Excavation and filling, Protection of front slope with good material, Sheet piling at front slope HWL
Prevention of Leak through Ground	Sheet piling at front slope toe for protection of ground water seepage
Erosion Protection Repair of Damaged Rivetment	Sand-bag piling, Concrete filling
Securing of Dyke Stability	Sand-bag' piling, Sheet piling for earth support, Counterweight fill
Repair of Crack and Gap of Concrete Dyke	Sand-bag piling, Concrete filling, Temporary coffering

Table 3.3 Permanent Restoration Technical Methods

Main Purpose	Methods
Securing of Dyke Resistance	Excavation and filling
Prevention of Leak through Dyke	do
Prevention of Leak through Ground	Sheet piling for protection of ground water seepage
Erosion Protection	Rivetment
Securing of Dyke Stability	Counter weight fill, Ground improvement
Securing of Concrete Dyke Stability	Reconstruction, retrofitting and repairing of retaining wall
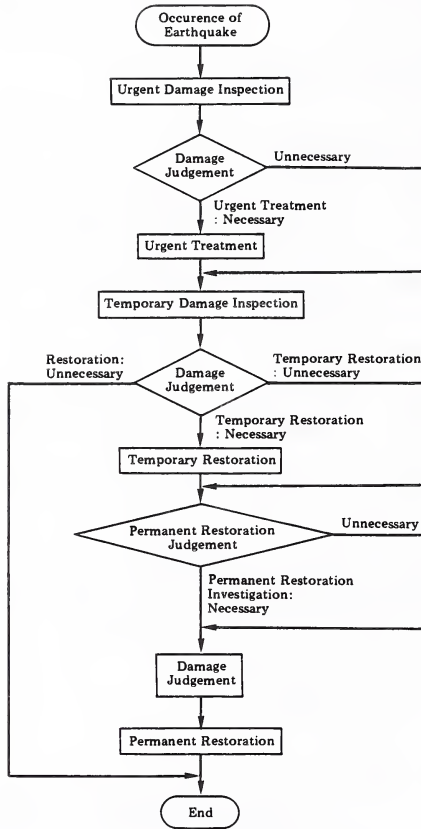
Fig. 3.1   Working Flow from Earthquake Occurence to Inspection
and Restoration

Table 4.1   Post-earthquake Function of Road

Situation	Definition
Connectivity	Situation to be connected from a specific point to a destination even if detour due to damage between the two points is needed.
Reliability	Situation able to go certainly to a destination within a desired time with safety tolerable after earthquake
Mass Trasportation	Situation able to serve for the same mass transportation as the road had although reliability is not guaranteed
Safety	Situation able to service for transportation with the same safety as the road had

Table 4.2 Major Check Points for Urgent Damage Inspection

Facilities				Check Point
Road Itself	Road	Flat Road		Large Subsidence of Road Surface
		Low ~ High Embankment		Large Subsidence of Road Surface, Large Subsidence and Failure of Embankment
		Natural and Cut Slope		Huge Failure of Slope, Large Fallen Stone on Road, Large Failure of Road
	Bridge	General		Fall-off of Bridge
		From the Surface		Slipping off and Gap of Hand Rail
				Sudden Change of Leveling
				Large Opening, Upheaval and Gap at Expansion Joint
		Side View	Superstructure	Sudden Change of Deformation and Leveling
			Substructure	Large Subsidence, Tilting, Large Cracks and Spalling-off of Concrete
	Tunnel			Large Slope Failure near Tunnel, Large Spalling-off of Covering Concrete
	Common Duct			Uplift to Ground Surface, Critical Damage of Storing Facilities
	Culvert and Underground Pedestrian Pass			Large Subsidence on Road Surface
	Pedestrian Bridge			Falling-off, Critical Failure of Pier
Other	Way-side Facilities			Collapse of Building on Road Secondary Disaster caused by Damage of Road Facilities
	Exclusive Use Facilities			Influence of Damage of Exclusive Use Facilities on Road
	Others			Critical Innaduation, Tsunami, Fire, etc.

Table 4.3 Damage Pattern of Bridges

- **Foundation**
  - Pile Foundation — 1 Failure of Pile Top, Residual Displacement
  - Direct and Caisson Foundation — 2 Residual Displacement
- **Sub-structure**
  - Pier
    - Reinforced Concrete Pier
      - 3 (At Bottom of Pier) Crack and Spalling-off of Concrete, Buckling and Cut of Reinforcing Bar, Tilting of Pier
      - 4 (At Cut-off Point) Crack and Spalling-off of Concrete, Buckling and Cut of Reinforcing Bar, Tilting of Pier
      - 5 (At Intermediate Height) Shear Crack and Spalling-off of Concrete, Exposure of Reinforcing Bar, Tilting of Pier
      - 6 (At Sudden Change Position of Cross Section and Construction Joint) Crack and Spalling-off of Concrete Buckling and Cut of Reinforcing Bar, Tilting of Pier
      - 7 (Flame Structure) Crack and Spalling off of Concrete, Buckling and Cut of Reinforcing Bar
    - Steel Pier — 8 Local Buckling, Cracks, Uneven Out-plane Residual Deformation, Tilting of Pier
  - Abutment — 9 Crack and Spalling-off of Concrete, Buckling and Cut of Reinforcing Bar, Tilting and Subsidence
- **Super-structure**
  - Concrete — 10 Crack and Failure around Support
  - Steel — 11 Residual Deformation and Failure of Members around Support
- **Bearing Support**
  - 12 Deformation and Failures of Support and Sole Plate
  - 13 Deformation and Failure of Stopper (Stopper of Upper Support, Side Block of Lower Support)
  - 14 Pulling-out, Blending and Cut of Anchor Bolt
  - 15 Looseness and Cut of Set Bolt (Pin and Roller Support)
  - 16 Pulling-out of Pin Cap, Cut of Cap (Pin and Roller Support)
  - 17 Pulling-out of Roller and Rocker (Roller and Rocker Support)
  - 18 Deformation and Failure of Up Lift Stopper for Preventing Up-lift
  - 19 Crack and Failure of Mortar under Support
  - 20 Crack and Failure of Seat Concrete
- **Expansion Joint**
  - 21 Falling-off of Joint Filler
  - 22 Failure of Face Plate
  - 23 Cut of Joint Rubber
  - 24 Failure of Anchor Concrete
  - 25 Opening and Contact of Joint
  - 26 Gap
- **Other** — 27 Failure of Hand-rail, Damper etc

201

Table 4.4   Major Temporal Repair and Restoration Methods for
Seismically Damaged Bridges

Purpose	Repair and Restoration Method
Prevention of Progress of Damage	a) Injection of Epoxy Regin b) Correction of Deformation, Installation of Stiffner or Temporal Members c) Installation of Falling-off Prevention Device d) Temporal Support of Superstructure
Safety for Transportation and Pedestrian	a) Covering Work on Road Surface including Expansion Joint b) Correction of Gap c) Temporal Repair of Hand Rail with Use of Steel Pipe

Table 4-5 Permanent Repair and Restoration of Reinforced Concrete Bridge Pier
Which Developed Bending Failure at Its Bottom

Level of Damage		Repair and Restoration Method	Design for Normal Load	Design by Ductility Analysis	
	Damage Patter Presented in Fig. 4-2			Yield Stage	Ultimate Stage
Before Yield of Reinforcing Bar	Before Stage 1	Injection of Epoxy Regin	Normal	Normal	Normal
		Covering by Reinforced Concrete	Hybrid	Hybrid	Hybrid
		Covering by Steel Plate	Hybrid	Hybrid	Hybrid
After Yield but Before Ultimate	Stage 2 and 3	Injection of Epoxy Regin	2/3 Es for Reinforcing Bar	2/3 Es for Reinforcing Bar	Normal
		Covering by Reinforced Concrete	Ignore Original Section	1/3 Es for Original Reinforcing Bar	Hybrid
		Covering by Steel Plate	Ignore Original Section	1/3 Es for Original Reinforcing Bar	Hybrid
After Ultimate	Stage 4, 5 and 6	Covering by Reinforced Concrete	Ignore Original Section	Ignore Original Section	Hybrid

Note   1) Normal: Usual design procedure in accordance with Design Specifications of Highway Bridge.

2) Hybrid: Original damaged section can be treated to work for load with new section.

Table 4-6 Classification of Damage Pattern and Damage Rank of
Road Embankment on Flat Ground

(a) Classification of Damage Pattern

Damage Pattern	Schematic Figure	Form of Damage
Type I		Slope failure, collapse, cracks and faulting are limited at the embankment shoulder.
Type II		Sliding failure, crack and faulting reach the central part of embankment crown.
Type III		Failure reaches to the subsoils, and the embankment does not show the original shape.
Type IV		Uniform settlement deforms the embankment with keeping the shape to a certain extent.
Type V		Settlement and cracks occur in in fills behind structures.
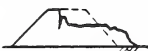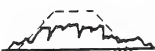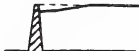
(b) Classification of Damage Rank

Damage Pattern	Damage Rank	Description of Damage Rank
I	β	$w \geqq 15$ cm, or $\delta \geqq 20$ cm
I	γ	$w < 15$ cm, and $\delta < 20$ cm
II	α	$w > 30$ cm, and $\delta > 50$ cm
II	β	$w \leqq 30$ cm, and $\delta \leqq 50$ cm
III	α	————
IV	β	$s \geqq 50$ cm
IV	γ	$s < 50$ cm
V	β	$s \geqq 20$ cm
V	γ	$s < 20$ cm

w : crack width, δ : faulting,   s : settlement

Table 4.7 Classification of Shape and Damage Rank of Road Embankments
on Inclined Ground

(a) Embankment Shape on Inclined Ground

Embankment of two sides slope	Embankment of one side slope	Cutting and Embankment

Damage ranks are specified as the damage pattern and rank of the embankments on inclined ground are almost coincidental.

(b) Classification of Damage Rank

Damage Rank	Description of Damage Rank
α	Embankment slides completely, and road surface and shoulder disappears.
β	Embankment deformation causes cracks and faulting of the road surface.
γ	No damage or hair crack on the road surface with no damage to the embankment.

Table 4.8 Temporary Restoration Technical Methods

Main Purpose	Methods
Protection of Embankment failure caused by Rainfall Seepage	Sand filling, Asphalt sealing, Sand-bag piling, Asphalt curb, Vinyl sheet, Temporary drainage
Protection of Embankment Failure caused by Traffic Load	Filling, Sand-bag piling, Sheet piling for Earth Support, Wooden pile
Securing of Traffic (Securing of Width of Road, Securing of Detour)	Filling, Paving, Sheet piling for Earth Support, Pier or Temporary Bridge, Detour
Securing of Traffic Safety (Treatment of Gap Settlement)	Run-off, Sand filling, Asphalt Patching

Table 4.9 Permanent Restoration Technical Methods

Treatment of Rainfall	Drainage ditch, Asphalt curb
Securing of Road Function	Filling, Paving, Asphalt sealing, Injecting asphalt into cave
Securing of Embankment Stability when Embankment is Problematic	Filling, Retaing wall, Grating Crib Works
Securing of Embankment Stability when Ground is Problematic	Counter weight fill, Ground Improvement, Underground Drainage, Sheet piling
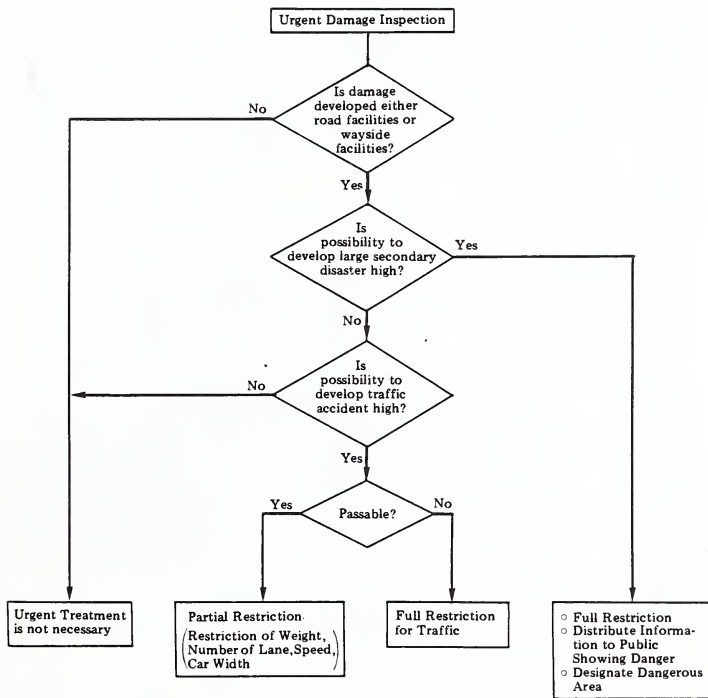
Fig. 4-1   Flow of Urgent Damage Inspection and Urgent Treatment

Observed Damage	1 Only Small Cracks	2 Diagonal Cracks (Not Penetrated)	3 Diagonal Cracks (Penetrated)	4 Spalling-off of Cover Concrete	5 Out-Plane Deformation of Reinforcing Bar	6 Cut of Reinforcing Bar and Tilting of Pier
Front View						
Side View						
Front View						
Side View						
Damage Degree	B: Slight Damage	B: Slight Damage	B: Slight Damage	C: Medium Damage	C: Medium Damage	D: Critical Damage
Residual Strength	P_u ($1.1 P_y \sim 1.3 P_y$)	P_u ($1.1 P_y \sim 1.3 P_y$)	$1.1 P_y$	$1.0 P_y$	less than P_y	less than P_y
Residual Deformability	70%	50%	30%	10%	0%	0%

Fig. 4-2   Damage Degree of Reinforced Concrete Pier which Sustained Bending Failure at Its Base

Damage Inspection for Temporal Repair and Restoration

Damage Judgement in view of Bearing Capacity

A. No Damage | B. Slight Damage | C. Medium Damage | D. Critical Damage | E. Falling off

Damage Judgement in view of Passage Condition

e. No Damage | b. Passable with Care | c. Unpassable

Total Judgement

A→a | B→a | A→b B→b C→a C→b | A→c B→c C→c

Permanent Repair and Restoration | Partial Restriction for Traffic | Full Restriction for Traffic | Full Restriction for Traffic | Full Restriction for Traffic

Damage Judgement in View of Bearing Capacity			
		A	B	C
Damage Judgement in View of Passage Condition	e	Not Needed	Not Needed	Partial Restriction
	b	Partial Restriction	Partial Restriction	Partial Restriction
	c	Full Restriction	Full Restriction	Full Restriction

Does Restrictions cause Critical Influence? — No / Yes

Does Restrictions cause Critical Influence? — No / Yes

Does Restrictions Cause Critical Influence? — No / Yes

Is Temporal Repair and Restoration feasible? — No / Yes

Is Temporal Repair and Restoration feasible? — No / Yes

Construction of Temporal Bridge

Watching for Progress of Damage

Temporal Repair and Restoration

Temporal Repair and Restoration (including Construction of Temporal Bridge)

Does Progress of Damage Occure?

Relief of Restriction | Relief of Restrictions | Relief of Restrictions

Consider Damage Degree as Critical

Go to D

Permanent Repair and Restoration

Fig. 4-3   Flow of Damage Judgement for Temporal Repair and Restoration of Bridge

209

Table 5.1   Summary of Damage of Sewage Facilities due to Major Past Earthquakes

Name of Earthquake, Magnitude (M), Date	Area	Seismic Intensity (JMA Scale) Agency	Damage to Sewerage System	
			Sewer Pipe System	Pumps and Treatment Plant
Kanto Earthquake;	Tokyo	VI	Damage to sewer pipe system was relatively small compared with those to other underground structures. Of total extension of 180 km, about 250 places mainly within boundary of downtown area and uptown area.	Minor damage to treatment plant was observed, but not so serious as to affect normal operation.
Niigata Earthquake; M = 7.9 June 16, 1964	Niigata City	V	Serious damage due to liquefaction was observed. About 70% of sewer pipe system of 35 km in total extension was damaged due to rising, collision between manholes and pipes, disalignment, etc. About 90% was damaged in monetary value.	Of 15 facilities, 11 facilities were damaged due to destruction of settling basins and rise of pumps caused by liquefaction. Functions of 8 facilities were lost due to serious structural damage.
Tokachi-oki Earthquake; M = 7.9 May 16, 1968	Hakodate City	V	Damage due to liquefaction was observed in reclaimed area. Rise was observed.	No damage.
	Muroran City	IV	Of 5.5 km in total extension, portion for 750 m laid in weak ground was settled.	Minor damages to two pumps were observed.

210

Table 5.1   Continued

Name of Earthquake, Magnitude (M), Date	Area	Seismic Intensity (JMA Scale)	Damage to Sewerage System	
			Sewer Pipe System	Pumps and Treat- ment Plant
Miyagi-ken-oki Earthquake; M = 7.4 June 12, 1978	Sendai City	V	Damages were observed in the area of weak ground and newly created housing site, but functions of sew- age system in these areas were main- tained. Of total ex- tension of about 690 km, branch pipe system for about 630 m in service was damaged. Serious damage was sufferred by sewer pipe system not in service at the time of earthquake.	Of 11 pumping equipments, func- tions of 9 pumps were lost due to power failure and damage to pressure pipe.
	Siogama City	V	Of total extension of about 27 km, portion for about 700 m laid under weak ground (reclaimed land) was damaged.	Damage was minor, and no failure of function was reported.
Nihon-kai- chubu Earth- quake; M = 7.7 May 26, 1983	Akita City	V	Damage to sewer pipe system due to liquefac- tion was reported. Of total extension of 286 km, relocated portion for 1.7 km and 93 manholes were damaged.	Damage due to to liquefaction was reported. For example, rise of puming equipment at Tsuchizaki and rainwater sediment- ation basin were observed.
	Noshiro City	V	Serious damage due to liquefaction was reported. Damage was observed as to re- located portion for about 8 km of total extension of 60 km.	No damage was ob- served as to dis- posal plant under construction.

211

Table 5.1 Continued

Name of Earthquake, Magnitude (M), Date	Area	Seismic Intensity (JMA Scale)	Damage to Water Supply System	
			Buried Pipe System	Pumps and Treat-ment Plant
San Fernando Earthquake; M = 6.6 Feb. 9, 1971	San Fernando Los An-geles	V — VI	Damage to pipe system considered to be caused by the change in the condition of ground resulting from dislocation of geologic formation was re-ported. About 3.8 km of pipe system in total was damaged (Re-stored later).	No serious damage was reported.

Table 5.2 Summary of Investigation Method

Investigation Method	Feature and Applicability
I. Direct Method	
I-1 Observation from Inside	Applicable to large-diameter pipe, man-hole and small-diameter pipe which is adjacent to man-hole
I-2 Direct Measurement from Inside	Method to measure the joint-opening, crack width; Applicable to large-diameter pipe and man-hole only; Necessary to shut off the flow and take measure to avoide the accident by noxious gas or lack of oxigen.
I-3 Survey	Survey of ground surface where pipe is burried or the level of man-hole tops; survey of pipe axis from inside by using special devices such as laser; Applicable to large and small diameter pipes, and possible to investigate precise dislocation.
I-4 Trailed TV Camera	Monitor the damage of pipe by using TV camera which is trailed inside the pipe; Measurable of the location of damage and degree of damage by video-sealer; Applicable to pipes which is larger than 20cm in diameter; There are two types of camera, one of which has only fore-sight and the other has fore-sight and lateral-sight.
I-5 Self-crawling TV Camera	Same as the "I-4 Trailed TV camera" but not necessary to traile the camera. Possible to investigate pipes inside from a man-hole.
I-6 Inserting TV Camera (for service pipe)	Monitor the damage of service pipe by TV camera which is mounted at the end of snakable rod and inserted from well; Applicable to larger pipe than 10cm in diameter.
I-7 Special Water-proof Camera	Moniter the damage of pipe by photo taken by the special water-proof camera; Applicable to large-diameter pipe and even to small-diameter pipe if the camera is mounted on skid or crawler of TV camera.
I-8 Observation or Measurement from Outside	Applicable to all kind of structures, but necessary of excavation for burried structure.
II Indirect Method	
II-1 Observation of Pipe Flow	Observe the pipe flow from man-holes; Applied for preliminary investigation.
II-2 Measurement of Pipe Flow	Measure the pipe flow by using flowmeter at man-hole.

Investigation Method	Feature and Applicability
II-3 Sounding by Rod	Know roughly the location of blockade of small-diameter pipe by insertion of rod.
II-4 Pumping Test between Man-holes	Know the inflow of groundwater by pumping out test of blocked section of pipe between man-holes.
II-5 Pumping Test at Joint or Crack	By using special device to block partially the water flow in the pipe at joint or crack, know the damage degree at joint or crack from the inflow of underground-water at this particular point.
II-6 Pore Water Test	Applicable to pipe of existing over ground water table; Block the pipe by packer, pore water into this block the section, measure the decrease of water table to know the damage.
II-7 Pneumatic Test and Smoke Test	Send smoke into pipe from man-hole, know the damage of pipe by observing the leakage of smoke; or send compressed air into the blocked section of pipe to know the damage from air-tightness.
II-8 Underground Rader	Know the location of burried pipe by underground rader.
II-9 Water-Quality Test	Know the possibility of inflow of groundwater by measurement of chlorine ion.

Table 5.3 Repairing Method of Damaged Pipe and Man-hole

(a) Pipes

	Damage Form	Method for Large-Diameter Pipe	Method for Small-Diameter Pipe
1	Breakage of Pipe	Concrete Coverage, Replacement	Replacement
2	Crack of Pipe	Resin Injection	Replacement
3	Breakage of Joint	Mortar Plug after V-form Cut	Improvement of Water-tightness by Chemical Grouting (Slight damage), Replacement (Heavy damage)
4	Dislocation at Joints	Sealing, V-form Cut and Mortar Plug, Bandage against Water Leake	Chemical Grouting using Packer, Replacement
5	Mixture of ① ~ ④	Concrete Lining, Replacement	Double Tubing, Replacement
6	Vertical Snaking	Improvement of the Lie by Special Chemical Grouting, Replacement	Improvement of the Lie by Special Chemical Grouting, Replacement
7	Lateral Snaking	Replacement if impossible to repair by ③~⑤	Replacement if impossible to repair by ②~⑤
8	Uplift, severe Dislocation of Pipe Axis	Replacement	Replacement

(b) Manholes

Damage Form	Repairing Method
Dislocation of Prefabricated Wall Joints	Replacement of Prefabricated Elements
Crack of Prefabricated Wall	Chemical Grouting (Slight Damage) Replacement of Damaged Elements (Heavy Damage)
Crack of Cast-in-place Wall	Resin Injection or Chemical Grouting (Slight Damage) Reconstruction (Heavy Damage)
Crack of Invert	Resin Injection (Slight Damage) Reconstruction (Heavy Damage)

Table 5.4 Actual Example of Repairing Method (Nihonkai-Chubu Earthquake)

Damaged Portion	Damage Form		Repairing Method
Pipes	Break		Replacement
	Leakage		Replacement
	Lateral Dislocation	More than 1/3 of Thickness of Pipe	Replacement
		Less than 1/3 of Thickness of Pipe	V-form Cut and Corkage
	Vertical Dislocation		Replacement
Cast-in-place Wall of Man-hole	Break		Reconstruction
	Crack		V-form Cut and Mortar Corkage
	Movement		Improvement of Invert
Prefabricated Wall of Man-hole	Break		Replacement
	Leakage		V-form Cut and Mortar Corkage
	Dislocation	Severe	Replacement with Excavation
		Slight	Improvement with Mortar
Invert of Man-hole	Break		Reconstruction
	Leakage		Improvement of Invert
	Crack		V-form Cut and Mortar Corkage
Service Pipe	Break		Replacement
	Projection		Improvement of

216

8.0
7.9 (The Tokachi-oki Earthquake)

Marginal line of lique-
faction given by
Kuribayashi and Tatsuoka

7.7 (The Nihonkai-chūbu Earthquake)

7.5 (The Niigata
7.4 Earthquake)
(The Miyagiken-oki Earthquake)

M (Magnitude in Richter Scale)

Monitary amount of
damage by unit length

○ 100,000 Yen/m
○ 10,000
○ 1,000
○ 100
∘ 10
• No damage

7.0

Marginal line of damage
to sewage system

50   100   200   500

Distance from Epicenter [km]

Fig. 5.1   Ground Motion to Cause Damage of Sewage System

(a) Uplift movement of manhole
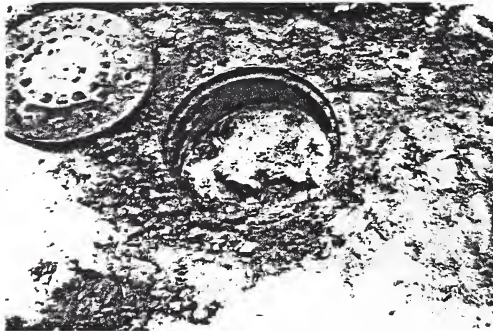
(b) Sand sedimentation in a manhole

Fig. 5.2 Damage of Sewage Facility due to the Ground Liquefaction

219

EFFECTS OF VERTICAL CONSTRUCTION JOINTS
ON THE DYNAMIC RESPONSE OF ARCH DAMS

BY

H. L Boggs[1] and J. R. Mays[2]

ABSTRACT

A finite element structural analysis of a double curvature thin arch dam which models the nonlinear behavior of the vertical contraction joints is presented. This static analysis represents a first step in a project at the Engineering and Research Center of the United States Bureau of Reclamation to examine the nonlinear behavior of a dam, foundation, and reservoir system subjected to seismic loading.

The "Curved Isoparametric Interface Surface Element," described in a technical note by Buragohain and Shah[1]* was coded and installed in the 1978 version of ADINA[2]. The element proved to be effective when a sufficiently fine mesh is used and when an appropriate integration order is used in the isoparametric element.

The static loading chosen to effect the opening of the vertical contraction joints consisted of gravity plus reservoir at approximately half height of dam plus a temperature increase of 24°F on the section of the dam above water level. To isolate the nonlinear effect of the joint opening, identical loads were applied to an identical model in which the vertical joints were allowed to carry tension.

The results of the two analyses are presented in the form of colored contour maps of arch and cantilever stresses on both the upstream and downstream faces of the dam. The inclusion of the nonlinear joint is clearly effective in reducing the calculated tensile arch stresses on the upstream face.

The load redistribution from the more flexible to the stiffer sections is more subtle but graphically shown as stresses in both the horizontal and vertical directions.

KEYWORDS: Arch Dam; Contraction Joints; Finite Element; Nonlinear Analyses

1. Introduction

1.1 General

Concrete arch dams during design are idealized as homogenous, isotropic and monolithic concrete structures. These assumptions are varied during construction but become actual after completion of construction. That is, during construction, concrete is placed as a heterogenous mixture of water, cement and aggregate which soon hardens into a homogenous mass. The material properties, not exactly equal in each direction, are sufficiently close to isotrophy. Current construction practices of horizontal lifts in vertical blocks, which when artificially and uniformally cooled to dissipate the heat of hydration, cause the blocks to shrink or contract thus separating the adjacent blocks at the formed joints. These contraction joints, which separate up to 3 mm, are soon filled with cement grout restoring the dam to a monolithic arch structure as was assumed in design. It is this last assumption during the life time of operation that may occassionally be violated.

---

[1]United States Bureau of Reclamation, Denver, Colorado 80225

[2]University of Colorado at Denver, Colorado 80202

*Refers to references at end of manuscript

1.2 Loads

Arch dams are designed to support a constant dead load, a fluctuating reservoir level, the annual concrete temperature variation from ambient air and reservoir temperature, ice and silt when appropriate. Except for some seasonal loads, most of these load combinations produce compression in the arches. Load combinations tending to produce tension in the arches occur when the cold winter temperatures act in concert with a full reservoir and late in the summer when the reservoir down from need and the temperture of the concrete is high. In this case the confining water pressure is insufficient to overcome expansion upstream from the increased concrete temperatures.

The potentially more severe but less frequent load is the earthquake which combines structural oscillations with the static loads occurring at that time. Generally the MCE (Maximum Credible Earthquake) events are sufficiently large to cause tension in both the horizontal and vertical directions on each face over the duration of the earthquake. The low reservoir/summer temperature load combination was selected to exercise the contraction joint finite element prior to analyzing the arch dam during an earthquake.

1.3 Analyses

Present analyses, using high speed large capacity digital computers, use linear elastic finite element modules. Throughout the duration, large tensions that develop are assumed not to cause structural distress to the dam. However, i the prototype, arch tension does not develop because of the formed cracks (contraction joints) and inherent weakness of the cement grout. At that instant in time, no horizontal tension exists, arch stiffness is reduced, and the loads are redistributed to the adjacent elements. This presumptive nonlinear action needs to be qualitatively and quantitatively determined. During an earthquake, relaxation of arch stiffness is expected to produce additional structural damping and mitigate the potential structural distress from the MCE.
At this time in the Bureau of Reclamation, a finite element has been developed to simulate the nonlinear no tension contraction joints. Initial analyses to confirm load redistribution were made with the aforementioned low reservoir and summer temperature load combination applied to two identical arch dams differing only in their ability to transmit tension across certain contraction joints. Following are descriptions of the finite element formulation, structural analyses, results and evaluation.

2. FINITE ELEMENT PROGRAM

2.1 General

The 1978 version of ADINA (Automatic Dynamic Incremental Nonlinear Analysis)[2] was selected as the finite element code to be used in this analysis. Modifications were made in the code to allow the addition of the interface element used to model the vertical contraction joints in the arch dam. A full Newton iteration procedure was added to complement the existing modified Newton procedure for maintaining control of equilibrium.

2.2 Interface Surface Element

The "Curved Isoparametric Interface Surface Element," described by D. N. Buragohain and V. L. Shah[1] in a technical note was coded and installed in ADINA. This element allows modeling of the contact surface between two adjacent blocks of a structure. The number of nodes on each surface of this element of zero thickness may vary from four to eight nodes. Two material models have been used. The first, which assumes both tension and compression capability, essentially glues the two construction blocks together. The second material models the compression but no tension property, characteristic of blocks which are in contact with each other. The stiffness of the joint element in the direction normal to the contact surfaces is controlled by the input material parameter K_n. So that significant overlapping does not

occur, K_n is chosen such that the stiffness of interface element is several orders of magnitude stiffer than the material in the adjacent blocks. Shear stiffness is controlled by a different material parameter K_s. The integration order and thus the number of integration points used in the normal isoparametric formulation of the element stiffness matrix is controlled by the input parameter INT.

The strain in the direction normal to the surface element as determined by the most recent displacement configuration of the nodes is examined at each integration point. If the strain indicates compression at this integration point, then full values of both K_n and K_s are used to evaluate the contribution to the element stiffness matrix from the integration point. If the sense of the strain indicates tension at the point, then both K_n and K_s are taken as zero. The element stiffness of the interface element is thus determined.

2.3 Verification of the Element

The verification and characteristics of the interface element were determined by modeling two cubes of material, one placed on the top of the other. The finite element model consisted of three-dimensional elements to model the cubes with the interface element used to model the contact region. A load was used such that theoretical results at the contact surface were known. Some sensitivity of integration order and relative values of stiffness were noted. Good results were achieved if the integration order of two or three and relative stiffness of no more than two orders of magnitude were used.

3. FINITE ELEMENT MODEL

3.1 Dam and Foundation

Morrow Point Dam was selected as the analytical model. This 465-foot-high double curvature arch dam has a minimum thickness of 12 feet, a maximum thickness of 75 feet, and a crest length of 720 feet. Twenty-noded three-dimensional finite elements were used to model the dam.

Two elements through the thickness of the dam resulted in 128 elements. The modulus of elasticity in the dam was taken as 3×10^6 lb/in^2. The foundation was extended approximately the height of the dam in all appropriate directions. Three-hundred twelve eight-noded elements having a deformation modulus of 2.5×10^6 lb/in^2 were used in the foundation. Morrow Point Dam, nearly symmetrical as constructed, was made symmetrical in this analytical exercise to reduce computational time and number of elements.

3.2 Vertical Construction Joints

Many vertical contraction joints exist in Morrow Point Dam. The finite element model, however, used only five vertical joints, placed symmetrically on the structure. A total of fifty 16-noded interface surface elements were used. Again, two elements were used through the thickness of the dam.

3.3 Complete Model

PATRAN[3], a commercially available computer code, was used to develop the geometry and finite element mesh for the complete model as shown on figure 1*. The resulting model consisted of 3,570 equations with a mean half band width of 202.

3.4 Loads

The final loads consisted of gravity, water elevation to approximately mid-height, and a positive temperature of 24°F throughout that section of the dam above the water level. This combination of loads was chosen to exercise the opening of the vertical contraction joints. The element birth option of ADINA was used to bring the five vertical contraction joints into existence after all loads were applied. This approximates reasonably well the order of block building and grouting of the contraction joints. The sequence of loading steps are: full gravity applied; vertical construction joints are born (grouted); waterload to 240-foot level applied; temperature of the dam above 240-foot elevation increases in 3°F increments until 24°F increase is

*See figures at end of manuscript

reached. The temperature load is uniform between faces and abutments.

4. PRESENTATION OF RESULTS

PATRAN[3] was used both as a preprocessor and a postprocessor for ADINA. PATRAN was used to prepare contours of equal stresses drawn separately on the upstream and downstream face of Morrow Point Dam. The two types of stress quantities drawn were the arch and the cantilever stresses on the faces. Both the arch and cantilever stresses are normal stresses lying in the plane tangent to the face of the dam at the point in question. The arch stress is in a horizontal plane while the cantilever stress is in a vertical radial plane. A complete translation code was written as an interface between ADINA and PATRAN. This translator resolved the global stresses into the arch and cantilever directions. The accumulative effect of this incremental loading on a linear elastic structure is graphically shown on figures 2 and 3 in the form of arch and cantilever stresses on the upstream face. Arch dam stresses from construction by vertical blocks are shown on figures 2a and 3a. Note on figure 3a the development of vertical tension near the crown cantilever where the downstream overhang is the greatest and simultaneously producing compression in the lower half where the undercutting is also greatest. This action with horizontal stiffness produces small horizontal stresses shown on figure 2a. The addition of water to mid-height alters the cantilever stresses little as shown on figure 3 but significantly increases the arch stresses as shown on figure 2. The incremental addition of temperature shows the rate of tension developed and magnitude of load necessary to produce sufficient arch tension for this analytical exercise. The significant change in arch and cantilever stresses are contained to the upper half of the dam where the loads are applied as seen on figures 2c-2f and 3c-3f. The effect on arch and cantilever stress from contraction joint opening, is shown on figures 4 and 5. To emphasize the dramatic load shift, the upstream and downstream arch and cantilever stresses are subdivided in the tension zones as shown on figures 6 and 7.

Evaluations

The load combination of low reservoir, summer temperatures and gravity produces a stress reversal to the normal reservoir/winter load combination that is of more concern to the designer. This latter load combination greatly influences the structural shape so as to cause compression in the arches, on both faces, base to crest, and between abutments. Similarly, most of the cantilevers are totally in compression, except small tensions along the abutment upstream face and the upper central section on the downstream face.

On figure 4a note the large area in tension caused by temperature expansion which completely disappears, figure 4b, if the interface element modeling the contraction joint is allowed to open rather than carry tension.

In the total elastic analysis, temperature expansion of the arches, causing tension on the upstream face, naturally causes compression on the downstream face. Relaxation of the arch stiffness via the contraction joint opening also tends to dissipate the downstream compression as shown in comparing figures 4c and 4d.

Temperature expansion also causes vertical tension in the cantilevers as is seen on figure 5a. Concurrently, the arch stiffness relaxation also reduces the cantilever restraint which simultaneously eliminates cantilever tension as is seen on figure 5b and compression on the downstream face, figures 5c and 5d.

The total dissipation of tension does not occur with the limited number of contraction joint elements as in this model as can be seen by recontouring the upstream stresses of the arches on figures 6a and 6b, and cantilevers, figures 7a and 7b. These small arch tensions would further dissipate by adding contraction joint elements in between the present configuration. All cantilever stresses in tension may not completely dissipate except in the upper part where no arch tension or compression exists. In other areas, the existence of arch compression signifies arch stiffness and does not relieve all cantilever tension.

225

Conclusions

Linear elastic analyses provide some measure of structural distress during load combinations producing tensile stresses such as during the low reservoir, summer temperature, and gravity load combination or as with an earthquake event. Reducing the element stiffness transfers sufficient load to adjacent structural components to mitigate or eliminate all tension.

Recommendation

Based on the load transfer following the reduced stiffness in elements not capable of tension, this finite element process is applicable to solving the in-elastic problem of arch dam structural response during an extreme seismic event.

REFERENCES

[1] Buragohain, D. N. and V. L. Shah, "Curved Isoparametric Interface Surface Element," Journal of the Structural Division, ASCE, Vol. 104, No. ST1, January 1978, pp. 205-209.

[2] "ADINA - A Finite Element Program for Automatic Dynamic Incremental Nonlinear Analysis," Report 82448-1 (Revised Dec. 1978), ADINA Engineering, December 1978.

[3] "PATRAN - G Users Guide", PDA Engineering, Santa Ana, CA.
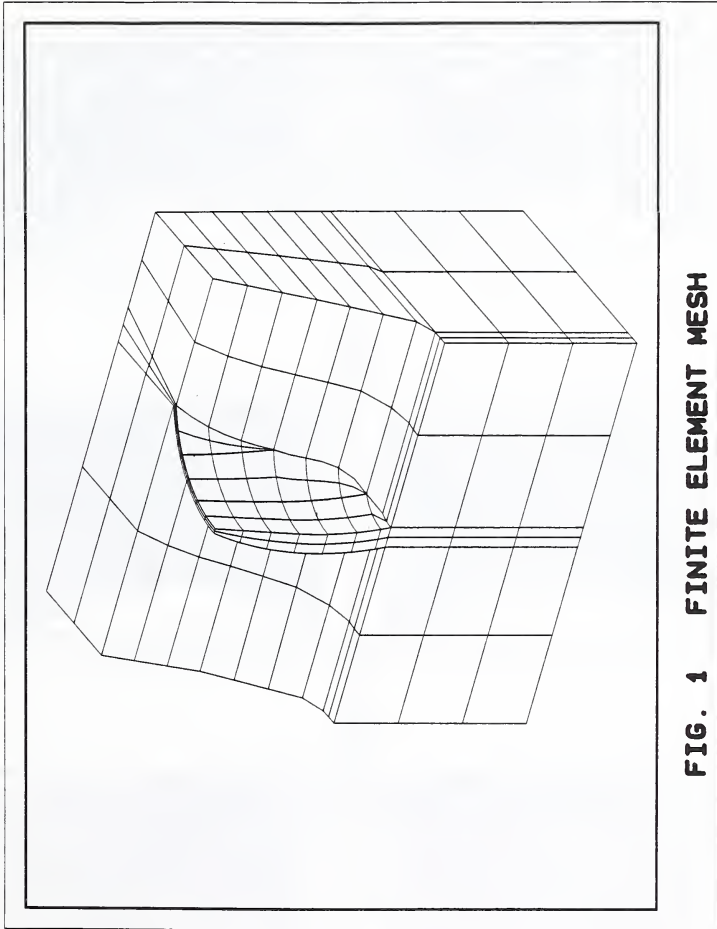
FIG. 1 FINITE ELEMENT MESH

FIG. 2 ARCH STRESSES (PSI) — UPSTREAM FACE

a GRAVITY LOAD ONLY

b GRAVITY + WATER

c GRAVITY + WATER + 6 F

d GRAVITY + WATER + 12 F

e GRAVITY + WATER + 18 F

f GRAVITY + WATER + 24 F
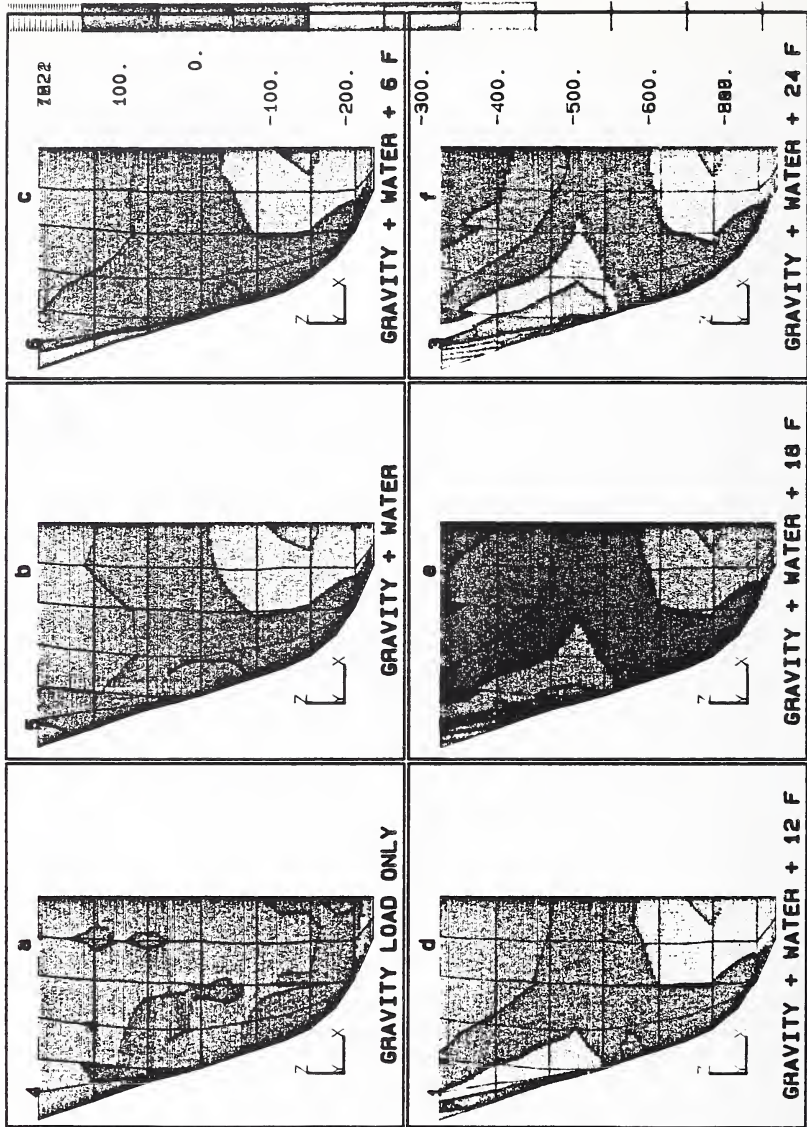
FIG. 3 CANTILEVER STRESSES (PSI) – UPSTREAM FACE

a GRAVITY LOAD ONLY

b GRAVITY + WATER

c GRAVITY + WATER + 6 F

d GRAVITY + WATER + 12 F

e GRAVITY + WATER + 18 F

f GRAVITY + WATER + 24 F

100.
0.
-100.
-200.
-300.
-400.
-500.
-600.

FIG. 4 ARCH STRESSES (PSI)

b - UPSTREAM FACE

243.
100.
0.
-100.
-200.

NO TENSION IN CONTRACTION JOINTS

d - DOWNSTREAM FACE

-300.
-400.
-500.
-600.
-798.

NO TENSION IN CONTRACTION JOINTS

a - UPSTREAM FACE

TENSION IN CONTRACTION JOINTS

c - DOWNSTREAM FACE
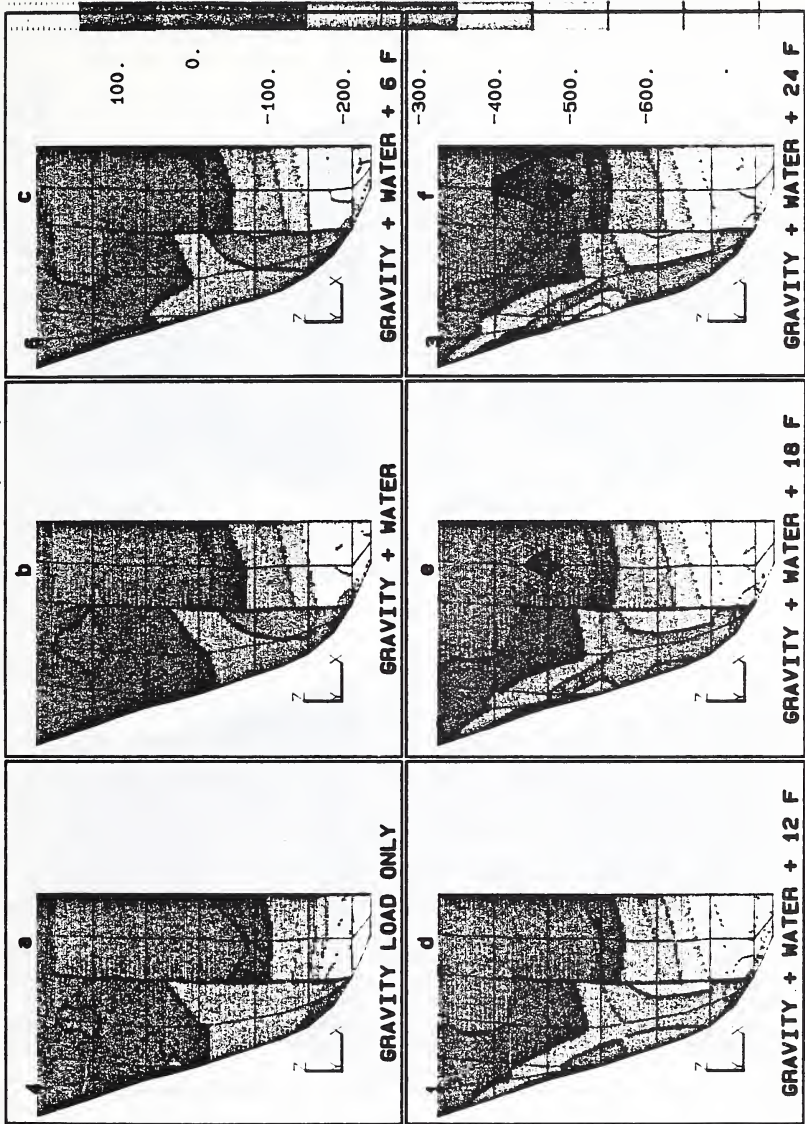
TENSION IN CONTRACTION JOINTS
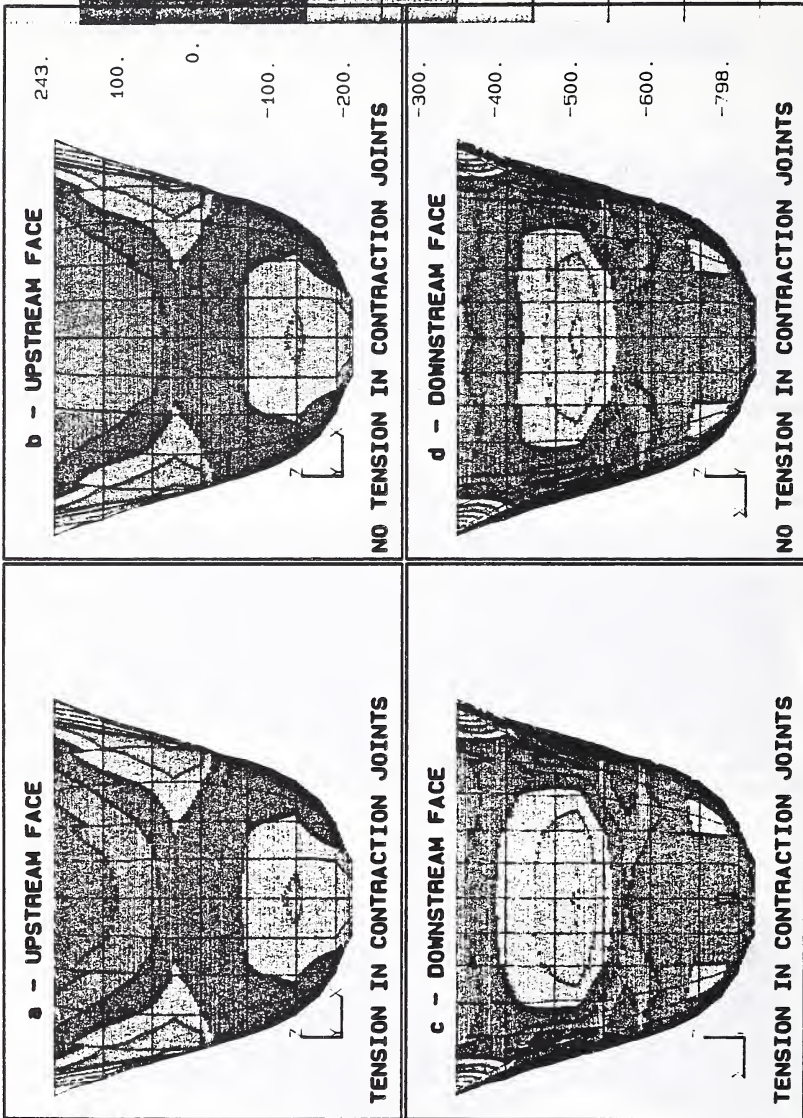
FIG. 5 CANTILEVER STRESSES (PSI)

a – UPSTREAM FACE

TENSION IN CONTRACTION JOINTS

b – UPSTREAM FACE

NO TENSION IN CONTRACTION JOINTS

c – DOWNSTREAM FACE
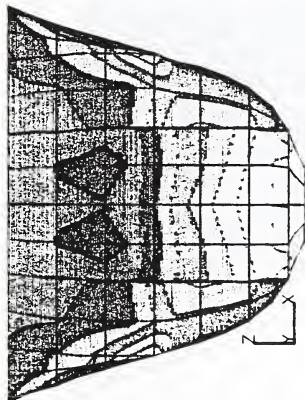
TENSION IN CONTRACTION JOINTS
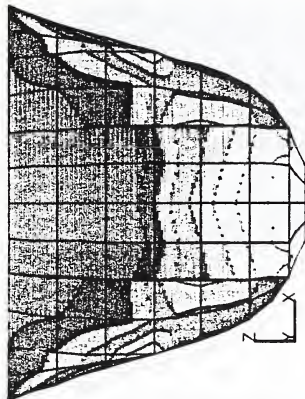
d – DOWNSTREAM FACE

NO TENSION IN CONTRACTION JOINTS

127.
100.
0.
-100.
-200.
-300.
-400.
-500.
-600.
-842.
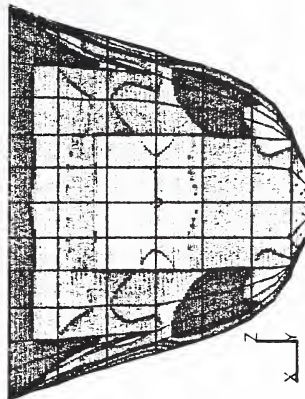
231

FIG. 6 ARCH STRESSES (PSI)

a - UPSTREAM FACE

b - UPSTREAM FACE

TENSION IN CONTRACTION JOINTS

NO TENSION IN CONTRACTION JOINTS

243.
150.
100.
50.0
0.
-50.0
-100.
-150.
-200.
-798.

FIG. 7 CANTILEVER STRESSES (PSI)

a – UPSTREAM FACE

TENSION IN CONTRACTION JOINTS

b – UPSTREAM FACE

NO TENSION IN CONTRACTION JOINTS

127.
150.
100.
50.0
0.
-50.0
-100.
-150.
-200.
-842.
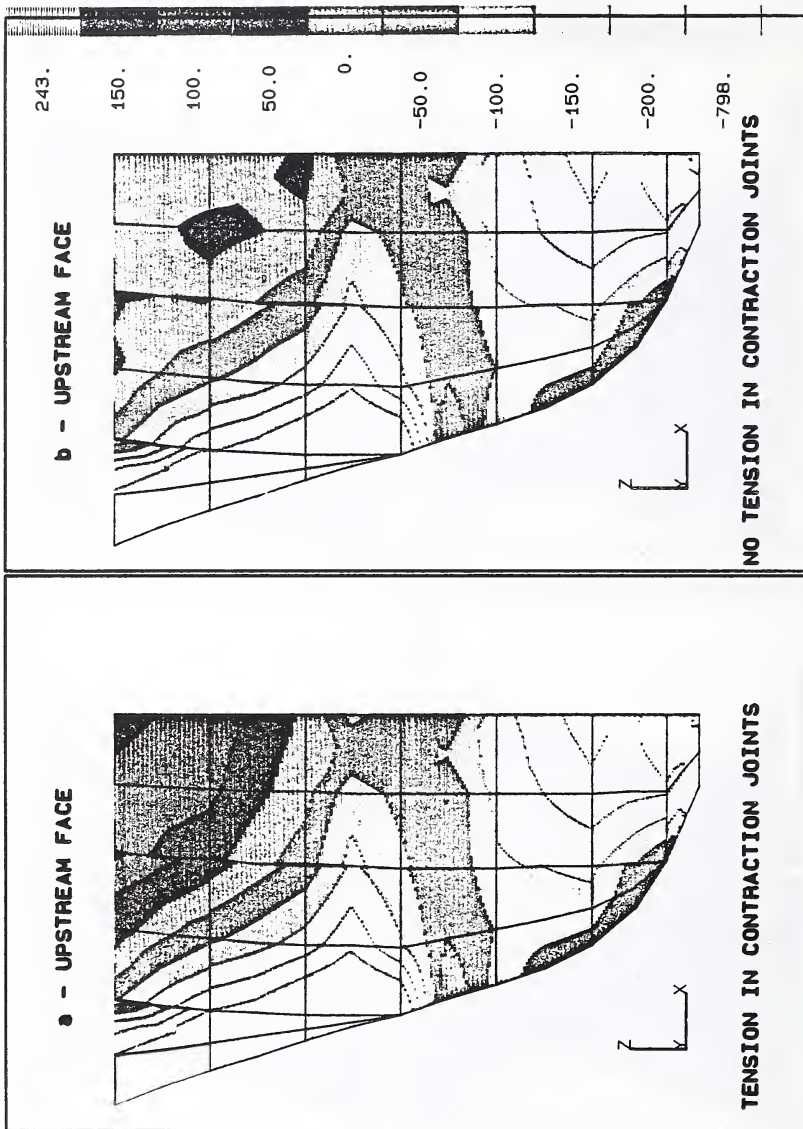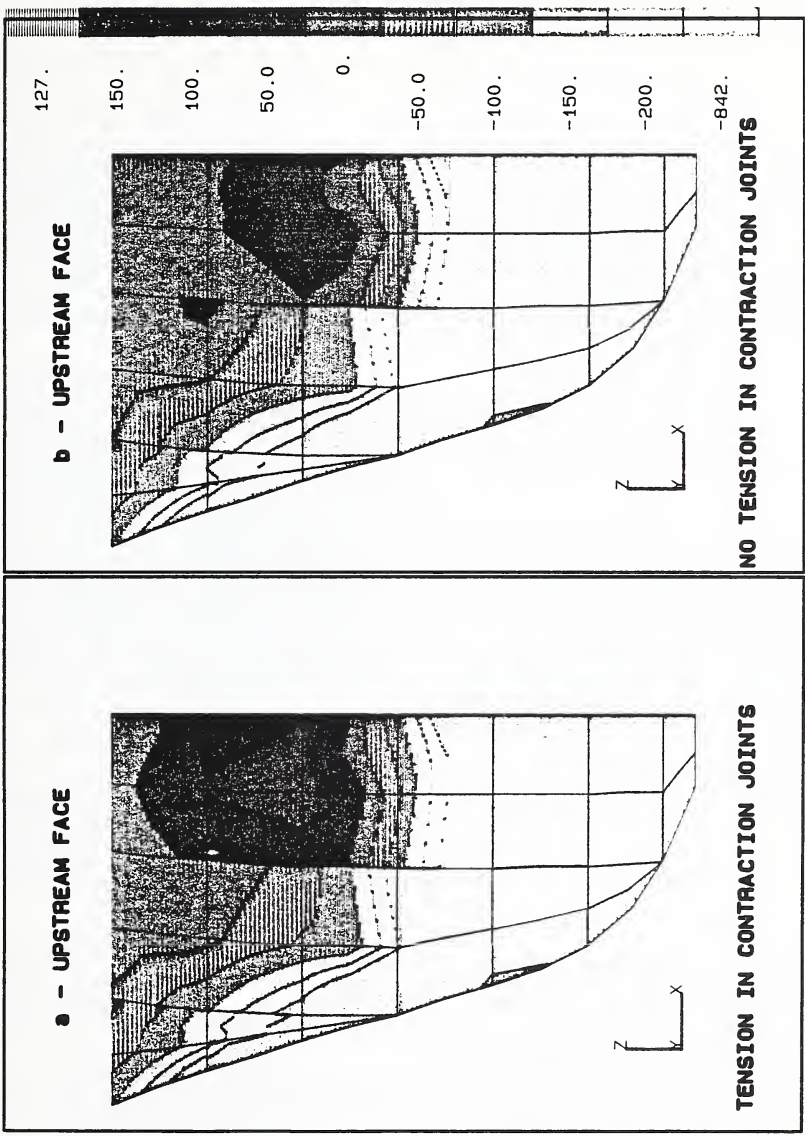
DECISION ANALYSIS FOR EMBANKMENT DAMS
UNDER SEISMIC LOAD
BY

T. A. Luebke[1]

ABSTRACT

Decision analysis may be defined as a process of systematic evaluation of alternative solutions to a problem where the decision is made under uncertainty. This method of analysis readily applies to seismic design and analysis of embankment dams because both the seismic event and response of the embankment are uncertain. The decision analysis does not replace the design process, but instead presents the risk and consequences of dam failure due to seismic loading for the various alternatives examined. The analysis is made up of two parts: (1) the hazard assessment and (2) the risk cost analysis of alternatives.

This paper presents a framework for decision analysis that may be applied to embankment dams in seismic areas. Simplified methods are described to determine the seismic risk of dam failure. Considerations in the determination of recurrence intervals for seismic events are briefly discussed. However, the paper concentrates on the application of the recurrence estimates in evaluating risk, and on the determination of potential for loss of life and adverse economic consequences. An example problem is provided to illustrate the use of decision analysis and the presentation of data for decisionmaking.

KEYWORDS: Dams; Hazard; Risk; Seismic

1. INTRODUCTION

Decisionmaking in situations where the outcome is uncertain is a difficult task to verify by quantitative procedures. Such decisions must be made for selecting appropriate dam designs in seismically active areas of the world. Our current understanding of the processes by which seismic activity occurs is somewhat limited, as is our ability to accurately predict the timing and magnitude of the next seismic event at a given source. Moreover, our ability to confidently predict the response of dam structures to seismic events is derived from empirical data. Although earthquakes occur on a relatively frequent basis around the world, our knowledge of how dams react to seismic events is generated from a relatively small data base. Given these significant uncertainties, dams located in seismic regions must be designed such that they will not represent a significant hazard to the public, while maintaining fiscal responsibility.

This paper presents a framework for decision analysis which provides a means for displaying uncertainty in a manner which allows an informed decision. The decision analysis does not provide answers, only information to be considered. The procedures are most useful when evaluating complicated problems where solutions are not obvious and justification for a particular course of action is required. A brief description of the decision analysis framework is provided, followed by an example problem to illustrate its use. The scope of the example problem is limited to seismic-related hazards and risks associated with a particular embankment dam.

2. DECISION ANALYSIS FRAMEWORK

The decision analysis framework consists of an organized investigation and presentation of alternatives for accepting or reducing potentially adverse consequences and/or risk associated with system failure or emergency operation. A general framework (reference 1) is depicted on Fig. 1.

The framework can be condensed and more easily understood by first identifying the two major phases in the formulation of information in this analysis: (1) hazard assessment and (2) risk cost analysis of alternatives.

The hazard assessment is performed to evaluate the consequences of dam failure and/or emergency operation (e.g., loss

---

[1] Bureau of Reclamation, PO Box 25007, Denver, Colorado 80225

of life, economic loss, environmental impact, etc.) for a given dam safety problem. This information is used to establish the minimum acceptable level of protection required, if the dam safety problem involves an existing structure. New structures generally will be designed to accommodate the maximum loading condition without catastrophic failure [e.g., PMF (probable maximum flood), MCE (maximum credible earthquake)]. The hazard assessment may often be effective in identifying alternatives. If an appropriate solution to the problem is identified and adequately justified at this stage, then a risk cost estimate for the existing condition and for various alternatives would not be required.

Once the minimum acceptable level of loading has been identified (based on appropriate input from the decision-maker), alternative courses of action are developed and may be compared using risk cost analysis of the adverse consequences (identified in the hazard assessment), the likelihood of adverse consequences, and the cost and benefits of corrective action. Depending on the results of the hazard assessment, the risk cost analysis may also be performed to determine whether a greater level of protection is economically justifiable.

The results of the hazard assessment and any required risk cost analysis form the basis for presenting information to the decisionmaker so that the site-specific conditions and options are well understood.

The decision analysis framework may be broken down into a stepwise process, with presentation of results for management decisions at appropriate points during the process. The framework is illustrated by an example problem in the following section of this paper.

3. EXAMPLE

3.1 Problem Definition

The example problem provided in this paper is partially based on data obtained from an existing dam. The analyses and judgments presented in this paper are solely for the purposes of illustrating the application of decision analysis for embankment dams under seismic load, and do not reflect final analytic results nor final judgments made.

The problem analyzed in this paper is the dam's ability to withstand potential seismic loading. If the dam is found to be subject to failure under seismic loading, alternative courses of action must be examined.

3.2. Pertinent Site Conditions

A description of pertinent site conditions is provided to summarize information which has a bearing on the analytic results. The example dam is located in the western United States. The reservoir serves as a link in cross-basin transfer of water along the south slope of the Uintah Mountains between two existing reservoirs. Dam construction was completed in 1975. Initial filling has taken place.

Major features include the dam embankment, spillway, and outlet works. The embankment is a zoned earthfill structure with a maximum height above streambed of approximately 130 feet and a crest length of 1,600 feet. The spillway is a box-type conduit structure with an uncontrolled ogee crest. Discharge capacity of the spillway at the maximum water surface is 850 ft^3/s. The outlet works is a cut-and-cover conduit structure. A steel pipe branch from the downstream control structure connects the outlet works to a pipeline feeding a nearby reservoir. The outlet works is also capable of discharging through a stilling basin into a creek. Discharge capacity of the outlet works at the top of active conservation is 5,430 ft^3/s.

Operating and failure discharges are released into the creek, which drops 1,400 feet over 21 river miles before its junction with a second creek, which descends 200 feet over 4 river miles to the main river. From this confluence, the river drops another 400 feet before entering a nearby reservoir 15 river miles downstream.

A review of construction records indicated that the embankment is a densely compacted fill with a clayey core and granular shell materials. A cutoff trench was provided to bedrock. However, geologic data indicated that alluvial deposits up to 20 feet in thickness remain under the shells of the embankment. The alluvial deposits consist of heterogeneous layers of silty to clayey fine sand, sand and gravel, organic silty sand, and peat. The finer grained materials (lacustrine deposits) were deposited in oxbows, ponds, and

marshes and are laterally discontinuous. The small amount of SPT (standard penetration test) results (all from preconstruction drilling) reported N values of 4 to 18 blows per foot. The upper portion of the foundation material was largely removed (including the peat and loose fine-grained material). However, some materials with low SPT blow counts still remain. The geologic sections indicated a general discontinuity of the lacustrine deposits and dominance of the gravelly streamfill deposits on some sections, but continuity of several hundred feet of the lacustrine deposits were reflected on other sections.

3.3 Potential Loading Conditions

Seismotectonic considerations for the example dam are summarized in Table 1. The table indicates seven distinct sources for MCE's between magnitude 6.5 and 7.5 within 90 km of the dam. Fig. 2 indicates the relationship of bedrock peak horizontal ground acceleration versus horizontal distance from source of energy release adapted from reference 2. The earthquake magnitude ranges from Table 1 are plotted onto Fig. 2, indicating that mean peak horizontal bedrock accelerations of between 0.10 and approximately 0.55 may occur at the damsite. Since it is known that the dam is in direct contact with bedrock at the cutoff trench and the alluvial fill under the shells is relatively shallow, the bedrock motion is not expected to attenuate prior to its loading the base of the dam.

It is important to note that the final seismotectonic considerations reported that surface faulting at the damsite and reservoir-induced seismicity were not considered to be potential hazards. Reservoir seiche waves and landslide-induced water waves were not felt to be significant issues.

3.4. System Response

An empirical assessment of the capability of the MCE's provided in Table 1 to produce liquefaction in the foundation soils (assuming they are liquefiable) can be made by plotting the MCE's for each source onto Fig. 3. The dashed lines on Fig. 3 represent the threshold boundary for earthquakes with the potential for producing liquefaction in liquefiable materials based on historical data. Although specific values are not available, it is implied that the lower boundary represents materials very susceptible to liquefaction. The fault

sources are plotted on the figure based on epicentral distance for the general range of earthquake magnitudes that fall above the line (capable of producing liquefaction). Note that each of the identified seismic sources are empirically capable of producing liquefaction.

It is assumed, for purposes of illustration in this paper, that more detailed analytic studies have been performed and support the findings of the empirical assessment. It is also assumed that liquefaction of the alluvial materials beneath the embankment shells will result in dam failure. The next step is to determine system response in terms of downstream flooding due to dam failure.

The active conservation pool for the example reservoir is expected to remain relatively constant, within 4 feet of top of active conservation at all times. Dam breach studies indicate that peak discharge resulting from dam failure will be 300,000 to 400,000 ft^3/s. This discharge will be reached within 30 minutes of the triggering seismic event. Inundation maps are prepared to depict the downstream areas affected by dam failure. Expected depth and velocity of the failure flood are considered. It is determined that the failure flood inflow to the downstream reservoir, located approximately 40 miles downstream of the example dam, can be completely stored.

3.5 Hazard Assessment

The hazard assessment is performed to evaluate the consequences of dam failure in terms of loss of life, economic impact, environmental impact, and other losses.

Buildings within the potential dam failure inundation area between the example dam and the downstream reservoir have been identified as follows:

Building	Location
1 residence	8 river miles below dam
5 residences and 2 commercial buildings	12 to 13 river miles below dam, near Highway 40
20 residences	20 to 40 river miles below dam

The total permanent resident population in the dam failure inundation areas has been estimated at around 80 to 100

people depending on the time of year. A few of the residences are vacation-type dwellings. However, during the late spring and summer, these units would probably be occupied and so a permanent residence population at risk of 100 was assumed under worst case conditions.

During the late spring and summer months, the local creeks and rivers provide recreational fishing and camping. There are, however, no established (State, Federal, private, etc.) campgrounds along the 40-mile stream course between the existing dam and the downstream reservoir.

Based on cursory field reconnaissance, it has been estimated that during the late spring and summer months the number of transitory people in the dam failure flood inundation area would range from 10 to 50 people for fishing and camping, and 5 to 10 people for other miscellaneous purposes during the daytime. At night it was estimated that there would be 5 to 20 campers in the flood plain area and 0 to 5 people traveling through the area for other miscellaneous reasons. It may be assumed that the transitory population would be more or less uniformly distributed along the flood reach, except for the undeveloped and relatively inaccessible reach 13 to 20 river miles below the dam, and that the spatial distribution of the resident population at risk would be according to structure locations, as presented in Table 2. The table indicates that the population at risk from dam failure is relatively small. However, the population is spread out over a large geographic area. Further, the transitory population cannot be easily contacted (e.g., by telephone) in the event of a failure.

Table 3 provides estimates of the time required for dam failure floodflow to reach each of the downstream areas.

The estimate of warning time available for the population at risk is based on the detection and warning capabilities of the system. A dam tender will not be onsite but the system will be operated and monitored (reservoir level and downstream discharge) by remote control on a 24-hour basis. The times at which people within the various river reaches are likely to be warned, both by telephone and in person, are shown in Table 4. The table also shows the number of residents and transitory visitors in each river reach, and when the failure flood arrives at each section. It was assumed that 30 minutes would be

required to detect the drop in reservoir level resulting from a sudden dam failure. At that point, monitoring officials would notify local authorities and begin telephoning residents in the upper reaches of the river.

It is estimated that 15 minutes would be required to notify local officials and begin warning residents by telephone of the probable dam failure flood. As shown in Table 4, it is estimated that neither telephone nor face-to-face warning can reach the population at risk before the failure flood arrived, except for river sections E, F, G, and H, where warnings can reach the residents shortly before the failure flood.

The probable loss of life resulting from downstream flooding can be estimated using the procedures described in reference 1. The reference includes an analysis of 24 historic dam failures and flash floods. These case studies have been evaluated to determine the relationship between the number of persons at risk, the amount of warning time available, and the number of fatalities resulting.

To estimate the loss of life, the population at risk is first divided into two groups: those people receiving adequate warning time to evacuate the flood area and inadequate warning time to evacuate the flood area. Based on empirical data from flash floods and dam failures, this break appears to be between those persons receiving more than and those receiving less than 90 minutes of warning. Separate predictive equations, shown below, may then be used to provide an initial (not site-specific) estimate of loss of life for these two subpopulations.

Loss of life, given 90 minutes or more warning = 0.0002 x (population at risk)

Loss of life, given less than 90 minutes warning = (population at risk)$^{0.6}$

These equations predict the loss of life that is likely to occur, based on historical averages, for a given population size and either adequate or insufficient warning time. Note that for the situation with less than 90 minutes warning the equation projects less than 100 percent fatalities. This is because historically many individuals at risk receive some minimal warning, while other persons detect the flooding on their own, and evacuate, while still

others are able to survive the
floodwaters.

These equations can be used to make
"baseline" projections of loss of life.
The estimates are usually adjusted up or
down if the particular setting poses
unusually threatening or unusually
benign conditions, compared to the
historical cases of dam failure and
flash flooding upon which the equations
are based. The equations provide esti-
mates of the most likely outcomes, given
the population at risk and warning time.
Many other factors (e.g., the ease of
evacuation from the flood plain, lethal-
ity of the flood in terms of depth,
velocity, and ability to carry debris,
etc.) can affect the actual outcome, and
these should be considered. The
reliability of prediction is much
greater for those cases involving ade-
quate warning.

The equations used to predict loss of
life require estimates of population at
risk for each flood and the estimated
warning time available for each popula-
tion. This information is shown in
Table 5.

As indicated in Table 5, a sudden dam
failure is likely to place up to
approximately 158 persons at risk
without adequate warning. However, this
condition will occur only during the
summer months. Fewer residents and far
fewer visitors are likely to be in the
area during the spring, fall, and
winter. The following table shows the
baseline estimated loss of life for the
maximum likely population at risk.

Baseline Loss of Life Estimates For
Sudden Dam Failure (Summer Season)

	Population at Risk	Potential Loss of Life
Insufficient warning (<90 minutes)	114-158	17-21
Baseline estimated total loss of life		17-21

In instances of sudden dam failure,
where some populations may receive no
warning of a flood, and where depths and
velocities may be considerable, it is

appropriate to revise the baseline
fatality estimates upward. One of the
worst cases of dam failure flooding,
with a population at risk of approxima-
tely this size and virtually no warning
(Laurel Run, PA, 1977), produced
approximately 30 percent fatalities. In
the present case, approximately 48 to
74 persons would receive no official
warning (reaches A through E) while
approximately 66 to 84 persons would
receive some advance warning. Applying
the 30 percent fatality rate only to
those receiving no warning produces a
revised fatality estimate of 26 to 36
$(26 = (48 \times 0.3) + 66^{0.6}; 36 = (74 \times 0.3) + (84)^{0.6})$.

The prior estimates of probable loss of
life are based on existing conditions.
Realistically, over the next few
decades, it is anticipated that local
use, recreational usage, and population
development between the example dam and
the downstream reservoir will probably
increase. As a rough quantitative indi-
cation of probable future changes, it is
estimated that the population at risk
will probably increase by less than
50 percent during the next two decades.
(The past two decades has seen a change
in permanent residents of about
one-third).

In addition to the estimated loss of
life, the magnitude of economic impact
resulting from dam failure is on the
order of $35 million to $110 million
depending on the availability of water
when the failure occurs (e.g., failure
during a relatively dry period will have
a greater economic impact than failure
in a wet period). The estimated impacts
can be divided into the following
categories:

    Loss of irrigation benefits - $8 to
      $81 million
    Cost to repair the dam - $15 million
    Downstream property damage -
      $10 million
    Loss of recreation benefits - $2 to
      $3 million

Environmental impacts and other losses
were determined to be insignificant for
this particular case.

In evaluating the adverse consequences
due to dam failure, the decisionmakers
first seek to determine the minimum
level of protection required. If there
is no significant incremental potential
for loss of life resulting from dam
failure (or other noneconomic factor),
the analysis may continue by evaluating
the likelihood of events to produce the

adverse impacts to determine an optimum level of expenditure to reduce the risks. However, if there is a significant incremental potential for loss of life, the maximum loading condition is chosen for design purposes. For earthquake loading, the maximum loading condition may be the MCE.

For the example dam, it has been shown that there is a significant incremental potential for loss of life in the event of sudden dam failure. Therefore, unless the population can be relocated, it was determined that the dam must be designed to withstand the MCE, regardless of the probability of occurrence of that event. The risk cost analysis of alternative actions would only consider alternative approaches to designing for the MCE.

For the purpose of illustration in this paper, it is assumed that the population can be relocated and the flood plain managed so that the potential for loss of life from dam failure is extremely low. It is assumed that the relocation can be accomplished for $10 million. Unless a means of precluding liquefaction can be found for less than $10 million, this alternative appears to be economically justified without consideration for the potential economic losses associated with project benefits and dam repair following dam failure. Further analysis of these issues is presented next.

3.6 Risk Cost Analysis

A risk cost analysis is performed to estimate the risk associated with the existing conditions and the risk reduction accomplished by alternative courses of action. This process facilitates comparison of proposed actions and leads to a good understanding of the nature of the problem.

Quantitative risk assessment requires consideration of the likelihood of dam failure and the adverse consequences resulting from dam failure. An evaluation of the probability of the seismic sources to produce liquefaction at the damsite can be performed based on the empirical assessment presented in a previous subsection of this paper. Table 1 presents a range of estimated recurrence intervals for each earthquake magnitude range from each source. Note that the four segments of the Wastach fault are treated as independent sources in the probability estimate. The recurrence (average return period) ranges reflect a range of uncertainty

for the corresponding range of earthquake magnitudes and do not reflect the assignment of a specific recurrence interval to a specific earthquake magnitude. Data in the last column includes some judgment of the time interval to the next seismic event based on the time elapsed since the last event.

From the seismotectonic information and the assumptions previously stated, a total annual probability of liquefaction due to the occurrence of seismic events is estimated using the following equation:

$$P_T = 1 - [(1-P_1)(1-P_2)(1-P_3)...(1-P_N)]$$

where P_T is the total annual probability and P_1, P_2, and P_N are the individual annual probabilities of the seismic events large enough to produce liquefaction at the damsite for each fault source (which equal the inverse of the recurrence interval).

For earthquake sources which have two distinct ranges of recurrence (e.g., the random earthquake in this problem), the following equation was used to estimate the individual annual probability from the fault source if the two earthquake ranges have a different capability of producing liquefaction at the damsite:

$$P_N = [(P_a - P_b) \times P_{DF_1}] +$$

$$[P_b \times P_{DF_2}]$$

where P_N is the total individual annual probability of liquefaction for the fault source, P_a and P_b are the annual probabilities for the two distinct ranges of recurrence, and P_{DF_1} and P_{DF_2} are the different probabilities that the seismic source is capable of producing liquefaction, if the deposits are susceptible.

The interpretation of the recurrence relationship for the random local vicinity earthquake is somewhat complicated because no specific epicentral distance is assigned to the earthquake magnitude; it simply represents a "near field" event. For this range of earthquakes, near field represents approximately from 2 to 20 km, with a worst case range of 2 to 5 km as plotted on Figs. 2 and 3.

P_{DF_1} has been assigned a value of 1.0 since the upper magnitude range consistently falls above the liquefaction threshold. P_{DF_2} has been assigned a value of 0.5 to reflect that the lower magnitude range generally plots below

the threshold of liquefaction. An engineering adjustment has also been made for the Wasatch fault sources at 68 km and 90 km to reflect the fact that much of the earthquake range falls below the threshold. A value of 0.75 and 0.50 has been assigned to the respective sources to obtain the probability of liquefaction. For all other seismic sources under consideration, it was assumed that liquefaction would occur (probability of 1.0) if the seismic event took place.

A separate calculation is performed for each extreme of the recurrence range (where applicable) so that the total estimated probability of liquefaction is also a range. The calculations are performed as follows:

Adjustments to obtain probability of seismic events capable of producing liquefaction

1. For random earthquake (least remote side of range):

$P_a = 10^{-2}$ $P_b = 10^{-3}$ $P_{DF_1} = 0.5$

$P_{DF_2} = 1.0$

Therefore, $P_N = [(0.01 - 0.001) \times 0.5] + [0.001 \times 1.0] = 5.5 \times 10^{-3}$

For random earthquake (most remote side of range)

The $P_N = 10^{-3} \times 1.0 = 10^{-3}$

2. For the Wasatch fault earthquakes that require adjustment:

Bountiful Segment:

$P_N = 2 \times 10^{-3} \times 0.5 = 1 \times 10^{-3}$
(least remote)

$= 10^{-3} \times 0.5 = 5 \times 10^{-4}$
(most remote)

Corner Canyon Segment:

$P_N = 10^{-3} \times 0.75 = 7.5 \times 10^{-4}$
(least remote)

$= 5 \times 10^{-4} \times 0.75 = 3.75 \times 10^{-4}$
(most remote)

Nephi Segment:

$P_N = 2 \times 10^{-3} \times 0.75 = 1.5 \times 10^{-3}$
(least remote)

$= 4 \times 10^{-4} \times 0.75 = 3 \times 10^{-4}$
(most remote)

Calculations of total probability of liquefaction

$P_T = 1 - [(1 - 0.001)(1 - 0.00075)$
$(1 - 0.002) (1 - 0.0015)$
$(1 - 0.0003) (1 - 0.0003)$
$(1 - 0.0055)] = 0.0113$ for the least remote side of range

$P_T = 1 - [(1 - 0.005)$
$(1 - 0.00375) (1 - 0.001)$
$(1 - 0.0003) (1 - 0.0001)$
$(1 - 0.0001) (1 - 0.001)]$
$= 0.0034$ for the most remote side of range

Based on the preceding calculations, the extreme worst case estimate for the annual probability of seismic events with the capability of producing liquefaction is on the order of from 1.1×10^{-2} to 3.4×10^{-3} which is from one to two orders of magnitude greater than the historical dam failure probability from all causes. It equates to a seismic event capable of producing an earthquake large enough to cause liquefaction in susceptible deposits occurring once every 90 to 300 years.

Assuming that property and population relocation has occurred, the adverse consequences resulting from dam failure due to liquefaction are estimated to result in economic losses from $25 million to $100 million. Then the range of annual seismic risk costs associated with the existing structure is from $85,000 to $1,100,000.

3.7 Alternative Actions

Based on the information provided in previous sections of this paper, three courses of action may be considered:

A. No action.

B. Relocation of the population and flood plain restrictions.

C. Modifications to the dam to preclude dam failure due to liquefaction.

D. Removal of the dam from service.

Alternative A was eliminated from consideration because there is a potential for failure due to loading conditions less than the maximum (in this case the MCE) which results in a significant potential for loss of life.

Alternative B eliminates the potential for loss of life at a cost of

$10 million. Using the present discount rate, the annual cost would be approximately $800,000.

Alternative C has been determined to cost $25 million for the least cost solution to the liquefaction problem. Using the present discount rate, the annual cost for modification of the dam would be approximately $2 million.

Alternative D has been determined to cost approximately $12 million in average annual lost project benefits.

The results of the decision analysis are provided to the decisionmakers. Various conclusions may be drawn from the analysis for the example dam. A possible decision may be that alternative B is selected while alternatives C and D are rejected due to their relatively high annual cost in comparison with the annual risk cost.

4. SUMMARY AND CONCLUSIONS

This paper has shown that a decision analysis framework may be useful in evaluating seismic risk associated with embankment dams. Analyses are provided to determine:

- The loading conditions that cause dam failure.

- The system response to the loading conditions.

- The adverse consequences of dam failure in terms of loss of life and economic impact.

- The probability (risk) of dam failure due to seismic loading.

Based on the analyses, alternative courses of action may be developed and compared to determine the most reasonable solution to the problem.

5. REFERENCES

(1) Bureau of Reclamation, "Guidelines to Decision Analysis," ACER Technical Memorandum No. 7, Denver, Colorado, March 1986.

(2) Seed, H. B., and Idriss, I. M., "Ground Motions and Soil Liquefaction During Earthquakes," Earthquake Engineering Research Institute, Berkeley, California, 1982.
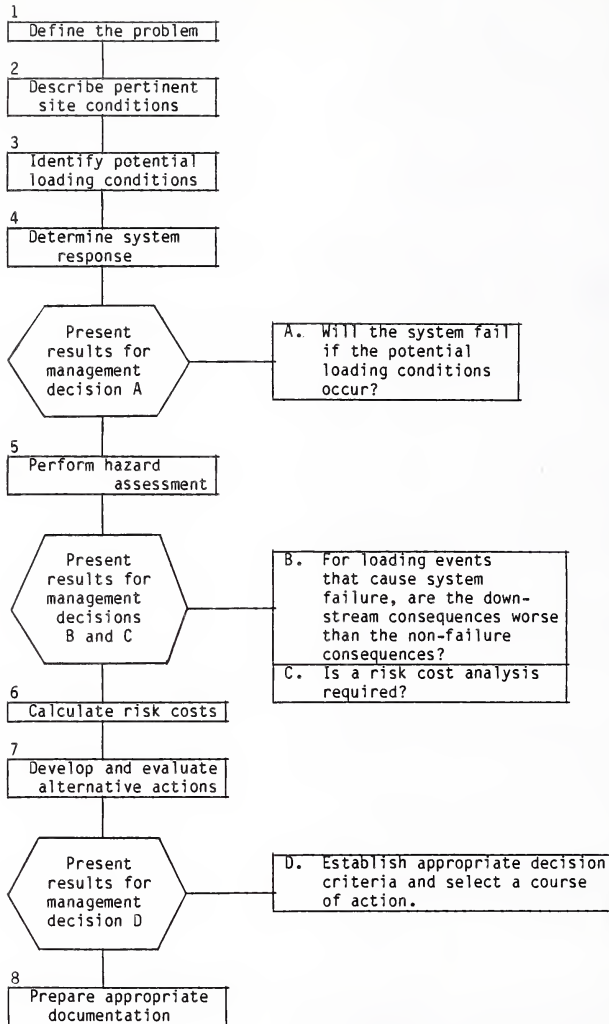
Figure 1. - General framework for decision analysis.

Table 1. - Magnitude and recurrence estimates for maximum credible earthquakes of possible concern to the example dam

Seismogenic structures	Magnitude range (M_s)	Epicentral distance (km)	Range of average return periods (k_a)*	Age of most recent event (k_a)*	Range of estimated annual probabilities of occurrence
Wasatch fault					
Brigham City-Bountiful Segment	6.5-7.5	90	0.5-1.0	0.3-0.5	2×10^{-3} - 10^{-3}
North Salt Lake City-Corner Canyon Segment	6.5-7.5	68	2.2-4.6	>0.13	10^{-3} - 5×10^{-4}
Alpine-Spanish Fork Segment	6.5-7.5	48	1.7-2.5	0.3-1.0	2×10^{-3} - 10^{-3}
Payson-Nephi Segment	6.5-7.5	68	0.5-4.0	0.3-0.5	2×10^{-3} - 4×10^{-4}
Strawberry fault	6.0-7.0	10	3-10	>3	3×10^{-4} - 10^{-4}
Stinking Springs fault	6.0-6.5	17	3-10?	-	3×10^{-4} - 10^{-4}
Random earthquake	6.0-6.5	Local vicinity	0.1-10?	-	10^{-3}
	5.0-6.0	Local vicinity	0.1-1.0?	-	10^{-2} - 10^{-3}

* k_a = 1,000 years.
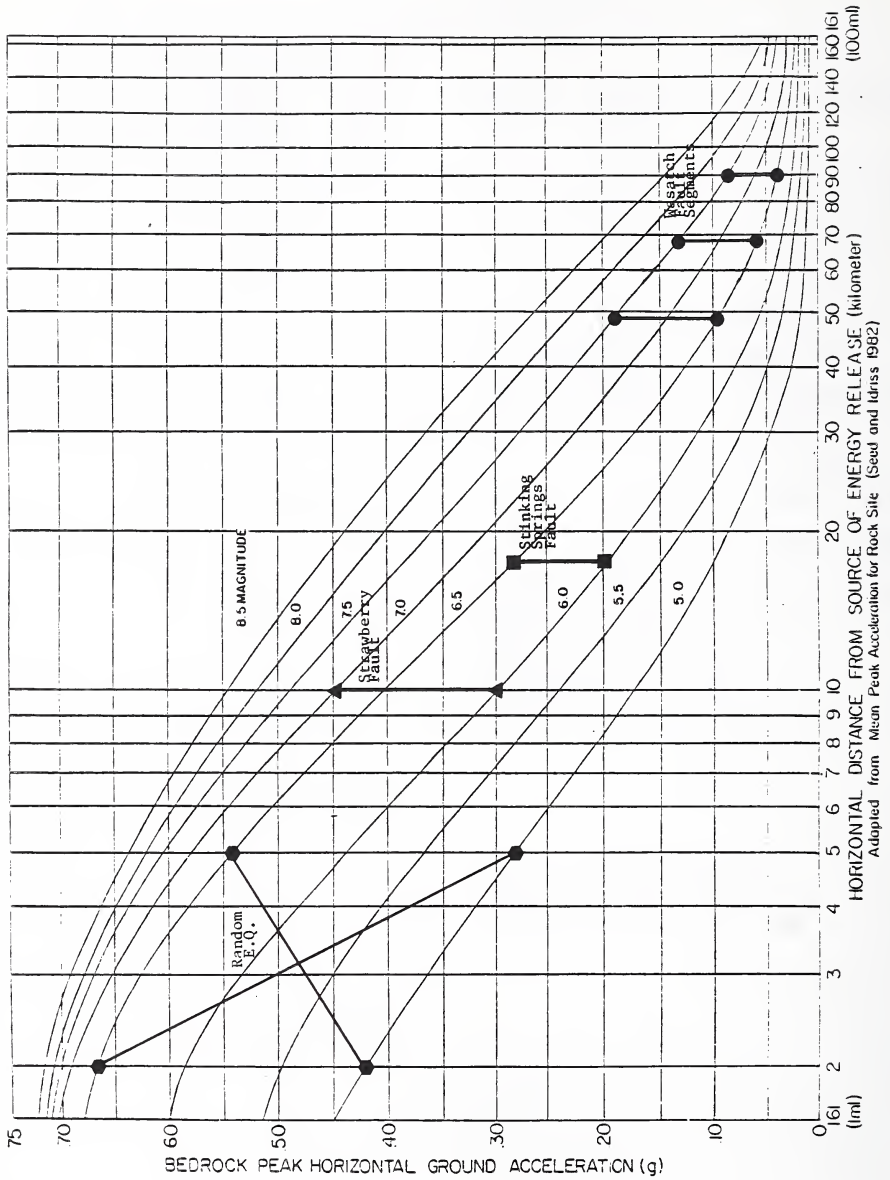
Figure 2. - Bedrock peak ground acceleration versus horizontal distance from source of energy release.

244
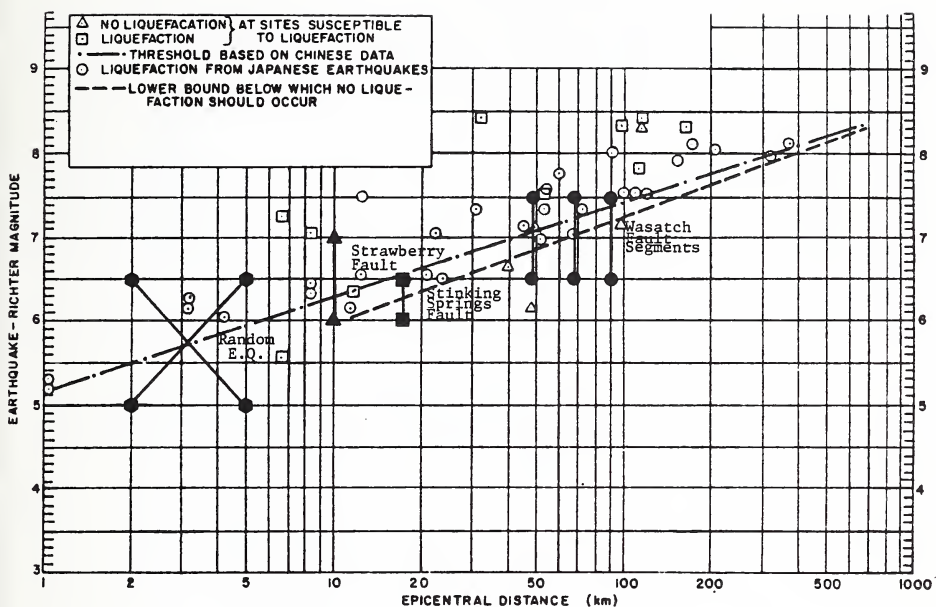
Figure 3. - Seismic potential at site vs. empirical liquefaction occurrence.

Table 2. - Total population at risk

River-mile location below the example dam	Total resident population at risk in flood area* (day or night)	Total transitory population at risk in flood area	
		Daytime	Night
A. 0 to 5 miles	0	2-8	1-3
B. 5 to 10 miles	4	2-8	1-3
C. 10 to 15 miles	20	2-8	1-3
D. 15 to 20 miles	0	0-2	0
E. 20 to 25 miles	16	2-8	1-3
F. 25 to 30 miles	20	2-8	1-3
G. 30 to 35 miles	20	2-8	1-3
H. 35 to 40 miles	20	2-8	1-3
Totals	100	15-60	5-25

*Assuming an average of four occupants per residential building.
NOTE: Totals may differ from column sums due to integer rounding of column values.

Table 3. - Flood travel times

River mile location below the dam	Time (in hours) after initiation of dam failure when initial dam failure flood waters reach center of area	Time (in hours) after initiation of dam failure when peak dam failure flood waters reach center of area*
A. 0 to 5 miles	0.1	0.8
B. 5 to 10 miles	0.5	1.0
C. 10 to 15 miles	0.8	1.2
D. 15 to 20 miles	1.2	1.6
E. 20 to 25 miles	1.4	1.8
F. 25 to 30 miles	1.8	2.2
G. 30 to 35 miles	2.4	2.7
H. 35 to 40 miles	2.9	3.3

*Based on assumption of 0.75 hour required for the dam failure.

Table 4. - Flood travel and warning times (in hours): Sudden dam failure

| River mile | 0 | 5 | 10 | 15 | 20 | 25 | 30 | 35 | 40 |
Study reach	A	B	C	D	E	F	G	H
Permanent population at risk	0	4	20	0	16	20	20	20
Transitory population at risk	2-8	2-8	2-8	0-2	2-8	2-8	2-8	2-8
Dam failure flood arrival (10,000 ft^3/s)	0.1	0.5	0.8	1.2	1.4	1.8	2.4	2.9
Telephone warning (beginning-ending)	NF	NF	0.75-1.25	NF	1.0-1.5	1.0-1.5	1.5-2.0	1.5-2.0
Face-to-face warning	NF	NF	NF	NF	NF	NF	1.0-2.0	1.0-2.0
Warning time (telephone) prior to 10,000 ft^3/s	-	0	0	-	0-0.4	0.3-0.8	0.4-0.9	0.9-1.4
(face-to-face)	(-)	(-)	(-)	(-)	(-)	(-)	(0.4-1.4)	(0.9-1.9)

t_0 = Dam failure.
$t_{0.5}$ = Detection of event and decision to warn, initiation of telephone and physical warnings.
NF   = Not feasible.

Table 5. - Probable warning times for sudden dam failure flood hazard

River mile location below the example dam	Resident population at risk in flood areas (day or night)	Transitory population at risk in flood areas (day and night)	Hours of warning prior to arrival of dam failure flood (Telephone)	(Face-to-face)
A. 0 to 5 miles	0	2-8	0	NF
B. 5 to 10 miles	4	2-8	0	NF
C. 10 to 15 miles	20	2-8	0	NF
D. 15 to 20 miles	0	0-2	0	NF
E. 20 to 25 miles	16	2-8	0-0.4	NF
F. 25 to 30 miles	20	2-8	0.3-0.8	NF
G. 30 to 35 miles	20	2-8	0.4-0.9	0.4-1.4
H. 35 to 40 miles	20	2-8	0.9-1.4	0.9-1.9
Totals:	100	14-58		

NF = Not feasible.

A NEW CRITERION FOR ASSESSING LIQUEFACTION POTENTIAL

BY

Susumu Iai, Hajime Tsuchida, and Setsuo Noda

ABSTRACT

One of the authors proposed a criterion in 1970 for assessing liquefaction potential. This criterion uses maximum acceleration of ground surface and SPT N-value of subsoils around ground water level. In the present study, the maximum acceleration is interpreted in terms of shear stress ratio and the SPT N-value of subsoils in terms of so called corrected N-value. Thus, the criterion proposed in 1970 is extended to incorporate the ability to predict depth of liquefiable layers. The extended version of the liquefaction criterion, namely the New Criterion, is compared with the criterion proposed by Seed and Tokimatsu, et al. in 1984. They are in good agreement.

1. INTRODUCTION

Great earthquakes have caused damages to some of the port structures in Japan. Among the various seismic effects to the port structures, liquefaction has caused one of the most serious damages. Therefore, a due consideration should be given for assessing liquefaction potential.

The Japanese port structures, the current design standard specifies the following methods for assessing liquefaction potential (1).

(1) a method using grain size accumulation curve and SPT N-value,
(2) a method using cyclic shear tests of sand specimen,
(3) a method using shaking table tests of sand layers.

Among these methods, the most suitable is chosen according to the degree of importance given to the structures. For most standard structure the method chosen is the grain size accumulation curve and SPT N-value. This method is based on a criterion for assessing liquefaction potential proposed by one of the authors in 1970 (2,3). This criterion will be designated as "the 1970 Criterion" hereafter.

Several great earthquakes have occurred in Japan and caused liquefactions since the proposal in 1970. The liquefaction case records by these great earthquakes have not been contradictory to the 1790 Criterion. However, the 1970 Criterion lacks the ability

Earthquake Resistance Structures Laboratory, Structures Division, Port and Harbour Research Institute, Ministry of Transport.

to predict the depth of liquefiable layers because it uses N-values of subsoils located around the ground water level. It has been sometimes difficult to decide how deeply the liquefiable site should be improved.

Therefore, the 1970 Criterion is extended to incorporate the ability to predict the depth of liquefiable layers. The report presents a method to extend the 1790 Criterion. The report also presents a comparison between the extended version of the 1970 Criterion, namely the New Criterion, and the criterion proposed by Seed and Tokimatsu, et al. in 1984 (15,17).

2. THE 1970 CRITERION

The 1970 Criterion is based on results of the shaking table tests and the liquefaction case records (2). Details were presented at the third joint meeting of U.S.-Japan Panel on Wind and Seismic Effects, UJNR in 1971 (3).

The procedure for assessing liquefaction potential by the 1970 Criterion is summarized as follows:

(1) Classify the soils by Fig. 1.
    Range (A): Easily Liquefiable Soil.
    Range (B) [(Bf) or (Bc)]: Liquefiable Soil.
    Other Ranges: Non-Liquefiable Soil.

(2) For soils in the ranges (A) or (B), obtain the critical N-value corresponding to the maximum acceleration of the design earthquake by Fig. 2. For example, critical N-value is 16, if the soil is in the range (A) and the maximum acceleration of the design earthquake is 300 gals. If the maximum acceleration is greater than 300 Gals, critical N-value is also 16 as indicated by the broken line for the soils in the range (A) for most of the cases.

(3) Investigate the SPT N-value of the layer around the water level. Compare this N-value with the critical N-value. If the N-value is greater than the critical N-value, the ground is judged not to liquefy at the design earthquake. If the N-value is smaller than the critical N-value, the ground is judged to liquefy at the design earthquake.

3. THE NEW CRITERION

3.1 Basic Rules of Liquefaction

The following basic rules of liquefaction have become widely accepted among geotechnical engineers in recent years.

(1) Liquefaction resistance depends on looseness or denseness of soils.

(2) Shear stress ration τ/σ_{vo}' (where τ: shear stress amplitude and σ_{vo}': vertical effective pressure) is a good index of liquefaction resistance because value of τ/σ_{vo}' which causes liquefaction does not depend on σ_{vo}':

(3) The τ/σ_{vo}' is greater, number of cyclic loadings necessary for liquefaction smaller.

These basic rules are used for the extension of the 1970 Criterion.

3.2 Relation Between SPT N-value and Effective Vertical Pressure

As mentioned earlier, the 1970 Criterion uses N-value of the layer around ground water level. Effective vertical pressure of such layers in Japanese port area is about 0.66 kgf/cm² . It is known that N-value depends not only on densities but also on effective vertical pressure. Therefore, if the 1970 criterion has to be applied to the layers at other effective vertical pressures, N-values of those layers have to be corrected for the difference in the effective vertical pressure. N-value corrected into the value at the effective vertical pressure of 0.66 kgf/cm² will be called "equivalent N-value" hereafter and sometimes designated as $(N)_{0.66}$.

A relation between N-value and effective vertical pressure for a fixed relative density was studied for the sands shown in Fig. 3 in the laboratory by several researchers (1,4-7). Ranges of the particle size distribution curves shown in Fig. 1 are also indicated in Fig. 3. The results of the relation for sands at range (A) are selected for the present study and are shown in Fig. 4 by broken lines. Average relation is given by the following equation.

$$(N)_{0.66} = \frac{N-1.828 \ (\sigma_{vo}'-0.66)}{0.399(\sigma_{vo}'-0.66)+1} \tag{1}$$

where $(N)_{0.66}$: equivalent N-value
$\quad$ N: N-value
$\quad \sigma_{vo}'$: effective vertical pressure in kgf/cm²

Solid lines in Fig. 4 correspond to this equation.

In addition to the laboratory study, there are several field investigations. Data shown in Fig. 5(a) are the results by one of them. They show a clear evidence of dependence of N-value on effective vertical pressure. If the N-values before the excavation are corrected by the equation (1), results become as shown in Fig. 5(b). Therefore, applicability of the equation (1) is confirmed.

3.3 Relation Between Maximum Acceleration and Shear Stress Ratio

If the 1970 Criterion has to be applied to the layers other than the layer around ground water level, intensities of ground shaking can be better specified in terms of shear stress ratio than maximum acceleration of ground surface as understood by one of the basic rules of liquefaction described in section 3.1. Relations between maximum acceleration of the ground surface and maximum shear stress ratio within the ground are shown in Fig. 6 by ground response analysis of typical ground conditions in Japanese port area as well as an empirical equation (3). These results indicate that the layer around ground water level in the Japanese port area receives a maximum shear stress ratio of about 1.4 times larger as a_{max}/g, where a_{max} is the maximum acceleration and g is the acceleration of gravity. Therefore, horizontal axis of Fig. 2 can be interpreted as maximum shear stress ratio if the value of maximum acceleration is divided by 0.7 g.

Instead of changing the horizontal axis of Fig. 2 into maximum shear stress ratio, maximum shear stress ratio can be interpreted in terms of equivalent acceleration if the maximum shear stress ratio is multiplied by 0.7 g. Namely,

$$\alpha_{ef} = 0.7 \ \frac{\tau_{max}}{\tau_{vo}'} \ . \ g \tag{2}$$

where α_{ef}: equivalent acceleration in gals
$\quad \tau_{max}$: maximum shear stress in kgf/cm²
$\quad \sigma_{vo}'$: effective vertical stress in kgf/cm²
$\quad$ g: acceleration of gravity (980 gals)

In this way, the 1970 Criterion shown in Fig. 6 can be applied to any layers other than the layer around ground water level.

Concerning the influence of the number of cyclic loadings mentioned at section 3.1, there was a proposal to determine the number of cyclic loadings by magnitude of the earthquake (9). However, it is known that ground motions are also greatly affected by other factors such as response characteristics of subsurface ground, distance from the epicenter, and source mechanism of the earthquake. Therefore, it is best to leave the influence of the number of cyclic loadings as an unknown factor and allow

a safety factor against this unknown factor for the time being.

3.4 Additional Factors

From the discussion described so far, it is evident that the 1970 Criterion can be applied to any layers other than the layer around ground water level if N-value and maximum acceleration of ground surface are interpreted

as equivalent N-value and equivalent acceleration. The knowledge acquired through recent years has made it possible to discuss the following additional factors.

(1) Range below 100 Gals

The knowledge obtained so far for the liquefaction at very small intensity of shaking is as follows:

a)   There has been no case records of liquefaction below 100 gals in Japanese port areas.

b)   The shaking table tests show that several sands liquefied at about 60 gals at their most loosely deposited conditions (2,3).

c)   There is a report that sand will not liquefy if level of shear strain is below 10^{-2}% (10).

If all these facts are considered, there may be a limit of equivalent acceleration below which no liquefaction takes place. However, at the moment, it is difficult to determine the exact level. Therefore, for the time being, it is safe to draw a line from the origin of Fig. 2 to the end of the lines (A) and (B) [(Bf) or (Bc)] in Fig. 2 as a critical N-value line.

(2) Range over 300 Gals

Recent studies confirm that dense sands do not liquefy and show a behavior so called cyclic mobility. Therefore, critical N-value shown by broken line in Fig. 2 can be reliable as a critical N-value in this range. It may be better to study the deformation of dense sands together with deformation of structures which will exhibit a dynamic interaction with the sands by earthquake motions.

(3) Influence of Fines Content

The 1970 Criterion roughly expresses difference of liquefaction resistances by particle size distribution curves shown in Fig. 1. Recent studies show silty sands within range (A) in Fig. 1 have lower critical N-value than clean sands of the same liquefaction resistance. Studies or specifications which show explicit relation of fines content (less than 74 μ) are shown in Figs. 7 and 8 (11-14).

Whether the critical N-value line for the silty sands can be obtained by parallel shift of the line or by magnifying the scale of N-value or acceleration coordinate remain an unresolved question. For the present study, the authors propose using a reduction factor of N-value as shown in Fig. 9, which is roughly harmonious to the results shown in Figs. 7 and 8.

(4) Allowance for the Possible Uncertainty of N-values and Others

From the discussions presented so far, a basis for the New Criterion has been established. Liquefaction potential will be determined by the comparison of equivalent N-value to the critical N-value which corresponds to the equivalent acceleration. However, if N-value is very close to the critical N-value, further studies on the liquefaction potential will be necessary because N-values always contain uncertainty as a representative indices of the liquefaction resistance at the ground layer under investigation. Moreover, influence by the number of cyclic loadings by the earthquake motions are not explicitly taken into account.

The regions of the uncertainties can be expressed in terms of safety factor for equivalent acceleration F_2 for the range of equivalent acceleration less than about 300 Gals and equivalent N-value less than about 16. It is difficult to specify the exact values of F_2 for the region of uncertainties but, roughly speaking, the region of uncertainties is considered $1/1.5 < F_2 < 1.5$. Fig. 10 shows this region.

For the range of greater equivalent acceleration and greater equivalent N-value, the safety factor for equivalent F_2 is not longer effective as understood by Fig. 10 because horizontal broken line of $(N)_{0.66} = 16$ is the critical N-value line in this range and it is parallel to the equivalent acceleration axis. Therefore, it is necessary to allow a safety factor for equivalent N-value in this range. The study of Tokimatsu and Yoshimi shows that, if N_1 (N-value at effective vertical pressure of 1 kgf/cm^2) is greater than 25, it is safe from liquefaction (12). This value of N_1 corresponds to 20 in equivalent N-value in this study. Therefore, $(N)_{0.66} = 20$ is taken as a border line of the uncertainty region in this study.

3.5 The New Criterion

The New Criterion is summarized as follows:

(1)   Soils are classified by Fig. 1.

(2)   Equivalent N-value is calculated by equation (1) for soils in the ranges (A) or (Bc) in Fig. 1. For soils in the range

of (Bf), no correction will be applied and N-value is considered to be the equivalent N-value.

(3) Equivalent acceleration is calculated by equation (2), where maximum shear stress ratio is computed by ground response analysis.

(4) Liquefaction potentials of soils in the range of (A) in Fig. 1 are judged by Fig. 11(a) and those in the range of (Bf) or (Bc) are judged by Fig. 11(b). If the layer of the soils in the range of (Bc) is overlain by impermeable layers, its liquefaction potential will be judged by Fig. 11(a) instead of Fig. 11(b).

(5) For the soils in the range of (A) in Fig. 1, critical N-value and associated boundaries of uncertainty regions are reduced by the reduction factor shown in Fig. 13 if fines content is greater than 5%.

(6) From the Fig. 15, following judgments are obtained.

Region I: Liquefaction takes place. Liquefaction is judged to take place.

Region II: Liquefaction likely takes place therefore, liquefaction is judged to take place, or further study such as laboratory tests of soils is recommended if improvement of liquefiable soils is economically or technically difficult.

Region III: Liquefaction does not likely take place. Therefore, liquefaction is judged not to take place; laboratory tests of soils is recommended if the structure is considered a critical facility.

Region IV: Liquefaction does not take place. Liquefaction is judged not to take place.

Extensive study on the applicability of the New Criterion has been carried out by using liquefaction case records in Japan. This part of the study will be reported in a separate report. The result of the study has confirmed the applicability of the New Criterion.

4. COMPARISON WITH THE CRITERION BY SEED, TOKIMATSU, ET AL. (1984)

Seed, Tokimatsu, Harder, and Chung have proposed a Criterion in October 1984, based on the comparative study of standard penetration test procedure among U.S., Japan, Argentina, and China (15). This Criterion will be called

the Criterion by Seed and Tokimatsu, et al., hereafter. This criterion was also presented at the 17th Joint Meeting of U.S.-Japan Panel on Wind and Seismic Effect, UJNR and in the reference 17 in 1985 (16). The New Criterion proposed in the present paper is compared with the Criterion by Seed and Tokimatsu, et al., in this chapter.

4.1 Dependence of N-value on the Effective Vertical Pressure

Dependence of N-value on the effective vertical pressure is shown in Fig. 12, in the normalized form by the equivalent N-value. Parameters used in the Criterion by Seed and Tokimatsu, et al., are relative densities, but those used in the New Criterion are equivalent N-values. Therefore, precise comparison is not possible. However, roughly speaking, they are in agreement.

4.2 Critical N-value

Critical N-values used by the criterions are shown in Fig. 13. The horizontal axis of Fig. 13 shows N-value at effective vertical pressure of 1 kgf/cm² obtained by the SPT procedure with rod energy ratio of 60% using a constant 1-3/8" diameter barrel. Because the rod energy ratio of Japanese SPT procedure is 78% by mechanical trip system (Tonbi) and 67% by rope and pulley system (15), average rod energy of 73% is considered to be the basis of the New Criterion in which no distinction is made of the methods of SPT. The New Criterion is shown in Fig. 13 taking these facts into account.

In overall, the criteria agree well with each other.

5. CONCLUSIONS

The following conclusions are obtained from the study.

(1) A criterion proposed by one of the authors in 1970 can be applied to the layer located around ground water level but not to the other layers. The present study makes it possible to apply the criterion to all the layers and thus makes it possible to predict the depth of liquefiable layers.

(2) The criterion thus obtained was compared with the criterion proposed by Seed and Tokimatsu, et al. in 1984. The results of the comparative study of SPT procedure between U.S. and Japan were taken into account for the comparison. They agree well with each other.

6.   REFERENCES

1)   Bureau of Ports and Harbours, Ministry of
     Transport: Design Standard for Japanese
     Port Facilities and the Guidance, Japan
     Port Association, March 1979 (In
     Japanese).

2)   Tsuchida, H., Prediction of Liquefaction
     of Sandy Subsoils and Countermeasures to
     Possible Damage Caused by the Liquefac-
     tion, Proceedings of the Annual Meeting of
     the Port and Harbour Research Institute,
     December 1970 (in Japanese).

3)   Tsuchida, H. and S. Hayashi, Estimation of
     Liquefaction Potential of Sandy Soils,
     Third Joint Meeting of U.S. Japan Panel on
     Wind and Seismic Effects, UJNR, May 1971.

4)   Gibbs, H. J. and W. G. Holtz, Research on
     Determining the Density of Sands by Spoon
     Penetration Testing, Proceedings of the
     Fourth International Conference on Soil
     Mechanics and Foundation Engineering,
     London, 1957, Vol. 1, pp. 35-39.

5)   Marcuson, W. F. III and W. A. Bieganousky,
     Laboratory Standard Penetration Tests on
     Fine Sands, Journal of Geotechnical Engi-
     neering Division, ASCE, Vol. 103, No. 6,
     June 1977, pp. 565-588.

6)   Marcuson, W. F. III and W. A. Bieganousky,
     SPT and Relative Density in Coarse Sands,
     Journal of Geotechnical Engineering Divi-
     sion, ASCE, Vol. 103, No. 11, November
     1977, pp. 1295-1309.

7)   Yoshida, Y., G. Kokusho, Y. Esashi, M.
     Sasaki, Standard Penetration Tests on
     Dense Sands (Second Report), 18th Japan
     Geotechnical Engineering Symposium, June
     1983, pp. 45-46 (in Japanese).

8)   Tatsuoka, F., T. Iwasaki, K. Tokida, S.
     Yasuda, M. Hirose, T. Imai, and M. Konno,
     Standard Penetration Tests and Soil Lique-
     faction Potential Evaluation, Soils and
     Foundations, Vol. 20, No. 4, December
     1980, p. 95-112.

9)   Seed, H. B. and I. M. Idriss, Simplified
     Procedure for Evaluating Soil Liquefaction
     Potential, Journal of the Soil Mechanics
     and Foundation Division, ASCE, Vol. 97,
     No. SM 9, September 1971, pp. 1249-1273.

10) Dobry, R., R. S. Ladd, F. Y. Yokel, R. M.
     Chung, and D. Powell, Prediction of Pore
     Water Pressure Buildup and Liquefaction of
     Sands During Earthquakes by the Cyclic
     Strain Method, NBS Building Science Series
     138, U.S. Department of Commerce, National
     Bureau of Standards, July 1982, 50p.

11) Ishihara, K., Stability of Natural
     Deposits During Earthquakes, Proceedings
     of 11th International Conference on Soil
     Mechanics and Foundation Engineering,
     August 1985, pp. 321-376.

12) Tokimatsu, K. and Y. Yoshimi, Criteria of
     Soil Liquefaction with SPT and Fines
     Content, Proceedings of Eighth World   ·
     Conference on Earthquake Engineering, July
     1984, Vol. 3, pp. 255-262.

13) Fire Defense Agency, Regulations on
     Controlling Hazardous Materials, 1978 (in
     Japanese).

14) Japan Gas Association and Committee on
     Safety of LNG Tanks: Provisions on LNG
     Underground Tanks, 1979 (in Japanese).

15) Seed, H. B., K. Tokimatsu, L. F. Harder,
     and R. M. Chung, The Influence of SPT
     Procedures in Soil Liquefaction Resistance
     Evaluations, Earthquake Engineering
     Research Center, University of California,
     Berkeley, Report No. UCB/EERC-84/15,
     October 1984, 50p.

16) Chung, R. M., H. B. Seed, A. G. Franklin,
     and J. A. Farrar, Re-evaluation of
     Liquefaction Resistance Curves, the 17th
     Joint Meeting of U.S.-Japan Panel of Wind
     and Seismic Effects, UJNR, May 1985.

17) Seed, H. B., K. Tokomatsu, L. F. Harder,
     and R. M. Chung, Influence of SPT Proce-
     dures in Soil Liquefaction Resistance
     Evaluations, Journal of the Geotechnical
     Engineering, ASCE, Vol. 111, No. 12,
     December 1985, pp. 1425-1445.
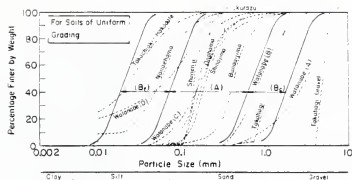
(a) For Soils of Uniform Granding
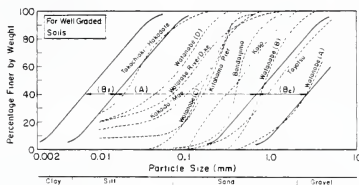
(b) For Well Graded Soils

Fig.1 Ranges of Particle Size Distribution Curves
of Liquefiable Soils
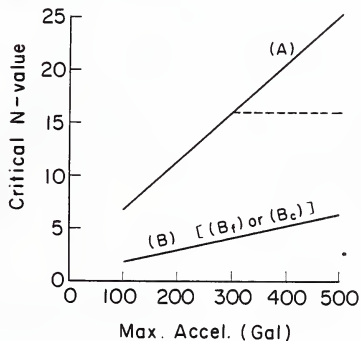
Fig.2 Critical N-values for Assessing
Liquefaction Potential
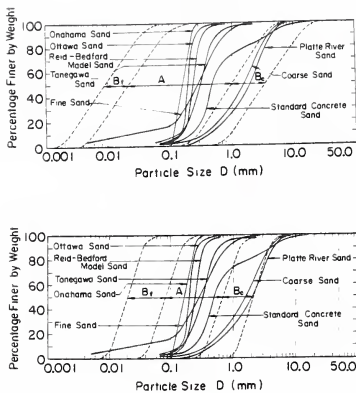
Fig.3 Particle Size Distribution Curves of Sands Used for Standard Penetration Tests In the Laboratory
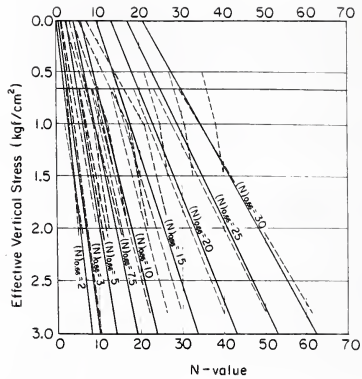
Fig.4 Relation Between SPT N-value and Effective Vertical Stress from the Laboratory Test Data
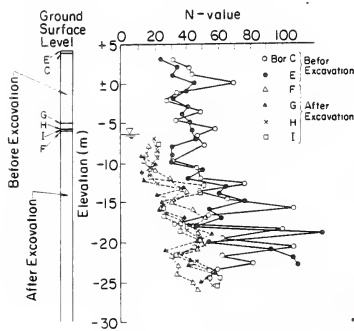
(a) N-values Before and After the Excavation
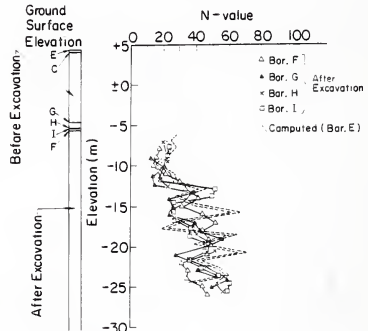
(b) Computed N-values and Those Measured After the Excavation

Fig.5 Comparison of N-values Before and After the Excavation
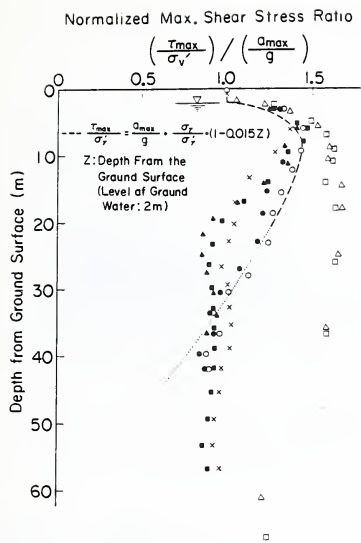
Fig.6 Distribution of Maximum
Shear Stress Ratio Normalised
by Maximum Acceleration of
Ground
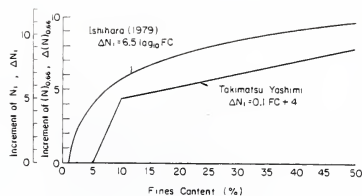
Fig.7 Increment of N-value in
Accordance with Fines Content
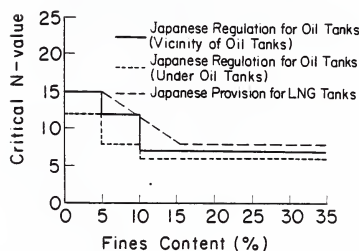
Fig.8 Provisions Explicitly Taking
Into Account the Influence of
Fines Content in Terms of
Variation in Critical N-value
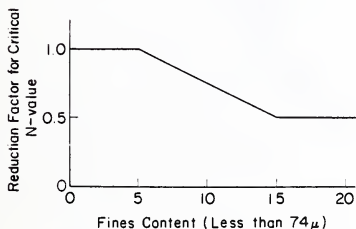
Fig.9 Proposed Reduction Factor for
Critical N-value
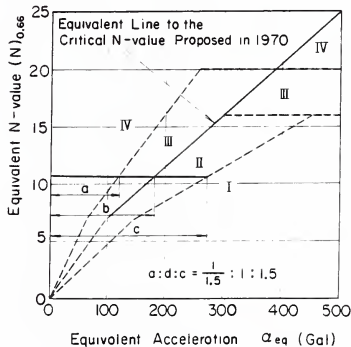
Fig.10 Critical N-value Line and
Associated Uncertainty Regions

255

4-2
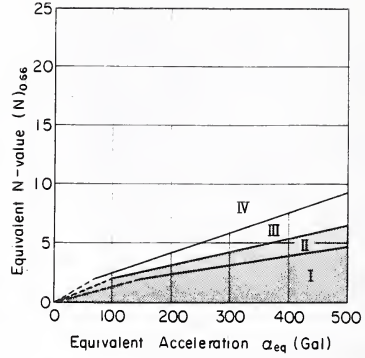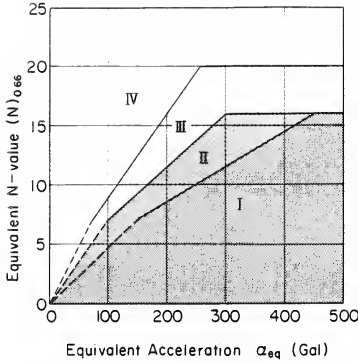
(a) For Soils in Range (A) in Fig.1   (b) For Soils in Range (Bf) or (Bc) in Fig.1

Fig.11 Proposed Chart for Assessing Liquefaction Potential
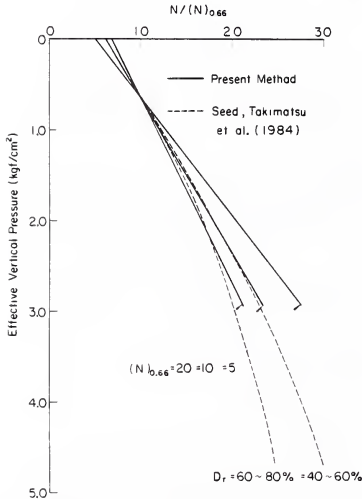
Fig.12 Comparison with the Criterion Proposed by Seed, Tokimatsu, et al. for the Relation of N-value and Effective Vertical Pressure
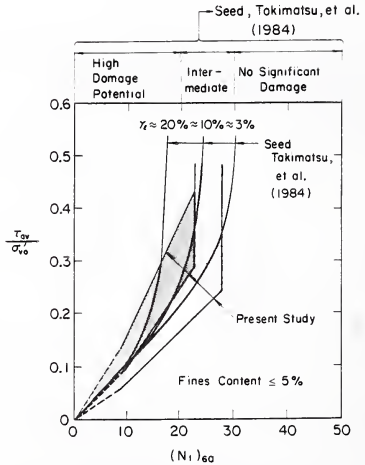
Fig.13 Comparison with the Criterion by Seed, Tokimatsu, et al. for Critical N-value (Clean Sands)

4-2

EARTHQUAKE SAFETY INVESTIGATION OF
EXISTING FACILITIES

BY

Joseph V. Tyrrell, P.E. [1]

ABSTRACT

The U. S. Navy has a large number of bases
located in areas where seismic risk is
high. Many bases are in costal areas and
areas founded on weak soils and hydraulic
fills. Experience from recent earthquakes
has led to increased design requirements and
some concern for the safety of existing
structures. Pilot studies have shown that
about 5% of the structures at these bases
are liable to experience serious damage. To
deal with the large inventory, at a
reasonable cost, a systematic investigation
procedure was developed. This paper
describes the methodology adopted.

KEYWORDS: earthquake safety; existing
facilities; earthquake investigations;
seismic

1. INTRODUCTION

The U.S. Navy has 55 major bases, as
well as a scattering of small facilities,
located in areas of high seismic risk in the
50 states, Puerto Rico, Guam, the
Philippines, and Naples, Italy (included
because of special problems). Other
overseas areas are not being investigated at
this time. This includes utilities, roads,
bridges, dams, and over 14,000 major
buildings. Even a superficial investigation
of existing structures on this scale could
be costly. Therefore, a strategy to reduce
the scope of the investigation was needed.

Several possible approaches were
considered. One plan was to limit the
investigation to the essential facilities.
This was discarded because we were concerned
with personnel safety as well as the
facility function. A second candidate
approach was to have experts scan the
facilities on-site and select buildings or
other facilities which require
investigation.

A field screening by experts was
incorporated as one step in the preliminary
work, but after the scope was first reduced
by computer screening. The scheme adopted
utilizes several layers of screening and two
levels of evaluation in order to minimize
the effort and its cost.

2. PROGRAM IMPLEMENTATION

The investigation program is handled by the
Naval Facilities Engineering Command's
(NAVFAC) six Engineering Field Divisions,
each of which serves a specific geographical
area. About 90% of the work is done thru
contracts with private A&E firms. NAVFAC HQ
provides funding and policy guidance. The
Western Division, located in San Bruno, CA.
assists NAVFAC HQ with coordination and
planning. The Naval Civil Engineering
Laboratory (NCEL), Port Hueneme, Ca. has
provided support in the form of research,
development and consultation.

The final product is recommendations for
needed improvements and draft programming
documents. The operating Commands at the
various naval activities determine what type
of funding is applicable and integrate
earthquake improvements with their other
requirements.

3. METHODOLOGY

The various steps in the evaluation process
are discussed in this section. Often it is
convenient to combine several of these steps
into one operation. A new tri-service
design manual for investigation of existing
facilities is now being prepared. The
Navy's designation for this manual will be
NAVFAC P 355.2 (ref. 1). The procedures
given in this manual are essentially the
same as those being used in the Navy's
Earthquake Safety program which consists of
the following steps:

a. Inventory Reduction (computer screening)
b. Consultation with the Activity
c. Site Seismicity Studies
d. Evaluation of Site Hazards and Utilities
e. Field Screening and Data Collection for
    Structures
f. Preliminary Structural Evaluation
g. Preliminary evaluation report
h. Follow-up Investigation of Site Hazards
    & Utilities
i. Detailed Analysis of Structures
    (Identified by Preliminary Evaluation)
j. Recommendations for Mitigations (if
    Required)

---

[1] Naval Facilities Engineering Command,
Consultant in Earthquake Engineering

k. Final Evaluation Report (with cost and
    programming data).

Steps one and two are usually completed
before a contract for an investigation is
prepared. In most areas, the balance of the
work is divided into two phases which are
contracted for sequentially. Results from
the first phase define the scope of work
required in the second phase. The process
continues to evolve and consequently not all
studies have been done in exactly the same
manner.

3.1 Inventory Reduction

The Navy is fortunate to have a good deal of
information on its facilities in an
automated data base. The real property
listing provides useful information on the
age, size, cost, and type of construction.
As a first cut, buildings with the following
attributes are eliminated:

a. Constructed after 1973
b. Area less than 3000 SF
c. Single story pre-engineered metal or
    timber structures
d. Structures with replacement cost less
    than $200,000
e. Earth covered structures, (6) structures
    scheduled for replacement within 5 years
f. Family housing.

This screening usually eliminates more than
half of the structures. In addition, where
there are identical structures, we try to
limit the investigation to just one since
the results may be inferred for the others.
A few of the structures eliminated may be
later reinstated as discussed below.

3.2 Consultation with Activity

The initial list produced by the computer
screening is presented to the Public Works
group at the Naval Activity in question.
They can effectively identify errors in the
computer listing and buildings that may not
warrant investigation for various reasons.
Sometimes the Activity will request
investigation of structures not included
after the initial screening. We either add
these candidates or explain why it is
unnecessary.

3.3 Site Seismicity Studies

A seismicity study is made to establish site
specific response spectra. This is used is
conjunction with the rapid evaluation method
described below. It is also used in
conjunction with the design of new essential
facilities in accordance with the new
tri-service design manual, Seismic Design
Guidelines for Essential Buildings [ref 2].

3.5 Evaluation of Site Hazards & Utilities

This is usually done in conjunction with a
site visit. Visual inspection and
discussion with the public works engineers
are the best sources. When appropriate,
soil reports for existing construction and
utility maps are scanned. At this point in
the investigation, attention is directed
toward the overall utility systems, not
utilities inside of buildings. The
reliability of utilities supplied from
outside sources is difficult to evaluate but
is essential in deciding what on-base
capacity is needed for emergencies.

3.6 Field Screening & Data Collection

NAVFAC or A&E engineers making the
evaluation visit the site and visually
screen the structures. Some structures
usually can be eliminated and sometimes an
additional structure may be recommended. In
some cases the need and type of upgrading
required may be obvious, and this may be
noted without further effort. When a listed
structure is found to be a valid candidate,
a walk thru inspection is made and notes
taken with regard to hazardous
non-structural components as well as
pertinent observations on the structural
system. The condition of materials should
be noted. Available drawings and
calculations are reviewed or collected for
subsequent review in the office. Photos are
useful for later reference.

3.7 Preliminary Structural Evaluation

In this phase any necessary data not
previously collected is obtained and the
information is evaluated. The "rapid
analysis" procedure developed by the firm of
John Blume/URS (ref 3) is applied to assess
vulnerability. In this method the key
structural elements are identified and their
capacities to resist earthquake forces
estimated, a typical summary sheet is shown
in Table 1 at the back of this manuscript. A
resistance curve for the structure can then
be compared to the earthquake demand.
Demand is determined from site response
spectra (for various degrees of damping)
developed by a seismicity study.

The calculations can be done fairly simply
and the results quickly obtained by a graph
showing the demand and resistance lines, see
Figure 1 at the back of the manuscript. The
ordinate is the spectral acceleration and
the abcissa is the period. When the initial
yield is reached, damage is assumed to be
zero. When the ultimate capacity is reached
(collapse mechanism developed) damage is
assumed to be 100%. The period of the
structure will lengthen and its ductility
changes as it experiences inelastic
deformation.

This evaluation method assumes that damage varies linearly between yield an ultimate. A point is found on the line connecting P_y and P_u such that the horizontal distance from P_y is to the horizontal distance to P_u inversely as the horizontal distances from the point to intersections with the demand spectra for elastic damping and damping at ultimate. "Percent of damage" is defined as the horizontal distance from yield to the point divided by the distance from yield to ultimate.

The Naval Civil Engineering Laboratory (NCEL) has provided modifications of the Blume/URS methods and developed computer programs for its application. This paper is not intended to provide a complete description of the rapid analysis technique. Anyone interested in the details of this method should obtain a copy of references 1 & 2.

The method is for preliminary evaluation only. It identifies which buildings are liable to be damaged and gives an indication of their relative vulnerability. It cannot be used for all structures.

3.8 Preliminary Evaluation Report

At this point in the procedure, it is necessary to determine what additional investigation is needed and its cost. Possible items include follow-up on site hazards and utilities, and detailed investigation of buildings which appear to be very vulnerable. As a rule of thumb, we consider buildings for further investigation if the rapid analysis indicates damage greater than 60%. Essential buildings with indicated damage greater than 30% may warrant further investigation.

Buildings that are subject to potential damage from site hazards may not be worth further structural analysis unless mitigation of the site hazard is feasible. Buildings with severe foundation problems may not be appropriate for further study.

This report also includes findings with respect to non-structural elements and recommendations for mitigations of non-structural problems with order of magnitude costs. It does not contain an itemized listing of every component although some major pieces of equipment may be described. In general, broad categories such as light fixtures are discussed. The investigator should provide sketches showing remedial measures.

3.9 Follow-up Investigation of Site Hazards & Utilities

The investigation of site hazards depends upon the unique conditions prevailing at each site. It might be necessary to determine the boundaries of area subject to tsunami, liquefaction, or slides. Gas lines and storage of hazardous materials pose a threat of secondary damage. Looping and redundancy in utilities provides increased confidence that operations will not be disrupted and that recovery can be carried out expeditiously.

3.10 Detailed Analysis of Structures

Structures recommended for further investigation after the preliminary evaluation are reviewed and a final list approved. The investigator may use whatever methods he feels necessary and appropriate. At this point it is not necessary to analyze the entire structure and determine stresses in each member. Instead an analysis that deals with typical segments of the lateral force resisting system is appropriate. It is our aim to do as much or as little analysis as is required to determine if deficiencies exist and their nature and extent. The need for upgrading is determined.

3.11 Recommendations for Mitigation

Under this task, the detailed analysis is continued to determine what effective mitigations are possible and their cost. Usually the results for typical lateral force resisting elements can be used to establish a budget estimate for upgrading. The first mitigation considered should allow the structure to meet 100% of the demand, unless this is not cost-effective. The minimum acceptable level of safety is that the structure's capacity be equivalent to at least 75% of the earthquake demand. If this cannot be accomplished, the report will usually indicate that upgrading is not feasible. However, if a lesser tangible improvement can be made at small expense, we will consider it. We rely on the investigator to determine whether there is more than one alternative worth considering.

3.12 Final Evaluation Report

The final report is expected to summarize all the investigations and present the recommended mitigations and their cost for the selected buildings. It also includes drafts, in the correct format, of documents that the Activity can use to request funding for remedial projects.

4. ECONOMIC ANALYSES

In order to justify upgrading, some form economic rationale or cost/benefit analysis is often required. We can evaluate structural effects fairly accurately although there is some uncertainty. Other elements of cost are more difficult to deal with. These include damage to non-structural elements, damage to equipment and building contents, secondary damage (fire, etc.), as well as injury of personnel. Additionally there is the loss of productive capacity while repairs are made. For the Navy, there is the question of military readiness. These factors are not amendable to precise quantification, however, an economic analysis is incomplete and may be misleading if they are not included.

5. PRIORITIES FOR UPGRADING

When there are a large number of facilities requiring upgrading, it is necessary to establish priorities. Some of the factors to be considered are:

a. Vulnerability of the structure
b. Vulnerability of contents
c. Feasibility - Cost/benefit of upgrading
d. Importance of facility - impact of loss
e. Occupancy (no. of people)
f. Expected service life of the facility

Requirements for upgrading for earthquake safety must, of course, be integrated with other requirements. The Navy spent some time considering systematic methods for prioritizing projects, but without complete success. However, each activity provides the prioritization for projects it recommends for funding, and at this level, no activity has so many upgrading projects that it requires a structured system. On further reflection, it is also apparent that an individual facility might be upgraded but still not be able to function because of damage to associated facilities. In order to substantially affect military readiness, a broad improvement program is needed.

The following priority order is suggested as most effective for improving overall safety as soon as possible:

a. Facilities needed for damage control and recovery
b. Utilities
c. Structures liable to collapse
d. Non-structural hazards (low cost items such as light fixtures, etc.)
e. Structures subject to serious damage
f. Essential structures subject to moderate damage
g. All other

6. STATUS & RESULTS

Investigations thru preliminary evaluation have been completed for about 90% of the facilities. The final reports have been produced for about 40%. If funding permits this pace to be continued, the investigations should be substantially finished by 1989. A total of 55 bases and more than 14,000 buildings will have been considered. The total cost is estimated to be 14 million dollars of which approximately 10 million is attributable to evaluation of structures. Site hazards, particularly liquefaction, have been identified at about 10 bases. About 5% of the existing structures, approximately 750, require structural upgrading.

Naval Activities have implemented expedient safety measures at many bases. These efforts have focused on minor utility improvements and non-structural elements. NAVFAC has issued a directive with regard to modernization and repair projects which has resulted in seismic upgrading of at least 130 buildings (some not yet fully completed). The general investigation of existing structures has resulted in upgrading of about 60 additional buildings with about 200 projects pending. At this point it is not possible to say what percentage of the deficient structures are likely to be upgraded.

The upgrading required may be anything from a few X braces to a completely new lateral force resisting system. Consequently, we have not been able to establish any accurate estimate of construction costs. A projection of an early sample indicated that total construction costs would be on the order of 200 to 300 million (not including hospitals). A decision to undertake or dismiss a few major projects could strongly affect this figure.

The cost of investigation though preliminary evaluation has been about $1,700 per building listed in the evaluation report (much less for the total buildings screened). The cost of detailed evaluation may vary widely depending upon the complexity of the building but has averaged about $25,000 per building. Overall cost is about $1,000 per building screened, but this figure is misleading because it includes site investigation of site hazards and utilities.

The most ambitious seismic upgrading project undertaken up to this time involves the Naval Hospital located in Oakland, California. Design for a modification to this 500 bed hospital with clinics and support facilities is complete and

construction is pending. The portion of cost associated with seismic upgrading is estimated to be about 27 million dollars.

Another pending project involves the Naval Support Activity at Naples, Italy. The site presently occupied is exposed to both tectonic and volcanic activity. For the past two and one half years, uplift associated with a magma intrusion and accompanied by tremors has been causing minor damage. The present facilities are leased. To construct facilities at a better site is estimated to require funding on the order of two hundred million dollars. Design for some of these facilities is underway.

7. SUMMARY

A methodology for investigating earthquake safety for a large inventory of facilities has been developed and implemented. Cost is minimized but still substantial, however, it is small compared to the potential losses which would result from a major earthquake.

The method is adaptable to a variety of requirements and purposes. A user can customize the method by changing the factors used for screening and evaluation. Each user is likely to have unique situations which determine how facilities are prioritized for upgrading.

In the event that the accurate prediction of earthquakes becomes a reality, the identification of facilities subject to serious damage would still be needed as a part of any warning system.

This type investigation has been feasible for the Navy and we feel that it will be cost effective. Applications in the public domain would involve many additional problems as well as political questions with respect to implementing mitigations. A broad upgrading of existing structures involves large expenditures and consequently warrants a plan to achieve the most cost effective results.

Judging by the Navy's experience, the extent of upgrading needed in the USA and world-wide necessitates accomplishment over an extended period of time. On the other hand, if a future large earthquake should cause massive damage, a crash program for upgrading may be the result.

REFERENCES

1. Seismic Design Guidelines for Upgrading Existing Buildings, TM 5-809-10-2/NAVFAC P 355.2/AFM 88-3, Chapt. 13.2, Departments of the Army, The Navy, and The Air Force, Washington, D.C.

2. Seismic Design Guidelines for Essential Buildings, TM 5-809-10-2/NAVFAC P 355.1/AFM 88-3, Chapt. 13.1, Departments of Army, The Navy, and The Air Force, Washington, D.C.

3. Puget Sound Naval Shipyard: Dynamic Analysis, Rapid Evaluation Method, and Cost Estimates for Damage, by Sigmund A. Freeman, Proceeding of the NAVFAC Structural Engineering Workshop, 1974.

TYPE A - STEEL STRUCTURES

	BUILDING			INITIAL YIELD				ULTIMATE				NOTE REF.
SEQ. NO.	HAVFAC NO.	DIRECT.	TYPE	T	S'_a	S'_d	ELEMENT	T	S'_a	S'_d	ELEMENT	
17	462	L	A2	0.25	0.40	0.2	X	1.2	0.54	7.	C & X	
		T		0.9	0.50	4.	C	1.1	0.57	6.	C & X	
18	469	L	A2	0.25	0.17	0.1	X	0.70	0.42	2.	C & X	
		T	A4	0.45	0.40	0.85	C					
19	494	L	A2	0.25	0.40	0.2	X	1.2	0.54	7.	C & X	3
		T		0.9	0.50	4.	C	1.1	0.57	6.	C & X	
20	818	EW	A2	0.2	1.2	0.2	X	1.1	0.45	5.	C	
		NS		0.1	2.4	0.1	X	0.45	1.6	3.	C	
21	851	L	A2	0.25	0.29	0.2	X	-	-	-	-	
		T		0.35	0.14	0.2	X	1.5	0.27	5.	C	

TABLE 1

KEY

T   Period in seconds
S'_a Spectral acceleration capacity in g's
S'_d Spectral displacement capacity (relative to ground) in inches
Element Symbols: C   Column; NS   Nonstructural; X   Diagonal Bracing
                  B   Brick wall; W   Wood wall; T   Tile wall

Building Types: AC   Mill bldg. with diagonal bracing
                  A3   Mill bldg. with diagonal bracing
                  A4   Mill bldg. without bracing or walls

Adapted from reference 3

Assumptions:
Damage 0% @ P_y
Damage 100% @ P_u
% Damage Linear Between
P_y & P_u
Damping, Linear Between
P_y (2%) & P_u (5%)

Example:
Earthquake Criteria for
10% Probability of Being
Exceeded. Damping at
2% and 5% (Appendix C)

Steel Building (#469L)
2% Damping @ Yield Capacity, P_y
5% Damping @ ULT. Capacity, P_u
(Table D-1, Appendix D)
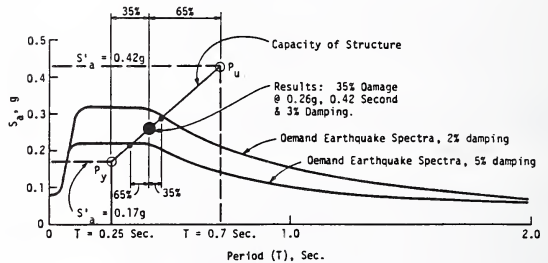
FIGURE 1

Adapted from ref. 3

262

THEMATIC MAPPING WORKS FOR SEISMIC DISASTER PREVENTION
IN GEOGRAPHICAL SURVEY INSTITUTE, JAPAN

BY

Masatoshi Nagaoka and Hiroyuki Matsuda[1]

ABSTRACT

The Geographical Survey Institute investigates earthquake disasters and landform conditions after major earthquakes occur. Based on the results of these investigations, the facts and findings about the relation between earthquake disasters and landform conditions of lowland are explained in this paper. The knick line was identified to have a relationship to slope failures. In addition, the viewpoint of historical evolution (development) of landforms is adopted to explain the increase of slope instability after investigating the Naganoken-Seibu Earthquake of 1984 (Ontake Landslide, etc.).

The Geographical Survey Institute is engaged in various geographic works including thematic map making of major areas in Japan, such as the Land Condition Map that addresses landform classification and the Land Use Map that addresses land use and urban function. This work is expected to contribute to the prediction of earthquake damages.

KEYWORDS: Earthquake disasters, Landform influence, Thematic mapping

1. INTRODUCTION

Earthquakes have distinguished characteristics in frequency and intensity. There have been many efforts to predict earthquakes scientifically and take measures against them administratively. The great Kanto Earthquake of 1923 and Fukui Earthquake of 1948 are two representative examples of disastrous earthquakes that affected big cities. Today, if large cities were subjected to such earthquakes, the damage could be unpredictably severe due to the congestion of people and buildings and falling debris.

To implement effective measures against earthquakes, it is necessary to be able to predict the location of the disaster-stricken area, the type of disasters, and their intensity.

Many investigations have been performed on understanding the relationship between natural condition of land and earthquake disaster in Japan. The Geographical Survey Institute performed investigations on all major earthquakes since 1948. Earthquake damage varies sharply with landform and ground

condition. It is effective to know ground condition in the plain by landform type based on landform classification, because classified landform type is closely related to the historical evolution (development) of landforms and is related to ground condition.

2. INVESTIGATIONS ON EARTHQUAKE DISASTERS PERFORMED BY THE GEOGRAPHICAL SURVEY INSTITUTE

The Geographical Survey Institute has performed post-disaster investigations of damages caused by major earthquakes since World War II. Included in these investigations are the relation between the damages and land conditions. Thematic maps were produced as investigative results. The results of the survey are discussed below.

2.1 Fukui Earthquake of 1948

An organized survey on earthquake damages and landform conditions was performed after the Fukui Earthquake in 1948. The following are the conclusions (reference 1):

a. Earthquake damages centered in alluvial lowland. Damage ratio of wooden houses was related to the thickness of soft ground.

b. Most of the destruction resulted from slippages of deep faults and accompanying earth movements.

c. Location of earthquake faults and earth movements could be estimated to some degree if tectonic landforms in alluvial lowlands were researched.

2.2 Chilean Earthquake Tsunami of 1960

Results of investigation on major tsunami-stricken places revealed that the scale of damages by this tsunami varied with regions. This regional difference in damages was found to be related to the difference in coastal landform as shown below (references 2 and 3):

---

[1] Geographical Survey Institute, Ministry of Construction, Kitasato, Yatabe-machi, Tsukuba, #305, Japan.

a. Even along the Rias Coast, damage intensity by the tsunami differed from place to place; it varies with submarine topography. The type of tsunami varied with the shape of the bay, such as the V-shaped bay (a submergence valley of a small river of the past), the W-shaped valley (a complex of V-shape bays), and the U-shaped bay (a submergence bay of a big river in the past).

b. Routes of intrusion, maximum reach from the shore and length of inundated period are deeply related with the landform of coastal plains.

c. By classifying shoreline and landform of coastal plains on the basis of the above, a regionally different type of tsunami and its risk can be estimated. In this sense, a landform survey on the coast forms give the basis of measures against a tsunami.

2.3 Niigata Earthquake of 1964

Unique damage from liquefaction at alluvial soft ground occurred following this earth-quake. The investigation of the damage and landform condition (aerial photographs, interpretation of landform, field survey, mapping of the damage, etc.) resulted in the following conclusions (references 4, 5 and 6):

a. Damages were serious along the former river beds. Also, major damage was found at interdune lowlands, backmarshes and banked-up lands (former lowlands or backmarshes).

b. Landform on ground surface is classified by characteristics such as geomorphic agent, formative age, shape and relief, structure, composed material, etc. The landform unit classified revealed that it is not only characteristic of landform itself but also the relation with surface geology and soil and drainage condition. Such detailed classification of landform, therefore, explains the reason of occurrence of regional difference in damage.

c. Consequently, earthquake damage potential at another place with similiar characteristics can be predicted to some degree by a microland-form classification map.

d. From the above, it was proven that a Land Condition Map which included damage made by the Geographical Survey Institute, was effective in predicting earthquake damage potential.

2.4 Izu-Hanto-Oki (Off Izu-Peninsula) Earthquake of 1974 and Izu-Oshima-Kinkai (Adjoining Sea of Izu-Oshima) Earthquake of 1978

After the investigation of the relationship between frequent landslides and local landform condition, the following conclusions were

obtained (reference 7):

a. Landslides frequently occurred around the knick line in mountain slopes.

b. In the relationship between landslide and dip division, it was revealed that the occurrence of landslides increased rapidly at 45 deg or greater slope according to landslide occurrence ratio by every dip unit. At slopes overlaid by tuff and/or pumice layer, however, landslides occurred even at about 25 deg.

2.5 Miyagi-Ken-Oki (Off the Coast of Minagi-Pref) Earthquake of 1986

The damage centered on newly prepared housing sites overlying hills. The following facts were revealed in connection with landform (reference 8):

a. Thicker banked-up layers resulted in greater damage to houses and ground. Sizable damage occurred at places where the slope before banking was large and where a terrace-like banked-up slope was one-sided.

2.6 Nihonkai-Chubu (Central Japan Sea) Earthquake of 1983

The following, similiar to preceding cases, were revealed (reference 9):

a. The highest percent of damage occurred to wooden houses at the banked-up former marsh.

b. Damage percentage was relatively high at the cut and leveled higher sand dunes, lower sand dune (groundwater level is high), inter-sand dune lowlands, banked-up flood plains and former river beds.

c. Damage percentage at a terrace and a table land was lower than that of any other type of landform.

2.7 Naganoken-Seibu Earthquake of 1984

The damage from this earthquake was reported at the 17th U.S.-Japan Joint Meeting (UJNR) in 1985. The author reported on geomorphological and geological characteristics of a large-scale landslide (Ontake Landslide), which occurred at the same moment when this earthquake occurred. That is, 3.4×10^7 m^3 of mountain mass suddenly began landsliding. This is shown in Fig. 1 as landform of prelandslide and postlandslide (stereoscopic). The main mass landslided along underlying pumice layer, and resulted in the reappearance of a V-shaped buried valley (reference 10).

Topographic profiles of landform change and landform classification maps of this landslide were produced. From the viewpoint of Quaternary historical evolution (development)

of landforms, the author studied:

a. Why did this large-scale landslide occur only at that site although the earthquake and heavy rainfall existed in the neighborhood?

b. Why, for the first time, did the landslide occur at the site despite the fact that no earthquake had been accompanied by a landslide before?

By reviewing historical factors connected to the occurrence of landslides, the following finding is obtained: a landslide occurs when the Instability Index I (reciprocal of "factor of safety") (reference 11) exceeds the critical value. The Instability Index is shown below.

$$I = \frac{L}{M} \times (V_f \times A + V_S + V_G)$$

where:

I = Instability Index (reciprocal of "factor of safety").
L = Land relief factor.
M = Slope material strength factor.
V_f = Final forcing variable for generating of landslide.
A = Amplification coefficient for V_F by site condition.
V_S = Step-up increase variables for slope instabilization.
V_G = Gradual increase variables for slope instabilization.

According to this equation, the geomorpho-logical process from the forming of the slope to the occurrence of the landslide is explained as follows (Fig. 2, reference 12):

a. A slope of V-shaped dissected valley (formed tens of thousands of years ago) in Pleistocene polygenetic volcano was overlaid by aeolian unconsolidated thin pumice layer. This layer was overlaid by alternating beds of lava and pyroclastics to develop a piled-up long slope. Subsequently, a lava layer covered the foot such as a "weighting banking."

b. With a decrease in the supply of debris from the slope due to downward tendency in temperature and ascension of forest line in Pleistocene (from ca. 10,000 years ago), downward erosion of valleys (50 m in relative height traced back from a geomorphic surface downward) and retreat of the knick point (falls, for instance), the slope was dug at the foot and became unstable (expression V_S and V_G as in the above equation). In the front of the V-shaped buried valley where "weighting banking" was removed by this erosion, a large-scale landslide had previously occurred caused by heavy rainfall and/or large earthquakes (V_F). The former large-scale landslide valley was formed in this process.

c. Later, the falls retrograded about 400 m, the valley bottom at the foot of the landslide site rapidly lowered its level. This caused deterioration of the slope of the mountain where the buried valley was hidden and intermittent creeps (estimated from existence of slid scarplets, etc.) advanced (V_S and V_G).

d. A large-scale landslide occurred from V_F, preceding rainfall of 160 mm and an earthquake with seismic intensity around VI. Groundwater catchment and storage were high because it underlaid a buried valley. The earthquake amplification (acceleration) was large because of a piled-up ridge (see the A factor in the above equation).

In this case, the direct factor V_F (final forcing variable for generation of landslide) and A (amplification coefficient for V_F by site condition) were large and played an important role for the occurrence of this landslide; but they alone did not cause it. It is important to realize that the Instability Index I first exceeded the critical value when V_F and A were added to the precedent facts that the level of the valley bottom already had been lowered and the slope had deteriorated; thus, the landslide. From this viewpoint, a and b above can be explained rationally. In addition, the viewpoint of the historical evolution (development) of slope landforms makes it possible to predict landslide site potential and reasonably explain the mechanism of occurrence of a landslide.

3. GEOGRAPHIC WORKS OF GEOGRAPHICAL SURVEY INSTITUTE

3.1 Earthquake Disaster and Landform Condition

Earthquake disasters are closely connected with landform condition. Disasters caused by earthquake movement and liquefaction are not directly affected by landform condition but by underground conditions. Reconstructing paleogeography by geomorphological methods and researching the historical evolution of landform provides a good understanding of underground condition; ground condition is determined by geomorphological place at the time of sedimentation (= landform formation). The ground condition of surface layer, not deeper than several meters, is closely related to microlandform (references 13 and 14). Therefore, it is possible to determine ground condition by reading the microlandform. It is possible to determine ground condition, such as evaluation of underground, by reading a Landform Classification Map. It is recommended to use this map from the viewpoint of earthquake disaster prevention. Fig. 3 shows a model of the relation between geographic place and sedimentary environment ground condition. Fig. 4 shows a sea level change since the last

glacial age which had a great influence on the sedimentary environment of the coastal plain.

The Geological Survey Institute published a Land Condition Map with landform classifications. The outline of this map is explained in Section 3.3.

Earthquake damages include not only direct damage of material and life but also overall damage to living and productive activity. It is necessary to collect various kinds of geographical data to predict such damages. For this purpose, the Geographical Survey Institute's Land Use Map and digital geographical data (Digital National Land Information) are available. These are explained in the following paragraphs.

3.2 Land Use Map

The map is categorized into three major divisions: urban area, agricultural land and forest. The urban area is subdivided into intermediate divisions and/or small divisions. Here, the regional planning division is used for Town Planning and Zoning Acts, and urban function is given special attention. The agricultural land and forest are subdivided into intermediate and/or small divisions, paying attention to the vegetations. Six different colors are used on the maps. By combining the shades of color and patterns, this map differentiates 35 land use divisions. Maps denoting land use (Fig. 5) are based on interpretations of aerial photographs by surveys and other data.

3.3 Land Condition Map

Before and after Typhoon 5919 (Isewan Typhoon, 1959), surveys on landform and flood disaster were performed in Nobi Plain. These surveys revealed that is was possible to predict the location and intensity of damage by characteristics and historical evolution (development) of landform, altitude, and history of reclamation. This experience accelerated the development of the Land Condition Map that focused on landform classification in lowlands. Investigations were then performed when earthquakes occurred. The results showed correlations between micro- landform ground conditions and earthquake disaster. Therefore, this type of landform classification map was considered useful.

Later, topographical classification and dip division of mountains were added to the map to understand slope disaster potentials. Since 1980, the information on underground features has improved. Contour lines of the base of alluvium deposits (= ground surface at last glacial stage) or isopach maps of soft layers were included as well as topographical classification.

The contents of the Land Condition Map include landform classification, ground elevation, and various organization and public facilities pertaining to land disaster and development. As seen in Fig. 6, maps were made mainly on the basis of the interpretation of aerial photographs and field survey. Units of the landform classification are classified into groups homogenous in morphological unit, morphogenesis (natural processes such as erosion by running water and sedimentation, volcanism, crustal movement, etc.), and formative age. Mountains and hill slopes are divided by slope and subdivided by shape of slope. Terrace and tableland are subdivided by formative age and elevation. Lowland is divided into general surface, relatively higher land, and well drained landform, and furthermore, subdivided by microtopography. An artificially deformed area, with bad conditions, is denoted so the former units of landform classification, before artificial deformation, can be shown. In addition to the above, land is contoured every 1 m to express subtle undulations on the ground surface.

3.4 Digital National Land Information

Information from maps such as the Land Use Map and the Land Condition Map is not always readily available as in the case of obtaining quantitative data from measuring. The Geographical Survey Institute initiated supplying various geographic digital data accurately corresponding to 1:25,000 topographical map. Now data, such as digital data, is more easily obtained.

The Digital National Land Information is stored on magnetic tapes. A large quantity of data can be processed and analyzed very fast by an electric computer. The data is stored as line data, e.g., data about shoreline, river channel, the administrative sector, roads and railroads, etc., and data as mesh (about 1 km^2).

4.0 SUMMARY AND FUTURE VIEW

Ground disaster accompanied by an earthquake is greatly affected by underground characteristics. The ongoing land condition survey by the Geographical Survey Institute is focused to know where earthquake disaster potentials lie. The Land Condition Map contains much useful information.

It was concluded that work needs to focus on the response characteristics of ground by computer analysis and liquefaction potential. Mappings on such were carried out. They were reported and discussed at UJNR meetings. There are "distribution map of ground motion" and "map of liquefaction potential" (mesh map) by Tokyo Metropolis (reference 15) as an example of mapping a large area. This mapping,

however, is based on the assumption that much borehole data can be obtained in urban areas in Japan.

It is necessary to scudy the landform classification of landforms in a tropical humid climate and an arid climate. Such landform classification maps at such places are expected to increase.

Furthermore, to inform map readers about the data contained on the maps, it will be necessary to produce not only general landform classification maps but also maps that meet various specified purposes such as an earthquake disaster hazard map and flood hazard map, etc. In that case, synthetic applied geomorphological evaluation is needed (reference 16). It is necessary to evaluation new characteristics of combined units including the characteristic of each landform classification unit. On the other hand, it is necessary to assume even changes of the original characteristic when natural and social (artificial) conditions are added to landform condition. Landform classification map expressions must be simplified by using colors and patterns to help map readers understand the similarity and contrast in the units of landform classification.

5. REFERENCES

(1)   Ogasawara, Y., "Earthquake Damage and Disastrophism," Journal GSI, Special Ser. 2, 13 p, 1949 (J).

(2)   Ohya, M., "Chilean Earthquake Tsunami and Coastal Landform (I)," Journal GSI, No. 26, p 6-13, 1961 (J).

(3)   Ohya, M., "Chilean Earthquake Tsunami and Coastal Landform (II)," Journal GSI, No. 27, p 12-19, 1962 (J).

(4)   Geographical Survey Institute, "Report on the Niigata Earthquake," 60 p, 1965 (J).

(5)   Kobayashi, M. and Magome, H., "Disaster of Niigata Earthquake of 1964 and Land Condition Survey," Journal GSI, No. 30, p 1-7. 1965, (J).

(6)   Takasaki, M., et al., "The Reration of the Damages Caused by the Niigata Earthquake and the Topographical Conditions in Niigata Plain," Rep. Cooperative Res. Disaster Prevention, No. 11, p 13-18, 1966 (J).

(7)   Geographical Survey Institute, "Report on the Izu-Oshima-Kinkai Earthquake of 1978," 56 p, 1979 (J).

(8)   Kobayashi, M., "Disastrous Ground Failure in a Residential Area of Large-Scale Cut-and-Fill in the Sendai Region Caused by the Earthquake of 1978," Bulletin of Geogr. Survey Institute, No. 24, p 15-25, 1980 (E).

(9)   Tsurumi, E., et al., "Relationship Between Seismic Disaster and Ground Condition in Noshiro Area, Akita Prefecture," reported at the 16th Joint UJNR Meeting, 1984 (J,E).

(10)   Nagaoka, M., et al., "Geomorphological Characteristics and Factors of the Large-Scale Landslide and Detritus Flow on the South Slope of Ontake Volcano Caused by Naganoken-Seibu Earthquake, 1984," reported at the 17 Joint UJNR Meeting, 1985a (J,E).

(11)   Hatano, S. and Nagaoka M, "Geomorphic Properties and Causal Factors of the 1984 Ontake Landslide, Analyzed by Time-Series Air-Photos," Bull. Volc. Soc. Japan, Ser 2, Vol 30, p 107-108, 1985 (J).

(12)   Nagaoka M. et al., "Casual Factors of Large-Scale Landslide as a Viewpoint of Postglacial Historical Evoaluation of Landforms - on the Case of Naganoken-Seibu Earthquake, 1984," Abstract of the 15 Meeting of Assoc. Quart. Res. Japan, No. 15, p 90-91, 1985b (J).

(13)   Tsurumi, E. et al., "Seismic Disasters and Land Conditions of Lowland," reported at the 14th Joint UJNR Meeting, 1982 (J,E).

(14)   Sunaga, H. and Kumaki, Y., "Earthquake Disaster and Landform Classification, Journal GSI, No. 56, p 24-31, 1982 (J).

(15)   Tokyo Metropolis, "Report on the Prevention of Earthquake Damages in the Tama-Region," 576 p, 7 maps, Tokyo Met. Gov., 1985 (J).

(16)   Kanabubo, T, "Present Situation and View of Landform Classification," Journal GSI, No. 56, p 5-6, 1982 (J).

(17)   Inokuchi, T., "Large-Scale Landslide and Rock Avalanches at the Head Source of the Denjo River," Natural Disaster Research Studies, No. 25, p 45-62, National Research Center for Disaster Prevention, 1985 (J).

(18)   Mizutani, T., "Disaster Prevention and Landform," Kokon-Syoin, 168 p, 1982 (J).

(19)   Ikeda, T., "Study on the Alluvial Deposits on Tokaido Region," Contribution Institute Geol. Paleontol., Tohoku University, No. 60, p 1-85, 1964 (J+E).

(   )   Kadomura, H., "Systematic Aerial Photo Analysis of Soft Ground Condition," Geogr. Rev. Japan, Vol 41, p 19-38, 1968 (J+E).

(   )   Kobayashi, M. et al., "Investigation on the Landform Condition and Earthquake Disaster," Report on the Miyagi-Ken-Oki

Note:

(J)   Written in Japanese only.
(J+E) Written in Japanese with English
       abstract.
(E)   Written in English only.
(J,E) Written in English and Japanese.

pre-landslide (solid line) :
1:5.000 Volcanic Map based on
1969.5 aerial photo. ×0.30.
G.S.I.

post-landslide(dotted line) :
1:5.000 map based on 1984.9
aerial photo. ×0.30. G.S.I.

⊢ knick point

⇡ : sliding direction of landslide
    (= projected direction
       of Fig.2)
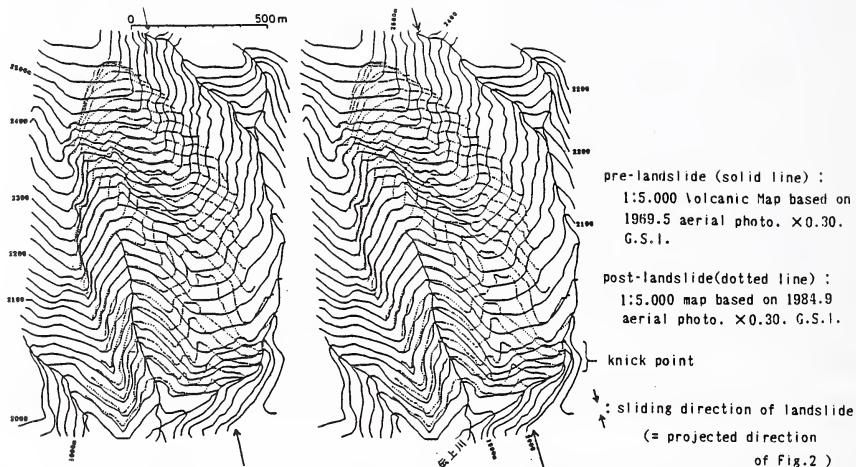
Fig. 1 Stereoscopic topography of the 1984 Ontake Landslide (reference 17).

A : ridge before the Landslide
B : valley formed by the Landslide
C : inferred valley bottom of ca.10000 years ago
D : lava flow surface at the left bank
E : valley on the right side of the lower reach

▢ : denudated part by the 1984 Ontake Landslide
--- : facies boundary
--- : inferred ground surface of ca.10000 years ago
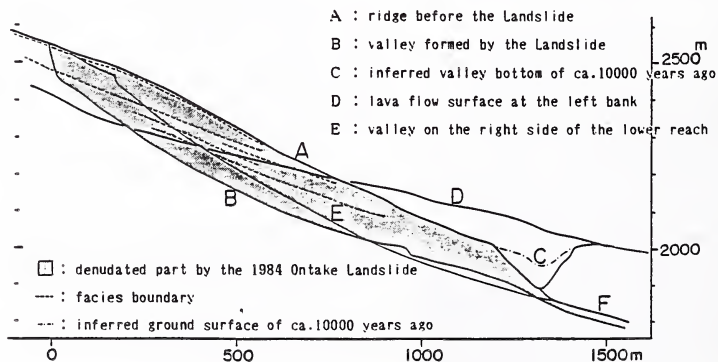
Fig. 2 Projected profile of 1984 Ontake Landslide (revised from reference 12).
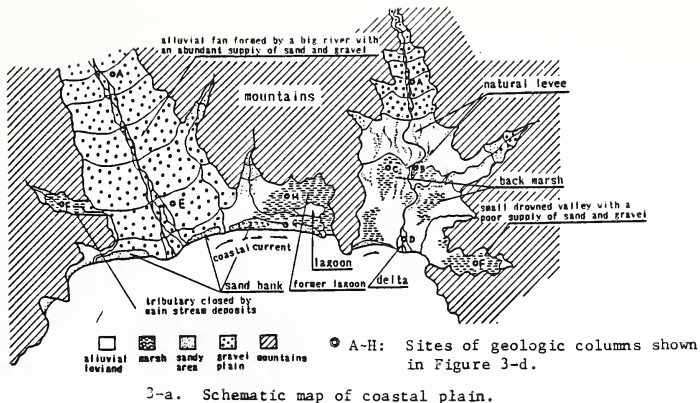
3-a. Schematic map of coastal plain.

○ A-H: Sites of geologic columns shown in Figure 3-d.
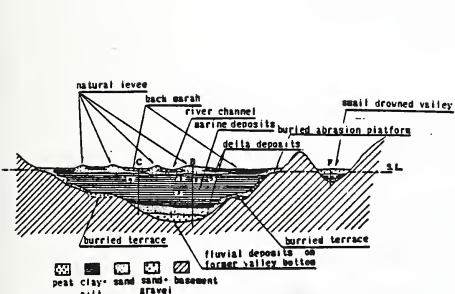
3-b. Schematic geologic section of alluvial (postglacial) deposits filling the drowned valley.
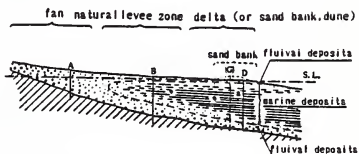
(a) Alluvial (postglacial) deposits of a big river flowing into a bay or a small river.
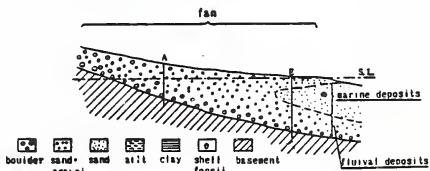
(b) Alluvial (postglacial) deposits of a big river whose alluvial fan directly faces the sea.

3-c. Schematic longitudinal geologic section of fluvial lowland.
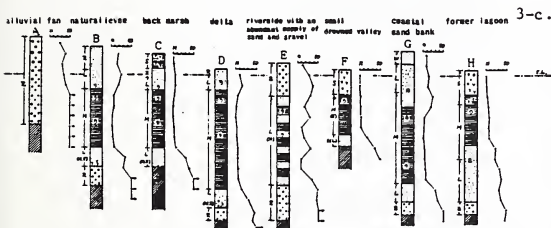
3-d. Schematic geologic columns of alluvial (postglacial) deposits in the lowland (compiled by the Geological Survey Institute from reference 19).
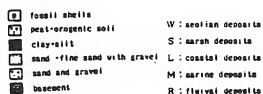
Fig. 3 Relationships of underground condition and landform-sediment environment of fluvial lowland (reference 19).

269
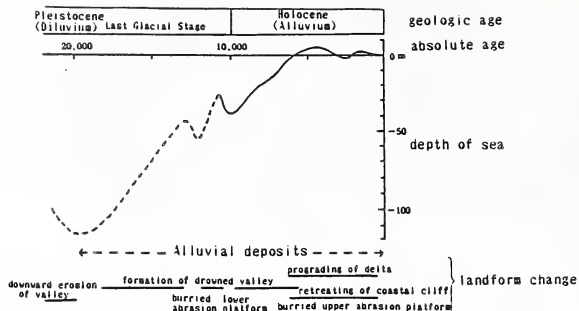
Fig. 4 Sea level change since the last Glacial Age (simplified by reference 18 from Kaizuka, 1976).

| Planning map | • Planning
• Base map making
• Preparing the photos
• Preparing the reference data |

| Preparatory work | • Photo-interpretation
• Analyzing the data
• Appearance of the planned area
• Checking the revised parts of the base map |

| Source material collection | • Source material collection in the public bodies
• Filling the source material |

| Field reconnais-sance survey work | • Observation of the field
• Checking the preparatory work carried out
• Confirming the changed land use after photographing
• Checking the map source material collected |

| Arrangement work | • Filing the data observed in the field
• Inking the data on the photos
• Arrangement of data on the overlay
• Ailling the reference maps |

| Compilation work | • Revision of the base map
• Land use classification by photo-interpretation
• Compiling the revision data map for drafting
• Tie-strip making
• Marginal information making
(Survey data: compiled manuscript) |

| Drafting work | • Revising the positive sheet of the base map
• Scribing the boundary sheet
• Mask-sheet making
• Making the compounded positive and negative sheets
(Drafting data: compounded positives and negatives for plating) |

| Map-reproduc-tion work | • Plating and reproducing
(Final data: Printed Land Use Map) |

Fig. 5 Work flow of the 1:25,000 Land Use Map.
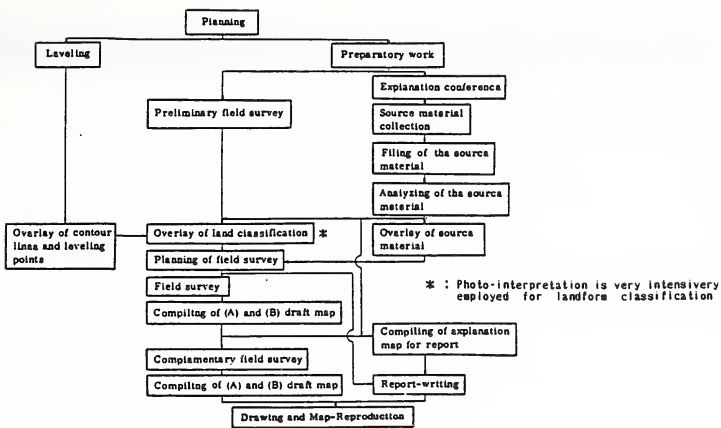
Fig. 6 Work flow of the 1:25,000 Land Condition Map.

THEME III

Storm Surge and Tsunamis

SATELLITE METHODS AND APPLICATIONS
IN MARINE ENVIRONMENTAL ANALYSIS

C. S. Barrientos, F. G. Everdale and R. P. Stumpf

Marine Environmental Assessment Division
Assessment and Information Services Center
National Environmental Satellite, Data and Information Service
National Oceanic and Atmospheric Administration
Washington, DC 20009 USA

ABSTRACT

Satellite can provide important data
for the study and monitoring of
processes, conditions, and changes in
the marine environment. Remote
sensing data have good spatial and
temporal resolution, thus providing
adequate information for analysis at
reasonable cost. Three
characteristics can be determined
directly on water by satellite
measurements, 1) surface temperature,
2) turbidity; and 3) water color.
Each of these characteristics can be
used to identify certain water masses
or water parcels to estimate the .
surface concentrations of sediment and
pigments. Overland, changes can be
seen by satellite from images taken at
different times. Similarity, changes
in the boundary between land and water
can be studied from time series
imageries.

Satellite data were used together with
conventional observations and modeling
to study the Chesapeake Bay and the
adjecent shelf waters. It was also
used to study the warming episode in
the eastern Pacific Ocean, to assess
the fishery situation in the
Philippines, and to determine the
feasibility of satellite applications
to fishery off West African countries.

1. INTRODUCTION

Satellite can provide important data
for the study and monitoring of
processes, conditions, and changes in
the marine environment because of
their synoptic and repetitive
coverage. Conventional oceanographic
data, such as that collected from
isolated moorings or from individual
cruises, have substantial spatial or
temporal limitations. Synoptic data
can be collected only at great
expense. Spatial variability cannot
be properly observed from a limited
number of discrete stations or
tracklines and cruises cannot often be
repeated. Satellites, however,
collect data at thousands of points
over the water and adjacent land
thereby providing essentially
continuous coverage. Certain sensors,
such as those on the NOAA weather
satellites, provided coverage as often
as two to four times a day, permitting
the modeling of dynamic estuarine and
coastal processes. However, they
cannot provide information on the
vertical structure of the water
column; therefore, a combination of in
situ measurements, remotely sensed
data, and modeling results are needed
in the study of estuarine and oceanic
processes.

At present, data obtained from
satellites yield information on
temperature, turbidity, and water
color. Each of these characteristics
can be used to identify certain water
masses or water parcels and to
estimate the surface concentrations of
sediment and pigments. Therefore,
satellites may aid in monitoring
fronts and plumes and in identifying
circulation patterns in Cheaspeake Bay
and on the adjacent shelf.

There are three satellites sensors of
potential use in estuarine waters:
the NOAA-n series Advanced Very High
Resolution Radiometer (AVHRR).
Nimbus-7 Coastal Zone Color Scanner
(CZCS), and Landsat Multispectral
Scanner (MSS) (Tables 1 and 2). These
sensors are on polar-orbiting
satellites; i.e., the satellites have
orbits oriented north-south in order
to allow coverage of the entire globe.
The sensors measure the radiance of
the reflected visible and near-
infrared light and the thermal
infrared energy emitted by the earth
and atmosphere. Each sensor system
has different characteristics, which
provide different advantages.

Landsat was designed for use over land, which has greater and more variable reflectance than does water. Accordingly, Landsat data has been shown to provide a good measure of suspended solids in turbid water. However, the satellite sensor is insensitive to slight changes in the reflectance of clear water. Landsat also has very high resolution, 80 m. To achieve this high resolution, the satellite has an overpass period of 16 days, thus limiting the temporal resolution.

The CZCS samples every three to five days in the mid-Atlantic with a resolution of 800 m. It has five reflected light bands and one thermal-IR band, all specifically designed for oceanic waters. It is quite sensitive to variations in water brightness, but it is not always usable for turbid waters, like those found in the upper Chesapeake Bay, that reflect enough radiance to saturate some channels on the radiometer. Algorithms for the CZCS data have produced estimates of oceanic chlorophyll content accurate to within 30 percent (Gordon et al., 1983). These results have permitted analysis of biomass on the shelf and in the Gulf Stream, and detection of some eddies and other features of circulation. Unfortunately, the error in these algorithms increases with turbidity, making them highly unreliable in many estuaries. Nonetheless, because the sensor's spectral bands were designed to collect measurements over water, this satellite sensor can provide useful information on estuaries. The CZCS is eight years old, well beyond its expected lifespan, and has failed in June 1986. Thus, we can no longer depend on it as future source of data. However, data collected during the eight years of operation are very useful in retrospective analysis.

The AVHRR sensor is on the NOAA-n polar orbiting satellites series. It measures radiance in two reflected (visible and near-infrared) bands and two or three thermal infrared bands. NOAA has developed regression equations to calculate sea surface temperature (SST) using data from the thermal channels (Strong and McClain, 1984). The sensors are intermediate in sensitivity between those of

Landsat and CZCS, making them useful in estuaries (Gagliardini et al., 1984). This satellite is designed for frequent sampling of the globe, twice per day with one satellite, and with two operational satellites, four overpasses (two daytime and two nighttime) may be recorded. The best resolution of the AVHRR is 1.1 km, making it useful for delineating the larger estuarine and oceanic features.

For application to Chesapeake Bay, the AVHRR and the CZCS systems are preferable because either sensor can include the entire Bay in one scene, and because either system has a high enough sampling frequency to aid in analyzing coastal dynamics and in verifying models. Biweekly sampling, like that done by Landsat, supplies more limited information on the dynamics of an estuary.

2. TEMPERATURE ANALYSIS

Using Planck's Law, we can calculate a temperature from the thermal infrared radiation detected by the satellite sensor. Due to atmospheric absorption and emission (primarily by water vapor), the thermal radiance reaching the satellite is not the same as that emitted by the surface of the water. Often the calculated black body temperature is lower than the surface temperature. A technique for atmospheric correction and calibration is required to determine the true surface temperature from the satellite data. The most accurate atmospheric correction entails the use of two or more thermal channels. Because CZCS has only one thermal-IR band, atmospheric corrections for CZCS are less accurate, although we can obtain reliable data on temperature gradients.

The AVHRR, through the use of regression equations developed at NOAA (Strong and McClain, 1984), provides excellent estimates of sea surface temperature using channels 3 and 4, and also channel 5, when available. These calculated, "multi-channel sea surface temperatures" (MCSST), are accurate to within 1 $^{\circ}$C when compared to ship and buoy data. Much of this 1 $^{\circ}$C diffence probably results from differences in the measured property ; buoys measure bulk temperatures of the

276

upper 0.5-1 m of water, whereas satellites receive radiation from the top millimeter or less of the water (skin temperature). Errors can also result from incomplete correction from the atmospheric effects, particularly for the effects of dust, fog, or thick haze. Because NOAA-6's channel 3 thermal data were noisy prior to September 1982, and the satellite did not have channel 5 (found only on NOAA-7 and NOAA-9), MCSST equations were not available for the April 1982 NOAA-6 imagery. Therefore, in this study, sea surface temperatures for the NOAA-6 imagery were determined by linear regression of channel 4 brightness temperatures against MCSST calculated from NOAA-7 data from the same day. The NOAA-6 temperatures matched the NOAA-7 temperatures to within 1 $^{\circ}$C (95 percent confidence level).

3. TURBIDITY DETERMINATION

Suspended materials provide useful tags of water parcels, and they indicate the extent of runoff, land erosion, and nutrient discharge. Visible or reflected infrared light provides an indication of the quantity of suspended materials by showing the turbidity of the water. However, monitoring and comparing imagery from different days requires a consistent and quantifiable property such as reflectance, or suspended sediment concentration. Determination of these quantities from the raw data requires several corrections of the total measured brightness.

Processing an image first requires the elimination of areas covered by clouds or showing discernible sunglint. Sunglint is the specular (mirror-like) reflection of sunlight off the surface of the water. It may provide useful information on surface phenomena, such as wave fields, but it prevents us from obtaining information on materials in the water, by masking the water column reflectances. The effect is similar to trying to see out a window at night and seeing only your own reflection. Water is a highly effective absorber of near-infrared radiation, therefore, both clouds and sunglint can usually be detected through the increased brightness they produce in near-infrared bands. In

the areas not containing clouds or sunglint we can obtain reflectance of the water column. To obtain reflectance in these areas, we must correct for both the radiance of the atmosphere between the earth and the satellite--known as path radiance--and the amount of total radiance reaching the surface (the incident irradiance).

Over water, path radiance frequently constitutes 50-90 percent of the total visible radiance detected by the satellite. It changes with the dust and water vapor content, and therefore can vary from one image to the next. In addition, the total path radiance generally increases toward the limbs of the image because of the greater thickness of the atmosphere. To obtain only the radiance leaving the water, we must substract the path radiance from the total radiance observed at each pixel by the satellite. The path radiance is usually determined as the radiance observed from the darkest pixels in the locale. In estuarine work, the path radiance is assumed uniform over the study area--a functional, albeit not ideal, correction. Areas near the limbs of the images are generally not usable.

The amount of radiance leaving the water depends on the amount entering; hence, there is need to correct for the incident irradiance. The incident radiance depends on the sun's elevation. Thus, water with a given sediment content will appear darker in the morning than at noon, and darker in the winter than in the summer. In contrast to the atmospheric correction, a calculation of the sun's elevation can be made quite precisely throughout the image, thereby allowing an estimate of the incident irradiance, using the solar constant multiplied by the sine of the solar elevation (Gordon et al., 1983). By dividing the atmospherically corrected water radiance by the incident irradiance, we obtain a form of reflectance that can be compared from one scene to the next with the same sensor band. We studied early morning and early afternoon scenes for the same day on 14 April 1982. Without the correction to obtain reflectance, the morning scene would show about 60 percent of the turbidity of the

afternoon scene. With the corrections, the turbidity becomes comparable in both scenes.

In the estuarine surface waters, reflectance (R) tends to vary directly with the common logarithm of the sediment concentration (n_s),

$$R \text{ <proportional> } \log_{10}(n_s)$$

so that a determination of reflectance can also show the amount and variability of suspended materials in the Bay (Munday and Alfoldi, 1979). For the study period, we do not have data on the concentrations or suspended solids, hence the results are shown as reflectance and not as concentrations. However, comparisons of reflectance (corrected turbidity) on different days can help show distribution patterns and paths of transport of suspended materials. In modeling, the suspended material may itself be of interest, or it may serve as a surrogate for other substances or organisms.

4. PIGMENT ESTIMATION

As described earlier, algorithms developed for the CZCS have given very good estimates of chlorophyll in oceanic and shelf waters. However, the techniques do not provide valid information in many estuaries, because the water's turbidity interferes with the atmospheric correction (Gordon et al., 1983). An algorithm developed in our Center in NOAA does permit the estimation of relative variations of the chlorophyll concentrations and the detection of algal blooms in turbid water such as found in Chesapeake Bay (Stumpf and Tyler, 1986). The technique is applicable to both AVHRR and CZCS data, although the CZCS, owing to its narrower bands and greater sensitivity, would tend to give results that are more specific to chlorophyll-a. The AVHRR, having broader bands, would respond to variations in other pigments, although it would be principally sensitive to chlorophyll. The corrected radiance as described in the previous section is necessary in these calculations.

We applied our analysis techniques for the pigments for April 1982 for AVHRR and CZCS imageries. Unfortunately,

the analyses can be displayed meaningfully only in color and not included here. The images showed that blooms appear in the western tributaries of Chesapeake Bay, the Rappahanock, Potomac, Patuxent rivers. The upper Bay, in the region of the turbidity maximum, contains low pigment concentrations. The frequent overpasses of the sensors permit study of diurnal variations in phytoplankton blooms. Many of the blooms result from algae transported into the area, so that modeling the drift would be helpful in predicting the onset of these blooms. Conversely, detection of blooms with satellites can provide data to aid the calibration of drift models.

5. IMAGE PREPARATION

The AVHRR and CZCS collect the data by scanning in a line across the satellite's path, collecting about 2000 radiance measurements on each line. Each measurement is called a pixel (picture element); the area of the earth viewed in each pixel determines the resolution, 1.1 km for AVHRR and 0.8 km for CZCS. As the satellite continues in its orbit, each scanline is slightly offset from the preceding one, thus an image results from the accumulation of these scanlines. The satellites take 1-2 minutes to produce an image of Chesapeake Bay. An image differs from a photograph, wherein all points are recorded simultaneously.

The original images contain distortions that are caused by the earth's curvature and the viewing angle of the satellite. To correct for the distortion, all the images were geometrically stretched to match certain points in the image with reference points on a Mercator projection. Because this commonly used techinque does not assure correspondence with a Mercator projection throughout the image, we call the result a pseudo-Mercator projection. On the resultant image the AVHRR data have a 1.2 km/pixel projection, and the CZCS data have a 0.9 km/pixel scale.

A total of 19 images were used in the Chesapeake Bay study (Table 3). We

included the Table here so that future users may recognized that these images have already been analyzed. Land and clouds were masked in the images using the near-infrared band (AVHRR channel 2, CZCS channel 5). Water absorbs near-infrared light quite effectively; therefore, a brightness threshold can generally be used to distinguish land and clouds from water. Highly turbid water may have the same reflectance as land, therefore some tributaries may be partially masked.

The temperature images were color-contoured in 1 °C intervals between 7 and 18 °C, where (for reference) the 7 °C contour contains the data from 6.95 to 7.95 °C. Temperatures outside that range were not distinguished.

The reflectance (turbidity) data were grouped into 16 classes and colored. Small values of reflectance should be interpreted as water that is relatively clear, i.e., the water does not contain large quantities of material, either organic or inorganic in suspension. Larger values of reflectance denote increasing quantities of suspended material in the upper water column. Reflectance indicates only the degree of water clarity or the relative quantity of materials in the water and does not indicate the composition of those materials.

6. SATELLITE IMAGERY ANALYSIS AND INTERPRETATION

The distributions of temperature and turbidity (reflectance) in the satellite imagery are used to infer some of the circulation dynamics and water quality of the Bay and the adjacent shelf and slope region. The region contains four principal water masses: the Bay waters, the shelf water, the slope water, and the Gulf Stream. Temperature imagery for the study period can be used to discern variations in all four. Reflectance, however, provides information only on the Bay waters; the sensitivity of the sensor and the quality of the atmospheric correction cannot discern variations in the reflectance of the comparatively clear offshore waters during this period.

7. ANALYSIS FOR CHESAPEAKE BAY

Insolation can significantly influence the surface skin temperature of the Bay. In the satellite imagery, the Bay cools by 1 to 4 °C at night, and warms throughout the day. Reduced vertical mixing during periods of reduced wind speeds may promote this variability. Satellite image for April 12, 1982 shows the low night-time temperatures in the Bay. The surface temperatures fall below 8 °C in the upper Bay and below 7 °C in the lower Bay (below the Rappahannock River). By early afternoon, (shown by the afternoon image), diurnal heating has greatly increased the temperature. The entire Bay has warmed by as much as 4 °C. <u>In situ</u> data taken in the Bay on this day correspond to the satellite-derived daytime temperatures. The shelf waters have warmed to a lesser extent (1 to 2 °C), while negligible changes appear in the slope and Gulf Stream waters. The difference between the day and night temperatures observed during the study period may result from either diurnal variations in the skin temperature or fog and mist over the Bay at night. If the variation is in the skin temperature, it does not necessarily indicate temperature fluctuations in the upper meter of the water column, because the skin temperature can react rapidly to changes in air temperature and sunlight.

The seasonal increase in surface temperature is evident during the study period. Some warming is evident on 15 April image analysis. By 23 April, the Bay and shelf have warmed substantially, about 4 °C throughout the area. Shallow waters, such as those in the sounds and tributaries, respond relatively quickly to changing insolation and air temperatures, while the deeper waters of the Bay and shelf respond more slowly. Thus, the western tributaries and eastern shore of the Bay contain warmer water than does the central Bay. Similarly, the lower Bay has warmer water than the adjacent shelf. Therefore, temperature can be used to infer transport of tributary water in the Bay and certain characteristics of the exchange of water between the Bay and the shelf.

The flows from the four largest tributaries, the Susquehanna, Potomac, Rappahannock, and James appear to hug the western shore. This is particularly evident on 12 April image and other data, where cool northern Bay and Susquehanna water follows the western shore, as does the 9 °C water leaving the Potomac River. The warm waters associated with the Rappahannock, York, and James Rivers appear to flow along the western shore down the Bay and out the mouth around Cape Henry.

The reflectance is generally highest in the upper reaches of the Bay and its tributaries, decreasing with distance downstream. The main Bay, Potomac River, and James River show turbidity maxima at the upper reaches with a rapid decrease in reflectance and fairly clear water downstream, as material supplied by the rivers settles from the surface. In the main Bay, lateral variations appear in the turbidity maximum.

The water of the central Bay, off the Potomac and Rappahannock Rivers is clearer and colder than the adjacent waters. These differences result from the greater depth of the water, which reduces both warming and sediment resuspension, and the greater distance from riverine and shoreline sources of sediment.

The thermal and turbidity fronts at the mouths of the Rappahannock, York, and James Rivers coincide. The Bay mouth plume shows a more complicated structure. The temperature and turbidity plumes do not always coincide, although the turbidity plume, owing to its low reflectance, is less pronounced than the plumes and fronts within the Bay.

The thermal plume's position is highly variable. Early on 12 April, the warmer Bay water appears to branch; one limb hugs the coast to the south for some 100 km, the other limb moves directly offshore, suggesting intense mixing. This structure may result from the 12 kn winds from the west pushing water offshore. In the afternoon the plume is oval, although tending southward. A bulge or turbid water appears off the mouth of the Bay at this time. A thermal plume is

distinct, despite the maximum flood tide at the mouth of the Bay. Small detached pools of 10 °C water are observed offshore. Two or three elongated filaments suggest intense mixing. Again, as on 12 April, the plume extends to the south. The 10 °C ribbon of water along the North Carolina cost may be simply warm nearshore water and not water from the Bay.

8. RESULTS FOR OFFSHORE WATERS

The water masses of the shelf, slope, and Gulf Stream show strong mixing and marked spatial variability in temperature during the period. The shelf waters are cooler (3 to 11 C) than the other water masses. Diurnal fluctuations in observed surface temperature occur in the shelf waters, but to a lesser degree than in the Bay. Near Cape Hatteras, the warm Gulf Stream (>15 °C) pinches off the shelf waters of the mid-Atlantic Bight. The Gulf Stream veers to the northeast from Cape Hatteras. Because the slope water originates as a mixture of shelf and Gulf Stream waters, it has intermediate temperatures to shelf and Gulf Stream waters. Thermal fronts sharply delineate the three water masses: the shelf break front between the slope (blue-green) and shelf (purple) waters, and the north wall of the Gulf Stream.

Gulf Stream eddies also can be tracked with the imagery. A warm core eddy, Eddy 12, having clockwise rotation, lies about 180 km off the mouth of the Bay. The eddy becomes increasingly evident through the study period because a filament of warmer Gulf Stream water wraps around it. The filament of 15 °C water develops on the SW side of the eddy (the eddy center is green). On the NE side, cold shelf water is apparently being advected onto the slope by the eddy. By 15 April, the filament has partially encircled the eddy and the cold water (10 °C) has moved around the eddy almost to the Gulf Stream. On 23 April, the filament has encircled the eddy and the cold water has moved between the eddy and the Gulf Stream. The eddy also appears in the chlorophyll pigment image. As the Gulf Stream has much lower chlorophyll

than the slope or eddy, the filament appears as a ring of lower chlorophyll water.

9. WARMING EPISODE IN EASTERN PACIFIC OCEAN

Periodically in the Pacific Ocean, there is a large global episode of abnormal meteorological and oceanic reversals of the circulation patterns causing some major environmental events worldwide. Some of the manifestations are good and some are disastrous. This event is generally referred to as "El Nino" Southern Oscillation (ENSO) episode. The last major ENSO was in 1982-83 which caused damages in the billions of dollars.

Normally in the Pacific Ocean, the trade winds from both hemispheres blow towards the west bringing warm water in the Western Pacific (Australia, Indonesia, and the Philippines), thus keeping the western Pacific warm and the eastern Pacific relatively colder. Part of this normal pattern is the presence of cold upwelling region off the coasts of Chile, Peru, and Ecuador. For reasons still unknown, this normal pattern is reversed every so often in which case we refer to as the ENSO episode. The strongest indication of ENSO is the warming in the eastern Pacific off the coast of South America. During the 1982-83 ENSO episode, we looked at the archive for satellite data for analysis of the event. It was during this event when we initiated our study of satellite applications for the eastern Pacific Ocean.

From October 1985 to May 1986, we requested that the NOAA Polar orbiter satellites collect AVHRR data for the coast of South America in Eastern Pacific region. The AVHRR data were of Local Area Coverage (LAC) type which has a resolution of about 1.1 km. Every two or three weeks during the period, we were able to obtain a series of two to four days of relatively clear imageries. The daily images were analyzed into a Mercator Projection, then composited to eliminate some of the clouds. Series of Sea Surface Temperature (SST) maps were produced which show the evolution of warming if there is any. During

early 1986, several groups have issued advisories of possible ENSO episode. However, our analysis showed that this was probably just the localized "El Nino" and not the large scale ENSO. We were able to reach that conclusion because of the better resolution (LAC, 1.1 km) data that we used.

10. ASSESS THE FISHERY SITUATION IN THE PHILIPPINES

Fishing industry is a major part of the livelihood in the Philippines. Majority of the population depends on fishing for their subsistence and the industry itself is a major component of the country's economy. It is important therefore to know the fishery situation around the Philippine islands.

Remote sensing data is ideal to determine the major oceanic features around the Philippines. By collecing AVHRR LAC imageries, we can determine the locations of warm and cold regions, and sharp temperature boundaries. These oceanic features are related to productivity and food abundance which indicates better fishing. We have coordinated our earlier efforts with the Philippine government officials and they have concluded that the correlation of the oceanic features with their fishing data (catch statistics and larval surveys) is very informative and useful. The information can provide them the understanding of the fishery stocks and assist them to save fuel during actual fishing voyage. We are continuing a series of analysis of imageries for the area. The main problem for this application in the Philippines is that very few times during the summer that we can find clear image.

11. APPLICATION OF SATELLITE IMAGERY

The National Oceanic and Atmopsheric Administration entered into an agreement with the U.S. Agency for International Development (AID), to study the feasibility of applying satellite imagery to the management of west African fisheries.

The geography, meteorology, and oceanography of the West African

coastal region provide for favorable conditions for strong upwellings. The relatively broad and shallow west African shelf has a well-defined seasonal upwelling which is easilly identified in satellite images. The upwelling cells extend to 80 km off the coast. The region of upwelling extends from Cape Bojador to below Cape Vert. The most intense upwelling occurs in the spring and is responsible to local winds along the coast.

We collected and analyzed satellite imagery for January through September 1983 to determined the feasibility of analysis of upwelling or other features of the environment using NOAA AVHRR data. We compared the observational characteristics of the several satellite systems available for adequacy of coverage and resolution. We found the Meteosat (European) was the best for temporal coverage (hourly) while the NOAA AVHRR was the best for spatial resolution (1.1 km). The French are presently providing basic maps of weekly sea surface temperatures of the region based on Meteosat imagery.

The West African fishery is dependent on the upwelling cells for nutrition and possibly life-cycle timing for reproduction. Each upwelling cell ages after being brough to the surface. The water is advected by surface flow, warmed by the sun, and has its nutrient contents depeleted by the grazing zooplankton. The fish in turn feed on the abundance of plankton. Observations indicate the local abundance of fish north of Dakar may be predicted somewhat by the earlier size and intensity of upwelling cells there, as the fish appear to migrate from one aging upwelling cell to a newer one in a slow southward movement. Because fisheries of the region are strongly linked to the upwelling cells, and because the upwelling intensity is highly variable, timely satellite images showing the intensity and location of these cells is valuable to fishermen and fisheries managers. The next task is to develop some kind of predictive indeces or measures of these indicators that the fishermen and managers concern can use.

12. SUMMARY

Data collected by satellites can show spatial and temporal changes in temperature, reflectance, and color (pigments) in the Bay and offshore. The high sampling frequency of the NOAA-n series and CZCS permits detection of daily and weekly variations in temperature. Temperature contrasts during the period were strong, the imagery showing fronts of 4-5 $^{\circ}$C and a temperature range of 15 $^{\circ}$C. Although turbidity showed slight changes over the study period, spatial variability in turbidity is quite evident in the images. The images show the turbidity maxima near the heads of the Bay and the major tributaries, and the clear water in the lower central Bay and offshore.

The Bay mouth temperature and turbidity plumes were neither well defined nor (apparently) persistent, thus movement during the period could not be inferred from a set of images. The greater temperature contrast offshore and the persistence of distinct features such as Eddy 12 did allow tracking of these features by satellite. This indicates that the movement of comparably distinct features within the Bay (such those produced by floods) could be traced.

Analysis of the imagery allows us to infer characteristics of the Bay's surface circulation for the conditions of the study period. The Susquehanna River waters produce a southward flow along the western shore, probably because of Coriolis force. As the Susquehanna and northern Bay waters move southward, they become less turbid. The temperature also changes because increasing time is available for mixing, sensible heat exchange and solar insolation. From the Patuxent River to the Rappahannock, a pool of clear and cooler water persists. This region is relatively deep and furthest from sources of suspended sediments and freshwater; hence it has low turbidity and the uniform and cooler temperatures. Plumes emanating from the Rappahannock and York Rivers are advected southward along the western shore. This water appears to merge with the James River plume and the

combined unit moves seaward along the coast around Cape Henry.

Most of the exchange of water with the shelf probably involves the central and eastern portions of the lower Bay. This Bay water closely resembles the shelf water in turbidity and temperature, hence the exchange cannot be readily seen in the images.

Our study of Chesapeake Bay and the adjacent shelf illustrated the utility of the approach in a complex environmental system. Adaptation to other areas is similar.

13. CONCLUSIONS

Satellites can provide important environmental information on Chesapeake Bay and the adjacent shelf. Using the satellite data, we can obtain a synoptic view of sea surface temperatures, particularly during the day, calculate the reflectances caused by suspended solids, and determine the presence and strength of phytoplankton blooms. Some characteristics of surface circulation can be inferred from the distributions of temperature and reflectance. With the presence of well defined features, the satellite data can be used to determine actual circulation, as shown by the movement of Eddy 12 on the shelf.

At present, satellites can provide accurate temperatures within 1 $^{\circ}$C. Reflectance values give an indication of the relative concentration of suspended solids; however, estiamtes of atual concentrations will depend on our ability to calibrate in situ data against remote measurements of reflectance. Similarly, the pigment index requires additional calibration in order to make it more widely applicable. However, the use of reflectance and a pigment index show the potential ability of satellites in studying and monitoring estuaries.

The temperature data can be used to initialize the surface temperature component of the MECCA circulation model. In addition, it can be used to verify the temperature distributions predicted by the model (section 6.6.3). Similarly, when material transport is added to the model, bloom and reflectance distributions could be compared with the model predictions. The synoptic coverage and availability of satellite data fill a void caused by the logistics and expense of conventional oceanographic measurements.

We have shown that satellite data together with other physical parameters (meteorlogic and oceanic) are useful indicators of fisheries. By understanding the major oceanic features (cold and warm pools, fronts, and productive regions), and relating them to fishery information, managers and policy makers will have additional information to based their decisions.

14. REFERENCES

1. Gagliardini, D.A., H. Karszenbaum, R. Legeckis, and V. Klemas. 1984. Application of Landsat MSS, NOAA/TIROS AVHRR, and Nimbus CZCS to study the la Plata River and its interaction with the ocean. Remote Sensing of Environment 15:21-36.

2. Gordon H.R., D.K. Clark, J.W. Brown, O.B. Brown, R.H. Evans, and W.W. Broenkow. 1983. Phytoplankton pigment concentrations in the Middle Atlantic Bight: comparison of ship determinations and CZCS estimates. Applied Optics 22: 20-36.

3. Munday, J.C. and T.T. Alfoldi. 1979. Landsat test of diffuse reflectance models for aquatic suspended solids measurements. Remote Sensing of Environment 8:169-183.

4. Strong, A.E. and E.P. McClain. 1984. Improved ocean surface temperatures from space--comparisons with drifting buoys. Bulletin American Meteorological Society 62(2):138-142.

5. Stumpf, R.P. and M.A. Tyler. Satellite detection of bloom and pigment distributions in estuaries. (Submitted to Limnology and Oceanography).

6. U.S. Department of Commerce. 1982. Tidal Current Tables, Atlantic Coast of North America. NOAA, National Ocean Survey, Rockville, MD.

Table 1. Spectral bands measured by AVHRR, CZCS, and Landsat MSS.
Numbers denote sensor channels.

```
                            Spectral Bands

              visible   |    near-IR         |       thermal-IR

   m    .4  .5  .6    .7  .8  .9   1.0          3.5   11  12   13
        |   |   |     |   |   |     |            |     |   |    |
AVHRR            1           2                   3      4    5

CZCS  1    2  3     4    5                                  6

Landsat MSS  4   |   5  |   6  |      7
```

Table 2. Characteristics of Satellite Sensors.

	Spatial Resolution (km)	Maximum Scan Angle from vertical	Image Width (km)	Coverage Period (days)
AVHRR	1.1	56	2000	1/2
CZCS	0.82	38	1500	6
Landsat MSS*	.08	6	180	18**

* Landsat Thematic Mapper, which has a spatial resolution of 30 m, began operating in fall of 1982.

** In 1979, the period was 9 days. Starting with Landsat 4 in fall 1982, the period between images changed to 16 days.

Table 3. Imagery of Chesapeake Bay used in this study.

Date	Time (EST)	Satellite	Orbit Number
10 April 82	0800	NOAA-6	14477
	1148	CZCS	17475
12 April 82	0805	NOAA-7	04143
	1045	CZCS	17502
	1429	NOAA-7	04141
14 April 82	0239	NOAA-7	04162
	0810	NOAA-6	14534
	1410	NOAA-7	04169
15 April 82	0230	NOAA-7	04176
	0740	NOAA-6	14548
	1137	CZCS	17544
	1400	NOAA-7	04183
16 April 82	1157	CZCS	17558
	1345	NOAA-7	04159
18 April 82	0810	NOAA-6	14591
	1050	CZCS	17585
23 April 82	0755	NOAA-6	14662
	1400	NOAA-7	04296
24 April 82	1058	CZCS	17668

DISCRIMINATION OF FLOODED AREAS CAUSED BY TSUNAMI OR STORM SURGE USING SATELLITE DATA

by

Atsushi Takeda[1]
Yoshinobu Tsuji[1]
Hiroshi Takahashi[1]

ABSTRACT

Sea water will damage vegetation in flooded areas caused by a tsunami or a storm surge. An examination to discriminate the flooded areas macroscopically of vegetation changes appearing in satellite images was made from the Tsunami caused by the Nihonkai-Chubu Earthquake in 1983.

1. INTRODUCTION

A macroscopical method using satellite data is used to detect flooded areas caused by tsunamis or storm surges. Traces of sea water from the flood remain for several months; vegetation changes from washing away, burying, and withering. These vegetation changes appear as spectral images of an earth surface observed from a satellite. Most parts of the earth surface are observed periodically by high-resolution spectral image sensors such as MSS and TM on LANDSAT satellites. A careful comparison of two images observing the same land area before and after a disaster provide useful information about traces of remaining sea water. This report addresses the flooded areas from the tsunami caused by the Nihonkai-Chubu Earthquake on May 26, 1983. The tsunami struck the coast of Minehama Village, Akita Prefecture in Northern Japan. Data used in this investigation was provided by MSS image data of LANDSAT.

2. DATA

Two scenes of satellite data were used for analysis of the examination. One is Scene No. 108-32 of LANDSAT-4 observed on July 12, 1983, one month and a half after the tsunami. The other is Scene No. 116-32 of LANDSAT-3, July 8, 1982, one year earlier. It was selected to compare the area, assuming that seasonal conditions of vegetation was almost equivalent except for the stricken areas. Each scene covers the areas required for analysis.

Data of each scene consist of 4 spectral images; Band 4 through Band 7, respectively. In the analysis, images from Band 5 and Band 7 were used. These two bands are important because they reveal vegetation changes. Band 5 $(0.6-0.7\mu m)$ involves an absorption band and Band 7 $(0.8-1.1\mu m)$ a reflection band of chlorophyl in green plants. The other bands are less important. The ground resolution of each image is 80m.

The ground data on actual flooded areas were referred to those reports of the field surveys made immediately after the tsunami by several groups. Fig. 1 shows a map of flooded areas based on the data.

3. ANALYSIS

To perform an objective description of differences between two images of each band obtained before and after the tsunami, quantitative analyses were made. Pre-processings, geometric corrections and optical sensitivity adjustments were performed, so the two images of each band coincident geometrically and optically except for the stricken areas. A sampling area P for an analysis, of 10km x 25km was cut out from an original image of 180km x 180km.

As the result of pre-processings, two sampling of band i (i=5, 7) are equivalent, if there is no change over the surface of sampling area, and pixels (pixel size; 80m x 80m) in each sampling image corresponding to a ground point $p(x,y)$ should have equal brightness. Consequently, the difference between the $\Delta B_i(x,y)$ should be zero. On the other hand, if $\Delta B_i(x,y)$ is not zero, it is suggested that there should be some change at the ground point corresponding to the pixels.

Thus, a subtracted image between two images of each band before and after the tsunami are shown in Fig. 2, where each pixel has a value of ΔB_i. Here, ΔB_i is defined as the difference of a value before the disaster from a value after it.

For a more quantitative expression, a standard deviation of ΔB_i, σ_B is calculated over a whole sampling image, and the pixels which lie on the land and $|\Delta B_i| \geq \sigma_B$ are selected as "significant difference pixel" = SDP. Fig. 3 a and b are a distribution map of SDP, where a SDP of $\sigma_B \leq |\Delta B_i| < 2\sigma_B$ and a SDP of $|\Delta B_i| \geq 2\sigma_B$ are indicated in ● and ○, respectively.

4. DISCUSSIONS

The false colored image after the tsunami shows 3 bright spots along the coast of Minehama Village. These spots are not clear in the image before the tsunami. On the other hand, it is found that positions of these spots coincide exactly with those of three large flood areas in Fig. 1.

[1]University of Tokyo, Hiratsuka Branch, Japan
[2]National Research Center for Disaster Prevention, Sakura, Ibaraki 305 Japan

The subtracted images of Band 5 and Band 7 have bright and dark spots, respectively, at the positions the false colored image has spots; a bright spot is positive, and a dark spot is negative ΔB_i.

Fig. 3 illustrates these facts clearly. The figure also shows that distributions of SDP are concentrated in a zone along the coast line; it does not expand into inland areas.

Almost all the SDPs in the two figures of Fig. 3 lie within the flooded areas in Fig. 1. Furthermore, the superimposed map of the two figures shows that distribution patterns of SDP are very similar to those of actual flooded areas except very narrow zones close to the shoreline.

Band 5 is an absorption band, and Band 7 is a reflection band of plants. When plants wither, absorption and reflection decrease; the brightness of Band 5 increases and that of Band 7 decreases. The results of the analyses agree to this inference.

A problem still remains. Few SDPs appear in a zone close to the shoreline where the tsunami intruded, and many black-pine trees died. Perhaps some plants on a dune are durable against sea water, wither several months after the flood, or revive soon after the damage.

5. CONCLUSION

Satellite data are useful for discriminating traces of flooded areas caused by a tsunami or a storm surge. This method will be used for field surveys immediately after the disaster. More similar analyses based on several satellite observations at different times are needed. The satellite data must keep pace with the vegetation cycles for more exact discrimination.

Only MSS images were available when the Nihonkai-Chubu earthquake occurred. Today, higher resolution pictures of Thematic Mapper image are available permitting greater detailed analyses of flooded areas.

6. ACKNOWLEGEMENTS

7. REFERENCES

(1) Akita Local Government (1984); Documents of the Nihonkai-Chubu Earthquake in 1983, Akita Local Govt. 420 pp. in Japanese.

(2) Forestry Div. of Akita Prefecture (1984); Documents of the Nihonkai-Chubu Earthquake, Green Waterbreak, 20 pp. in Japanese.

Fig. 2. Subtracted images (a)Band 5 (b)Band 7

Fig. 1. Flooded areas of the Tsunami of Nihonkai-Chubu Earthquake along the coast of Minehama Village, Akita Prefecture.

JAPAN SEA (NIHONKAI)

GONO LINE R.W.

MINEHAMA VILLAGE AKITA PREFECT.

140°01'E

40°16'N

0 1KM

287
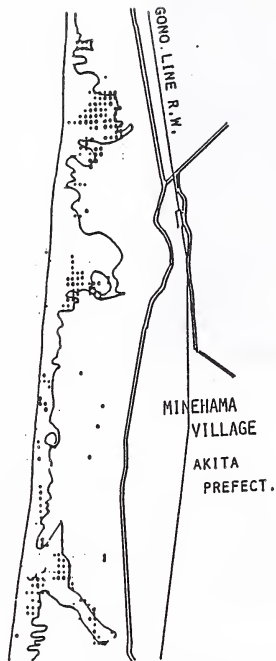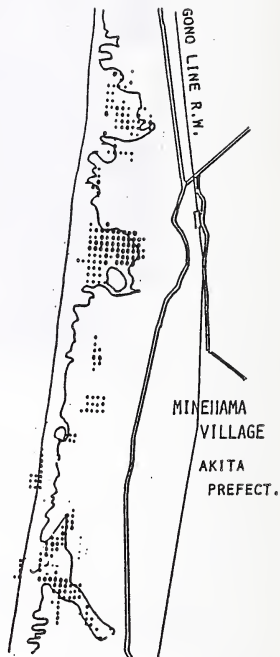
Fig. 3. Distribution map of SDP, (a) Band 5, (b) Band 7

FAULT DISPLACEMENT SEICHE WAVES ON
INLAND RESERVOIR AND LAKES
By

Robert L. Dewey[1]
and
Karl M. Dise[1]

ABSTRACT

Vertical displacements on faults that have been identified along the bottom and in the vicinity of inland lakes and reservoirs could induce seiche waves on the water surface that would create damage along the shoreline. Prediction of fault displacement seiche wave heights is important at the Bureau in order to assess the safety of dams exposed to this hazard. This paper pre- sents the Bureau's experience with com- puter analyses to predict seiche wave heights at a few dams potentially impacted by fault displacement waves. Wave characteristics and the parameters that influence the ultimate wave height at the dam are discussed. Evaluation of the wave's impact at the dam is also presented. Areas of analytical uncer- tainty are identified with recommen- dations for an appropriate conservative approach. Further research is suggested to reduce these uncertainties and advance the state-of-the-art.

KEYWORDS: Fault Displacement; Seiches; Seismic Risk; Waves

1. INTRODUCTION

If vertical displacements are expected on a fault located along the bottom or in the vicinity of a lake or reservoir, engineering designs at the water's edge need to account for the potential for extremely large waves impacting these structures during an earthquake. These waves can be called seiche waves. Seiche waves are created the moment vertical offset on the fault takes place. In an attempt to reach equilibrium, the volume of water that becomes higher immediately after the displacement prop- agates toward the lower end of the reservoir. Characteristics of the wave are primarily a function of the magni- tude of the fault displacement, the location of the faults, the shape of the reservoir, the bathymetry of the reser- voir bottom, and the reflectance of the shoreline, among other things. An appropriate model of these factors along with a good mathematical solution can lead one to predict the wave expected to impact the shoreline. Ever since this type of event resulted in overtopping Hebgen Lake Dam, Montana, the U.S. Bureau of Reclamation has attempted to predict fault displacement seiche wave heights at projects where that potential exists.

2. METHODS OF ANALYSIS

The computer program LSWAVE [1] was used to assist in the prediction of fault displacement seiche wave heights that may occur. The program was developed to simulate the propagation of waves throughout a reservoir or lake using numerical techniques. The waves that can be analyzed may be generated by a landslide entering the basin or by a bottom fault displacement. The equations of motion used in LSWAVE are the nonlinear, depth-averaged continuity and momentum partial differential equations derived from Navier-Stokes equations. Calculations are made for a variable-depth basin using an explicit finite difference method (a leapfrog scheme) for solving the partial dif- ferential equations. The forcing mecha- nism of the wave is incorporated into the continuity equation. A second forcing mechanism, drag induced water motion, is incorporated into the momen- tum equations. The equations and their solutions used in LSWAVE are presented in reference [1]. Varying boundary con- ditions are permitted to treat dam over- topping and shore reflectivity.

A body of water is modeled in LSWAVE by assigning water depths to the nodal points of a uniformly spaced grid. Land within grid boundaries is represented by

---

[1] Civil Engineer, U.S. Bureau of Reclamation, PO Box 25007, D-230, Denver, Colorado 80225.

by grid points that are assigned depths of 0.0. Fault movement is described by two lines: one of maximum displacement (the fault trace) and one of zero displacement (the hinge line). The reservoir floor instantaneously drops at time zero and displacements are calculated by linear interpolation at grid points located between the fault trace and the hinge line. The water surface grid points are displaced by an identical amount creating a discontinuity in the vicinity of the fault trace. Shoaling and reflection are accounted for by a Manning roughness coefficient and a CED (coefficient of energy dissipation).

Unless waves are totally reflected by the shoreline, wave energy is dissipated to some degree when it reaches the edge of the reservoir. One CED is selected to describe the dissipative capability of the entire reservoir shoreline. The CED can vary from 0.0 for totally reflective boundaries to 1.0 for totally transmissive boundaries. The slope and the roughness of the shoreline contribute to the CED. The sensitivity of the results to varying CED's should be studied for each analysis.

A grid of squares composed of up to 8,000 nodal points is required by LSWAVE to describe the reservoir bathymetry. There must be enough grid points to blanket the area of the reservoir and spaced such that at least six points are used to describe the expected wavelength. Thus, a square grid of a uniform spacing is applied to reservoir and shoreline features of all shapes and sizes.

Seismic movements modeled by the program LSWAVE could be considered static type rather than dynamic. The program assumes an instantaneous rupture along a fault on the lake bottom and calculates the resulting movement of the reservoir water surface for a given amount of time afterward. The instantaneous displacement of the water surface is an approximation of the effect of the dynamic release of energy over the entire lake bottom during the earthquake process. The assumption of instantaneous rupture could be slightly conservative because these displacements may take several seconds to propagate across the lake. Additional reverberant motions over a significant area surrounding the fault are not considered in this program. What is offered by the program is an approximation of the earthquake source.

Other input requirements, such as Manning's roughness coefficient, length of time history and time step, output options, etc., do not significantly influence the results and will not be discussed here. The following section presents cases that the Bureau has studied which demonstrate the use of LSWAVE for the fault displacement seiche wave analysis.

3. CASE HISTORIES

3.1 Lake Tahoe Dam (California/Nevada)

3.1.1 Description of Problem

Lake Tahoe occupies a graben that has been downdropped during Quaternary time relative to the Sierra Nevada to the west and the Carson Range to the east (see Fig. 1 and table 1)[2]. If a fault displacement were to occur, the lake bottom would be expected to drop like a trapdoor, hinged along another parallel fault on the opposite side of the lake. Keeping with theories of mass conservation, the lake water surface will simultaneously drop by the same amount to one side of the ruptured fault. Waves will then travel from both directions perpendicular to the ruptured fault to fill in where the water surface has dropped. Shortly after this hole begins to fill, waves will move out toward the shore and the dam. The distance that the wave travels, lake bottom topography, and shore outline contribute to the form of the wave. Lake Tahoe Dam is located on the northwestern shore of the lake basin where the lake bottom is relatively shallow and slopes are relatively gentle toward the middle of the lake. These factors can cause a wave to increase in height as it moves toward the dam. In fact, these effects, referred to as "shoaling," may produce a wave at the dam greater than the original fault displacement.

There are three possible cases of fault displacements within the shores of Lake Tahoe. The first is where the lake bottom just east of a fault running along the western side of the basin drops about 7 feet and decreases linearly eastward to 0 foot at a hinge on a fault running along the eastern side. This case is called "WE," the first letter standing for where the displacement occurs, the second letter standing for the hinge. The second case is just the opposite, "EW," where the fault along

the eastern side is displaced about 7 feet, dropping the lake bottom just west of the fault by that amount and decreasing linearly to 0 foot at the hinge located on the fault running along the western side. The third case involve dropping of the lake floor about 5 feet just south of a fault running along the north side. The displacement decreases linearly to 0 foot at the south edge of the lake basin on a hypothetical hinge formed at the bottom grid line. This case is called "NS."

Since Lake Tahoe is about 72,000 feet by 115,000 feet, the grid pattern selected was 69 by 110 spaces. Each grid point was 1,050 feet apart so that about six points would be used to model the expected wavelength of 6,200 feet. No more grid points or closer spacing was possible within the limits of LSWAVE's present computational capability.

Various CED's were selected to describe the percentage of the wave's energy absorbed by the shoreline. Selection of an appropriately conservative CED is discussed later.

3.1.2. Results and Interpretations

The results of the various computer runs are presented in table 2. Maximum wave heights were evaluated for all possible seismic cases and many values of CED. The prediction of the heights of waves expected at any point along the shoreline is dependent on the interpretation of the maxi um wave heights recorded at numerous other grid points in the vicinity of the point of interest.

Various interpretations can be made to predict the wave height at the dam depending on which grid points are selected and how they are examined. Fig. 2 shows numerous grid points along the shore of Lake Tahoe used to model the vicinity of the dam. Points on land are identified as X, points within the lake are identified as O. The dam is located near lake points labeled G and E.

Many interpretations were studied, but only the four shown in table 2 were considered reasonable. Interpretations that included corner points G, P, or U are not included in table 2 because the results at these points were anomalously high. Either numerical problems or an artifical compounding occurred at these points. Since the shoreline does not actually have sharp corners like this, averaging surrounding points or choosing

points not at a corner would afford a better interpretation. During an independent review, the U.S. Corps of Engineers [3] offered two of the interpretations shown in table 2. Relative to the Bureau's interpretations, the Corps' interpretations lead to higher expected waves for seismic cases WE and EW, and lower expected waves for seismic case NS. This is because the maximum wave heights increase from south to north and the Corps of Engineers' interpretations include more points that are north of the points used in the Bureau's interpretations.

Selecting just one interpretation over the others to best demonstrate the waves expected to impact the dam is difficult. Instead, it is prudent to formulate conclusions based on giving equal credence to the four reasonable interpretations.

The results in table 2 are fairly sensitive to the CED. The amount of wave energy reflected by the shoreline is dependent on:

- The slope of the shoreline.

- The roughness of the shoreline.

- The steepness of the incoming wave (height/length).

Fault displacement seiche waves are extremely long such that steepness is always very low. A relationship given in the Shore Protection Manual by the U.S. Corps of Engineers [4] between the wave steepness and the slope of the shoreline finds that at such small wave steepnesses, the effect of steepness becomes negligible with respect to the effect of the slope of the shoreline on energy dissipation. Although the average angle of Lake Tahoe's entire shoreline was calculated to be about 2.25 degrees, the angle of the northern two-thirds of the east shore and the southern one-third of the west shore is quite a bit higher (locally up to 10 degrees). Nevertheless, when accounting for roughness, a conservative estimate of the CED was determined to be 0.4.

3.1.3 Conclusions at Lake Tahoe

The highest value of maximum wave height selected from the four reasonable interpretations at a CED value of 0.4 offers a conservative estimate of the fault displacement seiche wave expected to impact Lake Tahoe Dam during a

seismic event. The controlling seismic event is a Richter magnitude 7.0 earthquake, displacing about 7 feet along the eastern fault and hinging along the western fault. The reasonably conservative upper bound value of the maximum fault displacement seiche wave height expected to impact Lake Tahoe Dam during that event is 11 feet. The buildup of such a large wave can be attributed to a considerable amount of shoaling as the wave approaches the dam.

Since the dam is comprised of both a concrete gate structure and two embankment fills that tie the concrete structure into the riverbank abutments, there are many potentially detrimental effects that such a wave can have on the structure. The two most critical effects were found to be sliding instability caused by the horizontal hydrostatic pressures of the wave tending to push the concrete structure downstream and washing away of the embankments by overtopping. The undrained behavior of the foundation soil was found to be dilative. Therefore, in the event of a sudden load caused by this fault displacement wave, the horizontal shear strength of the soil under the concrete structure will increase as the soil begins to strain so to resist the increased hydrostatic pressures. Surface protection of the embankments has been designed to prevent erosion during the temporary overtopping. Once these improvements have been constructed, Lake Tahoe Dam will be able to survive the expected seiche wave created by fault displacement through the water.

3.2. Jackson Lake Dam (Wyoming)

3.2.1. Description of Problem

Jackson Lake Dam is a composite earth-fill and concrete dam constructed between 1910 and 1916 on the Snake River in western Wyoming. The dam consists of a concrete gravity section with a miscellaneous fill embankment to the south and a hydraulic fill embankment to the north. The program LSWAVE was used to estimate the magnitude of fault displacement generated waves and the effect these waves have when they reach the dam. The study was conducted to determine if the dam's crest elevation should be raised to accommodate freeboard loss from these waves.

Most recent fault trace locations are shown in Fig. 3. Trace 1 has been observed along the shoreline and 1 mile to the west of Jackson Lake and it is considered to be the most likely

location for future rupture. Traces 2 and 3 were inferred from Jackson Lake bathymetry but no evidence of these faults was found outside the reservoir. There is inconclusive geophysical evidence for the existence of the Hermitage Point fault trace also shown in Fig. 3. Detailed study of large-scale aerial photographs along the postulated trace suggests that surface displacements have not occurred in the last 20,000 years. However, movement along this trace was thought to have the potential for creating the worst-case situation for fault displacement generation of waves, so it was included in this study.

Relationships between maximum fault displacements, net geodetic change, and distance from a fault trace are presented in Fig. 4 [5]. These relationships were developed based on displacement data associated with historic normal faulting in the Western United States along with observation of the basin width and the configuration of the Huckleberry Ridge Tuff in the Jackson Lake area. The maximum credible surface displacement along the Teton fault (traces 1, 2, or 3 on Fig. 3) was estimated to be 22 feet with the east side moving down relative to the west side. The maximum credible surface displacement along the Hermitage Point fault was estimated to be 5 feet, again down to the east. The net elevation change at Jackson Lake Dam and the location of the hinge lines for each of these events can be determined from Fig. 4. For the Teton fault, the net elevation change at the damsite would be down 13 feet and the hinge line would be located approximately 5 miles to the east of the dam. For the Hermitage Point fault, the net elevation change at the dam would be down 2 feet and the hinge line location would be approximately 1 mile to the east of the dam.

Jackson Lake was modeled using a grid 67 divisions wide by 99 divisions long. The grid spacing was approximately 668 feet square and seven grid points were used to represent the dam. Before the program could be run successfully, the reservoir boundary required smoothing and islands had to be removed by assigning 1-foot depths to grid points located within the island boundaries. The time step used was 4 seconds and the CED was varied from 0.30 to 0.75.

Best estimates for locations of the Teton and Hermitage Point faults were chosen for initial modeling attempts. Sensitivity to the choice of fault and

hinge line locations was then tested by arbitrarily moving these lines parallel, 2,000 feet in either direction.

3.2.2. Results and Interpretations

In each fault movement simulation, the estimated reservoir behavior was a combination of effects generated by a discontinuity in the water surface at the fault trace and by the tilting of the reservoir basin away from the dam. Initially, the water surface near the dam fell as water moved away from the embankment due to reservoir tilting (see Fig. 5a). At some time later, depending on the distance of the fault trace from the dam, the fault displacement induced wave reached the vicinity of the dam and the water surface rose again. The water surface then oscillated until all energy was dissipated at the shorelines or until the simulation was stopped (see Fig. 5b).

Varying the CED from 0.30 to 0.75 had little effect on results at the dam (see Fig. 6). Therefore, a value of 0.60 was used throughout the analysis.

Figs. 7 and 8 are plots of the time history of displacement for the water surface at a grid point next to the dam. Results of fault displacement along the Teton fault are presented in Fig. 7, while Hermitage Point fault displacement results are shown on Fig. 8. Water surface displacements represent the change in elevation from the assumed original water surface elevation of 6769 feet. The fault-induced elevation change of the dam crest is equal to the initial water surface elevation change at time zero. Therefore, the net difference between displacement at any time and displacement at time zero is the change in freeboard. The initial freeboard was assumed to be 11 feet.

Figs. 7 and 8 show the effects of changing the locations of the hinge lines and fault traces. Changing the location of the hinge lines had little effect on water surface displacement at the dam. Changing the location of the Teton fault significantly affected water displacement but changing the location of the Hermitage Point fault did not. For the best estimate location of the Teton fault, the minimum freeboard was 6.5 feet. When the fault was arbitrarily located 2,000 feet to the east, the minimum freeboard was 5.5 feet. For the best estimate location of the Hermitage Point fault, the minimum freeboard was 6.1 feet and changing the location 2,000 feet to the

east only decreased the freeboard by 0.5 foot.

In order to determine if boundary conditions at the grid points which represented the dam caused computational errors, water surface displacement versus time data were obtained for all grid point locations in the vicinity of the dam. Only slight differences were noted in the results. The shapes of the displacement versus time curves differed from grid point to grid point with some peaks sharper than others, but the periods were virtually identical and the maximum amplitudes were within approximately 0.5 foot.

3.2.3. Conclusions at Jackson Lake

Analytic results from studies presented in this report indicate that fault displacement induced waves will not overtop Jackson Lake Dam if the dam is rebuilt to its current crest elevation of 6780 feet. However, there are uncertainties in the results due to limitations in the ability to predict the actual fault displacement mechanism, in the ability of the computer code to adequately model these mechanisms, and in the small scale wave behavior in the vicinity of the dam. Constructive interference from several waves possibly generated by a multiple fault displacement event could conceivably create a wave that would overtop the dam but it is believed that the duration of the overtopping would be significantly shorter than the 18-minute period waves predicted in this report and that the overtopping would not be a recurrent phenomenon. The uncertainty of a conceivable dam failure caused by a fault-displacement induced wave overtopping the dam can be mitigated by placing slope protection material on the downstream slope.

4. CONCLUSIONS

Successful, conservative predictions of fault-displacement seiche wave heights can be made using the computer program LSWAVE. The amount of conservatism may tend to be high due to numerous uncertainties inherent in the analysis. Additional research and computer programming can eliminate some of these uncertainties and render more accurate predictions. Improvements to the program LSWAVE which are technically feasible at this time include:

- Allow for different types of grids:

Variable rectilinear
Curvilinear
Patched or subgrid features

- Develop a new solution scheme with dynamic time stepping.

- Allow for variable CED's along different sections of the reservoir shoreline.

- Allow for a more dynamic type of fault displacement and reservoir bottom drop.

These improvements were beyond the scope of the analyses presented in this paper. Without any of these improvements, conservative choices were made where the uncertainties exist. Areas within the LSWAVE model where conservatism may be introduced included:

- Selection of lower values of the CED.

- Selection of the most critical seismic case.

- Selection of the most critical interpretation of maximum wave heights at certain strategic grid points.

- Selection of the maximum fault offset possible and assume it occurs suddenly along the entire fault line resulting in a sudden drop of the reservoir bottom.

Accurate estimations of these parameters along with improvements to the program will lead to better, more reasonable engineering designs along a shoreline susceptible to fault displacement seiche waves. Nevertheless, the Bureau has demonstrated that fault displacement seiche waves can be predicted so that safe designs can be built accounting for what otherwise would be a catastrophic event.

5. REFERENCES

[1] Chiang, W., D. Divoky, P. Parnicky, and W. Wier, "Numerical Model of Landslide-Generated Waves," Tetra-Tech Report Number T-3427, Pasadena, California, November 1981. (Note: Program LSWAVE modified by Julie Heim, May 1984).

[2] U.S. Bureau of Reclamation, Memorandum, Subject: "Preliminary Seismotectonic Conclusions for Lake Tahoe Dam - Newlands Project, California-Nevada," February 10, 1984.

[3] U.S. Corps of Engineers, "Fault Displacement Seiche Wave Analysis Review," Coastal Engineering Research Center, Memorandums for Record, 26 April 1985 and 6 August 1985.

[4] U.S. Corps of Engineers, "Shore Protection Manual," U.S. Army Coastal Engineering Research Center, 1977 and 1984.

[5] U.S. Bureau of Reclamation, "Seismotectonic Study, Jackson Lake Dam, Minidoka Project, Wyoming," Seismotectonic Report 83-8, Engineering and Research Center, Denver, Colorado, September 1983.

Table 1. - Faults within Lake Tahoe [2]

Fault	Sense of displacement	MCE (M_s)	Estimated rupture length (km)	Amount of maximum surface displacement (m)
Tahoe (west side)	Normal, down to east	7	40 (24.9 mi)	1.8 - 2.1 (6.9 ft)
Tahoe (east side)	Normal, down to west	7	40 (24.9 mi)	1.8 - 2.1 (6.9 ft)
Tahoe (north side)	Normal, down to southeast	6-3/4	20 (12.4 mi)	1.2 - 1.5 (4.9 ft)

Table 2. - Summary of maximum fault-displacement seiche wave heights expected at Lake Tahoe Dam for different interpretations and various seismic cases.

Seismic cases			Bureau of Reclamation's interpretation		Corps of Engineers' interpretation [3]	
Fault	Hinge	CED	Dam (E)	1,050 ft east of dam (F)	Dam (H)	Three points surrounding dam (E, H, and I)
W	E	0.0	7.8	7.8	13.0	11.3
W	E	0.2	6.6	6.2	9.2	8.6
W	E	0.4	6.9	4.2	9.8	8.4
W	E	0.6	6.0	3.1	5.7	5.9
W	E	0.8	4.1	2.3	4.3	4.1
E	W	0.0	7.5	11.0	15.0	15.2
E	W	0.2	6.7	8.7	9.9	10.8
E	W	0.4	5.6	7.7	11.0	9.2
E	W	0.6	4.7	7.1	6.1	5.9
E	W	0.8	3.7	7.1	7.1	5.6
N	S	0.0				
N	S	0.2	4.9	5.5	5.5	5.1
N	S	0.4	4.7	3.9	2.6	3.3
N	S	0.6	2.6	1.9	2.2	2.0
N	S	0.8	1.7	0.80	0.90	1.2
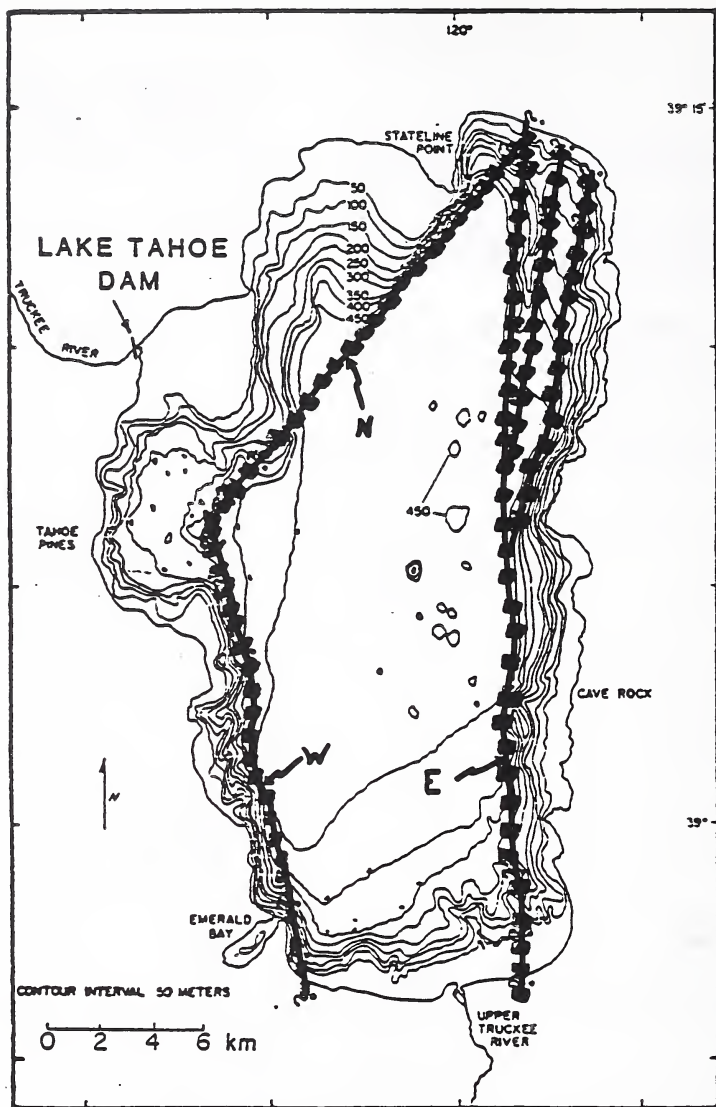
Figure 1. Bathymetric map of Lake Tahoe showing location of Lake Tahoe Dam and inferred Tahoe fault locations.

LEGEND

X = Grid point on dry land

◯ = Grid point within the lake
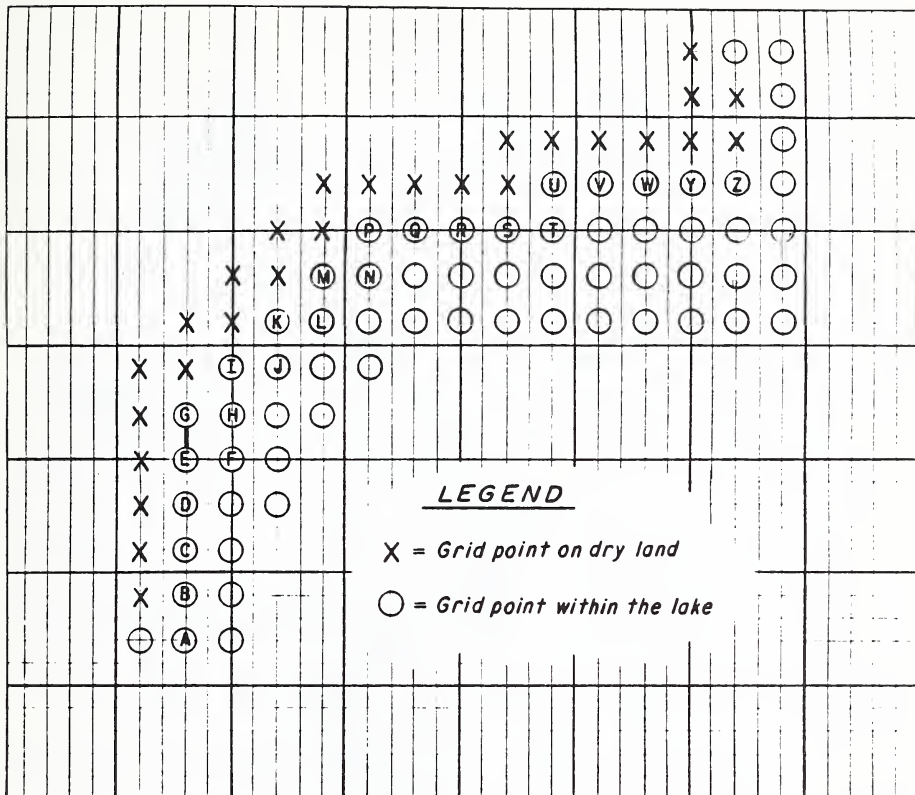
Figure 2. Grid points along the shoreline near Lake Tahoe Dam

297
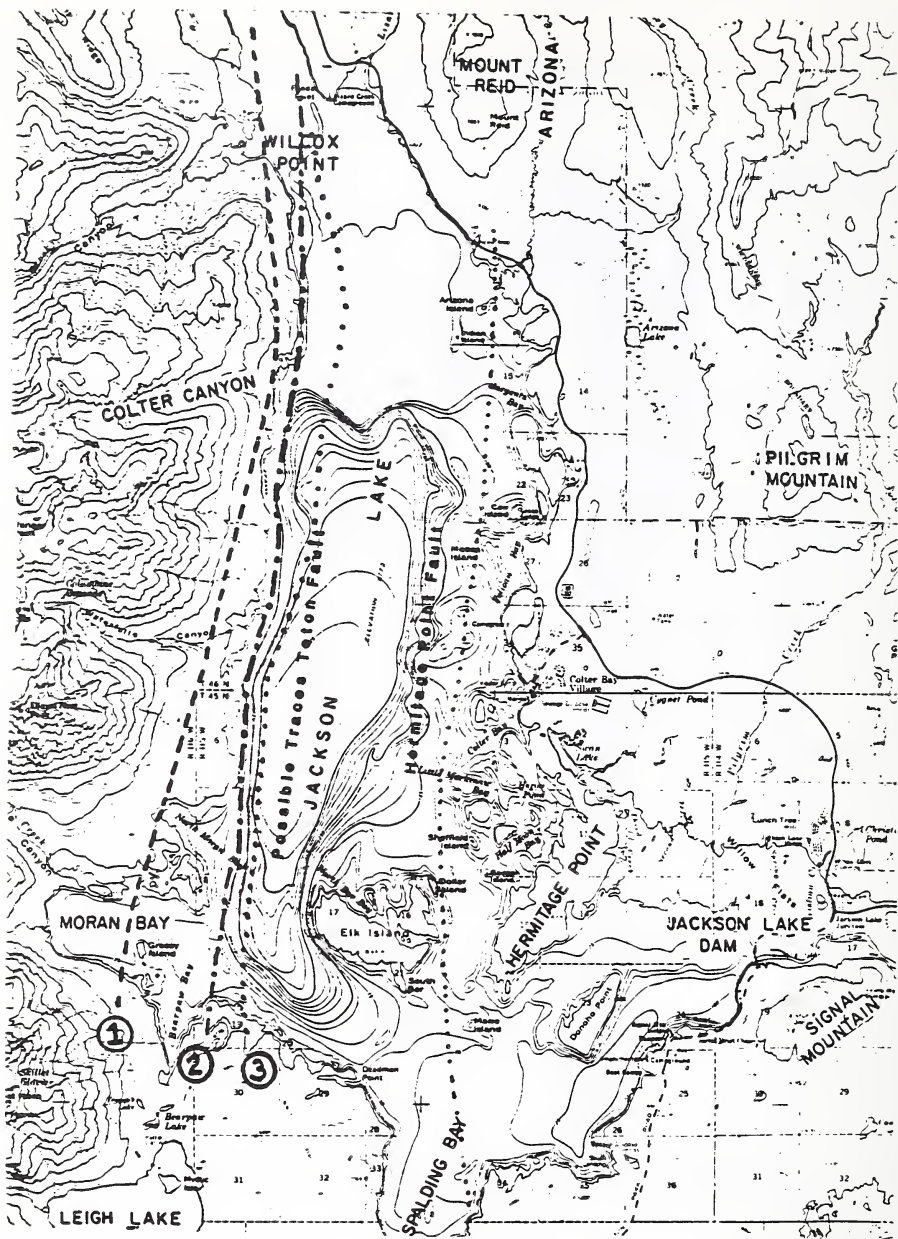
Figure 3. Possible locations of surface displacements within Jackson Lake Reservoir.
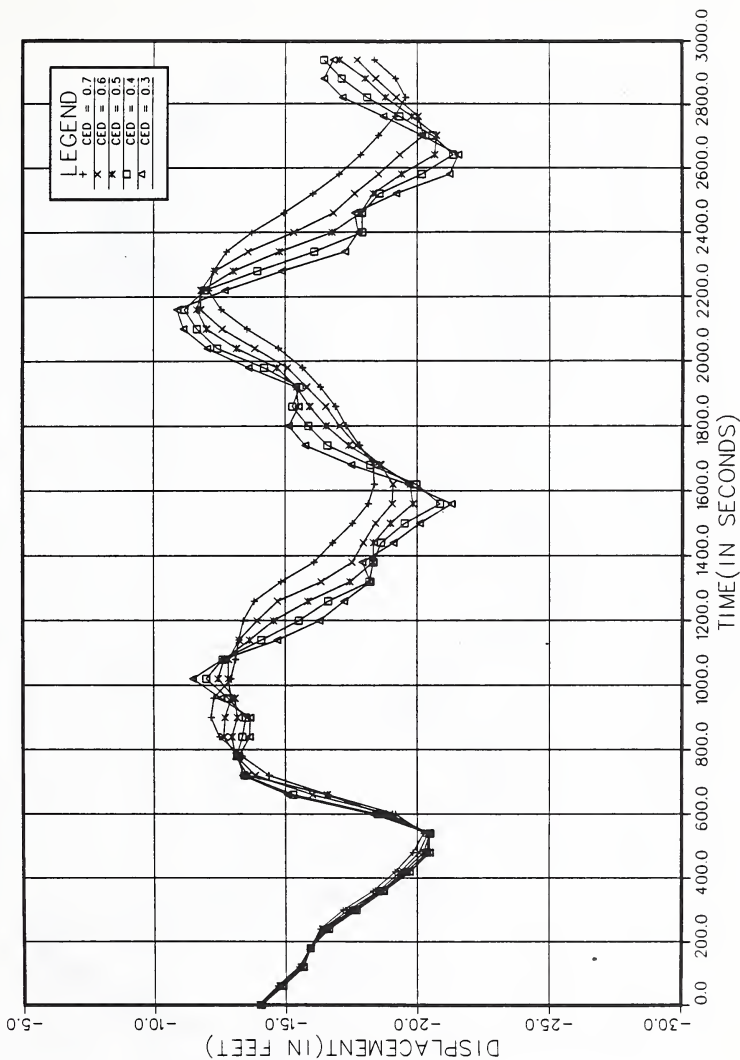
Figure 6. Water surface displacement vs. time for various coefficients of energy dissipation.

301
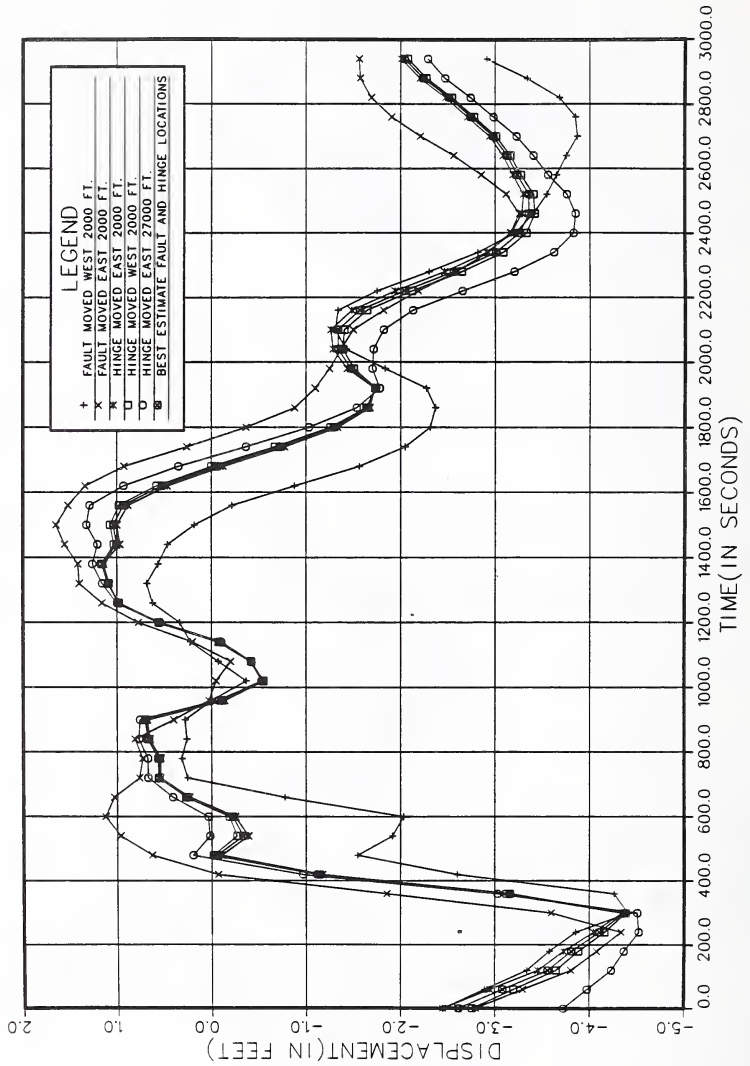
Figure 7. Water surface displacement vs. time
for various locations of the Hermitage Point fault trace and hinge line.

302
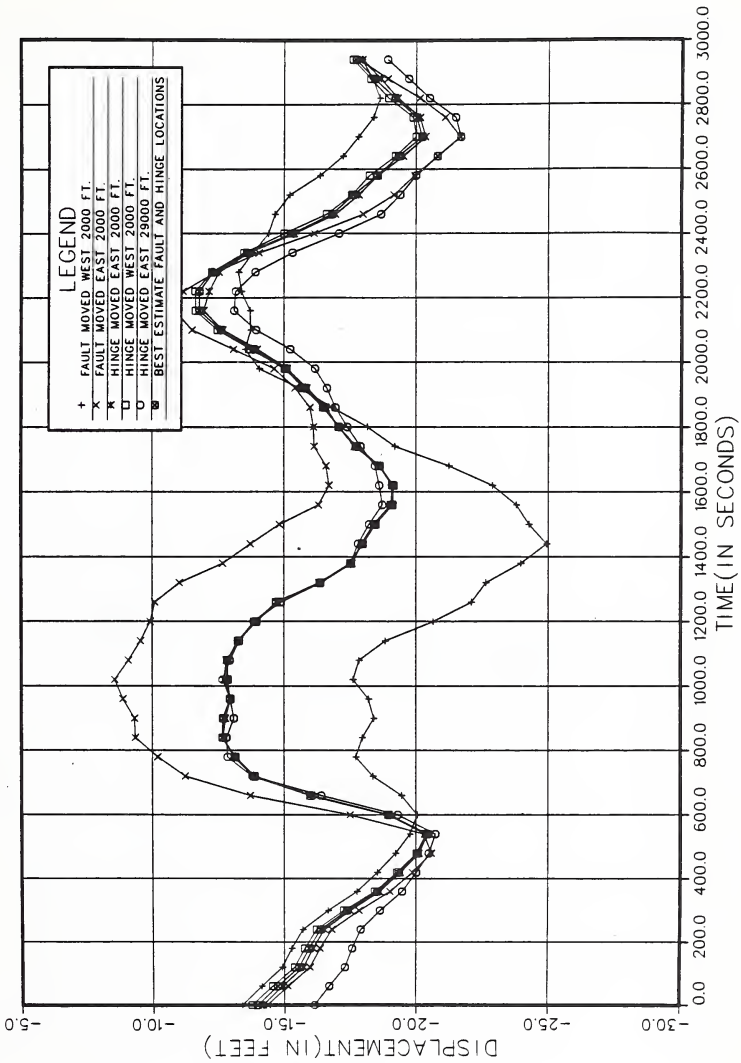
Figure 8. Water surface displacement vs. time for various locations of the Teton fault trace and hinge line.

U.S.-Japan Cooperative Research Program

U.S.–JAPAN COORDINATED EARTHQUAKE RESEARCH PROGRAM ON REINFORCED MASONRY BUILDINGS —SEISMIC CAPACITY OF REINFORCED MASONRY WALLS AND BEAMS—

BY

Shin Okamoto*, Yutaka Yamazaki*, Takashi Kaminosono*
Masaomi Teshigawara*, and Hisahiro Hiraishi*

ABSTRACT

As part of the U.S.-Japan cooperative research program on masonry building structures, work performed included testing many reinforced masonry walls and beams to investigate experimentally how the amount of shear reinforcement, axial stress, shear span ratio, reinforced concrete (R/C) slab and transverse walls affect shear and flexural behaviors of masonry walls and beams. To resist severe earthquakes, strength and deformation capacity are the most important factors for medium-rise masonry building structures. The major findings follow:

1) Increase in amount of shear reinforcement and spiral reinforcement was effective on deformation capacity.

2) Maximum shear stress increased with increasing of the axial stress.

3) Under the shear failure, the deformation and strength capacity of the walls were improved with the existence of the transverse walls.

4) The shear and flexural strength can be estimated by the empirical formulas specified for R/C.

1. INTRODUCTION

During 1984 and 1985 the Building Research Institute, Ministry of Construction, conducted seismic behavior test of masonry walls and beams. These tests were carried out under the U.S.-Japan Coordinated Earthquake Research Program on Masonry Building Structures. The purpose of this study was to investigate experimentally how the amount of shear reinforcement, axial stress, splices, confining of compression zone, transverse wall, shear span ratio, and R/C slab affect shear and flexural behaviors of masonry walls and beams. Thirty-five specimens were used in this study. They included 25 masonry blocks, 7 clay bricks, and 3 reinforced concrete specimens.

*Building Research Institute Ministry of Construction

2. SPECIMEN AND TEST SETUP

2.1 Materials

The concrete block masonry unit used for the specimens consists of two webs and two open ends with nominal dimensions of 20 cm thick, 40 cm wide, and 20 cm high. The clay brick masonry unit has the same shape as the concrete block unit, but the nominal dimensions are 20 cm thick, 30 cm wide, and 10 cm high. Those masonry units are shown in Fig. 1. The material properties of the specimens and the companion prism strength are tabulated in Table 1.

2.2 Specimens

Typical specimens are shown in Fig. 2. The specimens were constructed in running bond with a 50% overlap unit in alternate courses, and are fully grouted by concrete. The details of specimens are listed in Table 2. The specimens WTT1, WTT2 and WTC1 have transverse walls. The beam specimens GF1, GF2, and GS1 have R/C slab, they are 15 cm thick and 1 meter wide on each side of the beam.

2.3 Test Setup

The test setup (Fig. 3) employed in this study was the Building Research Institute's (BRI) Two-Directional Test Facility (BRI/TTF). The BRI/TTF is a computer-controlled loading apparatus which can apply in-plane force and displacement in three degrees of freedom at the top end of a specimen, there are two translations and one rotation. The bottom end of a specimen is fixed to the test floor. Specimen loading is accomplished by three servo-controlled hydraulic actuators which receive their instructions by computer-generated commands. In this test, two vertical actuators were controlled by the computer to restrain the rotation of the top end of the specimen and to keep constant vertical compressive stress.

2.4 Loading Rule

In principle, specified loading history was applied to each specimen. It consists of 1) one-cycle to the displacement corresponding to the elastic limit, 2) two-cycles to a drift angle of 1/400, 3) two-cycles to 1/200, 4) two-cycles to 1/100, and 5) one-cycle to 1/50.

3. TEST RESULTS OF WALLS

Figure 4 shows crack patterns at the final stage of some specimens. Table 3 lists the mean shear stress and drift angle at the maximum strength. This table also lists the ultimate stresses calculated by equations (1) and (2) described in the same table.

3.1 Effects of Axial Stress (WF1, WS4, WSN1, WSN2)

Figure 5 illustrates the relationships between the shear stress and the axial stress. The maximum shear stress increases from 16 kg/cm^2 to 23 kg/cm^2 with increases of the axial stress.

The specimen WF1 with an axial stress of 5 kg/cm^2 showed, 1) flexural yielding occurred about at drift angle of 1/500, 2) maximum strength occurred about at drift angle of 1/250, and 3) a 20% decreasing of the maximum shear stress was observed about at drift angle of 1/100. The specimens with the axial stress of 20 kg/cm^2 and more showed, 1) maximum strength occurred about at drift angle of 1/500, and 2) a 20% decreasing of the maximum shear stress was observed about at drift angle of 1/250.

3.2 Effects of Shear Span Ratio (WS1, WSR1, WS4, WSR4, WS7, WSR7)

Processes of crack propagation of each specimen had a similar tendency to a drift angle of 1/800. At first, flexural cracks were observed at the top and bottom parts of the specimens. Then shear cracks occurred at the wall corners and those were developed gradually with increasing number of loading cycles. When the drift angle reached to 1/400 (1/800 for the specimen WS1), the diagonal shear cracks occurred.

Figures 6 and 7 show the effect of shear span ratio (M/QD) on the shear stress vs. drift angle relationships. The maximum shear stresses of these specimens stand in the order of WSR1>WS1, WSR4>WS4, and WSR7=WS7. The specimens WS1 and WSR1 showed approximately 20% higher in shear stress compared with the specimens WS4 and WSR4, and also 30% higher than the specimens WS7 and WSR7. The specimens WS7 and WSR7 which have a shear span ratio of 1.14, failed in flexure and showed good deformation capacity. The concrete block masonry wall WS7 has a larger deformation capacity than clay brick masonry wall WSR7. In the case of the specimens which shear span ratios are 0.45 and 0.76, the clay brick masonry walls (WSR1 and WSR4) were superior to the concrete block masonry walls (WS1 and WS4) for the maximum shear stress and the deformation capacity.

3.3 Deformation Capacity (WF1, WF2, WFJ1, WFJ2, WFR1, WFR2, WFRC)

At first, flexural cracks appeared at the top and bottom. Thereafter, the crack width became wider, and flexural shear and shear cracks at both top and bottom parts appeared and developed according to an increase in drift angle. After a drift angle reached 1/200, diagonal shear cracks appeared in the specimens except specimens WF2 and WFJ2; this diagonal shear cracks became wider with an increase in the drift angle. The specimen WFR2 only failed at the upper part. This failure was caused by the incomplete filling of grout concrete at this portion. For specimens WF2 and WFJ2, compression failure and slippage occurred due to development of cracks which appeared before a drift angle of 1/200.

The strains of main longitudinal and vertical shear reinforcing bars of each specimen reached 0.2% through 2% at a drift angle of 1/400. Therefore, all specimens were supposed to be yielded in flexure before a drift angle of 1/400.

Figure 8 shows the effect of shear reinforcement. From this figure, the difference in deformation capacity depending on amount of shear reinforcement is observed for a drift angle which is larger than 1/200. The specimen WF2 showed stable deformation behavior without remarkable deterioration in strength even at a drift angle of 1/50, although the specimen WFR2 didn't show better deformation behavior at a drift angle of 1/50 than the specimen WFR1 because of partial failure at the upper part.

Figure 9 shows the effect of spiral reinforcement at critical compression zone. From the comparison of deformation behavior after a drift angle of 1/100, it was observed that the specimen WFJ1 showed a stable behavior while the specimen WF1 showed negative slope in positive loading. The load carrying capacity of each specimen at a drift angle of 1/50 is in order of WFJ2>WF2>WFJ1>WF1. This phenomena is explained by the reason why discrepancy of edge zone due to development of cracks and compressive failure might be prevented to some extent by the spiral reinforcement.

Figure 10 shows the comparison regarding splices in a wall panel. There is no remarkable difference in deformation capacity among three specimens in the figure.

3.4 Effect of Transverse Wall (WS4, WTT1, WS6, WTT2, WSRC, WTRC, WF1, WTC1

In the specimens WS4 and WSRC diagonal cracking occurred at the drift angle of 1/500 and after this cracking occurred the strength deterioration was severe. The specimens WTT1

and WTRC, which have a transverse wall at their edge, reached its maximum strength at a drift angle of 1/250 during positive loading, and 1/250 and 1/800 respectively during negative loading. The strength deterioration in these cases was medium, after reaching the maximum shear strength (Fig. 11).

The specimen WTT2 reached its maximum strength at a drift angle of 1/130 in positive loading and at 1/180 in negative loading. Its hysteresis loop was stable in comparing with that of WS6 specimen (Fig. 12).

WTC1 specimen reached its maximum strength at a drift angle of 1/250 in positive loading, and at 1/170 in negative loading. The mean shear stress of the specimen WTC1 was 1.4-1.8 times as much as that of the specimen WF1 at those drift angles, but the hysteresis loops of the two specimens were similar. Transverse wall of the specimen WTC1 inhibited the extent of the diagonal crack, but at the drift angle of 1/100, the transverse wall separated from the wall in the loading direction at its intersection (Fig. 13).

4. TEST RESULTS OF BEAMS

4.1 Effect of Shear Reinforcement (GS2, GS3, GSR1, GSR2)

Envelope curves of the mean shear strength versus drift angle relation for specimens GS2 and GS3, GSR1 and GSR2 are shown in Figs. 14 and 15. There are no difference between specimens GS2 and GS3 for ultimate shear strengths, but, after the drift angle exceeds 1/200, there is significant difference. The two specimens showed diagonal tension cracking which occurred at a drift angle from 1/300 to 1/200; there is no difference in the maximum shear strength. The amount of shear reinforcement affected the behavior of the specimen after the diagonal tension crack occurred. Specimen GS3, which has a large amount of shear reinforcement compared with the specimen GS2, maintained its maximum strength until a drift angle reached 1/100. The specimen GS2 lost its strength immediately after the diagonal crack occurred.

For GSR1 and GSR2 specimens, a diagonal tension crack occurred at a drift angle from 1/400 to 1/300. At this time, specimen GSR1 reached its maximum shear strength, it couldn't maintain that strength under a larger deflection. In specimen GSR2, the shear strength increased until a drift angle reached 1/50. After that, cracking occurred and compressive failure occurred where the critical compression was produced, which resulted in a reduction of shear strength.

4.2 Effect of R/C Slab (GS1, GS2, GF1, GF2, GF3)

Envelope curves of the mean shear strength versus drift angle relationships of specimens GF2 (a beam with R/C slab) and GF3 (a rectangular beam) are shown in Fig. 16. Those specimens GS1, GF1 (beams with R/C slab) and GS2 (a beam without R/C slab) are shown in Fig. 17.

Specimens GF2 and GF3 showed flexural failure. Their maximum shear strengths were produced at a drift angle in the range from 1/200 to 1/100. Those strength were 1.2 times as much as those estimated by the calculation where the slab reinforcement was accounted for GF2. The specimens GF2 and GF3 maintained the strength which is greater than the calculated strength until the drift angle reached 1/50, and 1/100, respectively.

The specimens GS1 and GS2, a pair of short span beams, reached their maximum shear strengths at drift angle of 1/250. Its strength was 1.38 to 1.52 times and 0.93 to 1.2 times larger than the corresponding calculated strength. In the calculation of shear strength, the effect of R/C slab was not considered. Specimen GS2 could not sustain its maximum strength after a drift angle reached 1/250, and deterioration of the strength was severe, while GS1 maintained the strength which is greater than the calculated strength until a drift angle was reached at 1/50.

The stress of the inner (near the beam) reinforcing bar in the R/C slab reached yield point under the loading cycle of 1/400, while the outer one reached its yield point under loading cycle of 1/200. In a short span beam with R/C slab (GF1 and GS1), all reinforcing bars in the R/C slab reached tension yield points under the large deflection; i.e. the drift angle exceeded 1/100.

5. CONCLUSIONS

1) The maximum shear stress increases with increasing of axial stress.

2) The specimen failed in flexure has good deformation characteristics. Compared with the flexural failure type specimen, the specimens failed in shear have 50% deformation capacity.

3) Increase in the amount of shear reinforcement (consequently increase in ratio of maximum shear strength to maximum flexural strength) improves deformation capacity of walls and beams.

4) The deformation capacity under a large amplitude of deformation is improved by the spiral reinforcement arranged at critical compression zone.

5) Splices of main longitudinal reinforcing bars have little affect on deformation capacity.

6) The larger the shear span ratio becomes, the smaller the maximum shear stress becomes.

7) The deformation capacity of the walls is improved with the existence of the transverse walls.

8) In rectangular masonry beams without R/C slab, the ultimate strength can be estimated by the equation specified for a R/C beam.

9) In the masonry beam with R/C slab, the shear strength is 1.45 times as much as the strength estimated by the equation specified for R/C beams without considering the effect of R/C slab.

6. ACKNOWLEDGEMENTS

Many personnel in BRI have offered invaluable help during the experiment. To all of them, the authors wish to convey their gratitude, especially to Dr. A. Baba, Messrs, M. Fujisawa, H. Isoishi, and T. Kawashima. The authors also wish the express their sincere gratitude to Mr. R. Kawai, Mr. T. Terada, Mr. M. Yamamoto, Mr. A. Nakaoka, and Mr. Y. Yamaguchi who participated in the experiments as visiting research members in BRI.

7. REFERENCES

(1) S. Okamoto, Y. Yamazaki, A. Baba, M. Teshigawara, and H. Hiraishi, "U.S.-Japan Joint Earthquake Research Program Involving Large-Scale Experiments on Masonry Building Structures - Japanese Side Research Plan-," the 17th Joint Meeting, U.S.-Japan Panel on Wind and Seismic Effects, UJNR, Tsukuba, Japan, May 12-24, 1985.

(2) T. Okada, H. Hiraishi, T. Kaminosono, and M. Teshigawara, "Flexural Behavior of Reinforced Masonry Walls and Beams," The 3rd ASCE Engineering Mechanics Specialty Conference, 1986.

(3) T. Kaminosono, H. Isoishi, Y. Yamaguchi, and R. Kawai, "Seismic Capacity of Reinforced Masonry Walls Including Effects of Axial Stress," The 4th Canadian Masonry Symposium, Canada, 1986.

(4) M. Teshigawara and H. Isoishi, "Seismic Behaviour of Masonry Beams," The 4th Canadian Masonry Symposium, Canada, 1986.

(5) Papers for the First Joint Technical Coordinating Committee on Masonry Research -U.S.-Japan Coordinated Earthquake Research Program-, Tokyo, Japan, August 26-27, 1985.

(5-1) H. Hiraishi, T. Kawashima, T. Terada, M. Yamamoto, and Y. Yamaguchi "Planar Test on Flexural Behavior of Reinforced Masonry Walls".

(5-2) M. Fujisawa, "Seismic Behavior of Reinforced Masonry Walls - Effect of Shear Span Ratio-".

(5-3) M. Teshigawara and H. Isoishi, "Seismic Behavior of Masonry Beams".

(5-4) M. Teshigawara, H. Isoishi, and A. Nakaoka, "Effect of Transverse Wall Attached to Reinforced Masonry Wall".

Table 1 Material Properties

a) Prism Compressive Strength

Specimen	Prism Compressive Strength (kg/cm²)
W S 1	1 8 3
W S 4	2 3 3
W S 7	1 8 3
W S R 1	2 7 3
W S R 4	2 5 7
W S R 7	2 1 8
W S N 1	2 3 3
W S N 2	2 3 3
W F 1	2 3 3
W F 2	2 1 9
W F J 1	2 1 9
W F J 2	2 1 9
W F L M	2 1 9
W F L 1	2 1 9
W F R 1	2 6 8
W F R 2	2 6 8
W T T 1	2 5 1
W T T 2	2 5 1
W T C 1	2 5 1
W S B 1	3 0 2
W S B 1 0	3 3 9
W S B 1	3 0 2
W S B 1 0	3 3 9
W S R C	2 7 3
W F R C	2 5 4
W T R C	2 5 2
G S 1	2 1 6
G S 2	2 1 2
G S 3	2 1 2
G S 4	2 1 2
G S R 1	2 7 5
G S R 2	2 7 5
G F 1	2 1 6
G F 2	2 1 6
G F 3	2 1 6

b) Reinforcing bars

	Specimen	σ_y (kg/cm²)
Flexural re-bars	W S 1, W S 4, W S 7, W S R 1, W S R 4, W S R 7, W S N 1, W S N 2, W T T 1, W T T 2, W S B 1, W S B 1 O, W S R C, W T R C	3,948.0
	W F 1, W F 2, W F J 1, W F J 2, W F L 1, W F R 1, W F R 2, W T C 1, W F B 1, W F B 1 O, W F R C	3,542.0
	W F L M	3,438.0
Shear re-bars (Vertical)	W S 1, W S 4, W S 7, W S R 4, W S R 7, W S N 1, W S N 2, W T T 1, W T T 2, W S B 1, W S B 1 O, W S R C, W T R C	3,791.0
	W S R 1	3,708.0
	W F 1, W F 2, W F J 1, W F J 2, W F L M, W F L 1, W F R 1, W F R 2, W T C 1, W F B 1, W F B 1 O, W F R C	289.0
Shear re-bars (Holizontal)	all "W" Specimens	3,620.0
Spiral	W F J 1, W F J 2, W F L 1	3,193.0
Flexural re-bars	G S 1, G S 2, G S 3, G S 4, G S R 1, G S R 2	3,833.0
	G F 1	3,500.0
	G F 2, G F 3	3,542.0
Shear re-bars (Vertical)	G S 1, G S 2, G S 3, G S 4, G S R 1, G S R 2	3,791.0
	G F 1, G F 2, G F 3	3,289.0
Shear re-bars (Holizonral)	G S 1, G S 2, G S 3, G S 4, G S R 1, G F 1, G F 2, G F 3	3,620.0
	G S R 2	3,791.0
Slab re-bars	G F 1, G F 2, G S 1	3,554.0

Table 2 Lists of Specimens

a) Wall Specimens

TRANSVERSE WALL / Pw		0		D13@400 (0.167%)		D13@200 (0.334%)		2D13@200 (0.668%)	
M/QD	At(cm²)	×	○	×	○	×	○	×	○
0.4S h/l= 180/200	D16 (1.99)								
	2D19 (5.74)			WS1,WSR1					
	2D2S (10.1)								
0.7S h/l= 180/120	D16			(WS3,WSR3)					
	2D19	(WSR2) (WSJ1) (WS2×2)		WS4 ,WSB1 WSR4 ,WSM1 WSM2,WF1,WFR1 WFL1,WSRC,WFJ1 WFLM,WFRC WSB1D (WSJ2)		WTT1 WTC1 WTRC	(WS5) (WSR5)	WF2,WFB1 WFR2 WFJ2 WFB1D (WS6) (WSR6)	WTT2
	2D2S	(WS8)		(WS11)			(WS9)	(WS10)	
1.13 h/l= 180/80	D16								
	2D19			WS7,WSR7					
	2D2S								

VERTICAL REINFORCEMENT D16@400

WS ; SHEAR FAILURE TYPE
WF ; FLEXURAL FAILURE TYPE
WT ; TT:T-SHAPE, TC:CROSS-SHAPE SPECIMEN
R ; CLAY BLOCK
J ; EFFECT OF LADDER STEEL

B1 ; 300mm LENGTH C/B SPECIMEN
RC ; R/C SPECIMEN
D ; OPEN JOINT SPECIMEN
N ; AXIAL FORCE SERIES SPECIMEN

Tests of specimens in pharenses were conducted by other investigators

b) Beam Specimens

R/C SLAB / Pw		D13@400 (2D10@400)*1 D13@400 *2		D13@200 D13@150*2		2D13@200 D16@150*2	
M/QD	At(cm²)	○	×	○	×	○	×
0.71 l/h= 120/95	2D16 (3.98)			GF1			
	2D19 (5.74)		(GF6,GFR4)				
	2D25 (10.1)	GS1	GS2,GSR1 (GSH1,GSB1) (GSH2)			GS3,GSR2	
1.18 l/h= 200/95	2D16						
	2D19	GF2	GF3(GFR1)		(GF4,GFR2)		(GF5,GFR3)
	2D25		GS4				

HORIZONTAL REINFORCEMENT D16@400

*1 FOR HOOP SERIES SPECIMEN
*2 FOR 300mm LENGTH UNIT SPECIMEN

GS ; SHEAR FAILURE TYPE
GF ; FLEXURAL FAILURE TYPE
R ; CLAY BLOCK

B1 ; 300mm LENGTH C/B SPECIMEN
H ; HOOP SERIES SPECIMEN

Tests of specimens in pharenses were conducted by other investigators

312

Table 3 Tests Results

Left table

Specimen	+/−	Test Results r_{max}	R_{max}	$R_{a,a}$	Calculated Results r_{aa}	r_{max}	$\frac{r_{max}}{r_{aa}}$	$\frac{r_{max}}{r_{aa}}$
WS1	+	30.73	1.720	2.220	38.11	16.58	0.806	1.853
	−	23.92	1.211	1.045			0.628	1.442
WS4	+	20.77	1.907	3.778	26.59	18.66	0.781	1.113
	−	19.40	1.579	5.833			0.730	1.040
WS7	+	20.21	9.359	8.205	20.08	16.36	1.007	1.235
	−	21.48	8.923	9.017			1.070	1.313
WSR1	+	31.25	2.010	1.769	40.07	17.49	0.780	1.787
	−	32.55	1.806	1.500			0.812	1.861
WSR4	+	23.60	2.510	6.625	27.09	19.46	0.871	1.213
	−	23.70	2.280	5.250			0.875	1.218
WSR7	+	19.62	6.809	6.051	20.23	17.30	0.970	1.134
	−	22.00	4.486	3.830			1.087	1.272
WSN1	+	25.95	2.111	4.778	36.41	20.27	0.713	1.280
	−	23.10	2.345	4.222			0.634	1.139
WSK2	+	26.30	2.407	4.556	43.96	21.88	0.598	1.202
	−	27.05	2.392	4.000			0.615	1.206
WSRC	+	21.24	1.989	5.278	26.76	19.79	0.794	1.073
	−	23.33	1.789	2.778			0.872	1.179
WF1	+	16.27	4.142	12.625	16.14	17.45	1.008	0.932
	−	15.96	2.503	9.375			0.989	0.915
WF2	+	16.88	10.381	20.500 ?	16.14	22.43	1.046	0.752
	−	15.99	2.688	20.500 ?			0.991	0.713
WFR1	+	17.03	4.926	7.679	16.73	18.26	1.018	0.933
	−	17.15	2.415	8.715			1.025	0.939
WFR2	+	17.27	4.963	10.938	16.73	23.56	1.032	0.733
	−	17.10	2.480	12.177			1.022	0.726
WFL1	+	16.16	5.092	16.000	16.14	17.08	1.001	0.946
	−	16.10	2.567	11.375			0.997	0.942
WFLR	+	16.88	5.040	18.561	16.14	17.08	1.046	0.988
	−	15.70	5.040	11.250			0.973	0.919
WFJ1	+	16.03	5.072	20.000 ?	16.14	17.08	0.993	0.939
	−	16.44	5.442	15.811			1.019	0.952
WFJ2	+	15.10	19.607	19.607 ?	16.14	22.43	0.936	0.673
	−	18.15	10.839	19.508 ?			1.124	0.809
WFRC	+	17.67	9.483	17.750	16.15	18.05	1.094	0.979
	−	16.61	5.047	11.750			1.029	0.921

Right table

Specimen	+/−	Test Results r_{max}	R_{max}	$R_{a,a}$	Calculated Results r_{aa}	r_{max}	$\frac{r_{max}}{r_{aa}}$	$\frac{r_{max}}{r_{aa}}$
WTT1	+	26.12	3.458	6.630	(26.67)	(19.17)	0.636	1.051
	−	24.02	5.080	9.990 ?	41.05	24.85	0.585	0.967
WTT2	+	37.27	7.740	9.300 ?	(26.67)	(24.52)	0.908	1.187
	−	38.81	5.500	7.150 ?	41.05	31.39	0.945	1.226
WTC1	+	23.05	4.120	11.750	(16.15)	(17.96)	0.853	0.975
	−	24.31	5.810	11.380	27.03	23.64	0.899	1.028
WTRC	+	24.52	4.494	21.063	(26.68)	(19.20)	0.597	0.986
	−	26.64	1.311	4.369	41.06	24.88	0.649	1.071
WFB1	+	15.56	2.320	19.940 ?	14.72	24.48	1.057	0.636
	−	14.20	2.390	20.210 ?			0.965	0.580
WFB10	+	15.80	10.120	36.072 ?	15.34	25.50	1.030	0.620
	−	14.69	5.240	21.072 ?			0.958	0.576
WSB1	+	23.34	4.240	9.750	25.30	20.30	0.922	1.150
	−	21.94	2.140	7.880			0.867	1.081
WSB10	+	24.54	4.660	8.130	25.40	21.32	0.966	1.151
	−	23.99	2.400	10.750			0.944	1.125
GF1	+	25.41	9.680	31.400	(10.16)	(18.35)	1.198	1.043
	−	23.98	4.960	19.400	21.22	24.36	1.130	0.984
GF2	+	18.49	5.150	21.600	(8.90)	(15.79)	1.190	0.966
	−	19.10	5.710	18.100	15.33	19.15	1.230	0.998
GF3	+	11.64	9.210	22.800	8.90	15.68	1.309	0.742
	−	10.47	5.110	12.000			1.177	0.668
GS1	+	27.96	4.680	11.200	(28.34)	(18.74)	0.710	1.109
	−	25.52	5.430	23.500	39.40	25.21	0.648	1.012
GS2	+	21.90	4.380	6.000	28.34	18.61	0.773	1.177
	−	16.91	3.463	7.300			0.597	0.909
GS3	+	20.11	5.060	11.500	28.34	20.81	0.710	0.966
	−	21.33	9.700	10.250 ?			0.753	1.025
GS4	+	17.70	4.620	4.800	17.01	17.13	1.041	1.033
	−	15.07	4.500	5.900			0.886	0.880
GSN1	+	17.43	6.830	10.300	28.34	21.56	0.615	0.888
	−	25.55	4.330	6.500			0.902	1.185
GSN2	+	29.45	7.630	10.900	28.34	26.55	1.039	1.109
	−	27.79	8.270	10.000 ?			0.980	1.047

313

τ_{max} : maximum shear stress obtained from test (kg/cm^2)
R_{max} : drift angle at τ_{max} $(10^{-3}rad.)$
$R_{0.8}$: drift angle at $0.8 \cdot \tau_{max}$ $(10^{-3}rad.)$
$\tau_{su} = \{ 0.053P_{te}^{0.23}(fm'+180)/(M/QD+0.12)+2.7\sqrt{\sigma_{wh}P_{we}}+0.1\sigma_{oe}\} B_{ej}/BD$ $- - -$ eq.1
   where M/QD : shear span ratio $1 \leqq M/QD \leqq 3$
          D : wall length or beam depth (cm)
          d : effective wall length or effective beam depth (cm)
          j : 7d/8 (cm)
          B : wall width or beam width (cm)
          B_e : equivalent width of wall or beam (cm)
          P_{te}: flexural reinforcement ratio $100 \times a_t/B_e d$ (%)
          fm': prism compressive strength (cm)
          σ_{wh}: yield strength of shear reinforcement (kg/cm^2)
          P_{we}: ratio of shear reinforcement
          σ_{oe}: vertical compressive stress (kg/cm^2)
                              (from A.I.J R/C Design Standards)
beam $\tau_{bu} = 2 \cdot 0.9$ $a_t \sigma_y d$ / ℓBD
wall $\tau_{bu} = 2 \{ 0.9$ $a_t \sigma_y d$ $0.4a_w \sigma_w+0.5ND(1-N/BDf_m')\} /hBD$ $- - -$ eq.2
     where a_t : cross sectional area of flexural reinforcement (cm^2)
              σ_y : yield strength of main vertical reinforcement (kg/cm^2)
              a_w : cross sectional area of vertical reinforcement (cm^2)
              σ_w : yield strength of vertical reinforcement (kg/cm^2)
              N : vertical compressive load (kg)
              h : clear height of wall (cm)
              ℓ : clear length of beam (cm)
                          (from A.I.J R/C Design Standards)
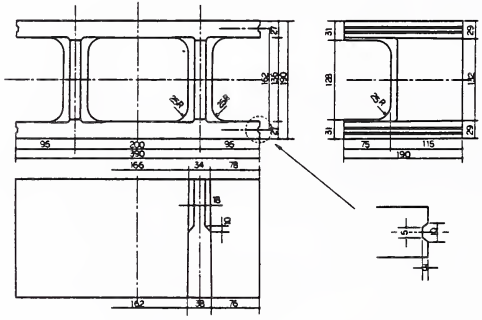
Fig. 1 Unit

a) Standard Concrete Block Unit
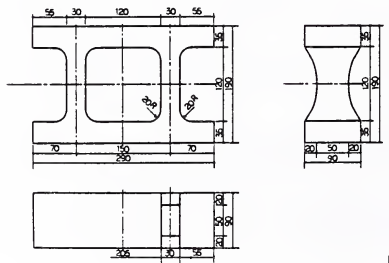
b) Standard Clay Brick Unit

314
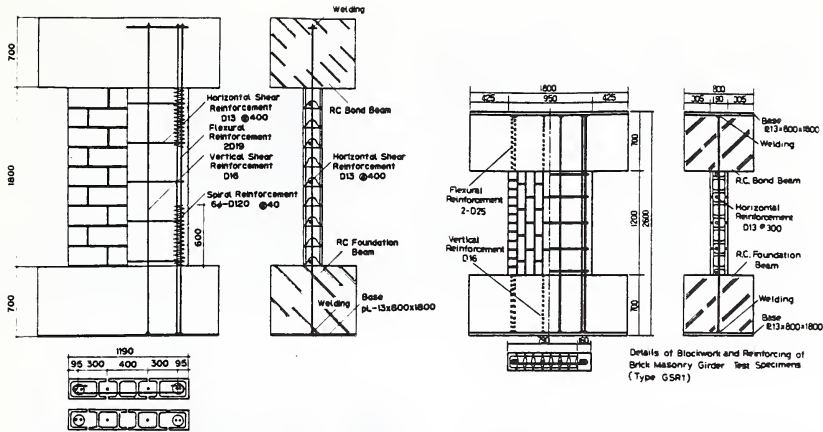
a) WFJ1   b) GSR1

Fig. 2 Test Specimen

Fig. 3 Loading System

315

a) WS4   b) WFJ2   c) WTT1   d) WS7

e) GF2   f) GF3
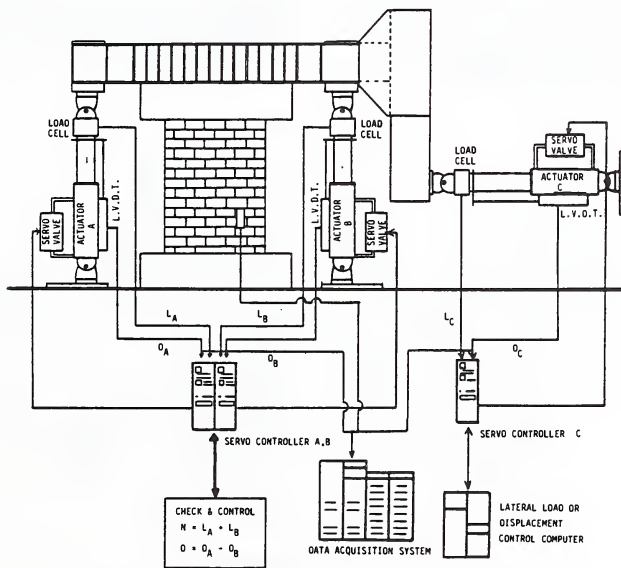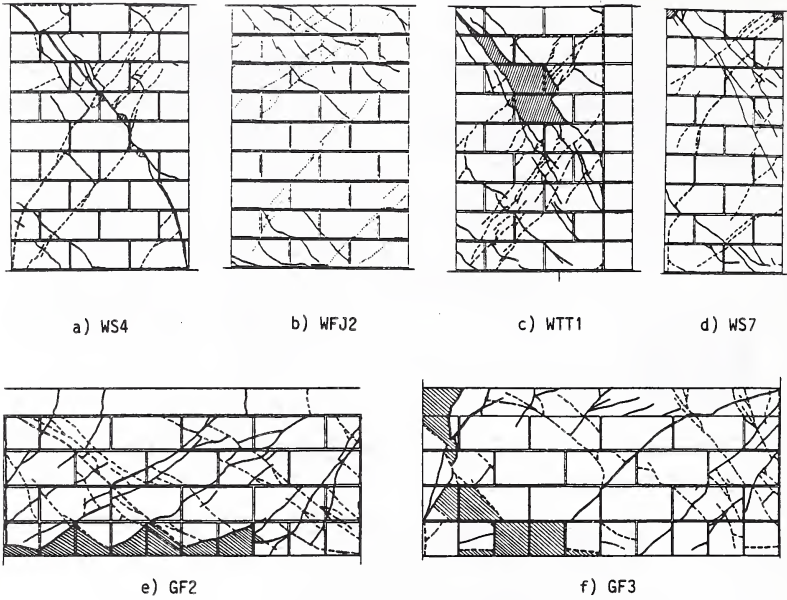
Fig. 4 Crack Pattern
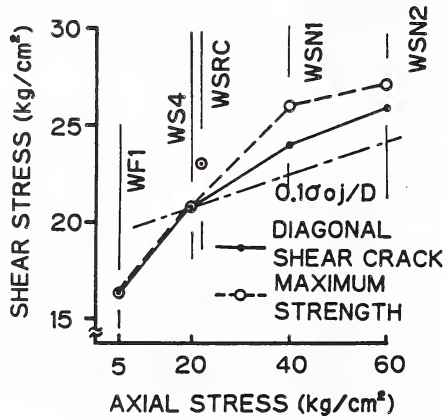
Fig. 5 Effect of Axial Stress

316
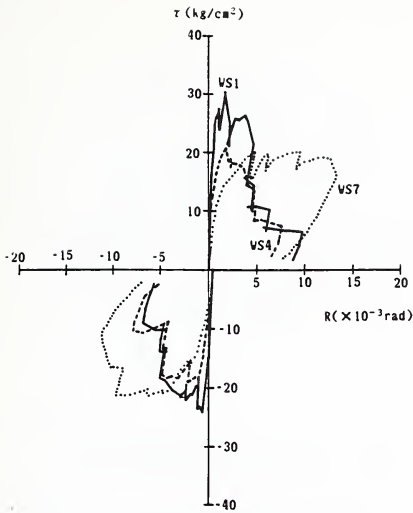
Fig. 6 Effect of Shear Span Ratio
(Concrete Block)
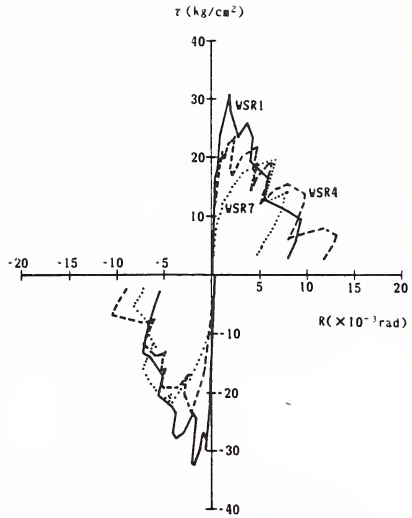
Fig. 7 Effect of Shear Span Ratio
(Clay Brick)
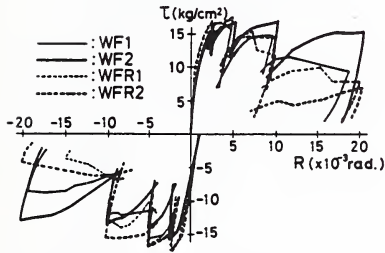
Fig. 8 Effect of Shear Reinforcement
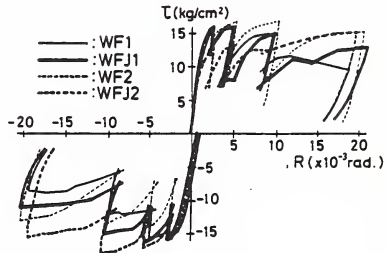
Fig. 9 Effect of Spiral Reinforcement

317
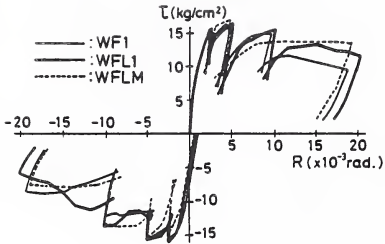
Fig. 10 Effect of Splice
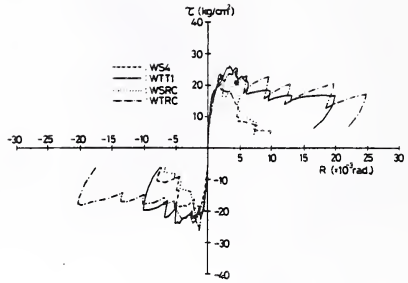
Fig. 11 Effect of Transverse Wall
(T Type Pw=0.167%)
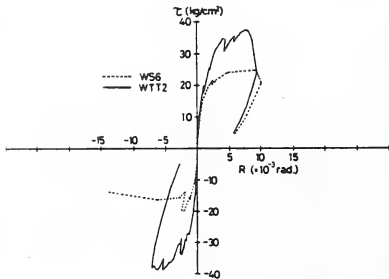
Fig. 12 Effect of Transverse Wall
(T Type Pw=0.667%)
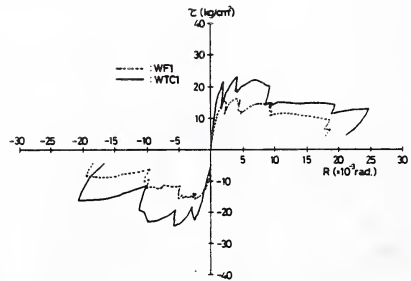
Fig. 13 Effect of Transverse Wall
(+ Type Pw=0.167%)

318
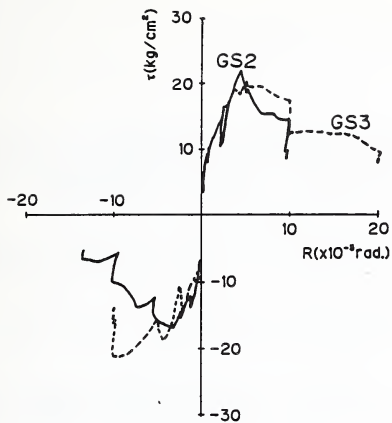
Fig. 14 Effect of Shear Reinforcement
(Concrete Block Beam)
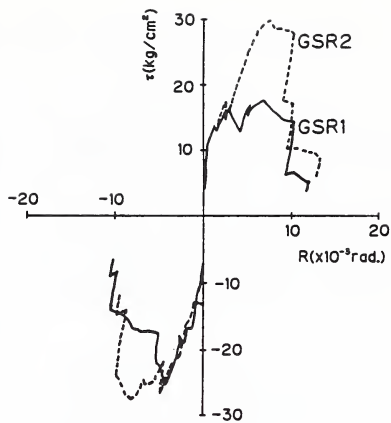
Fig. 15 Effect of Shear Reinforcement
(Clay Brick Beam)
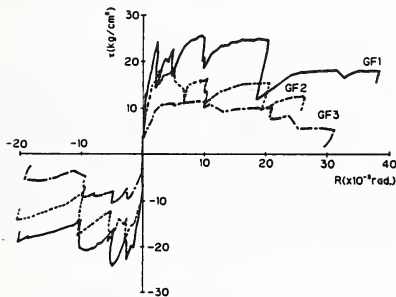
Fig. 16 Effect of R/C Slab
(Flexural Type)
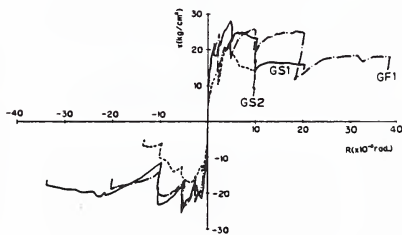
Fig. 17 Effect of R/C Slab
(Shear Type)

U.S.-JAPAN COORDINATED PROGRAM ON MASONRY RESEARCH

by

Shin Okamoto[1], James Noland[2], M.ASCE

ABSTRACT

An overview of the U.S.-Japan Coordinated Program
on Masonry Research is presented. The program
consists of parallel efforts in Japan and the
United States to develop design methods for rein-
forced masonry buildings located in areas of
seismic risk. Both programs rely heavily upon
experimental work to produce data and confirm
design methods. Both programs also include tests
of a full-scale reinforced masonry building
specimen to observe and verify system response.

1. INTRODUCTION

The U.S.-Japan Coordinated Program on Masonry
Research is the third in a series of building
research programs conducted by Japan and the
United Stated under the Auspices of the Panel on
Wind and Seismic Effects of the U.S.-Japan Natural
resources development program (UJNR). The first
two were conducted on reinforced concrete and
structural steel buildings.

The joint masonry programs are intended to obtain
experimental data and establish design methods
pertinent to design and construction of masonry
buildings in areas of seismic risk. However,
the knowledge and techniques developed in the
course of the two programs will also be appli-
cable to design and construction of masonry
buildings subjected to other types of loading.

The two research programs have begun. The pro-
gram in Japan began in 1984 and the U.S. program
commenced in 1985. This paper presents a brief
overview of each program.

2. PART I - OVERVIEW OF THE JAPANESE PROGRAM

2.1 Background

Masonry structural systems are known worldwide
as traditional and efficient with high durability,
fire resistance, sound and heat insulation, and
high flexibility in construction. The structural
system was imported to Japan from Europe with
little attention given to earthquake resistance
of masonry buildings as then constructed. The
masonry buildings constructed by the imported
concepts sustained extensive damage in the Great
Kanto Earthquake. Since then the construction of
masonry structures practically ceased in Japan
and little effort was made on the study of the
seismic resistance of masonry structural systems.

Because of the large demand· for building construc-
tion after World War II, Japan developed various
construction systems amenable to mass production
of buildings. Masonry buildings were generally

not built because of the problems then perceived
regarding masonry structures, e.g., tedious labor.
What is desired in building construction today
has changed. Now more value is placed on quality
then quantity. Versatility and variety are more
appreciated than uniformity.

It was natural, therefore, to reconsider masonry
structures. Since the late 1960's various types
of new masonry systems have been developed to
make construction more reliable and competitive.
The reinforced concrete block (RCB) system is
one example.

The Building Research Institute has contributed
a great deal to the improvement of masonry struc-
tural system. One current project is entitled
"Application of Small PC units to Urban Housing"
in which a high quality masonry unit will be
developed and a new earthquake resistant construc-
tion technique proposed.

Additional research is required to further
improve masonry design and construction techni-
ques for greater seismic safety thus enabling
greater utilization of this type of construction.
The immediate target of the Japanese part of the
U.S.-Japan joint research program will be the
development of a masonry construction system
applicable to low and medium rise building struc-
tures.

2.2 Research Team Organization

The organization of the Japanese masonry research
effort is shown in Figure 1 and its relationship
to the U.S. masonry research team organization.
The U.S. organization is presented in more detail
in Part 2 of this paper. Note that the Japanese
and U.S. research efforts are linked at the
government level by a coordinated research agree-
ment and at the project level by the Joint Tech-
nical Coordinating Committee on Masonry Research
(JTCCMAR).

Three major committees are included in the
Japanese masonry research organization, i.e., the
Technical Coordinating Committee on Masonry
Research (PROCMAR), and the Building Construction
Committee on Masonry Research (BLDCMAR). The

---
[1] Director, Production Department, Building
Research Institute Ministry of Construction,
Tsukuba, Japan.

[2] Principal, Atkinson-Noland & Associates.
Boulder, Colorado, U.S.A.

first committee, TECCMAR, coordinates technical research planning on materials, components, assemblies and full-scale experiments and will develop proposals for aseismic design guidelines for low and medium use reinforced masonry building structures in Japan.

PROCMAR was organized under a domestic cooperative research agreement between the Building Research Institute, the Japan Association for the purpose of promoting the U.S.-Japan research program in Japan on masonry structures. The members of PROCMAR include government officials, local self-governing body officials and representatives from many industrial organizations as shown in Figure 1.

There are many construction problems to solve in this research program to develop technology for the design and construction of low and medium rise reinforced buildings in Japan. The third committee, BLDCMAR, was organized under PROCMAR to address the problems concerning reinforced masonry building construction techniques.

2.3 Research Plan

The Japanese masonry research effort will take approximately five years and is composed of the following basic components:

1. Material Tests .
2. Static Tests of Walls
3. Static Tests of Beams
4. Static Tests of Wall and Beam Assemblies
5. Full-Scale Planar Static Tests
6. Shaking Table Tests of a Scale Model Specimen
7. A Full-Scale Five-Story Structure Test
8. Establishment of Aseismic Design Guidelines

The time schedule for the Japanese research effort is shown in Figure 2. During the first two years, fundamental tests of materials, of wall and beam components, masonry structural assemblies, and of a full-scale planar specimen are planned. A great deal of this has been done. The shaking table tests of a scale model specimen and a full-scale five-story structure will be done in the later part of the program.

2.4 Japanese Research Objectives

The final target for the Japanese side of the joint research program is to propose aseismic design guidelines for low and medium rise reinforced masonry building structures in Japan. Presently, only reinforced masonry buildings of 12 meters (one to three stories) are permitted. As a result of this program design guidelines for low-to-medium rise reinforced masonry building (up to five stories) will be proposed.

There are also many other objectives related to the structural design of masonry buildings such as:

1. To assure acceptable aseismic performance. Aseismic performance which is substantially equal to that to be required for wall type RC buildings in Japan will be expected for reinforced masonry buildings.

2. To propose decreased wall length rate. Revise 21 cm/m^2 in the present regulations:

   a) 15-18 cm/m^2 for five story buildings and,
   b) 12-15 cm/m^2 for three story buildings.

3. To eliminate the use of reinforced concrete collar beams. Reinforced concrete collar beams are required in reinforced masonry buildings under present regulations.

4. To simplify joint works of reinforced bars. Effectiveness of lap and mechanical joints of vertical reinforcing bars in walls must be established.

2.5 Review of Research Done in 1984

The following topics were addressed in 1984:

1. Masonry Units - Standard concrete and clay block units developed for use in the Japanese program are shown in Figures 3 and 4.

2. The predictions of the compressive strength of prisms based on the properties of block units, grout concrete and mortar has been investigated.

3. High lift grouting procedures have been studied using wall specimens 2½ units long (1000 mm or 39.4 in.) by 12 courses high (2400 mm or 94.5 in.).

4. Effectiveness of lap splices of reinforcing bars in masonry has been studied using six types of splice configuration. This included evaluation of spiral reinforcement around lap splices.

5. Anchorage of reinforcing bars in grouted masonry has been studied considering grout cover and proximity of the reinforcement to face shells of units.

6. Static tests of masonry wall and beam components were conducted. The major purpose was to investigate their deformation performance and shear capacity varying area of main reinforcement, shear reinforcement and shear-span ratio.

3. CONCLUSIONS

Masonry buildings of either concrete or clay unit masonry are at present few in Japan compared with the number of buildings of other materials, e.g., wood, concrete, and steel. This is because of the susceptibility to earthquake damage of masonry buildings previously constructed by methods imported from Europe one hundred years ago. It is expected that the five-year masonry research program just described on low-to-medium rise masonry buildings will allow and encourage greater numbers of such buildings in Japan.

4. ACKNOWLEDGEMENT

5. PART II - OVERVIEW OF THE UNITED STATES PROGRAM

5.1 Background

Load-bearing masonry buildings have been built in the United States for many years—nearly since the time European settlers first arrived. Masonry buildings are a significant percentage of buildings built from that time up to the 1930's and are generally unreinforced.

Reinforced concrete and structural steel buildings gradually became a larger and larger part of the construction market. Their use was and is encouraged by the great amount of research and development done and by the gradual improvement in design methods and codes.

In contrast, the use of masonry as the primary structural system declined in comparison to the use of steel and concrete possibly due to the perception that masonry design technology was not at the same level as that for steel and concrete and to the perception that masonry structures perform poorly in earthquakes.

While some U.S. research in structural masonry was done earlier, it beban to increase in the mid-to-late sixties and continues to increase. Masonry building code improvement has also recently been emphasized as exemplified by the 1985 Uniform Building Code and by the work of the joint ASCE/ACI Committee 530 on masonry. This author believes that some of the impetus for renewed interest in the structural use of masonry is due to its architectural flexibility and that it can be competitively economic for certain types of building plans. The introduction of reinforcement has been shown to provide the ductility required for adequate performance in earthquake conditions.

However, the design methodology is still basically a working stress approach based on the assumption of linear-elastic material behavior although the latest UBC does permit strength methods for certain applications. While many reinforced masonry structures have been built and have performed successfully, economic considerations and a better ability to predict ultimate behavior would make structural masonry a more viable alternative as a building system particularly for earthquake conditions. A need was recognized for complete strength-method design techniques for reinforced masonry based upon adequate experimental data to bring masonry structural technology to a level consistent with modern needs.

5.2 Research Team Organization

A team of masonry researchers known as the Technical Coordinating Committee for Masonry Research/ U.S. (TCCMAR/U.S.) was formed to identify the research necessary and to organize in a manner such that the research can be done in an orderly fashion. The organization of TCCMAR/U.S. and the basic research areas are depicted in Figure 1.

Funding is provided by The National Science Foundation (Dr. A.J. Eggenberger) and liason with the UJNR Committee on Wind and Seismic Effects is done by G.R. Fuller (HUD) and Dr. H.S. Lew (NBS). A single coordinator (J. Noland) is responsible for overall operation of the U.S. program with the advice and assistance of the Executive Panel. The Consultants Panel is composed of individuals highly qualified to provide basic guidance on the course and conduct of the program. Two were intimately associated with previous U.S.-Japan joint research programs.

A panel of Industry Observers was formed to provide industry perspective and to relay information about the program to the industry. The purpose of the Industry Participation Panel is to define ways in which the industry can assist the program and arrange for that assistance.

5.3 Research Plan

The U.S. masonry research program consists of a group of coordinated research tasks beginning with tasks which address basic material behavior, progressing to tasks addressing behavior of masonry structural components, e.g., walls, and finally to experiments on a full-size segment of a masonry building. Development of analytical methods for stress and strain analysis and system behavior will proceed in parallel with experimental tasks. The final task will be the preparation of recommendations for design procedures and building code provisions.

The research tasks which were identified by TCCMAR/U.S. fell into 10 categories as shown in Figure 1. The following is a more detailed list of research tasks in each category and their objectives.

Category	Task	Title-Purpose
1.0	1.1	Preliminary Material Studies – To establsih the range of continuity of masonry behavior to provide a basis for selection of the type or types of masonry to be used. To establish standardized materials test procedures for all the experimental tasks.
1.0	1.2	Material Models – To evaluate K1, K2, and K3 for the flexural stress-block. To determine uniaxial and biaxial material properties for analytical models (Tasks 2.1 and 2.2) including post-peak behavior. To evaluate non-isotropic behavior.
2.0	2.1	Force-Displacement Models for Masonry Component – To develop force-displacement mathematical models which accurately characterize reinforced masonry components under cyclic loading to permit pretest predictions for experimental results. To develop models suitable for parameter studies and models suitable for design engineering.
2.0	2.2	Strain Analysis Model for Masonry Components – To develop a strain model for reinforced masonry components in conjunction with Task 2.1 to enable regions of large strain to be identified thus assisting in experimental instrumentation planning. To develop a simplified model to be used to provide data for strength design rules and in-plane shear design procedures.
2.0	2.3	Dynamic Response of Masonry Buildings – To develop a generalized dynamic response model to predict inter-story displacements using specified time histories. To correlate force displacement models and to investigate force-displacement characteristics of structural components in the near-elastic and inelastic displacement range. To provide data for building test planning.
2.0	2.4	Dynamic Properties of Masonry Systems – To develop consistent unified, rationale for seismic design of masonry buildings considering elastic and inelastic response of masonry buildings and of the soil/structure interaction and related to seismic hazard zones.
3.0	3.1(a)	Response of Reinforced Masonry Story-Height Walls to Fully Reversed In-Plane Lateral Loads – To establish the behavior of story-height walls subjected to small and large amplitude reversals of in-plane lateral deflection, axial force, and bending moments considering aspect ratios, reinforcement ratios and patterns, and the effect of openings.
3.0	3.1(b)	Development of a Sequential Displacement Analytical and Experimental Methodology for the Response of Multi-Story Walls to In-Plane Loads – To develop a reliable methodology for investigating, through integrated analytical and experimental studies, the in-plane behavior of multistory reinforced hollow unit masonry walls. The methodology will be the basis of studying the response of a full-scale masonry research building.
3.0	3.2(a)	Response of Reinforced Masonry Walls to Out-of-Plane Static Loads – To verify the behavior of flexural models developed using material models, to evaluate the influence of mortar joint spacing, unit properties, reinforcement ratios and grouting upon wall behavior. To provide stiffness data for correlation with dynamic wall test results (Task 3-2(b)).
3.0	3.2(b)	Response of Reinforced Masonry Walls to Out-of-Plane Dynamic Excitation – To determine effects of slenderness, reinforcement amounts and ratios, vertical load and grouting on dynamic response, to verify mathematical response models, to develop design coefficients for equivalent static load methods.
4.0	4.1,	Wall-to-Wall Intersections and Floor-to-Wall Intersections of Masonry Buildings – To determine the effectiveness of

4.2 intersection details to connect masonry wall components, to construct a nonphenomenological analytical model of intersection behavior.

5.0 5.1 Concrete Plank Diaphragm Characteristics – To investigate experimentally concrete plank diaphragm floor diaphragms to determine modes of failure and stiffness characteristics including yielding capacity in terms of distortion as needed for masonry building models.

5.0 5.2 Assembly of Existing Diaphragm Data – To assemble extensive existing experimental data on various types of floor diaphragms, to reduce to a form required for static and dynamic analysis models.

6.0 6.1 Grouting Procedures for Hollow Unit Masonry – To identify methods of grouting hollow unit masonry such that the cavity is solidly filled and reinforcement is completely bonded.

6.0 6.2 Reinforcement Bond and Splices in Grouted Hollow Unit Masonry – To develop data and behavioral models on the bond strength and slip characteristics of deformed bars in grouted hollow unit masonry, to develop data and behavioral models on the bond strength and slip characteristics of deformed bar lap splices in grouted hollow unit masonry as needed for building modeling.

7.0 7.1 Small Scale Models – To experimentally evaluate the use of small-scale modeling for reinforced hollow-unit masonry walls by correlating test results with test results of full-scale walls of the same configuration. To determine if tests of small-scale specimens can reveal basic characteristics and failure modes of full-scale masonry specimens.

8.0 8.1 Limit State Design Methodology for Reinforced Masonry – To select an appropriate limit state design methodology for masonry. To select and document a procedure to compute numerical values for strength

reduction factors. To review program experimental research tasks assure that statistical benefits are maximized and proper limit states are investigated.

8.0 8.2 Numerical Reliability Indices – To develop numerical values of statistically-based strength reduction (i.e., $\emptyset$) factors using program experimentally developed data, other applicable data, and judgement.

9.0 9.1 Design of Reinforced Masonry Research Building, Phase I – To develop the preliminary designs of the potential research buildings which reflect a significant portion of modern U.S. masonry construction. To estimate interstory displacements using methods developed in Category 2 tasks and the associated load magnitudes and distributions. To select a single configuration in consultation with TCCMAR which will be used as a basis for defining equipment and other laboratory facilities in Task 9.2.

9.0 9.2 Facility Preparation – Define, acquire, install and check-out equipment required for experiments on a full-scale masonry research building.

9.0 9.3 Full-Scale Masonry Research Building Test Plan – To develop a detailed and comprehensive plan for conducting static load-reversal tests on a full-scale reinforced masonry research building.

9.0 9.4 Full-Scale Test – To conduct experiments on a full-scale reinforced masonry research building in accordance with the test plan and acquiring data indicated. To observe building response and adjust test procedures and data measurements as required to establish building behavior.

10.0 10.1 Design Recommendations and Criteria Development – To develop and document recommendations for the design of reinforced masonry building subject to seismic excitation in a manner conducive to design office utilization. To develop and document cor-

responding recommendations for
masonry structural code provi-
sions.

11.0   11.1   Coordination - To fully coor-
dinate the U.S. research tasks
to enhance data transfer among
researchers and timely comple-
tion of tasks. To schedule
and organize TCCMR and Execu-
tive Panel meetings. To
establish additional program
policies as the need arises.
To stimulate release of pro-
gress reports and dissemination
of results. To coordinate with
industry for the purposes of
informing industry and arrang-
ing industry support. To
interface with NSF and UJNR
on overall funding and policy
matters.

The names, affiliations and research task arrange-
ments of current TCCMAR/U.S. members are as
follows:

Task	Researcher	Institution
1.1	R. Atkinson	Atkinson-Noland & Assoc.
1.2(a)	A. Hamid	Drexel Univ.
1.2(b)	R. Brown	Clemson Univ.
2.1	R. Englekirk	AKEH Joint Venture
2.2	G. Hart	" " "
2.3	J. Kariotis	" " "
2.4	R. Ewing	" " "
3.1(a)	J. Noland/ B. Shing	Univ. of Colo.-Boulder
3.1(b)	G. Hegemier/ F. Seible	Univ. of Calif.-San Diego
3.2(a)	A. Hamid	Drexel Univ.
3.2(b1)	S. Adham	Agbabian Assoc.
3.2(b2)	R. Mayes	Computech
4.1	G. Hegemier	Univ. of Calif.-San
4.2	F. Seible	Diego
5.1	M. Porter	Iowa State Univ.
5.2	"	" " "
6.1	L. Tulin	Univ. of Colo.-Boulder
6.2	"	" " "
7.1	A. Hamid	Drexel Univ.
8.1	G. Hart	Univ. of Calif.-Los Angeles
8.2	TCCMAR*	--
9.1	J. Kariotis A. Johnson	Barnes-Kariotis Joint Venture
9.2	G. Hegemier	Univ. of Calif.-San Diego
9.3	TCCMAR*	--
9.4	TCCMAR*	Univ. of Calif.-San Diego
10.1	TCCMAR*	--
11.1	J. Noland	Atkinson-Noland & Assoc.

*
Task to be done by TCCMAR/U.S. or subgroup
thereof.

5.4 Task Coordination

The research tasks are interdependent, i.e.,
results from a given task may be required for the
execution of others and vice-versa. Analytical
tasks will generally require interaction with
experimental tasks on a fairly continuous basis
so that analytical model development may incor-
porate data as they are obtained. The needs of
the analytical tasks will in turn serve to define,
in part, the manner in which experimental tasks
are designed and conducted and the data to be
obtained.

The anticipated intra-task interaction is
depicted generally in Figure 2.

5.5 Schedule

The schedule for tasks comprising the U.S. pro-
gram is shown in Figure 3. Total time required
to complete the program is estimated to be
approximately six years.

5.6 Review of 1985 Progress

Task 1.1, Preliminary Studies was completed by
June 1985. Work was begun on Tasks 1.2(a & b),
2.1, 2.2, 2.3, 3.1(a), 5.1, 5.2, 6.2, 8.1 and
9.1 in the Fall of 1985; therefore results are
not yet available

6. CONCLUSIONS

The U.S. program was designed to provide a
strength design methodology for reinforced
masonry buildings based upon an integrated experi-
mental and analytical program of specific research
tasks. Study of the task descriptions will
reveal that only issues believed to be essential
to this development are addressed. Budget limi-
tations also restrict the number of parameters
which can be evaluated in these tasks. However,
the work will provide a unified framework and
reference point so that future research, as funds
become available, will be able to effectively
build upon the knowledge developed in this pro-
gram.

7. ACKNOWLEDGEMENT

U.S - JAPAN COORDINATED PROGRAM FOR MASONRY BUILDING RESEARCH
FIGURE 1 - TCCMAR ORGANIZATION (U.S.)
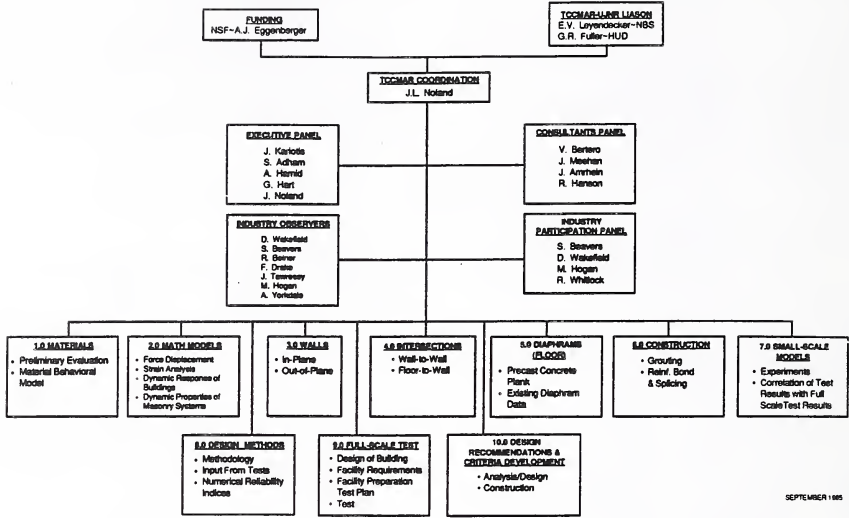
U.S.-JAPAN COORDINATED PROGRAM FOR MASONRY BUILDING RESEARCH
FIGURE 2 — TASK INGREDIENTS-DEPENDENCE CHART (U.S. PROGRAM)
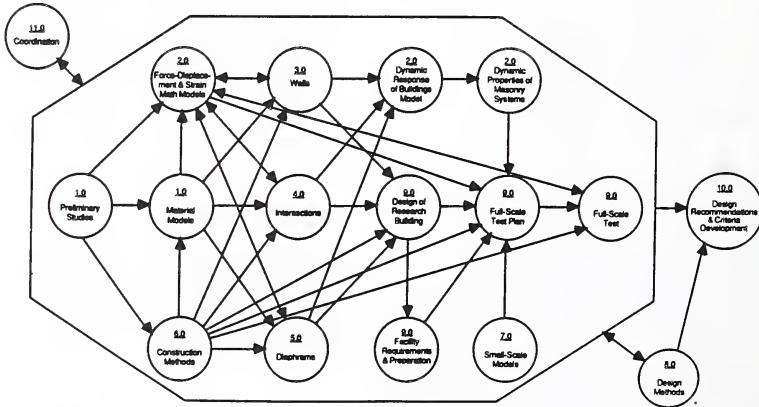
FIGURE 3 — TASK SCHEDULE (U.S. PROGRAM)

U.S.-JAPAN COORDINATED PROGRAM FOR MASONRY BUILDING RESEARCH

CATEGORY	TASK
1.0	1.1 PRELIMINARY STUDIES
	1.2 MATERIAL MODELS
2.0	2.1 FORCE-DISPLACEMENT MODEL
	2.2 STRAIN ANALYSIS MODEL
	2.3 DYNAMIC RESPONSE MODEL
	2.4 DYNAMIC PROPERTIES OF MASONRY SYSTEMS
3.0	3.1(a) IN-PLANE WALLS (STORY HEIGHT)
	3.1(b) SEQUENTIAL DISPLACEMENT- IN-PLANE WALLS
	3.2(a) OUT-OF-PLANE WALLS (STATIC-CONC. MAS.)
	3.2(b1) OUT-OF-PLANE WALLS (DYNAMIC-CONC. MAS.)
	3.2(b2) OUT-OF-PLANE WALLS (STATIC & DYNAMIC-CLAY MAS.)
4.0	4.1 WALL-TO-WALL INTERSECTIONS
	4.2 FLOOR-TO-WALL INTERSECTIONS
5.0	5.1 CONCRETE PLANK DIAPHRAMS
	5.2 EXISTING DIAPHRAM DATA
6.0	6.1 GROUTING PROCEDURE
	6.2 REINFORCEMENT BOND & SPLICES
7.0	7.1 SMALL-SCALE MODELS
8.0	8.1 LIMIT STATE DESIGN METHODOLOGY
	8.2 NUMERICAL RELIABILITY INDICES
9.0	9.1 DESIGN OF RESEARCH BUILDING
	9.2 FACILITY PREPARATION
	9.3 FULL SCALE TEST PLAN
	9.4 FULL SCALE TEST
10.0	10.1 DESIGN RECOMMENDATIONS & CRITERIA DEVELOPMENT
11.0	11.1 COORDINATION
	TCCMAR MEETINGS

Δ = PROPOSAL SUBMITTED

JULY 1985

BUDGET — U.S. COORDINATED PROGRAM FOR MASONRY BUILDING RESEARCH

Budget Request by Fiscal Year

| Category	Task	Task Title	Researcher	Institution	Total Fiscal FY '85,'86,'87	Fiscal '85	Fiscal '86	Fiscal '87	Fiscal '88	Fiscal '89	Fiscal '90	Fiscal '91
1.0	1.1	Preliminary Studies	Atkinson	Atkinson-Noland	$ 57,346	$ 57,346	$ —	$ —				
	1.2(a)	Material Models-Concrete Masonry	Hamid	Drexel Univ	71,712	39,839	31,873					
	1.2(b)	Materials Models-Brick Masonry	Brown	Clemson Univ	83,875	42,560	41,315					
2.0	2.1	Force-Displacement Model	Englekirk	AKEH Joint	191,779	54,944	50,000	86,835				
	2.2	Strain Analysis Model	Hart	Venture	164,935	52,615	40,000	72,320				
	2.3	Dynamic Response Model	Kariotis		174,240	52,950	40,000	81,290				
	2.4	Dynamic Properties of Masonry Systems	Ewing									
3.0	3.1(a)	In-Plane Walls (Story Height)	Noland / Shing	Univ of Colorado	147,474	—	77,041	70,433				
	3.1(b)	Sequential Displacement — Inplane Walls	Hegemier / Seible	UCSD	421,985	45,515	225,400	151,070				
	3.2(a)	Out-of-Plane Walls (Static-Conc. Masonry)	Hamid	Drexel Univ	89,552	—	41,500	48,052				
	3.2(b1)	Out-of-Plane Walls (Dynamic-Conc. Masonry)	Adham	Agbabian Assoc.	105,920	—	—	105,920				
	3.2(b2)	Out-of-Plane Walls (Static & Dynamic-Clay Masonry)	Mayes	Computech	204,743	5,992	40,038	158,713				
4.0	4.1	Wall-to-Wall Intersections	Hegemier / Murakami / Seible	UCSD	62,400	—	62,400	—				
	4.2	Floor-to-Wall Intersections										
5.0	5.1	Concrete Plank Diaphrams	Porter	Iowa State Univ	119,980	15,000	52,490	52,490				
	5.2	Existing Diaphram Data										
6.0	6.1	Grouting Procedures	Tulin	Univ of Colorado	83,748	46,773	36,975	—				
	6.2	Reinforcement Bond and Splices										
7.0	7.1	Small-Scale Models	Hamid	Drexel Univ	—	—	—	—				
8.0	8.1	Limit State Design Methodology	Hart	UCLA	80,668	36,088	21,798	22,782				
	8.2	Numerical Reliability Indices	TCCMAR*	—	—	—	—	—				
9.0	9.1	Design of Research Building	Johnson, Kariotis	Barnes Kariotis, Jv	21,920	21,920	—	—				
	9.2	Facility Preparation	Hegemier	UCSD	—	—	—	—				
	9.3	Full Scale Test Plan	TCCMAR*	—	—	—	—	—				
	9.4	Full Scale Test	TCCMAR*	—	—	—	—	—				
10.0	10.1	Design Recommendations and Criteria Development	TCCMAR*	—	—	—	—	—				
11.0	11.1	Coordination	Noland	Atkinson-Noland	121,355	42,275	41,540	37,540				
					2,393,632	516,817	802,370	884,445				

*The entire TCCMAR or subgroup thereof to be formed

JULY 1985

327

SEISMIC BEHAVIOR OF A FULL-SCALE K-BRACE STEEL BUILDING STRUCTURE

BY

Hiroyuki Yamanouchi*, Mitsumasa Midorikawa*, Isao Nishiyama* and Tatsuo Murota*

ABSTRACT

Full-scale seismic tests on a steel building were performed as a three-year research project from 1981. This research is part of the U.S.-Japan Cooperative Earthquake Research Program Utilizing Large-Scale Testing Facilities, to compare full-scale building behavior with scale model behavior and to assess the damage and safety levels of buildings subjected to earthquakes designed by current design practices.

This paper reports the results of seismic tests on a full-scale six-story steel building with concentric-K braces. A six-story, 2x2 bay, steel building was constructed at the Large Size Structure Laboratory of the Building Research Institute of the Japanese Ministry of Construction. The seismic tests were run as a six degree of freedom pseudo-dynamic system (on-line computer system). The input excitation was the NS component of the 1978 Miyagi-Ken-Oki Earthquake; and maximum intensity was set at three levels. To simulate working load conditions, the earthquake motion was scaled to 65 gal; for a moderate earthquake the peak intensity was set at 250 gal; the maximum earthquake was run at 500 gal.

The test results showed large capacity of the pseudo-dynamic testing technique, the importance of precise prediction of the interaction of the post-buckling behavior, local failure of the braces, the elasto-plastic behavior of the moment-resisting frame, and that of the three dimensional effects of the overall test building.

1. INTRODUCTION

As a part of the U.S.-Japan Cooperative Research Program Utilizing Large-Scale Testing Facilities (Ref. 7), a six-story, 2 by 2 bay, concentrically K-braced steel building was constructed in full-scale, and subjected to Miyagi-Ken-Oki simulated earthquake of different intensities by the pseudo-dynamic (PSD) test facilities (on-line computer-actuator test). To simulate working load conditions, the earthquake motion was scaled to 65 gal; for a moderate earthquake the peak intensity was set at 250 gal; the maximum earthquake was run at 500 gal. In a series of these seismic tests, the overall inelastic behavior and the

---

*Building Research Institute, Ministry of Construction

local behavior of the three dimensional full-scale structure were obtained, and considerations were carried out from various viewpoints.

2. FULL-SCALE TEST BUILDING

The test building was designed to satisfy the requirements of the 1976 Uniform Building Code and the 1981 Seismic Design Code of Japan. The plan and elevation are shown in Fig. 1. This building structure consisted of two unbraced moment-resisting frames (Frame-A and -C) and a concentrically K-braced frame (Frame-B). The dead load of the building was 523.6 tons (1154 kips) while the design dead load was 634.7 tons (1399 kips).

Member size of the test structure is shown in Table 1. Principal design criteria and details are: 1) The design base shear coefficient should be 0.197. 2) Live load and exterior wall weight should not be included in the design earthquake lateral forces. 3) Columns and girders should be wide flange shapes of ASTM A36 structural steel, and braces be square tubing section of ASTM A500 Grade B structural steel. 4) Girders and floor beams should act compositely with the floor using shear studs. 5) Braces should resist both tension and compression. 6) Girder-to-column connections should be moment connections in loading direction. 7) Column bases should be fixed. 8) Braces should be directly welded to surrounding frames without gusset plates.

3. TEST PROGRAM AND PROCEDURE

All tests, exclusive of free and forced vibration tests, were run as a six degree of freedom pseudo-dynamic (PSD) system. The input excitation was the NS component of the 1978 Miyagi-Ken-Oki Earthquake (Tohoku University). To maximize the amount of knowledge gained from the program, the test sequence in Table 2 was adopted, including the three level major seismic tests (the elastic PSD, inelastic PSD Moderate and inelastic PSD Final tests). At the head and end of the test sequence, the free and forced vibration tests were performed to obtain modal parameters and damping characteristics of the test structure.

The test structure was loaded by eight servo-controlled actuators through rigid loading beams installed at the edge of each floor. The

roof floor had two actuators, with a capacity of ± 100 ton (220 kips) load and ± 100 cm (39.4 in.) stroke, to prevent the test structure from overall torsion by displacements from the two jacks. At the 6th floor, two jacks were arranged with a capacity of ± 100 ton and ± 50 cm (19.7 in.). Only one of the two jacks were used in the PSD test control. The other actuator was controlled to generate the same load as the PSD-controlled actuator. Excluding the upper two floor levels, one actuator with the same capacity as the actuators at the 6th floor was set up for each floor. The PSD tests were run at time intervals of 0.01 sec. for the elastic level and 0.005 sec. for the moderate and final tests, respectively.

The basic instrumentation plan consisted of two phases. The first measured floor-level displacements and actuator forces for the PSD tests at each time step, by using digital-type displacement transducers and load cells. The second detected deformations of members of the steel skeleton, such as rotation angles of members, panel zone distortions of girder-to-column connections, and strains on structure components as girders, columns, braces and reinforcing bars in slabs, to estimate the load-deformation characteristics of the structural members of the building. Approximately 1,000 channels of data were collected for this purpose; the data were sampled at every fourth time step during the major three PSD tests.

4. OVERALL RESPONSE AND GROSS BEHAVIOR OF TEST STRUCTURE

Response waveforms of floor level displacements as a function of time, from the moderate and final tests are shown as solid lines in Figs. 2 and 3. In the moderate test, the girder panel-zone at the brace junction in the middle of the span failed at the 2nd floor. Also the braces at the 2nd, 3rd and 5th stories buckled slightly. The girder panel-zone was repaired by placing it with a new plate before the final test.

In the final test, at the 1st through 5th stories, the braces buckled in-plane and/or out-of-plane of the frame. In particular, the braces at the 2nd and 3rd stories buckled laterally 21 to 24 cm (8.27 to 9.54 in.) with local buckling and tearing at the mid-span and both ends. Many panel-zones of girder-to-column connections and member ends also suffered, mainly in the lower three stories. It should be noted that the maximum roof displacement reached was 22 cm (8.66 in.) and the maximum base shear was 331 tons (729 kips) at a displacement of 2.3 cm (0.91 in.) in the 1st story. Fig. 4 shows the relationship of story shear force vs. interstory displacement in the final test (solid lines). In this figure, it is shown that the lower stories

reached their load carrying capacity. On reaching this force level, several braces degraded. The vertical displacement at the brace junction reached 3.5 cm (1.38 in.) at the 3rd floor by a significant loss in capacity of the braces. Finally the test structure sustained an interstory drift angle of 1/57 at the 2nd story, and the north side brace at the 3rd story ruptured completely.

In Figs. 2, 3 and 4, analytical results are also shown in dotted lines. The DRAIN-2D computer program developed by Kanaan and Powell (Ref. 5) was used for the analysis. In this analysis, a degrading hysteresis model (Fig. 5) was applied to the post-buckling and cyclic behavior of braces. This model was developed by modifying the Jain-Goel-Hanson hysteresis rule of braces (Ref. 3). The comparison indicates that the analytical model is very good in predicting the overall behavior of the test building.

5. LATERAL ELASTIC STIFFNESS OF EACH STORY

Lateral elastic stiffness of each story is defined as a value of story shear divided by interstory drift. By the Elastic test, the stiffness of each story was obtained as listed in Table 3. On the contrary, an analytical stiffness of each story was obtained by using a computer program for static analysis on the basis of the DRAIN-2D. However, the results of this analysis (Analysis 0) had significant deviations from the test results as shown in Fig. 6. This discrepancy would be due to 1) three dimensional(3-D) effects of the framing of the test structure and 2) inaccurate estimation of each member's stiffness such as the stiffness of composite girders.

To study the effects of the above factors on the story stiffness in the Elastic test, further analysis were performed by taking the following items into account:

1) The nodal horizontal displacements at the nodes of B1 and the mid-span of the braced girders must be independent of those at the other nodes. Also reasonable shear stiffness of slabs between interior and exterior frames as a diaphragm effect may be effective; Analysis 1.

2) Axial deformations of B1-columns would be restrained by X-braces installed in the transverse direction; Analysis 2.

3) The stiffness of concrete should be taken into account to calculate the "negative" bending stiffness of composite girders in the Elastic test; Analysis 3.

4) Rigid zones in girder-to-column connection panels must be considered, which shorten the effective length of columns. Also

shear deformations of columns may be considered; Analysis 4.

Each analysis, herein, was done using the results from the preceding analyses. Fig. 6 shows how the analytical results changed from Analysis 0 to Analysis 4. From this figure, it is shown that the 3-D effects and rigid zones estimated for columns are significant to evaluate the actual story stiffness.

6. STORY SHEAR FORCE CARRIED BY BRACES AND BY MOMENT FRAMES

The ratio of story shear forces carried by seismic resistant braces and by moment frames is a basic parameter to design a steel structure with such braces and to evaluate the actual seismic performance, in particular, after buckling of the braces. The ratios were calculated for each story. Here, properties of the braces at each story are listed in Table 4. Effective slenderness ratio of the braces varied from 51.7 to 78.5 assuming an effective length coefficient K=0.7.

Fig. 7 gives time history ratios of story shear forces carried by the braces and by the moment frames to those induced by the actuator forces respectively, for the 2nd story in the final test (solid lines). This figure shows that the line on the braces turns down, and that on the moment frames turns up, having an intersection at the response time of 7.25 sec.. About the same time the north side brace began to develop severe buckling with the compressive strength much decreased. This showed that the deterioration of the brace capacity forced the moment frames into inelastic activity. On the contrary in the Elastic test and in the moderate test, the ratios were stable. Table 5 gives the ratios of the braces (in average) for the two tests. These values were close to those expected in the design process. For the final test, the ratios of the braces were well predicted by the analysis shown in Fig. 7 (dashed lines). However, this prediction was considerably disturbed by local failure such as local buckling, kinks, and cracking of the braces.

7. LOCAL BEHAVIOR IN THE FINAL TEST

7.1 Behavior of Braces

A pair of K-braces for each story carried about half-of-the-story shear force even after the buckling of compression brace. Therefore, the overall behavior of the test building depended on the behavior of the braces as shown in the preceding section in the final test.

The axial force vs. axial displacement relationships for a pair of the braces in the 2nd story are shown in Fig. 8. In this figure, the numerals in the boxes, such as [1] and [2],

show the locations of the members and/or sections in the test building as shown in Fig. 1. As seen from the figure, both braces showed rather large inelastic deformation under the axial thrust after buckling but they did not show tensile yielding.

The buckling strength of each brace of the test building is plotted and compared with European Column Curve (Ref. 4) in Fig. 9, where Column Strength Curve 2 for square tubing sections with residual stresses is shown. Herein, the nondimensional slenderness ratio λ for each brace is estimated that the effective buckling length is 70% of the clear length of each brace (K=0.7). The test results agree well with the Column Strength Curve 2.

The reason for no tensile yielding in the 2nd story braces (Fig. 8) resulted from the girder yield at the intersection of the braces under the vertical force produced by the difference of the axial force of the braces, and therefore the increase of the tensile force of one brace was interrupted by the reduction of the compression force of the other brace by buckling. Fig. 10 shows the time histories of the axial force of the 2nd story braces. The vertical displacement at the brace junction at the 2nd floor and of the story displacement in the 2nd story of the test building is shown. These time histories shows that the increase of the vertical displacement at the brace junction occurred when the initiation of the decrease of the compressive strength of the buckled brace started, it continued until the reverse of the increase of the story displacement.

The unbalance of the axial force of the braces affected the flexural yielding of the girder and the shear yielding of the girder panel-zone. The girder panel-zone showed large shear deformation; the hysteresis loop is stable as shown in Fig. 11. The maximum shear deformation amplitude reached 0.05 rad. but no cracks were observed in and around the shear panel.

7.2 Behavior of Girder-to-Column Panels (Joint Panels)

The strength of girder-to-column panels (joint panels) were designed to be much less than that of the adjacent members in this test building. The interior joint panels in the frames parallel to the loading direction were especially weaker in strength than exterior ones, relative to the strength of the adjacent members.

The shear deformation vs. panel moment relationships of the interior joint panels at the 4th floor are shown in Fig. 12. The panel moment was estimated as the sum of the face moment of the upper and lower columns (the moment diagram was evaluated from the readings of the strain gauges attached to the

intermediate sections of the columns). The calculated yield panel moment according to the AIJ (Architectural Institute of Japan) steel design standard (Ref. 1) is shown by the broken line in the figure. As seen in the figure, the joint panels show large inelastic shear deformation and the maximum amplitude of the shear deformation reached about 0.02 rad.. The plastic shear deformation in the joint panel of the braced-bay column (joint panel [5]) concentrates on one side, because the axial thrust in the column affected the increase of plastic shear deformation.

7.3 Behavior of Columns

Axial forces of the braced-bay columns became very large when the structure was subjected to large horizontal force. Axial force vs. axial deformation relationships are shown in Figs. 13 and 14 for 2nd and 3rd story interior braced-bay columns (B2-columns). They showed likely behavior of yielding. However, the calculated simple axial yield strength (Ny) is about 2 times as high as the force level corresponding to the apparent yielding.

The moment vs. axial force diagrams of both ends of each columns are shown in Figs. 15 and 16, respectively. Fig. 15 shows that the bottom end of the 2nd story B2-column should have yielded under the combination of flexural moment and axial force. As for 3rd story column, the combination of flexural moment and axial force is smaller than the yield criterion shown in Fig. 16. The joint panel adjacent to the top of the 3rd story column (joint panel [5]) showed a large amount of yielding (Fig. 12). According to the investigation by Nakao et al. (Ref. 6), the member adjacent to the yielded joint panel yields under a relatively small amount of flexural moment because of the stress distribution distorted as schematically shown in Fig. 17. This effect initiated the yielding of the top of the 3rd story column (Figs. 14 and 16).

7.4 Behavior of Girders

All the girders were designed to act compositely with the concrete slab using shear studs; their strength is much higher than the joint panels. Therefore the remarkable yielding was not observed in the girder. Here presented are the moment vs. curvature relationships measured at two sections of the 2nd floor girder in Frame-A (Fig. 18). Positive and negative stiffnesses calculated according to the AIJ recommendations (Ref. 2) and the stiffness of the bare steel girder are shown in the figure. Test results show fairly good agreement with calculated stiffnesses.

This figure shows apparent yielding under the positive bending and stiffness reduction under the negative bending at section [8]. The

theoretical full plastic moment of the composite girder is far larger. Slippage between the steel girder and the concrete slab explains the apparent yielding in the moment vs. curvature relationship. The composite girder is not able to sustain the increase of the flexural moment when the slippage occurred; then the moment vs. curvature relationship shows apparent yielding.

As for the stiffness reduction under the negative bending, the stiffness after the reduction is well agree with the stiffness estimated for bare steel (Fig. 18). The slippage between the steel girder and concrete slab or between the concrete slab and the reinforcing bars may be the reason for the stiffness reduction.

The stiffness at location [9] in the figure increases in the positive bending. The reason of this phenomenon is not yet explained.

7.5 Behavior of Transverse Braces

To restrain the torsional deformation of the test building under horizontal loading, transverse braces made of angle sections were installed in the exterior Frame-1 and -3 perpendicular to the loading direction. These transverse braces also restrained the vertical movements of the column ends which arose from the flexural deformation of the braced-bay frame.

The axial strains measured in the transverse braces are presented in Fig. 19. The figure shows that the transverse braces connected to the braced-bay columns (members [10] and [11]) were subjected to considerable strains, but those not connected to the brace-bay columns (members [12] and [13]) were subjected to almost zero axial strains. This occurred because the difference between the vertical displacements of the column in braced-bay and of the column in Frame-A or -C are relatively large. Yet, the difference between the vertical displacements of the column not in the braced-bay and of the column in Frame-A or -C is quite small. Moreover, the axial strains of the transverse braces were larger in higher stories. The flexural deformation of the braced-bay frame produced large vertical displacements in higher stories.

From the results of the strain measurement of the transverse braces, the three dimensional action (transverse action) should be considered for understanding the overall behavior of the test building.

8. CONCLUSIONS

1) The overall behavior and the local behavior of a full-scale K-braced steel structure were obtained with large capacity of the

pseudo-dynamic testing technique that simulates real earthquake responses.

2) Three dimensional effects of framing and more accurate estimations of members' stiffness resulted in close approximation of the analytical story stiffnesses to the experimental ones. From the consideration of the local behavior of transverse braces, it was shown that the three dimensional action by the transverse braces was important to understand the overall behavior.

3) The ratio between the story shear forces carried by the K-braces and by the moment frames were stable and predictable before the local failure of the braces. However, after such failure of the braces, the ratios changed so largely that further studies are needed to estimate the behavior of such failures.

4) Obtained local behavior was considered from various viewpoints and the behavior of many members and sections was made clear. Furthermore, data on the members and sections obtained in the test were verified to be reliable and useful for attaining knowledge about the behavior of individual members in actual structures.

9. ACKNOWLEDGEMENTS

10. REFERENCES

(1) Design Standard for Steel Structures, AIJ, Tokyo, 1970.

(2) Design Recommendations for Composite Constructions, AIJ, 1985.

(3) Jain, A. K., Goel, S. C. and Hanson, R. D., "Hysteresis Behavior of Bracing Members and Seismic Response of Braced Frames with Different Proportions," Report No. UMEE 78R3, University of Michigan, July, 1978.

(4) Johnston, B. G., "Guide to Stability Design Criteria for Metal Structure," SSRC, John Wiley & Sons, New York, 1976.

(5) Kanaan, A. E. and Powell, G. H., "General Purpose Computer Program for Inelastic Dynamic Response of Plane Structure," Report No. EERC 73-6, University of California, Berkeley, April, 1973.

(6) Nakao, M et al., "Strength and deformation capacity of joints and members in steel structures Part 3: Girder-to-Column Joints," Quarterly COLUMN 79, Nippon Steel Corporation, January, 1981 (in Japanese).

(7) U.S.-Japan Planning Group, "Recommendations for a U.S.-Japan Cooperative Research Program Utilizing Large-Scale Testing Facilities," Report No. UCB/EERC-79/26, Sept., 1979.

(8) Yamanouchi, H., Midorikawa, M., Nishiyama, I. and Kato, B., "Full-Scale Seismic Tests on a Six-Story Concentrically K-Braced Steel Building - U.S.- Japan Cooperative Research Program -," Proceedings of Special Conference of EM Division/ASCE, Laramie, Wyoming, August 1-3, 1984.

TABLE 1   MEMBER SIZE OF TEST STRUCTURE

COLUMN SCHEDULE

STORY \ MARK	C1	C2	C3	C4	C5
6-5	W 10 x 33 H-247.1x202.2 x7.37x11.05	W 10 x 33	W 10 x 49 H-253.5x254.0 x8.64x14.22	W 10 x 33	W 12 x 40 H-303.3x203.3 x7.49x13.08
4-3	W 10 x 39 H-252.0x202.8 x8.00x13.46	W 12 x 53 H-306.3x253.9 x8.76x14.60	W 12 x 65 H-307.8x304.8 x9.91x15.37	W 10 x 60 H-259.6x256.0 x10.67x17.27	W 12 x 72 H-311.2x305.8 x10.92x17.02
2	W 12 x 50 H-309.6x205.2 x9.40x16.26	W 12 x 65	W 12 x 79 H-314.5x306.8 x11.94x18.67	W 12 x 79	W 12 x 106 H-327.4x310.4 x15.49x25.15
1	W 12 x 65	W 12 x 87 H-318.3x308.0 x13.08x20.57	W 12 x 87	W 12 x 106	W 12 x 136 H-340.6x315.0 x20.07x31.75

GIRDER SCHEDULE

FLOOR \ MARK	G1	G2	G3	G4
RFL-6FL	W 16 x 31 H-403.4x140.3 x6.98x11.18	W 16 x 31 H-403.4x140.3 x6.98x11.18	W 18 x 35 H-449.6x152.4 x7.62x10.80	W 21 x 50 H-529.1x165.9 x9.65x13.59
5FL	W 16 x 31	W 18 x 35	W 18 x 35	W 21 x 50
4FL	W 18 x 35	W 18 x 35	W 18 x 35	W 21 x 50
3FL	W 18 x 35	W 18 x 40 H-454.7x152.8 x8.00x13.34	W 18 x 35	W 21 x 50
2FL	W 18 x 40	W 18 x 40	W 18 x 35	W 21 x 50

BRACE SCHEDULE

STORY \ MARK	BR1
6	Tube 4x4x1/5.56 Box-101.6x101.6x4.57x4.57
5	Tube 5x5x1/5.56 Box-127.0x127.0x4.57x4.57
4	Tube 5x5x1/4 Box-127.0x.127.0x6.35x6.35
3-2	Tube 6x6x1/4 Box-152.4x152.4x6.35x6.35
1	Tube 6x6x1/2 Box-152.4x152.4x12.7x12.7

333

TABLE 2   TEST SEQUENCE

1. Free and Forced Vibration Test (VT) #1
2. Each Floor Level Loading Test (FLL) #1
3. Trial Elastic Pseudo-Dynamic Test (PSD) #1
4. Elastic Pseudo-Dynamic Test #1&2
   (Maximum Input Acceleration 65 gal)
5. Pseudo-Dynamic Free Vibration Test #1
6. Trial Elastic PSD Test #2
7. Elastic PSD Test #3
   (Maximum Input Acceleration 65 gal)
8. Inelastic PSD Moderate Test
   (Maximum Input Acceleration 250 gal)
9. PSD Free Vibration (PSD-F) Test #2
10. Repair Works of Girder Panel
11. Each Floor Level Loading (FLL) Test #2
12. PSD Free Vibration (PSD-F) Test #3
13. Inelastic PSD Final Test
   (Maximum Input Acceleration 500 gal)
14. Each Floor Level Loading (FLL) Test #3
15. Free and Forced Vibration (VT) Test #2

TABLE 3   STIFFNESS OF EACH STORY

Story	Stiffness
6	64
5	92.5
4	127
3	152
2	183
1	220

(tonf/cm)

TABLE 4   BRACE PROPERTIES

Item / Story		A (cm^2)	r (cm)	L (cm)	L/r	KL/r (K=0.7)	P_{yn} (ton)	Pyp (A·F) (ton)
6	S	17.21	3.94	442.3	112.3	78.6	40.6	74.5
	N							
5	S	21.85	4.98	441.0	88.6	62.0	59.5	84.8
	N							
4	S	29.61	4.88	435.7	89.3	62.5	81.1	117.0
	N							
3	S	36.06	5.92	434.0	73.3	51.3	109.5	140.3
	N						113.8	147.8
2	S	36.06	5.92	432.9	73.1	51.2	109.6	140.3
	N						111.0	142.8
1	S	66.84	5.61	513.4	91.5	64.1	192.1	292.8
	N			512.4	91.3	63.9	191.3	290.1

TABLE 5   SHARE RATIO OF BRACES IN STORY SHEAR FORCES

STORY	ELASTIC	MODERATE	FINAL	ELASTIC ANALYSIS	DESIGN PROCESS	
					ELASTIC	ULTIMATE
6	0.59	0.59	0.59	0.67	0.74	0.76
5	0.67	0.67	0.67	0.72	0.78	0.49
4	0.71	0.71	0.71	0.73	0.78	0.51
3	0.75	0.75	0.75-0.51	0.76	0.82	0.56
2	0.72	0.72-0.67	0.72-0.26	0.72	0.78	0.48
1	0.83	0.83-0.65	0.83-0.64	0.81	0.85	0.58

FIG. 1 PLAN AND ELEVATION OF TEST STRUCTURE
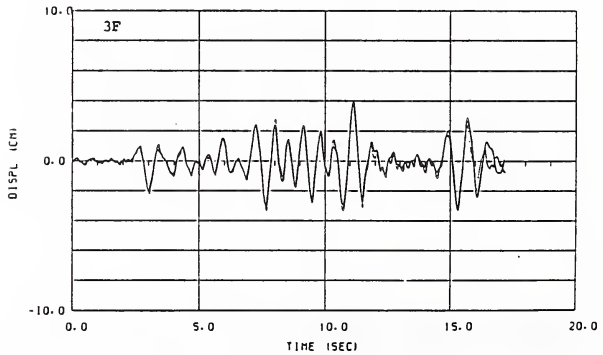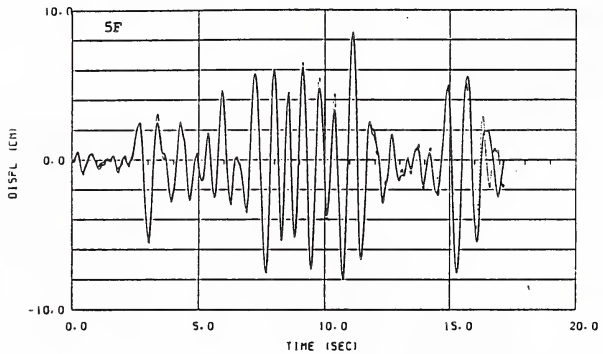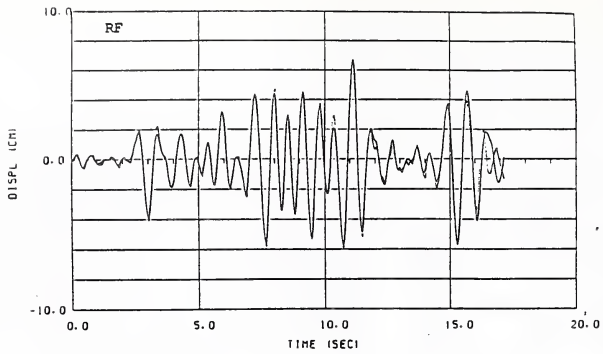
FIG. 2 FLOOR LEVEL DISPLACEMENTS (MODERATE)
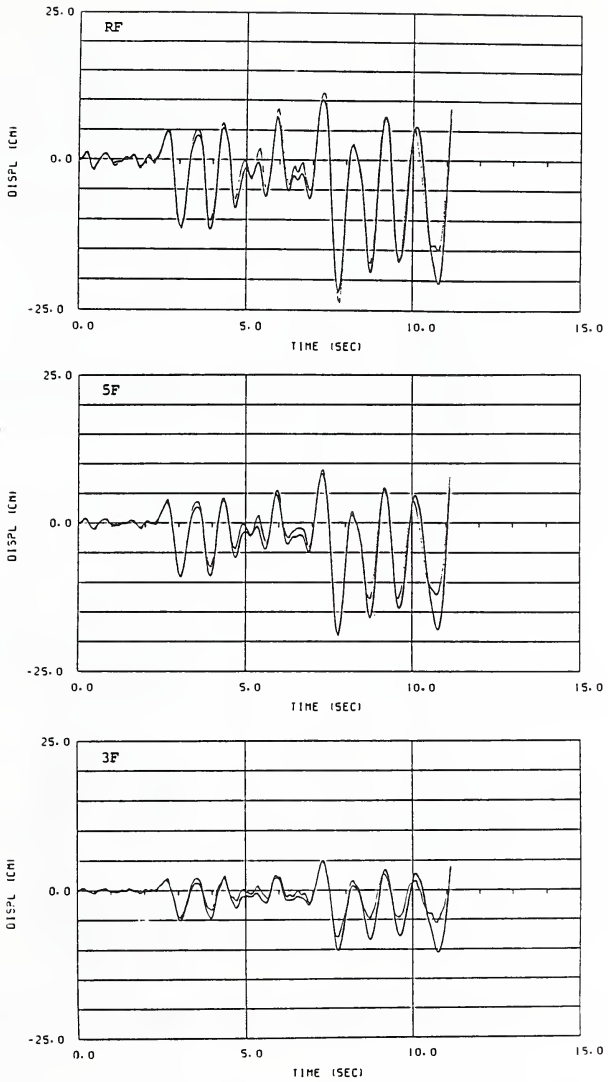
FIG. 3 FLOOR LEVEL DISPLACEMENTS (FINAL)

337
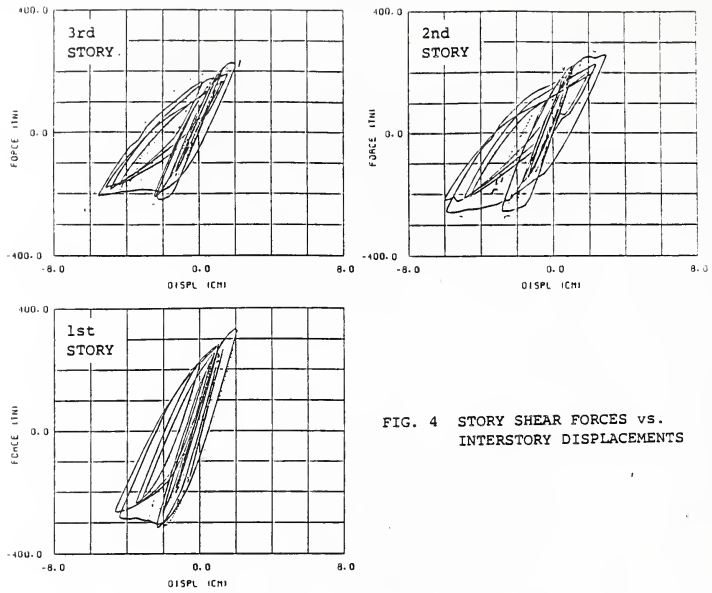
FIG. 4 STORY SHEAR FORCES vs.
        INTERSTORY DISPLACEMENTS
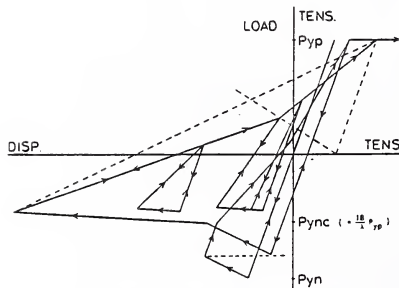
FIG. 5 HYSTERESIS MODEL OF BRACES
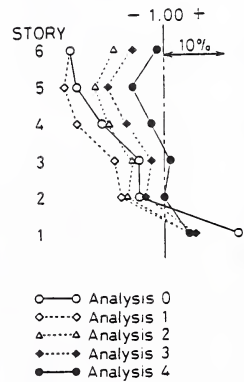
FIG. 6 DEVIATIONS OF ANALYTICAL
        STIFFNESS FROM THE TEST RESU
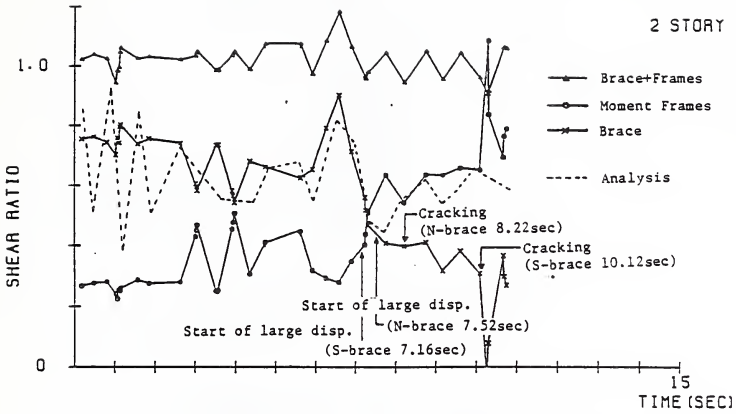
FIG. 7   RATIOS OF STORY SHEAR FORCES CARRIED BY BRACES AND BY MOMENT
FRAMES TO THOSE INDUCED BY ACTUATOR FORCES
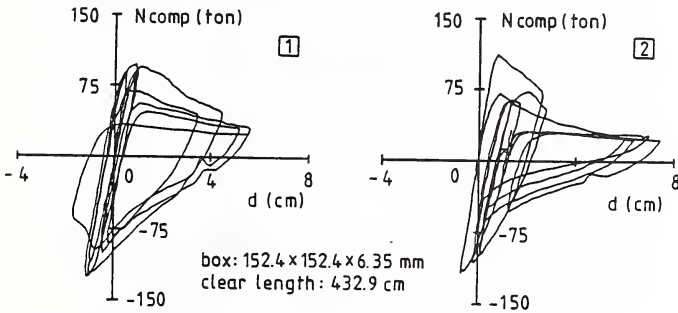
FIG. 8   AXIAL FORCE vs. AXIAL DISPLACEMENT
RELATIONSHIPS OF K-BRACES IN THE 2ND STORY
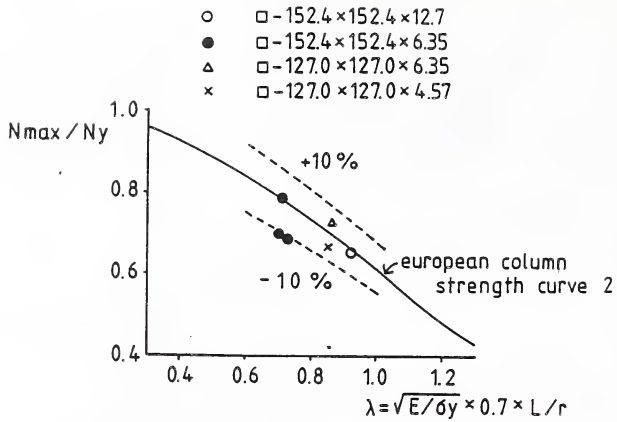
FIG. 9   BRACE BUCKLING STRENGTH
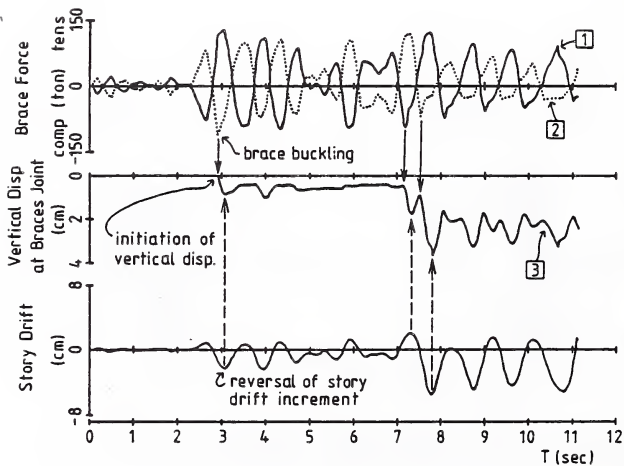
FIG. 10   TIME HISTORIES OF BRACE AXIAL FORCE, VERTICAL DISP.
AT BRACE JUNCTION AND STORY DISPLACEMENT
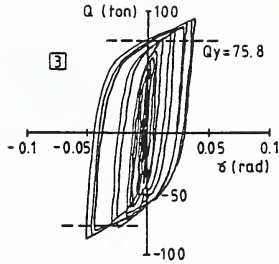
FIG. 11   SHEAR DEFORMATION OF THE GIRDER
PANEL-ZONE AT THE 3RD FLOOR
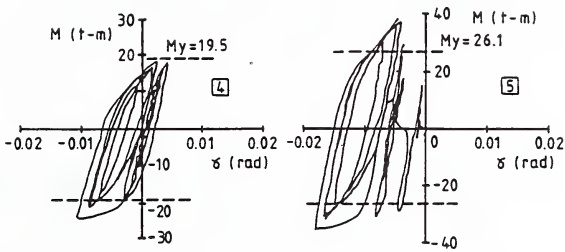
FIG. 12   SHEAR DEFORMATION vs. PANEL MOMENT RELATIONSHIPS
OF THE GIRDER-TO-COLUMN PANELS AT THE 4TH FLOOR
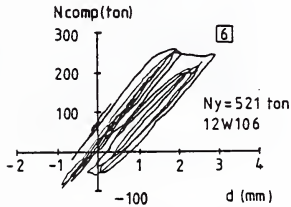
FIG. 13   AXIAL FORCE vs. AXIAL
DEFORMATION RELATIONSHIP
(2ND STORY B2-COLUMN)
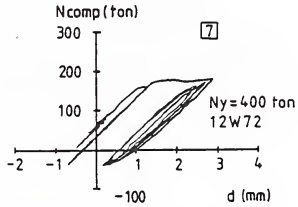
FIG. 14   AXIAL FORCE vs. AXIAL
DEFORMATION RELATIONSHIP
(3RD STORY B2-COLUMN)

341
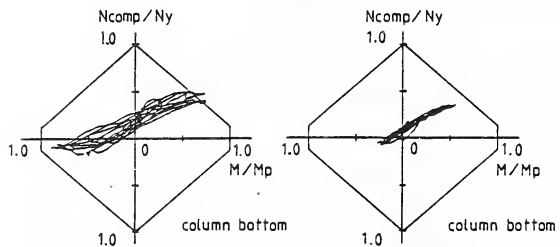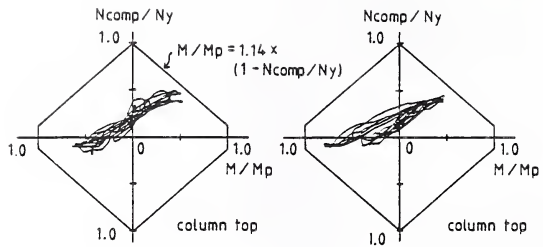
FIG. 15 M-N DIAGRAM
         (2ND STORY B2-COLUMN)

FIG. 16 M-N DIAGRAM
         (3RD STORY B2-COLUMN)
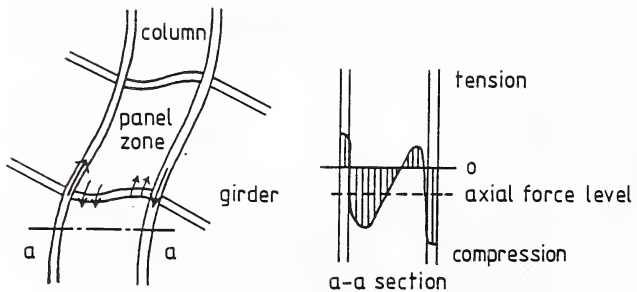
FIG. 17 DISTORTED STRESS DISTRIBUTION
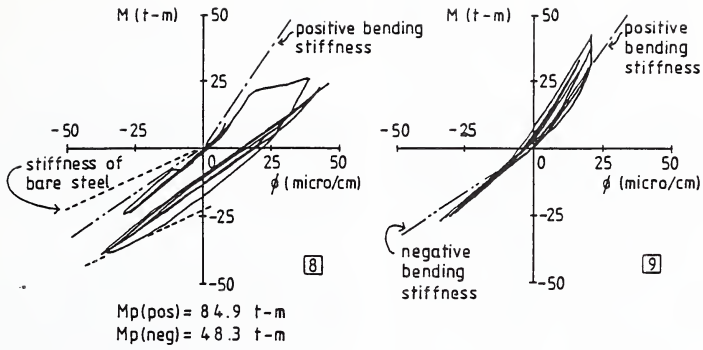
FIG. 18 MOMENT vs. CURVATURE RELATIONSHIPS OF THE 2ND STORY GIRDER
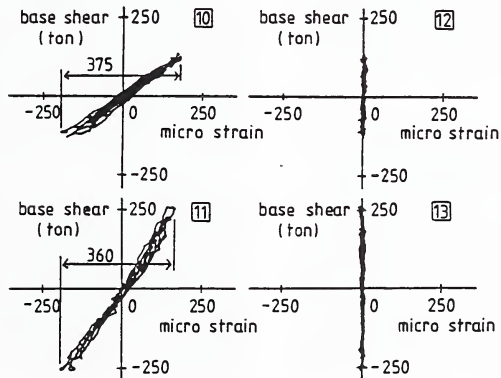
FIG. 19 STORY SHEAR FORCE vs. STRAINS IN THE TRANSVERSE BRACES RELATIONSHIPS

FULL-SCALE STUDIES OF STEEL STRUCTURES

by

Robert D. Hanson[1]

ABSTRACT

The US/Japan Cooperative Research Program in Earthquake Engineering Utilizing Large Scale Test Facilities was initiated in 1980 under the auspices of the UJNR Panel on Wind and Seismic Effects. The first phase of this program focused on a reinforced concrete test specimen, the second phase on a structural steel test specimen, and current program on masonry specimens. A summary of the USA activities and results in the Structural Steel phase of the program is given here. This information is extracted from the papers presented at the Sixth Joint Technical Coordinating Committee Meeting held in Maui, Hawaii from June 20 - 25, 1985 and does not include direct participation by Douglas Foutch, Subhash Goel and Charles Roeder in the full scale specimen tests in Japan. At this meeting nine major accomplishments of the program were identified and nine recommendations for future action were made. Because many of these actions require additional funding from the sponsoring government agencies and support of the UJNR Panel on Wind and Seismic Effects they are included herein in their entirety.

1. INTRODUCTION

Shortly after the US/Japan Cooperative Program was established with funding from the USA National Science Foundation, and the Government of Japan Ministry of Construction (Building Research Institute) and Science and Technology Agency (Disaster Prevention Research Institute), a Joint Technical Coordinating Committee (JTCC) was formed to provide and encourage cooperative technical interaction of all research investigators and to provide independent review of key technical decisions in research coordination. Professor Hajime Umemura and Professor Joseph Penzien have served as JTCC Chairmen and Professor Makoto Watabe and Professor Robert D. Hanson have served as JTCC Technical Coordinators for both the reinforced concrete and structural steel phases of the program. Other members of

the JTCC were principal investigators of the individual research tasks in Japan and the United States and prominent technical leaders. The independent members for the USA were Henry J. Degenkolb, Paul C. Jennings, Roy G. Johnston and Roland L. Sharpe.

The activities and milestones of the Cooperative Research Project are reflected in the papers and discussions held at the JTCC meetings. The First JTCC meeting was held in Tsukuba during January, 1981 prior to testing of the Full-Scale seven story reinforced concrete specimen. From this meeting the testing program for the specimen was agreed to be a single-degree pseudo-dynamic test program at four increasing levels of displacement response. The Second JTCC meeting was held in Tsukuba during July, 1981 to discuss the results of these four tests and to plan the repair and retests, nonstructural component additions, and preliminary designs for the steel test specimen. The Third JTCC meeting was held in Tsukuba during July 1982 to complete the design of the full-scale structural steel specimen, to review associated reinforced concrete and steel tests and analyses, and to develop a complete program of correlation studies for the reinforced concrete program.

The Fourth JTCC meeting was held in Tsukuba during June, 1983 to review the construction of the steel specimen, to establish the loading program for the full-scale specimen for multiple-degree pseudo-dynamic testing, and to review associated support tests and analyses of the reinforced concrete and steel studies. The Fifth JTCC meeting was held in Tsukuba during February, 1984 at the midpoint of the eccentric braced specimen test program. The earlier concentric braced specimen and eccentric braced specimen test results were presented, a program to complete the eccentric braced specimen tests was

---

[1] Dept. of Civil Engineering, Univ. of Michigan , Ann Arbor, MI 48109-2125

established, the nonstructural test program was reviewed, and associated supporting research activities were evaluated. The Sixth JTCC meeting was held in Maui, Hawaii during June, 1985 to review all support tests in the USA and Japan for the reinforced concrete and structural steel programs, to review the test results from the full-scale steel specimen including the nonstructural component phase, to discuss analytical studies, and to plan the activities necessary to complete these phases of the Program.

Because the preceding paper in this meeting provides data on the full-scale structural steel specimen tests, the following will provide only a brief summary of the USA associated support activities as reported to the JTCC at the Hawaii meeting. As a conclusion the 6JTCC Summary, Resolution, Recommendations and Accomplishments is quoted in its entirety.

2. EARTHQUAKE SIMULATION (SHAKING TABLE) OF 0.3 SCALE MODELS OF FULL-SCALE SPECIMEN

A dual structural system, consisting of a moment-resisting space frame and braced frame, was selected for the Test Structure of this phase of the program. Two different types of braced frames were studied: the first was based on the use of a concentric K bracing system; and the second used eccentric braces. The studies that were conducted at the University of California, Berkeley under the direction of Vitelmo Bertero can be grouped as follows: (1) Preliminary analytical studies conducted to review the soundness of the preliminary design of the building and to produce the analytical information required to determine the largest scale model for the two test structures that could be tested on the shaking table at Berkeley; (2) The final selection of the largest scale model (selected to be 0.305) and its design, the selection of the steel and of the concrete to be used and the problems encountered in the fabrication of the different components

of the model, and in their final assemblage and in their instrumentation; (3) The experimental and analytical studies conducted regarding the simulation and behavior of the composite construction used for the floor system of the two test structures; (4) Determination of the mechanical characteristics of the 0.3 models during the different stages of its construction; (5) Experiments conducted on the 0.3 scale models at the Berkeley earthquake simulator facility; (6) Comparison of experimental results with those obtained for the full-scale model tests conducted at Tsukuba, Japan, and those predicted analytically; and (7) Analysis of the implications of the results obtained on the states of the art and of the practice of seismic resistant design and construction of steel building structural systems based on use of braced and unbraced moment resistant frames. Conclusions and correlations of the 0.305-scale dynamic test results with the full-scale pseudo dynamic tests remain to be done.

3. CYCLIC TESTS OF FULL-SCALE COMPOSITE BEAM-COLUMN JOINTS

Cyclic tests of full-scale beam-column assemblages with composite metal deck and concrete slab was performed at Lehigh University under the direction of Professor Le-Wu Lu. Both interior and exterior joints with beams framing into the strong and weak directions of the columns were tested. These subassemblage test results will be compared and correlated with similar joints from the full-scale specimen tests in Tsukuba.

4. CYCLIC BEHAVIOR OF COMPOSITE FLOOR SYSTEMS IN ECCENTRICALLY BRACED FRAMES

Eccentrically braced steel frames can provide high elastic stiffness and large inelastic energy dissipation capacity. This makes this type of structural system a viable alternative for seismic design. Performance of these type of systems depends to a great extent on the behavior of the link sections in the

beams. The behavior of bare steel links has been extensively investigated in the past, however, the effects of the composite floor system in eccentrically braced frames has not been addressed.

An experimental investigation on bare steel floor beams and composite floor beams in eccentrically braced frames were made at the University of California, Berkeley under the direction of Professor Egor Popov. Behavior of both types of floor beams were subjected to cyclic loading with emphasis on the performance of the link. The performance of a composite floor beam's response to a simulation of the Taft earthquake was also made. The test results for the bare steel and composite floor beams were evaluated by comparing the elastic stiffness, strength, and ductility of the links, in addition to the restraint of the link by the slab. The effective width of the composite floor beams under cyclic loading was determined by measuring strain profiles.

The main conclusions were: (1) Composite short links designed as bare steel short links yield in shear and dissipate energy primarily through web yielding; (2) Composite short links have a greater yield and maximum strength compared to bare steel links under cyclic loading; (3) The composite floor system in eccentric braced frames increases the elastic stiffness of short links, in addition to effecting the rotational stiffness of the floor beams which frame into the ends of the link; (4) The composite floor system is not effective in providing restraint at the ends of the link to prevent lateral torsional buckling of the steel section. Transverse beams should be used to brace both ends of the link; (5) The shear lag effect is present in the composite floor system under cyclic loading. The longitudinal strain in the slab has a wider profile for positive moment compared to negative moment. The width of the profiles increases in slab sections through the link, whereas outside the link the profiles remain a constant width as the amplitude of link

distortion is increased; (6) The amount of link deformation to cause web buckling is independent of the link's deformation history, hence it is not a function of the amount of energy dissipated by the link. Web buckling occurs when the link deformation exceeds a specific accumulated value of deformation beyond the last zero shear crossing within the cycle of buckling. The specific value is related to section dimensions and stiffener spacing; (7) The web stiffeners should be designed in order to satisfy both the strength and rigidity criteria in order to avoid unfavorable post buckling performance of the link; and (8) The maximum forces developed in the jacks testing composite short links were greater compared to jacks forces developed in bare steel short link specimens. The forces in composite link specimens were, on the average, greater in V-brace EBF simulations compared to K-brace EBF simulations. To assure that braces remain elastic and do not buckle, the brace forces from a bare steel EBF collapse mechanism should be increased by a factor of 1.6 to 1.8 when designing the braces.

5. SMALL-SCALE MODEL TESTS OF STRUCTURAL STEEL ASSEMBLIES

In the steel phase of the project, tests were conducted on 1:12.5 scale specimens of beam-column assemblies, a braced frame, and an unbraced frame at Stanford University under the supervision of Professor Helmut Krawinkler. All of the small-scale specimens included floor slabs which consisted of concrete reinforced with wire mesh and were cast onto metal deck. Shear studs welded to the beams were used to make these slabs work compositely with the beams. The beam-column assemblies represent portions of the frame on the center column line and of the exterior frames. The braced frame specimen represents a model of the center unit of the concentrically braced prototype test structure including the floor slabs. The unbraced frame specimen is the braced frame specimen with the braces

removed. This specimen was tested to give information about the resistance of the moment frame in the braced frame specimen.

The major goal of this study was to assess the feasibility and limitations of small-scale model testing in earthquake engineering by testing models of steel structural assemblies and correlating the results with prototype tests. This correlation was made possible by the U.S.-Japan Cooperative Research Program in Earthquake Engineering in which full-scale prototype structures and components were tested. All small-scale models tested in this study were constructed at a scale of 1:12.5.

The three beam-column assemblies were replicas of full-size assemblies tested at Lehigh University. The prototype test of an exterior assembly with a column flange connection resulted in severe inelastic column panel zone deformation and ultimately fracture of the beam bottom flange next to the joint. This behavior was reproduced in the model tests. In the prototype test of an exterior assembly with a column web connection little inelastic shear deformation occurred in the joint region and the specimen deformed by inelastic flexure of the beam and column. Failure was by fracture of the lower beam flange. This was also reproduced in the model test.

The prototype test on an interior assembly with column flange connections resulted in severe inelastic shear distortion of the panel zone and ultimately fracture of the bottom beam flanges caused by high localized curvatures at the corners of the severely distorted joint. In the model test the inelastic deformations in the panel zone were reproduced, but the column web panel tore before the beam bottom flanges had flexed sufficiently to fracture.

The correlation between the results of the model braced frame test and the

prototype test was limited by the compromises which had to be made in loading and also by the absence of the two exterior moment frames in the model specimen. Despite these compromises the damage pattern in the prototype structure, represented by brace buckling, beam hinging, joint distortions, and ultimately fracture of the tubular braces, was reproduced in the model test. The model test predicted larger peak loads than the prototype test. This discrepancy is mostly due to the excessive strength of the model bracing members.

Based on the results of this study, the following major conclusions on small-scale modeling and structural behavior were drawn: (1) The experiments indicate that the overall cyclic inelastic load-deformation response of components and structures can be reproduced adequately in tests of carefully designed and detailed small-scale models; (2) The steel beam-column tests have shown that inelastic panel zone distortion and beam flexure can be properly simulated at small scales. In addition, the action of the composite floor slab can be simulated as shown by the load -deflection and moment-strain diagrams; (3) The braced frame test has demonstrated that the post-buckling response of complex bracing systems can be reproduced in model tests. However, this test has also shown that the buckling strength of braces is sensitive to material properties and connection details, which are parameters that are difficult to simulate accurately at small model scales; (4) Size effects in small-scale model tests will usually result in high predictions of strength (because of strain gradient effects) and ductility (because of improved fracture properties) under cyclic inelastic loading. In particular the improved fracture properties, together with fabrication problems, render model test results questionable for an evaluation of localized failure modes in structural connections; (5) and The small-scale model tests led to the same major

conclusions on structural behavior as the prototype tests. Amongst these conclusions the following deserve emphasis: (5a) Panel zone shear strength may limit the capacity of steel beam-column joints. Inelastic shear deformations of the panel zone are usually very ductile, absorbing considerable energy before failure occurs. Excessive shear distortions in joint panel zones may cause fracture of the beam flange welds due to the high curvatures at the joint corners; (5b) Composite floor slabs increase the strength of beams and joints in steel frames. At beam-column joints this increase in strength is limited by the bearing capacity of the concrete that transfers the slab stresses to the column. Under severe deformations the composite floor action is seen to deteriorate as the concrete surrounding the column is crushed; (5c) The strength of "K" braces in a braced frame deteriorates rapidly after first buckling. This will cause the formation of a "soft" story which may then be subjected to excessive drifts; (5d) Tubular braces are susceptible to severe local buckling after brace buckling. Under load reversals this local buckling may lead to crack initiation and fracture of braces.

6. PSEUDO-DYNAMIC TESTING: CONTROL ISSUES AND PERFORMANCE EVALUATION

The pseudo dynamic test method provides a means for testing of full scale structures subjected to simulated seismic ground motions. The method uses an on-line computer to calculate the appropriate displacement response of the structure, based on an analytical model of the inertia forces and the reaction forces due to the seismic ground acceleration and on direct measurements of the inelastic restoring forces. The structure is quasi-statically caused to deform according to the computed displacment response by use of electrohydraulic actuators. Experimental and theoretical research at The University of California, Berkeley under the direction of Stephen Mahin and at

The University of Michigan under the direction of Professor Robert D. Hanson have been cooperatively exchanged with colleaques at The University of Tokyo and The Building Research Institute (Tsukuba).

The pseudo-dynamic test method has been demonstrated to be a powerful and versatile procedure for assessing the seismic performance. In particular, it may provide insight on the seismic response of structures, that are too large, massive or strong for testing using available shaking tables. In addition, extension of the basic procedures will permit tests considering complex support excitations not possible with other means.

However, like all experimental procedures, the pseudo-dynamic method has inherent limitations and errors. These must be fully recognized in developing pseudo-dynamic test programs. In particular, the need for high performance control equipment and instrumentation must be taken into account.

A variety of future developments and investigations should be undertaken to make the pseudo-dynamic method more convenient and reliable. For example, the various implementation software algorithms developed in the U.S. and in Japan should be refined and integrated into a convenient package available to those interested in pseudo-dynamic testing. Various routines for self diagnosing of experimental errors, analytical substructuring, computer graphics, data analysis and etc. should be included. Guidelines for the use of such algorithm should be established. Additional research is needed related to numerical methods. This is especially true for methods associated with controlling the adverse effects of experimental errors and with substructuring methodologies. Experimental verification of these methods is essential.

One of the most important aspects to be

researched relates to understanding and improving the ability to control test specimens. At present, there are very few reliable guidelines available for selecting appropriate experimental equipment, or for establishing the various controller parameter settings, needed to assure test stability and accuracy. New controller designs to insure stability and to mitigate cross coupling effects in stiff systems should be investigated. In particular, digital controllers capable of combining the inner and outer control loops and implementing hybrid analysis capabilities in "real time" should be assessed. Not until reliable guidelines for the use of pseudo-dynamic test equipment are established can the method be used dependably.

For most structures tested by the pseudo-dynamic method, the response is dominated by the fundamental mode. However, spurious higher-mode responses can be excited by experimental errors. While high performance experimental equipment can be used to reduce these errors, their effects can be severely amplified if relatively large higher-mode frequencies are present in the test specimen. Under such condition, viscous or numerical damping is desired for eliminating the spurious higher-mode responses.

It is desired that the viscous damping ratios selected for the higher modes be much larger than that for the fundamental mode. Furthermore, since the nonlinear stiffness properties of that specimen are not accurately known, initial stiffness-dependent viscous damping has to be selected. Based on this approach, the damping characteristics may change as nonlinear deformation occur. However, it is imperative that these characteristics are not undesirably altered. To evaluate the variation of effective modal dampings in a nonlinear system, the complex eigen-value and approximate modal analysis techniques have been used to uncouple the equations of motion. The results of these studies show that

the higher-mode dampings do affect the response of the fundamental mode during nonlinear oscillations. In fact, for a softening-type non-linear system, the effective damping on the fundamental mode can be greatly increased by selecting large higher-mode dampings.

In view of the above problem, a modified Newmark's integration algorithm with frequency-proportional numerical damping has been proposed. It has been shown that the accuracy of this algorithm is comparable to that of the explicit Newmark's method. For softening-type nonlinear systems, a criterion has also been developed to ensure that numerical energy dissipation always remains positive. This preserves numerical stability as the fundamental frequency of a specimen is reduced by nonlinear deformations. Furthermore, based on the energy criterion developed, the numerical damping on the fundamental mode can be kept zero or arbitrarily small during nonlinear oscillations. This method, thus, seems to be more attractive than the initial stiffness-dependent viscous damping.

7. ANALYTICAL MODELS FOR FULL-SCALE SPECIMEN

A six-story, two bay, full-scale steel structure with eccentric bracing was tested by pseudo- dynamic method at the Building Research Institute, Tsukuba, Japan, during January-March, 1984. The two exterior frames are unbraced moment-resisting frames with one column in each oriented for weak-axis bending, and the interior frame is braced with eccentric K-bracing in the north bay. The floor system consists of formed metal decking and cast-in-place lightweight concrete which acts compositely with the girders and floor beams.

The main pseudo-dynamic testing of the structure consisted of three parts. S21^{o}W component of the 1952 Taft earthquake was used in the elastic and inelastic tests with peak acceleration of 65 and 500 gals, respectively, (1 gal

= 1 cm/sec^2). The final large amplitude test was performed as steady state responses to three sinusoidal ground acceleration pulses of one cycle each.

Based on the analytical study of the elastic and inelastic response of the Phase 2 structure at The University of Michigan under the direction of Professor Subhash Goel, the following conclusions can be drawn: (1) The refined analytical model seems to represent the global behavior of the structure quite accurately. The agreement between the analytical results and those from the elastic and inelastic tests was excellent; (2) The elastic response seems to be very sensitive to the fundamental period; and (3) The assumed characteristics of the hysteresis behavior of shear links had significant influence on the inelastic response. More information is needed on the behavior of these elements.

8. SYSTEM EVALUATION OF ELASTIC PSEUDO-DYNAMIC FULL-SCALE TEST DATA

The low-amplitude pseudo-dynamic test data from a six-story, two bay full-scale steel structure with eccentric bracing was analyzed using a system identification technique at the California Institute of Technology under the direction of Professor James L. Beck. Properties of the first three modes of the structure were identified and the calculated response due to these modes when subjected to the earthquake ground accelerations used in the test was found to be in excellent agreement with the displacements and pseudo-velocities from the test. However, the pseudo-accelerations from the test did not agree well with those calculated from the identified three-mode model because the third mode gave unreasonable large accelerations in the test. This is attributed to an instability in the experimental method that is produced by the cumulative effects of feedback of errors in the computer control system. The identified natural periods of the first three modes of the structure were 0.553, 0.191 and

0.102 second.

The following conclusions were made from this study: (1) The feedback of control and measurement errors into the computer model used to produce the experimental displacements in the elastic test produced a cumulative error of large amplitude in the pseudo-acceleration at frequencies around 10 Hz. However, these errors have an insignificant effect on the displacements and pseudo-velocities, where the high-frequency content was greatly reduced; (2) For similar amplitudes to those in the elastic test (peak acceleration and displacement of 30%g and 1.4 cm respectively at the roof), a linear model based on two classical normal modes should give an excellent approximation to the response of the structure; and (3) At these amplitude levels, the equivalent viscous damping factors for the first three modes are 1.2%, 2.1% and 2.2% of critical. The damping of the fundamental mode is consistent with the value of 1.23% reported for a pseudo-dynamic free vibration test performed after the elastic test. Part of the damping was artificially introduced as numerical viscous damping in the computer model used to produce the experimental displacements. Also, the displacement overshoots programmed into the computer control system apparently contributed some damping. The energy dissipated by the structure itself produced equivalent viscous damping factors less than 0.8%, 1.7% and 0.2% for the first three modes. These low values of damping compared with values of 3% to 8% from the earthquake response of tall buildings in the field is most likely due to the absence of energy dissipation by nonstructural components and the smaller amount of radiation damping produced by the relatively stiff foundation for the test structure.

9. SUMMARY, RESOLUTION, RECOMMENDATIONS AND ACCOMPLISHMENTS - 6JTCC

9.1 Summary

The Sixth Joint Technical Coordinating Committee Meeting for U.S.   -Japan Cooperative Research Program Utilizing Large-Scale Testing Facilities was held at Kaanapali, Maui, Hawaii, U.S.A., from June 20th through June 25th 1985. Thirteen U.S. and five Japanese JTCC members plus twelve observers participated in the meeting.

On the first day of the meeting (June 20th), after the opening session, (1) support tests in both countries and full-scale tests for RC phase were all reported, and then (2) future tasks for RC phase were discussed. On the second day, (1) steel phase on full-scale tests of concentric K brace system:, (2) of eccentric K brace, as well as (3) of moment frame system, and then (4) U.S. steel support test results were reported and discussed. On the third day, (1) the latter half of U.S. steel support test results and (2) behaviors and analytical results on non-structural elements of steel full-scale tests were reported and discussed. On the fifth day (June 24th Monday), Japanese steel support test results, as well as (2) analytical studies on steel full-scale tests were reported and discussed. Brief introduction of recent aspects on masonry phase was reported.

Following the discussion on future tasks of steel phase, accomplishments of the program were identified and potential future tasks of U.S.-Japan earthquake engineering cooperative research program were discussed. On the final day, at concluding session, the statement of accomplishments was agreed and the following resolution and recommendations were adopted.

9.2 Resolution

Members of the JTCC recognize this meeting to be the tenth anniversary of the Review Meeting of the U.S.-Japan

Cooperative Research in Earthquake Engineering with emphasis on the Safety of School Buildings, also held in the State of Hawaii in 1975, at which meeting the recommendation for the current U.S.-Japan Cooperative Program in Earthquake Engineering Utilizing Large-Scale Testing Facilities was compiled and signed, marking the very beginning of the project. They agree that the meeting was successful and fruitful for both countries in a cordial atmosphere at Kaanapali, Maui, and they are pleased to acknowledge the fine arrangements for the meeting and the great effort and excellent performance of all principal investigators, and in particular, the continuing encouragement and guidance by Professor J. Penzien and H. Umemura.

9.3 Recommendations

(1) The experimental and analytical accomplishments of the program have important consequences to the practice of earthquake resistant design and earthquake engineering research. Reports of individual research efforts and correlation studies should be completed at the earliest possible time. The implications of these studies should be prepared for the design and research professionals as soon as possible.

(2) The reports, papers, photographs and data developed in this program should be fully documented and made available according to the schedule given in Attachment 1.

(3) The Structural Steel program must be completed at the earliest possible time by performing the necessary correlation studies amongst the various experiments and with appropriate analytical studies. These results should be reported as recommended in (1) and (2) above.

(4) Exchange of research investigators should be implemented to hasten data

interpretation and correlation study completion. These individuals who were active participants in the experimental research program will provide the most effective exchange.

(5) The results of the experimental and analytical studies in this program have provided significant benefits as outlined in the ACCOMPLISHMENTS. The results and specimens of the current program can be effectively and economically utilized to investigate additional variations of framing suggested from analytical parameter studies. This is a cost effective extension of the existing program.

(6) The possibility of new phase for a cooperative program should consider systems such as (a) mixed structures and (b) inventive bracing systems. A planning group for the new phase should be organized.

(7) For quicker and smoother information exchange to achieve well-coordinated reports and papers, frequent national JTCC meetings should be held in each country.

(8) A seventh JTCC meeting is necessary for correlation of the various aspects of the U.S. and Japanese support programs and to discuss the significance of preliminary conclusions. The meeting should be held in California during the last quarter of 1986.

(9) To carry out the above recommenda- tions, the sponsoring government agencies in both countries are urged to provide the necessary funds on a timely basis.

9.4 Accomplishments of the U.S.-Japan Cooperative Research Program Utilizing Large-Scale Testing Facilities

This unique research program combines full-scale, small-scale, subassembleage

and component test with analytical investigations of specific building structures. These experiments were carried out using static, static cyclic, on-line computer and dynamic shaking table tests at unique facilities in the United States and Japan by the best researcher available in the two countries. The coordinated research activities, scientific and personnel exchanges have produced results which could not have been achieved by individual efforts in the U.S. of in Japan.

The participants at the 6th JTCC have identified some of the major accomplishments achieved at this time and provide the following list arranged by scientific and technical accomplishments. This list is not meant to b exhaustive and it does not contain those anticipated from the final stages of the structural steel phase of the program.

(1) Significant Contribution to the Understanding of the Real Behavior of Buildings During Earthquake

These test structures closely resembled real dual framed buildings. The contributions and inter- action of these dual systems are more fully appreciated and may lead to better building with less cost. The incorporation of interior and exterior walls, glazing and cladding added stiffness to the structure, thereby changing the dynamic characteristics of the building. The static tests of these elements provide insight to the large deformation characteristics.

(2) Demonstration of the Need for Integrated Analytical and Experimental Studies of Structural Behavior

In the elastic range it is dangerous to rely on prediction of response on a deterministic basis because of the sensitivity of the response to building period and the sensitivity of the building period on mathematical models

of the structure which may not include
adequate three dimensional effects,
shrinkage, loss of composite action, and
axial load effects of dead and live
loads. In the inelastic range initial
damage will predicate the subsequent
response and damage. Our current models
are not sufficiently developed for
independent reliance on analytical
studies for systems not experimentally
verified.

(3) <u>On-Line Computer (Pseudo-Dynamic)
Test Control Method Established</u>

The traditional static cyclic test
methods are predetermined before the
test begins. They are not capable of
reflecting the changes in force and
displacement distributions caused by
inelastic action or damage to portion of
the structure. Realistic loading
patterns are essential to accurately
represent earthquake loading and to
follow the resulting inelastic response.

(4) <u>Confirmation of the Validity and
Reliability of Scale-Models for
Studies of Overall Structural
Response</u>

This cooperative program with full size
and various scale models have confirmed
the validity and reliability for overall
structural response, and this has
important economic consequences for
future structural testing.

(5) <u>Confirmation of the Validity and
Reliability of Large-Scale Component
Tests for Studies of Local
Structural Behavior</u>

The program has shown that large-scale
component tests are necessary to define
local detail behavior. In designing
these tests it is important that
rational load programs should be
established for that portion of the
structure.

(6) <u>Three-Dimensional Effects of
Monolithic Structures Can Not Be
Neglected</u>

Actual behavior of buildings requires
analytical and experimental modeling to
realistically represent the three
dimensional characteristics even for ·
planar loading. The necessity for this
modeling for multi-directional
earthquake considerations is
selfevident.

(7) <u>Advances in Structural Testing
Technology and Efficient Utilization
of Experimental Facilities and
Research Funds</u>

The coordinated testing program,
involving full-scale and reduced-scale
structural components, assemblies and
complete frames and utilizing
quasistatic, pseudo-dynamic and truly
dynamic (earthquake simulators) testing
techniques has demonstrated the
advantages and disadvantages of
different experimental approaches. In
addition, the problem has resulted in
significant advancements in the
technologies of testing large-scale
multi-story structures. These
advancements will make possible more
efficient and cost-effective
utilizations of existing and planned
experimental facilities in the future.

(8) <u>Synergistic Effect of Coordinated
Multi-Institutional Cooperative
Research Programs</u>

The benefits of active coordinated
interchange between key research
personnel during the execution of a
research program directed at a common   ·
goal has been demonstrated. The
utilization of the unique research
facilities at specific institutions can
be effectively utilized in this manner.
This provides an economical utilization
of personnel and facilities.

(9) <u>The U.S.-Japan Cooperative Research
Program Has Developed an Open, Full
Exchange of Scientific Research
Ideas, Concepts and in Earthquake
Engineering</u>

This program has developed a mutual
respect and trust among the U.S. and
Japanese researchers. This relationship
allows the open, full exchange of
technical information beyond the
immediate scope of the research program.
This relationship should be maintained
to the mutual benefit of both countries.

Mexico City and Chilian Earthquakes

EARTHQUAKE DAMAGE IN MEXICO CAUSED BY THE
SEPTEMBER 1985 EARTHQUAKES

BY

Edgar V. Leyendecker
William C. Stone
Felix Y. Yokel[1]

ABSTRACT

Following the September 19, 1985 Mexico City earthquake, a team consisting of four engineers and one seismologist from the National Bureau of Standards (NBS) and the United States Geological Survey (USGS) was dispatched to Mexico City to provide technical advice to the US rescue effort and to asses structural damage. This report is primarily based on data gathered by the team, but it also contains a compilation of other available information. The report addresses the origin and characteristics of the observed ground motion, the ability of buildings designed in accordance with present and proposed seismic design provisions to resist this type of ground motion, and observed data on structural and foundation failures.

1. INTRODUCTION

On September 19, 1985, an earthquake of magnitude 8.1 struck the western coast of Mexico near the town of Lazaro Cardenas in the State of Michoacan (See figure 1). A team of engineers and seismologists from the National Bureau of Standards and the United States Geological Survey was sent to Mexico following the earthquake to provide technical assistance and to study its effects.

Despite a distance of more than 400 kilometers from the epicenter, the earthquake caused widespread damage in central Mexico and was felt as far north as Houston, Texas. The city was shaken on Friday, September 20 by a magnitude 7.5 aftershock with an epicenter 100 kilometers southeast of the main earthquake.

2. BACKGROUND

The earthquakes which struck Mexico City on September 19 and 20 originated in a narrow seismic zone that runs 2500 kilometers along the western coast of Central America from Panama to central Mexico west of Puerto Vallarta. A zone (figure 2) of intense seismicity has been formed where the Cocos plate dips beneath the North American plate, giving rise to earthquakes along the coast and volcanoes inland in central Mexico. Mexico City lies in a broad basin formed approximately 30 million years ago by faulting of an uplifted plateau. Subsequent volcanic activity closed this basin resulting in the formation of historic Lake Texcoco upon which the Aztec capital was built.

The expansion of Mexico City by the Spaniards led to the gradual draining of Lake Texcoco. With a population of about 18 million, Mexico City is the world's largest population center and the site of more than one million man-made structures. The photograph in figure 3 was taken a few days after the earthquake and shows little evidence of widespread damage. In fact about 330 buildings were severely damaged or collapsed as shown in figure 4. Buildings in the 6 to 15 story range were particularly hard hit. Some of the reasons for the damages are discussed in this paper.

Today, much of the city rests on lake deposits (figure 5) made up of highly plastic clays and sands with thicknesses of more than 50 meters. These lake deposits have long been identified as a factor making Mexico City particularly vulnerable to earthquakes. When unconsolidated material underlies a site, the seismic shaking is modified from what it would have been on competent rock. The general trend in the lake bed region of Mexico City is for

---

[1] National Bureau of Standards, Gaithersburg, Maryland 20899

unconsolidated sediments to increase the amplitude of ground shaking at higher periods leading to what is generally termed soil amplification. In the center of the historic district, where many buildings between five and 20 stories high did match the natural period of the quake, devastation was widespread. Dots shown in figure 6 mark the locations of damaged or destroyed buildings. Practically all of the most seriously affected area was confined within a five by five kilometer area just east of the U.S. Embassy.

3.   STRUCTURAL PERFORMANCE

The twelve story reinforced concrete structure shown in figure 7 housed the Ministry of Communications and transport, and the nation's main microwave transmitter. Failure of this structure precipitated a near total collapse of long-distance telecommunications between Mexico City and the rest of the world, a factor which complicated the coordination of international rescue efforts.

The SCT accelerograph station (figure 8), located on the grounds of the telecommunications center, provides a good indication of response in the historic district, where most of the structural damage occurred. At the communications center the predominant acceleration component was east-west with a period of approximately two seconds. Vertical accelerations were negligible.

The East/West ground motion records (figure 9) indicated peak free field accelerations of 0.17g with peak to peak ground displacements of 42 cm. because of the long duraton of the Earthquake structures with a natural period close to the predominant two second period of the earthquake had ample opportunity to be driven to resonance.

The reason why so many apparently well-designed structures collapsed in the central portion of Mexico City is best explained by the design response spectrum from the communications center site (figure 10). Structures with natural periods in the vicinity of two seconds, which is about 5 to 20 stories, were subjected to lateral accelerations of up to one G, nearly six times the highest lateral acceleration previously recorded. This large amplitude, combined with the

exceptionally large number of stress reversals, contributed to the majority of the collapses. The solid horizontal line in figure 10 shows the current Mexico city building code design spectra for non-ductile frames, which was based on previous earthquake records for the valley of Mexico. Thus, even buildings designed entirely in accordance with the code were severely under strength for this quake.

Hospitals are one of the most critical facilities in any disaster. However, major portions of three of the city's largest hospitals collapsed. Some 1200 people were buried as six buildings collapsed at the Centro Medico and Mexico General Hospital (figure 11), one of the largest medical complexes in Latin America.

Yet another 400 medical personnel and patients were trapped in the Maternity wing of the Juarez Hospital, eight blocks south of the Presidential Palace. Like the General Hospital, this nine story reinforced concrete frame structure collapsed towards the east, exhibiting localized failures at the beam-to-beam joints of each floor. The Juarez Hospital received considerable media attention as rescue personnel continued to retrieve survivors as late as ten days after the earthquake by tunneling through the debris between the floor slabs. Heavier rigging equipment and more rapid slab cutting techniques -- such as an oxygen lance -- may have substantially reduced the time required to remove the debris and reach possible survivors.

Taller concrete buildings, such as apartments over 5 stories, were particular victims of earthquake damage. The 14 story Nuevo Leon Complex consisted of three independent wings separated by construction joints. The two northern-most wings, each containing 196 apartments, apparently collapsed from overturning due to column failure on the east side of the building.

Heavy damage was also sustained in the Juarez apartments (figure 12), just west of the Medical Center. Two eight story, and one thirteen story reinforced concrete flat slab structures collapsed in this area.

The southern half of the thirteen story complex, separated by a non-structural joint, remained standing but required demolition.

Perhaps the most impressive failure was that of the two southern towers in the Consumo Pino Suarez, a government office complex just west of the Juarez Hospital. These 14 and 21 story buildings utilized an exterior welded box column frame and an integral composite slab system. These were among the few steel structures to collapse as a result of the earthquake. Despite heavy truss floor beams very little ductility appears to have been developed due to buckling of the truss braces under reversed loading. However, the collapse appears to have been initiated by column buckling in the 21 story tower, as evidenced by substantial listing to the south of the one of the remaining identical structures.

4. POUNDING PROBLEMS

Another common cause of building damage was drift interaction between adjacent structures (figure 13). Here two buildings of similar height were built too closely together. Their natural period was close to the period of the earthquake allowing the structures to undergo lateral displacements sufficient to allow them to "hammer" each other. The structure on the left, in this case, lost the battle for survival. This phenomena was more pronounced when buildings of unequal height were involved.

Despite the many collapses there were also many success stories. Well designed masonry infill frame structures, in general, safely dissipated earthquake energy in the shear walls, as evidenced by well developed x-cracking in the masonry. Steel frame structures, such as the 43 story Latin American tower, recorded little damage principally because their natural periods of vibration were significantly longer than the charcteristic ground motion period for the sites on which they were constructed. Would these towers, have performed equally well in the unconsolidated soil near the airport where the natural period of the quake was much longer and the duration sufficient to drive any structure with a period near 4 seconds to fatal resonance?

Many tall concrete structures whose design met the requirements of the building code did perform well. Given the magnitude and duration of the quake the performance of the city as a whole -- with its one million structures -- can only be considered impressive.

5. SUMMARY

In summary, the primary causes of structural failures were unusually high accelerations combined with an exceptionally long duration of shaking. The high accelerations were caused by amplification due to local soil conditions. The coincidence of the period of ground shaking with the natural period of a large number of buildings, and foundation failures due to a loss of soil shear capacity led to the catastrophic damages.

6. ACKNOWLEDGEMENT

Figure 1.   Location map showing epicenters of main 8.1 earthquake and 7.5 aftershock.
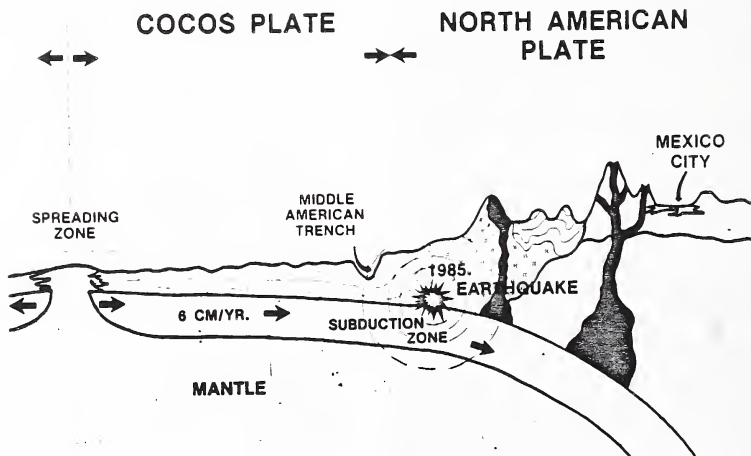
Figure 2.   Geoligic profile showing interactin between the Cocos and North American plates.

Figure 3. Aerial view of Mexico City looking south.

Type of Construction	Condition	Year of Construction			Number of Stories				Total
		<1957	1957-1976	>1976	<5	6-10	11-15	>15	
Reinforced Concrete fram	Collapse	27	51	4	27	46	8	1	82
	Serious	16	23	6	10	28	6	1	45
Steel frame	Collapse	7	3	0	4	3	1	2	10
	Serious	1	1	0	0	0	2	0	2
Flat slab/ waffle slab	Collapse	8	62	21	36	49	5	1	91
	Serious	4	22	18	5	26	12	1	44
Masonry	Collapse	6	5	2	11	2	0	0	13
	Serious	9	13	1	22	1	0	0	23
Other	Collapse	4	8	2	12	2	0	0	14
	Serious	0	4	2	2	4	0	0	6
Collapse		52	129	29	89	103	14	4	210
Serious		30	63	27	40	58	20	2	120
TOTAL		82	192	56	129	161	34	6	330

Figure 4. Structural damage summary.

361

Figure 6. Approximate damage map in the historic district.

Figure 5. Plan view of the Valley of Mexico, including location accelerograph stations.

362

Figure 7. Aerial view of Communications Center (SCT).
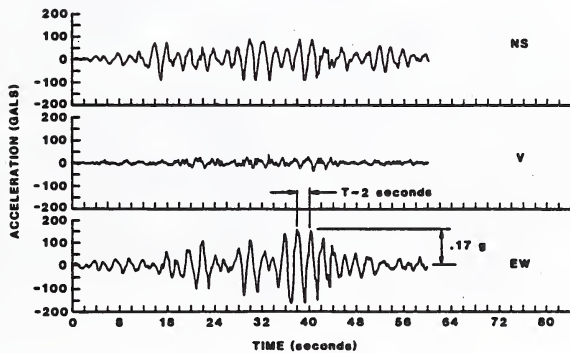
Figure 8. Acceleration records at the SCT.

363
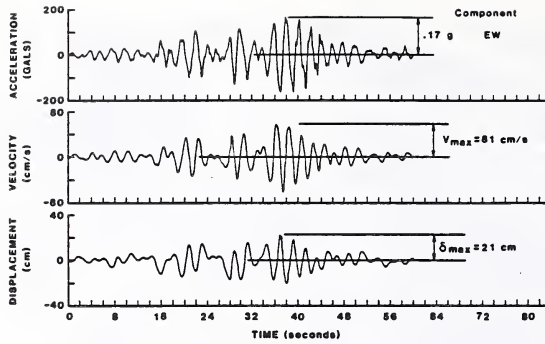
Figure 9. East - west ground motion at the SCT.
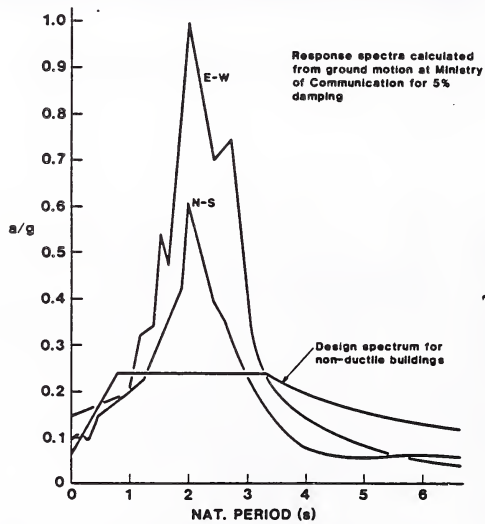
Figure 10. SCT response spectra.

364
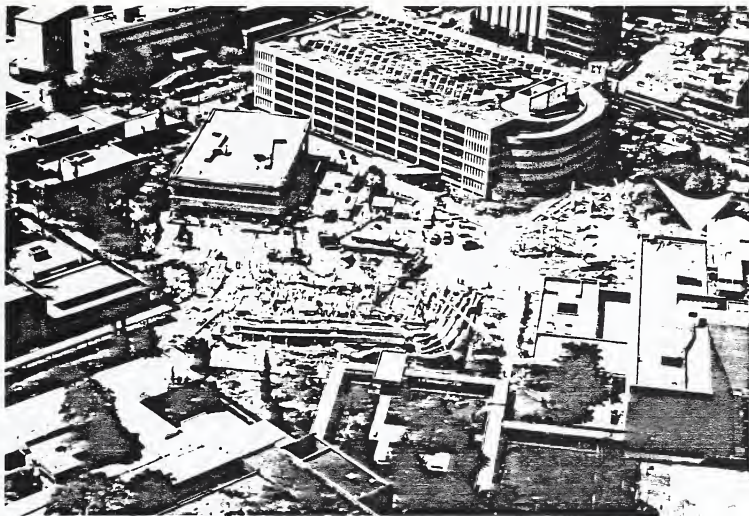
General Hospital
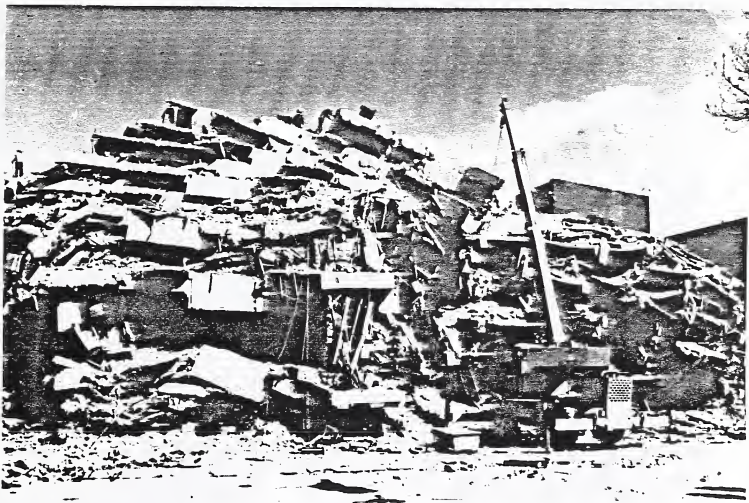
Juarez Hospital

Figure 11. Examples of hospital damage.

Nuevo Leon

Juarez

Figure 12. Examples of housing damage.
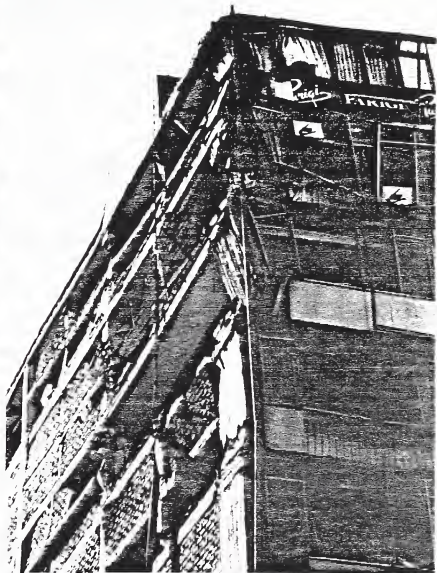
Pounding of equal height buildings
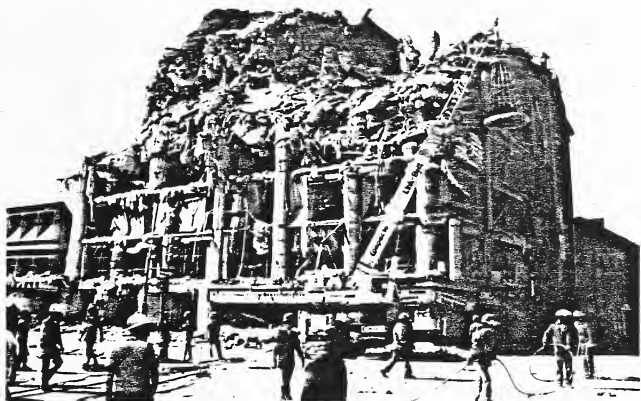
Pounding of unequal height buildings.

Figure 13. Building interaction.

367

JAPAN-MEXICO TECHNICAL COOPERATION ON DAMAGE EVALUATION, REPAIR AND STRENGTHENING FOR BUILDINGS DAMAGED BY 1985 MEXICO EARTHQUAKE

BY

Masaya Hirosawa(I) and Tatsuo Murota(II)

ABSTRACT

The government of Japan dispatched a team of experts to Mexico from September 30 to October 7, 1985 to negotiate a cooperation on restoration of buildings damaged from the September 19-20, 1985 Mexico Earthquakes. A report on recommendations on damage evaluations was prepared for the Department of Federal District of Mexico.

1. INTRODUCTION

A team of experts visited the Mexico City earthquake site during September 20 - October 7, 1985. Their mission was to negotiate cooperation to renovate buildings damaged by the September 19-20, 1985 earthquake. In this negotiation, it was agreed by both sides that the Japanese government shall dispatch experts and donate equipments as technical cooperation on investigation, judgment and retrofitting of damaged buildings. Based on this recognition, a second expert team was dispatched to Mexico during October 19 to November 22. The team was sponsored by the Japan International Cooperation Agency. Its mission:

(1) to investigate and analyze typical building damage in Mexico City,

(2) to recommend damage evaluation guidelines and repair and strengthening methods after modifying those used in Japan,

(3) to donate equipments and documents useful for applying these damage evaluation guidelines and repair and strengthening methods and

(4) to recommend methods to decrease possible damage to buildings in future earthquakes in Mexico.

2. MEMBERS

The second mission consisted of 22 experts from disciplines of earthquake engineering and building construction. They were selected from the Ministry of Construction, universities, local building administration offices and construction corporations. Names and affiliations of members are:

|	
Norihisa Ishikawa Mission Leader	Senior Coordinator, Division of Building Standards, Bureau of Housing, Ministry of Construction
Tsuneo Okada	Professor, Institute of Industrial Science, University of Tokyo
Masaya Hirosawa	Director, Planning Division, building Research Institute, Ministry of Construction
Mizuno Yamada	Manager, Design Department, Building Construction Division, Taisei Corporation
Hisahiro Hiraishi	Senior Research Associate, Structural Engineering Division, Building Research Institute, Ministry of Construction
Kazuyoshi Ohshima	Assistant Division Chief, Division of Building Design, Department of Building and Repair, Secretariat of the Ministry of Construction
Shinji Takiguchi	Assistant Division Chief, Division of Supervising, ditto
Yuji Najima	Coordinator, Division of Building Design, Department of Building and Repair, Bureau of Construction (Kanto Area), Ministry of Construction
Tatsuo Murota	Head, Building Aerodynamic Section, Structural Engineering Division, Building Research Institute, Ministry of Construction

(I) Director, Research Planning and Information Dept., Building Research Institute, Tsukuba, Japan

(II) Director, Structural Engineering Dept., BRI

Toshihide Kashima	Research Associate, Structural Engineering Division, ditto
Hideo Tsukagoshi	ditto
Toshikazu Kawashima	ditto
Hideaki Kishida	Professor, Department of Science and Technology, Graduate School of Tokyo Institute of Technology
Tadao Minami	Associate Professor, Earthquake Research Institute, University of Tokyo
Masaya Murakami	Professor, Department of Architectural Engineering, Faculty of Engineering, Chiba University
Junichi Sato	Assistant Division Director, Building Standard Division, Bureau of Urban Planning, Tokyo Metropolitan Government
Toshiyasu Yanagihara	Technical Director, Architecture Division, Government of Shizuoka Prefecture
Hiroaki Eto	Assistant Supervising Researcher, Structural Engineering Department, Technical Research Institute, Ohbayashi Corporation
Shunsuke Sugano	Chief Research Engineer, Division of Structural Engineering, Department of Research Development, Technical Research Laboratory, Takenaka Komuten Co., Ltd.
Kazuo Tamura	Ohsaki Research Institute, Shimizu Construction Co., Ltd.
Toshiyuki Noji	Chief Research Engineer, Technical Research Institute, Mitsui Construction Co., Ltd.
Tsuneyoshi Hagiwara	Chief Research Engineer, Soil Mechanics and Foundation Department, Institute of Construction Technology, Kajima Corporation

3. TIME TABLES OF TECHNICAL ACTIVITIES

The five members in the preceding list departed Tokyo and arrived at Mexico City on October 19. On the 21st, they held a meeting at the Department of Federal District of Mexico with Mr. Noreña, Secretario General de Obras and Mr. Rivas, Coordinator Técnico Operativo, where objectives of technical cooperation and tentative schedule of technical activities were confirmed. During the following week, the members visited the sites of damaged buildings in central parts of Mexico City with Mr. Ortiz, Subdirector de la Coordinación Técnica Operativo, who had been nominated as the DDF's senior counterpart of this mission, to select some damaged buildings as the objects of investigation. During this period, they visited universities and consulting engineers to collect information and held discussions to learn more about the building damages. The other 17 members arrived in Mexico on October 28. From October 30 to November 6, they investigated three damaged buildings in some details: a 12 story office building and a 4 story school buildings. From November 7 to 12, a 9 story apartment building was investigated. In addition to these investigations, quick inspection of safety and damage evaluation were made on other 16 buildings. Microtremors were observed in 46 buildings. This work was performed under the cooperation of Technical staffs of DDF and engineers of consultant corporations in Mexico City. Table 1 shows the technical activities time table.

4. TECHNICAL REPORT

A technical report entitled "Recommendations on Damage Evaluation, Repair and Strengthening for Buildings Damaged by the September 19-20, 1985 Mexico Earthquakes" was submitted to the Department of Federal District of Mexico by the Mission on Nov. 21. This report consists of five chapters;

Chap. 1 contains objectives, members committed and timetables of technical activities. Chap. 2 are describes the earthquakes damage evaluation guidelines for damaged buildings; guidelines for quick inspection of safety and two levels of damage evaluation, which are revisions of the damage evaluation guideline developed recently in Japan based on damage observations, strengthening practices and various kinds of structural tests. Chap. 3 describes some methods to repair and strengthen buildings, currently adopted for Japanese buildings. Comments about the repair and strengthening of substructures are also contained in this chapter. Chap. 4 contains twenty case examples of applications of guidelines and methods on existing Mexico City buildings, four cases address damage evaluation and repair and strengthening, and sixteen case examples address quick inspections for

determining the safety and level-1 damage
evaluation.   Chap. 5 is a summary of
recommendations to DDF from the Mission.

Table 1 Time Table of Technical Activities

Oct.   Nov.
21   28   4   11   18

Selection of Damaged Buildings
        to be investigated

Collection of Informations

            Investigation of
            #1 to #3 Building

                    Investigation of
                        #4 Building

            Micro Tremor Observation

            Collection of Information
            about Soil and Foundations

                    Analysis of Data, Report Making

◇   ◇   ◇   ◇   ◆
Meeting with DDF   Delevery Ceremony
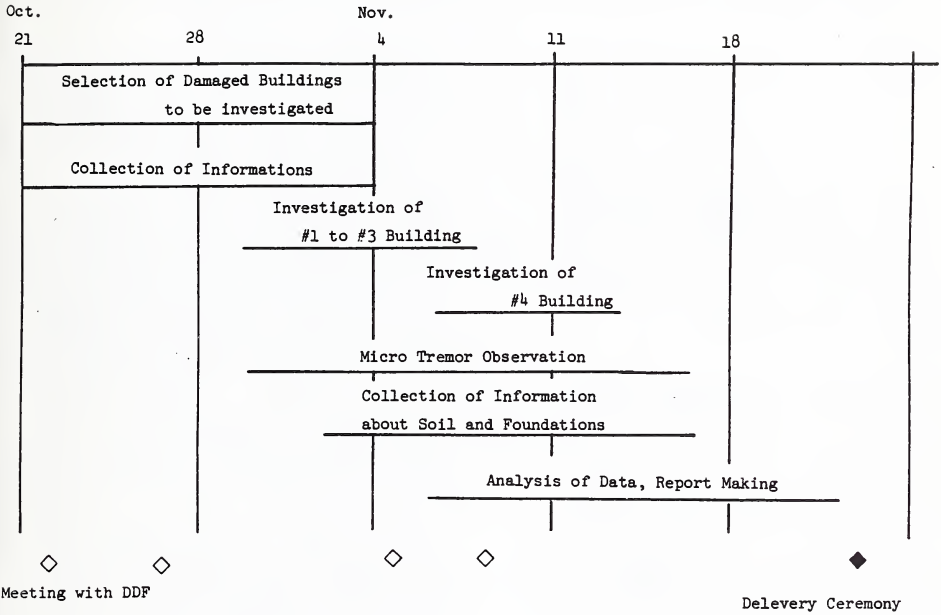
ASPECTS OF STRONG MOTION FROM THE MICHOACAN, MEXICO, EARTHQUAKE OF SEPTEMBER 19, 1985

John G. Anderson[1], James N. Brune[1], Jorge Prince[1],
Enrique Mena[2] Paul Bodin[1], Mario Onate[2],
Roberto Quaas[2], Shri Krishna Singh[2]

ABSTRACT

Strong motion accelerograms from the Mexico earthquake of September 19, 1985 provide the most complete picture to date of the damage-producing motions of a magnitude 8+ earthquake. The success in obtaining these records was significantly enhanced due to close cooperation between the fields of seismology and earthquake engineering, and also between U.S. and Mexican scientists.

INTRODUCTION

Strong motion accelerographs are operating in Mexico as the result of two major sources of support. The first general category is instruments installed and maintained entirely from any of several Mexican sources for funds. The agency in Mexico which maintains all of these instruments is the Instituto de Ingeniería (II), at the Universidad Nacional Autónoma de México. Instruments in this category include all accelerographs in Mexico City and many digital and analog accelerographs scattered throughout Mexico. The second category includes the Guerrero accelerograph network, described here, and the Baja California accelerograph network (Anderson et al., 1982) has been installed with support from the U.S. National Science Foundation in a cooperative effort between II personnel and personnel at the Institute of Geophysics and Planetary Physics, at the University of California, San Diego.

GUERRERO ARRAY

The Guerrero array consists of 30 digital accelerographs which were installed for the specific purpose of obtaining strong motion records from a large ($M > 8$) earthquake. The array was strategically located in Guerrero and Michoacan, Mexico, in two seismic gaps, with the expectation, obtained from seismological research, that these locations were high probability areas for such a large earthquake. Figure 1 shows a space-time diagram of Mexico to illustrate that prior to the 1985 events, the Michoacan region was a seismic gap. This was the basis of the placement of the accelerographs in that location. Actually, prior to the September 1985 earthquakes, we were uncertain about the seismic potential of the Michoacan region, where there were no certain prior earthquakes. In the Guerrero gap, in contrast, there were several large earthquakes at about the turn of the century (1899, 1908, 1909, 1911).

Table 1 lists all of the stations in the Guerrero array. The 1985 earthquakes occurred at a time when installation of the array was about 65 percent complete. Therefore there are only 16 accelerograms for the earthquake from that array.

Figure 2 shows the locations of instruments in the Guerrero array which recorded the 1985 earthquakes. Most of the units are in the Mexican state of Guerrero, in the Guerrero gap, but several instruments were located in Michoacan, and were in the immediate vicinity of rupture during the September 1985 event.

MEXICO CITY ACCELEROGRAPHS

Table 2 lists Mexico City vicinity accelerographs which recorded the September earthquake and Figure 3 shows the locations of those which were located in Mexico City in more or less free field conditions. The soil conditions in Mexico City vary widely, from relatively firm soils or volcanic flows in the hills zone to soft clay in the lake zone as indicated in Table 2 and Figure 3.

SEISMOLOGICAL CHARACTERISTICS

Before discussing the strong motion it is useful to review some seismological characteristics of the Sept. 1985 Mexico earthquake. Several parameters are listed in Table 3. For comparison, Table 3 also shows some of the characteristics of the March 3, 1985 Chile earthquake. The Chile earthquake is important for being about the same size, and also for producing strong motion records from near the faulting.

Figure 4 is modified from Scholz (1982). It shows the relationship of two parameters from several earthquakes which have occurred in a strike slip environment and several which have occurred in subduction thrust zones, such as in Mexico. According to all purely elastic models, for a long earthquake which ruptures the entire width of the seismogenic zone the seismic moment is proportional to the product of the rupture length, L, and the rupture width, W, squared. The constant of proportionality is the stress drop, which may vary from one earthquake to another. This figure shows that the stress drop appears to increase as the seismic moment increases. The Mexico and Chile earthquakes have been added to the figure. These two earthquakes are not anomalous based on Figure 4. The point for the Mexico earthquake is a little low (ie, stress drop appears to be a little higher than other events of the same size), but considering the uncertainties in interpretation of rupture width which have not yet been resolved, it is consistent with the other points.

In contrast to this result, Houston and Kanamori (1986) have looked at the spectrum of teleseismic P-waves in the frequency range of 0.05 to 1 Hz. While these spectra are similar at frequencies less than 0.1 Hz, from 0.1 to 1.0 Hz the Mexico earthquake spectra are depleted relative to Chile and relative to a worldwide average. The lower amplitudes in Mexico appear to correlate with a less complex rupture process than that found for the Chile event.

STRONG GROUND MOTION

Levels of Peak Motions

Table 4 lists all peak accelerations, peak velocities, and peak displacements for the main shock from the Guerrero array. Table 5 lists peak accelerations, velocities, and displacements which are available from the Mexico City vicinity. Figure 5 shows peak accelerations which were recorded in the Chile and the Mexico earthquakes. The peak values in the Mexico earthquake are much less scattered than in Chile, and except for the points in Mexico City, the Mexico points almost seem to provide a lower bound to the Chile points. These peak accelerations are at a higher frequency than the frequencies which were studied by Houston and Kanamori (1986), but if it is allowable to extrapolate between the two frequency bands,

[1]Institute of Geophysics and Planetary Physics, University of California, San Diego, La Jolla, California, U.S.A.

[2]Instituto de Ingeniería, Universidad Nacional Autónoma de Mexico, Mexico City, Mexico

the lower peak accelerations may be consistent with the teleseismic results.

There is however one other factor which is important in evaluating these peak accelerations, namely site effects. The site conditions in Michoacan and Guerrero are uniform. All stations were placed on the most competent rock outcrop consistent with the target location. Only one station (El Cayaco) was not sited on rock. Compressional wave velocities measured from rock samples taken at many of the sites have a median value of about 4 km/sec, with the variation among sites sampled to date ranging from a low of 1.6 km/sec to a high of 5.6 km/sec. The high value in this preliminary set was obtained from the site at La Villita. Samples from the other stations above the source zone are not completed yet, but the rock samples are similar to others which have measured about 4 km/sec.

In contrast to this situation, the site conditions in the Chilean data set are not uniform, and are not yet as well documented. Conditions described in Bolt and Abrahamson (1986) are evidently obtained from geological maps of the area rather than field inspection. Some of the accelerograms which are nominally listed as coming from rock sites show apparent ringing, probably caused by local site conditions. Therefore it is likely that to some extent the lower levels obtained near the faulting in Mexico are the result of differing site conditions.

From the Mexican data alone, there is clear evidence that the site conditions are important. The accelerations in Mexico City were unambiguously amplified by local site conditions. In addition, an II accelerograph, Zacatula 4.3 km from the La Villita accelerograph recorded peaks in acceleration of 1.5 to 2.5 times those recorded at La Villita. Peak velocities at Zacatula were also amplified by a similar amount. The Zacatula station is situated on a river terrace deposit of probable Quaternary age. The deposit is an indurated cobble conglomerate with a high density of cobbles ranging in size mostly from 5 to 25 cm.

Appearance of Accelerograms

Figure 6 shows the north-south component of all accelerograms from the Guerrero array. Figure 7 shows the east-west acceleration from those Mexico City sites which are shown in Figure 3. At the stations above the faulting (Caleta de Campos, La Villita, La Union) the duration of strong shaking is fairly long (over 30 seconds) but at stations farther to the southeast, the duration is shorter. This is because the rupture on the fault propagated to the southeast during the event, so that the arrivals in that direction are compressed in time. In Mexico City, the durations are much longer than in the source region. At the station CDA and SCT, the strong shaking lasted over 60 seconds (only the most significant part of these records is shown), and the total duration of these accelerograms exceeds 180 second.

Anderson et al. (1986) have demonstrated that above the fault, the accelerograms can be integrated to obtain a permanent offset. The offset obtained is consistent in magnitude and direction with that expected from the earthquake mechanism. Vertical offsets are also apparently consistent with observed uplift along the coast.

Figures 8 to 13 show a selection of accelerograms and response spectra from the Guerrero array. These records have been filtered at low frequencies, with the cutoff in the vicinity of 0.15 Hz, so the static displacements are not visible. Figures 14 to 16 show the same information for a selection of records from the Mexico City vicinity.

Because of the unprecedented building damage in Mexico City for the earthquake and because the damage was in large part caused by amplified 2 second energy, an important question is whether or not the earthquake source energy at 2 second period was anomalous compared, for example, with previous large Mexico earthquakes. A survey of the velocity and displacement records outside of the Mexico City basin (Figures 8–13) shows obvious high amplitudes at these periods, e.g. especially records from Caleta de Campos, La Villita, Papanoa, Teacalco, and CUIP. Some records from the coast show local maxima in the response spectra at 2 seconds (e.g. Caleta de Campos and La Villita) but at all stations closer than El Cayaco (Figure 2) the response spectra also attain even higher values of periods shorter than 2 seconds. The highest peaks with velocity response spectra near 2 second period on the near-source stations Caleta de Campos and La Villita (∼60 cm/sec) for zero damping are smaller than the response spectra peaks near the same period for 1971 San Fernando (Pacoima Dam > 150 cm/sec, near 1.5 second period) and 1940 Imperial Valley (El Centro > 110 cm/sec, near 2.0 second period) (EERL 72-80, 73-81). Thus there does not appear to be any clear indication of anomalously high source energy near 2-seond period, but a final conclusion awaits a more thorough comparison with other Mexico earthquakes. Earth structure effects (e.g. energy focusing) also might have been partly responsible for the unusual damage for the earthquake.

CONCLUSIONS

Earthquake hazards are distributed widely around the world, and the need to measure the strong motion in the vicinity of strong earthquakes is an international problem. The success in obtaining accelerograms from the epicentral area of the Mexico earthquake is a result of application of seismological information about the relative likelihood of earthquakes, and international cooperation to put the instruments in one of these locations.

ACKNOWLEDGMENTS

REFERENCES

(1) Anderson, J.G., J.N. Brune, J. Prince, and F.L. Vernon III (1983). Preliminary report on the use of digital strong motion recorders in the Mexicali Valley, Baja California, *Bull. Seism. Soc. Am.*, 73, 1451-1468.

(2) Anderson, J.G., P. Bodin, J. Brune, J. Prince, and S. Singh (1986). Strong ground motion of the Michoacan, Mexico earthquake, (invited paper *Science*, accepted for publciation).

(3) Bolt, B. And N. A. Abrahamson, Seismological features, *in* Earthquake Engineering Research Institute report on the March 3, 1985 Chile earthquake (in press), (1986).

(4) EERL, Analyses of strong motion earthquake accelerograms, Vol. III - Reponse Spectra, Part A - Acclerograms IIA001IIA020, Earthquake Engineering Research Laboratory, Calif. Institute of Technology, Pasadena, Calif. 272 pp., (1972).

(5) EERL, Analyses of strong motion earthquake accelerograms, Vol. III - Reponse Spectra, Part C - Acclerograms IIC041IIC055, Earthquake Engineering Research Laboratory, Calif. Institute of Technology, Pasadena, Calif. 191 pp., (1973).

(6) Houston, H. and H. Kanamori, Source characteristics of the 1985 Michoacan, Mexico earthquake at short periods, (Geophys. Res. Letters, in press), (1986).

(7) Instituto de Ingeniería de la Universidad Nacional Autónoma de México, El temblor del 19 de septiembre de 1985 y sus efectos en las construcciones de la Ciudad de México, Informe Preliminar Instituto de Ingeniería, UNAM, Mexico City, (1985).

(8) Scholz, D. H., Scaling laws for large earthquakes, conse-quences for physical models, *Bull. Seism. Soc. Amer.* 72, 1-14 (1982).

(9) Sykes, L. and R. Quittmeyer (1981). Repeat times of great earthquakes along simple plate boundaries, in D.W. Simpson and P. G. Richards, eds., *Earthquake Prediction: an International Review*, 217-247.

Table 1.
Accelerograph Stations in the Guerrero Array Which Were
Installed Prior to the September 19, 1985 Earthquake

Station	Location Lat.°N	Long.°W	Instrument Type	S/N	Geology
Caleta de Campos	18.0727	102.7552	DSA-1	261	metavolcanic
La Villita	18.0475	102.1840	DSA-1	260	gabbro
La Union	17.9824	101.8054	DSA-1	259	Metavolcanic
Zihuatenejo	17.6030	101.4550	DCA333	106	tonalite
Papanoa	17.3278	101.0399	DCA333	111	weathered plutonic
El Suchil	17.2258	100.6418	DCA333	109	plutonic
Atoyac	17.2113	100.4309	DSA-1	256	weathered plutonic
El Paraiso	17.3444	100.2145	DSA-1	257	plutonic
El Cayaco	17.0452	100.2664	DSA-1	258	
Coyuca	16.9967	100.0900	DCA333	107	schist/gneiss
El Ocotillo	17.0378	99.8749	DCA333	110	weathered gabbro
Xaltianguis	17.0950	99.7201	DSA-1	253	granodiorite
El Ocotito	17.2500	99.5106	DCA333	104	weathered plutonic
La Venta	16.9129	99.8159	DSA-1	252	granitic gneiss
Cerro de piedra	16.7692	99.6326	DCA333	112	weathered gneiss
Las Mesas	17.0070	99.4565	DSA-1	254	weathered granitic/gneiss
San Marcos	16.7760	99.4077	DSA-1	255	granitic gneiss
Las Vigas	16.7560	99.2359	DCA333	108	plutonic
Tonalapa	18.0975	99.5594	DSA-1	249	met. shale
Teacalco	18.6174	99.4528	DSA-1	248	volcanic tuff

Station	Code	Lat.° N Long.° W	Type/N0	Accelerograph Comp.	Nat. Freq.	Damp. G.	Site Description
Cd. Univ. D.F	CU01	19.330 99.183	DCA333 -121	S00E VERT N90W	33.0 31.0 32.0	0.64 0.66 0.70	Rock basalt. 1st floor of 3-story Idel main Ibldg. Hilly zone
Idel Patio	CU1P	19.330 99.183	DCA310 -154	N00E VERT N90W	31.0 31.3 31.4	0.73 0.66 0.68	Rock, basalt. Free field. Idel yard.
Mesa Vibra-dora C.U.	CUMV	19.330 99.183	DCA333 -145	S00E VERT N90W	31.0 31.0 30.0	0.70 0.66 0.75	Rock, basalt. Shaking table. Free field.
Sismex Puebla	SXPU	19.043 98.212	DCA310 -148	N00E VERT N90E	32.0 32.0 31.0	0.71 0.77 0.74	Hard soil, sand and gravel. Free field. Puebla Valley.
Tacubaya, D.F.	TACY	19.403 99.194	DCA333 -168	S00E VERT N90W	30.0 30.0 30.0	0.70 0.70 0.70	Hard soil. Free field. Hill zone, D.F.
Sismex Viveros	SXV1	19.358 99.171	DCA310 -133	N00E VERT N90W	30.4 32.0 33.0	0.66 0.80 0.78	Soft soil, clay. Free field. Transition zone. D.F.
C. de Abastos Frigorifico	CDAF	19.368 99.088	DCA333 -114	S00E VERT N90W	31.0 31.0 31.0	0.70 0.70 0.70	Very soft soil. Free field. Texcoco lake bed zone, D.F.
C. de Abastos Oficina	CDAO	19.368 99.088	DCA333 -115	S00E VERT N90W	31.0 31.0 31.0	0.70 0.70 0.70	Very soft soil, clay. 1-story bldg. Texcoco lake bed zone, D.F.
Secretaria de Comunicaciones y Transportes	SCT1	19.393 99.147	DCA333 -144	S00E VERT N90W	30.0 30.0 30.0	0.75 0.66 0.70	Very soft soil, clay. Free field. Texcoco lake bed zone, D.F.
Tlahuac Bombas	TLHB	19.279 99.008	SMA1 -4590	N00E VERT N90W	18.3 19.0 18.5	0.60 0.60 0.60	Soft soil, clay. Free field. Xochimilco lake bed zone
Tlahuac Deportivo	TLHD	19.293 99.035	SMA1 -4591	N00E VERT N90W	18.3 19.0 18.5	0.60 0.60 0.60	Soft soil, clay. Free field. Xochimilco lake bed zone

Table 3.
Characteristics of Mexico and Chile Earthquakes

Event	Michoacan	Michoacan	Chile
Date	Sept. 19, 1985	Sept 21, 1985	Mar. 3, 1985
Time	13:17	01:37	22:46
M_S	8.1	7.5	7.8
M_0 (dyn-cm)	0.9–1.5×10^{28}	1.4×10^{27}	1.1×10^{28}
L (km)	170	70	125
W (km)	50	40	90

Station	$R1$	$R2$ (1)	Trigger (2)	Dur. (3)	Comp. (4)	A_{max} (5)	V_{max} (6)	D_{max} (7)	V_{max} (8)	D_{max} (9)
Caleta	22.7	0.0	13:17:	49.4	N	138	25.9		16.70	5.73
de		0.0			W	141	19.5		12.64	3.22
Campos		0.0			DN	89	16.9		7.11	1.88
		0.0	13:18:	25.6	N	40	4.1	4.4		4.04
		0.0			W	51	4.8	3.2	5.96	1.18
		0.0			DN	24	3.3	2.0	2.91	0.88
La Villita	43.7	0.0	13:18:	64.0	N	125	25.9		16.11	6.67
		0.0			W	122			10.51	3.77
		0.0			DN	58	11.0		4.72	1.21
La Union	84.0	0.0	13:18:	62.8	N	166	28.0		20.34	6.95
		0.0			W	148	14.4		11.70	4.16
		0.0			DN	129	17.7		11.72	3.89
Zihuatenejo	134.6	8.0	13:18:	71.8	N	103	20.8	34.9	15.86	5.96
		8.0			W	161	17.9	17.2	18.34	4.62
		8.0			DN	105	14.6	22.1	10.23	3.80
Papanoa	187.9	63.0	13:18:	59.5	N	162	14.0	21.2	9.67	2.85
		63.0			W	117	7.7	12.9	6.13	1.57
		63.0			DN	84	10.4	14.6	8.38	1.81
El Suchil	230.4	112.0	13:18:	60.0	N	102	16.0	17.5	11.61	2.95
		112.0			W	81	7.1	7.9	6.36	1.49
		112.0			DN	51	6.8	9.2	5.96	1.16
Atoyac	251.1	135.0	13:18:	42.2	N	53	8.0	13.9	5.44	2.04
		135.0			W	59	4.6	5.5	3.67	0.89
		135.0			DN	60	8.3	8.6	6.68	1.61
El Paraiso	266.3		13:18:		N					
					W					
					DN					
El Cayaco	275.0	152.0	13:18:	25.6	N	41	5.2	10.0	3.75	1.31
		152.0			W	48	3.5	2.3	2.91	0.68
		152.0			DN	24	5.4	9.0	3.81	1.32
Coyuca	294.1	175.0	13:18:	38.8	N	42	9.0	12.4	7.82	2.83
		175.0			W	35	3.6	5.3	3.16	1.19
		175.0			DN	19	4.2	7.8	3.33	0.91
La Venta	324.3	206.0	13:18:	10.2	N	18	5.5	2.7	4.30	1.29
		206.0			W	21	3.6	1.5	2.62	0.88
		206.0			DN	16	3.3	1.5	3.20	0.98
Cerro de	348.9	225.0	13:18:	25.5	N	27	5.9	9.2	2.59	0.69
Piedra		225.0			W	15			2.52	0.57
		225.0			DN	13	3.8	7.1	3.07	0.79
Las Mesas	354.9	237.0	13:18:	14.1	N	22	4.6	5.1	1.90	0.51
		237.0			W	18	3.2	3.3	2.84	0.66
		237.0			DN	19	4.5	3.3	3.85	0.98
Xaltianguis	325.3	207.0	13:18:		N	25				
		207.0			W	18				
		207.0			DN	20				
El Ocotito	340.2	223.0	13:18:		N	49			7.65	2.92
		223.0			W	54				
		223.0			DN	21			3.72	1.48
Teacalco	332.5	244.0	13:18:	38.4	N	49	9.4	12.6	7.38	3.68
		244.0			W	24	5.4	6.0	4.74	1.36
		244.0			DN	27	5.8	10.3	4.41	1.62
El Ocotillo	312.7									
San Marcos	370.0									
Las Vigas	387.5									
Tonalapa	318.3									

NOTES

1. Epicentral distance (km), based on epicenter at 18.182° N, 102.573° W, origin time 13:17:47.8.

2. Closest distance to outline of aftershock zone (km).

3. Origin time of accelerogram.

4. Duration (seconds) of accelerogram.

5. Orientation, while nominal, is expected to be accurate.

6. Peak acceleration (cm/sec^2).

7. Peak velocity (cm/sec). This is obtained from an integration which did not employ a high-pass filter at low frequencies, made possible because the accelerograph is digital. There are some uncertainties in this, however, and these values are preliminary.

8. Peak displacement (cm). Obtained from the unfiltered velocities. The same notes apply. For some records, the peak velocity and peak displacement are reduced merely because the instrument did not run long enough to recognize their presence.

9. Peak velocity (cm/sec). To obtain these values, a high pass filter with a corner at about 0.015 Hz has been applied. The much lower values present in this case result because there are very strong low frequency signals period about 20 seconds) which have been filtered out from the records. The low frequencies are physically meaningful, and can be shown to correlate from one accelerogram to the next along the coast.

10. Peak displacement (cm). Filtered records. See note 9.

TABLE 5.
Strong Motion Data from Mexico City and Vicinity
Sept. 19, 1985 Mexico Earthquake ($M_S = 8.1$)

Station	$R\,1$ (1)	$R\,2$ (2)	Trigger (3)	Dur. (4)	Comp. (5)	A_{max} (6)	V_{max} (7)	D_{max} (8)	V_{max} (9)	D_{max} (10)
Teacalco	332	244	13:18:	38.4	N	51.3	9.4	12.6	7.38	3.68
		244			W	24.7	5.4	6.0	4.74	1.36
		244			DN	27.1	5.8	10.3	4.41	1.62
CU01	379	289		60.0	S	28.1			10.20	5.54
					W	33.5			9.38	7.19
					UP	21.6			8.23	6.65
CUIP	379	289		60.0	N	31.7			10.25	6.17
					W	34.7			9.37	7.71
					UP	21.9			7.99	6.61
CUMV	379	289		60.0	S	37.4			9.19	5.70
					W	38.8			11.01	4.45
					UP	20.1			8.40	4.57
SXPU	469	379		85.3	N	29.6			7.18	3.10
					E	32.6			6.63	2.65
					UP	15.9			4.06	1.67
TACY	380	290		156.0	S	34.4			14.29	11.96
					W	33.2			9.81	8.62
					UP	19.2			9.29	7.61
SXVI	381	291		60.0	N	44.1			11.48	9.10
					E	42.4			12.20	7.47
					UP	18.2			5.84	6.96
CDAF	389	299		60.0	S	80.5			24.85	15.02
					W	94.6			37.57	18.88
					UP	27.2			8.90	8.17
CDAO	389	299		180.0	N	69.2			34.98	25.02
					E	80.4			41.86	24.67
					UP	35.7			11.34	8.92
SCT1	385	295		180.0	S	98.0			38.74	19.12
					W	167.9			60.50	21.94
					UP	36.6			9.00	7.58
TLHB	394	304		150.0	N	135.9			64.10	36.61
					W	106.7			44.61	39.29
					UP	24.0			9.39	6.78
TLHD	392	302		150.0	N	117.7			34.90	20.76
					W	111.6			36.06	22.07
					UP	59.3			17.01	6.87

NOTES

1. Epicentral distance(km), based on epicenter at 18.182 N, 102.573 W, origin time 13:17:47.8.

2. Closest distance to outline of aftershock zone (km). Taken to be 90 km less than distance to epicenter.

3. Origin time of accelerogram.

4. Duration (seconds) of accelerogram.

5. Orientation, while nominal, is expected to be accurate.

6. Peak acceleration (cm/sec²).

7. Peak velocity (cm/sec). This is obtained from an integration which did not employ a high-pass filter at low frequencies, made possible because the accelerograph is digital. There are some uncertainties in this, however, and these values are preliminary.

8. Peak displacement (cm). Obtained from the unfiltered velocities. The same notes apply. For some records, the peak velocity and peak displacement are reduced merely because the instrument did not run long enough to recognize their presence.

9. Peak velocity (cm/sec). To obtain these values, a high pass filter with a corner at about 0.015 Hz has been applied. The much lower values present in this case result because there are very strong low frequency signals (period about 20 seconds) which have been filtered out from the records. The low frequencies are physically meaningful, and can be shown to correlate from one accelerogram to the next along the coast.

10. Peak displacement (cm). Filtered records. See note 9.

Figure 1. Top: map of Mexico with epicenters of large historical earthquakes identified by year, and depth in parentheses when event is known to be deep.
Bottom: Space-time diagram in which epicenters are projected down and plotted at year of occurrence. Deep events and events located far inland and thus not clearly related to subduction are deleted. Larger events are highlighted. Guerrero gap and former Michoacan gap are illustrated.

Figure 2. Map of coastal Mexico, epicenters and aftershock zones of 1985 events, and locations of strong motion stations in Guerrero array on September 19, 1985. Short dashed lines show limits of aftershocks of large earthquakes in this region since 1951. Peak accelerations, in cm/sec^2, are given for each station, for the north, east, and vertical components, respectively, in parentheses.
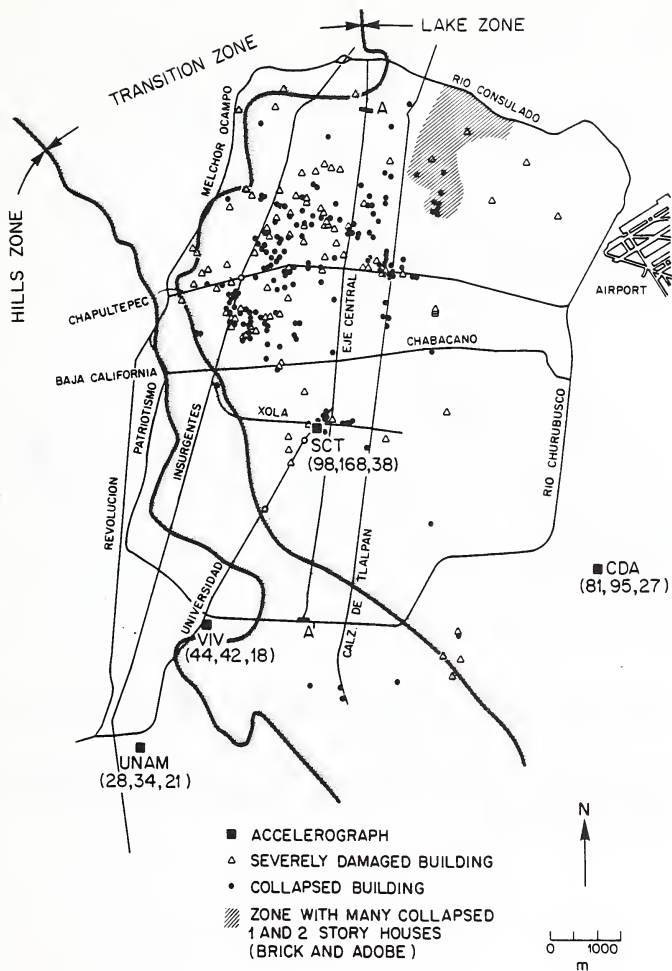
Figure 3. Mexico City map showing free-field accelerograph stations, generalized soil classification, and sites of worst building damage from Instituto de Ingeniera (1985) preliminary report. Peak accelerations (cm/sec^2) for the north, east, and vertical components,respectively, are given in parentheses by each station.
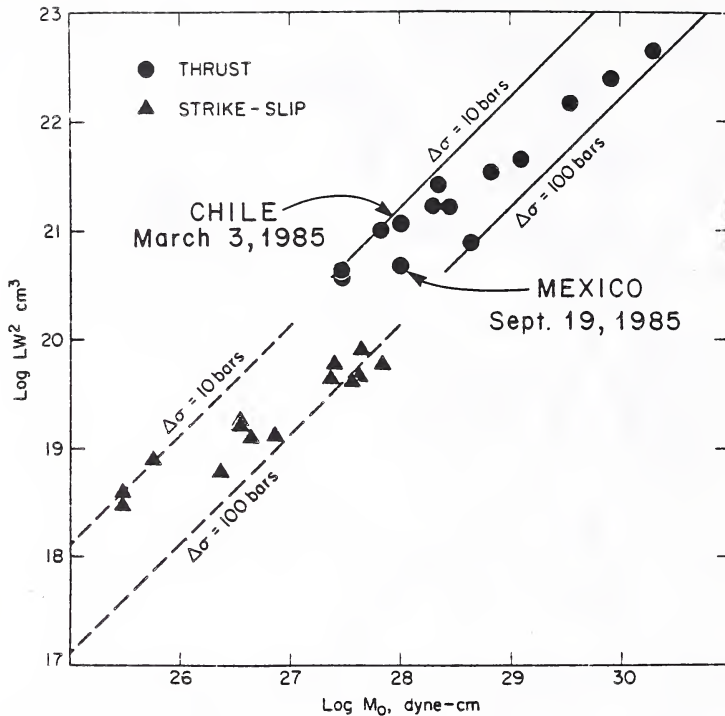
Figure 4. Plot of log LW^2 versus log M_0 for the large interplate earthquakes from the data set of Sykes and Quittmeyer (1981). The lines of slope 1 are constant stress drop lines, assuming $C=0.6$ for the thrust events, and 0.3 for the strike-slip events (after Scholz, 1982).
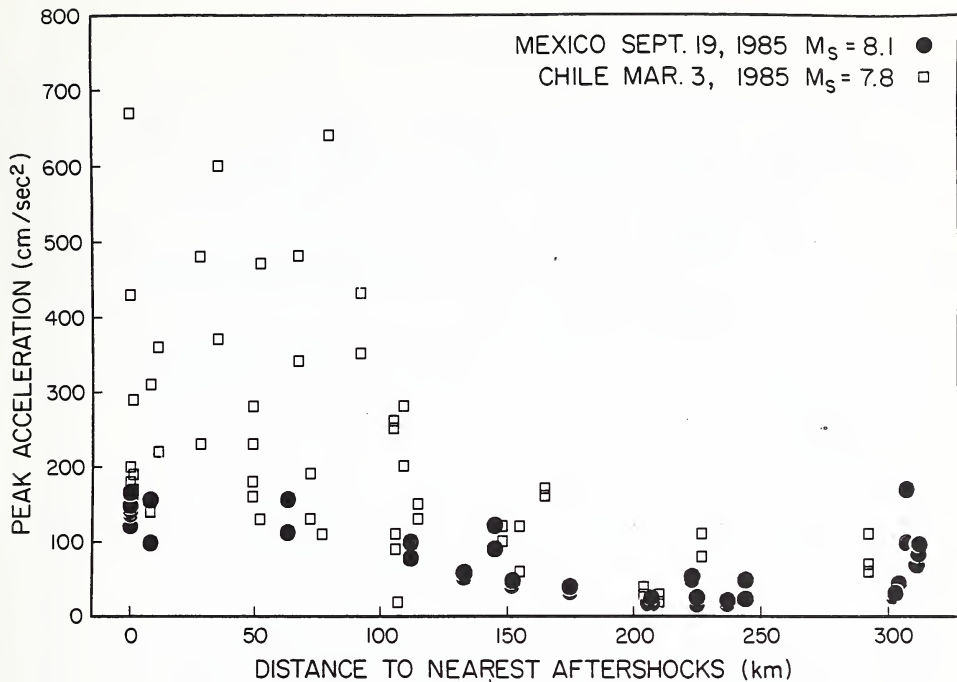
Figure 5. Peaks of horizontal components of acceleration plotted against distance outside the boundary of the aftershock zone (Figure 2).
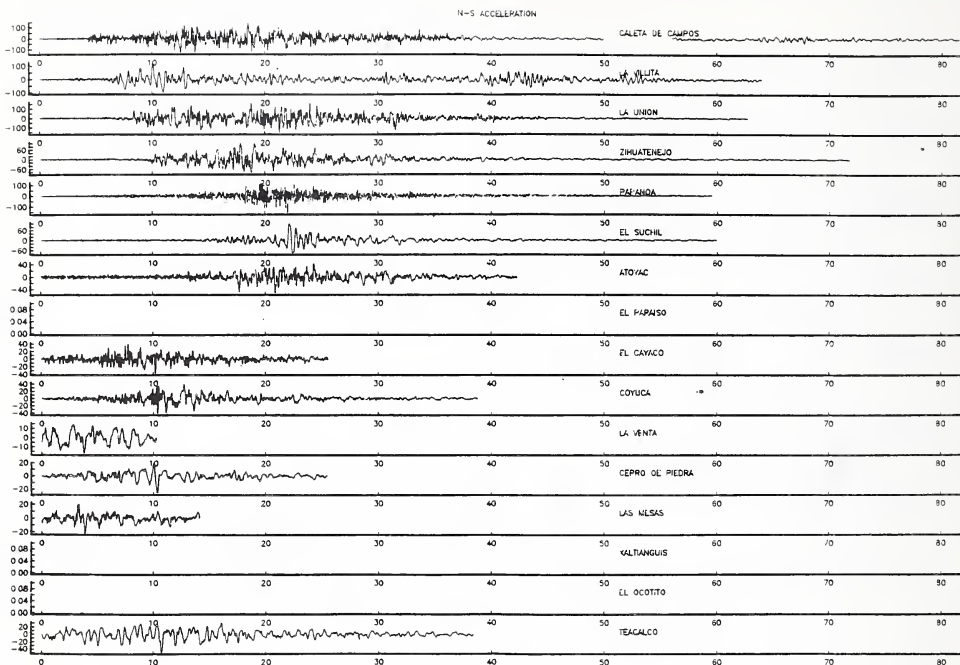
Figure 6. North-south component of acceleration for stations above the aftershock zone. Vertical separation of traces is proportional to separation of the projection of stations onto the trench. Time, T_0, is the origin time of the earthquake.[1] The clock correction at Caleta de Campos is uncertain.

EAST−WEST ACCELERATION
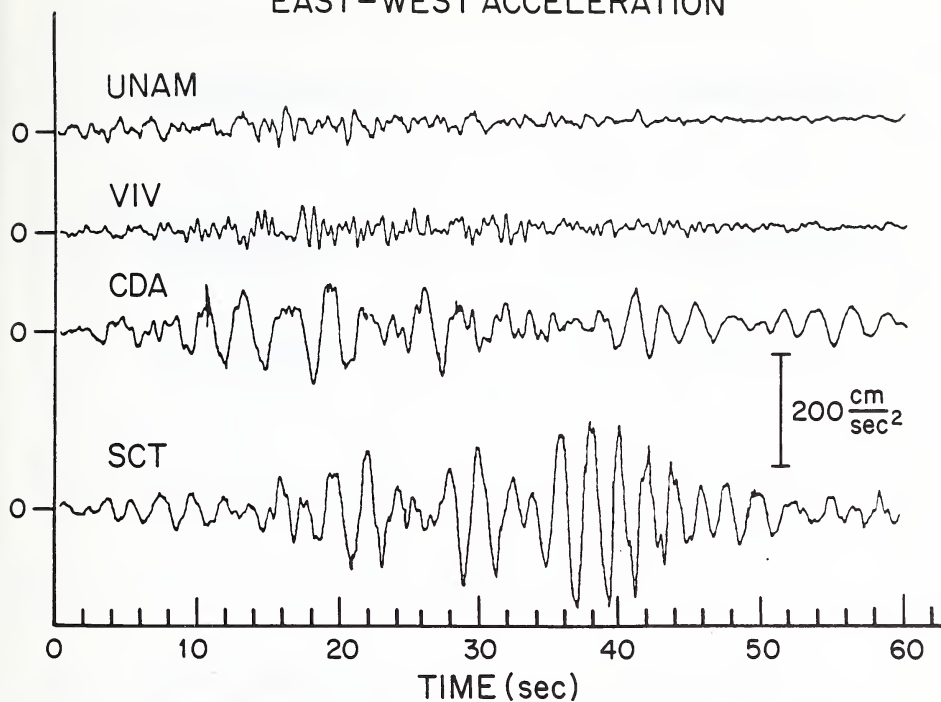
Figure 7. Most significant one-minute segments of the east-west acceleration recorded on the free-field accelerographs in Mexico City. Complete accelerograms are longer 100 sec of motion preceded the segment of the SCT record shown here. No time correlation exists among these traces.
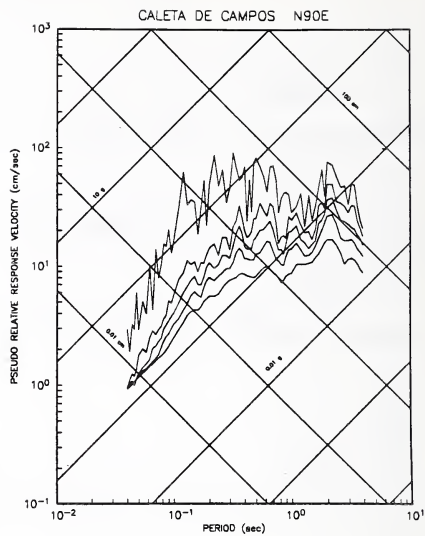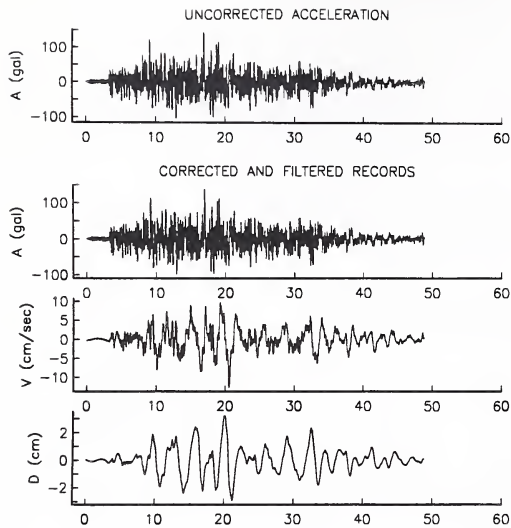
Figure 8. East west acceleration, velocity, displacement, and pseudo relative velocity response at Caleta de Campos, September 19, 1985
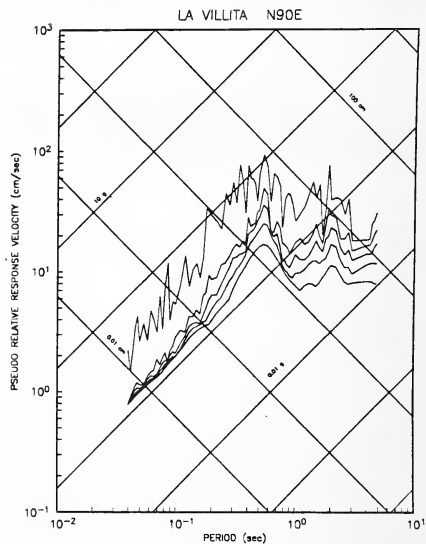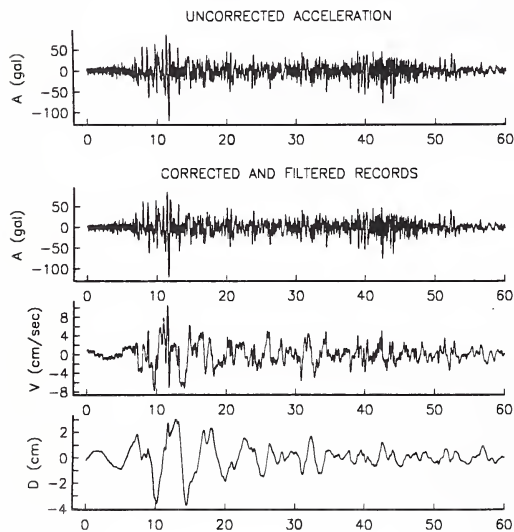
Figure 9. East west acceleration, velocity, displacement, and pseudo relative velocity response at La Villita, September 19, 1985
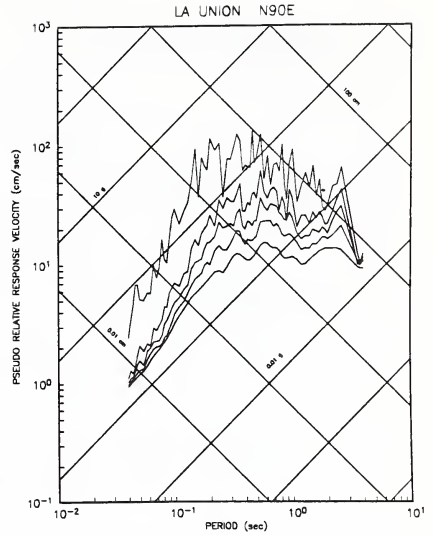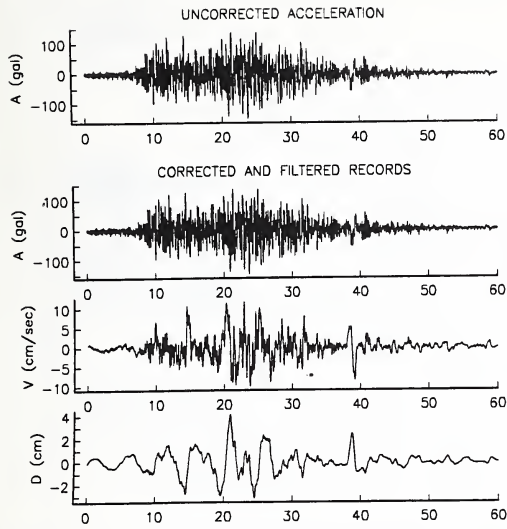
Figure 10. East west acceleration, velocity, displacement, and pseudo relative velocity response at La Union, September 19, 1985
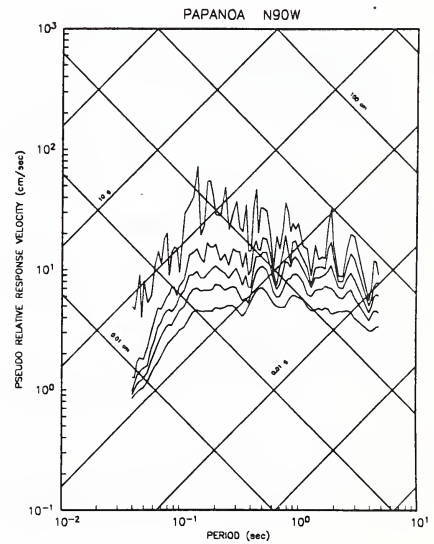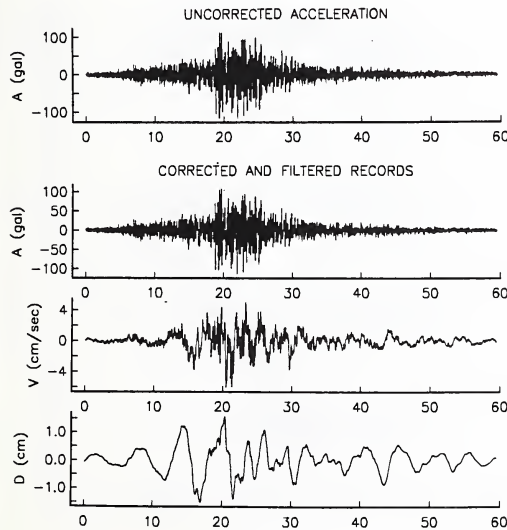
Figure 11. East west acceleration, velocity, displacement, and pseudo relative velocity response at Papanoa, September 19, 1985
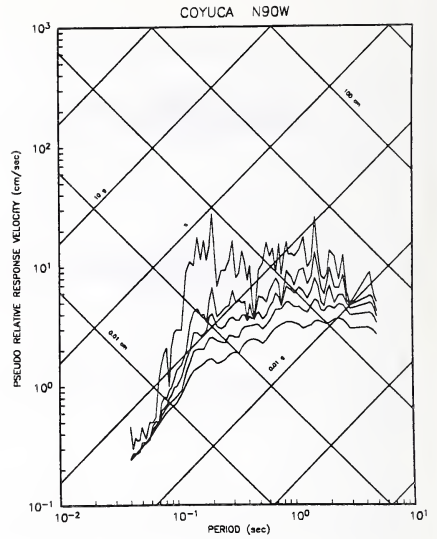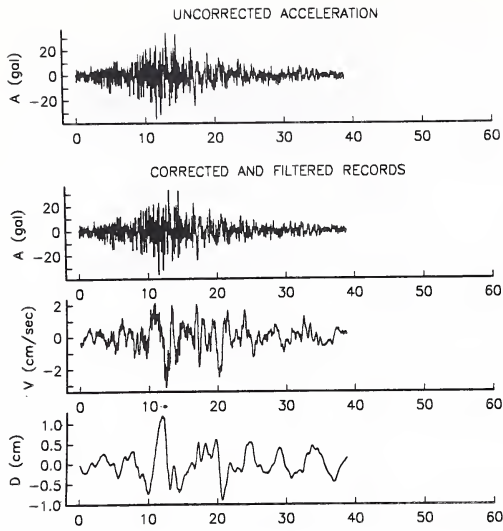
Figure 12. East west acceleration, velocity, displacement, and pseudo relative velocity response at Coyuca, September 19, 1985
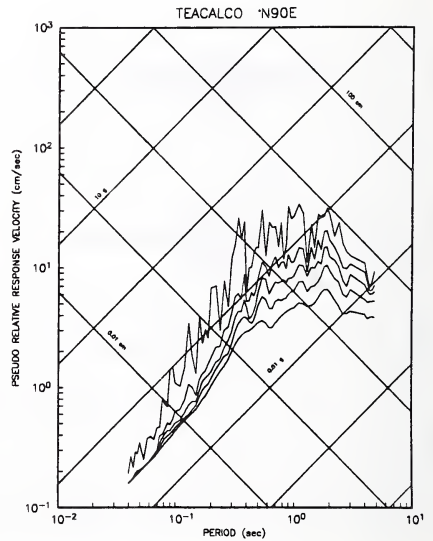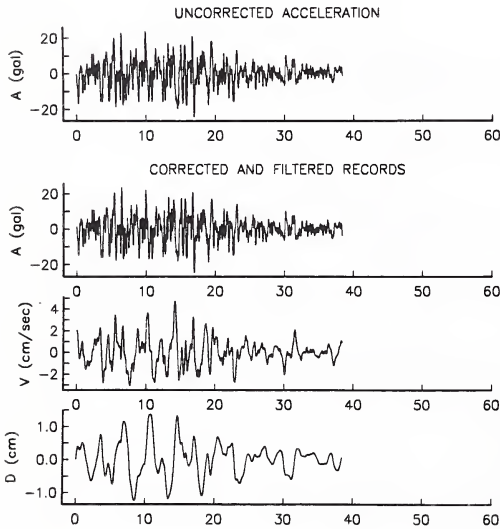
Figure 13. East west acceleration, velocity, displacement, and pseudo relative velocity response at Teacalco, September 19, 1985
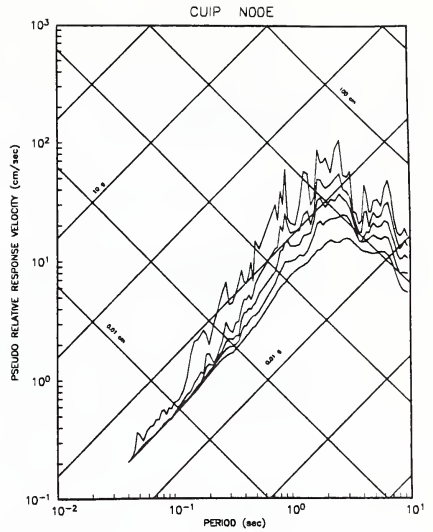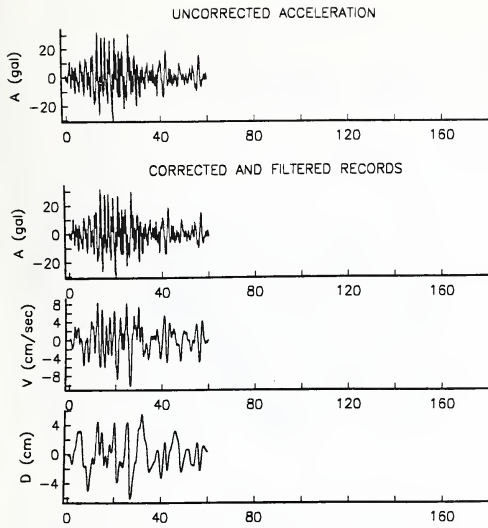
Figure 14. East west acceleration, velocity, displacement, and pseudo relative velocity response at Instituto de Ingenieria patio, September 19, 1985
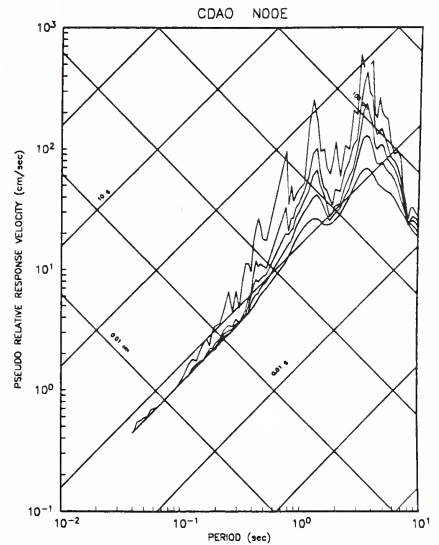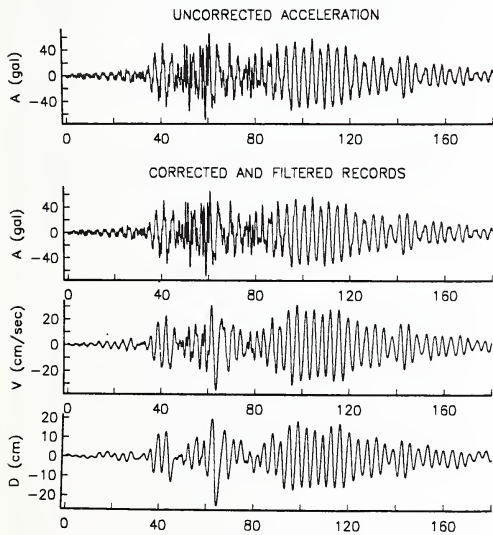
Figure 15. East west acceleration, velocity, displacement, and pseudo relative velocity response at C. de Abastos Oficina, September 19, 1985
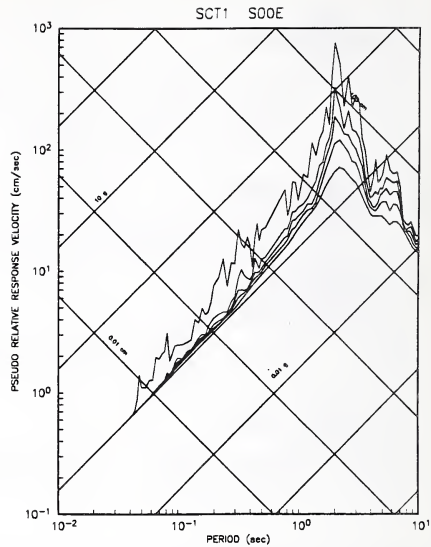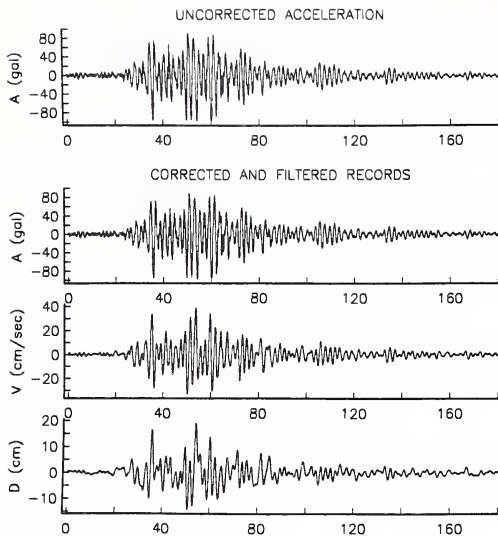
Figure 16. East west acceleration, velocity, displacement, and pseudo relative velocity response at Secretaria de Comunicaciones y Transportes September 19, 1985

SEISMIC DAMAGE TO PORT FACILITIES BY THE 1985 CHILE EARTHQUAKE
AND
IMPROVEMENT OF SEISMIC SAFETY OF THE DAMAGED PORTS

BY

Hajime Tsuchida and Setsuo Noda

ABSTRACT

The March 3, 1985 earthquake (M=7.7) in the
middle of Chile caused serious damage to
facilities in the Port of Valparaiso and the
Port of San Antonio. This paper presents the
seismic damage to these facilities and the
investigation of the causes of damage based on
damage reconnaissance and stability analyses.
Damage reconnaissance and planning for restora-
tion work were performed as a technical coope-
ration project between Chile and Japan. This
cooperative project is described.

1. INTRODUCTION

On March 3, 1985, an earthquake of magnitude
7.7 occurred in central Chile; it resulted in
lines lost and damaged engineered structures.
The Port of Valparaiso and the Port of San
Antonio were affected by severe ground shaking;
many port facilities suffered serious damage.
Cargo handling capacities of both ports were
greatly affected. Major damage took place on
quaywalls and cranes. However, some quaywalls
suffered no damaged even though they were
located in the vicinity of other damaged ones.

This report presents a description of the
damage to port facilities and the stability
analyses used to assess damaged quaywalls.

The Japanese government sent a team of Japanese
experts to chile. Cooperation with Chilean
port engineers for evaluating the stability of
the damage facilities was expanded as the
technical cooperation effort focus on the
restoration plan of the damaged facilities.

3. EARTHQUAKE AND GROUND MOTIONS

The location of the focal area is shown in Fig.
1 (see locations of the Port of Valparaiso and
the Port of San Antonio). Event data of the
earthquake are listed in Table 1. The seismic
intensities in the Modified Mercalli scale in
Valparaiso were 7 to 8 and those in San Antonio
were 8. The maximum accelerations around
Valparaiso and San Antonio are listed in Table
2 (1). The Accelerographs used at the sites
were the SMA-1 accelerographs with a natural
period of 0.03 second.

Port and Harbour Research Institute, Structures
Division, Ministry of Transport.

3.1 Damage in Port of Valparaiso

3.1.1 Outline of the Port

The Port of Valparaiso is the largest seaport
in Chile and is the center of foreign trade for
exporting fruits and copper and for importing
industrial products. The socioeconomics
activities of Chile are centered in the
Santiago region approximately 100 km east of
the port. The port consists of mooring
facilities for 10 berths, a breakwater, 14
warehouses, and 31 wharf cranes. A plan view
of the port is shown in Fig. 2; the berth
numbers are indicated.

The mooring facilities were completed between
1915 through 1932. The seismic resistance of
these facilities structure were not taken into
consideration. The structures for eight berths
are gravity type quaywalls using concrete
blocks (Berth Nos. 1 through 6 and 8) and
concrete caissons (Berth No. 7). Baron Pier
(Berths Nos. 9 and 10) consists of reinforced
concrete slab-beams and concrete foundation
piers. Diameters of the foundation piers are
4.0 m. Similar concrete foundation piers also
were used in the front part of the gravity type
quaywall of Berth No. 4 to sustain the seaside
crane railing. The breakwater was constructed
with the concrete blocks founded on the rock
mound. The breakwater extends offshore to a
water depth of 45 m.

To better understand the seismic stability of
the facilities at the Port of Vaparaiso; the
quaywalls at the Port of Valparaiso were
damaged by the 1971 earthquake and the port
operations were affected for many months (2).

In particular, the quaywalls for Berths Nos. 4
and 5 are tilted with a maximum horizontal
displacement of 5 cm at the ground level and a
subsidence of the backfill up to 40 cm. Damage
to the quaywalls for Berths Nos. 6 and 7 were
observed. The displacements were up to 30 cm.

3.1.2 Subsoil Conditions

According to the topographic survey and to the
borings, the original sea bottom existed at
about -10 m near the land side end of Berths
Nos. 6 and 8 and at about -35 m at Berth No. 7.
Therefore, the original sea bottom is sloping
steeply towards offshore.

The surface layer of the area, covering approximately Berths Nos. 4 through 8, is medium fine sand or silt having N-value of SPT about 20 and its thickness is 5 to 10 m. The surface layer at the area around Baron Pier is soft silty soil about 5 m thickness. A sand or gravel deposit lies under the surface layer and this underlying layer has N-value of SPT not less than 40 and it has been considered as the bearing stratum for the port facilities. The base rock formation was found at depth between about -10 m to -17 m. As an example, the boring log at the Berth No. 1 is shown in Fig. 3.

3.1.3 Damage to Mooring Facilities

The damage to the mooring facilities and to the adjacent yards were severe than the damage to the buildings. The major types of damage were: i) sliding of the concrete blocks and the caissons (gravity elements) toward the sea, ii) tilting and settlement of quaywalls, and iii) settlement, cracking, and opening of the joints of the apron pavements. The damage is shown in Figs. 4 through 6. The damage to the mooring facilities is summarized in Table 2.

The amount of horizontal sliding of quaywalls toward the sea are different depending on the berths: less damage at Berths Nos. 1 through 3 and heavier damage at Berths Nos. 4 through 8. However, the sliding is in decimeter scale. Tilting was observed at Berths Nos. 5 and 7.

As shown in Photo 1, the crane railings and the railway tracks deformed and settled. The settlement was observed in the berth aprons and the back-of-port yard in decimeter scale.

The copeline displacements were clear at berths Nos. 4, 5, 6, and 8. The displacement at Berths No. 5 is shown in Photo 2. The copeline displacement towards the sea was measured as 170 cm maximum, which included the displacement caused by the 1971 earthquake.

3.1.4 Damages to Wharf Cranes

Damage to wharf cranes at Berths Nos. 6 through 8 was severer than at Berths Nos. 1 through 3. About half of the wharf cranes were damaged at the portal legs and the rings. Damage to the legs was caused by local buckling from large compressive stress. Some damage to the legs might have been caused by cargo striking the legs. Derailing of land side wheels and buckling of the land side truck frames were observed at most of the wharf cranes at Berths Nos. 6 through 8. No damage occurred to the heavy cargo handling crane at Berth No. 4 and to the cranes at the Berths Nos. 9 and 10. A wharf crane at Berth No. 7 collapsed.

3.2 Damage at San Antonio Port

3.2.1 Outline of the Port

The Port of San Antonio shares, with the port of Valparaiso, the role of chief seaports of the country. Major cargos through the Port of San Antonio are cooper for exportation and wheat for importation. The cargos through the port sustain the socioeconomic activities in the Santiago region. A plan view of the port is shown in Fig. 7; the berth numbers are indicated. At the time of the earthquake, the port consisted of mooring facilities for 7 berths, a tanker berth, 2 breakwaters, 3 warehouses, and 15 wharf cranes.

The structures of the mooring facilities are gravity type quaywalls at Berths Nos. 1 and 2, steel sheet pile bulkheads at Berths Nos. 3 and 4, and open type wharves at Berths Nos. 5 through 7. The mooring facilities at the port also suffered damage from the 1971 earthquake.

The quaywall structures at Berths Nos. 1 and 2 suffered heavy tilting experiencing a maximum displacement of over 60 cm at the ground level and subsidence up to 60 cm at the apron and the yard behind. Longitudinal cracks in the yard behind Berths Nos. 1 through 3 also were observed. The warehouses were heavily damaged and had to be demolished. A group of undamaged steel silos were disassembled for safety purposes.

3.2.2 Subsoil Condition

The geological formation of the port area consists of 2 layers. The upper layer is divided into two sub-layers. The upper sub-layer extends uniformly over the port area and consists of fine sand deposit. The lower sub-layer consists of clayey deposits. The clayey soil of the lower sub-layer is dominant at the onshore side of the port area, while the sandy soil of the upper sub-layer is dominant at the offshore side of the port area near the breakwater. The upper sub-layer of the sands has N-value in SPT 20 and is considered as sediments of littoral and drift from the Maipo River. The lower layer is composed of dense sand or gravel. From an engineering point of view, this is the bearing layer for the port facilities structural foundation. Its hardness is not less than 50 N-value. The layer was found at the depth of approximately -19 m. In the port area, the depth of the boundary between the two layers varies. This implies marine abrasion in the past. As an example, the boring log at Berth No. 1 is shown in Fig. 8.

3.2.3 Damage to Mooring Facilities

The damage to mooring facilities at this port was heavier than at the Port of Valparaiso.

Complete collapses of the quaywalls with severe
subsidence of the apron took place at the
Berths Nos. 1 and 2. Some cranes were partly
damaged. Also other mooring facilities experi-
enced some damage. The damage is summarized in
Table 3. Figs. 9 through 11 and Photos 3
through 7 show the damage at the Port of San
Antonio.

3.2.4 Damage to Wharf Cranes

The damage to wharf cranes at Berths Nos. 1 and
2 was heavy. As shown in Photo 6, all 7 of the
wharf cranes experienced severe damage or
collapse. At Berth No. 5, however, there is no
damage to the wharf cranes. At Berths Nos. 6
and 7, no damage to wharf cranes were reported
although it appears that the wharf cranes may
experience difficulty operating due to rail
deformation.

4. STABILITY ANALYSES AND DAMAGE CAUSES

4.1 Stability Analyses

For planing the restoration work, it is
important to analyze stability and stresses of
the structures during the seismic ground
motions and to learn how the damage was caused.
The stabilities of the mooring facilities and
the cranes were analyzed by the seismic coeffi-
cient method which is currently being used for
earthquake proof design of many structures.
Details of the method is available in many
references (3). In the analyses, the factor of
safety for the stability of the structures were
calculated for the seismic coefficients of sev-
eral different values, to find the condition
which gives the factor of safety of unity.
This condition may be considered as the criti-
cal condition. No loading on the apron of the
wharf and the crane were considered in these
analyses.

4.2 Mooring Facilities at Port of Valparaiso

The quaywalls at Berths Nos. 1 through 8 became
the critical condition for the seismic coeffi-
cients (from 0.09 to 0.15), depending on the
berth. According to the empirical formula
about the relationship between the seismic
coefficient and the peak ground acceleration,
the seismic coefficient 0.09 and 0.15 corre-
spond to peak ground acceleration of 0.09 g and
0.15 g, respectively (4). One of the peak
ground accelerations recorded near the Port of
Valparaiso was 0.29 g (Table 2). It should be
noted that the formula gives somewhat conserva-
tive seismic coefficients. Even when using the
conservative coefficients, the magnitude of the
earthquake ground motions exceeded what the
quaywalls could withstand.

4.3 Mooring Facilities at Port of San Antonio

The quaywalls at Berths Nos. 1 and 2 became the
critical condition for sliding when the seismic
coefficient was 0.07, and for overturning at
0.11. Similar to the quaywalls in the Port of
Valparaiso, it may be concluded that the cause
of damage to the quaywalls at Berths Nos. 1 and
2 was from intense seismic ground motions.

On the sheetpile bulkhead at Berth No. 4, the
seismic coefficient 0.17 corresponds to the
critical condition. This bulkhead suffered no
evident of structural damage.

The critical condition on the L-shaped
retaining wall behind the open-type wharf at
Berth No. 5 occurred when the seismic
coefficient is 0.17.

In the Port of San Antonio, evidences of
liquefaction were found at several locations.
However, the degree of liquefaction influence
to the damage of structures in this port is not
year clear. Soil testing for assessing lique-
faction potential is under way. The influence
will be studied in detail after completion of
testing.

4.4 Wharf Cranes

The wharf cranes at the Port of Valparaiso and
Port of San Antonio were not designed to resist
the effects of seismic ground motions. How-
ever, according to stability analyses, it
appears that the wharf cranes can maintain
stability against earthquake ground motions
equivalent to the horizontal seismic coeffi-
cient of about 0.2. Therefore, it is concluded
that the wharf cranes may have sufficient
stability and strength of its members. The
stress and the instability from loading cargo
may be severer than seismic ground motions. It
can be presumed that the collapse of some wharf
cranes was caused mainly by the unfavorable
performance of wharf cranes foundations, such
as the quaywalls.

5. TECHNICAL COOPERATION

5.1 The First Mission

Immediately after the earthquake, the Chilean
government requested the technical cooperation
of the Japanese government. Major objectives
of the cooperation were:

i) to assess the structural reliability of
   the damaged port facilities.

ii) to advise the Chilean government about the
    investigations necessary for designing and
    planning the restoration work.

The Japanese government organized the mission of 6 experts (referred to the first mission, hereafter) and sent the delegation to Chile from March 23 to April 5. The first mission focused on the field investigation of the ports, preparing some analyses, and presenting a report to the Chilean government. The report included surcharge restriction of each berth when it was necessary.

The first mission reported to the Japanese government that the Port of Valparaiso should be modernized, especially for the container cargo, and that the restoration work should be planned taking the possible modernization into consideration.

5.2 The Second Mission

According to the report of the first mission, the Japanese government decided to expand the technical cooperation to include port planning for the modernization. To make necessary arrangement for further technical cooperation, the second mission was organized with 7 members. They visited Chile from May 27 to June 11. The technical cooperation consisted of dispatching experts and studying the following items: i) present situation of port facilities, ii) immediate restoration plan, iii) master plan, and iv) restoration and improvement plan. A part of the study would be performed by the Chilean engineers under guidance of the Japanese study team.

5.3 Experts and Study Team

To implement the agreement, three experts were sent to Chile for two months during the first time and two experts for about one and half months during the second time. The experts pro-vided advise and technology transfer to the Chilean government engineers. The team visited Chile for about two months to collect necessary information and to discuss the matter with the Chilean government staff. A portion of the study is being performed in Japan. The study is expected to be complete in about 11 months.

6. REFERENCES

1) Saragoni, R. H., P. S. Gonzales, and M. B. Fresard, Analisis de los Acelerograms del Terremoto del 3 de Marzo de 1985, SES I 4/1985, Departamento de dIngenieria Civil, Universidad de Chile, 1985.

2) Lastrico, R. M. and Joaquin Monge, Engineering Aspects of the July 8, 1971 Earthquake in Central Chile, Proceedings of the 5th World Conference on Earthquake Engineering, Vol. 1, June 1973, pp. 468-477.

3) Bureau of Ports and Harbours, Ministry of Transport, Technical Standards for Port and Harbour Facilities in Japan, The Japan Association for Ports and Harbours, 1980.

4) Noda, S. and T. Uwabe, Relation Between Seismic Coefficient and Ground Acceleration for Gravity Quaywall, Proceedings of the 6th World Conference on Earthquake Engineering, 1977, pp. 1963-1968.

location	Components			Ground condition	Distance from ports
	NS	EW	UD		
Univ.Federico Santa Maria	0.164	0.179	0.125	Rock	1.4 km east from Baron Pier at Valparaiso Port
El Almendral	0.163	0.293		Reclaimed land	0.8km south from Baron Pier at Valparaiso Port
Llilleo	0.669	0.426	0.852		5km south from San Antonio Port

Table 2 Maximum acceleration around ports

Description	Berth No.						
	1 to 3	4	5	6	7	8	9 and 10
Displacement of copeline seewards	Not remarkable less than 10cm	Slight 4cm	170cm Max.	74cm Max.	20cm Max.	60cm Max.	Negligible
Horizontal sliding of quaywall elements	10-15cm Max. but 70cm at the connection with berth 4	70cm Max.	Slight	Heavy sliding partly at the offshore end	Slight	Heavy sliding totally	–
Tilting of quaywall seewards	Negligible	None	Remarkable	Negligible	1- 2°	Negligible	–
Gap between quaywall elements	Observed but minimal	10-20 cm Max.	Observed but minimal	Parts remarkable	30cm at the end units	Remarkable	–
Settlement of apron and back-of-port yard	less than 15cm but 30cm partly at Berth 4	Heavy 35cm	Heavy 35cm	20cm	Heavy 40cm	Heavy 30cm	None
Settlement of railings	Slight at Berths 1 and 2, but max. 10cm at berth 3	10cm Max.	Heavy	3-5cm but 18cm Max.	Heavy	Heavy 20cm	None
Assessment of overall damages	I	III	III	II	III	III	0

Legend:Extent of damages 0: No damage I: Slight II: Medium III: Severe IV: Great -: not applicable

Table 3 Extent of damage to berths at Valparaiso port

Description	Berth No.				
	1 and 2	3	4	5	6 and 7
Displacement of copeline seawards	Collapsed	70cm-100cm	Negligible	Negligible	Maybe occur
Horizontal sliding of quaywall elements	Collapsed	–	–	Slight	–
Tilting of quaywall seawards	Collapsed	–	–	Slight	–
Gap between quaywall elements	Collapsed	–	–	Nil	–
Settlement of apron and back-of-port yard	Great	Severe	Slight	40cm at back-of-deck yard	60cm at the rear end of deck
Settlement of railings	Great	Heavy	Slight	Nil	Negligible
Assessment of overall damages	IV	III	I	II	IV

Legend:Extent of damages 0: No damage I : Slight II : Medium III: Severe IV: Great –: not applicable

Table 4 Extent of damage to berths at San Antonio port

Valparaiso : Boring No.1

Scale (m)	Level (m)	description	N-value 10 20 30 40	Vp (m/sec)	Vs (m/sec)
0 —	3.93	silty sand		270	110
	-1.32	clean fine sand, homogeneous, soft compaction medium			
	-4.67	silty sand,homogeneous, soft compaction		1780	200
5 —		fine to medium sand,soft compaction			
10 —	-9.17				
	-10.87	similar stratum 6.30~9.50			
15 —	-12.67	fine coarse sand medium to high compaction		810	410
	-15.17	sand with silt,medium compaction			
20 —	-16.17	fine and medium gravel		200	800
	-20.17	Altered rock			

Fig. 3 Boring log of Berth 1 at Valparaiso port
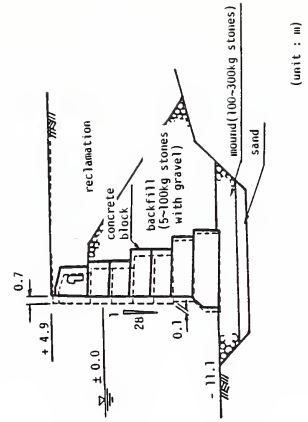
Fig. 4 Cross section of Berths 1-3 and 5 at Valparaiso port

reclamation
concrete block
backfill (5~100kg stones with gravel)
mound(100~300kg stones)
sand

+ 4.9
± 0.0
- 11.1
0.7
28
0.1

(unit : m)

Fig. 1 Location of epicenter, Valparaiso and San Antonio

Santiago
Valparaiso
Epicenter
San Antonio
Llolleo

50km
0
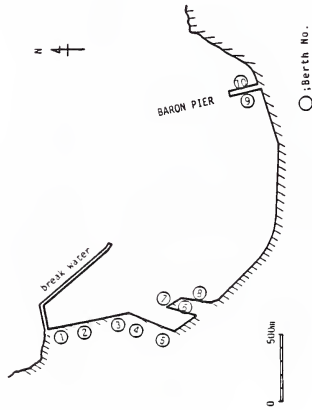
Fig. 2 Plan of Valparaiso port

BARON PIER
break water
○ ;Berth No.
N
0   500m

397

Fig. 7 Plan of San Antonio port

Fig. 8 Boring log of Berth 1 at San Antonio port

Fig. 5 Cross section of Berth 4 at Valparaiso port

Fig. 6 Cross section of Berths 6 and 8 at Valparaiso port

398

Fig. 11 Cross section of Berths 6 and 7 at San Antonio port

(unit : m)
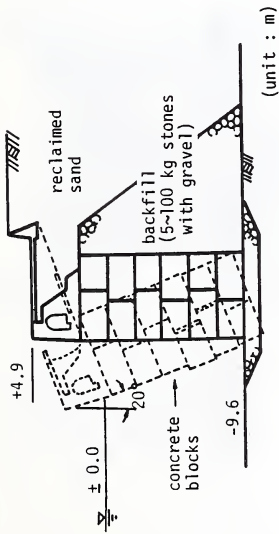
Fig. 9 Cross section of Berths 1 and 2 at San Antonio port
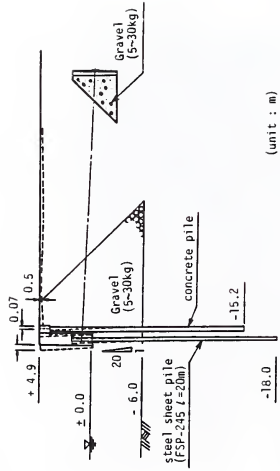
Fig.10 Cross section of Berth 3 at San Antonio port

399

Photo 3 Opening between Coping and Apron of Berth 3 at San Antonio Port

Photo 4 Settlement of Back Yard of Berth 5 at San Antonio Port
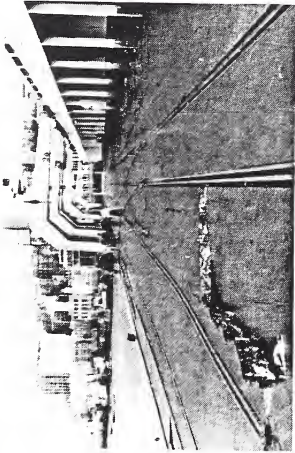
Photo 1 Damge to Apron and Crane Raling of Berth 8 at Valparaiso Port
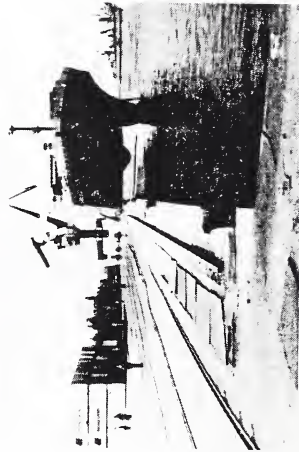
Photo 2 Copeline Deformation of Berth 5 at Valparaiso Port

Photo 5 Settlement of Apron of Berth 6
at San Antonio Port

Photo 6 Collapse of Wharf Crane of Berths 1
and 2 at San Antonio Port

Photo 7 Hole due to Liquefaction of Berth 3
at San Antonio port

401

OBSERVATION OF THE STRUCTURAL
DAMAGE CAUSED BY THE 3 MARCH 1985
CHILE EARTHQUAKE

Summary of a Talk

by

Mete A. Sozen[1]

Following by 10 seconds an event that appeared to be a precursor shock of magnitude (body-wave) 5.2, a major earthquake of body-wave magnitude 6.9 and surface-wave magnitude 7.8 (NEIS) struck 40 km off the coast of San Antonio, Chile, at 7:47 p.m. local time on 3 March 1985. The resulting strong ground motion affected a large area which more than half the population of Chile lives. The affected zone includes coastal towns of Valparaiso and Vina del Mar. The total direct and indirect damage was estimated to approach two billion dollars (U.S.).

Because of the occurrence of major events in that area with a return period of almost a century and because of the expectation of another event between the years 1980 and 2000, an extensive strong-motion instrument network had been installed in the region as a joint project of the Organization of American States and the University of Chile. This network yielded 31 strong-motion recordings with horizontal accelerations ranging up to 0.67g. This collection of strong-motion data is certainly the most important aspect of the 3 March 1985 Chile earthquake from the viewpoint of structural engineering because structural damage was, on the whole, light for recent construction. The number of casualties attributed to the earthquake was 176 which also indicates that structural performance was generally satisfactory, considering the number of population centers affected. Had such a convincing collection of strong-motion data not been available, the event might have been dismissed as one corresponding to relatively weak ground motion, despite its magnitude. As in the past, the few failures would have been attributed to flaws in design or construction. The successes would have been ignored.

An important feature of the strong-motion data obtained for this event caused by a subduction fault is its spatial distribution. Figure 1 shows the scatter in the variation of the maximum horizontal acceleration with epicentral distance. The data in Figure 1 have been plotted to linear x- and y- scales. Figure 2 shows the same data plotted logarithmically. Even though the logarithmic representation appears to imply the existence of a trend, it does not change the facts which require serious study in view of the practice of using the epicentral distance as the dominant factor in estimating ground-motion intensity.

The acceleration response spectra calculated ($\beta = 0.02$) for the 1940 El Centro N record ($A_{max} = 0.33g$) and the 1985 Vina del Mar record S20W record ($A_{max} = 0.36g$) are compared in Figure 3. (The spectrum for Vina del Mar was based on values reported by R. Sarragoni.) In terms of instrumental indication, the two events would be expected to have comparable damage potential. But the overall record of the large inventory of buildings in Vina del Mar was quite good. Given that the design-code requirements for lateral strength were comparable to those used in zones of high seismicity elsewhere in the world and that the detail requirements for the reinforced concrete buildings were not demanding, it follows that detailed studies of the reasons for the satisfactory performance of the Vina del Mar buildings may have a very strong impact on building construction for earthquake resistance.

[1]Department of Civil Engineering, University of Illinois, Urbana, IL

VARIATION OF MAX. ACCELERATION WITH DISTANCE

Figure 1

Figure 2

Figure 3

405
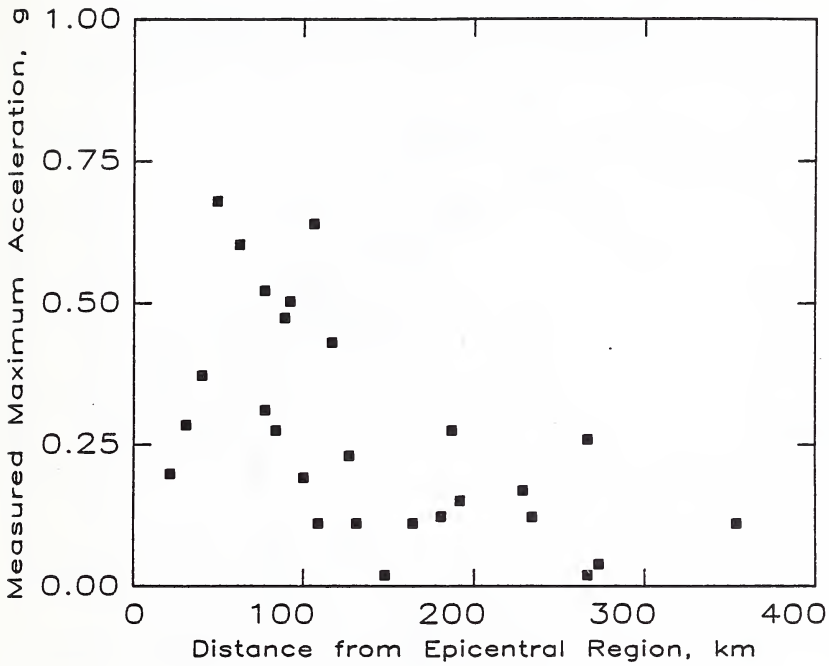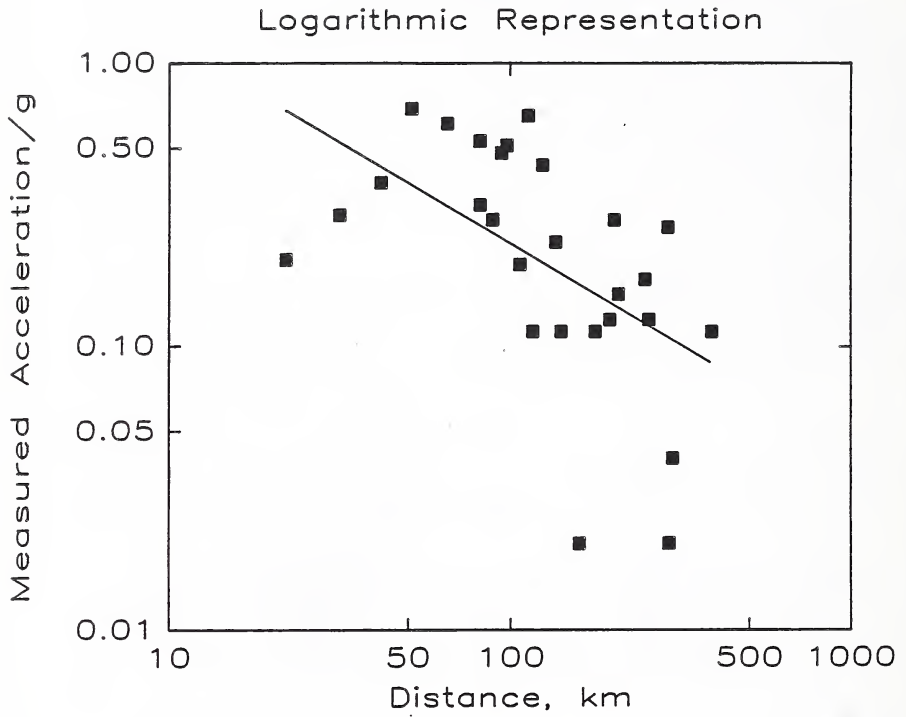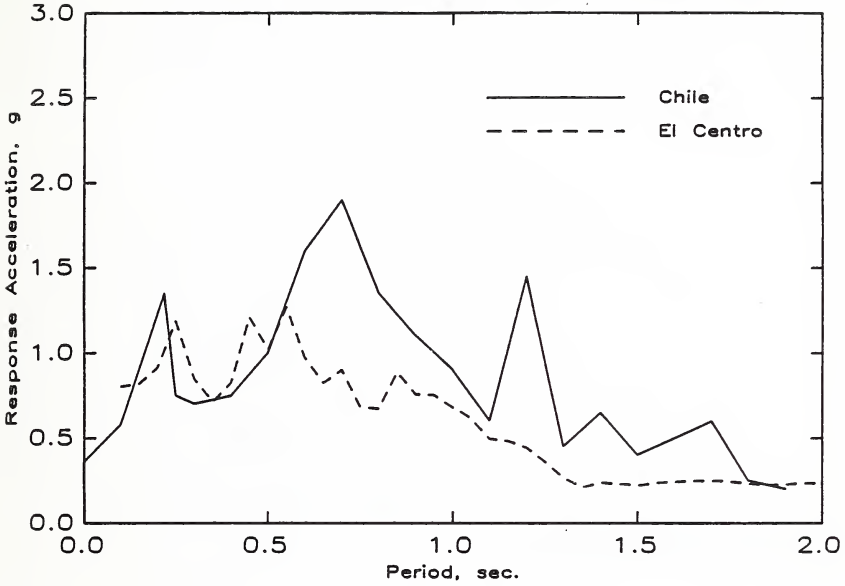
**Papers Not Presented Orally
But Included In The Proceedings**

SPATIAL STRUCTURE OF THE WIND IN THE MARINE BOUNDARY LAYER

BY

Keikichi Naito*, Tatsuo Hanafusa**, and Tokunosuke Fujitani**

ABSTRACT

This study investigated the temporal and
spatial structures of the wind in the marine
boundary layer. For this purpose the array of
instrumented towers is located at the seaside.
The results of preliminary analysis of low-wind
speed data are presented. The eddy is hori-
zontally isotropic in unstable condition, but
is elongated along the mean wind direction in
stable condition. In unstable condition the
lateral coherence function of longitudinal
velocity component followed exponential decay
formula, but that of lateral component followed
approximately the theoretical formula derived
from the theory of isotropic turbulence.

1. INTRODUCTION

There have been many studies of turbulent
characteristics of the wind in the marine
boundary layer. However, there remains insuf-
ficient knowledge of the spatial structure of
the offshore wind, because wind measurements at
various points on the sea surface are difficult
to perform. In the present study, an array of
instrumented towers is located at the seaside.
The preliminary observation begun in 1984, and
overall data collection started in March of
1985. High winds have not been observed, but
the results of preliminary analysis of low-wind
speed data are presented.

2. OBSERVATIONAL SITE AND INSTRUMENTATION

The observational site is located at the
seacoast of the Pacific Ocean, about 100 km
east of Tokyo. The shoreline is straight and
the topography is flat and open. One 36 m and
three 20 m towers form the observational array
which is parallel to the beach about 70 m down-
wind from the shoreline. The dunes of 2 m high
are located about 30 m apart from the array as
shown in Fig. 1. The separation distances of
20, 40 and 80 m are used. Three 3-cup anemome-
ters are provided at 10, 20 and 35 m for verti-
cal wind profile measurement and two resistance
thermometers are installed at 10 and 35 m. The
2-dimensional sonic anemometer at 35 m high can
measure wind speed and direction, and these
data are fed into the automatic sequence con-
troller for unmanned operation of the data

* Meteorological Satellite Research Division.
**Meteorological Research Institute, Japan
  Meterological Agency, Tsukuba, Ibaraki 305,
  Japan.

acquisition system. The 3-dimensional sonic
anemometer-thermometers are provided at the
20 m level of each tower for measuring
fluctuations of wind velocity components and
temperature.

The preliminary observation was executed by
using a 36 m and two 20 m towers.

3. AERODYNAMIC CHARACTERISTICS OF THE SITE

In this study, the observation was performed
near the seacoast, thus it is necessary to
evaluate the effect of the modification of the
wind field induced by the change of surface
roughness at the land-sea interface. Following
the equations of Jackson (1) and Wood (2), it
is possible to evaluate the height of the
internal boundary layer developed from the
land-sea interface. The roughness height over
a sandy beach is assumed to be 0.1 cm. The
estimated value of the internal boundary layer
height is about 2 m or 3 m. This value is
small enough to compared it to the lowest
observational height of 10 m.

To ascertain the aerodynamic characteristics of
the site, vertical wind profiles are obtained.
The wind speed ratios averaged for total
sampling duration are shown in Fig. 2. The
profile follows the logarithmic law; the
estimated roughness length is about 0.08 mm,
which is compatible with other results obtained
over open ocean. Result suggests that the
observed wind, at this site, has the
characteristics of offshore wind.

4. RESULTS AND DISCUSSION

The data discussed in this study were obtained
under stable and unstable conditions. A sam-
pling rate of 50 or 100 msec was used for mea-
surements and in the analysis raw data were
averaged for every 1 second. The data were
divided into sub-data blocks for 10 minutes,
and turbulence statistics were computed for
each sub-data block.

To investigate the spatial extent of the eddy,
the integral scales of each velocity component
were evaluated from correlation functions. The
integral scale of longitudinal component (u)
was evaluated from autocorrelation curve by
assuming Taylor's hypothesis. In unstable con-
dition, the block-to-block and tower-to-tower
variabilities of the integral scale are not so
large. On the other hand, in stable condition
both variabilities are somewhat larger. The
mean values of integral scale of u component

are 126 m in unstable and 81 m in stable conditions, respectively. The lateral extent of the eddy was evaluated from the lateral spatial correlation of lateral velocity component(v). The cross correlation analysis shows that the correlation of v component is larger than that of u component and also the correlation of vertical velocity component (w) is negligibly small with the separation distance longer than 20 m. The correlation peak of u component shifts progressively as increasing separation distances. In stable condition, the correlation of v component is also larger than that of u component and the correlation of u component with the separation distance longer than 20 m are very small. Figure 3 shows the variations of the cross correlation in lateral direction. In the preliminary observation, the separation distances are insufficient to carry out the numerical investigation. Therefore, in the present study, the exponential decay assumption was applied to these data. Estimated integral scales of each velocity component for longitudinal and lateral directions are given in Table 1. The main features of this table shows that in unstable condition the scale of u component was almost the same as that of v component. This fact suggests that the eddy seemed to be horizontally isotropic in unstable condition. Meanwhile, in stable condition, the scale of u component was about 3 times larger than the scale of v component, that is, the eddy was elongated along the mean wind direction.

Figure 4 shows the lateral coherence of u and v components in unstable and stable conditions. In unstable condition the coherence of u component can be well expressed by the exponential decay function, and the broken line is corresponding to the curve with the decay parameter k=8. On the other hand, the coherence of v component is determined by a slightly different formula. The similar shape to this curve can be derived theoretically from the homogeneous and isotropic turbulence (Kristensen and Jensen (3)). As mentioned before, the eddy in unstable condition was horizontally isotropic, thus, the present result obtained here is probably reasonable. In stable condition, lateral coherences also are well expressed by the exponential decay formula.

5. CONCLUDING REMARKS

To investigate the spatial structure of the offshore wind, the instrumented tower array is provided near the seacoast and preliminary observation was executed. The evaluated integral scales of turbulence suggest that the eddy is horizontally isotropic in unstable condition and is elongated along the mean wind direction in stable condition. The lateral coherence functions except v component in unstable condition can be described by

exponential decay formula. The coherence of v component in unstable condition can be described by different formula approximately similar to the theoretical result of homogeneous and isotropic turbulence. The authors executed the overall measurements using good collected data. They will present the results of their detailed analysis in the near future.

6. REFERENCES

1) Jackson, N. A., 1976, The Propagation of Modified Flow Downstream of a Change in Roughness, Q. J. Roy. Met. Soc., 102, 924-933.

2) Wood, D. H., 1982, Internal Boundary Layer Growth Following a Step Change in Surface Roughness, Boundary Layer Met., 22, 241-244.

3) Kristensen, L. and N. O. Jensen, 1979, Lateral Coherence in Isotropic Turbulence and in the Natural Wind, Boundary Layer Met., 17, 353-373.

Table 1 Integral scales for each velocity component.

Stability	Direction	U	v	w
Unstable	Longitudinal	126m	218m	37m
	Lateral	52m	134m	–
Stable	Longitudinal	81m	77m	26m
	Lateral	17m	28m	–
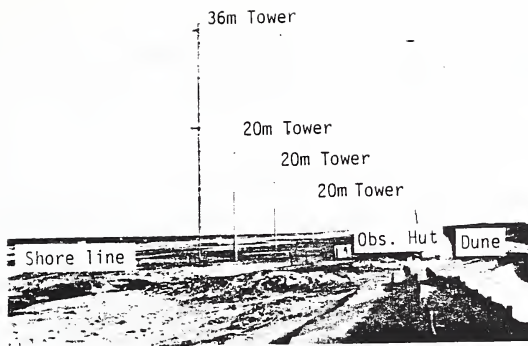
Fig. 1   View of tower array.
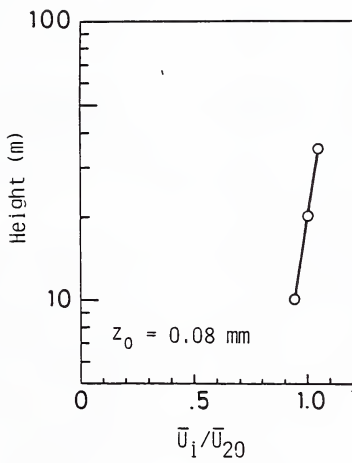
Fig. 2   Vertical wind profile.
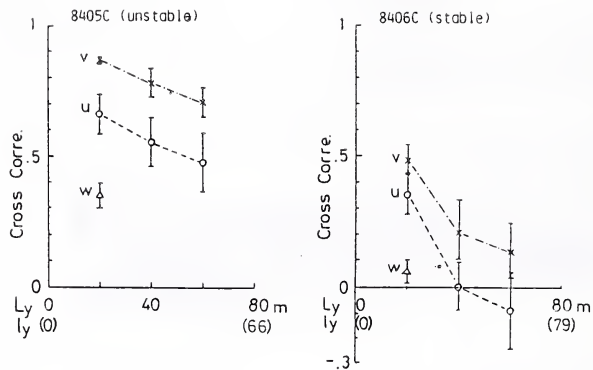
Fig. 3 Spatial crosscorrelation for lateral direction.
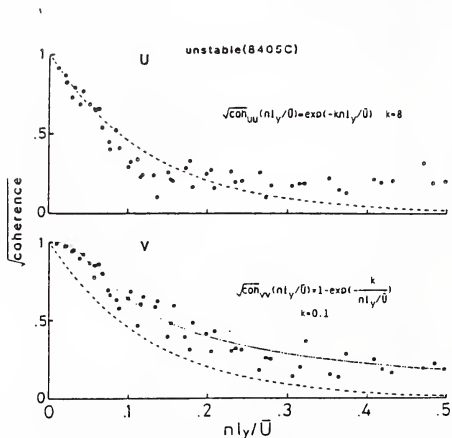
Fig. 4 Lateral coherence of u and v components.

LOADING TEST ON THE CONNECTION
OF CONCRETE FILLED STEEL TUBES

BY

Hirohiko Tada [1], Hiroshi Shinohara [II], Koichi Minosaku [III],

Akira Takizawa [IV], and Jun Hikino [IV]

ABSTRACT

Concrete filled steel tubes have good load-resisting performance as a composite structure composed of steel and concrete. However, it is important to examine the load-resisting performance of the connection using concrete filled steel tubes to reflect the actual design of bridge piers in urban expressways and monorails.

Five different models of the connection were made; static loading tests were performed to investigate the difference of the load-resisting behavior with respect to the existence of filled concrete, studs and diaphrams, and understand the region of filled concrete.

Loading test results showed little difference in the capacity and the performance of deflection of each speciment; on the whole the specimens with filled concrete show good loading-resisting peformance.

1. INTRODUCTION

As described in previous reports [1]-[4], concrete filled steel tubes (hereafter called "CFST") have large capacity and good ductility as a composite structure composed of steel and concrete. The application of CFST to bridge piers in urban expressways and monorails require large capacity and aseismatic performance. However, the peformance of CFST is confirmed for simple members such as a beam and a column. There is no complete data on its peformance for applying to actual structures.

There is concern that the collapse of the connection leads to the collapse of a structure in cases when the CFST is not adequately designed.

In general, conditions required for the connections required for the connection are:

(1) withstand collapse before bridge piers show original strength and ductility.

(2) possess ample strength and rigidity to be satisfied with the assumption in the calculation that the part of connection is a rigid point.

Against these requirements, there are many studies on connections of steel piers, and practical design methods, presented by Okumura et al. .

There are few studies about the connection when using CFST as a column; the design method and structual details are not filled concrete, its connection needs to have higher load- resisting performance than a steel column.

The author intented to determine the desirable CFST connection in this loading test. Five models of the connection in rigid frame piers were made, and static loading tests were performed to investigate the difference of the load-resisting behavior with respect to filled concrete, studs and diaphrams and the region of filled concrete. Then, the estimation of the specimens rigidity by two dimensional finite element method and the comparison of test results and theoretical results by the calculation program for beding capacities under changeable axial force were performed.

I)   Director of Structure and
      Bridge Department, PWRI
II)   Chief of Bridge Division,
      Structure and Bridge
      Department, PWRI
III) Research Engr. of Bridge
      Division, Structure and
      Bridge Department, PWRI
IV)   Research Asst. of Bridge
      Division, Structure and
      Bridge Department, PWRI

2. OUTLINE OF TEST METHOD

2.1 Specimens

As described in the introduction, five types of models of the connection in rigid frame typed piers were made to determine the desirable type of connection CFST. The dimensions and the specifications for each specimen are indicated in Table-1 and Fig.-1. Ready-made steel tubes with thin walls were used as a column.

Beams were made of steel plates. Stiffened plates are attached to eliminate local deflection from concentrated forces near the applied point of force. Double rigid steel plates are arranged at the lower edge so the specimen can be fixed in the bed of the testing machine.

In the design of specimens, the beam is designed to fail only after the collapse of its column connection. This was done to understand the difference of the load-resisting behavior for each specimen with the following features (see. Fig. -2)

Type A ----This is the standard specimen without filled concrete in the beam and column. A diaphram is attached to prevent local buckling in the inside of a colunm adjacent to the lower flange of a beam.

Type B ----This specimen has filled concrete in the column in part of the beam; it does not have a stud or a diaphram. A thin steel plate is fixed in place of the form to fill into concrete in the designated part of beam.

Type C ----This specimen has filled concrete in the column to determine the need for concrete in a beam.

Type D ----This specimen is similar to Type B, but a solid diaphram is arranged in a beam. This diaphram is expected to prevent the sliding in the boundary between steel and concrete and the volume expansion of concrete in the plastic region.

Type E ----This specimen is similar to Type B, but studs are arranged near the joint between the beam and column. The stud is expected to prevent sliding in the boundary between steel and concrete and the separation of concrete from steel due to the difference of Poisson's ratio in steel and concrete.

The Concrete used has specifications as shown in Fig.-2 so compressive strength of 240kg/cm^2 can be obtained. Average compressive strength of three cylinders is (10 cm in length and 20cm in diameter), at seven days is 251kg/cm^2.

2.2 Loading method

Loading tests are performed using the 3000 ton large universal structual testing machine installed in PWRI's structure engineering laboratory. Each specimen is fixed in the testing machine bed by bolts not subjected to eccentric force. Photo-1 shows the specimen.

A static load is applied to the top plate of the specimen until specimen's horizontal displacement reaches the allowable stroke of the testing machine controlling the load in the region of low load and the displacement in the region of high load. The upper edge is possible to move freely in the horizontal direction and the rotation by the above equipment for loading.

2.3 Measuring method

Strain gauges and displacement indicators are set as shown in Fig.-3(a) and (b). Strains on the surface of steel and displacements at prescribed points are measured at fixed loads. Particularly, three directional guages are attached on the surface of steel near the joint between a column and a beam so detailed distribution of the stress can be measured. Also, the change of deflectional angle at the joint and the lower edge is indirectly measured by setting the rolling typed displacement indicators. The separation of mill scale and the out-of-plane deflection are observed during the tests.

414

3. TEST RESULTS AND DISCUSSION

3.1 General

Type B to Type E with filled concrete in the columns show large capacity and sufficient ductility in comparison with Type A without concrete. Figs. 4(a) to (e) show the situation after loading for each specimen (ref. Photo -2 and 3). Type A indicates large out-of-plane deflection near the joint in a column at almost maximum load, and its deflection grows in proportion to the increment of load. Simultaneously, the separation of mill scale is seen only at lower flange.

Type B shows the separation of mill scale near the joint in a column at a load of 170 ton. Thereafter, the out-of-plane deflection near the joint in the lower flange of a beam is observed.

It is recognized that the performance of Type C to Type E is approximately same as that of Type B. However, Type C indicates the mode of local buckling toward the inside of a beam near the joint. This probably results because this specimen type does not have filled concrete in the beam. Also, the out-of-plane deflection near the joint in beams of Type D and Type E is slight compared with that of Type B. This may be caused by the stud and diaphram. Filled concrete prevents the out-of-plane deflection toward the inside of steel and the arrangement of studs controls the out-of-plane deflection toward the outside of steel.

3.2 Capacity

Table-3 shows theoretical results and test results related to three kinds of load.

The following are assumed in the calculation of capacities.

(1) No slip occurs in the boundary between steel and concrete. That is, the distribution of longitudinal strains at a section follows the assumption of the plane preservation (bending cracking load and steel yielding load).

(2) Neither shear failure nor local buckling occurs.

(3) The tensile strength of concrete is negligible in the calculation of steel yielding load and load corresponding to the full-plastic resisting moment.

(4) The stress-strain relationships of steel and concrete follows the relationship as shown in Fig.-5(a), (b) respectively.

Based on these assumptions, the section is divided into small elements as shown in Fig.-6, and numerical analysis is performed using Newton-Raphson method with two parameters, which are the position of neutral axis e and the local P.

In the analysis, the initial values of the veritical load and the position of neutral axis, P_o, e^o, are obtained by the elastic theory, and in turn are corrected in accordance with equation-(1 to equation-(4), so that the equilibrium of force can be satisfied and strains of upper or lower fiber at a section become prescribed become prescribed values.

(1) To axial force

$$F_n = N + \left(\sum_{k=1}^{m} (\sigma_{sk} \cdot A_{sk} + \sigma_{ck} \cdot A_{ck}) - \sum_{j=1}^{n} (\sigma_{sj} \cdot A_{sj} + \sigma_{cj} \cdot A_{cj}) \right) = 0$$

(2) To bending moment

$$F_m = M - \left(\sum_{k=1}^{m} (\sigma_{sk} \cdot A_{sk} \cdot Z_{sk} + \sigma_{ck} \cdot A_{ck} \cdot Z_{sk}) \right.$$
$$\left. - \sum_{j=1}^{n} (\sigma_{sj} \cdot A_{sj} \cdot Z_{sj} + \sigma_{cj} \cdot A_{cj} \cdot Z_{sj}) \right) = 0$$

$\cdots (1)$

in which, N ; Axial force due to external force(kg)

Column : $N = P \cdot \cos \theta$

Beam : $N = P \cdot \sin \theta$

M ; Bending moment due to exteral force (kg.cm)

Column : $M = P \cdot \cos \theta \times (11.2 + e) + P \cdot \sin \theta \times 168$

Beam : $M = P \cdot \cos \theta \times 109.5 - P \cdot \sin \theta \times e$

$$\Delta p = - \frac{F_m(p,e) \cdot G_{n,e} - F_n(p,e) \cdot G_{m,e}}{G_{m,p} \cdot G_{n,e} - G_{n,p} \cdot G_{m,e}}$$

$$\Delta e = - \frac{F_n(p,e) \cdot G_{m,p} - F_m(p,e) \cdot G_{n,p}}{G_{m,p} \cdot G_{n,e} - G_{n,p} \cdot G_{m,e}}$$

$\cdots \cdots \cdots \cdots (2)$

$$G_{n,p} = \frac{F_n(p + \Delta po, e) - F_n(p,e)}{\Delta po} , \quad G_{n,e} = \frac{F_n(p, e + \Delta eo) - F_n(p,e)}{\Delta eo}$$

$$G_{m,p} = \frac{F_m(p + \Delta po, e) - F_m(p,e)}{\Delta po} , \quad G_{m,e} = \frac{F_m(p, e + \Delta eo) - F_m(p,e)}{\Delta eo}$$

$\cdots (3)$

$$\Delta po = \frac{p}{1000} , \quad \Delta eo = \frac{e}{1000}$$

$\cdots \cdots \cdots \cdots (4)$

It is assumed that the capacity of all specimens are determined by the capacity of a column as in the design of specimens from Table-3. This is also realized from the fact that the out-of-plane deflection is large near the joint. However, as long as the Type C without filled concrete in a beam is concerned, the influence of the out-of-plane deflection in a beam upon the capacity is realized because the capacity of this specimen is larger than the load correspond-ing the full-plastic resisting moment. Its capacity is slightly smaller than that of Type B, D, E. Type A indicates the incre-ment of out-of-plane deflection from near the steel yielding load, and its capacity is considerably smaller than the load corresponding to the full-plastic resisting moment. Filled concrete inside a column or a beam has sufficient resistance against the load and holds the increase of strength after steel yielding. This occurs because filled concrete prevents the development of out-of-plane deflection of steel.

Compared calculated values with measured values for the steel yielding load, a measured values are smaller than calculated values in all specimens. And especially, measured values of Type A and Type C related to a column are comparatively smaller than calculated values. Therefore, the influence of shear lag is needed in the case of connections as Types B, D, and E, and certainly for Types A and C.

3.3 Rigidity and ductility

Fig. 7 to 10 show the relationships between the vertical load and vertical displacement, horizontal displacement, the ratio of vertical displacement to horizontal displacement, and the deflectional angle at the joint respectively. Furthermore, the results of linear analysis by the finite element method, in which specimens are replaced to the two dimensional plate model as shown in Fig. 11, are indicated in Fig. 7 & 8, and Fig. 10. S-line shows load-displacment relationships provided that flexual rigidity of only steel is taken into account, and S+C-line indicates both concrete and steel. The ratio of Young's modulus in steel and concrete is considered in the evaluation for rigidity of filled concrete. The plate thickness and the plate width of analytical model are determined so that a fiber strain $\overline{\quad}$ in specimens and the analytical model can be coincide. That is, area of cross-section A and section modulus W in the following equation are made to be equal in specimens and the analytical model.

$$\sigma = \frac{M}{W} + \frac{P}{A} \qquad \cdots \cdots \cdots (5)$$

in which: M; Moment due to external force

P; Axial force due to external force

Fig.-3 indicated previously that bending cracks occur; and the relationship between the load and the displacement becomes unlinear in Type B to Type E. However, it is found from Fig.-7 and 8 that the relationship between the load and the displacement including that of Type A are almost linear up to the steel yielding load, the thereafter the displacement becomes larger.

Compared the slope of the straight line of Type A with that of Type B to Type E before the steel yielding; it is realized that the rigidity of specimens becomes large by the effect of filled concrete. For instance, the displacement of Type B to Type is almost 50% of that of Type A at 50 ton load. Furthermore, the ductility of Type B to Type E is improved by filled concrete compared with that of Type A because the load decreases in Type A and not observed in Types B to E.

The relationship between the load and the ratio of horizontal displacement to vertical displacement shown in Fig.-9 is dispersed by the setting error and measuring error in the range of small load. Thereafter, its relation continues to be an almost constant value; it increases near the maximum load. This means that the deflection of a column abruptly increases near the maximum load, and the capacity of specimens is determined by the capacity of the column.

It is determined that both filled concrete and steel resist the load in theoretical calculation, because measured values of Types B to E in Fig.-7 and Fig.-8 lie on S+C-line approximately. Measured values of horizontal displacement of Type A in Fig.-8 lie on almost S-line, but measured values of vertical displacment of Type A in Fig.-7 is considerably larger than theoretical values. This reason is Type A is affected severely by the shear lag and the out-of-plane deflection compared with other specimens.

3.4 Characteristics of strain

Fig.-12 and -13 show the relationship between the load and the tensile strain at positions indicated. Fig.-14(a) to (e) show the distribution of longitudional strains in a column at representative loads. First, it is shown from Figs. -12 to -13 that type a beam yields after column yielding near a load of 60 ton; there is little increase of strain in a beam after column yielding. This means that only the column goes toward collapse. Types B to E suggest almost the same relationships between the load and the strain. The strain in a beam increases after column yielding because the column does not collapse (due to the filled concrete). It is determined from Fig.-14 that the influence of shear lag in Type C and Type A is larger than that of other specimens.

4. CONCLUSION

The following results were obtained from these loading tests.

(1) The influence of shear lag can be reduced.

(2) The out-of-plane deflection can be controlled, and the strength in the plastic region is expected.

Large carrying capacity greater than the full-plastic resisting moment and good ductility resulted.

The ductility and characteristics of strain, Type B, Type D and Type E which have filled concrete in the column and the beam are desirable types of connection when concrete filled steel tubes are used as a column.

It was determiend that the rigidity of concrete filled steel tubes in the elastic region can be evaluated as a composite structure provided that the ratio of Young's modulus in concrete and steel is taken into consideration.

REFERENCES

1) Narita, N., Saeki, S., Kanai, M., Oshio T., "Behavior of Concrete Filled Steel Tubes (Part 1; Compression Members)", Technical Memorandum of PWRI No. 1771, February, 1982.

2) Narita, N., Saeki, S. Kanai, M., "Behavior of Concrete Filled Steel Tubes (Part 2; Bending Members)", the 15th Joint Meeting of U.S.-Japan Panel on Wind and Seismic Effects, UJNR, May, 1983.

3) Saeki, S., Minosaku, K., Takizawa, A., "Behavior of Concrete Filled Steel Tubes (Part 3; Beam-Column Members)", the 16th Joint Meeting of U.S.-Japan Panel on Wind and Seismic Effects, UJNR, May, 1984.

4) Tada, H., Shinohara, H., Minosaku, K., Takizawa, A., Hikino, J. J., "A Study on Behavior of Concrete Filled Steel Tubes", Proc. of the 2nd J Task Committee, September, 1985.

5) Okumura, T., Ishizawa, N., "The Design of Knee Joints for Rigid Steel Frames with Thin Walled Section", Transactions of the Japan Society of Civil Engineers, No. 153, May, 1968.

Table.1 Specifications for Specimens

Type of specimens		A	B	C	D	E
Column	Diameter (mm)	609.6	609.6	609.6	609.6	609.6
	Thickness (mm)	9.5	9.5	9.5	9.5	9.5
	Designation	STK41	STK41	STK41	STK41	STK41
	Yield strength (kg/cm²)	3,500	3,500	3,500	3,500	3,500
	Breaking strength (kg/cm²)	4,800	4,800	4,800	4,800	4,800
Beam	Width (mm)	450	450	450	450	450
	Height (mm)	450	450	450	450	450
	Thickness (mm)	19	19	19	19	19
	Designation	SS41	SS41	SS41	SS41	SS41
	Yield strength (kg/cm²)	3,000	3,000	3,000	3,000	3,000
	Breaking strength (kg/cm²)	4,500	4,500	4,500	4,500	4,500
Concrete	Column	without	with	with	with	with
	Beam	without	with	without	with	with
Concrete strength (kg/cm²)		—	251	251	251	251
Stud		without	without	without	without	with 9.5φ×80
Diaphram		without	without	without	with t=16mm (SS41)	without
Remarks					effect of diaphram	effect of stud

Table.2 Specification for concrete

Nominal strength	Unit (m³)	Cement C (kg)	Water W (kg)	W/C (%)	Fine aggregate (kg)	Coarse aggregate (kg)	Slump (cm)	Air content (%)
240	1.0	251	148	59.0	839	1,119	8.0	4.0
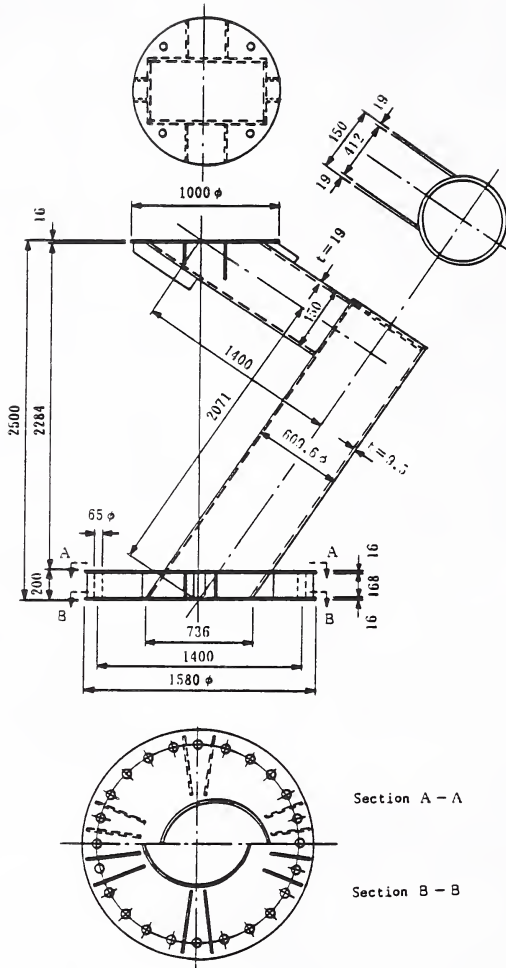
Fig.1 Configuration of Specimen

420

(a) Type−A

(b) Type−B

Filled Concrete

(c) Type−C

Diaphram

(d) Type−D

(e) Type−E

Stud
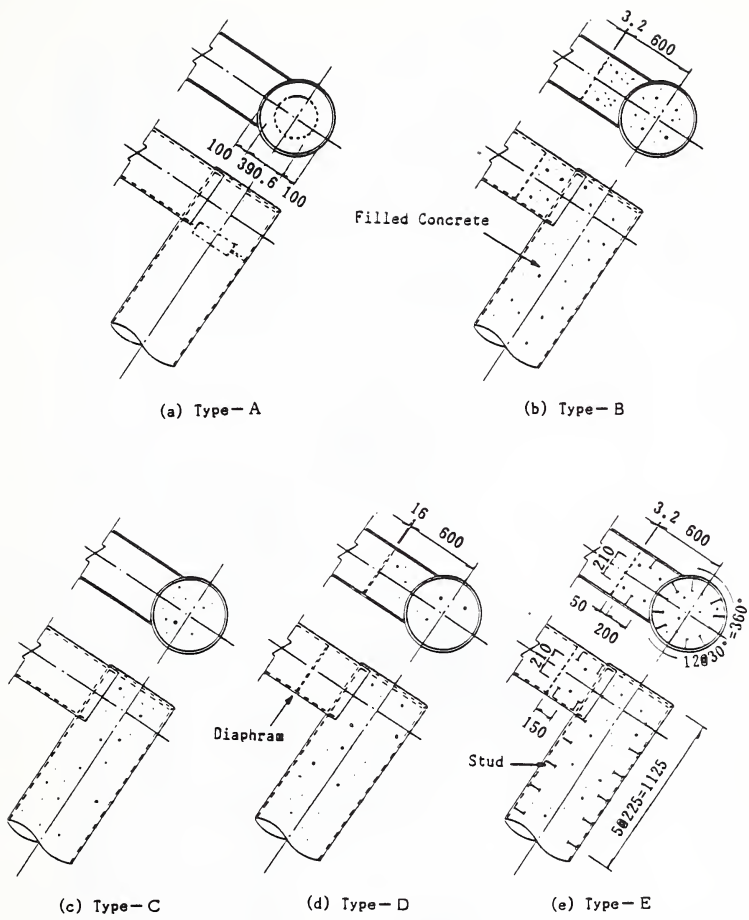
Fig.2 Detail of Connection Part

Section A-A

Section 1 2 3 4 5

Section B-B

Section C-C

□ : One-Directional Guage

○ : Three-Directional Guage

(a) Mesuring Position of Strains

→ : Displacement Indicator

○ : Mesuring Position of Displacement

(b) Mesuring Position of Displacement

Fig.3 Mesuring Method
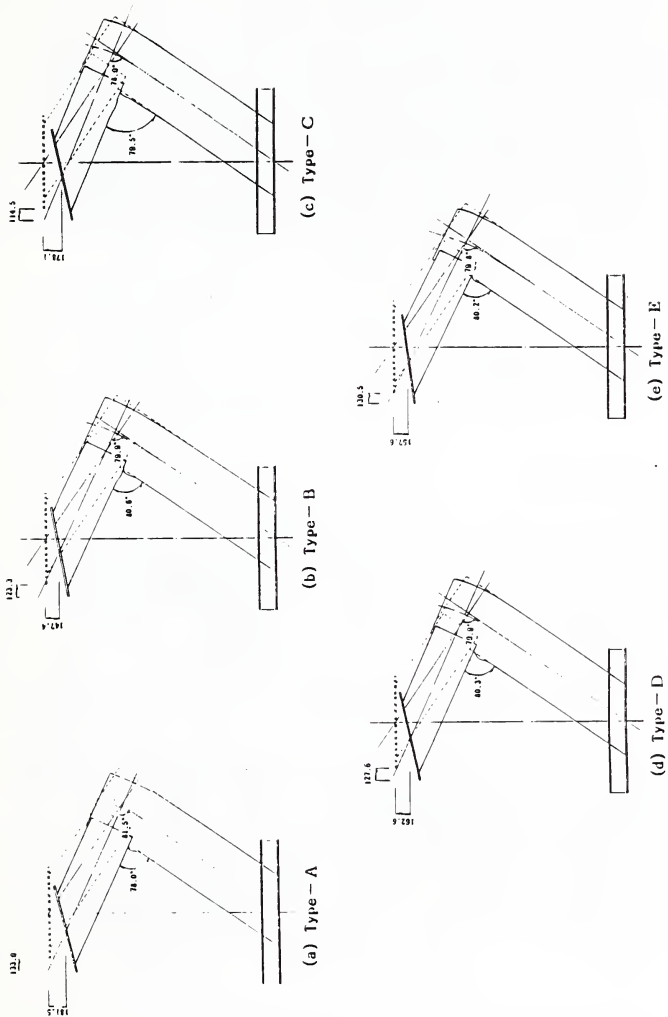
Fig.4 Situation of Specimens after Loading

(a) Type – A

(b) Type – B

(c) Type – C

(d) Type – D

(e) Type – E

423

Table.3 Theoretical and Experimental Resistance

Specimen		Bending Cracking Load			Steel Yielding Load						Maximum Load		
					Tension Side			Compression Side					
Type		Measured Value Pce	Calculated Value Pcc	Pce/Pcc	Measured Value Pye	Calculated Value Pyc	Pye/Pyc	Measured Value Pye	Calculated Value Pyc	Pye/Pyc	Measured Value Pue	Calculated Value Puc	Pue/Puc
A	Column	–	–	–	57.3	96.5	0.59	75.8	80.4	0.94	88.4	113.1	0.78
	Beam	–	–	–	72.2	165.8	0.44	–	143.0	–	–	186.1	–
B	Column	–	10.5	–	121.5	105.9	1.15	140.0	117.5	1.19	177.2	148.2	1.21
	Beam	–	15.3	–	102.9	165.8	0.62	–	165.2	–	–	192.1	–
C	Column	–	10.5	–	77.9	105.9	0.74	131.0	117.5	1.11	165.7	146.2	1.13
	Beam	–	15.3	–	87.1	165.8	0.53	–	143.0	–	–	186.1	–
D	Column	–	10.5	–	97.6	105.9	0.92	130.2	117.5	1.11	176.8	146.2	1.21
	Beam	–	15.3	–	93.0	165.8	0.58	103.1	185.0	0.62	–	192.1	–
E	Column	–	10.5	–	116.1	105.9	1.10	123.0	117.5	1.05	173.5	146.2	1.19
	Beam	–	15.3	–	97.3	165.8	0.59	98.3	165.2	0.60	–	192.1	–

1) Calculated Value of Maximum Load indicates Load corresponding to the full-plastic resisting moment.
2) Each Load shows values of Section A-A in a column and Section B-B in a beam.

(a) Steel   (b) Concrete
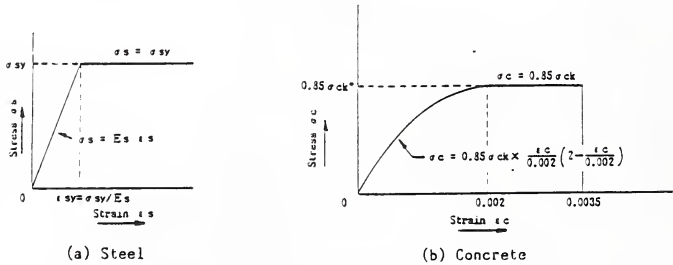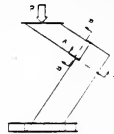
Fig.5 Stress—Strain Curve

(a) Column   (b) Beam   (c) Strain Distribution   (d) Stress Distribution
(i) Steel   (ii) Concrete
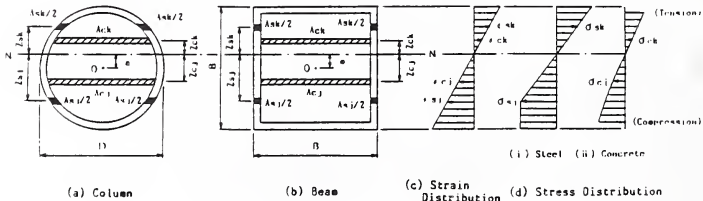
Fig.6 Element Division of Section for the Strength Calculation

Fig.9 Relation of Load and the Ratio of Vertical Displacement to Horizontal Displacement

Fig.10 Relation of Load and Deflectional Angle
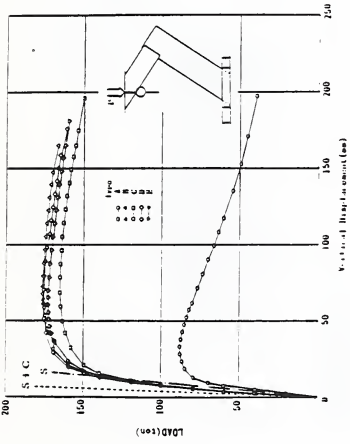
Fig.7 Relation of Load and Vertical Displacement
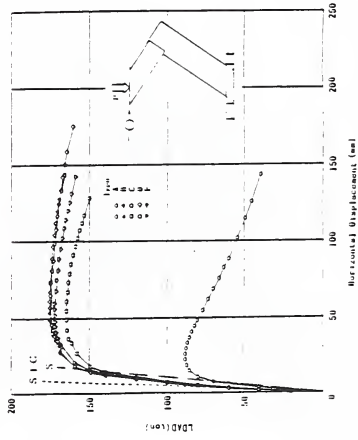
Fig.8 Relation of Load and Horizontal Displacement

425

Fig.12 Relation of Load and Strain in a Column
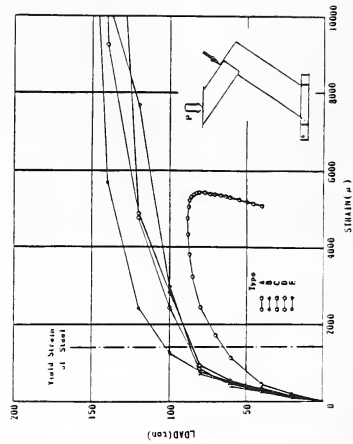
Fig.13 Relation of Load and Strain in a Beam

Input Data		Plate Thickness (cm)		
	Width B (mm)	Type-A	Type-B,D,E	Type-C
Column	B_1	45.72	1.922	9.266	9.266
	B_2	7.62	5.987	7.924	7.924
Beam	B_3	30.00	1.789	7.550	1.789
	B_4	7.50	18.260	21.830	18.260

Note : Young's Modulus $E=2.1\times10^6$ kg/cm Poisson Ratio $\nu=0.3$

Fig.11 Two-Dimensional Finite Element Model
for the Displacement Calculation

426
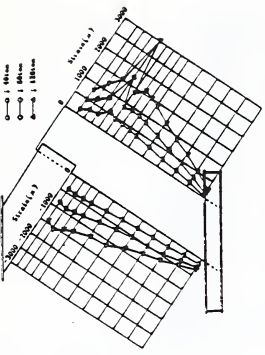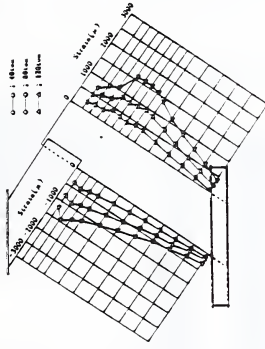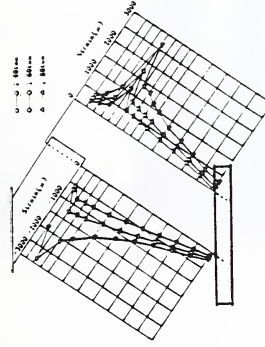
(a) Type-A

(b) Type-B

(c) Type-C
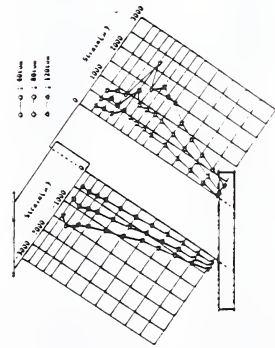
(d) Type-D
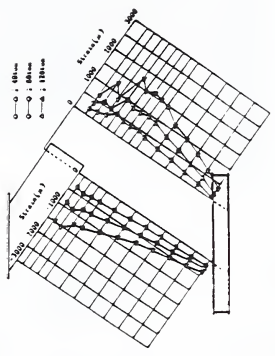
(e) Type-E

Fig.14 Distribution of Longitudinal Strains in a Column

427
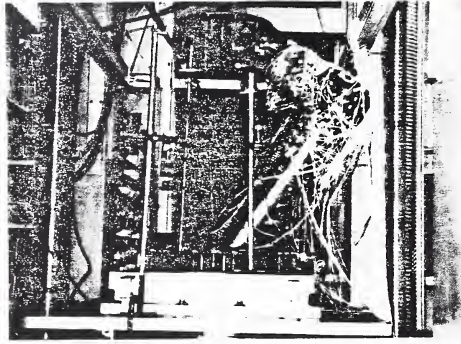
Photo.1 Setting Situation of Specimen
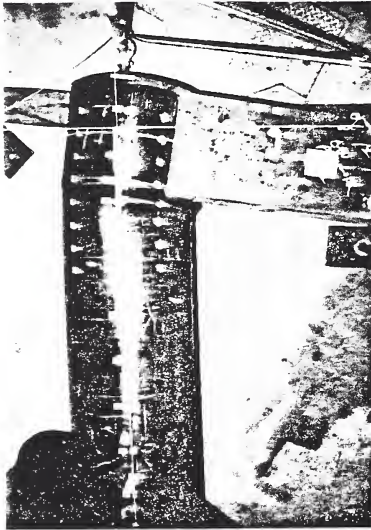
Photo.2 Situation after Loading
(Type-A)
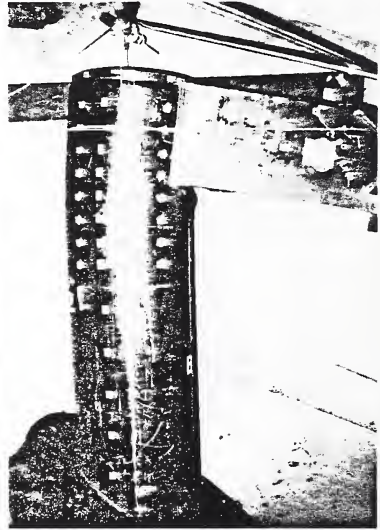
Photo.3 Situation after Loading
(Type-B)

DEFORMATION CAPACITY OF STEEL TRUSS GIRDER

BY

Isao Nishiyama[1], Tatsuo Murota[2], Nagahide Kani[3], and Shin-ichi Ina[3]

ABSTRACT

The aim of this research is to make clear the relation between the deformation capacity of steel truss girder and the slenderness ratios of the individual members or the failure mode of the steel truss girder. Six steel truss girders, composed of double angle section chords and braces, were loaded monotonically. Five girders of H-section chords, arranged by their weak axis in the plane of the girders, and circular tube braces were tested by cyclic loading.

The following results were obtained: (1) large deformation capacity can be anticipated, in a steel truss girder, if the slenderness ratio of individual members are small. (2) Steel truss girders of chord failure type should be restrained from its lateral buckling to ensure deformation capacity. (3) Steel truss girders of brace buckling failure type have little deformation capacity without slippages of joint bolts. (4) Overall deformation characteristics of steel truss girders can be evaluated as the sum of the deformation characteristics of the individual members which construct the girder. (5) Inelastic behavior of steel truss girders are largely affected by the plastic deformation of a few individual members near the end of the girder.

INTRODUCTION

According to the current seismic design standard in Japan (Ref. 1), both strength and deformation capacity are required for steel building structures. For full web members, many experimental investigations were conducted and the deformation capacity and the strength was well documented. For open web members such as trusses, however, research is needed to evaluate the deformation capacity. To obtain the fundamental data on the deformation capacity of steel trusses, bending tests were performed in two test series.

In the first, monotonic loading tests of six steel truss girders with double angle section chords and braces were performed. Here, the

[1] Research Engineer, Structure Engineering Department, Building Research Institute, Tsukuba, Japan.
[2] Director of Structure Engineering Department, BRI.
[3] Member of Structure Tech. Special Committee, Japan Federation of Architect Office Association, Tokyo, Japan.

rough consideration was done on the relation between the deformation capacity and the slenderness ratios of the chords and braces of the truss girders.

In the second series, cyclic loading tests were performed on five steel truss girders with H-section chords arranged by their weak axis in the plane of the girders and circular tube braces. The interaction of the inelastic behavior of the girders and the sectional shapes, slenderness ratios of the individual members used, or failure modes of the girders was considered. Moreover, each axial deformation of the individual member of the truss girder was measured. From the measured axial deformations, the overall deformation of the truss girder was estimated. The estimated deformation was compared with the overall deformation directly measured in the test.

2. TEST SPECIMEN

2.1 Series 1 Test

The representative shape of the six test specimens and its joint detail are shown in Fig. 1. Both top and bottom chords were made of a double angle section (2L-65x65x8). Diagonal braces also were made of a double angle section (2L-50x50x4). The ends of the braces were frictionally connected to the chords through the gusset plates by three high-strength-bolts. Only the depth and the shear span length of the truss girders were varied but the sections used and joint details were common in these specimens. See Figure 1 for and chords and braces. CU-, CD-, and B- are top chord, bottom chord, and diagonal brace respectively. The number, in these indexes, is counted from the left-hand side end of each girder. The dimensions of the test specimens are summarized in Table 1. The mechanical properties of steel are listed in Table 2.

2.2 Series 2 Test

The representative shape of the five test specimens is shown in Fig. 2. Both top and bottom chords were made of H-section members arranged by their weak axis to coincide with the plane of the truss girder. The braces were circular tubes, and the angle between chord and brace was 60 degree. Chord-to-brace joints were of fillet welding using gusset plates, which were arranged with a right angle to the

plane of the strong axis of the truss girder and inserted into the circular tube braces by cutting slits. Failure modes and slenderness ratios of the members, which seemed to fail, varied for each specimen. The dimensions of the test specimens are listed in Table 3. The mechanical properties of steel are listed in Table 2.

3. OUTLINE OF LOADING AND MEASUREMENTS

3.1 Series 1 Test

The test set-up and the measuring instrumentations are schematically shown in Fig. 1. Both ends of the test specimen were pin-roller supported and monotonic vertical force was applied concentrically just on the top of the vertical stiffener to induce triangularly distributed bending moment.

Lateral deflections were fully restrained at both ends and intermediate loading position of the test specimen. The rigid part of the specimen shown in Fig. 1 was much higher in rigidity than the testing part, so the rotation about the weak axis of the truss girder did not arise at the position of loading.

Measurements were conducted so the deformation of the specimen, as a cantilever beam, could be computed from measured data.

3.2 Series 2 Test

The test set-up is shown in Fig. 3. The test specimen is a cantilever type girder; one end fixed to the reaction wall and the other end subjected to vertical force by an actuator through T-shaped loading-rig. The out-of-plane truss deformation were laterally restrained at the *-marked locations in Fig. 3.

Three loading cycles were started from negative loading. They were carried out with the final collapse under the last positive loading, where the upward loading is considered positive loading in Fig. 3. Vertical and rotational deformations at both ends of the testing part of the specimens and axial deformations of CU-1 and -2, CD-1 and -2, and B-1, -2 and -3 were measured as shown in Fig. 4.

Axial strains of the members near the end subjected to maximum stresses were measured in both series of tests, but they are not referred to in this paper.

4. TEST RESULTS

4.1 Series 1 Test

Maximum strength and failure mode etc. of each specimen are summarized in Table 4. The applied load (shear in the testing part) vs.

displacement relationships of the specimens are shown in Fig. 5 to Fig. 10.

The yield strength of the specimen T-66-21 was about 14 tonf; after the yielding load carrying capacity increased to 16.4 tonf by strain hardening until it was interrupted by the buckling of B-1 brace (Fig. 5). However, the deterioration of the load carrying capacity was relatively small even after the buckling of the brace. The severe reduction of the strength of the specimen was observed after the lateral buckling of the girder. As for the maximum strength, the test result determined by brace buckling is far smaller than that calculated as tabulated in Table 4. The high stress concentration and the large eccentricity of diagonal brace is not considered in the calculation.

In specimen T-66-40 (Fig. 6) and in specimen T-99-40 (Fig. 7), brace yielding began at about 15 tonf, and the deformation increased with slippages of the high-strength-bolts connecting the braces to the chords. The broken lines in Figs. 6 and 7 show the reduction of load carrying capacity by the slippages. In the specimen T-66-40, the load carrying capacity increased to 16.2 tonf until disturbed by the buckling of the B-1 brace. After the reduction of the load carrying capacity, the trapezoid frame, which consists of CU-1, B-2, CD-1 and the vertical stiffener at the loading position, showed relatively stable restoring force characteristics. The stable strength was about 12.0 tonf.

The specimen T-132-60 failed by brace buckling as did specimens T-66-40 and T-99-40, but no slippage was observed, thus its deformation capacity was poor.

Both ends of the buckled braces rotated about each middle bolt of the end-connections, so the effective buckling length of the braces could be considered to be the length between both middle bolts.

Lateral buckling occurred at 12.9 tonf in the specimen T-132-40 (Fig. 8) and at 11.1 tonf in the specimen T-165-60 (Fig. 10). After the lateral buckling, the load carrying capacity decreased in both specimens. These specimens, in which lateral buckling occurred in the early stage of loading, showed little deformation capacity.

The elastic energy absorption capacity defined by $Eo=Qy \cdot \delta y/2$ and the overall energy absorption capacity Ek were estimated from the load vs. displacement relationships, and the specific value Ds in the Japanese seismic design standard (Ref. 1) was calculated from Eq. (1). According to the current seismic design standard in Japan, the value Ds of most ductile steel structure is defined to be 0.25 and it increases as the structure becomes less

ductile. The estimated values are listed in Table 5, where Qy is

$$Ds = \sqrt{\frac{1}{Ek/Eo}} \qquad (1)$$

the yield strength, δy is the yield displacement estimated by the division of yield strength by elastic stiffness, and Ek is the energy absorbed until the load carrying capacity of the truss decreases to k% of yield strength. The calculated Ds-values from Ek with k=100% widely varied from 0.26 to 0.58. These calculated results show that a truss girder can have large deformation capacity if individual members are selected with small slenderness ratio.

4.2 Series 2 Test

These test results are summarized in Table 6. The load vs. displacement relationships of the specimens are shown in Figs. 11 to 15. In these figures, the displacement is measured vertically at the right-hand side end of the specimen and the upward displacement is positive.

Both specimens A and E showed plastic flows (flat portions) in the load vs. deformation relationships under the positive loading, produced by the tensile yielding of the CD-1 prior to the reduction in strength by the buckling of the CU-1. The slenderness ratio, λ, of the CU-1 in the specimen E was 34, and it was much larger than that of the specimen A, so the ratio of the buckling strength of the CU-1 to the tensile yield strength of the CD-1 was relatively smaller in the specimen E than in specimen A. Therefore, the flat portion of the load vs. deformation relationship was shorter in specimen E than in specimen A. Under the negative loading, the load carrying capacity decreased just after buckling of CD-1 (λ>10). The deterioration slope in specimen E was much steeper than in specimen A, because the slenderness of the buckling member in specimen E is larger than that in specimen A.

Axial force vs. axial deformation relationships of the principal members of the truss girder are shown in Figs. 16a to 16f for specimen A, where the axial force was calculated based on the assumption that was the determine truss. The CU-1 and CD-1 mainly shows the inelastic behavior; the others remained elastic. Measured axial displacements for the members and calculated ones for the other members are used to estimate the overall girder deformation. The estimated overall deformation is shown in Fig. 11 as the dotted line. From the comparison of the solid line (test result) and the dotted line (evaluated results), it can be concluded that the overall deformation of the

truss girder can be predicted from the deformation of each individual member.

The specimens B, C and D reached their maximum strength by brace buckling in positive and negative loadings showing non-ductile hysteresis loop. Especially in specimen B, a very brittle type of snap through buckling (Ref. 2) occurred. After the reduction of the strength by such brace buckling, these specimens showed rather stable hysteresis loops, which resulted from the contribution of the frame activity prescribed on the trapezoid frame action in the specimen T-66-40 in the series 1 test. The practical yield strength of this stable loop can be explained by a virtual work method considering the positions of the yield hinges as shown in Fig. 17.

From these test results in general, truss girders of the type of brace buckling failure is non-ductile. Of course, the specimens T-66-40 and T-99-40 showed relatively large deformation capacity in spite of their brace failure. The reason for failure; joint bolts slipped before brace buckling. In general design practice, however, it is not realistic to design the joint bolts to slip prior to brace buckling.

5. SUMMARY AND FUTURE PLAN

The following results are obtained from the eleven girder tests:

(1) The steel truss girder is usually non-ductile, but rather large deformation capacity can be anticipated if the slenderness ratio of each individual member is selected small.

(2) Generally the steel truss girder of brace failure type is non-ductile because it is accompanied with sudden drop in the load carrying capacity. But after the reduction in strength by brace buckling, the load carrying mechanism of the truss changes into frame mechanism by chord members, and the hysteresis loop becomes stable. Relatively large deformation capacity is expected in cases where slippage occurs in the joints.

(3) Steel truss girder of chord failure type should be restrained from its lateral buckling to ensure the deformation capacity.

(4) Overall steel truss deformation can be estimated as the sum of the deformation of each individual member, of which the truss is composed.

(5) The inelastic behavior of steel truss girders are largely affected by the

plastic deformation of a few individual
members near the end of the girder.

In the future, the axial behavior of the member
under various end support conditions should be
studied to correctly estimate the deformation
capacity of the truss. Moreover, the evalua-
tion method of the deformation capacity of the
frame should be studied through experiments and
analysis. Areas requiring further studies will
be addressed in a future plan.

6. ACKNOWLEDGEMENTS

7. REFERENCES

(1) Japanese Building Standard Law and its
     Enforcement Order, The Outline of the
     Standard is Simply Summarized in "Intro-
     duction to the Building Standard Law," The
     Building Center of Japan, 1986.

(2) Suzuki, H. and H. Nabana, "Behavior of
     Rigidly Joined Steel Truss Beam Part 2
     Snap Through Buckling of a Truss with Weak
     Diagonals," Proceedings of AIJ Annual
     Meeting, 2373, Oct. 1989 (in Japanese).

TABLE 1 DIMENSIONS OF TEST SPECIMENS (SERIES 1)

specimen	chord and brace	shear length (cm)	depth (cm)	angle (deg)	slenderness ratio#	
					chord	brace
T-66-21	chord: 2L-65x65x8 Ac=19.5cm ixc=1.94cm iyc=3.04cm	200	50		66	18
T-66-40		200	90		66	46
T-99-40		300	90		99	46
T-132-40	brace: 2L-50x50x4 Ab=7.78cm ixb=1.53cm iyb=2.38cm	400	90	60	132	46
T-132-60		400	130		132	76
T-165-60		500	130		165	76

Slenderness ratio of chord member is calculated as the division of the shear length by the radius of gyration,iyc. The effective buckling length of chord member will be obtained by multiplying 0.73x0.7 to the value in the table. In the calculation of the slenderness ratio of brace, the buckling length of the brace is considered to be the length between both middle bolts of the end-connections.

TABLE 2 MECHANICAL PROPERTIES

test series	member	tensile strength ($tonf/cm^2$)	yield strength ($tonf/cm^2$)
1	L-65x65x8	4.46	2.93
	L-50x50x4	3.96	2.88
	G.PL-9	4.20	2.86
2	H-194x150 flange x6x9 web	4.93 5.03	3.45 3.50
	H-150x150 flange x7x10 web	— 5.01	3.90 3.10
	H-148x100 flange x6x9 web	4.88 5.09	3.30 3.50
	P-89.1x4.2	3.97	3.63
	P-89.1x3.2	4.73	4.08
	P-60.5x3.2	4.25	3.92

P: circular tube

433

TABLE 3   DIMENSIONS OF TEST SPECIMENS (SERIES 2)

speci-men	chord	brace	depth (cm)	shear length (cm)	slenderness ratio#	
					chord	brace
A	H-194x150 x6x9	P-89.1 x4.2			22(11)	32
B	H-194x150 x6x9	P-89.1 x3.2			22(11)	32
C	H-194x150 x6x9	P-60.5 x3.2	100	480	22(11)	47
D	H-150x150 x7x10	P-89.1 x4.2			22(11)	32
E	H-148x100 x6x9	P-89.1 x4.2			34(17)	32

Numerals in the parentheses are the slenderness ratios of the CD-1 chords. The buckling length of chord members are considered to be 70% of the actual length.

TABLE 4   TEST RESULTS (SERIES 1)

specimen	maximum strength (tonf)	yield strength (tonf)	stable strength (tonf)	failure mode	estimated failure mode & (corresponding strength) (tonf)
T-66-21	16.4	14.0		lateral buckling, B-1 buckling	lateral buckling(14.2) cf. brace buckling(19.0)
T-66-40	16.2	15.0	≒12.0	B-1 buckling	brace buckling(17.1)
T-99-40	15.5	15.4	≒ 9.0	B-5 buckling	lateral buckling(16.9) cf. brace buckling(17.1)
T-132-40	12.9	11.4		lateral buckling	lateral buckling(10.8)
T-132-60	14.8	11.2	≒ 5.0	B-5 buckling	brace buckling(13.8)
T-165-60	11.1	10.0		lateral buckling	lateral buckling(11.2)

TABLE 5   ENERGY ABSORPTION CAPACITY OF SERIES 1 TEST SPECIMEN

specimen		Eo(tonf·cm)	Ek(tonf·cm)					
			k=100%	90%	80%	70%	60%	50%
T-66-21	energy E	7.20	103.19	111.22	118.57	126.88	134.81	135.15
	Ds-value		0.26	0.25	0.25	0.24	0.23	0.23
T-66-40	energy E	6.85	48.51	55.31	85.91	126.22	126.22	126.22
	Ds-value		0.38	0.35	0.28	0.23	0.23	0.23
T-99-40	energy E	11.31	61.73	61.73	61.73	61.73	70.75	89.95
	Ds-value		0.43	0.43	0.43	0.43	0.40	0.35
T-132-40	energy E	15.10	44.89	52.96	60.68	67.18	72.66	86.58
	Ds-value		0.58	0.53	0.50	0.47	0.46	0.42
T-132-60	energy E	5.04	25.61	26.70	27.54	28.44	29.11	29.77
	Ds-value		0.44	0.43	0.43	0.42	0.42	0.41
T-165-60	energy E	8.28	33.93	37.96	41.87	45.01	47.94	59.13
	Ds-value		0.49	0.47	0.44	0.43	0.42	0.37

TABLE 6   TEST RESULTS (SERIES 2)

speci-men	loading direc.	maximum strength (tonf)	stable strength (tonf)	failure mode	estimated failure modes & (corresponding strength) (tonf)
A	pos.	26.6		CD-1 yield,CU-1 buckling	CD-1 yield(28.1),CU-1 buckling(31.3)
	neg.	-24.5		CD-1 buckling	CD-1 buckling(28.0)
B	pos.	25.6	11.3	B-3,B-1 buckling	CD-1 yield(28.1),brace buckling(29.0)
	neg.	-23.7	-9.6	B-4,B-6 buckling	CD-1 buckling(28.0) cf:brace buckling(29.0)
C	pos.	16.6	8.5	B-3,B-5,B-1 buckling	brace buckling(17.5)
	neg.	-14.9	-7.1	B-4,B-2 buckling	brace buckling(17.5)
D	pos.	28.4	17.0	B-3,B-1 buckling	CD-1 yield(31.2),brace buckling(33.6)
	neg.	-26.7	-15.6	B-4,B-6 buckling	CD-1 buckling(31.0) cf:brace buckling(33.6)
E	pos.	18.5		CD-1 yield,CU-1 buckling	CD-1 yield(18.8),CU-1 buckling(20.4)
	neg.	-17.2		CD-1 buckling	CD-1 buckling(18,6)

FIG. 1 TEST SPECIMEN, TEST SET-UP AND DEFORMATION MEASUREMENTS (SERIES 1)

436
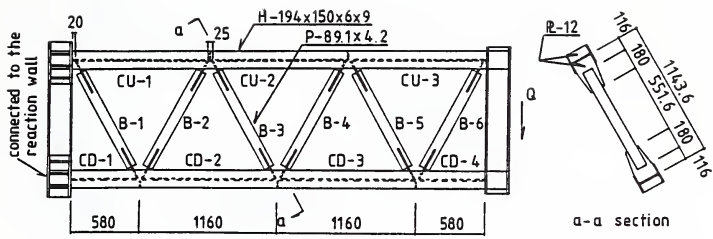
FIG. 2 TEST SPECIMEN (SERIES 2)
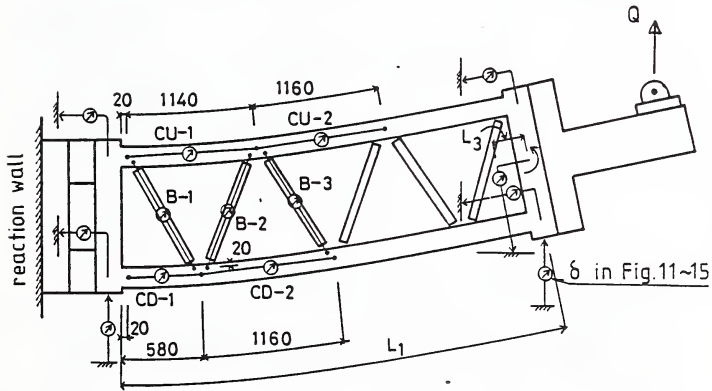
FIG. 4 DEFORMATION MEASUREMENTS (SERIES 2)
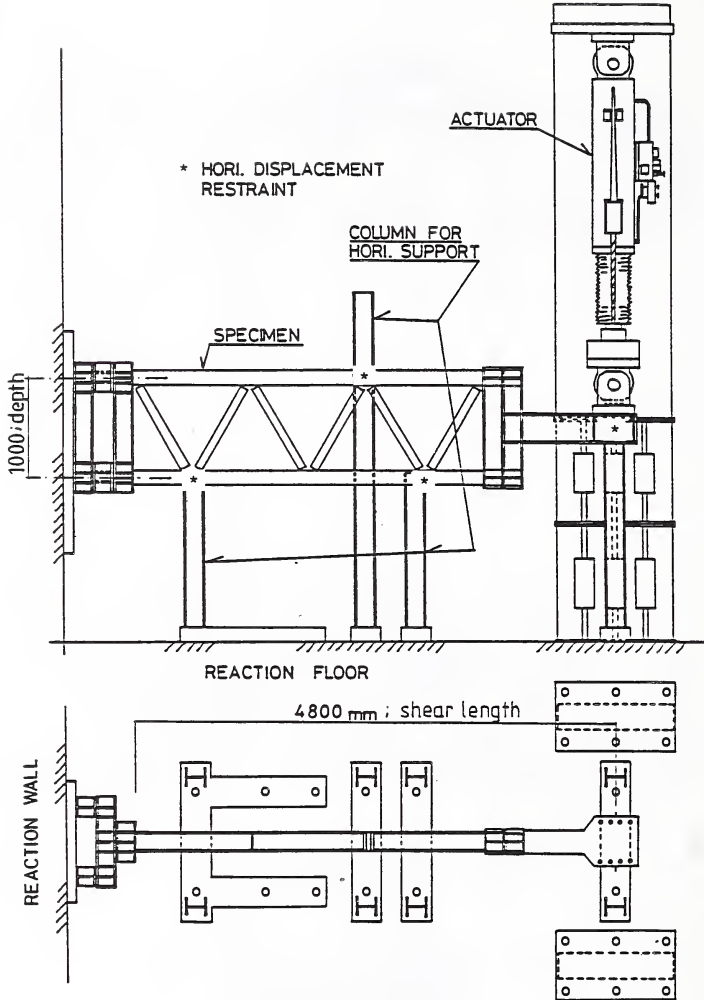
FIG. 3 TEST SET-UP (SERIES 2)
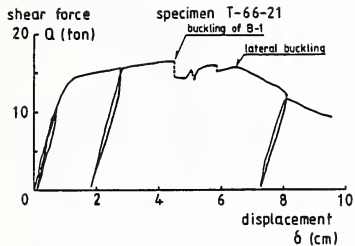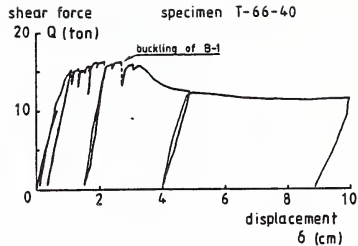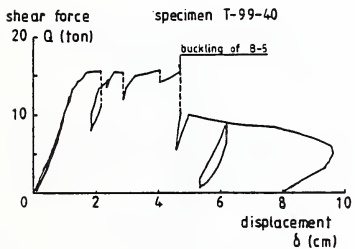
shear force specimen T-66-21

20 Q (ton) buckling of B-1

lateral buckling

10

0 2 4 6 8 10

displacement
δ (cm)

FIG. 5 LOAD vs. DISPLACEMENT RELATION

shear force specimen T-66-40

20 Q (ton)

buckling of B-1

10

0 2 4 6 8 10

displacement
δ (cm)

FIG. 6 LOAD vs. DISPLACEMENT RELATION

shear force specimen T-99-40

20 Q (ton)

buckling of B-5

10

0 2 4 6 8 10

displacement
δ (cm)

FIG. 7 LOAD vs. DISPLACEMENT RELATION

shear force specimen T-132-40

20 Q (ton)

lateral buckling

10

0 2 4 6 8 10

displacement
δ (cm)

FIG. 8 LOAD vs. DISPLACEMENT RELATION

shear force specimen T-132-60

20 Q (ton)

buckling of B-5

10

0 2 4 6 8 10

displacement
δ (cm)

FIG. 9 LOAD vs. DISPLACEMENT RELATION

shear force specimen T-165-60

20 Q (ton)

lateral buckling

10

0 2 4 6 8 10
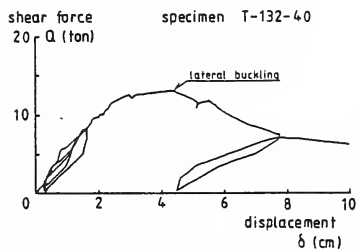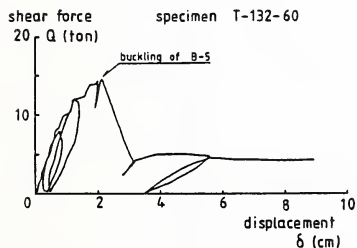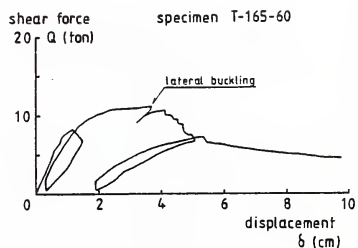
displacement
δ (cm)

FIG. 10 LOAD vs. DISPLACEMENT RELATION
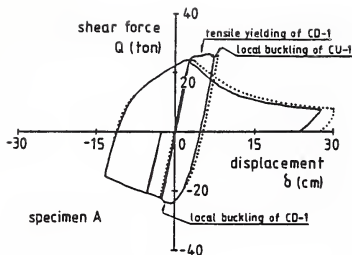
FIG. 11   LOAD vs. DISPLACEMENT RELATION
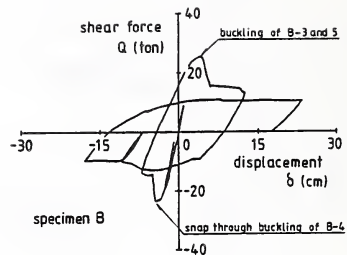
FIG. 12   LOAD vs. DISPLACEMENT RELATION
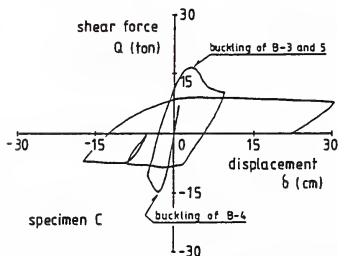
FIG. 13   LOAD vs. DISPLACEMENT RELATION
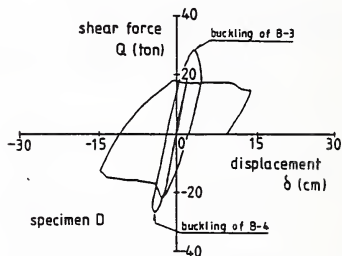
FIG. 14   LOAD vs. DISPLACEMENT RELATION
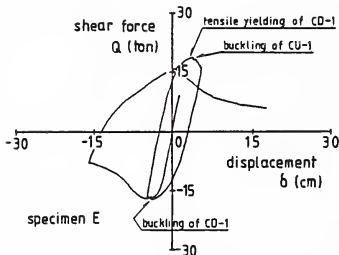
FIG. 15   LOAD vs. DISPLACEMENT RELATION
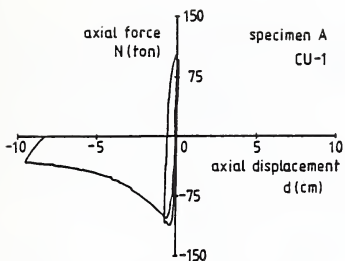
FIG. 16a AXIAL FORCE vs. AXIAL
DEFORMATION RELATIONSHIP
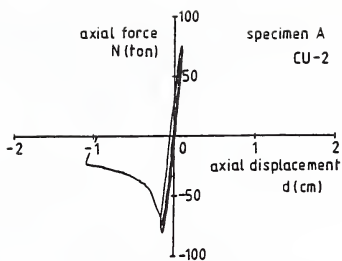
FIG. 16b AXIAL FORCE vs. AXIAL
DEFORMATION RELATIONSHIP
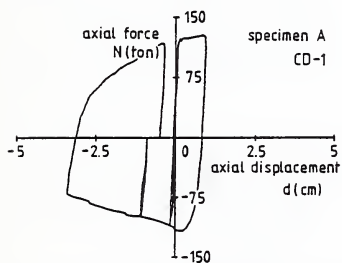
FIG. 16c AXIAL FORCE vs. AXIAL
DEFORMATION RELATIONSHIP
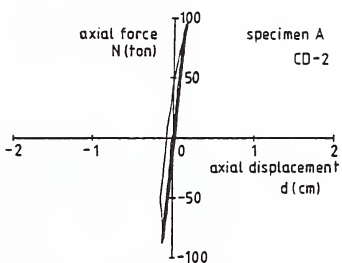
FIG. 16d AXIAL FORCE vs. AXIAL
DEFORMATION RELATIONSHIP
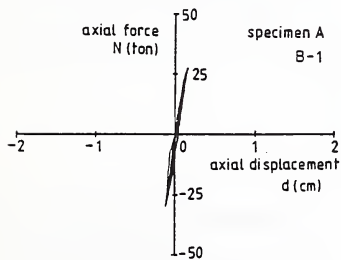
FIG. 16e AXIAL FORCE vs. AXIAL
DEFORMATION RELATIONSHIP
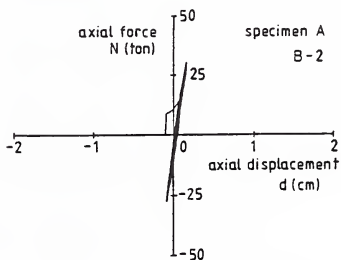
FIG. 16f AXIAL FORCE vs. AXIAL
DEFORMATION RELATIONSHIP
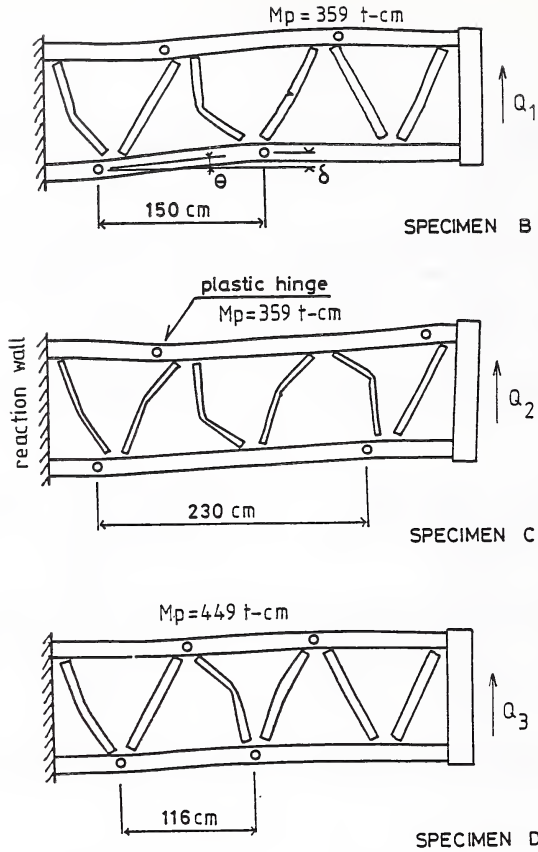
$Q_1 = 4 \times 359/150 = 9.6$ ton

$Q_2 = 4 \times 359/230 = 6.2$ ton

$Q_3 = 4 \times 449/116 = 15.5$ ton

FIG. 17   OBSERVED HINGE PATTERNS OF BRACE BUCKLED SPECIMENS

FIELD INVESTIGATION OF SEISMICALLY DAMAGED SITES BY USE OF VIBRATORY CONE PENETROMETER

BY

Yasuyuki Koga*, Yasushi Sasaki**, Yoshihiro Itoh***, and Osamu Matsuo***

ABSTRACT

Liquefaction investigations were carried out at various sites using a newly developed vibratory cone penetrometer (VCPT). The results obtained by these investigations were compared with the cyclic triaxial test results on undisturbed samples taken from these sites, and the effect of overburden pressure, etc. were examined. The liquefaction strength obtained from VCPT and cyclic triaxial tests at a seismically damaged river dike were compared.

1. INTRODUCTION

In Japan and the United States, the standard penetration test (SPT) is most generally used as an in-situ test method for assessing liquefaction potential of soils during earthquakes. But there can be a problem that the blow counts (or N-values) from the SPT are influenced by the quality of the bore hole and it is not necessarily appropriate to investigate the liquefaction potential at many points using the SPT in structural foundations with wide area or long length.

To solve this disadvantage, a method using the vibratory cone penetrometer (VCPT) was developed at the Public Works Research Institute (PWRI) to supplement the SPT in assessing liquefaction potential at a site. Field and indoor tests using this apparatus have been carried out.

The VCPT and some tests results were introduced in the past UJNR Joint Meeting[1]-[3].

This paper presents the estimation formula of liquefaction potential of the ground by use of VCPT. Also, a comparison with detailed investigation and analysis of the damaged dikes due to liquefaction in the Nihonkai-chubu Earthquake is described.

2. OUTLINE OF VIBRATORY CONE PENETROMETER

The vibratory cone penetrometer was developed to satisfy the following objectives:

(1) to obtain liquefaction strength of soils along the depth,

(2) to record liquefaction strength of soils accurately including loose silty fine sands with fine contents,

(3) to precisely measure liquefaction strength of soils at sites,

(4) to obtain liquefaction strength of soils at sites rapidly, and to easily record data at many sites,

(5) to perform in-situ tests inexpensively.

The VCPT apparatus is similar to the Dutch Cone Penetrometer. A basic difference, a small electric vibrator is installed inside the vibratory cone as illustrated in Fig. 1.

When the vibrator is turned on, the vibratory cone body vibrates around its axis. By this excitation, the soil's pore water pressure surrounding the cone may build up as in the case of saturated sandy ground. Therefore, penetration resistances under the condition using the vibrator will become smaller than those without excitation.

Although the effects of the vibrator on soils surrounding the cone might be different from actual earthquakes, the pore water pressure increase is an indicator of vulnerability of the in-situ soils against liquefaction. The difference between penetration resistances with and without cone excitation will reflect in-situ liquefaction resistance of soils.

Fig. 2 shows an example of in-situ measurement of penetration resistances. As shown in this figure, the penetration resistances decrease when the vibrator is used. This difference can be expressed by the degree of penetration resistance decrease D which is defined by the following equation.

$$D = \frac{Q_c^s - Q_c^v}{Q_c^s} \tag{1}$$

---

*Head, Soil Dynamics Division, Construction Equipment and Method Department, Public Works Research Institute
**Head, Ground Vibration Division, Earthquake Disaster Prevention Department, do
***Researcher, Soil Dynamics Division, Construction Equipment and Method Department, do

where D : degree of penetration resistance
              decrease,
       Q_c^s: penetration resistance without
              operation of vibrator (kgf/cm^2),
       Q_c^v: penetration resistance with
              operation of vibrator (kgf/cm^2).

The value of D, the degree of penetration
resistance decrease is nondimensional and can
have any value between zero and one. When soil
has value of D close to one, the soil can be
regarded vulnerable to liquefaction during
earthquakes.

Table 1 summarizes the main features of the
vibratory cone.

3. LIQUEFACTION STRENGTH AND DEGREE OF PENETRATION RESISTANCE DECREASE

The VCPT measures a penetration resistance
(bearing capacity) in the ground with the
application of an external vibration. The
dynamic shear stress which is generated in a
ground during earthquakes is considered to
increase roughly in proportion with the depth
of overburden pressure. Therefore the cyclic
shear stress is controlled roughly to be
proportional to the overburden pressure in a
cyclic triaxial test which is widely used as a
laboratory test method. Meanwhile the magni-
tude of the acting vibration force in the VCPT
is considered almost constant irrespective of
the depth. This is the same as in the case of
the SPT where a constant falling energy is
given irrespective of the depth. Therefore it
is expected that the penetration resistance
decrease D which was introduced as Eq. (1) to
represent the liquefaction potential may be
influenced by the overburden pressure under the
condition of a constant liquefaction strength R_ℓ
(stress ratio). In other words, the penetra-
tion resistance decrease D may not necessarily
uniquely correspond to the liquefaction
strength R_ℓ.

Fig. 2 shows a test result at Showa-Ohashi in
Niigata prefecture where relatively uniform
loose sand layer is deposited. This figure
illustrates that an average value of penetra-
tion resistance D decreases as the depth
increases.

Table 2 summarizes the vibratory penetration
test results where the cyclic triaxial test
results of undisturbed samples are available.
In Fig. 3 the relation between the penetration
resistance decrease D and the liquefaction
strength (stress ratio) R_ℓ is plotted with
different marks according to overburden pres-
sure. The solid curve shows an experimental
equation between D and R_ℓ, which was proposed
during the 16th UJNR meeting, Fig. 3 shows that
though the obtained results are distributed
around the curve, the scatter is fairly large.

The relation between R_ℓ and D was examined
assuming it is influenced by the overburden
pressure as the vibratory load is constant
along the depth as mentioned above. Fig. 4
shows the relation between D and the liquefac-
tion strength (stress) r_ℓ with different marks
according to overburden pressure. The figure
shows that the relation between D and r_ℓ may be
separated as groups according to overburden
pressure. The experimental formula which
relates D, r_ℓ and σ_v' can be in several
different equation forms. Eq. (2) below is a
tentatively proposed formula;

$$r_\ell = 0.2\sigma_v'^2 \cdot (1-D)^2 - \left(\frac{0.144}{\sigma_v' + 0.4} \right) + 0.3 \qquad (2)$$

where σ_v': effective overburden pressure
              (kgf/cm^2),
       r_ℓ: estimated liquefaction strength
              (stress) (kgf/cm^2).

Fig. 5 illustrates a comparison between r_ℓ
calculated from Eq. (2) and the measured
values. The figure shows a fairly good
agreement where r_ℓ is small (say r_ℓ <0.3
kgf/cm^2) but the scatter is large where r_ℓ
becomes large.

To examine the cause of scatter between the
estimated value from Eq. (2) and the measured
value of liquefaction strength, the difference
between them and grain characteristics are
compared in Fig. 6. $R_{\ell_{20}}*$ is a calculated
liquefaction strength (stress ratio) using Eq.
(2), and $R_{\ell_{20}}$ a measured value. Fig. (a) shows
that the difference decreases as the mean
diameter D_{50} increases, though the scatter is
large, which suggests that Eq. (2) provides a
little smaller value where D_{50} gets small.
Fig. (b) shows the relation between the
difference and the fine grain content FC; a
clear relationship is not observed.

4. INVESTIGATION OF A DAMAGED SITE BY USE OF THE VCPT

The Nihonkai-chubu Earthquake of May 26, 1983
caused embankment damages in many places from
liquefaction. Several damages to Iwaki-gawa
river dike in Aomori prefecture were observed
among the various damaged fill sites. Soil
tests and surveys including cyclic triaxial
tests on undisturbed samples were performed
using the VCPT.

A detailed case study based on test results
were performed to clarify the damage mechanism.
Fig. 7 shows a soil investigation result of a
damaged river dike where settlement of 20-50 cm
occurred. An analysis was conducted to calcu-
late a seismically induced permanent deforma-
tion of a dike. A similar analysis method was
used as a degradation of a static rigidity.
Following two strain potential

444

characteristics; (1) liquefaction strength under the condition without initial shear before earthquakes, (2) cumulative strain characteristics under superimposed stress conditions of initial and seismic shear stresses before and during earthquakes. The latter characteristics were obtained from cyclic triaxial test results. The former characteristics (liquefaction strength) were estimated with emphasis on cyclic triaxial test results on undisturbed samples from the site. Using both characteristics a model for the analysis was constructed. Liquefaction strength (stress ratio) $R_{\ell_{20}}$ from cyclic triaxial test results, that for analysis, and that obtained from the VCPT are shown in Fig. 7. This shows good agreement of the liquefaction strength from the VCPT and that of the model for the analysis. The latter indicates more subtle change of ground strength.

Fig. 8 illustrates a calculated permanent deformation of a dike against the earthquake. For the dike crest settlement, the observed value from a damage investigation is 20-50 cm, the calculated value is 46 cm, which indicates that the analytical method and properties used are both rational. This further suggests that the VCPT can give an in-situ liquefaction strength with good approximation.

5. CONCLUSION

The following concerns the VCPT which was developed at PWRI:

(1) It is necessary to consider the effect of overburden pressure to estimate the liquefaction strength of the ground from the measured penetration resistance decrease.

(2) An experimental formula to give the liquefaction of the ground from the measured penetration resistance decrease was tentatively proposed.

(3) The above experimental equation gives a little smaller value when the average diameter of the soil gets small.

(4) The liquefaction strength was estimated from the VCPT at the site where a dike was seismically damaged. A detailed ground investigation and analysis was conducted. There were good agreement with the permanent deformation analysis and with the measured settlement.

6. REFERENCES

1) Sasaki, Y. and Koga, Y. "Vibratory Cone Penetrometer to Assess the Liquefaction Potential of the Ground," 14th Joint Meeting, UJNR, 1982.

2) Sasaki, Y., et al., "U.S.-Japan Cooperative Research on In-site Testing Procedure for Assessing Soil Liquefaction (No. 1)," 16th Joint Meeting, UJNR, 1984.

3) Sasaki, Y., et al., "In-situ Test for Assessing Liquefaction Potential Using Vibratory Cone Penetrometer," 17th Joint Meeting, UJNR, 1985.

4) Lee, K. L., Seismic Permanent Deformations in Earth Dams, Report No. UCLA-ENG-7497, School of Engineering and Applied Science, University of California at Los Angeles, 1974.

① Porous metal
② Pore pressure transducer
③ Load transducer of
   point resistance
④ Load transducer of
   side friction
⑤ Take-out cable for
   transducer
⑥ Vibrator
⑦ Power source cable for
   vibrator
⑧ Penetrating rot
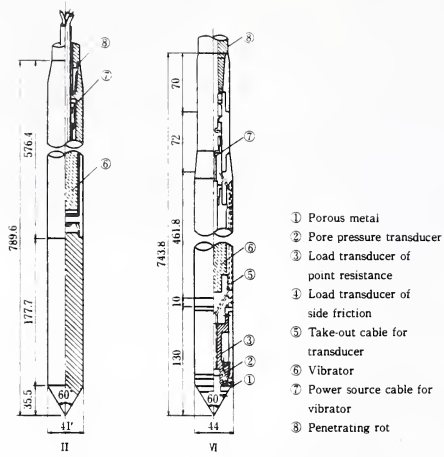
Fig. 1   Vibratory Cone
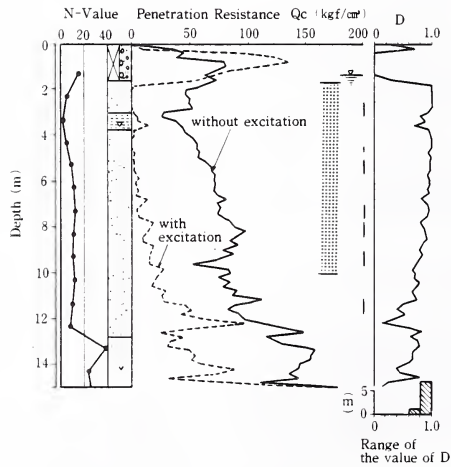
Fig. 2   Example of In-situ Measurement of VCPT Showa-Ohashi Bridge Site
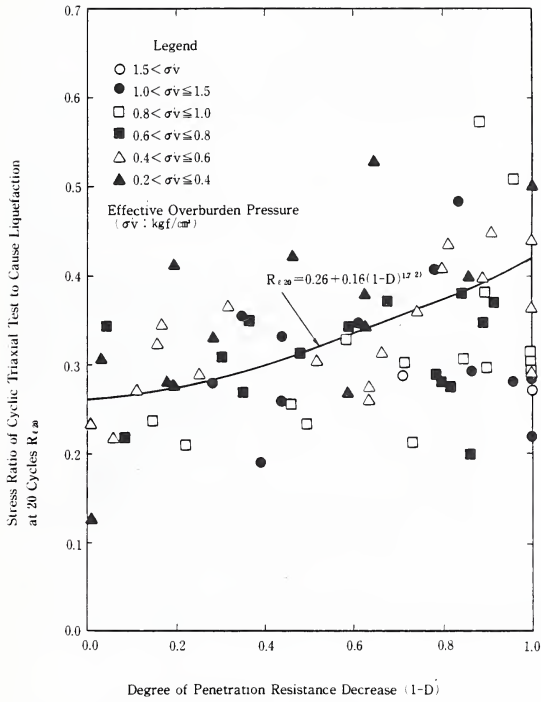
Fig. 3   Relation between Liquefaction Strength and Degree of Penetration Resistance Decrease
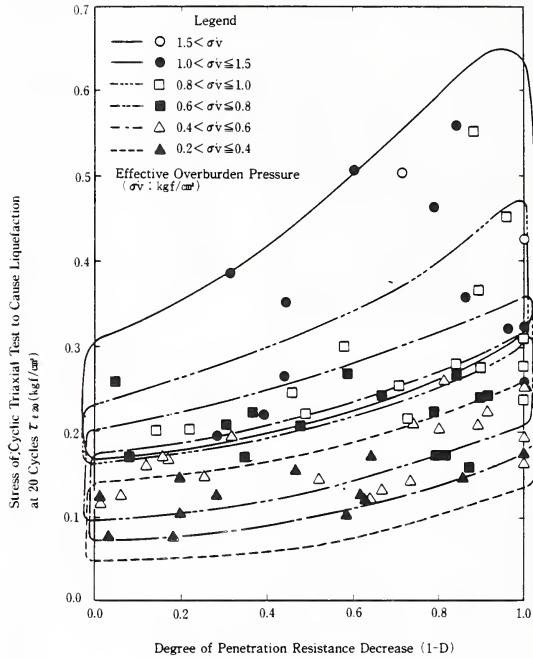
Fig. 4   Relation between Liquefaction Strength and Degree of Penetration Resistance Decrease
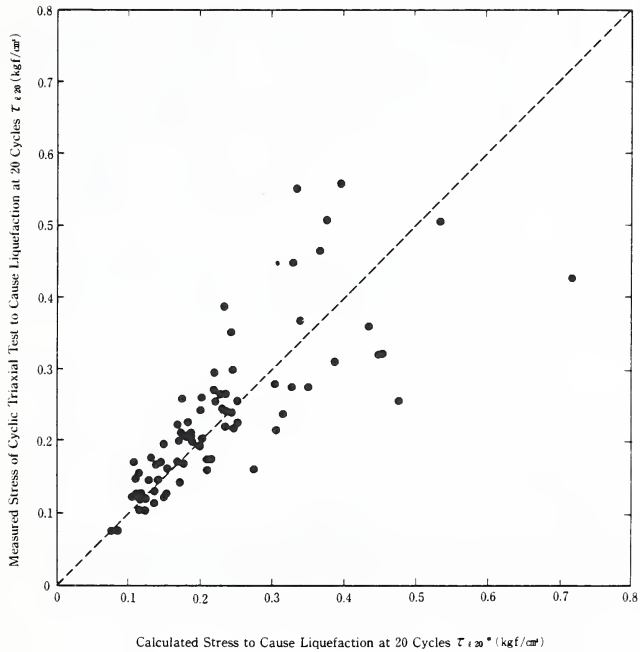
Fig. 5   Comparison of Measured and Calculated Stress to Cause Liquefaction

The y-axis is labeled: Measured Stress of Cyclic Triaxial Test to Cause Liquefaction at 20 Cycles $\tau_{\ell\,20}$ (kgf/cm²)

The x-axis is labeled: Calculated Stress to Cause Liquefaction at 20 Cycles $\tau_{\ell\,20}{}^*$ (kgf/cm²)
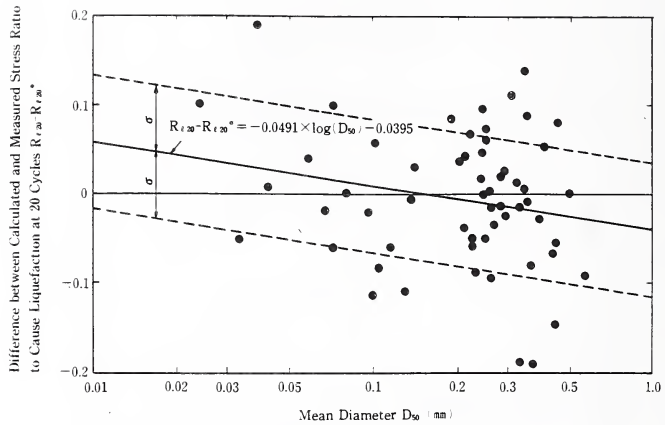
(a) Effect of Mean Diameter
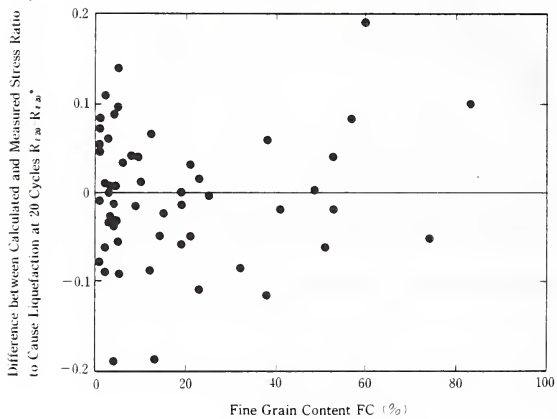
b) Effect of Fine Grain Content

Fig. 6　Effect of Grain Size Characteristics
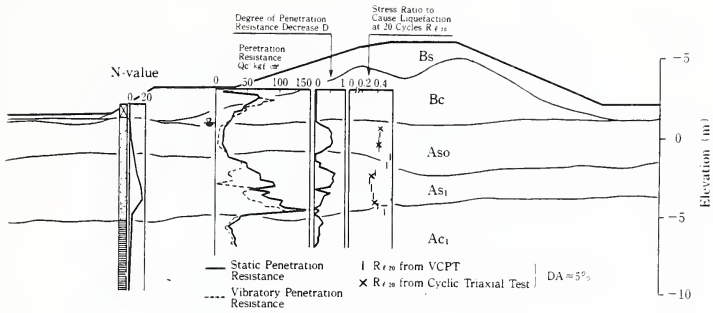
Fig. 7   Ground Investigation Result
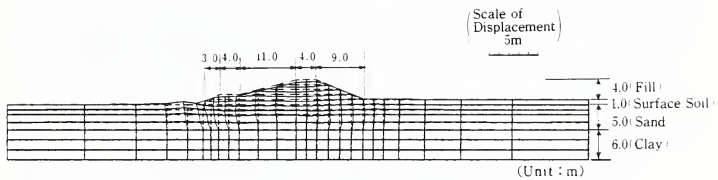
Fig. 8   Deformation after the Earthquake

Table 1　Vibratory Cone

a) Comparison of Vibratory Cone

	Standard	Vibratory Cone	
	Cone	Il	VI
Diameter　(mm)	35.7	41	44
Length　(mm)	205	789.6	743.8
Apex Angle	60°	60°	60°
Weight　(kg)	1.1	6.3	6.7
Vibrator	Without	With	With
Sensor	Without	Without	With

b) Specification of Vibrator

Item	Size, etc.	
	II	VI
Diameter	41mm	31mm
Length	576mm	431.5mm
Frequency	200Hz	
Power Source	AC 3φ 48V 200Hz	
Centrifugal Force	80kgf	80kgf

c) Specification of Transducers

Symbol	Item	Type	Capacity	
			II	VI
qc	Load Transducer of Point Resistance	Strain Gauge	1tf	5tf
fc	Load Transducer of Side Friction	Strain Gauge	1tf	———
P	Pore Pressure Transducer	Strain Gauge	2kgf/cm²	5kgf/cm²
S	Displacement Transducer of Penetration	Potentiometer	106cm	

Table 2 Summary of VCPT & Cyclic Triaxial Test Result

SITE	Z (m)	Qc^s (kgf/cm²)	Qc^v (kgf/cm²)	D	$\sigma v'$ (kgf/cm²)	$R_{\ell 20}$	$\tau_{\ell 20}$ (kgf/cm²)	N値	D_{50} (mm)	FC (%)
A- 1- 1	2.28	64.00	12.00	0.813	0.27	0.280	0.076	5.0	0.223	4.0
A- 1- 2	3.33	35.00	30.00	0.143	0.36	0.400	0.144	11.3	0.210	3.4
A- 1- 3	4.73	84.00	67.00	0.202	0.49	0.410	0.201	15.5	0.220	12.0
A- 2- 1	3.31	42.00	12.00	0.714	0.78	0.330	0.125	9.0	0.200	12.0
A- 2- 2	4.85	31.00	5.00	0.839	0.52	0.325	0.169	5.3	0.240	0.5
A- 2- 3	10.80	80.00	23.00	0.713	1.05	0.290	0.204	9.7	0.250	3.5
A- 3- 1	3.77	60.00	94.00	0.000	0.53	0.365	0.193	3.3	0.370	4.0
A- 4- 1	4.08	35.50	6.00	0.831	0.48	0.347	0.167		0.250	3.0
A- 4- 2	2.96	12.80	2.60	0.797	0.38	0.272	0.102		0.225	5.5
A- 5- 1	6.42	78.00	3.40	0.956	0.75	0.343	0.257		0.310	2.0
A- 6- 1	3.41	43.60	11.20	0.743	0.50	0.291	0.146		0.262	3.0
A- 6- 2	8.93	53.00	38.70	0.270	1.00	0.214	0.214		0.230	12.0
A- 7- 1	5.09	108.80	52.40	0.518	0.65	0.316	0.205		0.200	5.5
A- 7- 2	4.84	39.10	36.30	0.634	0.63	0.353	0.222		0.190	57.0
B- 1- 1	1.80	59.00	2.00	0.966	0.25	0.304	0.076	8.9	0.350	1.0
B- 1- 2	4.85	44.00	14.00	0.682	0.53	0.368	0.195	5.0	0.450	0.5
B- 1- 3	6.55	46.00	14.00	0.696	0.68	0.310	0.211	7.0	0.400	1.0
B- 1- 4	9.84	26.00	26.00	0.000	0.98	0.315	0.309	8.4	0.260	1.0
B- 2- 1	2.85	40.00	0.50	0.988	0.35	0.348	0.122	3.3	0.058	53.0
B- 2- 2	4.43	55.00	0.50	0.991	0.49	0.233	0.114	5.8	0.222	20.5
B- 2- 3	5.37	65.00	4.00	0.938	0.58	0.215	0.125	9.0	0.250	13.5
B- 2- 4	7.32	75.00	6.00	0.920	0.77	0.217	0.167	12.0	0.260	19.0
B- 2- 5	8.13	91.00	13.00	0.857	0.84	0.238	0.200	11.0	0.240	23.0
B- 2- 6	9.38	72.00	16.00	0.778	0.96	0.210	0.202	10.0	0.245	19.0
B- 2- 7	11.38	92.00	36.00	0.609	1.15	0.190	0.219	10.0	0.295	15.0
B- 3- 1	2.43	65.00	42.00	0.354	0.32	0.528	0.169	3.8	0.038	60.0
B- 3- 2	3.18	17.00	10.00	0.412	0.38	0.268	0.102	2.7	0.072	51.0
B- 3- 3	5.04	68.00	50.00	0.265	0.52	0.275	0.143	23.0	0.225	18.5
C- 1- 1	16.50	40.92	42.74	0.000	1.57	0.272	0.427	4.0	0.330	13.0
C- 2- 1	2.38	15.04	3.00	0.801	0.36	0.410	0.146	3.0	0.024	83.0
C- 2- 2	8.47	81.30	47.04	0.421	0.91	0.330	0.299	14.0	0.100	38.0
C- 3- 1	5.45	121.04	98.37	0.187	0.60	0.435	0.261	15.0	0.240	5.0
C- 3- 2	3.43	101.58	90.74	0.107	0.95	0.385	0.367	12.0	0.140	21.0
C- 4- 1	3.27	45.64	28.82	0.369	0.75	0.340	0.119	9.0	0.080	49.0
C- 4- 2	9.35	93.38	97.90	0.000	0.90	0.305	0.274	10.0	0.105	32.0
C- 5- 1	6.71	55.30	25.10	0.546	0.36	0.255	0.245		0.320	9.8
C- 5- 2	8.25	36.60	34.40	0.644	1.10	0.352	0.387		0.340	5.0
C- 5- 3	12.30	205.40	123.20	0.400	1.47	0.345	0.507		0.350	4.1
C- 5- 4	15.38	90.80	64.50	0.290	1.74	0.290	0.505		0.067	52.6
C- 6- 1	4.38	43.00	5.10	0.881	0.59	0.270	0.159		0.340	3.7
C- 6- 2	7.88	120.90	101.60	0.160	0.90	0.310	0.279		0.390	2.8
C- 7- 1	2.95	71.50	45.50	0.364	0.46	0.260	0.120		0.430	2.3
C- 7- 2	3.32	41.30	52.20	0.000	0.55	0.290	0.160		0.570	1.9
C- 7- 4	8.33	165.30	81.40	0.508	0.94	0.235	0.221		0.280	9.3
C- 7- 5	10.62	167.10	160.20	0.041	1.15	0.280	0.322		0.130	23.4
C- 8- 1	8.63	206.00	91.00	0.558	1.02	0.260	0.265	12.0	0.290	9.0
C- 9- 1	10.95	114.00	123.00	0.000	1.11	0.290	0.322	9.0	0.100	38.0
C-10- 1	6.75	149.00	150.00	0.000	1.16	0.220	0.255	9.0	0.370	4.0
D- 1- 1	5.73	41.20	32.50	0.211	0.63	0.280	0.176	2.6	0.033	74.3
D- 1- 2	8.18	67.00	74.80	0.000	0.82	0.290	0.208	13.0	0.260	5.4
D- 1- 3	9.33	113.70	102.00	0.103	0.92	0.300	0.276	14.0	0.440	5.2
D- 2- 1	2.46	17.10	11.40	0.333	0.41	0.315	0.129	1.0	0.098	41.2
D- 2- 2	3.51	13.50	7.00	0.481	0.48	0.305	0.146	2.0	0.136	25.0
D- 2- 3	5.56	71.70	24.90	0.653	0.63	0.270	0.170	10.0	0.490	3.4
D- 2- 4	7.21	101.90	80.10	0.214	0.78	0.290	0.226	17.0	0.265	5.0
E- 1- 1	4.88	59.10	51.00	0.137	0.80	0.200	0.160		0.440	
F- 1- 1	3.45	25.60	11.90	0.535	0.36	0.422	0.152			
F- 1- 2	5.83	70.80	52.80	0.254	0.57	0.368	0.210			
F- 1- 3	6.53	93.30	75.90	0.186	0.62	0.278	0.175			
F- 2- 1	6.94	52.40	35.10	0.330	0.65	0.373	0.242			
F- 3- 1	6.94	133.50	122.20	0.085	0.65	0.373	0.242			
F- 4- 1	5.44	48.50	43.30	0.107	0.52	0.400	0.208			
F- 4- 2	7.34	72.60	60.90	0.161	0.69	0.383	0.264			
F- 5- 1	8.34	58.30	34.20	0.413	0.78	0.345	0.269			
F- 5- 2	10.30	146.80	128.90	0.122	0.96	0.575	0.552			
F- 5- 3	12.34	122.30	96.10	0.214	1.14	0.407	0.464			
F- 6- 1	3.33	13.70	21.00	0.357	0.33	0.377	0.124			
F- 6- 2	12.53	123.90	104.00	0.161	1.16	0.483	0.560			
F- 7- 1	3.45	26.70	53.70	0.000	0.35	0.501	0.175			
F- 7- 2	7.21	114.50	102.10	0.108	0.69	0.350	0.242			
F- 7- 3	9.34	150.10	143.80	0.042	0.88	0.510	0.443			
F- 8- 1	5.25	42.10	38.40	0.098	0.50	0.450	0.225			
F- 8- 2	6.10	72.20	72.10	0.001	0.58	0.442	0.256			
G- 1- 1	14.43	24.60	17.40	0.293	0.83	0.307	0.255	3.6	0.042	60.0
G- 1- 2	17.43	27.30	12.00	0.560	1.27	0.330	0.352	3.4	0.072	49.0
G- 1- 3	19.35	40.80	35.00	0.135	1.22	0.295	0.360	4.8	0.115	35.0

AN INVESTIGATION ON A TWELVE-STORY OFFICE BUILDING
DAMAGED BY THE 1985 MEXICO EARTHQUAKE

by

Hisahiro Hiraishi
Masaya Hirosawa
Hideo Tsukagoshi
Toshihide Kashima
Toshikazu Kawashima[1]

ABSTRACT

The 1985 Mexico City Earthquake caused serious damage particularly to reinforced concrete buildings. A team of experts was dispatched to Mexico October 19 to November 22, under sponsorship by the Japan International Cooperation Agency. Their objective was to evaluate damaged buildings to judge the necessity for repairing and strengthening and to propose a plan for strengthening appropriate buildings.

This report describes the detailed damage observation and analyses and a plan to strengthen a twelve story reinforced concrete office building.

The following conclusions were derived from the observation and analyses:

1) Torsional vibration occurred during the earthquake due to the existence of exterior brick walls.

2) Significant settlement occurred and shear walls did not perform as expected because of insufficient bearing capacity of friction piles.

3) A wrong location of the cut-off of top reinforcements of beams resulted in a critical section occuring at a different location in the structural design. As a result, the beams' flexural strength was extremely small.

4) The base shear coefficients corresponding to the ultimate stage were 0.07 and 0.08 for longitudinal and transverse directions, respectively (due to 2 and 3 above).

5) Consequently, a drastic increase in strength was needed to strengthen the building.

1. INTRODUCTION

The 1985 Mexico Earthquake with a magnitude of 8.1 caused serious damages to Mexico City buildings. Although damage statistics are not yet available, it is estimated that 7,000-8,000 lives were lost, 400-500 buildings totally collapsed, and about 1,500 buildings were evaluated for necessary repair and strengthening.

The objective of the team of experts dispatched to Mexico City during October 19 to November 22 was: to evaluate buildings damaged, to decide the necessity for repair and strengthening, and to propose a plan to strengthen buildings.

This paper describes the investigation and analyses of a damaged twelve-story office building.

2. OUTLINE OF THE BUILDING

The 12 story building had a trapezoid plan with 5 spans in the longitudinal direction and 3 spans in the transverse direction and a basement, as shown in Fig. 1 and Photos 1 and 2. The basement and the first and second stories were used for parking.

The structural feature of the building is as follows:

1) The building had the center core consisting of one and two shear walls in the longitudinal and transverse directions, respectively.

2) The columns were flat section in the longitudinal direction, and the flat ratio was 1/2.

3) Floor system was Losas Planus (Mexican style waffle slab); beams and sub-beams were placed within the slab.

4) Brick walls reinforced by reinforced concrete braces were wholly placed in two exterior frames out of four exterior frames.

5) There were one in-situ reinforced concrete friction pile and two piles, under interior and exterior columns, respectively, having a triangular section of 55 cm x 55 cm x 55 cm, and 26m long.

6) The Building was constructed during 1980 to 1982.

3. DAMAGE OBSERVATIONS

3.1 General Description of Damage

---
[1]All authors from Ministry of Construction, Building Research Institute, Tsukuba, Japan

The general description of damage is summarized as follows:

1) Failure of beams connected to non-structural reinforced concrete walls on the north side of the building and the adjacent slabs.

2) Cracking on the floor slabs due to settlement of the elevator core.

3) Failure of capitals on the exterior columns on the east, north, and south sides.

4) Failure of short span beam between the C and D frames on the south side.

5) Failure of extremely short beams in the basement.

6) Failure of columns and beams at the anchorage of reinforcements in the exterior brick walls (east and south sides).

7) Failure of exterior brick walls.

8) Failure of lumped slabs in the parking space.

Torsional vibration is considered to have occurred during the earthquake due to the existence of exterior brick walls on the east and south sides and the lumped slabs for parking in the first through third floors. Bond splitting cracks were observed in columns.

3.2 Structural Damage

Significant beam damage was seen at the capitals except for damage of the beams between the frames 1 and 2 which were connected to the non-structural reinforced concrete walls on the north side and for damage of the short span beams in the frame 1 between the frames C and D. Large column damages were observed at the anchorage of reinforcements in the exterior brick walls except in the basement. Some damage examples on columns and beams are shown in Photos 3-5. Here, notation S, F, B mean shear, flexure, and bond splitting failures, respectively, and notation II, III, IV, and V mean small, moderate, severe damages, and collapse, respectively. Observed crack patterns on the columns and shear walls on the frames 1, 3, A, D, and F are illustrated in Figs. 2-6. Cracks running at 45 degrees in both directions on shear walls indicated that they carried seismic forces reversibly.

Examples of crack patterns on the 10th floor are given in Figs. 7 and 8. The following statements are from the crack observations.

1) On floors above the first floor, cracks of 3.0mm in width run parallel to the frames B and E at the locations 1,500mm-1,800mm apart from the frame lines. These locations correspond to the end of capitals where the amount of upper reinforcements suddenly decreased and reinforcing bars yielded. These cracks resulted from settlement of the elevator

core.

2) Cracks of 3.0mm in width running perpendicular to frame A also were seen between frames 1 and 2.

3) On the lower side of floors, radiating cracks from the column top were observed.

3.3 Non-Structural Damage

Damage on brick walls in the frame lines was investigated. They were classified into 6 categories as shown in Fig. 9. Typical patterns of failure for each type of brick walls are shown in Table 1.

Exterior walls of east and south facades were type x, and most were damaged as shown in Photo 4. The detail of anchorage of reinforced concrete braces of x type is shown in Fig. 10; such anchorage caused severe damage to beams (damage to columns if anchored into column), as seen in Fig. 4. The structural engineer who designed this building said that the x type brick walls were considered an earthquake resisting member in structural calculation. However, the efficiency of the brick walls is quite doubtful for such buildings in which ductility is required, although it may be effective for stiff buildings.

Crack patterns on the lumped slabs in the parking space are illustrated in Fig. 11. As large cracks were observed specially between the frames D-F, the lumped slab between the frames 1-4 and frames E-F were considered to have acted as a brace, and the slab between the frames 1-2 and E-F were considered to have acted as a flexural member. This fact may explain that the building vibrated in torsional modes to produce severe damage to the fourth through sixth stories rather than to the first through third stories.

The non-structural RC-walls on the north side were located outside of frame A. The columns at each end of the walls were connected to the corner column of the frame 1 or the beams on the frame A between the frames 1 and 2 (see Fig. 1). The foot of the wall was connected to the retaining wall at the basement just outside of frame A. The shear cracks on the walls indicate possibly that large seismic forces were carried by this wall. Concrete crushed at the foot of the wall and shear failure in the beams on the frame A between the frames 1 and 2 and the large cracks in the floor systems around the wall were induced by the failure of the wall (see Photo 6).

3.4 Collision

This building collided with the adjacent buildings in the east and south sides (see Photo 7). The building on the south side was particularly damaged.

3.5 Settlement and Tilting of the Building

Settlements of the floor systems were measured at the basement, first, tenth, and twelfth floors by bench mark leveling. The largest settlements occurred around the elevator core. The inclinations of the building were measured by transit to determine the considerable distortion of the building (see Fig. 13).

4. STRENGTH TESTS OF CONCRETE

Strength of concrete was measured by the Schmidt hammer tests at 23 points in each floor and the tests on the three concrete core samplings taken from the column at the same location for all the stories. The average strength of concrete estimated from the Schmidt hammer tests was 205 kg/cm2 for the whole building. The same quantity measured by sampling tests varied between 210 and 400 kg/cm2. The average strength of concrete at the middle part of columns was 248 kg/cm2.

5. ESTIMATION OF FAILURE MECHANISM

Fig. 14 shows the estimated failure mechanism from the crack patterns, where the cracks of the width of 1mm and the length of 50cm were considered to be the threshold value for the hinge occurence. Shear failure was not observed in this frame. Notation o and x mean flexural yielding hinges corresponding to each directional response, respectively. For the frames 1 and 3, the hinges x appear at many locations between the frames D and F. This is possibly a result from the settlements of the frames C and D. There are seen, however, the hinges o between the frames A and C and the hinges x between the frames D and F, suggesting possible severe oscillations of the building in both directions. Since the hinges appear in more than half of beams in the transverse direction, the building is considered to have oscillated severely in this direction.

6. EVALUATION OF LATERAL STRENGTH AND SEISMIC CAPACITIES

Bearing capacities and seismic safety estimated by the third Level Screening Procedure for evaluation of seismic capacity are described for the undamaged state of the building. In calculating bearing capacity of the building, two methods were employed. In the first method, the nodal moment distribution method for limit analysis was applied to the building whose base was fixed at the basement. In the second method the virtual displaement principle was used for evaluating bearing capacity of the building with its base fixed at the ground level. The horizontal strength of frame structures and shear walls were first calculated separately and then added to give the total bearing capacity of the building.

Lists of structural indices (Is=Eo x SD x T) are tabulated in Table 3. The values for the first were 0.061 in the longitudinal direction and 0.082 in the transverse direction.

The bearing capacity was re-evaluated by applying the virtual displacement principle under the assumption of reversed triangle distribution of external forces. The derived story shear forces are tabulated in Table 4. The base shear coefficients corresponding to the ultimate state, are 0.07 and 0.08 for the longitudinal and transverse directions, respectively. The low values of bearing capacities, resulted from cutting of the reinforcements in the upper side of slab-systems at the end of capitals. This action resulted in extremely low beam strength and insufficient bearing capacity of the foundation was not allowed to increase the strength of the shear walls. The calculated ultimate lateral strength, where all reinforcement in the upper side of the capitals is assumed to be effective, is twice that calculated based on real condition as mentioned before.

7. PROPOSED PROCEDURE OF STRENGTHENING

Figure 18 proposes an example for possible repair and strengthening procedures. The target level of strengthening is set at 0.25 of the strength index and 2.5 of the ductility index being considerably higher than the existing bearing capacity of 0.07-0.08 in the undamaged building. Four shear walls are installed at the corners in both directions, each is expected to carry the base shear coefficient of 0.05. This arrangement of shear walls is effective to prevent torsional motions of the building. Existing shear walls are thickened to prevent shear failure in future earthquakes.

The following local reinforcements of elements also are recommended:

(1) Non-structural RC walls on the north side should be removed. The surface concrete of the floor slabs near the wall is chipped and recast after the welded mesh wire is placed.

(2) Shear walls are installed in place of the short columns in the basement. Short span beams on the frame 1 between the frames C and D should be improved by removing the brick wall or by providing a slit between the beams and the brick wall.

(3) Since the target strength of the building is relatively low, the members and structures should be ductile enough to avoid failure in shear and bond splitting.
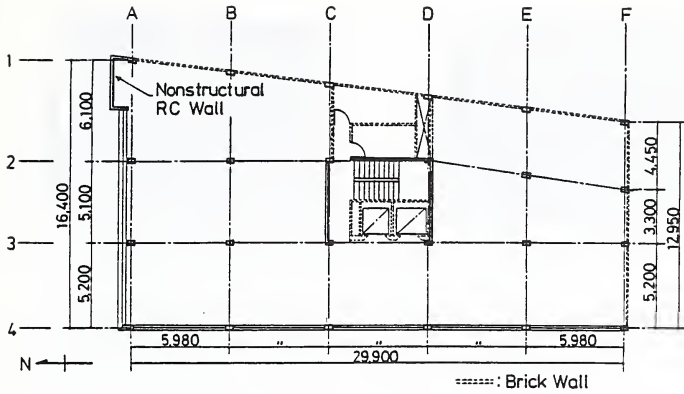
Fig. 1 Typical Plan
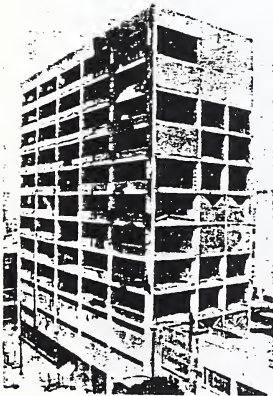
Photo. 1 South West Side

Photo. 2 North Side
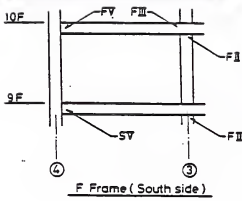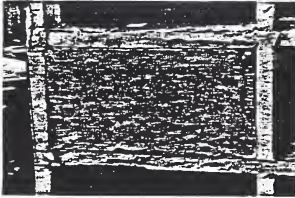
Photo. 3   Damage Degree of the Members
(No. 1)
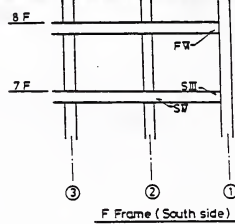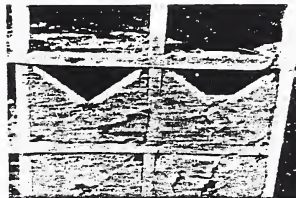
Photo. 4   Damage Degree of the Members
(No. 2)

Photo. 5   Damage Degree of the Members (No. 3)
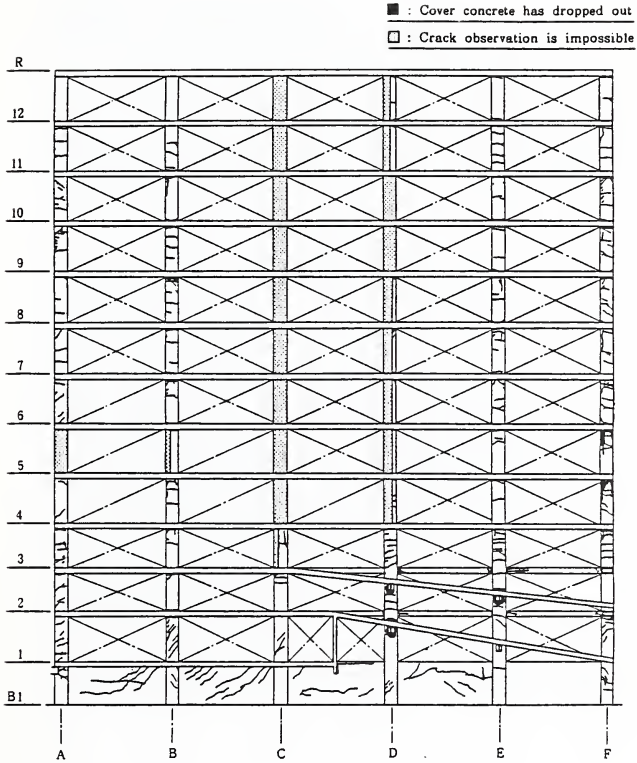
Fig. 2 Crack Pattern of 1 Frame (West Side)
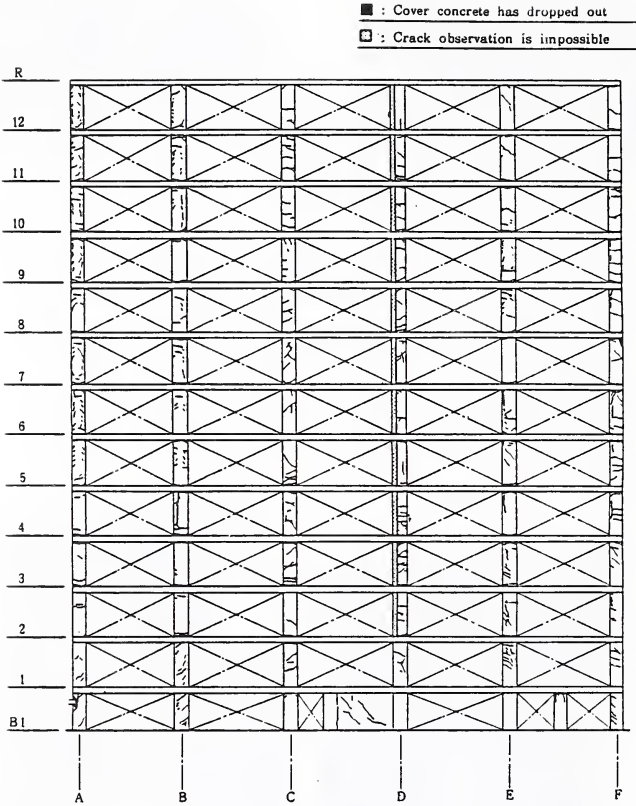
Fig. 3 Crack Pattern of 3 Frame (West Side)
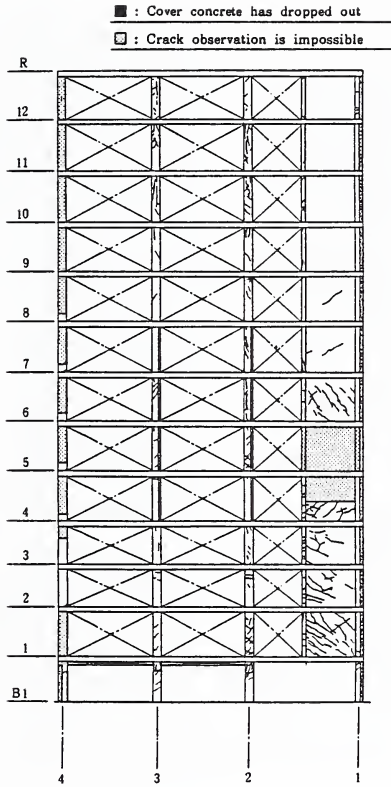
Fig. 4 Crack Pattern of A Frame (South Side)
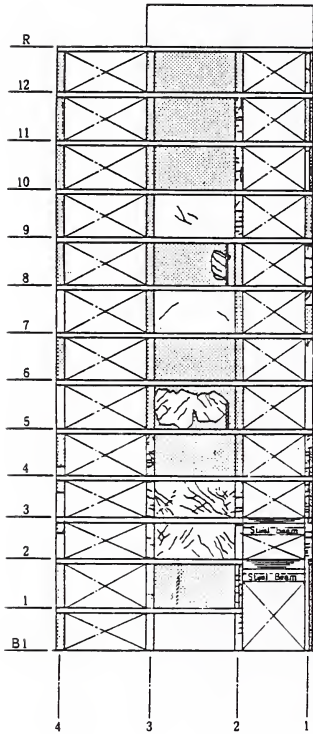
Fig. 5   Crack Pattern of D Frame
(South Side)
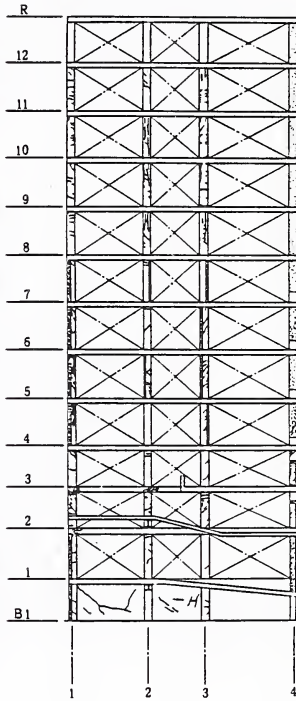
Fig. 6   Crack Pattern of F Frame
(North Side)
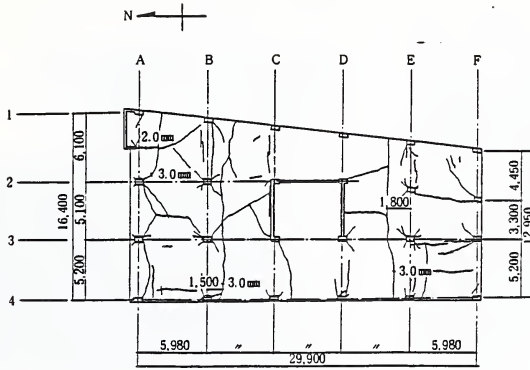
Fig. 7 Crack Pattern of 10th Floor System (Upper)
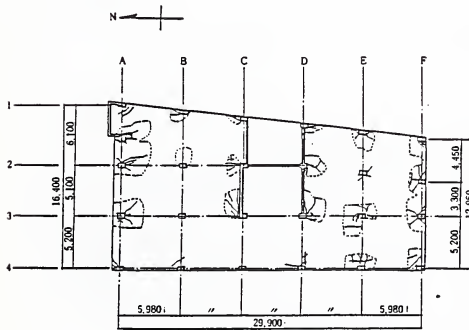
Fig. 8 Crack Pattern of 10th Floor System (Bottom)

X Type   P Type   M Type

S Type   H1 Type   H2 Type
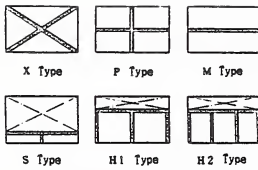
Fig. 9   Construction Types of Brick Wall

Beam
Anchore bar 4#2.5
Column
Length of connection
Reinforcing bar 4#2.5
2 @ 30
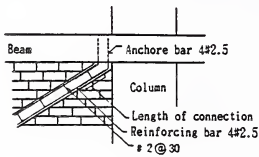
Fig.10   Anchoring of Diagonal

Reinforcing Bars

Table 1   Typical Failure Patterns of

Brick Wall

Type	Damage	Construction Type
X	1) Crush at corner 2) Crush at crossing point 3) Collapse of anchored bars 4) Collaps e of connected bar at corner	1) 2)
P M	1) Diagonal crack	1)
S	1) Diagonal crack 2) Crush at bottom	1)
H1 H2	same as above	same as above

2F → 1F Ramp
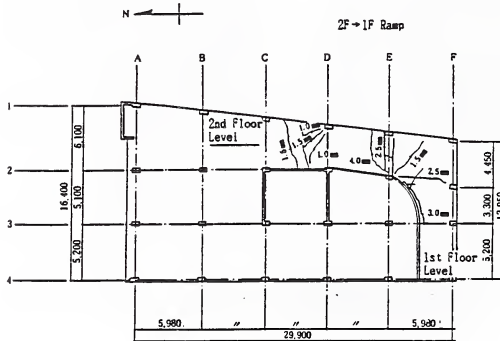
Fig.11   Crack Pattern of Ramp
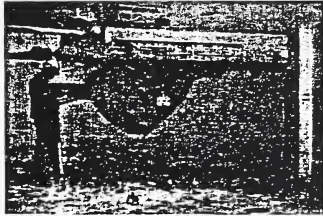
Photo 6   Failure Pattern of Non-Structural
          R/C Wall at North Side
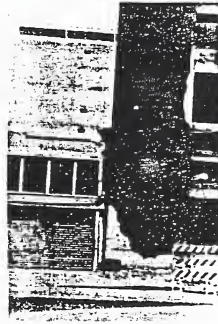
Photo 7   Collision at East Side
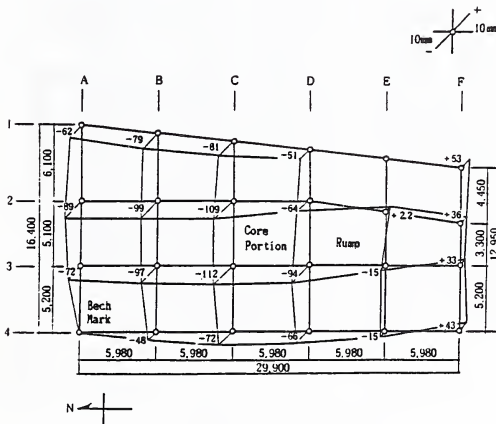
Fig.12   Settlement of Basement Floor System (Unit:mm)

Fig.13 Permanent Deformation of Floors

Fig.14 Failure Mechanism

Table 2 Seismic Index of Structure Before Earthquake

Story	Longitudinal			Span		
	C	F	Is(Eo)	C	F	Is(Eo)
12	12900 / 37.08	1.5 / 1.0	0.303*1 (0.384)	105.27 / 5155	2.37 / 1.5	0.402*1 (0.362)
11	149.49 / —	1.5 / —	0.167	179.96 / —	1.5 / —	0.202
10	139.81 / —	1.5 / —	0.107	184.54 / —	1.5 / —	0.141
9	171.44 / —	1.5 / —	0.102	197.89 / —	1.5 / —	0.117
8	180.21 / —	1.5 / —	0.089	210.58 / —	1.5 / —	0.104
7	189.02 / —	1.5 / —	0.082	248.11 / —	1.5 / —	0.107
6	196.84 / —	1.5 / —	0.077	283.49 / —	1.5 / —	0.110
5	202.93 / —	1.5 / —	0.073	292.20 / —	1.5 / —	0.105
4	208.17 / —	1.5 / —	0.071	299.68 / —	1.5 / —	0.102
3	220.54 / —	1.5 / —	0.072	294.41 / —	1.5 / —	0.096
2	237.30 / —	1.5 / —	0.075	298.58 / —	1.5 / —	0.094
1	196.44 / —	1.5 / —	0.061	264.38 / —	1.5 / —	0.082

Values in parentheses mean values at stage of beam yielding

Table 3 Lateral Strength

③ ④	①				②			
	⑤		⑥		⑤		⑥	
	Q	Cs	Q	Cs	Q	Cs	Q	Cs
12	331.82	0.08	0.47	139.02	0.43	30.24	0.14	386.9	0.17
11	737.00	140.48	0.20	1789.4	0.24	96.30	0.13	1133.1	0.15
10	1162.16	13061	0.12	18454	0.16	136.16	0.12	1625.0	0.14
9	1397.36	17144	0.11	1678.0	0.13	175.84	0.11	206.95	0.13
8	1972.54	19021	0.09	2103.0	0.11	206.33	0.11	296.32	0.12
7	2317.72	16002	0.06	246.11	0.10	238.64	0.10	290.82	0.12
6	2702.80	18684	0.07	2934.0	0.10	293.76	0.09	310.30	0.11
5	3190.09	20293	0.09	2922.0	0.09	2647	0.09	325.02	0.11
4	3592.9	20617	0.09	296.99	0.08	301.44	0.08	354.72	0.10
3	3802.64	22054	0.09	264.41	0.07	314.00	0.08	368.50	0.08
2	441153	23730	0.03	298.5	0.07	322.37	0.07	376.33	0.09
1	4026.69	19644	0.04	286.38	0.03	326.56	0.07	394.29	0.08

① Nodal moment distribution method for limit analysis

② Limit analysis by assumed hinge mechanism

③ Story ④ Weight ⑤ Longitudinal ⑥ Span

Additional shear wall for strengthening

Thickness-increased shear wall for strengthening
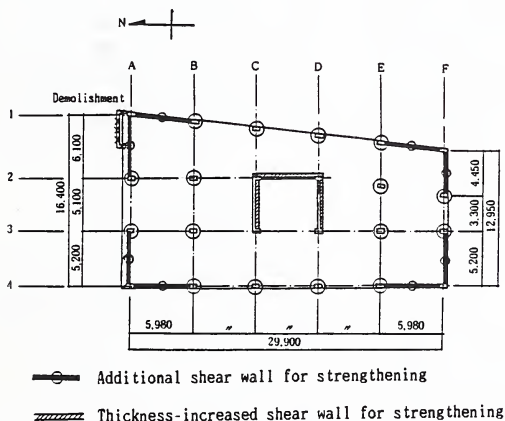
Fig.15 Proporsal of Strengthening

467

PRACTICAL APPROACH FOR DETERMINING STAGE FREQUENCY

BY

H. Lee Butler and Thomas A. Hardy[1]

ABSTRACT

The Corps of Engineers has to provide reliable
estimates of coastal flooding from surges in
order to make sound engineering decisions
regarding the design, operation, and
maintenance of various coastal projects.
Potential of flooding due to tropical storms
(hurricanes) is greater for coastal regions
along the Atlantic and Gulf of Mexico Coasts
of the United States while extratropical
storms (northeasters) affect coastal areas
from the mid-Atlantic to Canada. Storm surges
provide a higher water level on which short
period surface waves can propagate, subjecting
beaches and structures to wave forces not
ordinarily experienced. There is a need for
procedures to analyze the impacts of storm
surge and related wave forces for the purpose
of establishing design criteria for coastal
structures, providing data for an economic
analysis of coastal projects, or developing
evacuation plans.

Use of time-dependent numerical models for
simulating water levels and flows in open
coastal waters, estuaries, bays, or lakes has
become a standard practice. When these
numerical schemes are used conjunctively with
statistical techniques, a modeling procedure
can be developed to estimate the magnitude and
frequency of occurrence of storm-induced water
levels in coastal regions. It is not the
purpose of this paper to discuss any
particular hydrodynamic, wave, or probability
model development, but rather to discuss the
practical application of these techniques to
coastal regions.

Two flood frequency studies will be used as
examples to illustrate appropriate solution to
modeling difficulties. The first is a dual-
grid model study to investigate flood levels
on the south coast of Long Island, New York,
including open coast, inland bays and flood
prone land areas. Analysis of improvements to
provide adequate protection for the area
against storm tides also was conducted. A
second study involves the conjunctive use of
hydrodynamic, wave, physical, and probability
models, applied on a single nearshore grid, to
provide estimates of flood frequencies and
wave overtopping volumes in an area north of
Boston, Massachusetts.

1.0 INTRODUCTION

Efficiency in design of coastal protection is
becoming more and more important. Development
of coastal regions, costs of damages from
storm-induced water levels, and costs of
protection from these waters are all
increasing. Adequate protection for coastal
regions is desired; however, due to monetary
constraints, the amount of water level
protection that can be considered adequate
becomes a question for which there is no easy
answer. Therefore, inherent in any coastal
protection project (new or rehabilitation
effort), there is a need to develop the best
possible estimate of the stage-frequency
relationship for the project area, as well as
an estimate of the error in this relationship.

When applying numerical and statistical models
to estimate storm-induced flood levels for
open coast and inland situations, various
problems are encountered. These include, but
are not limited to, selection of an
appropriate model basin; procedures for model
calibration and verification; appropriate
treatment of wind-wave generation and wave
setup in the surf zone; barrier island
overtopping and routing of flood waters into
inland bays; wave overtopping of structures;
applicable probability models; and
optimization of the number of computer runs
necessary for meaningful statistical results.

This paper focuses on the type of models used
for stage frequency analysis, calibration and
verification procedures, and statistical
techniques for reducing computer effort. Two
applications are briefly discussed to point
out how modeling techniques and procedures
were applied to efficiently derive stage
frequency relationships for coastal flooding.

2.0 MODELS

2.1 Storm/Tide Models

The storm surge equations (5, 6) are
descriptive of a variety of other long-wave
applications in open coastal waters. These
equations are familiar with most readers and
will not be described in this paper. Many
techniques and grid constructions are
available for use in coastal areas. The
applications to be discussed later used the
Waterways Experiment Station Implicit Flooding
Model (WIFM). The numerical and hydrodynamic
features of WIFM are discussed in Butler (1).
WIFM solves the vertically integrated, time-
dependent, shallow water wave equations of

---

[1] U.S. Army Engineer Waterways Experiment
Station, Coastal Engineering Research
Center, Vicksburg, MS 39180-0631

fluid motion using an alternating direction implicit finite difference algorithm. The model allows sugrid barriers and utilizes a stretched numerical grid which permits concentration of grid resolution in areas of interest.

In order to model storm surge it is usually necessary to extend the computational grid past the edge of the continental shelf and into deep water. Since it also is desirable to have small cell sizes in areas of interest, a very large number of grid cells may be necessary to model a study area using a single grid. Consequently, in locations with a wide continental shelf, a two grid system is usually developed. Fine resolution is required in nearshore regions. Development of a single grid to resolve fine scale nearshore features and, at the same time, cover the required expanse of the adjacent continental shelf, would result in a very inefficient model to simulate hundreds of storms. The outer (global) grid contains an approximate description of the inland system thereby eliminating possible contamination of nearshore boundary conditions. Boundary conditions are saved from global grid simulations to drive the inner (nearshore) grid which contains sufficiently fine resolution to describe flood propagation into shore, through various inlets, into back bays, and over flood-prone inland areas. This same technology is used when only separate models for open coast and inland surge are available. Grid construction will be discussed later in sections on model application.

To insure the appropriateness of all model assumptions, tests should be made with varying grid limits, time steps, and sensitive channel depth representation. Sensitivity to model boundary conditions also should be tested. Having accepted an appropriate grid, the model should be calibrated and verified for the astronomical tide. Tidal data are usually more available for checking model performance or can be collected without much difficulty. Following model tests for tidal representation, several historical storms should be simulated to compare model water level predictions with observed levels and observed extent of flooding.

2.2 Wave Models

Wind-generated surface waves force an increase in the time-averaged water level in the surf zone. The magnitude of the effect for hurricanes can be an increase of 2 meters or more. Thus, in areas where the principal storm surge is due to wind stress and barometric effects, there is an additional rise in the water level due to the presence of waves. This wave setup is not essentially periodic on the time-scale of the surface waves but varies with the general sea state

and is restricted to the surf zone. The cause of the rise is the divergence of the wave radiation stress caused by dissipation of wave energy in the surf zone.

A number of complications occur in the estimation of wave setup during storms. Primary among these is the estimation of the radiation stress tensor for storm wave spectra. Since the sea state during a storm is not well represented by a simple monochromatic wave train, estimation of the tensor involves adequate estimation of the directional wave spectrum in shallow water. This must take into account spectral wave transformations in shallow water including shoaling, refraction, diffraction, wave growth, and breaking. The results are highly site dependent. Both monochromatic and spectral models have been used to model wave setup in storm conditions.

Wave setup may not be significant in all cases; some problems may involve estimation of flooding due to waves overtopping a structure. A steady state, shallow water, directional spectral wave model is used to perform wave simulations in an example of a single grid application. The required simulations actually called for the use of a time dependent model but the cost of using such a model was prohibitive. In lieu of a truly transient simulation, the model was run once for each hour of each event and the resulting wave climate was taken to be representative of the conditions existing for the entire hour.

2.3 Probability Methods

There are several possible approaches to establishing frequency curves where the scarcity of data in the immediate study area requires a modeling approach. The two most common are called the historical method and the joint probability method (JPM). In the historical method, a series of historical events is recreated with the pertinent data being saved in the necessary locations. In effect, it is like operating a time machine with the hindsight to know what data to collect and where to collect it. Probability is assigned to each event by a standard ranking method. For the JPM, the storm type is parameterized. For example, hurricane windfields can be defined by three parameters: central pressure deficit, radius to maximum winds, and forward speed. Then an ensemble of synthetic events is simulated representing those events which are possible in the study area. Probability is assigned to individual events by assigning probabilities to parameter values which determine that event. If the parameters are independent, then the probability of the event would be the product of the probabilities of the component parameters. In the two examples discussed below, the JPM was used along with a

modification of the historical approach.

3.0 DUAL GRID APPLICATION

A study to investigate the frequency of storm plus tide flood levels along the coast and within the bays of southern Long Island, New York, was recently completed at WES (3). The study involved development of two numerical models, collection of field data for model calibration, computation of coastal and back-bay stage frequencies, and analysis of alternative barrier and inlet configurations.

A coarse global grid was constructed to cover the New York Bight from a point south of Atlantic City, New Jersey, to beyond Cape Cod, Massachusetts (and includes New York Harbor and Long Island Sound). The purpose of the global grid was to model large-scale tidal and meteorological events, providing the boundary conditions for a smaller, high-resolution grid of the main study area. The high-resolution nearshore grid covers the south-central shore and back-bay areas of southern Long Island and has variable grid size resolution of 270 to 1200 m.

Both numerical grids were tested and calibrated for the M2 astronomical tidal constituent, and verified for a mixed tide condition. Bathymetric and topographic information describing barrier island and inlet configurations for five severe historical storms was developed and the storms were hindcasted. Due to the severity of the historical and hypothetical storms to be simulated for developing a statistical data base, a scheme to model breaching of the barrier island system was implemented.

The JPM approach was used to develop stage frequencies for hurricanes, northeaster, and tide events along the south shore of Long Island. Five hurricane parameters were used: forward speed, radius of maximum wind, central pressure deficit, track direction, and landfall point. Probability distributions for each parameter were obtained by a thorough review of the historical occurrence of hurricanes in the New York Bight. It was determined that three forward speeds, three radii, five landfall points with three track directions, two track directions for bypassing storms, and six pressure deficits were needed to represent the range of hurricane parameters which could occur. Thus, 918 hurricane events were modeled, each with its own probability of occurrence (namely, the product of the probabilities of the component parameters). The actual number of storm events modeled was reduced. Sensitivity tests determined that water levels resulting from different pressure deficits could be linearly interpolated. Therefore, modeling hurricanes with only two values of central pressure deficits was necessary.

Northeasters were modeled by choosing 27 historical storms which were found to be representative of the 41-year period, 1940 through 1980. Historical data were used to develop a partial duration stage frequency curve of significant northeaster surge levels at Sandy Hook, New Jersey. Sandy Hook is at the entrance to New York Harbor. Probabilities of simulated storms were assigned according to how much of the partial duration probability distribution each storm represented.

Global grid simulations were carried out for surge without tide. Tides were incorporated through the convolution of tidal values with output of the surge-only numerical simulation. This procedure is valid in the open Bight area where nonlinear effects of combining surge and tide are negligible. The convolution procedure produced more than 600,000 possible hurricane surge-tide combinations and over 18,000 northeaster surge-tide combinations. These storm sets were ranked by height, and through the use of their probabilities, stage-frequency relationships were developed for open-coast locations throughout the study area.

For nearshore grid simulations, it was necessary to reproduce the statistics of the thousands of possible global surge-tide events with a much smaller ensemble of events for nearshore simulation. A random sampling of roughly 6000 hurricane plus tide events was further reduced to three sets of 17 storm-tide events, with each set chosen to represent a range of storms from moderate to very severe. Weaker events were not emphasized due to the dominance of northeasters for return periods below 25 to 50 years. Tests showed that 40 northeaster plus tide simulations could reliably represent the full set of extratropical events. Probabilities of each nearshore event were assigned according to how much of the nearest open-coast stage frequency curve each event represented. Stage frequencies were developed from the results of these simulations. This procedure replaced the typical approach of routing all the open-coast surge events into the back-bay areas. It also provided a clean statistical method to account for the nonlinear effects involved in routing flood waters through inlets and over the barrier islands. The method also provides for measuring confidence in the results (4). The technique used is known as the bootstrap, and provides an estimate of the error of the stage frequency by determining the variation possible in each component's probability distribution. This variablity is due to the construction of the distribution from a finite set of historical events.

4.0 SINGLE GRID APPLICATION

The use of a two grid approach is not always

necessary for investigating flood frequency via numerical modeling. A good example of a single nearshore grid application is a recent study conducted at WES (2). The study location is a residential area, just north of Boston, Massachusetts. Over fifty years of tidal stage data (Boston Harbor) and wind data (Boston's Logan Airport) were available. This information was the key to reducing the computational effort in establishing flood frequencies in Broad Sound. A second factor in adopting the single grid approach was the lack of hurricane influence on the stage frequency curve at Boston.

The purpose of this study was to determine flood levels in the back-bay reaches of the Saugus-Pines River system as well as develop the frequency of water volumes caused by storm waves overtopping seawalls protecting a residential area called Roughans Point. Flooding caused by wave overtopping is an annual occurrence. In order to determine the economic viability of possible protective measures, it was necessary to establish the frequency of the flood levels caused by wave overtopping for both the existing conditions and the proposed protective measures.

Wave overtopping is a complex phenomenon which is governed by a number of sometimes interdependent variables such as tide, storm surge, wave height and period, and structure height and slope. To study this problem five models were used in conjunction. A numerical storm surge model (WIFM) calculated the still-water level. A numerical spectral wave model estimated the characteristics of the waves which would attack the structures at the water levels predicted by the surge model. A physical model produced an analytical relationship for determining overtopping rates given water level, wave height and period, and structure characteristics. A flood routing model calculated the maximum stage in the interior of Roughans Point caused by each simulated event. A probability model chose events to simulate, assigned probabilities to those events and constructed the stage frequency curves.

If all of the variables which determine wave overtopping were independent, then a joint probability approach would work well for determining probabilities associated with specific overtopping volumes. The probability of a volume would then be the product of the separate variable probabilities. Unfortunately, storm surge, wind and wave variables are not independent. Therefore, an alternative approach was developed which would link the probability of an overtopping volume to historic storm meteorology.

Defining maximum storm surge as the maximum difference between measured and predicted water levels during a storm, a 20-year partial duration series (PDS) of maximum surge was established at the Boston tide gage adjacent to the study area. A synthetic surge plus tide event was created by combining a time history of a surge from the PDS with a randomly chosen astronomical tide. This was done with the assumption that the historic storm which caused the surge was independent of tide, i.e. the storm could have occurred at any phase of any tide during storm season. A large array of synthetic surge plus tide events was created by repeating the above process 500 times for each surge time history.

A probability of exceedence curve for the still-water level can be reliably established at the nearby Boston tide gage due to its long record. A semi-random selection procedure was developed using this curve as a basis for choosing events to simulate and for assigning probabilities to these synthetic events. In a sense the exceedence curve for the Boston Harbor gage was used to replace the need for a global grid. In order to judge the accuracy of the selection process, the total number of events simulated was divided into three sets. The sets were individually processed, creating three overtopping exceedence curves. The range of variation among these three curves gives an estimate of the accuracy of the process.

For areas where stage frequency curves were computed for the still-water level resulting from the combination of surge and tide, only the surge and probability models were necessary. These areas included both open coast and estuarine locations. The model showed the inlet to the Saugus-Pines River system efficiently conveyed flood levels to the river flood plains. This meant that the entire study area tended to flood to approximately the same level.

For Roughans Point, multiple combinations of possible seawall-revetment structures were modeled. Major differences amoung the combinations were evident at the lower return periods with combinations of a wide berm revetment and a cap on the existing east seawall providing the greatest protection. At higher return periods the protection differential offered by the various structure combinations tended to diminish.

5.0 CONCLUSIONS

Two example flood frequency studies were used to describe appropriate solutions to various modeling difficulties. Both dual- and single-grid approaches were discussed. Practical problems of routing flood waters over protective dune systems were solved. An efficient procedure for selecting a minimal number of storm plus tides events to simulate in a nearshore region was developed. Innovative use of five modeling systems to

compute wave overtopping frequencies was
described.

6.0 ACKNOWLEDGEMENTS

7.0 REFERENCES

(1) Butler, H. Lee, "Evolution of a Numerical
Model for Simulating Long-Period Wave Behavior
in Ocean-Estuarine Systems," Estuarine and
Wetland Processes with Emphasis on Modeling,
Marine Science Series, Vol. 11, Plenum Press,
New York, NY, 1980.

(2) Hardy, Thomas A., and Crawford, Peter L.,
"Frequency of Coastal Flooding at Roughans
Point, Broad Sound, Lynn Harbor and the
Saugus-Pines River System, " Technical Report
in publication, U.S. Army Waterways Experiment
Station, CE, Vicksburg, MS.

(3) Hardy, Thomas A., Prater, Mark D., and
Butler, H. Lee, "Fire Island to Montauk Point,
New York, Storm Surge Model Study," Technical
Report in publication, U.S. Army Waterways
Experiment Station, CE, Vicksburg, MS.

(4) Prater, Mark D., Hardy, Thomas A.,
Butler, H. Lee, and Borgman, Leon E.,
"Estimating Error of Coastal Stage Frequency
Curves," 19th International Conference on
Coastal Engineering, ASCE, Houston, TX, 3-7
Sept, 1984.

(5) Reid, R.O., and Bodine, B.R., "Numerical
Model for Storm Surges in Galveston Bay,"
Journal of Waterways and Harbors Division,
ASCE, Vol. 94, No. WW1, Proc. Paper 5805,
Feb 1968, pp. 33-57.

(6) Welander, P., "Numerical Prediction of
Storm Surges," Advances in Geophysics, Vol. 8,
Academic Press, New York, NY, 1961.

Task Committee Reports

Report of Task Committee on

(A) STRONG-MOTION INSTRUMENT ARRAYS AND DATA

Date: May 13, 1986

Place: National Bureau of Standards
            Gaithersburg, MD USA

Attendees: Japan Side - H. Tsuchida, Chairman (PHRI)
                             K. Ohtani (NRCDP)

                U. S. Side - A. G. Brady, Chairman (USGS)
                             H. Meyers (NOAA)

I. Activities and Principal Accomplishments to Date

Catalogs of strong-motion earthquake records observed both in the
United States and Japan are being exchanged. U.S. data are
published in the "Seismic Engineering Program Report," and the
Japanese data are published in "Strong-Motion Earthquake Records
in Japan."

Discussions were held on the possibility and the necessary
support for accepting a team of scientists and engineers,
together with their instruments, immediately following a large
earthquake in the host country (see No. 10, following).

II. Future Programs

Both sides of the Task Committee plan to continue their respective
efforts in the following ten points, 1 to 10, and to initiate three
points, 11, 12, and 13.

1.   After an earthquake which has caused damage
      to structures or an earthquake during which
      maximum acceleration exceeding about 0.1g has
      been recorded, the task committee of the
      country where the earthquake has taken place
      will provide a list of the strong-motion
      earthquake records for the counterpart of the
      task committee. The list contains maximum
      component acceleration of each record. If
      there is such a list compiled by any organiza-
      tion, the list mentioned above may be replaced
      by it.

2.   Every year the task committee will exchange
      catalogs of the strong-motion earthquake
      records during the previous year. The
      catalog contains maximum component accelerations
      and wave forms of major records. If there is
      such a catalog compiled by any organization,
      the catalog mentioned above may be replaced
      by it.

3.   The Task Committee makes appropriate arrangements
      to provide digitizable copies of records when
      they are requested. In addition, arrangements
      will be made to provide information on the
      characteristics of the site and structures at
      the locations where such records are obtained.

4.   When the organizations taking part in the
      Panel publish reports on strong-motion
      earthquake records, these organizations will

distribute copies of the reports to the other organizations of the Panel interested in them. The Task Committee exchanges lists of the organizations and their Panel representatives who wish to receive the reports.

5. The Task Committee will continue to exchange digitized data on all the major strong-motion earthquake records recovered in both countries, under the conditions mutually acceptable to the agencies involved in acquisition of the data.

6. The Task Committee will exchange technical information concerning seismometers and accelerometers to be developed, and the deployment and installation of instruments with emphasis on bore-hole instruments, and the design of seismic arrays.

7. The Task Committee plans to assist and cooperate, where possible, in the following areas:

    a. Assistance and cooperation with governmental organizations in other seismic areas, in order to promote high quality strong earthquake motion observations in all seismically active areas of the world.

    b. Assistance and cooperation with any international effort to record strong ground motion close to the source of a large magnitude shock.

8. The Task Committee feels the UJNR Panel on Wind and Seismic Effects should play a major cooperative role in the implementation of relevant parts of the Resolution of the International Workshop on Strong-Motion Earthquake Instrument Arrays held May 1978, in Honolulu, Hawaii. The exchange of complete information on all aspects of the program, as it develops particularly in Japan and the United States, will be carried out in the manner of our standard exchange when appropriate. Particularly with unique data from arrays, or deep bore-hole instruments in the U.S. and Japan, Task Committee Chairmen will retain the responsibility of relaying information on their existence and subsequently of transferring the digital data from such institutions as, in the U.S., the USGS, CDMG, USC, and UCSD; and, in Japan, PWRI, BRI, PHRI, MRI, and NRCDP.

9. The Task Committee recommends collaborative studies involving strong-motion instrumentation and interpretation of resulting strong-motion data sets for purposes of earthquake hazard reduction.

10. The Task Committee will study the possibility of exchange of scientists, engineers, and appropriate equipment in a timely fashion for the observations following large earthquakes in either country. As the largest and most interesting aftershocks occur immediately

following the main earthquake, recovery of
the most useful aftershock data requires that
the response to major earthquakes be initiated
as rapidly as logistics permit.

11.   The task committee will hold a workshop on
Strong-Motion Earthquake Observation in the
San Francisco area in August 1987. The
details of the workshop program will be dis-
cussed between both Task-Committee chairmen
and include array and network planning,
recording instrumentation, digitizing hardware,
and the digitization of representative records.

12.   The Task Committee recognizes that another
workshop on Processing of Seismic Strong
Motion Records to be held in Vancouver in
August 1987 is significantly relevant and
would complement the Panel's Workshop. The
Task Committee urges that the Panel members
contribute to this workshop.

13.   The Panel discussed the occasional, but extended,
unavailability of existing strong-motion data of engineering
significance from very large earthquakes outside the US and
Japan.   The Task Committee considered dealing appropriately
with US and Japanese data.   The Task Committee chairmen will
extend their committee's study to encourage the appropriate
dissemination of world-wide data having engineering significance
and prepare a report for the next Panel meeting.

Report of Task Committee on

(B) LARGE-SCALE TESTING PROGRAM

Date: May 13, 1986

Place: National Bureau of Standards,
          Gaithersburg, MD, U.S.A.

Attendees: Japan Side - K. Ohtani, Chairman (NRCDP)

              U. S. Side - E.V. Leyendecker, Chairman (NBS)
                           J. J. Burns (NRC)
                           J.B. Scalzi (NSF)

I.   Activities and Principal Accomplishments to Date

The main activities related to this task committee during the
past year are as follows:

1.   The UJNR Panel on Wind and Seismic Effects
     endorsed the Implementing Arrangement for
     Cooperation in the U.S.-Japan Earthquake
     Research Program Involving Large-Scale
     Experiments of Masonry Structures during the
     17th meeting in Tsukuba.

2.   The Joint Technical Coordinating Committee on
     the Masonry Research (JTCCMAR) was held in Tokyo
     in August 1985. Coordinated research on
     masonry structures were discussed.

3.   Support tests on masonry research continued
     on the Japanese side and were initiated on
     the U.S. side.

4.   Active exchanges of U.S. and Japanese
     researchers have occurred under the program
     and have been very useful.

5.   Testing of the full-scale steel structure and
     support tests have been completed in both
     countries. Analytical studies are currently
     in progress.

II. Future Programs

The status of the U.S.-Japan Joint Program of reinforced concrete,
steel and masonry structures were reviewed. The Task Committee
adopted the following resolutions as a result of discussion.

1.   The Panel of each country should collect
     copies of reports for all coordinated
     research conducted in that country in a
     single set. Each country should exchange a
     set of these reports.

2.   The major aspects and conclusions of the
     steel test programs in each country should be
     synthesized into a single report. The
     dissemination activities for accomplishments
     of the U.S.-Japan cooperative research
     program on steel and reinforced concrete
     structures should be encouraged and supported
     by each side.

3.   To assure effective exchange of information
     on masonry structures, continuing and

expanded personnel exchange is encouraged
under the coordinated research program.

4. The Task Committee will review progress of
    the Joint Research Program and continue to
    reassess the need for testing of other types
    of structures and report its findings and
    recommendations to the Panel.

5. The Task Committee recommends that the Panel
    endorse the Coordinated Research Program on
    Large-Scale Testing of Masonry Structures.

6. The 2nd meeting of the Joint Technical
    Coordinating Committee on Masonry Research is
    scheduled for the fall of 1986 in Denver,
    Colorado.

7. Construction of a full-scale five-story masonry
    building will begin in the BRI laboratory in
    Tsukuba in Japanese fiscal year 1986.

8. Task Committees (B), Large-Scale Testing
    Program and Task Committee (D), Evaluation of
    Performance of Structures should maintain
    closer liaison to facilitate the planning of
    instrumentation and analysis for full-scale
    test structures.

9. Technical exchange of information on masonry
    structures should continue to be exchanged
    through this Task Committee.

10. Exchange of information on large-scale testing
    facilities and large-scale testing programs should
    be encouraged.

Report of Task Committee

(C) TASK COMMITTEE ON REPAIR AND RETROFIT OF EXISTING STRUCTURES

Date: May 14, 1986

Place: National Bureau of Standards
           Gaithersburg, MD, U.S.A.

Attendees: Japan Side - H. Yamanouchi (BRI)

                  U.S. Side - J. B. Scalzi, Chairman (NSF)
                              A. G. Franklin (WES)
                              R. D.Hanson (MICH)
                              R. McConnell (VA)
                              A. J. Eggenberger (NSF)

I.   Activities and Accomplishments to Date

In Japan the following activities have been carried out:

1.   The Japan National Project - Post - Earthquake
     Measures of Buildings and Structures Damaged
     by Earthquake has been completed as a
     five-year plan from 1981 to 1985.

     Research products are summarized as "Manuals
     for Repair Methods for Damaged Structures and
     Buildings".

2.   "Total System for Aseismic Design, Inspection
     and Repair and Retrofit of New or Existing
     Building. Equipment and Non-Structural
     Element for Official Use" was compiled by
     Government Buildings Department, Ministry of
     Construction in March, 1985 and is still
     under trial use.

In the U.S. the following activities have been carried out:

1.   Studies on base isolation and supplemental
     damping devices have been in progress which
     may be of benefit in repair and retrofit of
     existing structures.

2.   Research has been initiated on techniques to
     assess current material and mechanical
     properties in structures which are aging or
     showing the effects of weathering or excessive
     use. Such information is essential in
     developing retrofit measures.

3.   Research on methods to assess the performance
     of existing and damaged structures is
     continuing along with research on methods to
     repair and retrofit such structures.

II. Future Programs

1.   Continue and expand the exchange of reports,
     books and special publications related to
     repair and retrofit of existing structures.

2.   A cooperative workshop on repair and retrofit
     should be held in the near future. Possible
     date might be in conjunction with the May
     1987 UJNR meeting to be held in Japan.

3. Exchange information and give consideration to possible cooperative efforts to study methods to quickly and economically assess the characteristics and residual structural capabilities of material which may have suffered degradation due to weathering, aging, misuse or change of use and on methods to upgrade the capabilities of such materials where required. Develop methods of analysis for predicting the structural capacities of structures containing such materials.

4. Share information such as handbooks and on specific completed projects such as evaluations of particular designs for which retrofit studies have been carried out and which may provide specific validation of retrofit design methods.

5. Arrange for the evaluation of the reports and manuals on seismic retrofit of concrete structures of building and contents and of historical structures which were prepared under the UNIDO Balkans Project.

6. Carry out research to evaluate the potential structural benefits and relative economics of using base isolation and supplemental damping devices for retrofitting existing structures. Such devices may be of particular interest for historical or monumental structures.

7. Devote increased attention to developing methods to assess nonstructural items in existing structures which could pose severe hazards and/or cause loss of service. Develop methods for retrofit or repair of important non-structural elements.

8. Cooperate with Committee D "Evaluation of Performance of Structures" to identify and encourage coordinated U.S.-Japan papers on computer programs which are useful for the evaluation of existing structures and which could be used to guide repair and retrofit decisions.

9. Join with Committee H to recommend that the Panel endorse the initiation of a coordinated research program on remedial measures to mitigate or prevent damage due to liquefaction failures.

Report of Task Committee on

(D) Evaluation of Structural Performance

Date: May 13, 1986

Place: National Bureau of Standards
           Gaithersburg, MD, USA

Attendees: U. S. Side: G. R. Fuller, Chairman (HUD)
                        P. E. Gurvin (STATE)
                        J. Z. Mirski (VA)
                        J. B. Scalzi (NSF)
                        R. J. Smith (ARMY)

           Japan Side: H. Yamanouchi, Chairman (BRI)
                        H. Okada (BRI)

I.   Activities and Principal Accomplishments to Date

In responses to the need for better understanding of current
safety evaluation methodologies, Task Committee D organized three
U.S. -Japan workshops on the evaluation of the performance of
existing buildings for resistance to earthquakes.

The First Workshop, held in Japan in 1983, treated five theme
areas: (1) Overview of evaluation of buildings for seismic
resistance, (2) Practical methodology, (3) Computer programming,
(4) Evaluation of structural performance through full scale
tests, and (5) Post-earthquake evaluations. The Second Workshop
was held in the U.S. in 1984 on (1) Safety evaluation methods,
(2) Evaluation methods applied to benchmark structures, and (3)
Damage and analysis of other structures. The Third Workshop was
held in Japan in 1985 and concentrated on additional comparisons
of evaluations of benchmark structures and on updating information
on methodologies.

Those three workshops, participated in by over 30 from the
U.S. side and over 30 from the Japanese side, were very successful.
The detailed methods reported on ranged from rapid classifications
of groups of buildings to detailed dynamic analysis of individual
structures.

Methods developed in Japan and in the U.S. were "tuned" to the
characteristics of typical buildings in each country. Comparative
analyses of benchmark structures reflected that Japanese seismic
design approaches are relatively more conservative.

The comparisons also reveal that the various methods are suitably
accurate for the expected level of evaluation for buildings with
good arrangement of lateral strength elements, and that a general
idea of expected damage level can be estimated. However,
additional developments are required to validate and improve the
methods to make them more useful, especially for buildings of
unusual geometry or with special secondary elements, and to
include effects of soil-structure interaction.

Three volumes of proceedings of the First to Third workshop are
scheduled to be published in 1986 by Cornell University, under a
grant from the U.S. National Science Foundation.

The U.S.Chairman distributed copies of a paper by Gergely, White,
and Fuller on "Seismic Performance of Existing Buildings" to be
presented at the U.S. Earthquake Engineering Conference in
Charleston, S.C. in August 1986. This paper summarizes the
results of the three U.S. Japan Workshops, and discusses the
methodologies used to evaluate six benchmark structures.

The Task Committee then discussed the status of various related projects, and objectives and possible future activities to be pursued. It was recommended that each side investigate the possibility of obtaining useful information on evaluating performance of buildings after the 1985 Mexican Earthquake.

II.   Future Programs

The Task Committee reconfirmed the objectives and recommendations of the May 17, 1984 meeting concerning analysis, instrumentation, and post-
earthquake evaluation of benchmark structures; and agreed to continue activities of the Task Committee on the following tasks:

1.   Encourage the continued exchange of literature, analyses, and research reports relative to assessment of seismic resistance of buildings.

2.   Expand the inventory of existing buildings in each country that have been evaluated and instrumented, and then observed after any future seismic activity. Continue to evaluate other buildings in each country using Japanese and American methods of analysis.

3.   Develop recommended evaluation and screening methods for determination of seismic resistance of existing buildings and identify research needs to improve evaluation technology.

4.   Concentrate on the evaluation of several structural steel buildings in each country using Japanese and U.S. methodologies. These buildings will be from six to ten stories in height.

5   Propose conducting a Fourth Workshop on "Evaluation of Seismic Resistance of Existing Buildings" to be held in Japan prior to the 19th UJNR Meeting. The main objective of this workshop will be to present conclusions and recommendations for methodologies to analyze seismic strength of buildings.

Report of Task Committee on

(E) NATURAL HAZARD ASSESSMENT AND MITIGATION THROUGH LAND USE
PROGRAMS

Date: May 14, 1986

Place: National Bureau of Standards,
           Gaithersburg, MD, U.S.A.

Attendees: Japan Side - M. Nagaoka, Temporary Chairman (GSI)

               U. S. Side - S. T. Algermissen, Chairman (USGS)
                            A.G. Brady (USGS)

I.   Activities and Principal Accomplishments to Date

      1.   The US-Japan Workshop on "Urban Earthquake
            Hazards Reduction," sponsored by the U.S. Earth-
            quake Engineering Research Institute (EERI)
            was held at Stanford University in July
            1984. Attendees included UJNR members
            Dr.Kazuhiko Kawashima and Dr. John B. Scalzi,
            and representatives of the Government of
            Shizuoka Prefecture: Messrs. Toshiroh
            Sugiyama and Katsunori Imado. The final
            report from EERI was published in July 1985
            and was distributed to Task Committee (E)
            members.

      2.   The Geographical Survey Institute (GSI) of Japan
            has conducted thorough reviews of research
            and work on the effects of topographical and
            geological conditions on seismic damage.

            The Public Works Research Institute (PWRI) of
            Japan has proposed a procedure for assessing
            direct and indirect losses from earthquake
            disasters, and the direct and indirect losses
            were evaluated for the Miyagi-ken-oki earthquake
            of 1978 and the Nihon-kai chubu earthquake of
            1983.

            The Building Research Institute (BRI) of Japan
            has conducted the development of automatic
            computer programs for analyzing the expected
            ground intensity at an arbitrary site, and has
            made analyses of the response characteristics
            of ground having an irregular surface and
            heterogeneity.

      3.   The U.S.Geological Survey conducts a broad based
            program in natural hazards reduction. This
            program includes assessment of: (1) earthquake
            ground motion; (2) soil liquefaction potential,

            (3) landslide potential; and (4) earthquake
            economic losses.

      4.   Several papers pertaining to Task Committee (E)
      were presented at the 18th Joint Panel Meeting:

                  a.   Sessions 2 and 4 "Earthquake
                        Engineering"
                  b.   Session 5 "Storm Surge and Tsunami"
                  c.   Session 7 "Technical Cooperation
                        related to the Mexican Earthquake
                        and Chilean Earthquakes"

5. A discussion was held concerning the possibility of revising the name of the Task Committee. It was pointed out that the term "Land Use Programs" has a rather narrow meaning in English. The Task Committee recommends that the Panel endorse the change of name of the Task Committee to "Natural Hazard Assessment and Mitigation through Land Use Programs".

II. Future Programs

1. Both sides will continue to exchange technical information on the following subjects:

   a. Evaluation of, and mapping procedures for seismic risk.
   b. Maps of geological conditions, soil liquefaction potential, seismic risk, and tsunami risk.
   c. Seismic response characteristics of ground having an irregular surface, and heterogeneity.
   d. Planning methodologies for earthquake disaster mitigation in large populated cities.
   e. Socio-economic aspects of earthquake disasters and evaluation procedures for them.
   f. Direct and indirect losses from earthquakes and evaluation procedures for them.

2. Both sides will continue to promote coordinated research and exchange of specialists in natural hazard assessment and mitigation through land use programs.

3. The U.S. Chairman will furnish to Task Committee members future reports on natural hazard assessment and mitigation through land use programs being coordinated or sponsored by the Federal Emergency Management Agency (FEMA), the Interagency Coordinating Committee of the National Earthquake Hazards Reduction Program (ICC/NEHRP), the U.S. Geological Survey (USGS), the National Science Foundation (NSF), and the National Academies of Science and Engineering.

4. The possibility of holding workshops on (1) techniques of earthquake loss estimation; and (2) evaluation of seismic risk and mapping procedures, was discussed. It was agreed that further consideration of these workshops would be undertaken during the coming year.

Report of Task Committee on

(F) DISASTER PREVENTION METHODS FOR LIFELINE SYSTEMS

Date: May 14, 1986

Place: National Bureau of Standards,
           Gaithersburg, MD, U.S.A

Attendees: U.S. Side - S. C. Liu, Chairman (NSF)
                           H.S. Lew (NBS)
                           C. Scheffey (DOT)

               Japan Side - Y. Sasaki, Temporary Chairman (PWRI)
                            H. Tada (PWRI)

I.   Activities and Principal Accomplishments to Date

A US-Japan Workshop on Seismic behavior of Buried Pipelines and
Telecommunication Systems was held in December at the Public
Works Research Institute, Japan. The proceedings of this workshop
were published by Columbia University and were distributed to the
Workshop participants, appropriate members of the UJNR Panel on
Wind and Seismic Effects, and other interested parties.   In
Japan, the Ministry of Construction has completed a 5-year
(1981-1985) research project on the development of repair
technology for seismically damaged structures. As a result of
this project, a Manual of Repair Methods for Civil Engineering
Structures Damaged by Earthquakes (Draft) was prepared by PWRI.
In the Manual procedures of damage surveys and repair work for
buried sewer pipelines are described. An outline of the results
of this research project was introduced at the 18th UJNR Joint
Meeting of the Panel on Wind and Seismic Effects. PWRI is also
conducting a dense instrument array measurement program at PWRI
campus and in Shizuoka Prefecture to identify ground motions
applicable to seismic design of buried pipeline structures. An
outline of the dense instrument array program was presented at
the 18th UJNR Joint Meeting. The Ministry of Construction is
promoting the construction of cable box systems (CAB systems)
under urban highways, in order to install aerial cables (for
electricity and telecommunication) into underground cable boxes,
and has prepared Technical Standards for CAB Systems (Draft). In
conjunction with these activities, PWRI has proposed a seismic
design procedure of CAB systems and conducted dynamic experiments
for examining the seismic safety of CAB systems. An outline of
the Technical Standards for CAB Systems (Draft) and the dynamic
experiments was reported during the 18th UJNR Joint Meeting.

In U.S., a study program to assess the design and operating
standards for lifeline systems has been initiated by the Building
Seismic Safety Council (BSSC) under the support of the Federal
Emergency Management Agency (FEMA).

The American Society of Civil Engineers (ASCE) through its
Technical Council on Lifeline Earthquake Engineering (TCLEE) and
the American Society of Mechanical Engineers (ASME) have developed
and published several design manuals and advisory notes dealing
with the seismic design of lifeline systems. These efforts are
made with contributions from investigators supported by the
National Science Foundation (NSF).

NSF has continued the support of a number of research projects
dealing with lifeline earthquake engineering. For example, there
is an International Symposium/Workshop between U.S., Japan, and
Taiwan on lifeline system in 1985, and a research project on
telecommunication systems and another project on field experiments
of buried pipelines. The workshop proceedings and the project
reports have been exchanged through the UJNR channels.

The strong motion array project in Taiwan (SMART) has been
continuously operated and new data has been recorded. In 1985
NSF supported a new project in conjunction with the SMART array in
deploying a instrumentation system to measure the soil responses
during the earthquakes. The data recorded from these projects
will be continuously exchanged between the two countries.

II. Future Programs

1. The members of the Task Committee will
   facilitate the continued exchange for
   technical information and cooperation in
   research on specialized problems listed as
   follows:

   a. Seismic damages to lifeline systems
   b. Seismic design procedures for
      lifeline systems
   c. Procedures and instrumentation to
      detect and inspect damage and the
      behavior of lifeline structures
      including buried pipelines.
   d. Repair and retrofit methodology for
      lifeline systems
   e. Estimation of reliability of lifelines
   f. Management and public education on
      importance of lifeline systems
   g. Investigation of needs for large-scale
      testing of lifeline systems.

2. It is recommended to initiate a US-Japan
   coordinated research project on seismic
   behavior, seismic design method, and seismic
   reliability of buried pipelines and similar
   lifeline systems. In order to make up a
   specific program of the future US-Japan
   coordinated research project including a
   possible workshop on Lifeline Earthquake
   Engineering, it is also recommended to hold a
   planning meeting of the Task Committee during
   the Charleston conference in August 1986.

3. The Third U.S. National Conference on
   Earthquake Engineering will be held in
   Charleston, South Carolina in August, 1986.
   Since a special session on lifeline earthquake
   engineering is being scheduled, it is
   proposed that Task Committee (F) members
   participate in the special session.

4. The Task Committee recognizes the importance
   and potential impact to the engineering
   practice of the Manual of Repair Methods for
   Civil Engineering Structures Damaged by
   Earthquakes (Draft and in Japanese) prepared
   by PWRI, and recommends that consideration be
   given to translate this document into English
   for wide distribution to the U.S. earthquake
   community.

Report of Task Committee on

(G) WIND CHARACTERISTICS AND STRUCTURAL RESPONSE

Date: May 14, 1986

Place: National Bureau of Standards,
             Gaithersburg, MD, U.S.A.

Attendees: Japan Side - H. Okada, Chairman (BRI)

             U.S. Side - R. D. Marshall, Chairman (NBS)

I.   Activities and Principal Accomplishments to Date

     Noting that:

             a.   High winds frequently cause loss of
                  life and extensive property damage.
             b.   The knowledge derived from the
                  exchange of high wind data and
                  information on wind effects can be
                  useful in reducing loss of life and
                  property damage,
             c.   Insufficient knowledge exists on
                  the effects of high winds on
                  structures and methods for modeling
                  these effects, and
             d.   The needs for wind data for various
                  applications and new projects are
                  increasing.

The Task Committee carried out the following activities;

        1.   The following documents were exchanged:

             a.   Report entitled "Hurricane Alicia -
                  Glaveston and Houston, Texas,
                  August 17-18, 1983," published by
                  Committee on Natural Disasters,
                  Commission on Engineering and
                  Technical Systems, National
                  Research Council, USA.

             b.   Report entitled "Performance
                  Requirements and Preliminary Design
                  of a Boundary Layer Wind Tunnel
                  Facility," NBS Report No. NBSIR85-3168,
                  May 1985.

             c.   Design and construction details of
                  Japanese boundary layer wind
                  tunnels were provided during the
                  past year. This information is in
                  addition to data on Japanese wind
                  tunnels published in 1984.

        2.   Some instruments capable of measuring high
             winds at coastal or sea regions were installed
             or prepared in Japan: Kashima coast observation
             with several masts 20 to 30 m high, an
             off-shore tower 20 m high at Hiratsuka, wind
             measurements at long span bridges in the
             Setonaikai Sea, et al.

        3.   Comprehensive measurements of surface
             pressures and internal pressures acting on a
             full-scale low-rise building situated in open

terrain. This proposed three-year study is
under consideration by the National Science
Foundation, USA.

4.   Development work was initiated by BRI for a
       research effort involving wind pressures
       acting on high-rise and on low-rise buildings.
       A priority area for high-rise buildings is
       the reliable measurement of internal pressures
       in buildings with large open interiors. The
       motivation for additional studies of low-rise
       buildings is to improve on the quality of
       measured surface pressures such as those
       reported in the Aylesbury study in England.

5.   Concerning high wind effects, particular
       investigations continued in the U.S.A. on
       various projects, such as wind loading and
       strength prediction of glass cladding and
       wind loading and response of transmission towers.

II.   Future Programs

1.   Exchange observation reports of high winds.

2.   Encourage interaction between meteorologists
       and engineers to identify the types of wind
       data required for future use in establishing
       extreme wind distributions; in determining
       wind loading on buildings and structures; in
       understanding the urban wind climate;and in
       considering design issues involved with the
       wind generation of energy.

3.   Encourage the establishment of minimum
       requirements for the simulation of atmospheric
       boundary layers in wind tunnels and the
       exchange of boundary layer wind tunnel test
       results, including comparisons with corresponding
       full-scale situations.

4.   Exchange information on criteria, techniques
       and instrumentation for structural modeling
       in boundary layer wind tunnels. Also
       encourage the exchange of information of
       measurements made on actual structures and on
       comparisons with predictions from wind tunnel
       studies of these structures.

5.   Expand the exchange of engineers and meteoro-
       logists, and encourage the mutual use of
       available research facilities in the two
       countries.

Report of Task Committee on

(H) Soil Behavior and Stability During Earthquakes

Date: May 13, 1986

Place: National Bureau of Standards
Gaithersburg, MD, USA

Attendees: U.S. Side - A. G. Franklin, Chairman (WES)
F. G. McLean (USBR)
R. L. Dewey (USBR)

Japan Side - Y. Sasaki, Chairman (PWRI)
M.Nagaoka (GSI)

I. Activities and Accomplishments to Date

1. Exchange of relevant documents on soil
    behavior during earthquakes was made. From
    the Japanese side, eight papers were submitted
    and from the U.S. side, three papers were
    submitted to the Eighteenth Joint Meeting of
    the Panel.

2. Following the resolution of the Seventeenth
    Joint Meeting, a workshop on In-Situ Testing
    for Evaluation of Soil Liquefaction Susceptibility
    was held in San Francisco, California, in August,
    1985. There were 10 representatives from the
    Japanese side and 14 from the U.S. side.

3. Under the auspices of the UJNR, Mr. Takashi
    Tsuchida of the PHRI is being hosted by WES
    as a visiting engineer, working on liquefaction
    of fine-grained soils and dynamic behavior of
    embankment dams. The term of this visit is
    for one year beginning in November 1985.

4. Under the auspices of the UJNR, Dr. Nobuyuki
    Narita of the PWRI visited the geotechnical
    centrifuge at the University of Colorado and the
    Engineering and Research Center of the USBR. He
    discussed with the USBR the visit to the PWRI of
    Mr. Jeffrey Farrar of the USBR as an exchange
    researcher hosted by the Japanese government.

II. Future Programs

1. Proceedings of the 1985 workshop on In-Situ
    Testing for Evaluation of Soil Liquefaction
    Susceptibility will be published.

2. Mr. Jeffrey A. Farrar will visit the PWRI in
    October and November 1986.

3. The committee recommends that the panel
    endorse the initiation of a cooperative
    research program on remedial measures to
    mitigate or prevent damage due to liquefaction
    failures.

4. When requested, the Task Committee will
    assist in arrangements for visits to earth
    embankments including fill dams and foundations

which have been subjected to significant
ground motions.

5.   The Task Committee encourages the maximum
     exchange of information on the following
     areas of earthquake engineering which are
     currently of intense interest to both
     U.S. and Japanese engineers.

     a.   Liquefaction potential of soils
     b.   In-situ testing methods for
          evaluation of soil liquefaction
          potential
     c.   Seismic stability of embankment
          structures and natural slopes
     d.   Remedial treatment of embankments
          and foundations to improve seismic
          stability
     e.   Seismically induced permanent
          displacements in earth structures
     f.   Seismically induced settlements of
          soils and foundations
     g.   Earthquake effects on semi-buried
          concrete structures
     h.   Earthquake effects on retaining walls
     i.   Centrifuge testing facilities and
          methods
     j.   Laboratory testing of models of
          geotechnical structures
     k.   Field performance data showing
          full-scale seismic response of
          earth dams

6.   The Task Committee requests that the Panel encourage
     visits and exchanges of engineers and scientists
     between U.S. and Japanese government research organizations,
     and that the Panel assist such exchanges by providing
     the channels of communication for making the arrangements,
     and endorsing such visits and exchanges as UJNR
     activities, when appropriate.

Report of Task Committee on

(I) STORM SURGE AND TSUNAMI

Date: May 14, 1986

Place: National Bureau of Standards,
          Gaithersburg, MD, U.S.A.

Attendees: U.S. Side - C. S. Barrientos, Chairman (NOAA)
                         H. Meyers (NOAA)
                         C. Astill (NSF)
                         R. L. Dewey (USBR)

             Japan Side - K. Ohtani, Temporary Chairman, (NRCDP)
                          H. Tsuchida (PHRI)

I.   Activities and Principal Accomplishments to Date

     1.   The U.S.side (NOAA) supplied the Japan side
          (MRI) with digital records of tsunamis affecting
          Japan. MRI has examined the records and identify
          the differences with their data. The U.S. side
          (NOAA) will make the necessary adjustments to
          conform with the Japanese information.

     2.   The Japan side (PWRI) has sent copies of
          photographs taken right after the Mihonkai-
          Chubu Earthquake tsunami to the U.S. (NOAA).
          These photographs are important information in
          understanding tsunami effects.

     3.   The U.S. side (NOAA) has provided the Japan
          side (MRI) with the Pacific Ocean Bathymetry
          Data Base. The data base is used in modeling
          tsunamis and in producing tsunami propagation
          charts. Based on the bathymetry data, three
          charts were produced by NOAA and the charts
          were given to the Japanese members during the
          18th Panel meeting.

     4.   A report by NOAA (SE-39) on tsunamis in Peru-Chile
          was given to the Japan side during the 18th
          meeting.

II. Future Programs

     1.   The Task Committee supports the continuation
          of exchange of data and information on
          tsunami and storm surge. The Committee also
          supports exchange of researchers whenever
          possible.

     2.   The Task Committee proposes to hold a Second
          Tsunami and Storm Surge Workshop in connection
          with the 19th Panel Meeting in Japan. Details
          of the workshop will be arranged by the Task
          Committee Chairmen with the approval of the
          Panel Chairmen. Specifically the workshop
          will address computational and experimental
          methods in tsunami and storm surge. The
          U.S. National Science Foundation will
          consider providing partial support for the
          U.S. side to attend the Workshop.

This proposed workshop is subject to the final approval of the Japan Task Committee members.

3. The U.S.side (NOAA) and the Japan side (MRI) will work together on tsunami propagation studies which will include producing tsunami propagation charts.

4. The U.S. side (NOAA) will give to the Japan side the report and documentation of the Storm Surge Model, SLOSH (Sea, Land and Overland Surges from Hurricanes).

Report of Task Committee on

(J) WIND AND EARTHQUAKE ENGINEERING FOR TRANSPORTATION SYSTEMS

Date: May 13, 1986

Place: National Bureau of Standards,
          Gaithersburg, Maryland, U.S.A.

Attendees: Japan Side - H. Tada, Chairman (PWRI)

            U.S. Side - C. F. Scheffey, Chairman (FHWA)
                         H. S. Lew   (NBS)
                         J. B. Scalzi (NSF)

I.   Activities and Principal Accomplishments to Date

The major accomplishments of Task Committee (J) during the past
year were as follows:

   1. Summaries of wind and earthquake research on
       bridges conducted by both countries were
       presented to the 18th Joint Meeting, and
       exchange of information was made.

   2. The coordinated research study on the seismic
       performance of bridge piers and columns was
       begun in 1983, and the following experiments
       were conducted.

       a. performance of reinforced concrete
           piers and columns subjected to
           dynamic cyclic loading
       b. model tests on the failure of
           reinforced concrete piers
       c. testing full-scale concrete columns
           and associated small-scale model
           tests
       d. behavior of concrete filled steel
           tubes

   3. The report which consists of a compilation of
       bridge research papers from recent UJNR
       Meeting was published and sent to the
       Japanese Task Committee in June, 1985.

   4. The Second U.S.-Japan Bridge Workshop was
       held in San Francisco, California, in August
       19-22, 1985 with cooperation from organizations
       concerned in both countries.   Thirteen
       U.S. and twelve Japanese members participated
       in the workshop. Exchange of technical
       information was made and comprehensive
       discussion were held on future cooperative
       programs. The proceedings made by U.S. side
       were distributed to the participants of the
       both countries in December 1985. Some of the
       subjects are:

       a. Research on aerodynamic stability
           of suspension bridges and cable-stayed
           bridges
       b. Laboratory experiments on the
           seismic behavior of reinforced
           concrete piers and columns including
           concrete-filled steel tubes

494

    c. Repair procedure for seismically
       damaged bridge structures
    d. Experimental field testing of
       bridges including forced and
       ambient vibration measurements
    e. Experimental and analytical studies
       on the effects of soils on the
       behavior of bridge structures
    f. Strengthening procedures for
       existing bridges
    g. Strong motion instrumentation of
       bridges, corresponding data
       processing and parameter identification
    h. Seismic design and construction
       procedures of highway bridges

5. Dr. H. Tada, Chairman of Task Committee (J),
stayed in the U.S. for one month beginning in
August 9, 1985 and visited laboratories and
organizations related to the Panel on the
basis of personnel exchange program of the
UJNR Panel.

II. Future Programs

As a result of comprehensive discussions, the Task Committee (J)
hereby resolves to carry forth with the following programs:

1. Continue with the coordinated experimental
research study on the seismic performance of
bridge piers and columns, and review the
progress of the study at the intermediate
stage.

2. Develop a coordinated research study, both
theoretical and experimental, on the seismic,
aeroelastic, and aerodynamic response of
cable-supported bridges. A specific proposal
for reciprocal testing of models in turbulent
flow is to be developed by the co-chairman.

3. Encourage the continued exchange of information
and research personnel through the Panel on
Wind and Seismic Effects of UJNR.

4. Mr. Koichi Minosaku, researcher of Bridge
Division, PWRI, MOC, will be a guest researcher
at the Center for Building Technology, NBS,
U.S.A. for 10 months beginning in September,
1986, to perform cooperative experimental
research on the seismic performance of bridge
piers and columns. This assignment is part
of the personnel exchange program of the UJNR
Panel.

5. The Task Committee endorses the initiation of a
coordinated and expanded program of research on remedial
measures to mitigate or prevent damage to existing bridges
by the natural hazards of earthquakes and strong winds.

6. The Task Committee proposes the third Bridge Workshop
to promote cooperative research on wind and
seismic-resistant design of long span bridges and
strengthening of existing bridges. The Workshop will
be held in Japan in conjunction with the 19th
joint meeting of the Panel or in October, 1987, in
conjunction with the completion of Honshu Shikoku
Bridges, Kojima-sakaide Route. Details of the
Workshop should be determined based on discussion
between the Task Committee Chairmen.

4. TITLE AND SUBTITLE

Wind and Seismic Effects - Proceedings of the 18th Joint UJNR Panel Conference

5. AUTHOR(S)

Noel J. Raufaste, Editor

6. PERFORMING ORGANIZATION (If joint or other than NBS, see instructions)

NATIONAL BUREAU OF STANDARDS
DEPARTMENT OF COMMERCE
XMWASHNNGXONMMMCXMMMMX Gaithersburg, MD 20899

7. Contract/Grant No.

8. Type of Report & Period Covered

FINAL

9. SPONSORING ORGANIZATION NAME AND COMPLETE ADDRESS (Street, City, State, ZIP)

10. SUPPLEMENTARY NOTES

☐ Document describes a computer program; SF-185, FIPS Software Summary, is attached.

11. ABSTRACT (A 200-word or less factual summary of most significant information. If document includes a significant bibliography or literature survey, mention it here)

The 18th Joint Meeting of the U.S.-Japan Panel on Wind and Seismic Effects was held at the National Bureau of Standards, Gaithersburg, Maryland, from May 12 through May 15, 1986. This publication is the proceedings of the Joint Meeting, and includes the technical papers and the members of task committees and formal resolutions.

Subjects covered in the papers presented to the panel include: (1) wind engineering, (2) earthquake engineering, (3) storm surge and tsunamis, (4) U.S.-Japan cooperative research program, and (5) Mexico City and Chilian Earthquakes.

12. KEY WORDS (Six to twelve entries; alphabetical order; capitalize only proper names; and separate key words by semicolons)

accelerograph; codes; design criteria; disaster; earthquakes; earthquake hazards; geotechnical engineering; ground failure; liquefaction; pipeline; seismicity; solids; standards; structural engineering; structural response; tsunami; wind loads; winds

13. AVAILABILITY

☒☒ Unlimited

☐ For Official Distribution. Do Not Release to NTIS

☐ Order From Superintendent of Documents, U.S. Government Printing Office, Washington, D.C. 20402.

☒☒ Order From National Technical Information Service (NTIS), Springfield, VA. 22161

14. NO. OF PRINTED PAGES

488

15. Price

$36.95